Cosmic Shear and the Intrinsic Alignment of Galaxies

Dissertation

zur

Erlangung des Doktorgrades (Dr. rer. nat.)

der

Mathematisch-Naturwissenschaftlichen Fakultät

der

Rheinischen Friedrich-Wilhelms-Universität Bonn

vorgelegt von

Benjamin Joachimi

aus

Rheine

Bonn, 2010

Angefertigt mit Genehmigung der Mathematisch-Naturwissenschaftlichen Fakultät
der Rheinischen Friedrich-Wilhelms-Universität Bonn

1. Gutachter: Prof. Dr. Peter Schneider
2. Gutachter: Prof. Dr. Andreas Eckart

Tag der Promotion: 04. November 2010
Erscheinungsjahr: 2010

To strive,
To seek,
To find,
And not to yield.

Lord Alfred Tennyson, Ulysses

Abstract

Cosmology has recently entered an era of increasingly rich observational data sets, all being in agreement with a cosmological standard model that features only a small number of free parameters. One of the most powerful techniques to constrain these parameters and test the accuracy of the concordance model is the weak gravitational lensing of distant galaxies by the large-scale structure, or cosmic shear. This thesis investigates the optimisation of present and future cosmic shear surveys with respect to the extraction of cosmological information and deals with the characterisation and control of the intrinsic alignment of galaxies, a major systematic in cosmic shear data.

A detailed derivation of the covariance of the weak lensing convergence bispectrum is presented, clarifying the relation between existing formalisms, providing illustration, and simplifying the practical computation. The results are then applied to forecasts on cosmological constraints by cosmic shear two- and three-point statistics with the proposed Euclid satellite. Besides, a novel method to assess the impact of unknown systematics on cosmological parameter constraints is summarised, and several aspects concerning the weak lensing analysis of the Hubble Space Telescope COSMOS survey are highlighted.

A synopsis of the current state of knowledge about the intrinsic alignment of galaxies is given, including its physical origin, modelling attempts, simulation results, and existing observations. Possible corrections to the prevailing model of intrinsic alignments are suggested, before presenting new observational constraints on matter-intrinsic shear correlations using several galaxy samples from the Sloan Digital Sky Survey. For the first time a data set with only photometric redshift information is included, after developing the formalism for correlation function models that take photometric redshift scatter into account. The intrinsic alignment signal of early-type galaxies is found to increase with galaxy luminosity and to be inconsistent with the default redshift evolution of a widely used model, both with high confidence.

Moreover the nulling technique is developed, a method to remove gravitational shear-intrinsic ellipticity correlations from cosmic shear data by solely relying on the well-known redshift dependence of the signals, and its performance on realistically modelled cosmic shear two-point statistics is investigated. Subsequently, the principle of intrinsic alignment boosting, an inverse and likewise geometrical approach capable of extracting the intrinsic alignment signal from cosmic shear data, is derived. Both techniques are shown to robustly remove or isolate the intrinsic alignment signal, but are subject to a significant loss of statistical power caused by the similarity between the redshift dependence of the lensing signal and shear-intrinsic correlations in combination with strict model independence.

As an alternative ansatz, the joint analysis of various probes available from cosmic shear surveys is considered, including cosmic shear, galaxy clustering, lensing magnification effects, and cross-correlations between galaxy number densities and shapes. The self-calibration capabilities of intrinsic alignments and the galaxy bias in the combined data are found to be excellent for realistic survey parameters, recovering the constraints on cosmological parameters for a pure cosmic shear signal in presence of flexible parametrisations of intrinsic alignments and galaxy bias with about a hundred nuisance parameters in total.

Contents

Chapter 1

Introduction

Cosmology is targeted on a physical description of the Universe as a whole and takes a special place among the disciplines of physics, as there exists only a single 'object' of interest from which one can collect empirical data. Yet, the ensembles studied to infer properties of the large-scale structure of the cosmos are among the largest in physics and comprise billions of constituents. To arrive at a consistent picture of the Universe, physical laws have to be applied to the largest possible scales, and to unveil its origin, the physics on scales smaller than those reached hitherto by laboratory experiments have to be probed. Fundamental cosmological questions drive some of the most forefront research in modern physics but were also posed at the very beginnings of man's rational understanding of nature, playing a relevant part in the evolution of human society over the past centuries.

These dichotomies underline the comprehensiveness as well as the challenges inherent to the task of establishing a general model of the Universe. In addition, cosmologists face the problems of being restricted to essentially a single point in space and time, and of receiving cosmological information almost entirely in the form of electromagnetic radiation. As a consequence, only a very limited part of the Universe is in principle accessible through observations, which in turn are only available for cosmological objects that emit or absorb photons.

In spite of these intricacies, a concordance model of the cosmos has emerged in the past two decades whose success is comparable to the feats of the standard model of elementary particle physics. At the end of the twentieth century, after a long time of 'data starvation', cosmology entered a prosperous era of immense and rich data sets, provided by novel, both ground- and space-based observational facilities. To date, all major observations by various mutually independent cosmological probes are consistent with this standard model, featuring only six free parameters which could already be constrained with fair precision.

However, despite the success of the concordance model, it remains deeply unsatisfactory as regards the requirements of a comprehensive physical theory because – again not unlike the standard model of elementary particle physics – central elements remain unexplained. The most important issue is the fact that according to the concordance model only about 5 % of the total energy budget of the Universe today are composed of matter whose existence has been confirmed in laboratory experiments, including protons, neutrons, electrons, neutrinos, and photons. Astronomical observations agree that another 20 % of this budget are covered by dark matter, supposedly massive elementary particles that interact only gravitationally and via weak nuclear forces, and that in particular do not emit light. The remaining 75 % are made up of the even more exotic dark energy, a component which causes the late-time acceleration of the expansion of the Universe but which is otherwise obscure.

Not only are thus 95 % of the energy content of the cosmos of unknown nature, but in addition the concordance model rests on two fundamental constituent theories which have not

been verified by cosmological observations (yet), namely the validity of general relativity on cosmological scales and the inflationary paradigm, setting the initial conditions for structure formation.

One of the main challenges for cosmology in the near future is therefore to pin down the properties of dark matter and dark energy with high precision, test general relativity and modified theories of gravity on large scales, and possibly collect evidence for one of the various models of inflation by exploiting upcoming new data sets of unprecedented richness. Complementary to established methods probing anisotropies of the cosmic microwave background, the large-scale galaxy distribution, or indicators of the cosmological distance ladder, weak gravitational lensing on cosmological scales, or cosmic shear in short, has recently emerged as the potentially most powerful technique to shed light on the issues listed above.

Gravitational lensing refers to the general relativistic effect of the bending of light paths in gravitational potentials. Regarding cosmological scales, the light of distant galaxies is continously deflected by the large-scale matter distribution along the line of sight to an observer on Earth, causing very small distortions or shears on the shapes of the galaxy images. Correlating millions of these background galaxies, the shear signal can be extracted and used to infer statistical properties of the intervening matter distribution. This in turn allows one to constrain cosmological parameters by probing both the geometry of the Universe and the growth of the large-scale structure.

The smallness of the cosmic shear effect on the shape of a galaxy image is an observational challenge wherefore the first detections were reported only a decade ago. Since then the method has been rapidly maturing, with various ground- and space-based weak lensing surveys upcoming or in advanced planning stages. Among the central issues for cosmic shear research are therefore the optimisation of future surveys and moreover, with the increasing statistical accuracy of measurements, the control of systematic effects potentially jeopardising cosmological parameter estimates. Of particular importance in this respect is the intrinsic alignment of galaxies which can mimic a cosmic shear signal and which has been identified as the major astrophysical source of systematic errors.

It is the scope of this thesis to investigate both of these aspects, i.e. the optimisation of cosmic shear surveys and their analysis as well as the elimination of systematics due to intrinsic alignments, aiming at a contribution to prepare cosmic shear for the upcoming era of high-precision cosmology, which in turn is going to have a significant share in constraining and consolidating the standard model of cosmology. The thesis is organised as follows:

We begin with a brief overview on cosmology in Chap. 2, outlining the central ingredients of the concordance model such as the metric structure and the different matter components populating the cosmos. The important processes in the early phases of the Universe as well as the formation and evolution of structure are summarised. We also highlight the current knowledge about the free parameters in the concordance model and the main probes used to constrain them, before detailing potential shortcomings in the standard picture and the possible extensions or modifications that could eventually resolve them.

In Chap. 3 the basic theory of weak gravitational lensing is presented, focusing on its application to the large-scale structure of the Universe via the cosmic shear effect. We elucidate how the gravitational shear can be inferred from galaxy images and derive the statistics used to extract information from the shear field, as well as their dependence on cosmology. Finally, the status quo of cosmic shear measurements is discussed by reviewing the observations of the past ten years and providing an outlook on the surveys of the coming decade.

Chapter 4 is dedicated to various aspects concerning the optimisation of cosmic shear surveys, beginning with an in-depth study of the covariance of the weak lensing bispectrum. Subsequently, detailed forecasts of the performance of the cosmic shear survey by the planned

Euclid space mission are presented, followed by the synopsis of a novel technique to incorporate the effects of unknown systematics into the predictions on cosmological parameter constraints. Furthermore some key points in the optimisation of the analysis of the Hubble Space Telescope COSMOS weak lensing survey are discussed. The work presented in this chapter can also be found in Joachimi et al. (2009), Laureijs et al. (2009), Kitching et al. (2009), and Schrabback et al. (2010).

The remainder of this work focuses on the intrinsic alignment of galaxies and its control in cosmic shear analyses, beginning in Chap. 5 with an overview on the current knowledge about the origin and properties as well as models and observations of intrinsic alignments. We then present the first study of intrinsic alignments in a data set with photometric redshift information, the MegaZ LRG sample. After incorporating photometric redshift uncertainty into the modelling of the signal, we constrain an intrinsic alignment model using several galaxy samples from the Sloan Digital Sky Survey, measuring for the first time a clear redshift and luminosity dependence of intrinsic alignments among red galaxies. The implications for cosmological parameter estimation with cosmic shear data by the constraints on the intrinsic alignment model we obtain are also discussed.

Due to the currently still limited understanding of the intrinsic alignment of galaxies, models of this systematic signal have not evolved past a relatively simplistic stage, thereby hindering an efficient and reliable removal of the intrinsic alignment contamination from cosmic shear surveys. In Chap. 6 a model-independent method to remove gravitational shear-intrinsic ellipticity cross-correlations from cosmic shear data, the nulling technique, is developed. Using only the well-known characteristic redshift dependence of intrinsic alignments, linear combinations of cosmic shear statistics are constructed which are free of the systematic. We introduce the basic formalism and determine optimised weightings for these linear combinations. The capabilities of intrinsic alignment removal and the inherent loss of information on cosmology are assessed in detail for realistic cosmic shear survey properties. The content of this chapter is largely congruent with the work of Joachimi & Schneider (2008, 2009).

In Chap. 7 we use a methodology similar to the foregoing chapter to create an 'inverse' approach to the nulling of intrinsic alignments. By means of the resulting boosting technique, one is able to extract an intrinsic alignment signal directly from the galaxy sample used for the cosmic shear measurements. This is achieved by suppressing the lensing signal, again in a model-independent manner. We develop the formalism, demonstrate the constraining power of boosting, and establish a quantitative link to the nulling technique. The work presented in this chapter is based on Joachimi & Schneider (2010).

The considerable information loss inherent to nulling causes this technique not to be the method of choice for planned large cosmic shear measurement campaigns. Therefore we investigate another method to eliminate contaminations by intrinsic alignments in Chap. 8 which compensates the loss of statistical power due to a low level of assumptions on the form of the intrinsic alignment signal by adding correlations between galaxy number densities as well as between number density and galaxy shape to the analysis. The performance of this self-calibration ansatz is then examined in detail, with realistic assumptions about the cosmic shear survey properties and all contributing cosmological signals. This study closely follows Joachimi & Bridle (2009).

Finally, in Chap. 9 we provide an overall summary of and general conclusions on the research presented in this thesis. Moreover an outlook is given on future work that is immediately associated with the results found, listing also more general tasks required to render cosmic shear a vital constituent of precision cosmology.

Chapter 2

Principles of cosmology

Within the past two decades cosmology has taken a leap from a data-starved science to a thriving field with a multitude of large and rich data sets. The same time span saw the swift emergence of a standard picture of the Universe which is consistent with the whole variety of modern cosmological observations while featuring only of the order 10 free parameters, its success rivalling the standard model of elementary particle physics. In the following the principles of the concordance model of cosmology will be outlined, beginning with the description of the overall structure of spacetime in Sect. 2.1. In Sect. 2.2 the constituent components of the Universe are introduced. A brief account on the evolution of the Universe from its early phases to the present-day structure we observe is given in Sects. 2.3 and 2.4. The current estimates for the values of the free parameters of the concordance model and the observations that lead to them are summarised in Sect. 2.5, together with an outline of remaining challenges as well as potential extensions or alternatives to the theory.

2.1 Homogeneous world models

A model of the Universe as a whole must originate from a theory of gravity since it is the only fundamental interaction that acts on cosmological scales. Although the local Universe is largely ionised, electromagnetism does not play a role on large scales as any net charges are quickly evened out. Hence we will make use of General Relativity (Einstein 1916) to determine the overall spacetime structure of the cosmos.

The wealth of structure which we observe in the sky, and the corresponding complexity of spacetime, hinders straightforward progress. However, on scales larger than about 300 Mpc the distribution of galaxies appears rather uniform around us (see e.g. the Sloan Digital Sky Survey; Abazajian et al. 2009). As the visible Universe has a radius of several Gigaparsecs, the simplifying assumption of isotropy on large scales is therefore justified. Further support comes from the observed isotropy of the cosmic microwave background radiation (see Sect. 2.3), yielding an image of the structure of the Universe from a much earlier hot phase.

Moreover, avoiding the usage of anthropic arguments leads to the generalisation of the Copernican Principle to cosmological scales. Assuming that the position of Earth in the Universe is not special from others, much like it was found that Earth is located neither at the centre of the solar system nor of our Galaxy, large-scale isotropy should also be found by every other observer, resulting in a homogeneous universe. These well-reasoned postulates of isotropy and homogeneity on large scales are summarised under the term ‘cosmological principle’.

It is important to keep in mind that our view of the cosmos is very limited because most of the information arrives in the form of photons and thus originates from electromagnetic interactions. Since photons move with the speed of light, this information is in addition restricted

to the backward light cone of our present position in spacetime. Thus, we would hardly be able to detect a complicated spacetime structure. A further assumption implicitly contained in what follows is the validity of the fundamental laws of physics, not only in the local Universe but also at all other points in spacetime (although changes in the fundamental constants with cosmic time are currently under scrutiny).

Central to General Relativity are the Einstein field equations (see e.g. Dodelson 2004),

$$G_{\mu\nu} = -\frac{8\pi G}{c^4} T_{\mu\nu} \; ; \quad \mu, \nu = 0, \ldots, 3 \; , \tag{2.1}$$

relating the sources of gravity contained in the energy-momentum tensor $T_{\mu\nu}$ to the Einstein tensor $G_{\mu\nu}$. Here G denotes Newton's constant and c the speed of light. The Einstein tensor is a function of the four-dimensional spacetime metric $g_{\mu\nu}$ and its first and second derivatives. Any sources of energy, or equivalently matter, in $T_{\mu\nu}$ cause the spacetime around them to be curved, and the metric resulting from (2.1) deviates from the Minkowski case. Within this picture the gravitational force acting on a test particle can be regarded as the inertial force on this particle moving freely through non-Euclidean space. The path of light is not a 'straight' line (in the Euclidean sense) anymore, but follows a geodesic. Consequently light can be deflected in gravitational potentials, leading to the gravitational lensing effect which will be further dealt with in Chap. 3.

A solution of (2.1) that describes the overall metric of the Universe should respect the assumptions of the cosmological principle. In a series of publications between 1922 and 1936 Friedmann, Lemaître, Robertson and Walker (Friedmann 1922, 1924; Lemaître 1927; Robertson 1935, 1936; Walker 1936) investigated such world models and introduced a homogeneous and isotropic metric, which is one of the simplest non-trivial solutions of (2.1) and describes an expanding universe. This FLRW metric can be given in the following form:

$$c^2 \mathrm{d}\tau^2 = c^2 \mathrm{d}t^2 - a^2(t) \left\{ \mathrm{d}\chi^2 + f_\mathrm{k}^2(\chi) (\mathrm{d}\theta^2 + \sin^2\theta \, \mathrm{d}\phi^2) \right\} \; , \tag{2.2}$$

where τ is the eigentime, t is the cosmic time, $a(t)$ the cosmic scale factor and χ the comoving distance. Furthermore we have introduced the comoving angular diameter distance

$$f_\mathrm{k}(\chi) = \begin{cases} 1/\sqrt{K} \sin(\sqrt{K}\chi) & K > 0 \\ \chi & K = 0 \\ 1/\sqrt{-K} \sinh(\sqrt{-K}\chi) & K < 0 \; , \end{cases} \tag{2.3}$$

where $1/\sqrt{|K|}$ is interpreted as the curvature radius of the spatial part of spacetime. For $K > 0$ ($K < 0$) one speaks of a closed (open) universe; $K = 0$ corresponds to a flat universe. In the latter case, i.e. for an Euclidean spatial geometry, the term in curly brackets of (2.2) can be recognised as ordinary three-dimensional polar coordinates.

Observers whose motion is solely due to cosmic expansion are called comoving observers. For them $\mathrm{d}\chi = \mathrm{d}\theta = \mathrm{d}\phi = 0$, so that their eigentime is the cosmic time, see (2.2). Comoving observers rest in the comoving coordinate frame $\boldsymbol{x}$, which is related to physical coordinates $\boldsymbol{r}$ via $\boldsymbol{r} = a(t)\boldsymbol{x}$. The scale factor is chosen to be unity today, i.e. $a(t_0) \equiv 1$. Note that due to the assumption of homogeneity a is a function of time only.

The expansion of spacetime causes all comoving observers to see the recession of surrounding objects. The velocity due to expansion amounts to

$$\boldsymbol{v} = \dot{a} \, \boldsymbol{x} = \frac{\dot{a}}{a} \, \boldsymbol{r} = H(a) \boldsymbol{r} \; , \tag{2.4}$$

where $H(a) \equiv \dot{a}/a$ is the Hubble parameter, the normalised rate of cosmic expansion. Then the observed velocity difference between two objects at a distance $\Delta\boldsymbol{r}$ reads

$$\Delta\boldsymbol{v} = \boldsymbol{v}(\boldsymbol{r} + \Delta\boldsymbol{r}) - \boldsymbol{v}(\boldsymbol{r}) = H(a) \Delta\boldsymbol{r} \; . \tag{2.5}$$

This distance-velocity relation states that objects surrounding a comoving observer recede, the more distant, the faster. Equation (2.5), specialised to today and an observer on Earth, results in the local Hubble law $v_{\rm esc} = H_0\, D$, where $H_0 \equiv H|_{a=1}$ denotes the Hubble constant and D the distance from Earth. This relation was observationally confirmed by Hubble (1929), thereby proving the expansion of the Universe and dismissing stationary, more complex solutions of (2.1) devised by Einstein. The Hubble constant is a key parameter of cosmological models. It is often convenient to use a dimensionless variant, writing $H_0 = h100\,\mathrm{km\,s^{-1}\,Mpc^{-1}}$, where h is of order unity.

The FLRW metric can be obtained from (2.1) for a diagonal energy-momentum tensor of the form $T_{\mu\nu} = \mathrm{diag}\,[\rho(a)c^2, p(a), p(a), p(a)]$ if specified locally in Cartesian coordinates[1]. This expression for $T_{\mu\nu}$ corresponds to a perfect fluid which is at rest in comoving coordinates and can be fully described in terms of its density ρ and its pressure p. Inserting an energy-momentum tensor of this form into (2.1), one obtains two equations governing the evolution of the scale factor, the first being the Friedmann equation

$$H^2(a) = \left(\frac{\dot{a}}{a}\right)^2 = \frac{8\pi G}{3}\,\rho(a) - \frac{Kc^2}{a^2}\,, \tag{2.6}$$

and the second an equation of motion

$$\frac{\ddot{a}}{a} = -\frac{4\pi G}{3}\left(\rho(a) + \frac{3p(a)}{c^2}\right)\,. \tag{2.7}$$

To derive an explicit expansion history, both the density and the pressure of the matter components entering $T_{\mu\nu}$ have to be specified. Different types of matter are characterised by the way their pressure and density are interrelated via an equation of state. We will further discuss the relevant matter constituents of the Universe in Sect. 2.2.

In the foregoing equations we used the cosmic scale factor a to describe the evolution of spacetime. This choice is not unique as there is a range of quantities suitable to characterise cosmic epochs, and these will be used interchangeably henceforth. One option is to use the cosmic time t which is related to $a(t)$ via $\mathrm{d}t = \mathrm{d}a/\dot{a} = \mathrm{d}a/(aH)$, resulting in

$$t(a) = \int_0^a \frac{\mathrm{d}a'}{a'\,H(a')}\,. \tag{2.8}$$

To obatin this expression, it was assumed that the Universe started in a Big Bang (see the following section), the onset of time at $a = 0$. Note that setting $a = 1$ in the upper limit of integration then yields the cosmic time as of today, i.e. the age of the Universe. One can alternatively relate epochs to the temperature of the dominating matter component, which is particularly common to describe processes in the early Universe.

The redshift z is frequently used because it is most closely related to direct observables. It is defined as the relative shift of observed spectral features at wavelength λ with respect to the rest frame wavelength λ_0, $z \equiv \lambda/\lambda_0 - 1$. The shift of wavelength due to cosmic expansion can locally be interpreted as a Doppler shift caused by the recession of objects wherefore the relative change in wavelength is given by $\mathrm{d}\lambda/\lambda = \mathrm{d}v/c$. Using the Hubble law (2.5) in its infinitesimal form and the definition of the Hubble parameter, one can write $\mathrm{d}v = H\mathrm{d}r = c\,H\mathrm{d}t = c\,\mathrm{d}a/a$ and thus $\mathrm{d}\lambda/\mathrm{d}a = \lambda/a$, i.e. λ is proportional to the scale factor. Inserting $\lambda_0 = a\lambda$ into the defining equation for the redshift, the important relation

$$\frac{1}{a} = 1 + z \tag{2.9}$$

[1]To specify $T_{\mu\nu}$, a coordinate system has to be chosen. Consequently, $T_{\mu\nu}$ will in general depend on the metric $g_{\mu\nu}$, complicating the solution of (2.1).

follows.

Due to the finite velocity of light the observation of an object at a certain distance along the backward light cone necessarily implies that this object is seen as it was at some time in the past. Hence, time and distance measurements on cosmological scales are closely related, and one can equivalently use measures of distance to characterise epochs. Consider a radial light ray on our backward light cone for which (2.2) simplifies to $c\,\mathrm{d}t = -a\,\mathrm{d}\chi$ since for light rays $\mathrm{d}\tau = 0$ and for radial motion $\mathrm{d}\theta = \mathrm{d}\phi = 0$. Expressed in words, this relation means that the light of an object at comoving distance χ observed today was emitted at cosmic time t. Making use of $\mathrm{d}t = \mathrm{d}a/\dot{a} = \mathrm{d}a/(aH)$ again, one finds

$$\chi(z) = \int_0^\chi \mathrm{d}\chi' = \int_a^1 \frac{c\,\mathrm{d}a'}{a'^2 H(a')} = c\int_0^z \mathrm{d}z'\, H^{-1}\left(\frac{1}{1+z'}\right) , \tag{2.10}$$

where (2.9) was used to arrive at the second equality.

In contrast to a stationary Euclidean space the notion of physical distance is not uniquely defined in an expanding, potentially curved spacetime. As a consequence the basic methods of distance determination via relating a measured flux to a known luminosity, and relating a measured angular separation to a known physical one, do not yield identical results anymore (Etherington 1933). Since this work focuses on gravitational lensing where angular separations are measured, and hence it is natural to employ the distances defined via the latter method, all physical distances referred to in the following are by default angular diameter distances, given by $D_\mathrm{A} = a\, f_\mathrm{k}(\chi(a))$.

The principle of relativity sets c as the maximum velocity with which information can be transmitted. As will be detailed below, we have compelling evidence that a has always been monotonically increasing, so that the Universe must have had a beginning when at least formally $a = 0$. Consequently light has only had a limited amount of time to travel through the cosmos, and hence there is only a finite volume of space that can have been in causal contact since the Big Bang. The comoving horizon, i.e. the comoving distance light has travelled since $a = 0$ until today, is defined as

$$\chi_\mathrm{hor}(a) = \int_0^a \frac{c\,\mathrm{d}a'}{a'^2 H(a')} . \tag{2.11}$$

Regions with separation vectors outside a sphere of radius χ_hor have never had physical interactions. Subtly different, the comoving Hubble radius

$$\chi_\mathrm{H}(a) = \frac{c}{aH(a)} \tag{2.12}$$

defines the volume which is in causal contact at the epoch corresponding to a. As of today, $\chi_\mathrm{H}(a=1) = c/H_0$, where c is the speed at which signals travel, and $1/H_0$ approximately gives the time these signals have had to propagate since the Big Bang, see (2.8).

One would expect that, as the age of the Universe increases, more and more objects enter the sphere around an observer defined by the Hubble radius and come into causal contact. However, cosmic expansion counteracts this effect and can potentially move objects out of the Hubble sphere again. Hence, while χ_hor obviously always increases with time, the Hubble radius can become smaller at certain epochs. Demanding $\mathrm{d}\chi_\mathrm{H}/\mathrm{d}t < 0$, (2.12) yields the condition $\ddot{a} > 0$ for this to happen. Therefore striking differences between the evolution of χ_hor and χ_H can appear in periods of accelerated expansion like for instance during inflation, see Sect. 2.3.

2.2 Matter components

Within the perfect-fluid approximation discussed in the foregoing section the different ingredients of the Universe are characterised by their density and its evolution with scale factor, and an equation of state which relates pressure to density. One differentiates between ordinary matter or 'dust', radiation, and dark energy, depending on the form of the equation of state.

Cosmological dust is understood as matter at zero pressure which is thermally cold, i.e. whose constituents have velocities much smaller than c. In this category fall non-relativistic baryonic[2] as well as dark matter. The latter constitutes an essential part of the cosmological standard model although its nature is still unknown. However, various independent astronomical observations give strong evidence for its existence, for instance the flat rotation curves of spiral galaxies out to large radii, mass-to-light ratios of galaxies and galaxy clusters which are inexplicable by baryonic matter alone, and the level of structure formation in the present-day Universe.

The latter fact also speaks against hot dark matter which would still have been relativistic at the onset of galaxy formation and thus could have streamed freely out of the shallower gravitational potentials, thereby suppressing the formation of structure in particular on small scales. This disqualifies light neutrinos as candidates for dark matter although they fulfil the requirements on longevity and of either very weak or no electromagnetic interactions. They can merely add a small contribution to the dark matter density, but still future cosmological surveys of the large-scale structure will be able to provide competitive constraints on e.g. the neutrino masses (Massey et al. 2010). For current analyses of neutrino properties from cosmology see e.g. de Bernardis et al. (2009); Thomas et al. (2010); Debono et al. (2010).

To fit the picture of structure formation, cold dark matter (CDM) is required, so that candidate dark matter particles have to be massive in order to be non-relativistic already in the early Universe, or else have to be created non-thermally, e.g. by decay. Theories of particle physics suggest massive neutrinos, axions (hypothetical light particles solving the problem of strong CP violation in quantum chromodynamics), or weakly interacting massive particles (WIMPs) like the lightest stable supersymmetric particle as the major constituents of dark matter (Amsler et al. 2008; see also Feng 2010 for an extensive review), none showing any evidence as to their existence so far. Cosmological probes such as weak gravitational lensing will contribute decisively to narrowing down the properties of dark matter particles like for instance self-interaction cross sections (Heavens 2009; Massey et al. 2010), see Sandick (2010) for a current status.

Alternatively dark matter could consist of astrophysical objects such as primordial black holes or dark planetary or stellar bodies, summarised under the term of MACHOs (massive astrophysical compact halo objects). Indeed is has been found that MACHOs could contribute up to 20 % of the dark matter in the halo of the Milky Way, but they cannot make up the total amount (Alcock et al. 2000). It has also been suggested that the lack of baryonic mass is mimicked by a change in the law of gravity due to modified Newtonian dynamics (MOND, Milgrom 1983a,b,c). However, MOND is inconsistent with observations, most evidently proven by recent observations of a collision of two galaxy clusters, the so-called bullet cluster (Clowe et al. 2006; see also Bradač et al. 2008). The galaxies of these clusters are still located at the centres of the gravitational potential, as measured by gravitational lensing, although the intra-cluster medium, which contains the bulk of the baryonic matter, has been stripped off due to the collision. Hence, this observation gives support to the conviction that baryons are not the dominant matter component in galaxy clusters, and that this dominating component must

[2]In cosmology the term 'baryonic' is not used in its strict sense but usually comprises neutrons, protons, and electrons, i.e. those long-lived fermions which are the building blocks of all visible objects.

be nearly collisionless. Note that relativistic modifications of gravity like Tensor-Vector-Scalar (TeVeS) theories (Bekenstein 2010) can fit current observations (see Reyes et al. 2010, though), but they are not competitive due to the significantly larger number of free parameters in these models.

The evolution of the matter density ρ_m with a can best be studied by means of the expression

$$\mathrm{d}\{\rho(a)c^2a^3\} = -p(a)\,\mathrm{d}\{a^3\}\ , \tag{2.13}$$

which is derived from (2.6) and (2.7). For illustration, (2.13) can be identified with the first law of thermodynamics, $\mathrm{d}U = -p\,\mathrm{d}V$, where U is the internal energy of the component fluid under consideration, and where the volume V scales with a^3. Recalling that the pressure for ordinary matter vanishes, one arrives at $\mathrm{d}\{\rho_\mathrm{m}(a)a^3\} = 0$, from which one concludes $\rho_\mathrm{m}(a) \propto a^{-3}$. In other words, due to the conservation of mass $\rho_\mathrm{m}(a)$ is proportional to the inverse of the volume.

The second type of matter, radiation, comprises all constituents which are relativistic, i.e. have a velocity near or at the speed of light, e.g. photons or the almost massless neutrinos in the early phases of the Universe. Therefore they exert radiation pressure $p_\mathrm{r}(a) = (1/3)\,\rho_\mathrm{r}(a)\,c^2$, which, after inserting into (2.13), results in $\rho_\mathrm{r}(a) \propto a^{-4}$. Illustratively the additional factor of a^{-1} in the dependence of ρ_r on the scale factor, compared to the matter density, stems from the depletion of energy due to cosmological redshift. In cosmologically more recent times the radiation density has been dominated by the cosmic microwave background. Even though radiation governed the energy budget at early times, its contribution decreased rapidly due the strong dependence on a, so that for the bulk of cosmological time its influence on the expansion history can be neglected.

Finally, dark energy is by far the most obscure and yet the dominant contribution to the matter-energy budget of the Universe at the present epoch. That a third type of matter exists is strongly suggested by the recent accelerated expansion of the Universe (Freedman et al. 2001), as confirmed by a number of independent observations (see e.g. Schrabback et al. 2010), which cannot be explained in terms of a universe populated by dark matter, baryonic matter, and radiation alone. Moreover CMB observations demonstrate that the Universe is spatially flat to high accuracy while ordinary matter cannot provide more than about 30 % of the density needed to render the Universe flat.

The most obvious source of dark energy is vacuum energy whose existence is well established by measurements of the Lamb shift and the Casimir effect. To all fundamental interactions only differences in energy are relevant, except for gravity which couples to all sources of energy and momentum. Hence the energy level of the ground state of any field is important to gravitational interaction and should enter (2.1). Since the energy ground state should be Lorentz-invariant, the energy-momentum tensor has to be proportional to the Minkowski metric (Carroll et al. 1992), which in conjunction with the energy-momentum tensor of a perfect fluid leads to the equation of state

$$p_\Lambda = w\,\rho_\Lambda\,c^2\ , \tag{2.14}$$

with $w = -1$. The constant density ρ_Λ has then to be inferred from a particle physics model. However, current estimates differ by more than 100 orders of magnitude from the actually measured density (Carroll et al. 1992; Durrer & Maartens 2008). Apart from this severe fine-tuning problem the approach cannot explain either why the dark energy and matter densities are of about the same size or, in other words, why dark energy has started to dominate the matter-energy budget of the Universe only fairly recently. This coincidence problem needs to be explained by a theory of dark energy unless one is willing to accept anthropic arguments.

Originally, a term of the form (2.14) was not introduced as part of the energy-momentum tensor, but as an additional contribution to the left-hand side of (2.1), i.e. a modification of

gravity. Einstein proposed a new term $\Lambda g_{\mu\nu}$ in (2.1), with Λ the cosmological constant, in order to obtain solutions for a stationary universe. Dismissed after the discovery of the expansion of the Universe by Hubble, Λ is today re-considered as a possible explanation for the dark energy phenomenon. The additional term $\Lambda g_{\mu\nu}$ is allowed in the Einstein-Hilbert action, but the value of Λ is not constrained at all by General Relativity, so that the coincidence problem remains. Note however that any fundamental physical constant, for instance also Newton's constant, is a free parameter and requires a certain amount of fine tuning to permit the formation of the Universe as it is observed today.

Although there are currently no signs of a deviation from $w = -1$ (e.g. Serra et al. 2009), a plethora of theories proposing dynamical dark energy scenarios has emerged in recent years. They suggest a variable equation of state parameter $w(a)$ and/or a speed of sound of less than c, and hence the clustering, of dark energy. Since the accelerated expansion of spacetime is a recent phenomenon, it is widespread practice to do a first-order Taylor expansion of the equation of state parameter around $a = 1$ (Chevallier & Polarski 2001; Linder 2003),

$$w(a) = w_0 + (1 - a)\, w_a = w_0 + \frac{z(a)}{1 + z(a)}\, w_a \;, \tag{2.15}$$

and use the two parameters w_0 and w_a to constrain the dynamics of dark energy. In this work we will adopt this parametrisation, but will not consider any clustering of dark energy.

A popular model for dynamical dark energy is quintessence[3], postulating a scalar, dynamical field which only couples to gravity. There are extensions ('k-essence', Armendariz-Picon et al. 2000) which introduce a non-standard kinetic energy of the field and thus allow for a coupling of dark energy to the background evolution of ordinary matter. This modification can solve the coincidence problem, but contains several new fundamental issues like causality problems (Durrer & Maartens 2008). Furthermore, attempts are made to unify dark matter and dark energy into a single model (Basilakos & Plionis 2009; Camera et al. 2010). However, in all these cases the Lagrangians of the newly introduced fields have at least as many free parameters as the more 'classical' representations presented above.

The acceleration of spacetime expansion can be explained without introducing dark energy at all if one is willing to abandon other fundamental assumptions of the concordance model. For instance, dropping the Copernican principle, one can study spherically symmetric but inhomogeneous solutions of (2.1), so-called Tolman-Bondi-Lemaître models (Lemaître 1933). In this picture an accelerated expansion could be observed if Earth is located deep inside a large underdense region of space (Moffat 2009), but this creates of course new severe coincidence problems. Note that this void scenario is related to studies of the 'backreaction' of spacetime inhomogeneities due to structure evolution on the evolution of the homogeneous background.

Just like the cosmological constant is indistinguishable from the concept of vacuum energy, there are degeneracies between dynamical dark energy models and theories of modified gravity, depending on whether changes of (2.1) are assigned to the left- or right-hand side of the equation (Kunz & Sapone 2007; Durrer & Maartens 2008). Hence the phenomena assigned to dark energy might as well be caused by the breakdown of General Relativity on cosmological scales where the theory is, in contrast to solar-system scales, not well tested yet. Among the wealth of suggestions for alternative theories of gravity, the $f(R)$-models for which the Einstein-Hilbert action of General Relativity is modified by a function of the Ricci scalar R (e.g. Durrer & Maartens 2008), or the higher-dimensional DGP model motivated by string theory (Dvali et al. 2000) are the most advanced ones. Even these theories are subject to inconsistencies such as

[3]The term 'quintessence' refers to dark energy constituting the fifth component which can in principle determine the expansion history of the Universe, besides baryonic matter, dark matter, radiation, and spatial curvature.

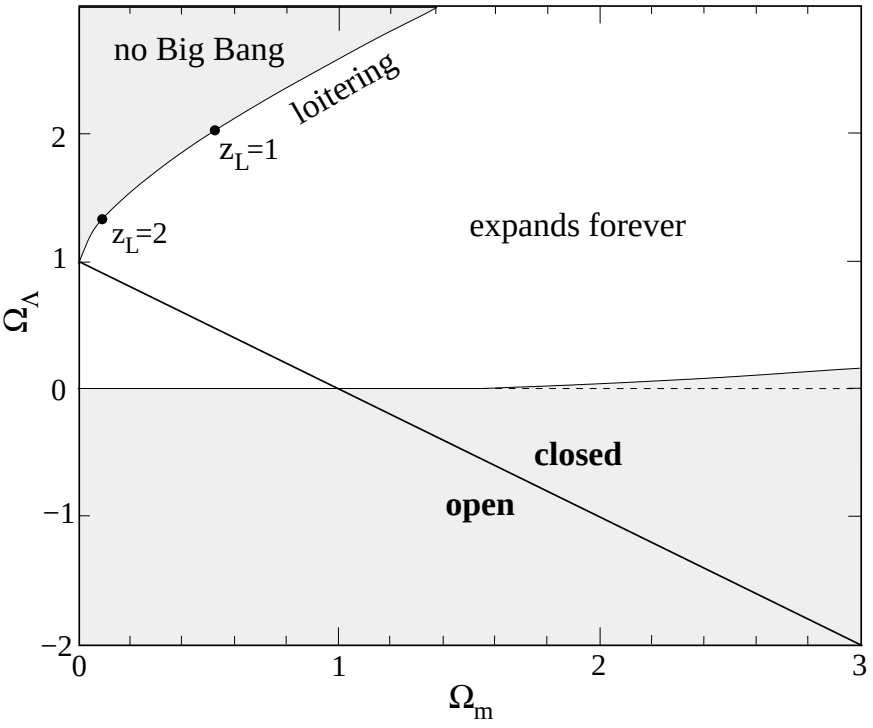

Figure 2.1: Expansion histories for different values of Ω_m and Ω_Λ. A total density parameter $\Omega_0 = \Omega_\mathrm{m} + \Omega_\Lambda$ of unity, indicated by the straight line, separates an open from a closed universe. The shaded area in the lower part of the diagram marks regions in the parameter plane for which the Universe will eventually recollapse. In the upper left shaded part universes without Big Bang can be found; z_L indicates the maximum observable redshift for a given Ω_m (from Peacock 1999).

ghosts (unphysical properties due to a missing well-defined energy ground state) and are in their basic versions incompatible with present observations (e.g. Durrer & Maartens 2008; Thomas et al. 2009; Zhao et al. 2010).

Having worked out the dependence on a for the three types of matter, one still needs to specify an absolute value of the density of each component at a certain epoch, these values entering the cosmological model as free parameters. To this end, one specialises the Friedmann equation (2.6) to today and sets $K = 0$, yielding

$$\left(\frac{\dot{a}}{a}\right)^2\Bigg|_{t=t_0} = H_0^2 = \frac{8\pi G}{3}\,\rho_\mathrm{cr}\;, \tag{2.16}$$

where ρ_cr is the total density today (provided that $K = 0$), called critical density. It is used to define dimensionless density parameters

$$\Omega_\mathrm{x} := \frac{\rho_\mathrm{x}}{\rho_\mathrm{cr}} = \frac{8\pi G\rho_\mathrm{x}}{3H_0^2}\;, \tag{2.17}$$

where x can stand for the subscripts b (baryons), m (ordinary matter), Λ (dark energy), r (radiation), or 0 (total density). Note that Ω_m comprises both baryons and dark matter. While only the sum of baryonic and dark matter is relevant for the expansion history, Ω_b enters separately into equations of structure formation, see Sect. 2.4.

Relaxing the condition $K = 0$, but keeping $a = 1$ in (2.6), results in

$$Kc^2 = H_0^2(\Omega_0 - 1)\;, \tag{2.18}$$

i.e. one can relate the spatial curvature to the total density parameter. After having inserted the evolution equations of the three types of matter given above, (2.6) finally takes on the form

$$H^2(a) = H_0^2\left\{\Omega_\mathrm{r}\,a^{-4} + \Omega_\mathrm{m}\,a^{-3} + (1-\Omega_0)\,a^{-2} + \Omega_\Lambda\right\}\;. \tag{2.19}$$

Apart from early times, i.e. very small a, the radiation contribution can be neglected as it decreases with a^{-4} and $\Omega_\mathrm{r} \ll 1$, so that Ω_m and Ω_Λ determine the expansion history of the Universe. Characteristic properties of the expansion history for different values of Ω_m and Ω_Λ are shown in Fig. 2.1. The fact that one can observe galaxies with redshifts larger than 7 in conjunction with very robust lower bounds $\Omega_\mathrm{m} > 0.1$ excludes expansion histories which have a minimum a. It is also known to high confidence that $\Omega_\Lambda > 0$ and $\Omega_\mathrm{m} < 1$, so that the Universe is expected to expand forever. Hence, the scale factor is monotonically increasing for all times. This implies that the Universe must have started in an initial state with – formally – zero extension and infinite density and temperature, dubbed the Big Bang.

2.3 The early Universe

With a description of the expansion history at hand, one can investigate the physical processes that have taken place at different epochs, governing the appearance of the Universe. Observational evidence demands the beginning of the Universe in a Big Bang, so that it must have been in an extremely hot and dense state in its early phase. Within the first few minutes after the Big Bang a multitude of important processes and transitions have occurred, determined by the level of mean kinetic energy of the particles present. Hence, we choose to specify epochs in terms of the characteristic temperature of the particle ensemble instead of cosmic time or scale factor in the following.

At energy scales significantly larger than about 1 TeV physics is poorly understood and has not yet been explored in laboratory experiments. Consequently one can only hypothesise about the numerous processes that must have occurred in the early Universe above correspondingly high temperatures. Theories about these processes covering the vast range of energy scales above 1 TeV need to make predictions about present-day observables in order to be falsifiable. One of the best-established of these theories, central to the cosmological standard model, is inflation (Guth 1981; Linde 1982).

The simplest inflationary models postulate a scalar quantum field with constant energy density, which is located in a state of false vacuum, i.e. not in the global minimum of its potential. Around the energy scale at which electroweak and strong interactions are assumed to unify (Grand Unified Theories), the vacuum energy of this field starts to dominate over radiation due to the a^{-4} dependence of Ω_r. Inserting a constant energy density into the Friedmann equation (2.6) leads to an accelerating, exponential growth, i.e. an inflationary expansion of spacetime. Note that the explanation of the late-time acceleration of expansion via vacuum energy is exactly analogous. When trying to unify the concepts of inflation and dark energy, one is again faced with the discrepancy of the involved energy scales of more than a hundred orders of magnitude though.

The temperature drops rapidly due to adiabatic expansion, which modifies the potential, so that the scalar field starts to move down its potential to reach its true vacuum state. The shallower the potential, the longer does the field 'roll' towards its minimum. This process is described in terms of a hierarchy of so-called slow-roll parameters $\boldsymbol{\eta}$, defined as functions of the scalar field potential and its derivatives. When the ground state is reached, the energy difference between false and true vacuum is released, decreasing the vacuum energy density and reheating the Universe to the temperature it had at the beginning of inflation. Radiation starts to dominate again, marking the end of the exponential growth (for more details see e.g. Bartolo et al. 2004).

During inflation spacetime is assumed to have expanded by at least about 60 e-folds, the precise number depending on the time span inflation lasted, and thus on the values of the slow-

roll parameters. Despite the current lack of direct observational evidence inflationary scenarios have become an integrative part of the cosmological concordance model. They provide a number of testable predictions such as the vanishing curvature of spacetime. Most notably they solve the horizon and flatness problem of non-inflationary cosmological models in a natural way, which can be seen as follows.

As demonstrated in Sect. 2.1, accelerating expansion is equivalent to a decreasing Hubble radius χ_H, see (2.12). As a consequence, χ_H has been much smaller than the comoving horizon (2.11) ever since the end of the inflationary phase. At the time the CMB was generated, regions with angular separation of more than about 1 deg were not in causal contact, i.e. outside the Hubble sphere. Yet the CMB has a uniform temperature over the whole sky which can only be explained if essentially all scales are within the comoving horizon χ_hor. The necessary difference between the size of the horizon and of χ_H originates from the exponential expansion of space during inflation.

To understand the flatness problem, consider the evolution of the density parameters with scale factor,

$$\Omega_\mathrm{x}(a) = \frac{\rho_\mathrm{x}(a)}{\rho_\mathrm{cr}(a)} = \left(\frac{H_0}{H(a)}\right)^2 \frac{\rho_\mathrm{x}(a)}{\rho_\mathrm{cr}(a_0)} \,, \tag{2.20}$$

where $a_0 = 1$. Note that if no argument is specified as in the remainder of this work, the density parameters are evaluated today, i.e. $\Omega_\mathrm{x}(a_0) \equiv \Omega_\mathrm{x}$. In an early phase of the Universe we can neglect the influence of dark energy, which yields for the evolution of the todal density parameter, making use of (2.19),

$$\begin{aligned} \Omega_0(a) &\approx \frac{\Omega_\mathrm{r}(a_0)a^{-4} + \Omega_\mathrm{m}(a_0)a^{-3}}{\Omega_\mathrm{r}(a_0)a^{-4} + \Omega_\mathrm{m}(a_0)a^{-3} - (\Omega_0(a_0)-1)\,a^{-2}} \\ &= 1 + \frac{\Omega_0(a_0)-1}{\Omega_\mathrm{r}(a_0)a^{-2} + \Omega_\mathrm{m}(a_0)a^{-1} - (\Omega_0(a_0)-1)} \approx 1 + a^2\,\frac{\Omega_0(a_0)-1}{\Omega_\mathrm{r}(a_0)} \,, \end{aligned} \tag{2.21}$$

where $a \ll 1$ was used in the second approximation. Thus, if $|\Omega_0(a_0) - 1| \ll 1$ as we indeed observe, $|\Omega_0(a) - 1| \lll 1$ must have held for $a \ll 1$, requiring very fine tuning of the curvature of spacetime. In case the total energy density is governed by inflation so that $\rho_0 \approx \rho_\mathrm{infl.} = \text{const.}$, (2.6) yields a scale factor $a \propto \sinh(\tilde{H}t)$ or $a \propto \cosh(\tilde{H}t)$, depending on the sign of K, where $\tilde{H}^2 = H_0^2\rho_\mathrm{infl.}/\rho_\mathrm{cr}(a_0)$. If inflation lasts long enough, these solutions approach an exponential, which then leads to $H(a) = \dot{a}/a = \tilde{H}$, i.e. a constant rate of expansion. Inserting this result into (2.20), one sees that the constant energy density and the constant expansion rate $\tilde{H}$ imply $\Omega_0(a) \equiv 1$. In summary, the phase of rapid expansion causes every spatial geometry of spacetime to appear flat, yielding a plausible explanation for the total density parameter being very finely tuned to unity (see also Kolb & Turner 1990).

Besides, all inflationary theories predict the creation of gravitational waves which would imprint a clear signature on the B-mode polarisation of the CMB (Dodelson 2004), expected to be for instance measured in the near future by the Planck satellite. As will be detailed in Sect. 2.4, quantum fluctuations in the scalar field which are increased to macroscopic scales due to the inflationary expansion serve as the seeds for structure formation. Finally, more complicated models of inflation than the single-field version outlined above predict density fluctuations of matter which are not purely stochastic and hence display non-Gaussianity. This primordial non-Gaussianity would e.g. leave an observable signature in higher-order CMB statistics (Fergusson & Shellard 2007) and on the large-scale galaxy distribution (Dalal et al. 2008; see also Giannantonio & Porciani 2010).

A further process that must have taken place in the high-energy Universe but whose nature is still completely unknown is baryogenesis. The symmetry between matter and antimatter was

broken at an early epoch since otherwise matter and antimatter would have fully annihilated. The surplus in matter remaining after annihilation corresponds to the total of observable matter in the present-day Universe. At scales below the order of 100 MeV there exist electrons, photons, neutrinos, protons, neutrons and to a slightly lesser extent their respective anti-particles. In addition, WIMPs or other dark matter particles may be present, but at these energies they interact only via gravity. All elementary particles with sub-second lifetimes have decayed and cannot be created anymore due to the lack of highly energetic particle collisions. As long as reaction rates are larger than the expansion rate of the Universe, characterised by $H(a)$, the particles still in existence are in equilibrium, their energies following a thermal distribution.

At energies of about 1 MeV the reaction rate for neutrinos, which couple to other particles only via weak nuclear forces, has decreased so far that neutrinos stop interacting with other particle species. From then on, they move freely through the Universe, still following a thermal distribution. Cosmic expansion transforms this thermal distribution into one with temperature $T = T' a'/a$, where the so-called freeze-out of the neutrinos took place at epoch a'. Hence one expects today an isotropic neutrino background with a temperature of $T_{\nu,0} = 1.9\,\mathrm{K}$; however, due to the extremely low neutrino energies it is unobservable.

After neutrino decoupling weak interactions between neutrons and protons are hampered, so that the equilibrium between neutrons and protons terminates. The free neutrons start to decay with a lifetime of approximately 900 s. When mean energies have decreased to 100 keV, nuclear physics comes into play. Nearly all remaining neutrons at that time are then bound into deuterons, which in turn combine immediately to ^{4}He nuclei. From the time spans and energies involved in these processes one predicts abundances of 75 % hydrogen, 25 % helium and traces of deuterium and heavier elements such as lithium and beryllium. This prediction of Big Bang Nucleosynthesis is in precise agreement with current observations (see Dodelson 2004 and references therein).

At $\sim 1\,\mathrm{eV}$, corresponding to a temperature of the Universe of roughly 10000 K, typical particle energies lie in the range of electronic transitions in atoms, but the (re-)combination of nuclei, mostly hydrogen, and free electrons could actually take place only at about 3000 K when the number of photons with energies higher than 13.6 eV, which could re-ionise hydrogen from the ground state, had decreased sufficiently. Hence, at around $z \sim 1100$ the Universe finally becomes neutral. Since only few charged particles are left, photons decouple and form a background radiation analogous to neutrinos. Due to the annihilation of electrons and positrons below mean energies of 0.5 MeV, the photon gas has received extra energy, so that the background radiation today follows a Planck law with a slightly higher temperature of $T_{\gamma,0} = 2.73\,\mathrm{K}$, its flux peaking in the microwave regime.

2.4 Structure formation

In an ideal homogeneous and isotropic universe the density of all matter components remains homogeneous throughout cosmic history, so that structures would never form. As soon as density perturbations occur, they evolve under their mutual gravitational influence and can eventually form the rich structure of the Universe we observe today. The formation and evolution of structure is usually studied by assuming a homogeneous background set by the FLRW model. Of course, density fluctuations also lead to structure in spacetime and hence may in principle affect the expansion history. This 'backreaction' is a matter of on-going investigation and could serve as a possible explanation of the dark energy phenomenon (e.g. Brandenberger 2000; Wiltshire 2008), but it remains questionable whether backreaction effects are strong enough to be of relevance (Kasai et al. 2006).

As discussed in the foregoing section, the initial seed for structure formation is provided by inflation, which enlarges quantum fluctuations in its scalar field to macroscopic scales. To describe perturbations in the matter density quantitatively, one uses the matter density contrast

$$\delta(\boldsymbol{x},t) = \frac{\rho(\boldsymbol{x},t) - \bar{\rho}(t)}{\bar{\rho}(t)} \ , \tag{2.22}$$

where $\bar{\rho}(t)$ is the mean density given by the FLRW model. Due to their original quantum nature, the perturbations can only be predicted in a statistical way. In the prevailing single-field, slow-roll theory of inflation, density fluctuations are created purely stochastically and can be described in terms of a Gaussian random field. Then the perturbations are fully characterised by their power spectrum, defined via

$$\left\langle \tilde{\delta}(\boldsymbol{k},t)\ \tilde{\delta}^*(\boldsymbol{k'},t) \right\rangle = (2\pi)^3\ \delta_{\mathrm{D}}^{(3)}(\boldsymbol{k}-\boldsymbol{k'})\ P_\delta(k,t) \ , \tag{2.23}$$

where δ_{D} is the three-dimensional Dirac delta distribution. Furthermore the Fourier transform of the matter density contrast,

$$\tilde{\delta}(\boldsymbol{k},t) = \int \mathrm{d}^3x\ \delta(\boldsymbol{x},t)\ \mathrm{e}^{-\mathrm{i}\boldsymbol{x}\cdot\boldsymbol{k}} \ , \tag{2.24}$$

with the comoving wavenumber k as the Fourier variable, was introduced. Note that the power spectrum is the Fourier transform of the two-point correlation function of the density contrast. Since the distribution of the perturbations is assumed to be statistically homogeneous and isotropic, $P_\delta(k,t)$ depends only on the modulus of $\boldsymbol{k}$.

The angular brackets in (2.23) denote the ensemble average, supposed to be taken over a large number of realisations of the random field. However, as in all of cosmology one is faced with the problem that only a single realisation, i.e. only one Universe, is observable. One usually proceeds by working under the ergodic hypothesis, taking the average over large numbers of (approximately) statistically independent patches of the one available realisation instead. While holding for Gaussian random fields, potential limitations of ergodicity are currently under investigation (e.g. Marinucci & Peccati 2010).

Single-field inflation then predicts a scale-invariant primordial power spectrum of the form

$$P_\delta(k,t) \propto k^{n_\mathrm{s}} \quad \text{with} \ \ n_\mathrm{s} = 1 - f\left(\boldsymbol{\eta}\right) \ , \tag{2.25}$$

where $f\left(\boldsymbol{\eta}\right) \ll 1$ is a function of the slow-roll parameters. Both the predicted Gaussianity of the initial density perturbations and the value of $n_\mathrm{s} \lesssim 1$ are well in agreement with observations, see Sect. 2.5. The limiting case $n_\mathrm{s} = 1$ in (2.25) is called Harrison-Zeldovich power spectrum and is frequently employed in computations, also in this work.

The initial perturbations in the matter distribution set up by inflation, one can now follow the evolution of density fluctuations, which depends on the matter component dominating the expansion at the considered epoch. By inspection of (2.19), one finds that radiation has the strongest dependence on $a(t)$, so that it dominates at early times, both before and after the inflationary period. Later on, matter determines the expansion history. The transition takes place when radiation and matter density are of equal size, i.e. $\rho_\mathrm{r}(a_\mathrm{eq}) = \rho_\mathrm{m}(a_\mathrm{eq})$. This condition leads to $a_\mathrm{eq}^{-1} = 1 + z_\mathrm{eq} \approx 4000$ for current values of the cosmological parameters. Nowadays dark energy governs the expansion of the Universe, but the era of matter domination has ended only comparatively recently, at $z < 1$, which is related to the coincidence problem discussed in the foregoing section. Note that although we assume throughout this work that dark energy does not cluster and remains homogeneous for all times, it still influences structure formation via the expansion history.

If one considers scales much smaller than the horizon, whose size is of the order of the curvature radius of spacetime, the evolution can be followed in a Newtonian approach. It comprises a continuity equation encoding mass/energy conservation, the Euler equation as an equation of motion, and the Poisson equation which links sources of gravity to the gravitational potential. Clustering is governed by dark matter, so that pressure which becomes important for baryons can be neglected. Dark matter is collisionless or very nearly so, but is here considered as a perfect fluid, i.e. one can assign a unique velocity to every point in space. This approximation is fair as long as the involved scales are not too small and the evolution is not followed for too long. The three basic equations are transformed to comoving coordinates and written in terms of the deviations from the homogeneous solution. In addition, the equations are Taylor-expanded in the density contrast around small δ and truncated after the first order, to be able to perform analytic calculations. These steps result in the set

$$\frac{\partial\delta(\boldsymbol{x},t)}{\partial t}+\frac{1}{a}\nabla_x\cdot\boldsymbol{v}(\boldsymbol{x},t) = 0\,, \tag{2.26}$$

$$\frac{\partial\boldsymbol{v}(\boldsymbol{x},t)}{\partial t}+\frac{\dot{a}}{a}\,\boldsymbol{v}(\boldsymbol{x},t) = -\frac{1}{a}\nabla_x\Phi(\boldsymbol{x},t)\,, \tag{2.27}$$

$$\nabla_x^2\Phi(\boldsymbol{x},t) = \frac{3H_0^2\Omega_\mathrm{m}}{2a}\,\delta(\boldsymbol{x},t)\,, \tag{2.28}$$

where $\boldsymbol{v}(\boldsymbol{x},t)$ is the peculiar velocity and $\Phi(\boldsymbol{x},t)$ the comoving gravitational potential. The symbol ∇_x denotes the gradient with respect to comoving coordinates.

Inserting (2.26) to (2.28) into one another yields a second order, homogeneous differential equation for δ,

$$\ddot{\delta}(\boldsymbol{x},t)+\frac{2\dot{a}}{a}\,\dot{\delta}(\boldsymbol{x},t)-\frac{3H_0^2\Omega_\mathrm{m}}{2a^3}\,\delta(\boldsymbol{x},t)=0\,, \tag{2.29}$$

which can be solved by separating the dependences on space and time, $\delta(\boldsymbol{x},t):=D(t)\Delta(\boldsymbol{x})$. One of the two solutions of (2.29) decays with time and is thus irrelevant for structure formation, whereas the second, growing solution is described by the growth factor $D_+(t)$. In the growth factor the time dependence of the density perturbations is encoded, which is determined by the dominant component of matter at each epoch. For instance, on sub-horizon scales in the matter dominated era one finds $D_+(t)=a(t)$ for the dark matter component. Similar calculations can be made for the other components of matter which cluster, including pressure for baryons and radiation, and following a relativistic ansatz on super-horizon scales. For matter and radiation the growth factor mostly shows a power-law behaviour as a function of scale factor. For a more detailed account of perturbation theory and the evolution of structure see for instance Peacock (1999), Bernardeau et al. (2002a), and Dodelson (2004).

Characteristic changes in the evolution take place at a_enter, i.e. the scale factor of the epoch at which perturbations enter the sphere defined by the Hubble radius (2.12), and start to have physical interactions, and at a_eq, i.e. when matter starts to dominate over radiation. Figure 2.2 outlines the different evolution of the density fluctuations of the matter components that cluster for a given, fixed comoving wavenumber $\boldsymbol{k}$. Note that, although baryons and dark matter have been treated identically in their effect on expansion history, their perturbations evolve differently because baryons are coupled to photons which have pressure.

When radiation perturbations enter the horizon, pressure counteracts gravity, so that oscillations occur. Moreover the further growth of perturbations is hindered. The same applies to all other matter components as long as radiation is dominant. After a_eq dark matter fluctuations can grow, whereas baryons are still tightly coupled to radiation via Compton scattering until recombination, marked by a_rec. After recombination baryons fall into the potential wells

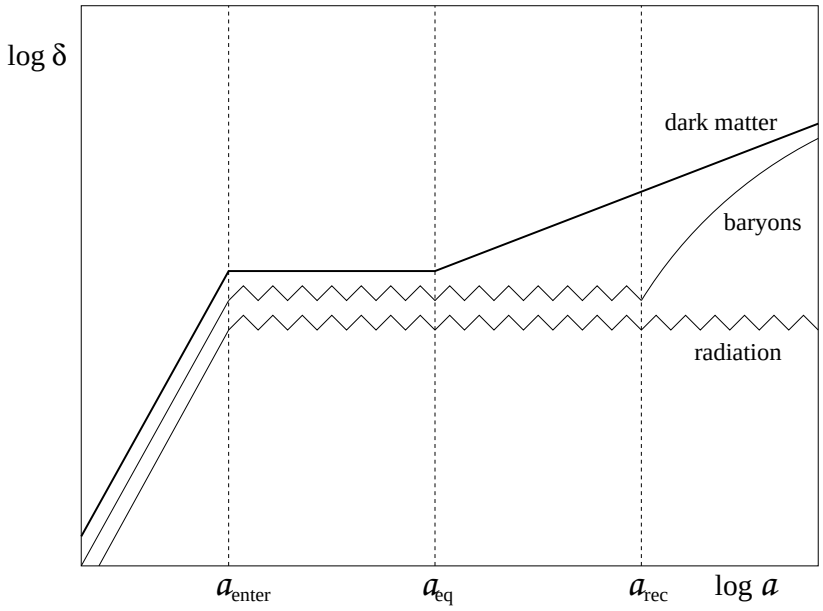

Figure 2.2: Sketch of the evolution of the density contrast δ for different matter components at fixed wavenumber. Curves are offset with respect to each other. Super-horizon fluctuations ($a < a_{\rm enter}$) grow $\propto a^2$, provided that $a_{\rm enter} < a_{\rm eq}$. In the matter-dominated era ($a > a_{\rm eq}$) dark matter fluctuations grow $\propto a$. Wiggly lines correspond to oscillating density contrast, where δ can obtain negative values. Here only the maximum amplitudes are plotted. Recombination takes place at $a_{\rm rec}$ (from Joachimi 2007).

of dark matter. The quantity $a_{\rm enter}$ is a function of the wavelength corresponding to the extent of a perturbation, so that the evolution of dark matter fluctuations differs for different wavenumbers. Small-scale perturbations, corresponding to large k, enter the horizon earlier. If this happens before $a_{\rm eq}$, dark matter overdensities do not grow anymore before matter starts to dominate the expansion, see the sketch. As a consequence, the power of modes with large wavenumbers is suppressed – the larger k, the stronger.

The various transitions are collected into the transfer function $T(k)$, defined via

$$\frac{\tilde{\delta}(\boldsymbol{k}, a_0)}{\tilde{\delta}(\boldsymbol{k}_{\rm l}, a_0)} \equiv T(k)\, \frac{\tilde{\delta}(\boldsymbol{k}, a_i)}{\tilde{\delta}(\boldsymbol{k}_{\rm l}, a_i)}\ , \tag{2.30}$$

where $a_i \ll \{a_{\rm enter}, a_{\rm eq}\}$ and where $\boldsymbol{k}_{\rm l}$ denotes a small wavenumber for which density fluctuations are still linear today. Note that in this work we use cosmic time t, scale factor a, and comoving distance χ interchangeably to denote the dependence on epoch of the density contrast, the power spectrum, and related quantities. The normalisation by linear density contrast is done in order to eliminate a 10 % decline of these scales during the epoch of radiation-matter equality (see e.g. the discussion in Dodelson 2004). The transfer function is calculated numerically, including further effects by e.g. neutrinos and baryons. Fit formulae which are in common use were provided by Bardeen et al. (1986), Efstathiou et al. (1992), and Eisenstein & Hu (1998).

Taking into account the considerations made above, including (2.25) and (2.30), one obtains the matter power spectrum for arbitrary times,

$$P_\delta(k, t) = A\, k^{n_{\rm s}}\, T^2(k)\, D_+^2(t)\ , \tag{2.31}$$

which is still given in the approximation of linear perturbations. The normalisation, here given by a constant A, is usually expressed in terms of σ_8, the root-mean square of matter fluctuations in spheres of radius $8h^{-1}$Mpc today, which is of order unity. On scales smaller than approximately 10 Mpc the root mean square of the density contrast exceeds unity today, so that already on considerably larger scales and at earlier times the linear approximation has to break down. Apart from special cases such as stable clustering (Davis & Peebles 1977; Smith et al. 2003) the fully non-linear treatment of (2.26) to (2.28) is done numerically. If

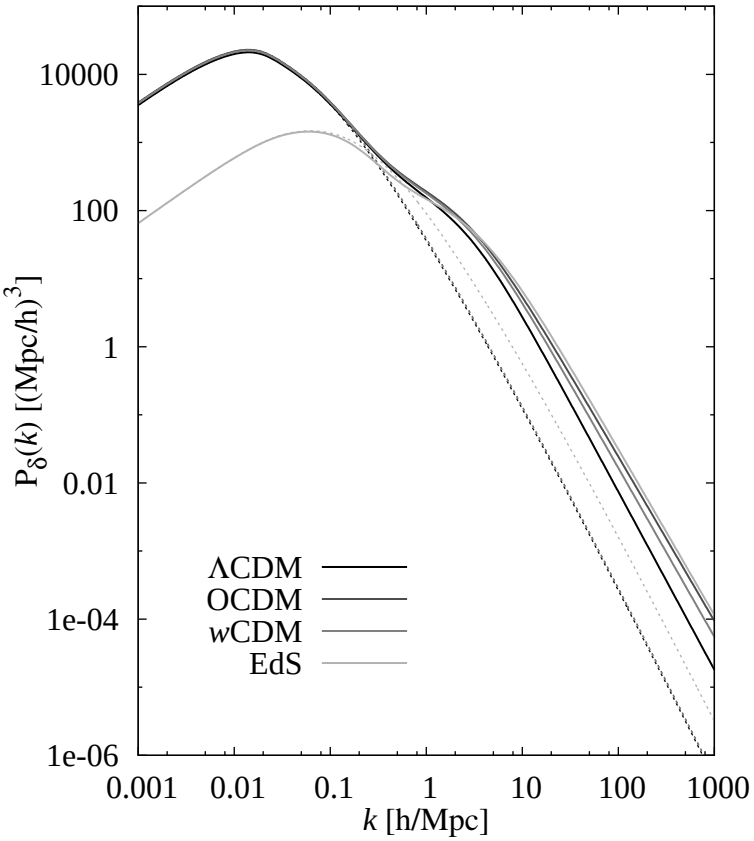

Figure 2.3: Dark matter power spectrum for different spatially flat cosmological models. Dotted curves correspond to the linear power spectrum, solid lines to the non-linear power spectrum computed according to Smith et al. (2003), with the modifications discussed in Sect. 4.3. From black curves to lighter shades of grey the results for the cosmological models ΛCDM ($\Omega_\mathrm{m} = 0.25$, $\Omega_\Lambda = 0.75$, $w_0 = -1$), OCDM ($\Omega_\mathrm{m} = 0.25$, $\Omega_\Lambda = 0$), wCDM ($\Omega_\mathrm{m} = 0.25$, $\Omega_\Lambda = 0.75$, $w_0 = -0.5$), and EdS ($\Omega_\mathrm{m} = 1$, $\Omega_\Lambda = 0$) are displayed. The other cosmological parameters have been fixed at their fiducial values, in particular $w_a = 0$ and $\sigma_8 = 0.8$. All power spectra have been calculated at $z = 0.5$.

only dark matter is considered, merely gravitational forces need to be modelled, so that N-body simulations are effective in producing fully non-linear power spectra. Peacock & Dodds (1996) have given widely used analytic fit formulae for the non-linear power spectrum using such simulations, supplemented by the more accurate approximations of Smith et al. (2003). However, these fit formulae do not incorporate the more recent developments in modelling like variable dark energy or modified gravity, so that new simulations and possibly new fits are required, see e.g. McDonald et al. (2006) and Beynon et al. (2010), but also the case study in Sect. 4.3.

In Fig. 2.3 both linear and non-linear matter power spectra are plotted for different cosmological models, including ΛCDM, an open universe without dark energy (OCDM), a model with variable dark energy (wCDM), and an Einstein-de Sitter universe (EdS). They all have in common that they increase for small k according to an approximate Harrison-Zeldovich slope. Modes which enter the horizon before a_eq are suppressed (as discussed in Fig. 2.2), so that P_δ turns over for increasing k. Non-linear clustering enhances the power for large k, corresponding to small spatial scales at which gravitational potentials are deep and the density contrast large. The position of the peak of P_δ is determined by the so-called shape parameter $\Gamma \approx \Omega_\mathrm{m}\, h$. Since we keep Γ and the power spectrum normalisation fixed for the ΛCDM, OCDM, and wCDM models, they coincide on large scales up to the peak. Therefore non-linear scales of the matter power spectrum need to be probed to differentiate between them. It is interesting to note that the wCDM model with $w = -0.5$ mimics closely the behaviour of an OCDM universe, even on small scales. Due to the largely different Ω_m the power spectrum in an EdS universe has a clearly shifted peak and can thus readily be distinguished on all scales from the other equally flat models.

Non-linear evolution does not only enhance the power spectrum on small scales, but also generates non-Gaussian density fluctuations, irrespective of whether the initial density field

parameter	value	$1\,\sigma$ error
h	0.704	+0.013; -0.014
Ω_m	0.272	$\pm$ 0.007
Ω_Λ	0.728	+0.015; -0.016
Ω_b	0.0456	$\pm$ 0.0016
σ_8	0.761	+0.049; -0.048
n_s	0.963	$\pm$ 0.012

Table 2.1: Current values and $1\,\sigma$ errors of important cosmological parameters, assuming a ΛCDM cosmology (Spergel et al. 2007; Komatsu et al. 2010). Note that the radiation density is dominated by the CMB and amounts to $\Omega_\mathrm{r} = 8.6 \times 10^{-5}$.

was purely Gaussian distributed or not. Consequently the power spectrum does not capture all information anymore. One can in addition study higher-order spectra, defined via

$$\left\langle \prod_{i=1}^{N} \delta(\boldsymbol{k}_i, t) \right\rangle_\mathrm{c} = (2\pi)^3\, \delta_\mathrm{D}^{(3)} \left(\sum_{i=1}^{N} \boldsymbol{k}_i \right)\; P_\delta^{(N)}(\boldsymbol{k}_1, \, ... \, , \boldsymbol{k}_N, t) \; , \tag{2.32}$$

where the subscript c denotes the connected part of the correlator (see Bernardeau et al. 2002a for details). For $N = 2$ (2.32) is equivalent to the definition of the power spectrum (2.23) while the case $N = 3$ corresponds to the defining equation of the bispectrum. In what follows we will identify $B_\delta \equiv P_\delta^{(3)}$ for ease of notation. To study non-Gaussianity in the large-scale structure, one can thus measure three-point statistics or alternatively obtain statistics of galaxy clusters which should trace the positions of the peaks of highest density in the underlying dark matter distribution.

2.5 The concordance model and beyond

Currently all cosmological observations can be explained by means of a simple, consistent framework that has a surprisingly small number of free parameters. This concordance model of cosmology is a ΛCDM universe, a homogeneous and isotropic expanding spacetime featuring cold dark matter and a cosmological constant or non-evolving, non-clustering dark energy, depending on the interpretation. This description of the cosmos contains in its basic form only six free parameters whose current best-fit values and $1\,\sigma$ uncertainties are summarised in Table 2.1. These constraints have been obtained by a wealth of different and mostly independent methods of which we will present an overview below.

As noted earlier, the CMB constitutes a snapshot of the Universe at $z \sim 1100$ and consists of a near-perfect thermal Planck spectrum in every direction. At the time photons decoupled from the other matter components to form the background radiation, structure formation had already begun and left a small (of the order 10^{-5}) but characteristic imprint on the angular photon distribution. The resulting anisotropies in the CMB have been measured to high accuracy, the best constraints to date shown in Fig. 2.4 (see Komatsu et al. 2010 for details).

Within the sound horizon at the time of recombination the oscillations in the baryon-photon fluid cause strong features in the anisotropy power spectrum (the Doppler peaks), whose positions and relative heights are sensitive to Ω_b and Ω_m. By relating the sound horizon scale, corresponding to the position of the first Doppler peak, to the angle under which it is observed in the CMB, an angular diameter distance can be calculated, which depends on the spatial geometry of the Universe via (2.19) and allows one to constrain in particular the curvature of space. On super-horizon scales, i.e. for multipoles $\ell \lesssim 200$, the anisotropy power spectrum is dominated by the Sachs-Wolfe effect, plus the integrated Sachs-Wolfe effect generated after recmobination (e.g. Giannantonio et al. 2006), which depend on both curvature and dark energy. Otherwise dark energy is only weakly constrained by CMB measurements because it was clearly

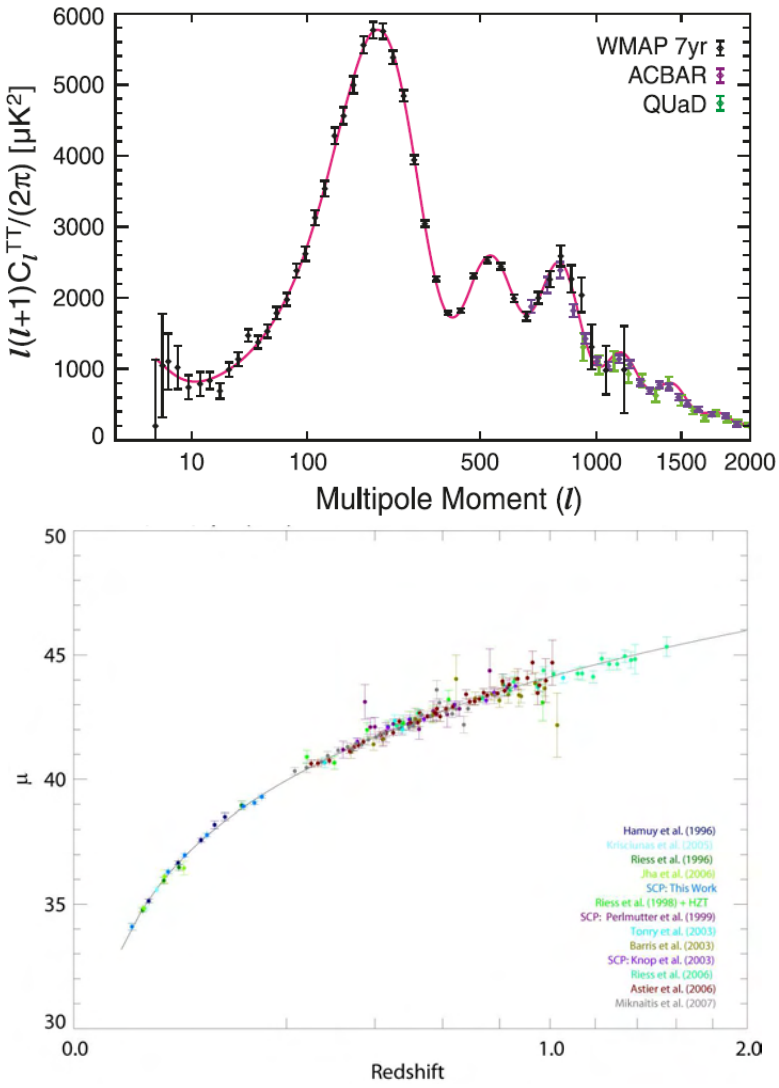

Figure 2.4: *Top panel*: CMB anisotropy power spectrum as a function of multipole moment. The best-fitting power spectrum for a flat ΛCDM cosmology is shown as solid curve (from Komatsu et al. 2010). *Bottom panel*: Distance modulus μ as a function redshift. As μ is a linear function of the logarithm of the luminosity distance, this plot shows the distance-redshift relation, and hence the data probes the Hubble parameter (2.19). The curve corresponds again to the best-fitting flat ΛCDM cosmology (from Kowalski et al. 2008).

subdominant in the early Universe, but combining CMB measurements with data probing more recent epochs still yields a powerful tool to pin down the properties of dark energy.

Furthermore the measurement of luminosity distances can be used to determine cosmological parameters. Type Ia supernovae are the most luminous standard candles and can thus be observed out to high redshifts. Comparing the inferred distances, or equivalently the distance modulus, to the observed redshift as shown in Fig. 2.4 probes the expansion history. Observations of type Ia supernovae about a decade ago first revealed the existence of the dark energy phenomenon by indicating that the luminosity distance of objects at relatively low redshifts was larger than in an empty universe with constant expansion. This implied that in recent times the expansion has started to accelerate which is only possible if $\Omega_\Lambda > 0$.

A further probe of expansion history, this time via angular diameter distances, is provided by baryonic acoustic oscillations (BAO). As sketched in Fig. 2.2 baryons started to be attracted by the gravitational potentials of dark matter after having decoupled from radiation. To a certain extent, dark matter particles also fell into the potential wells of the baryons, which had escaped the dark matter potentials while still coupled to photons. The oscillations of the baryon-photon fluid at that time, also prominent in the CMB power spectrum, have thus left an imprint, albeit weak, on the dark matter distribution. These oscillations, or 'baryonic wiggles', show up in the matter power spectrum, thereby providing basically a measure of the sound horizon scale at a range of smaller redshifts, see Fig. 2.5. This physical scale can then

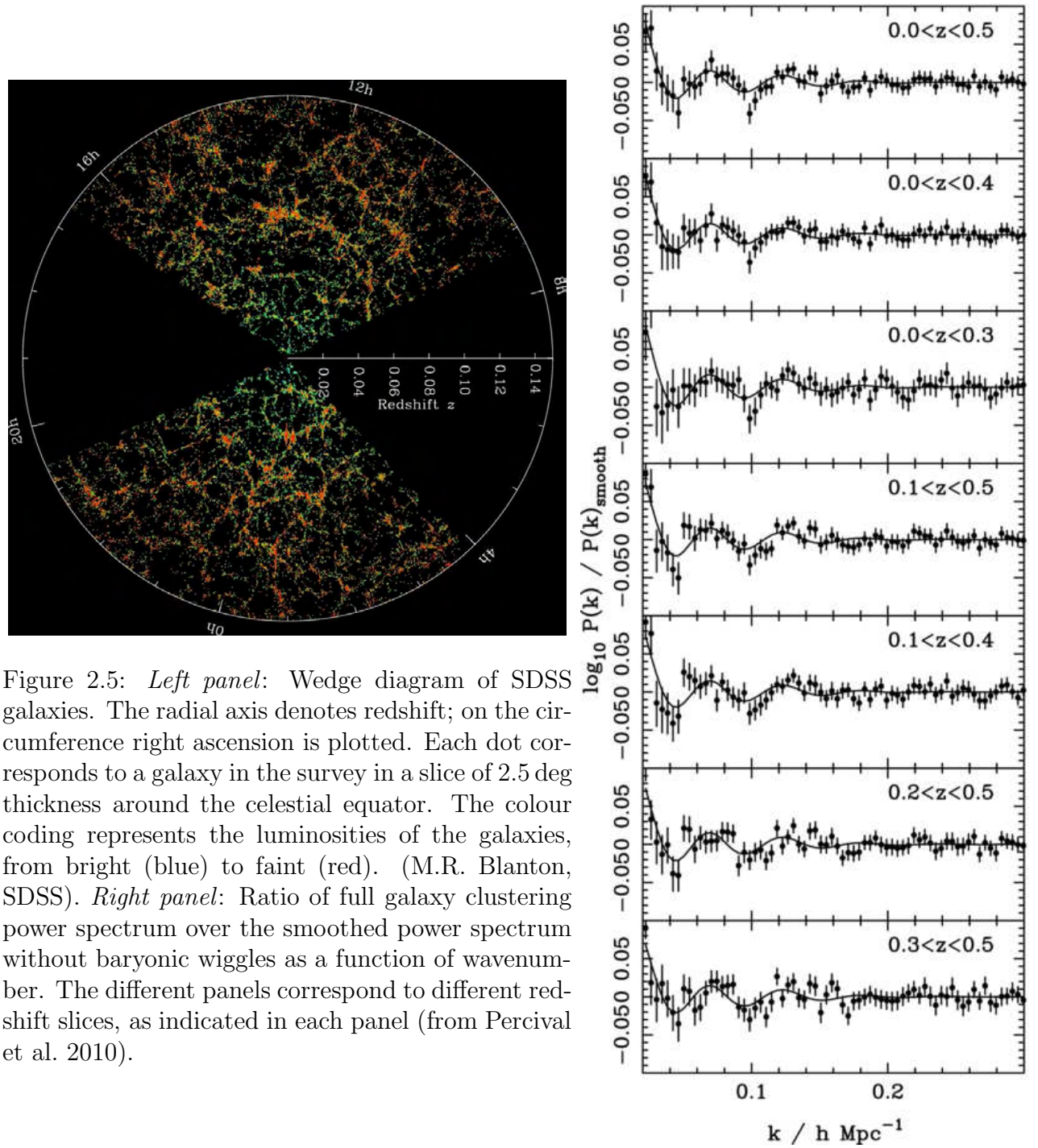

Figure 2.5: *Left panel*: Wedge diagram of SDSS galaxies. The radial axis denotes redshift; on the circumference right ascension is plotted. Each dot corresponds to a galaxy in the survey in a slice of 2.5 deg thickness around the celestial equator. The colour coding represents the luminosities of the galaxies, from bright (blue) to faint (red). (M.R. Blanton, SDSS). *Right panel*: Ratio of full galaxy clustering power spectrum over the smoothed power spectrum without baryonic wiggles as a function of wavenumber. The different panels correspond to different redshift slices, as indicated in each panel (from Percival et al. 2010).

be related to the angle under which it is observed, yielding angular diameter distances. Note that BAOs are observed in the galaxy distribution instead of the matter distribution, but the usual assumption that galaxies trace the underlying dark matter well is expected to hold on the relatively large scales that BAOs are restricted to.

The more recent Universe can be probed not only via its expansion history but also by its structure and the evolution thereof. However, to proceed by studying the visible matter, one has to assume an unambiguous, at least in a statistical sense, relation between the density contrast of the number density of galaxies δ_g and the density contrast of dark matter as used in the foregoing section. The baryons which formed galaxies should reside close to the centres of the gravitational potentials of dark matter and hence trace the underlying dark matter density structure, at least on larger scales. Then the three-dimensional distribution of galaxies, measured by galaxy

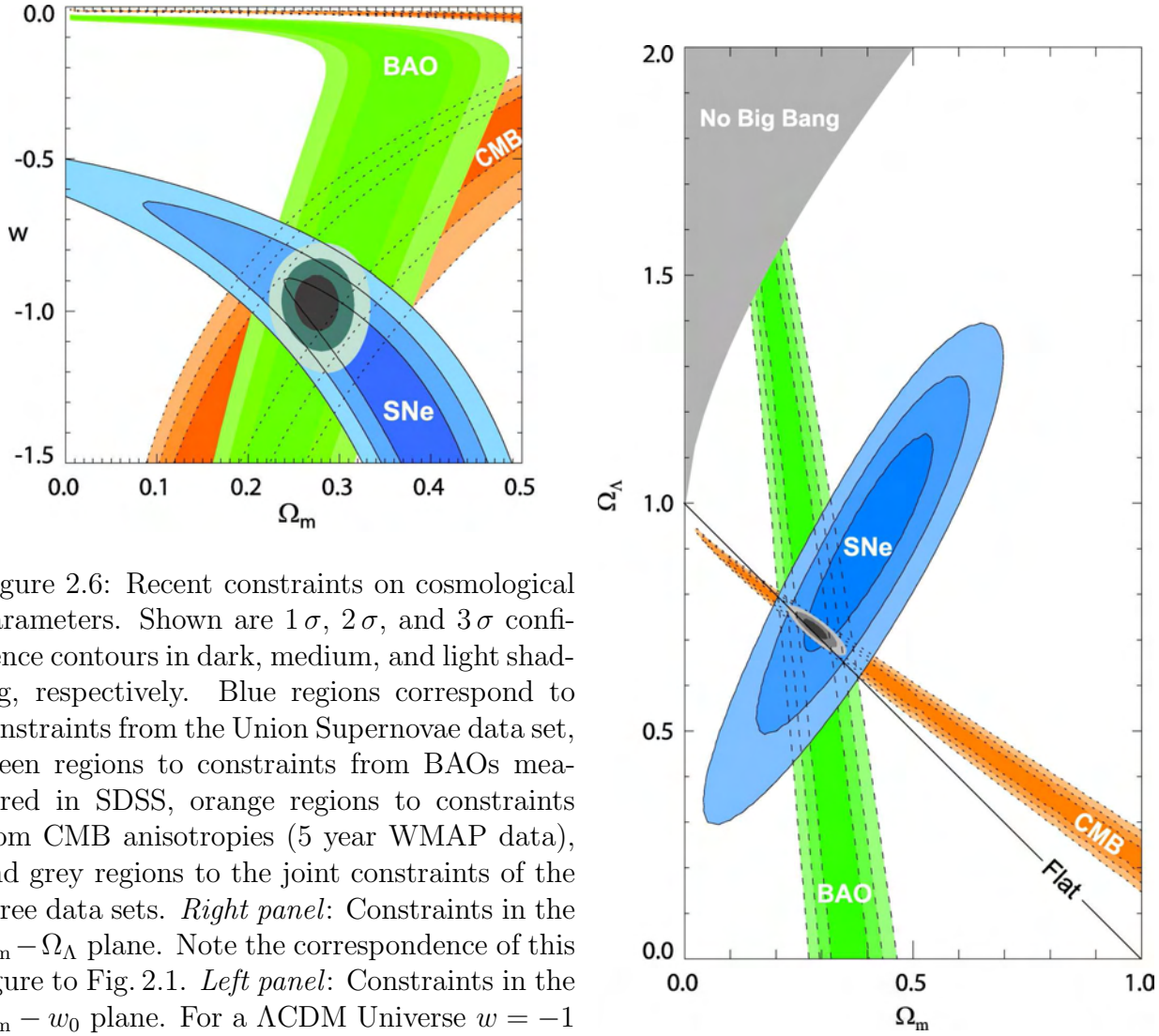

Figure 2.6: Recent constraints on cosmological parameters. Shown are $1\,\sigma$, $2\,\sigma$, and $3\,\sigma$ confidence contours in dark, medium, and light shading, respectively. Blue regions correspond to constraints from the Union Supernovae data set, green regions to constraints from BAOs measured in SDSS, orange regions to constraints from CMB anisotropies (5 year WMAP data), and grey regions to the joint constraints of the three data sets. *Right panel*: Constraints in the $\Omega_\mathrm{m} - \Omega_\Lambda$ plane. Note the correspondence of this figure to Fig. 2.1. *Left panel*: Constraints in the $\Omega_\mathrm{m} - w_0$ plane. For a ΛCDM Universe $w = -1$ holds (from Kowalski et al. 2008).

redshift surveys such as the Sloan Digital Sky Survey (SDSS, see Abazajian et al. 2009 and Fig. 2.5), should represent a powerful probe of the dark matter power spectrum (2.31) and its dependence on cosmology. Further methods that fall into this category are measurements of the abundance of galaxy clusters, which trace the largest dark matter potentials, and the Lyα forest, whose absorption features are caused by baryonic matter within the large-scale structure filaments.

A technique capable of mapping dark matter directly via the gravitational force it exerts and hence avoiding the problem of the relation between the baryonic and dark matter distribution is weak gravitational lensing. Due to its additional dependence on angular diameter distances via the lensing geometry, weak lensing probes both expansion and structure growth and is therefore the potentially most powerful method to narrow down the properties of dark matter and dark energy. Weak lensing, or cosmic shear as its application to cosmology is usually referred to, is the main topic of this work and will be dealt with in more detail in Chap. 3.

All methods, including the most important ones mentioned here, give a consistent view on the Universe, as is demonstrated by the exemplary confidence contours shown in Fig. 2.6. The overlap of the allowed parameter regions is remarkable, producing tight constraints that exclude vanishing Ω_Λ with high confidence, strongly favour spatial flatness, and prefer constant dark energy with $w = -1$, and hence the interpretations as vacuum energy or a cosmological

constant.

Despite the success of the concordance model it remains deeply unsatisfactory as it depends vitally on a number of still purely hypothetical concepts. About 95 % of the matter-energy content of the Universe are of unknown form. While both observational evidence and candidate particles abound in the case of dark matter, the nature of the dark energy phenomenon, claimed to make up three quarters of the matter budget, remains totally obscure. Moreover, in the ΛCDM framework the existence of any structure relies on the concept of inflation which is supported by current observations but again lacks a firm grounding in fundamental physics. Scalar fields are popular in elementary particle physics and as possible explanations for many theories of both inflation and dark energy, but actually none has been proven to exist so far.

Therefore it is essential to acquire more data to either confirm the ΛCDM paradigm and exclude alternative theories or to extend the currently prevailing picture and provide more physically motivated explanations of the phenomena observed. All fundamental assumptions inherent in the concordance model have to be put to the test, among them the validity of General Relativity on cosmological scales (e.g. Daniel et al. 2010; see also Uzan 2009), the constancy in time and space of physical constants (e.g. Gutiérrez & Lopéz-Corredoira 2010), and the large-scale homogeneity and/or isotropy of space, which are related to the cosmological and Copernican principle, see Sect. 2.1. When striving towards further insight into the physics of the cosmos, it has to be kept in mind that information will always be restricted to the backward light cone, limiting fundamentally our ability to distinguish between cosmological models (Kolb & Lamb 2009).

Yet, even on a long-term scale astronomical observations are likely to be the only sources of information on dark energy and will prove central to reveal the nature of dark matter. Hence, cosmologists take an effort to turn methods such as cosmic shear into efficient and robust cosmological probes, aiming at a unified and consistent picture of the four fundamental forces of nature and the standard models of particle physics and cosmology.

Chapter 3

Weak gravitational lensing

According to General Relativity, massive objects induce a local perturbation of the curvature of spacetime. Through this curved spacetime light takes the shortest possible path by moving along null geodesics, i.e. geodesics with tangent vectors of length zero. As a consequence the light path in the vicinity of a celestial body may appear bent to a distant observer. Similar to an optical collecting lens, astrophysical objects can thus focus the light of a background light source (see e.g. Refsdal & Surdej 1994), motivating the name gravitational lensing for this effect.

The gravitational deflection of background starlight by the Sun, measured during a Solar eclipse in 1919, turned out to be twice as large as predicted by a Newtonian approach. This finding marked the first observational confirmation of General Relativity, contributing considerably to the common acceptance of the theory (Eddington 1920). While Einstein calculated parameters of the lensing effect by a Milky Way star and concluded it to be unobservable (Einstein 1936), Zwicky claimed (and anticipated) that lensing of an extragalactic source by a galaxy would be observable and that corresponding lens systems would abound (Zwicky 1937a,b). It still took more than four decades before the first gravitational lens system was discovered by Walsh et al. (1979). Then observations and discoveries quickly accumulated, in particular by virtue of the development of CCDs and radio interferometry.

Since the 1990's gravitational lensing has become a standard tool of astronomy, with applications ranging from the study of magnified high-redshift galaxies to quasar time delay measurements, micro-lensing of dark astrophysical objects in the halo of the Milky Way, and the discovery of Earth-like extra-solar planets. Its strongest virtue lies in the fact that the deflection of light is sensitive to the total matter content entering the energy-momentum tensor, irrespective of its physical state. Therefore lensing can be used to directly map the distribution of dark matter, providing valuable observational support for its existence (e.g. Clowe et al. 2006). The theory of gravitational lensing, which will be outlined in the following, is particularly 'clean' in the sense that it is based solely on gravity and does not invoke the complex processes inherent to baryonic physics.

This work concentrates on weak gravitational lensing, comprising all methods that infer lensing from an ensemble of objects in a statistical way due to the weakness of the effect. In Sect. 3.1 a general overview on gravitational lens theory is presented before turning to the problem of measuring the small shear effect induced by lensing from observational data in Sect. 3.2. Section 3.3 is devoted to the principle of cosmic shear, the weak gravitational lensing effect by the large-scale structure of the Universe. Measures of cosmic shear are introduced in Sect. 3.4, and in Sect. 3.5 a brief account of the current status and future prospects of cosmic shear measurements is provided.

3.1 Gravitational lens theory

Consider a gravitational lens system consisting of a light source in the background, an isolated massive structure like a galaxy and its halo acting as the lens, and an observer on Earth. In any relevant astrophysical situation the distances between light source and lens as well as between lens and observer are large compared to the line-of-sight extension of the lens. Thus, in analogy to the thin-lens approximation in optics, it is fair to approximate the light paths between source and lens and between lens and observer as straight, with a single deflection taking place in a plane perpendicular to the line of sight containing the lens. This assumption alters the calculation of gravitational light deflection from an application of General Relativity to essentially a simple geometric problem.

Only the deflection angle in the lens plane has to be provided by General Relativity because it is this quantity into which gravitational physics enter. As detailed in Bartelmann & Schneider (2001), see also Joachimi (2007), the deflection angle $\hat{\boldsymbol{\alpha}}$, defined as the difference in direction between in- and outgoing ray, is given by

$$\hat{\boldsymbol{\alpha}}(\boldsymbol{\xi}) = \frac{2}{c^2}\int_0^{\chi_\mathrm{hor}} \mathrm{d}\chi\, \nabla_\perp \Phi(\boldsymbol{\xi},\chi)\;, \tag{3.1}$$

where Φ denotes the gravitational potential of the lens. The gradient is taken with respect to the two spatial coordinates perpendicular to the line of sight while the integration runs over the comoving distance. Here and in the following, $\hat{\boldsymbol{\alpha}}$ and other angles are written as two-dimensional vectors as they are in addition assigned a direction perpendicular to the line of sight. The comoving vector $\boldsymbol{\xi}$ is also two-dimensional and lies in the lens plane. Equation (3.1) states that the deflection angle at a certain position $\boldsymbol{\xi}$ in the lens plane is given by the transverse changes in the gravitational potential, integrated over the line of sight.

For a point mass M located at $\boldsymbol{\xi} = 0$ the deflection angle (3.1) reads (Bartelmann & Schneider 2001)

$$\hat{\boldsymbol{\alpha}}(\boldsymbol{\xi}) = \frac{4GM}{c^2}\frac{\boldsymbol{\xi}}{|\boldsymbol{\xi}|^2}\;, \tag{3.2}$$

where G is Newton's constant. This finding can be generalised to arbitrary mass distributions by assuming that the lens is composed of an ensemble of point masses m_i, so that

$$\begin{aligned}\hat{\boldsymbol{\alpha}}(\boldsymbol{\xi}) &= \frac{4G}{c^2}\sum_i m_i\,\frac{\boldsymbol{\xi}-\boldsymbol{\xi}_i}{|\boldsymbol{\xi}-\boldsymbol{\xi}_i|^2} \approx \frac{4G}{c^2}\int \mathrm{d}^2\xi' \int_0^{\chi_\mathrm{hor}} \mathrm{d}\chi\,\rho(\boldsymbol{\xi}',\chi)\,\frac{\boldsymbol{\xi}-\boldsymbol{\xi}'}{|\boldsymbol{\xi}-\boldsymbol{\xi}'|^2} \\ &= \frac{4G}{c^2}\int \mathrm{d}^2\xi'\,\Sigma(\boldsymbol{\xi}')\,\frac{\boldsymbol{\xi}-\boldsymbol{\xi}'}{|\boldsymbol{\xi}-\boldsymbol{\xi}'|^2}\;,\end{aligned} \tag{3.3}$$

where in the last step the surface mass density

$$\Sigma(\boldsymbol{\xi}) \equiv \int_0^{\chi_\mathrm{hor}} \mathrm{d}\chi\,\rho(\boldsymbol{\xi},\chi) \tag{3.4}$$

was defined. The approximation in (3.3) requires that the change in the separation of the actual light ray from its fiducial, undeflected path is small across the line-of-sight extension of the lens, so that the value of the impact parameter $\boldsymbol{\xi}-\boldsymbol{\xi}'$ for the individual mass elements m_i becomes independent of the comoving distance. Again, this is ensured by the thin-lens approximation which holds true to high accuracy in all astrophysical situations. Consequently, the mass distribution of the lens can be projected onto the lens plane, its properties characterised by the surface mass density.

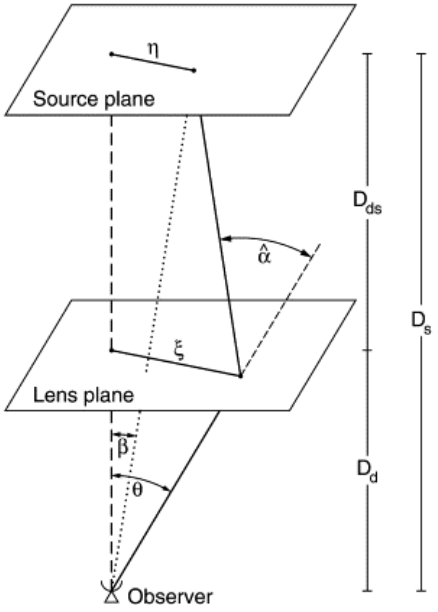

Figure 3.1: Sketch of the geometry of lens mapping. The dashed line denotes the optical axis. The light of a source at position $\boldsymbol{\eta}$ in the source plane is deflected at position $\boldsymbol{\xi}$ in the lens plane by the angle $\hat{\boldsymbol{\alpha}}$. The image is observed under an angle $\boldsymbol{\theta}$ whereas in absence of gravitational lensing it would be observed under an angle $\boldsymbol{\beta}$ (from Bartelmann & Schneider 2001).

With the relevant physics encoded in (3.3), one can now link this result to the geometrical situation, which is shown in Fig. 3.1. Following the notation of this figure, the angular diameter distances from source to observer D_s, from lens to observer D_d and from source to lens D_ds are defined. Note that $D_\mathrm{s} = D_\mathrm{d} + D_\mathrm{ds}$ holds approximately in the local Universe, but is generally not valid in an expanding spacetime. From the figure one can read off the relations $\boldsymbol{\xi} = D_\mathrm{d}\,\boldsymbol{\theta}$ and $\boldsymbol{\eta} = D_\mathrm{s}\,\boldsymbol{\beta}$, where $\boldsymbol{\eta}$ is the position of the light source in the source plane. The vectors $\boldsymbol{\xi}$ and $\boldsymbol{\eta}$ are (or would be, in case of the source plane) observed under the angles $\boldsymbol{\theta}$ and $\boldsymbol{\beta}$, respectively. Throughout, the small-angle approximation $\sin x \approx \tan x \approx x$ has been used. The origin in each plane is located at the intersection with the optical axis. By means of simple geometric relations, evident from Fig. 3.1, one can derive the lens equation

$$\boldsymbol{\theta} = \boldsymbol{\beta} + \frac{D_\mathrm{ds}}{D_\mathrm{s}}\,\hat{\boldsymbol{\alpha}}(\boldsymbol{\xi}) \equiv \boldsymbol{\beta} + \boldsymbol{\alpha}(\boldsymbol{\theta})\;, \tag{3.5}$$

where $\boldsymbol{\alpha}(\boldsymbol{\theta})$ is the scaled deflection angle. The lens equation yields the observed positions of the lensed image $\boldsymbol{\theta}$ for a given true position of the source $\boldsymbol{\beta}$ and the deflection angle $\boldsymbol{\alpha}$.

Equation (3.3) can then be rewritten in the form

$$\boldsymbol{\alpha}(\boldsymbol{\theta}) = \frac{4G}{c^2}\frac{D_\mathrm{d}D_\mathrm{ds}}{D_\mathrm{s}}\int \mathrm{d}^2\theta'\,\Sigma(\boldsymbol{\theta}' D_\mathrm{d})\,\frac{\boldsymbol{\theta}-\boldsymbol{\theta}'}{|\boldsymbol{\theta}-\boldsymbol{\theta}'|^2} = \frac{1}{\pi}\int \mathrm{d}^2\theta'\kappa(\boldsymbol{\theta}')\,\frac{\boldsymbol{\theta}-\boldsymbol{\theta}'}{|\boldsymbol{\theta}-\boldsymbol{\theta}'|^2}\;. \tag{3.6}$$

In the second step we defined the dimensionless surface mass density or convergence

$$\kappa(\boldsymbol{\theta}) \equiv \frac{\Sigma(\boldsymbol{\theta} D_\mathrm{d})}{\Sigma_\mathrm{cr}} \quad \text{with} \quad \Sigma_\mathrm{cr} = \frac{c^2}{4\pi G}\frac{D_\mathrm{s}}{D_\mathrm{d}D_\mathrm{ds}}\;, \tag{3.7}$$

where the constants and distances were absorbed into the critical surface mass density Σ_cr. Moreover, one defines a scalar quantity, the deflection potential

$$\Psi(\boldsymbol{\theta}) \equiv \frac{1}{\pi}\int \mathrm{d}^2\theta'\kappa(\boldsymbol{\theta}')\ln|\boldsymbol{\theta}-\boldsymbol{\theta}'|\;, \tag{3.8}$$

yielding the relations

$$\boldsymbol{\alpha}(\boldsymbol{\theta}) = \nabla\Psi(\boldsymbol{\theta})\;; \quad \nabla^2\Psi(\boldsymbol{\theta}) = 2\kappa(\boldsymbol{\theta})\;. \tag{3.9}$$

These definitions create a triple of quantities $\{\kappa, \alpha, \Psi\}$ which is equivalent to the matter density, the gravitational field, and the gravitational potential in three-dimensional problems of gravitation. Note that the last equality in (3.9) is a two-dimensional Poisson equation.

If $\beta \ll 1$, i.e. if observer, lens and source are nearly aligned, the lens equation (3.5) can have more than one solution for $\boldsymbol{\theta}$. This corresponds to the realm of strong lensing, where lensing effects can be studied on individual images of the background object (see e.g. Kochanek 2006). If the modulus of $\boldsymbol{\beta}$ is much larger than the modulus of the deflection angle, the position of the image of the source is basically unaltered, i.e. $\boldsymbol{\theta} \approx \boldsymbol{\beta}$. Still, gravitational lensing leaves a distinct imprint via the differential deflection of the light of the source.

First, the differential deflection changes the solid angle under which the source is seen. Since the process of lensing obviously is not related to absorption or emission of photons, the intensity or equivalently the surface brightness remain the same. As a consequence, the observed flux from the source changes, leading to a magnification or demagnification of the background object. Second, images of the source can also be distorted due to the tidal gravitational field of the lens. Both effects are described by the Jacobian matrix of the lens mapping

$$A_{ij}(\boldsymbol{\theta}) \equiv \frac{\partial \beta_i}{\partial \theta_j} = \delta_{ij} - \frac{\partial^2 \Psi}{\partial \theta_i \partial \theta_j} \,, \tag{3.10}$$

where the second equality follows from (3.5) and (3.9). Introducing the gravitational shear γ as a complex quantity

$$\gamma = \gamma_1 + \mathrm{i}\gamma_2 \quad \text{with} \quad \gamma_1 = \frac{1}{2}\left(\frac{\partial^2 \Psi}{\partial \theta_1^2} - \frac{\partial^2 \Psi}{\partial \theta_2^2}\right); \quad \gamma_2 = \frac{\partial^2 \Psi}{\partial \theta_1 \partial \theta_2} \,, \tag{3.11}$$

the Jacobian matrix can be rewritten as

$$A(\boldsymbol{\theta}) = \begin{pmatrix} 1-\kappa-\gamma_1 & -\gamma_2 \\ -\gamma_2 & 1-\kappa+\gamma_1 \end{pmatrix} = (1-\kappa)\,\mathrm{id}_2 - |\gamma| \begin{pmatrix} \cos 2\varphi & \sin 2\varphi \\ \sin 2\varphi & -\cos 2\varphi \end{pmatrix} \,. \tag{3.12}$$

The second equality provides an illustrative understanding. The convergence κ yields isotropic focusing, whereas γ quantifies distortions of the image (plus anisotropic focusing). Sources with circular isophotes are mapped into elliptical images, where a combination of κ and $|\gamma|$ determines the length of the major and minor axes, while the polar angle of γ, denoted by φ, describes the orientation of the ellipse. Note that the angular dependence of γ is given by the angle 2φ which maps γ onto itself after a rotation by π, characterising γ as a polar. Since the unlensed image of the source is not observable, neither the focusing nor the shear effect can be measured directly for a single object in weak lensing, but both effects can be inferred from an ensemble of background galaxies.

Plugging (3.8) into (3.11) yields a relation between shear and convergence,

$$\gamma(\boldsymbol{\theta}) = \frac{1}{\pi} \int \mathrm{d}^2\theta' \; \mathcal{D}(\boldsymbol{\theta} - \boldsymbol{\theta'}) \; \kappa(\boldsymbol{\theta'}) \quad \text{with} \quad \mathcal{D}(\boldsymbol{\theta}) = \frac{\theta_2^2 - \theta_1^2 - 2\mathrm{i}\theta_1\theta_2}{|\boldsymbol{\theta}|^4} \,. \tag{3.13}$$

This convolution simplifies in Fourier space to a simple multiplication of the form

$$\tilde{\gamma}(\boldsymbol{\ell}) = \mathrm{e}^{2\mathrm{i}\beta} \; \tilde{\kappa}(\boldsymbol{\ell}) \,, \tag{3.14}$$

where β is the polar angle of the angular frequency $\boldsymbol{\ell}$, which is the Fourier variable corresponding to the angle $\boldsymbol{\theta}$. A tilde is used to denote Fourier transforms. If one is able to measure the shear, one readily obtains the convergence which in turn is related to the projected matter density, see (3.7). This can be exploited to construct celestial maps of the distribution of gravitating mass (see Kaiser & Squires 1993).

The magnification μ is defined as the ratio of the flux of the lensed image over the flux of the source. The flux in both the lens and source planes is given by the integral over the intensity in the plane. Since the intensity is not affected by lensing, only the mapping from source plane coordinates $\boldsymbol{\beta}$ to lens plane coordinates $\boldsymbol{\theta}$ is relevant, producing a factor $\det A$, see (3.10). Thus the magnification is given by

$$\mu = \frac{1}{\det A} = \frac{1}{(1-\kappa)^2 - |\gamma|^2} \approx 1 + 2\,\kappa\;. \tag{3.15}$$

To arrive at the second equality, (3.12) was inserted. The final expression holds approximately for $\kappa, |\gamma| \ll 1$ and is obtained by dropping the term quadratic in γ, doing a Taylor expansion around $\kappa = 0$, and truncating after the first order. Equation (3.15) is also valid in cosmic shear if the lensing potential and κ are defined such that the basic relations of lens mapping (3.9) still hold (Bartelmann & Schneider 2001), see Sect. 3.3.

Magnification effects can be observed via their influence on number density counts in flux limited surveys. Gravitational lensing locally stretches the sky, thereby enhancing the flux of galaxies within that region but reducing the observed number density of objects with a given luminosity in the field. If $n(>S, \boldsymbol{x})$ denotes the observed number density of galaxies with flux larger than S in a region specified by the comoving vector $\boldsymbol{x}$, one thus finds

$$n(>S, \boldsymbol{x}) = \frac{1}{\mu(\boldsymbol{x})}\; n_0\left(> \frac{S}{\mu(\boldsymbol{x})}, \boldsymbol{x}\right)\;, \tag{3.16}$$

where $n_0(>S, \boldsymbol{x})$ is the galaxy number density in absence of lensing. Note that the possible dependence of μ on angular position and redshift or comoving distance has been made explicit by adding the argument $\boldsymbol{x}$. The first term of μ in (3.16) corresponds to the depletion of counts due to the stretching of the sky and the second term containing μ to the enhancement of flux above the detection limit S. The bigger part of this work will concentrate on exploiting the shear effect of weak lensing, but we are going to include lensing magnification into our considerations in Chaps. 5 and 8.

3.2 Shear measurement

Faint galaxies are abundant on the sky and thus serve as good background sources for measuring the lensing effect by foreground structures. However, the practical measurement of the gravitational shear is anything but straightforward due to the smallness of the lensing effect. Furthermore the typical background galaxy image has low signal-to-noise, small angular extent, and does neither have a smooth nor an intrinsically circular shape. Besides, the measurement of shears is very sensitive to atmospheric and instrumental effects. For the remainder of this work we will assume that the non-astrophysical issues in shear measurement have been accurately dealt with, but due to their importance we provide a brief overview on the practicalities of obtaining the shear in the following.

Galaxy images on the sky are not circular, either due to an intrinsically triaxial light distribution or due to an inclination of disks with respect to the line of sight. To first approximation the isophotes of galaxies are elliptical, and would remain so when lensing acts upon them, but measurements of this ellipticity are complicated by complex structures and the pixelisation of the image on the CCD. Suppose a galaxy image has a brightness distribution $I(\boldsymbol{\theta})$. Then one can define the first brightness moment of this distribution to mark the centre $\boldsymbol{\theta}_\mathrm{c}$ of the image,

$$\boldsymbol{\theta}_\mathrm{c} = \frac{\int \mathrm{d}^2\theta\; I(\boldsymbol{\theta})\; H\left[I(\boldsymbol{\theta}) - I_\mathrm{thr}\right]\; \boldsymbol{\theta}}{\int \mathrm{d}^2\theta\; I(\boldsymbol{\theta})\; H\left[I(\boldsymbol{\theta}) - I_\mathrm{thr}\right]}\;, \tag{3.17}$$

where $H\,[I]$ is the Heaviside step function. Via this definition $\boldsymbol{\theta}_\mathrm{c}$ is the centre of light within a limiting isophote of intensity I_thr. Note that weight functions of the intensity other than $H\,[I]$ are possible in (3.17). The quadrupole moment of the brightness distribution constitutes a symmetric tensor

$$Q_{ij} = \frac{\int \mathrm{d}^2\theta\; I(\boldsymbol{\theta})\; H\,[I(\boldsymbol{\theta}) - I_\mathrm{thr}]\;\; (\theta_i - \theta_{\mathrm{c},i})(\theta_j - \theta_{\mathrm{c},j})}{\int \mathrm{d}^2\theta\; I(\boldsymbol{\theta})\; H\,[I(\boldsymbol{\theta}) - I_\mathrm{thr}]}\;; \quad i,j = \{1,2\}\;. \tag{3.18}$$

The three independent components of the quadrupole can then be used to define an ellipticity of the image as

$$\epsilon \equiv \frac{Q_{11} - Q_{22} + 2\mathrm{i}\,Q_{12}}{Q_{11} + Q_{22} + 2\sqrt{\det Q}}\;. \tag{3.19}$$

Both (3.18) and (3.19) are not unique, e.g. a widely used alternative for ϵ, sometimes called polarisation, employs a different normalisation (Bartelmann & Schneider 2001). The choice of the numerator in (3.19) implies that ϵ has the same polar transformation behaviour under rotations as γ. If the isophotes of an image are perfectly elliptical with major axis a and minor axis b, then one finds $|\epsilon| = (1 - b/a)/(1 + b/a)$. Then the phase of the complex quantity ϵ describes the orientation of the ellipse with respect to the θ_1-axis.

Analogous definitions to (3.18) and (3.19) can be made for the intrinsic ellipticity ϵ^s of an unlensed galaxy image. With these definitions at hand, Seitz & Schneider (1997) showed that the measured ellipticity ϵ is related to the lensing induced shear and the intrinsic ellipticity via

$$\epsilon = \frac{\epsilon^\mathrm{s} + g}{1 + \epsilon^\mathrm{s} g^*} \approx \epsilon^\mathrm{s} + g \approx \epsilon^\mathrm{s} + \gamma \quad \text{with} \quad g \equiv \frac{\gamma}{1 - \kappa}\;, \tag{3.20}$$

where g is called reduced shear. The approximations made in (3.20) are valid for sufficiently weak gravitational fields, i.e. $\kappa, |\gamma| \ll 1$. Hence, under these assumptions the observed ellipticity is just the sum of the gravitational shear γ and the intrinsic ellipticity ϵ^s.

However, the intrinsic shape of a lensed galaxy is not directly accessible via observations. Besides, the contribution from ϵ^s to the measured ellipticity is in general about two orders of magnitude larger than the shear, so that only by averaging over many galaxy images in a region of the sky can the shear be obtained as the expectation value of the ellipticity, $\langle\epsilon\rangle = \gamma$. This relation holds under the viable condition that the intrinsic shapes of galaxies are randomly oriented in the sky, so that $\langle\epsilon^\mathrm{s}\rangle = 0$.

Since the distribution of matter is isotropic on large scales, the expectation values of all quantities bearing a phase, so in particular also the shear γ, should vanish. Therefore one considers second-order (or higher) statistics of the shear field instead, some of which we will present in Sect. 3.4. These measures are all based on correlators of the ellipticities of two populations of galaxies i and j, $\left\langle\epsilon_i\epsilon_j^*\right\rangle = \left\langle\gamma_i\gamma_j^*\right\rangle$. This equation holds if the intrinsic ellipticities of different galaxies are uncorrelated, and if the intrinsic ellipticities are not correlated with the shear of other galaxies. Although this assumption has been standard hitherto in both theory and observations, it is in general not true, as will be detailed in Chap. 5.

Using the relations given above, it is in principle possible to determine the gravitational shear from data. However, reading off ellipticities of galaxies from a telescopic image is a highly non-trivial task. First of all, one has to observe a large number of galaxies to beat down the noise due to intrinsic shapes. Hence, observations are preferentially deep, increasing the number of faint galaxies as much as possible, and in addition made in the optical or near-infrared band, where the sky is populated densest. Faint galaxies are small in angular extent, often similar to the size of the point spread function (PSF).

For space-based observations the PSF is determined by the optical system of the telescope. Its size can be very small, but also anisotropic, thereby mimicking a shear. Ground-based PSFs are governed by the blurring due to Earth's atmosphere and at best have a full width half maximum of 0.5 to 1 arcseconds, depending on the site. Hence, in this case galaxy images are circularised by the PSF, leading to an underestimation of the shear. In spite of the larger size of the PSF, anisotropy can still be induced by e.g. telescope jitter. Obviously the properties of the PSF have to be specified to high accuracy for shear measurements. Usually this is achieved by interpolating the PSF obtained from point sources in the field such as stars. In practice the translation from stellar point spread functions to the PSF at the position of the galaxies is further complicated by e.g. a colour dependence of the PSF (see Cypriano et al. 2010).

Moreover the requirements on the optical system and the data reduction pipeline are also high because camera distortions or an inaccurate astrometric calibration can again be a source of artificial shear. A small field of view would reduce this problem, but large-area surveys are highly desirable to improve the statistics. The image quality and consequently the shear measurement suffers from various other aspects such as saturated stars, fringing, bad pixels, charge transfer inefficiency due to radiation damage, temporal and spatial focus variations, gaps on multi-chip detectors etc.

Even if all these effects have been successfully treated, the direct application of (3.18) is hampered by pixelisation, i.e. the fact that information about the flux of a galaxy is only available on a relatively coarse grid. In addition, galaxy images may not be isolated due to close-by masks or neighbouring galaxies. Voigt & Bridle (2010) have shown that the obtained ellipticity can even depend on the choice of the threshold intensity in (3.18) if the galaxy has an ellipticity gradient, i.e. a change of the isophotal shape with radius.

It is evident that a lot of effort has to be put into the measurement of image ellipticities in order to avoid the introduction of systematic errors. The most widely used implementation to arrive at unbiased estimators of the shear is the KSB scheme (Kaiser et al. 1995). Other approaches include the fitting of complete sets of functions to the galaxy image, e.g. shapelets (Réfrégier 2003), or modelling the original galaxy image before applying a gravitational shear and the PSF convolution to reproduce the observed brightness distribution (e.g. Kuijken 1999). Erben et al. (2001) have shown that KSB causes systematic errors on the shear of the order 10 %, so that it is not suited for upcoming high-precision weak lensing studies. There is active research going on in the comparison of shear measurement methods (Heymans et al. 2006a; Massey et al. 2007a; Bridle et al. 2010) and the development of new techniques (e.g. Bernstein 2010).

Weak lensing statistics have a wide range of applications and can for instance be measured in the outer regions of galaxy clusters to determine the total mass and the density profile of the cluster halo (e.g. Israel et al. 2010). Although the shear induced by a single galaxy halo is too small to be detected, one can superpose sets of foreground lenses and background sources in order to obtain statistical properties of the density distributions of galactic haloes and correlations between visible and dark matter – a method known as galaxy-galaxy lensing (see Chap. 8). Finally, one can consider the weak lensing effect by the large-scale structure of the Universe, which shall be dealt with in detail below.

3.3 Foundations of cosmic shear

The shear effect on the images of distant galaxies is generated by the continuous deflection and distortion of light by all the intervening matter inhomogeneities along the line of sight, see Fig. 3.2 for an illustration. Hence cosmic shear differs fundamentally from other variants of weak

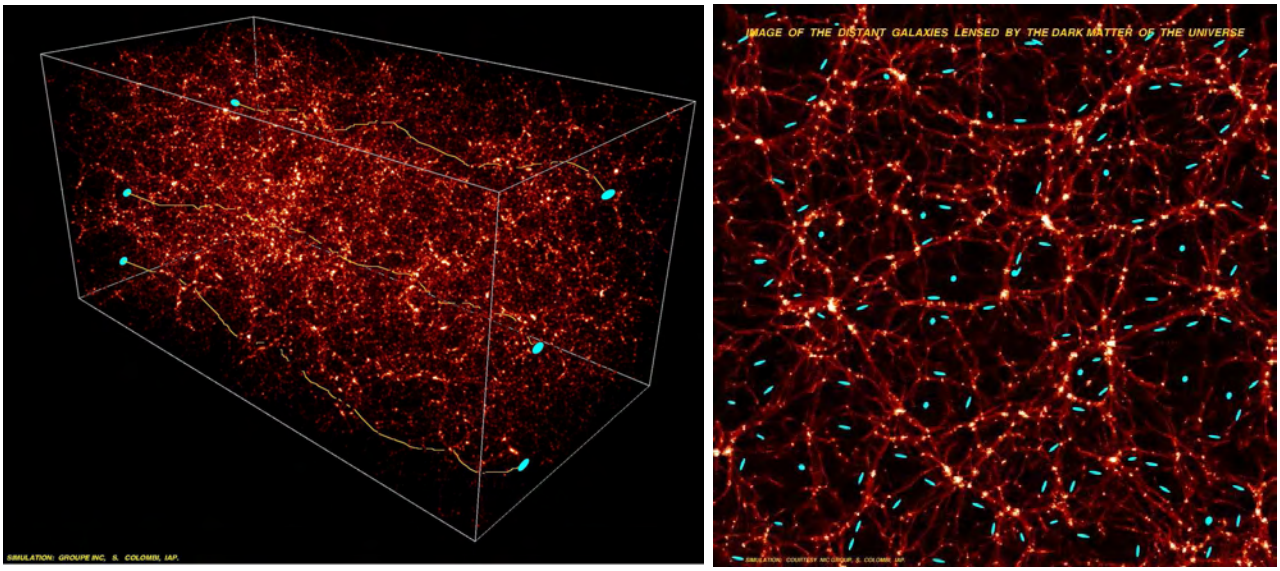

Figure 3.2: Cosmic shear observed through a simulated dark matter distribution. *Left panel*: Simulated ray paths through an N-body simulation. Image ellipticities are given both at the start and the end of the light paths. Note that the light deflections have been exaggerated. *Right panel*: Projection along the line of sight as it would be seen by an observer (S. Colombi).

gravitational lensing for which the deflection stems from a localised mass concentration. This implies in particular that the thin-lens approximation cannot be applied anymore. Technical details about the derivation of the cosmic shear formalism can be found in Bartelmann & Schneider (2001), see also Schneider (2006) and Joachimi (2007).

One considers the transverse separation of two light rays which start at the observer and are separated by an angle $\boldsymbol{\theta}$. These light rays then propagate through the inhomogeneous Universe, where the changes in the separation of the rays are determined by the transverse gradient of the gravitational potentials at the positions of the light rays. A key step to proceed analytically is the application of the Born approximation, implying that the potential gradients are measured at the positions of the unperturbed light rays instead of the true ones. The Born approximation is valid if the difference between deflection angles of neighbouring light rays is small, which holds true if the gravitational potentials are shallow. Moreover, the coupling between light deflections at different redshifts is neglected, enabling one to calculate the effective light deflection via simply integrating over the contributions along the line of sight. Limitations of and corrections to these important assumptions are discussed in Schneider et al. (1998), see also Hilbert et al. (2009) for a comparison with ray-tracing simulations.

After applying the Born approximation and neglecting lens-lens coupling, one obtains a net deflection angle, measured with respect to an arbitrarily defined nearby fiducial ray, of

$$\boldsymbol{\alpha}(\boldsymbol{\theta},\chi) = \frac{2}{c^2}\int_0^\chi \mathrm{d}\chi' \, \frac{f_\mathrm{k}(\chi-\chi')}{f_\mathrm{k}(\chi)} \, \nabla_\perp \Phi\left(f_\mathrm{k}(\chi')\boldsymbol{\theta},\chi'\right) \;, \tag{3.21}$$

for the image of a source that is located in direction $\boldsymbol{\theta}$ and at a comoving distance χ (Bartelmann & Schneider 2001). As before, $\nabla_\perp\Phi$ denotes the gradient of the gravitational potential perpendicular to the line of sight. Note that $\boldsymbol{\alpha}(\boldsymbol{\theta},\chi)$ is not uniquely defined due to the arbitrariness of the reference light ray.

To keep the lens mapping formalism, one can now use (3.9) to define an effective lensing potential and an effective convergence from (3.21), the latter reading

$$\kappa(\boldsymbol{\theta},\chi) = \frac{3H_0^2\Omega_\mathrm{m}}{2c^2}\int_0^\chi \mathrm{d}\chi' \, \frac{f_\mathrm{k}(\chi')\, f_\mathrm{k}(\chi-\chi')}{f_\mathrm{k}(\chi)} \, \frac{\delta\left(f_\mathrm{k}(\chi')\boldsymbol{\theta},\chi'\right)}{a(\chi')} \;, \tag{3.22}$$

where the Poisson equation (2.28) was employed to replace the gravitational potential by the matter density contrast. Via (3.22) we have defined an equivalent lens plane for each comoving distance χ to the background light source by projecting the matter density contrast between the source and the observer along the line of sight.

Usually the large number of galaxies used as sources for cosmic shear analyses are spread out along the line of sight. If one denotes the distance probability distribution of a population i of source galaxies by $p^{(i)}(\chi)$, one obtains a source-averaged convergence as

$$\kappa^{(i)}(\boldsymbol{\theta}) \equiv \int_0^{\chi_\mathrm{hor}} \mathrm{d}\chi \; p^{(i)}(\chi) \; \kappa(\boldsymbol{\theta}, \chi) \; , \tag{3.23}$$

where the upper limit of integration is the maximum comoving distance at which objects can be observed, i.e. the comoving horizon distance given by (2.11). Plugging in (3.22) and rearranging the integration over χ and χ', one arrives at

$$\begin{aligned} \kappa^{(i)}(\boldsymbol{\theta}) &= \frac{3H_0^2\Omega_\mathrm{m}}{2c^2} \int_0^{\chi_\mathrm{hor}} \mathrm{d}\chi \int_\chi^{\chi_\mathrm{hor}} \mathrm{d}\chi' \; p^{(i)}(\chi') \; \frac{f_\mathrm{k}(\chi) \; f_\mathrm{k}(\chi'-\chi)}{f_\mathrm{k}(\chi')} \; \frac{\delta\left(f_\mathrm{k}(\chi)\boldsymbol{\theta}, \chi\right)}{a(\chi)} \\ &= \frac{3H_0^2\Omega_\mathrm{m}}{2c^2} \int_0^{\chi_\mathrm{hor}} \mathrm{d}\chi \; \frac{g^{(i)}(\chi) \; f_\mathrm{k}(\chi)}{a(\chi)} \; \delta\left(f_\mathrm{k}(\chi)\boldsymbol{\theta}, \chi\right) \; , \end{aligned} \tag{3.24}$$

where in the second step the lensing efficiency

$$g^{(i)}(\chi) \equiv \int_\chi^{\chi_\mathrm{hor}} \mathrm{d}\chi' \; p^{(i)}(\chi') \; \frac{f_\mathrm{k}(\chi'-\chi)}{f_\mathrm{k}(\chi')} \tag{3.25}$$

was defined. The lensing efficiency $g^{(i)}(\chi)$ corresponds to the average ratio $D_\mathrm{ds}/D_\mathrm{s}$ of distance between lens and source over distance between source and observer, weighted by the distance probability distribution of source galaxies.

Now we are interested in the power spectrum of the convergence as given by (3.24). To this end, the Fourier transforms of the convergence and the density contrast are introduced,

$$\tilde{\kappa}^{(i)}(\boldsymbol{\ell}) = \int \mathrm{d}^2\theta \; \mathrm{e}^{\mathrm{i}\boldsymbol{\ell}\cdot\boldsymbol{\theta}} \; \kappa^{(i)}(\boldsymbol{\theta}) \; ; \tag{3.26}$$

$$\delta\left(f_\mathrm{k}(\chi)\boldsymbol{\theta}, \chi\right) = \int \frac{\mathrm{d}^3k}{(2\pi)^3} \; \mathrm{e}^{-\mathrm{i}\boldsymbol{k}_\perp\cdot\boldsymbol{\theta} f_\mathrm{k}(\chi)} \; \mathrm{e}^{-\mathrm{i}k_\parallel\chi} \; \tilde{\delta}(\boldsymbol{k}, \chi) \; , \tag{3.27}$$

where $\boldsymbol{k}_\perp$ is the component of the three-dimensional wave vector in the plane perpendicular to the line of sight, and correspondingly, $k_\parallel$ lies parallel to it. Note that the second argument of the Fourier transform of the density contrast denotes the cosmic epoch, like for δ in real space. With the convenient abbreviation

$$q^{(i)}(\chi) \equiv \frac{3H_0^2\Omega_\mathrm{m}}{2c^2} \; \frac{g^{(i)}(\chi) \; f_\mathrm{k}(\chi)}{a(\chi)} \; , \tag{3.28}$$

one can then write the Fourier transform of the convergence as

$$\tilde{\kappa}^{(i)}(\boldsymbol{\ell}) = \int \mathrm{d}^2\theta \int_0^{\chi_\mathrm{hor}} \mathrm{d}\chi \int \frac{\mathrm{d}^3k}{(2\pi)^3} \; q^{(i)}(\chi) \; \tilde{\delta}(\boldsymbol{k}, \chi) \; \mathrm{e}^{-\mathrm{i}\boldsymbol{\theta}\cdot(\boldsymbol{k}_\perp f_\mathrm{k}(\chi) - \boldsymbol{\ell})} \; \mathrm{e}^{-\mathrm{i}k_\parallel\chi} \; , \tag{3.29}$$

where (3.26), (3.24), and (3.27) were used successively.

The two-dimensional power spectrum of the lensing convergence is defined in analogy to (2.23) via

$$\left\langle \tilde{\kappa}^{(i)}(\boldsymbol{\ell}) \; \tilde{\kappa}^{(j)\,*}(\boldsymbol{\ell'}) \right\rangle = (2\pi)^2 \; \delta_\mathrm{D}^{(2)}(\boldsymbol{\ell} - \boldsymbol{\ell'}) \; P_\kappa^{(ij)}(\ell) \tag{3.30}$$

for two galaxy populations i and j. From (3.29) one can derive the necessary two-point correlation of convergences,

$$\begin{aligned}\left\langle\tilde{\kappa}^{(i)}(\boldsymbol{\ell})\;\tilde{\kappa}^{(j)\,*}(\boldsymbol{\ell'})\right\rangle &= \int \mathrm{d}^2\theta \int \mathrm{d}^2\theta' \int_0^{\chi_\mathrm{hor}} \mathrm{d}\chi \int_0^{\chi_\mathrm{hor}} \mathrm{d}\chi' \int \frac{\mathrm{d}^3k}{(2\pi)^3} \int \frac{\mathrm{d}^3k'}{(2\pi)^3} \left\langle \tilde{\delta}(\boldsymbol{k},\chi)\;\tilde{\delta}^*(\boldsymbol{k'},\chi')\right\rangle \\ &\quad \times q^{(i)}(\chi)\;q^{(j)}(\chi')\;\mathrm{e}^{-\mathrm{i}\boldsymbol{\theta}\cdot(\boldsymbol{k}_\perp f_\mathrm{k}(\chi)-\boldsymbol{\ell})}\;\mathrm{e}^{-\mathrm{i}k_\parallel\chi}\;\mathrm{e}^{\mathrm{i}\boldsymbol{\theta'}\cdot\left(\boldsymbol{k}'_\perp f_\mathrm{k}(\chi')-\boldsymbol{\ell'}\right)}\;\mathrm{e}^{\mathrm{i}k'_\parallel\chi'} \\ &= \int \mathrm{d}^2\theta \int \mathrm{d}^2\theta' \int_0^{\chi_\mathrm{hor}} \mathrm{d}\chi \int_0^{\chi_\mathrm{hor}} \mathrm{d}\chi' \int \frac{\mathrm{d}^3k}{(2\pi)^3}\;P_\delta\left(|\boldsymbol{k}|,\frac{\chi+\chi'}{2}\right) \\ &\quad \times q^{(i)}(\chi)\;q^{(j)}(\chi')\;\mathrm{e}^{-\mathrm{i}\boldsymbol{\theta}\cdot(\boldsymbol{k}_\perp f_\mathrm{k}(\chi)-\boldsymbol{\ell})}\;\mathrm{e}^{\mathrm{i}\boldsymbol{\theta'}\cdot(\boldsymbol{k}_\perp f_\mathrm{k}(\chi')-\boldsymbol{\ell'})}\;\mathrm{e}^{-\mathrm{i}k_\parallel(\chi-\chi')}\;. \end{aligned} \tag{3.31}$$

In order to arrive at the second equality, the definition of the three-dimensional matter power spectrum (2.23) was inserted and subsequently the k'-integration over the Dirac-delta distribution executed. Note that the density contrasts in the correlator were evaluated at different epochs, so that we have chosen the mean of the comoving distances involved to specify the epoch for which the power spectrum is computed. As will be demonstrated shortly, this assumption is uncritical. In the next step the integration over angles is performed, yielding two more Dirac-delta distributions. Via the transformation $\delta_\mathrm{D}^{(2)}(\boldsymbol{\ell}-f_\mathrm{k}(\chi)\boldsymbol{k}_\perp)=\delta_\mathrm{D}^{(2)}(\boldsymbol{\ell}/f_\mathrm{k}(\chi)-\boldsymbol{k}_\perp)/f_\mathrm{k}^2(\chi)$ one is able to perform the integration over $\boldsymbol{k}_\perp$, which results in

$$\begin{aligned}\left\langle\tilde{\kappa}^{(i)}(\boldsymbol{\ell})\;\tilde{\kappa}^{(j)\,*}(\boldsymbol{\ell'})\right\rangle &= 2\pi\int_0^{\chi_\mathrm{hor}} \mathrm{d}\chi \int_0^{\chi_\mathrm{hor}} \mathrm{d}\chi' \int \mathrm{d}k_\parallel\;\frac{q^{(i)}(\chi)\;q^{(j)}(\chi')}{f_\mathrm{k}^2(\chi)} \\ &\quad \times P_\delta\left(\sqrt{\left(\frac{\boldsymbol{\ell}}{f_\mathrm{k}(\chi)}\right)^2+k_\parallel^2}\,,\frac{\chi+\chi'}{2}\right)\;\delta_\mathrm{D}^{(2)}(\boldsymbol{\ell'}-\frac{f_\mathrm{k}(\chi')}{f_\mathrm{k}(\chi)}\boldsymbol{\ell})\;\mathrm{e}^{-\mathrm{i}k_\parallel(\chi-\chi')}\;. \end{aligned} \tag{3.32}$$

Since $P_\delta(k)\to 0$ for $|\boldsymbol{k}|\to 0$, see (2.31), one can to good approximation assume that the power vanishes on sufficiently large spatial scales, and consequently if χ and χ' differ significantly. Thus it is fair to apply the so-called Limber approximation, i.e. to replace χ' by χ in the arguments of the slowly varying functions $q^{(i)}(\chi)$ and $f_\mathrm{k}(\chi)$, and to assume $(\chi+\chi')/2\approx\chi$. As a consequence the χ'-integration can be performed, yielding another delta distribution, which in turn renders the $k_\parallel$-integration trivial. The final result is

$$\left\langle\tilde{\kappa}^{(i)}(\boldsymbol{\ell})\;\tilde{\kappa}^{(j)\,*}(\boldsymbol{\ell'})\right\rangle = (2\pi)^2\;\delta_\mathrm{D}^{(2)}(\boldsymbol{\ell}-\boldsymbol{\ell'})\int_0^{\chi_\mathrm{hor}}\mathrm{d}\chi\;\frac{q^{(i)}(\chi)\;q^{(j)}(\chi)}{f_\mathrm{k}^2(\chi)}\;P_\delta\left(\frac{|\boldsymbol{\ell}|}{f_\mathrm{k}(\chi)},\chi\right)\;. \tag{3.33}$$

The comparison of (3.30) and (3.33) yields the Fourier version of Limber's equation (Kaiser 1992; for the original real-space variant see Limber 1953),

$$\begin{aligned}P_\kappa^{(ij)}(\ell) &= \int_0^{\chi_\mathrm{hor}}\mathrm{d}\chi\;\frac{q^{(i)}(\chi)\;q^{(j)}(\chi)}{f_\mathrm{k}^2(\chi)}\;P_\delta\left(\frac{\ell}{f_\mathrm{k}(\chi)},\chi\right) \\ &= \frac{9H_0^4\Omega_\mathrm{m}^2}{4c^4}\int_0^{\chi_\mathrm{hor}}\mathrm{d}\chi\;\frac{g^{(i)}(\chi)\;g^{(j)}(\chi)}{a^2(\chi)}\;P_\delta\left(\frac{\ell}{f_\mathrm{k}(\chi)},\chi\right)\;, \end{aligned} \tag{3.34}$$

where in the second equality (3.28) was re-substituted. Limber's equation states that the convergence power spectrum is given by the line-of-sight projection of the three-dimensional matter power spectrum, weighted by the lensing efficiencies of the correlated source populations. By also making use of Limber's approximation, relations between higher-order statistics of cosmic shear and the matter density contrast, such as the bispectrum, of a form similar to (3.34) can be derived, see Sect. 4.1. Note that due to (3.14) the convergence power spectrum and the power spectrum of gravitational shear, which is more closely related to actual observables, are

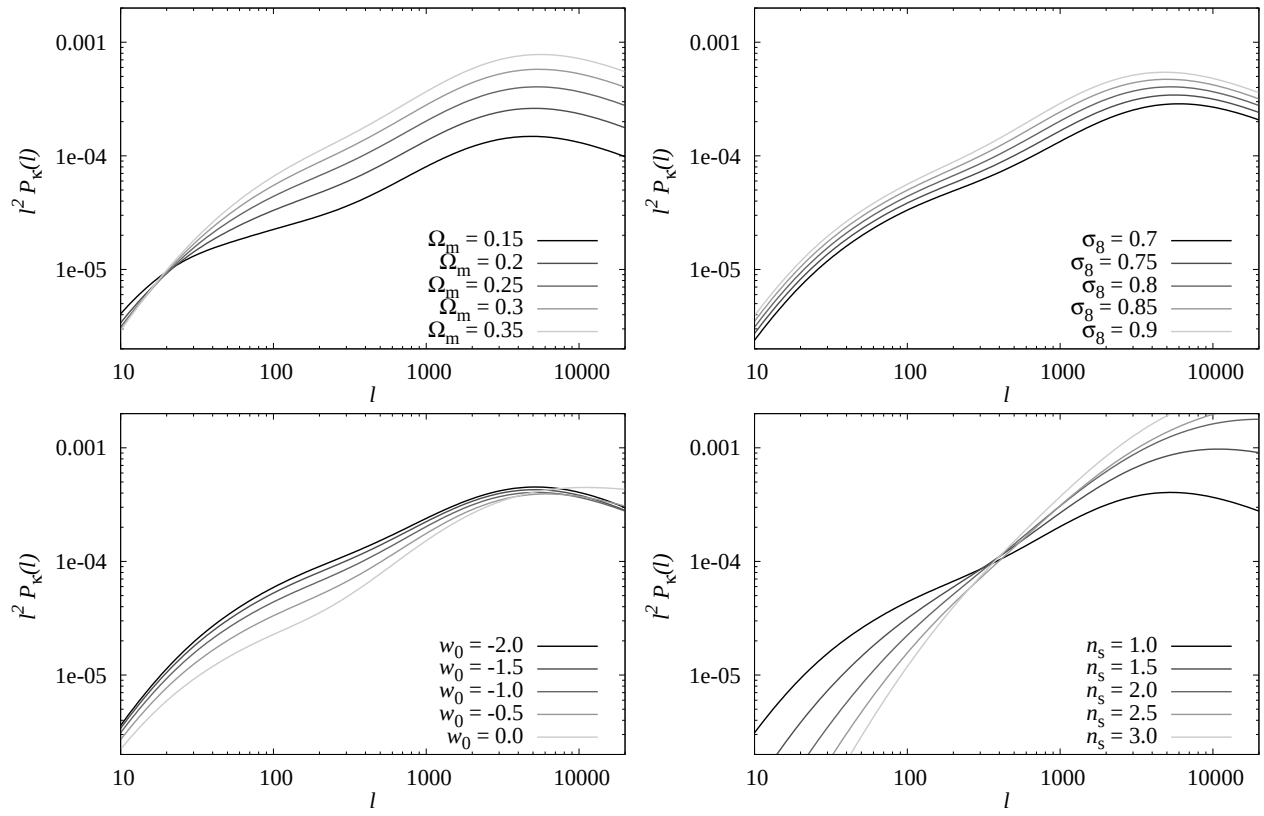

Figure 3.3: Dependence of the convergence power spectrum on cosmological parameters. In each panel one of the parameters is varied while keeping all other parameters at their values in the fiducial, spatially flat cosmology, given by $\Omega_\mathrm{m} = 0.25$, $\Omega_\mathrm{b} = 0.05$, $\sigma_8 = 0.8$, $n_\mathrm{s} = 1.0$, $h = 0.7$, $w_0 = -1.0$ and $w_a = 0$. In clockwise direction starting from the upper left panel, the parameters Ω_m, σ_8, n_s, and w_0 are varied, each as indicated in the legends. Note that since spatial flatness is kept, $\Omega_\Lambda = 1 - \Omega_\mathrm{m}$ is also varied in the first case.

identical. In the following we will omit the subscript κ of the power spectrum whenever it is unambiguous to do so.

By virtue of (3.34) it becomes evident that when obtaining the convergence power spectrum through cosmic shear observations, one can probe both the large-scale structure via the matter power spectrum and the expansion history which determines the physical distances entering (3.25). For this reason cosmic shear is particularly sensitive to most of the standard cosmological parameters, as is demonstrated in Fig. 3.3 where we show the change in convergence power spectrum when varying one parameter at a time.

As expected, the amplitude of the power spectrum directly scales with σ_8^2. The same holds true for the matter density parameter because of the prefactor in (3.34), but other dependencies via the transfer function and distances also play a role. Since we keep spatial flatness, $\Omega_\Lambda = 1 - \Omega_\mathrm{m}$ varies as well and thus modifies the growth factor and the Hubble parameter entering the distances. For low angular frequencies the overall dependence on Ω_m is only small, so that a change in Ω_m causes a tilt of the convergence power spectrum. The parameters Ω_m and σ_8 are constrained tightest by cosmic shear, but display a characteristic degeneracy due to their similar scaling, see Sect. 3.5.

Cosmic shear is also sensitive to the initial conditions of structure formation, e.g. to the slope of the primordial power spectrum n_s, as well as to dark energy. A change of n_s directly affects the slope of the three-dimensional matter power spectrum for all wave numbers. Due to

the integration over comoving distances and the χ-dependence in the first argument of P_δ in (3.34), as well as due to the amplitude of the power spectrum being fixed at $k \sim 2\pi/(8\,\mathrm{Mpc}\,h^{-1})$ via σ_8, this dependence is spread to all angular frequencies in the convergence power spectrum. Generally, a steeper slope of the matter power spectrum at small k due to a larger n_s causes an overall steeper P_κ. A modification of the dark energy equation of state in terms of w_0 leaves an imprint in the shape of the convergence power spectrum which is most pronounced at intermediate scales.

3.4 Measures of cosmic shear

As already discussed in Sect. 3.2, all meaningful measures of cosmic shear have to be at least quadratic in the shear or, in practical terms, the galaxy ellipticity. In the following an overview over a range of second-order cosmic shear measures, suited for different purposes, is presented. All of them are linearly related to the power spectrum, rendering (3.34) the central equation to connect cosmic shear measures to the underlying cosmological model.

Before defining cosmic shear measures, it is important to note that the real and imaginary part of the shear γ are not independent of each other. This follows from the fact that γ can be obtained from the scalar quantities Ψ or κ, see (3.11) and (3.13). The interdependence of the shear components can be expressed in the form of a local constraint on the second derivatives of γ via

$$\boldsymbol{u}(\boldsymbol{\theta}) \equiv \nabla\kappa(\boldsymbol{\theta}) = \begin{pmatrix} \frac{\partial\gamma_1(\boldsymbol{\theta})}{\partial\theta_1} + \frac{\partial\gamma_2(\boldsymbol{\theta})}{\partial\theta_2} \\ \frac{\partial\gamma_2(\boldsymbol{\theta})}{\partial\theta_1} - \frac{\partial\gamma_1(\boldsymbol{\theta})}{\partial\theta_2} \end{pmatrix} , \tag{3.35}$$

which follows from (3.9) and (3.11). From the condition that a gradient field is curl-free, one obtains the constraint equation

$$\nabla \times \boldsymbol{u}(\boldsymbol{\theta}) = \frac{\partial^2\gamma_2(\boldsymbol{\theta})}{\partial\theta_1^2} - \frac{\partial^2\gamma_1(\boldsymbol{\theta})}{\partial\theta_1\,\partial\theta_2} - \frac{\partial^2\gamma_2(\boldsymbol{\theta})}{\partial\theta_2^2} = 0 . \tag{3.36}$$

This condition ensures that when the convergence is calculated from the shear via (3.14) and then transformed back to real space, it is still a purely real quantity.

However, due to noise and remaining systematics, as well as due to physical processes such as lensing contributions beyond the Born approximation (Schneider et al. 1998), source redshift clustering (Schneider et al. 2002b), or the intrinsic alignment of galaxies (see Sect. 5.1), (3.36) will in general be violated for realistic data. Hence, it is useful to split up the vector field $\boldsymbol{u}$ into a curl-free and a divergence-free part and write

$$\nabla^2\kappa_\mathrm{E} = \nabla\cdot\boldsymbol{u} ; \quad \nabla^2\kappa_\mathrm{B} = \nabla\times\boldsymbol{u} . \tag{3.37}$$

Since the shear γ is a polar like the polarisation of an electromagnetic field, this decomposition is performed in analogy to the electromagnetic case, thus inheriting the terms E-mode for the curl-free and B-mode for the divergence-free mode. Therefore (3.36) is equivalent to the statement that gravitational lensing in the Born approximation only generates E-modes, i.e. produces a curl-free field $\boldsymbol{u}$. B-modes violate (3.36), causing an imaginary contribution to the convergence after transformations via (3.14). Hence, one rewrites the convergence as a complex quantity to account for B-modes,

$$\kappa(\boldsymbol{\theta}) = \kappa_\mathrm{E}(\boldsymbol{\theta}) + \mathrm{i}\;\kappa_\mathrm{B}(\boldsymbol{\theta}) . \tag{3.38}$$

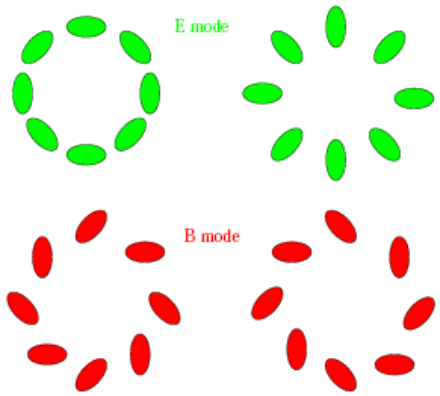

Figure 3.4: Sketch of the orientation of galaxy images due to an E-mode (top row) and B-mode (bottom row) shear field. The sketches on the left correspond to a matter overdensity, those on the right to an underdensity in the centre. Note that to first order, only E-modes are generated by gravitational lensing (from van Waerbeke & Mellier 2003).

Similarly, the deflection potential is turned into a complex quantity. The corresponding convergence power spectra are now defined via

$$\begin{aligned}
\langle\tilde{\kappa}_{\rm E}(\boldsymbol{\ell})\,\tilde{\kappa}^*_{\rm E}(\boldsymbol{\ell'})\rangle &= (2\pi)^2\,\delta^{(2)}_{\rm D}(\boldsymbol{\ell}-\boldsymbol{\ell'})\,P_{\rm E}(\ell)\;;\\
\langle\tilde{\kappa}_{\rm B}(\boldsymbol{\ell})\,\tilde{\kappa}^*_{\rm B}(\boldsymbol{\ell'})\rangle &= (2\pi)^2\,\delta^{(2)}_{\rm D}(\boldsymbol{\ell}-\boldsymbol{\ell'})\,P_{\rm B}(\ell)\;;\\
\langle\tilde{\kappa}_{\rm E}(\boldsymbol{\ell})\,\tilde{\kappa}^*_{\rm B}(\boldsymbol{\ell'})\rangle &= (2\pi)^2\,\delta^{(2)}_{\rm D}(\boldsymbol{\ell}-\boldsymbol{\ell'})\,P_{\rm EB}(\ell)\;,
\end{aligned} \tag{3.39}$$

where the assignment of galaxy populations was suppressed throughout for clarity. The E-mode power spectrum is generated by lensing and therefore given by (3.34), while the B-mode power spectrum vanishes under ideal circumstances, but contains in general contributions by the effects listed above. Due to the parity invariance of the shear field (see Schneider 2003 for details) the cross-power spectrum $P_{\rm EB}(\ell)$ is expected to be identically zero because B-modes change sign under parity transformation, whereas E-modes do not.

Figure 3.4 shows the possible alignments of galaxy images which correspond to the two modes. The E-mode and hence weak lensing causes tangential alignment around mass overdensities, which is also prominent in the much stronger shear effect around galaxy clusters, or a radial orientation indicating an underdense region in the centre. Due to their curl, B-modes introduce a net orientation into the shear field, which cannot be generated by gravitational lens mapping.

Taking into account that gravitational lensing only allows for certain orientations of galaxy images, it is convenient not to measure shear and ellipticities in terms of their real and imaginary parts, but via the tangential and cross components, defined as

$$\epsilon_+ \equiv -{\rm Re}(\epsilon\,{\rm e}^{-2{\rm i}\phi})\;;\quad \epsilon_\times \equiv -{\rm Im}(\epsilon\,{\rm e}^{-2{\rm i}\phi})\;, \tag{3.40}$$

where ϕ denotes the polar angle of the separation vector $\boldsymbol{\theta}$ of two galaxies. Note that this separation vector and hence the tangential and cross component of ϵ are defined for each pair of galaxies individually. Again, the factor of 2 in the exponent reflects the properties of a polar. Similar expressions can be given for γ and $\epsilon^{\rm s}$. A rotation of the galaxy image by 45° transforms a tangential ellipticity into a cross ellipticity, just like the patterns of E-modes are turned into the ones of B-modes in Fig. 3.4.

With the definitions (3.40) one can define the cosmic shear measure that is most practical to be directly applied to data, the two-point correlation functions

$$\xi_\pm(\theta) \equiv \langle\gamma_+\gamma_+\rangle\,(\theta) \pm \langle\gamma_\times\gamma_\times\rangle\,(\theta)\;. \tag{3.41}$$

Provided one has obtained an unbiased estimate of the ellipticity ϵ_i of every galaxy in the survey catalogue, as was outlined in Sect. 3.2, the correlation functions can be measured by means of

the unbiased estimators (Schneider et al. 2002a)

$$\hat{\xi}_{\pm}(\theta) = \frac{1}{N_{\rm p}(\theta)} \sum_{i,j} \left(\epsilon_{i\,+}\epsilon_{j\,+} \pm \epsilon_{i\,\times}\epsilon_{j\,\times}\right) \Delta_\theta\left(|\theta_i - \theta_j|\right) \ , \tag{3.42}$$

where $\Delta_\theta(\vartheta)$ is a bin selection function that is one in case ϑ lies within a bin centred on θ, and vanishes otherwise. The number of galaxy pairs in this bin is given by $N_{\rm p}(\theta) = \sum_{i,j} \Delta_\theta\left(|\theta_i - \theta_j|\right)$. The strength of the correlation functions is their insensitivity to an irregular survey geometry caused e.g. by the masking of bright stars, chip defects, and detector gaps.

Furthermore, Schneider et al. (1998) defined the aperture masses

$$M_{\rm ap}(\theta) = \int {\rm d}^2\vartheta\ Q(|\boldsymbol{\vartheta}|,\theta)\ \gamma_+(\boldsymbol{\vartheta}) \ ; \quad M_\perp(\theta) = \int {\rm d}^2\vartheta\ Q(|\boldsymbol{\vartheta}|,\theta)\ \gamma_\times(\boldsymbol{\vartheta}) \ , \tag{3.43}$$

where the weight function $Q(\vartheta,\theta)$ is axially-symmetric and vanishes for $\vartheta > \theta$. See Schneider (1996) for the derivation of the further conditions that $Q(\vartheta,\theta)$ has to fulfil, and Schneider et al. (1998) and Crittenden et al. (2002) for explicit functional forms. The aperture masses measure the weighted tangential or cross shear in circular apertures of radius θ. Since these apertures have to be placed on the image, $M_{\rm ap}$ and $M_\perp$ are sensitive to any irregularities in the survey aperture when directly estimated from the data. As second-order measures one then uses the dispersion of $M_{\rm ap}$, $\left\langle M_{\rm ap}^2\right\rangle$, and likewise for $M_\perp$.

The advantages and limitations of the measures introduced above can best be understood by considering their relation to the E- and B-mode power spectra. Noting that $\gamma_+\gamma_+ + \gamma_\times\gamma_\times = \gamma_1\gamma_1 + \gamma_2\gamma_2 = \gamma\gamma^*$, and placing one of the galaxy images at the origin without loss of generality, one can write for the correlation function

$$\xi_+(\theta) = \langle\gamma(0)\ \gamma^*(\boldsymbol{\theta})\rangle = \int \frac{{\rm d}^2\ell}{(2\pi)^2} \int \frac{{\rm d}^2\ell'}{(2\pi)^2}\ {\rm e}^{{\rm i}\boldsymbol{\ell'}\cdot\boldsymbol{\theta}}\ \langle\tilde{\gamma}(\boldsymbol{\ell})\ \tilde{\gamma}^*(\boldsymbol{\ell'})\rangle \ , \tag{3.44}$$

where in the second step the gravitational shear was Fourier transformed. By means of (3.14) the correlator of shears can be replaced by a correlator of convergences, so that after insertion of (3.39) one arrives at

$$\xi_+(\theta) = \int_0^\infty \frac{{\rm d}\ell\ \ell}{2\pi}\ J_0(\ell\theta)\left\{P_E(\ell) + P_B(\ell)\right\} \ . \tag{3.45}$$

The quantity $J_\mu(x)$ denotes the Bessel function of the first kind of order μ which is defined as

$$J_\mu(x) \equiv \frac{1}{\pi{\rm i}^\mu} \int_0^\pi {\rm d}\varphi\ \ {\rm e}^{{\rm i}x\cos\varphi} \cos\left(\mu\varphi\right) \ . \tag{3.46}$$

The other relations can be calculated analogously (e.g. Schneider et al. 2002b), yielding

$$\begin{aligned}
\xi_-(\theta) &= \int_0^\infty \frac{{\rm d}\ell\ \ell}{2\pi}\ J_4(\ell\theta)\ \left\{P_{\rm E}(\ell) - P_{\rm B}(\ell)\right\} \ ; \\
\left\langle M_{\rm ap}^2\right\rangle(\theta) &= \int_0^\infty \frac{{\rm d}\ell\ \ell}{2\pi}\ \frac{576 J_4^2(\ell\theta)}{(\ell\theta)^4}\ P_{\rm E}(\ell) \ ; \\
\left\langle M_\perp^2\right\rangle(\theta) &= \int_0^\infty \frac{{\rm d}\ell\ \ell}{2\pi}\ \frac{576 J_4^2(\ell\theta)}{(\ell\theta)^4}\ P_{\rm B}(\ell) \ .
\end{aligned} \tag{3.47}$$

Evidently these second-order measures of cosmic shear are all linear functionals of the convergence power spectra, each employing a different filter. The two aperture masses offer a

possibility to separate E- and B-modes since $\langle M_{\rm ap}^2 \rangle(\theta)$ is only sensitive to E-modes as induced by gravitational lensing, whereas $\langle M_\perp^2 \rangle(\theta)$ has merely contributions from B-modes, i.e. in practice it serves as a measure of noise and systematics. The broad filter J_0 of ξ_+ leads to a strong signal, but also to strong correlations between different angular scales because, for every given angle θ, the power spectra are integrated over a wide range of angular frequencies. In contrast, a narrow filter yields a lower signal, but provides a good estimate of the power spectrum. In fact, the filter of $\langle M_{\rm ap}^2 \rangle(\theta)$ can be replaced by a Dirac-delta distribution with an error of only 10 % (Bartelmann & Schneider 1999). The filters in (3.45) and (3.47) also determine the covariance properties of the shear measures, see Schneider et al. (2002a) and Joachimi et al. (2008).

Given the orthogonality relations of the Bessel functions, it is possible to invert (3.47), which results in case of the correlation functions in

$$\begin{aligned} P_{\rm E}(\ell) &= \pi \int_0^\infty {\rm d}\theta\, \theta \left\{ \xi_+(\theta)\, J_0(\ell\theta) + \xi_-(\theta)\, J_4(\ell\theta) \right\} \;; \\ P_{\rm B}(\ell) &= \pi \int_0^\infty {\rm d}\theta\, \theta \left\{ \xi_+(\theta)\, J_0(\ell\theta) - \xi_-(\theta)\, J_4(\ell\theta) \right\} \;. \end{aligned} \tag{3.48}$$

Inserting these equations back into (3.47), one can infer interrelations between the correlation functions ξ_+ and ξ_-, and moreover give other cosmic shear measures such as the aperture masses in terms of $\xi_\pm$ (Crittenden et al. 2002). With these relations at hand, it is preferable to use the correlation functions as the primary observable due to their insensitivity to gaps etc., and subsequently compute other measures such as $\langle M_{\rm ap}^2 \rangle(\theta)$, allowing for an EB-mode separation and a more direct probe of the convergence power spectra.

To compute the aperture masses from correlation functions, $\xi_\pm(\theta)$ has to be known down to a galaxy separation of $\theta = 0$, which infeasible for realistic data, e.g. due to the finite size of galaxy images. Instead of placing circular apertures, Schneider & Kilbinger (2007) have thus suggested to measure the shear in annuli with a non-vanishing inner radius, resulting in the ring statistics. This approach has been generalised recently to complete orthogonal sets of EB-mode integrals which are second-order measures that are again linear in $\xi_\pm$ and contain the full cosmic shear information that can be separated into E- and B-modes (Schneider et al. 2010). Note that since (3.37) depends on the second derivatives of the shear, constant and linear contributions to γ cannot be uniquely assigned to E- or B-modes and hence are not contained in these measures.

As noted before, the convergence power spectrum is the second-order measure which is most directly related to the predictions of the cosmological model via (3.34). In principle it is possible to extract the power spectrum itself from the measured ellipticities, but simple power spectrum estimators are highly susceptible to a complex survey geometry (Joachimi et al. 2008). While it should be possible to transfer de-biasing methods such as the pseudo-C_ℓ formalism of the CMB (e.g. Hivon et al. 2002) to the context of cosmic shear, it currently seems more favourable to apply correlation function estimators of the form (3.42) to the data and constrain cosmology by making use of the relations (3.45) and (3.47). As long as a manipulation of second-order cosmic shear measures does not affect angular scales, one can use any measure for its investigation and adapt the formalism to other second-order measures, employing the relations of this section. For this reason we will, without loss of generality, restrict our considerations mostly to the convergence power spectrum, profiting from its simple modelling and convenient noise properties (Joachimi et al. 2008).

The considerations made in this section can be generalised to correlations between the gravitational shear of two distinct populations of source galaxies, which were incorporated into the formalism of Sect. 3.3. Usually the different galaxy populations are defined such that they

are ordered in redshift, with their redshift probability distributions $p^{(i)}(z) = p^{(i)}(\chi)\,\mathrm{d}\chi/\mathrm{d}z$[1] having as little overlap as possible. Thereby one can create a tomographic view of the lensing effect by the large-scale structure. This cosmic shear tomography has recently been applied to current data sets, see e.g. Sect. 4.3, and will become the standard analysis method of future cosmic shear surveys (see Heavens 2003 for a different approach to the inclusion of redshift information). The division of the cosmic shear source galaxy population into a moderate number of redshift bins improves constraints on cosmological parameters (e.g. Hu 1999) and is vital to eliminate systematic effects. The influence of the quality of redshift information on the control of the intrinsic alignment of galaxies will be a major topic of this work.

The large number of source galaxies necessary to render cosmic shear a powerful probe of cosmology (several billion for planned all-sky surveys) prohibits the usage of spectroscopy to determine accurate redshifts. Instead one has to rely on multi-filter colour information to infer photometric redshifts. Various algorithms that estimate photometric redshifts, for instance via the fitting of template galaxy spectra or via neural networks trained by example spectra, are available, see Abdalla et al. (2008) and references therein for an overview and a comparison of different codes. The uncertainty related to the measurement of photometric redshifts causes a significant spread of the redshift probability distributions $p^{(i)}(z)$ when dividing the source galaxies into photometric redshift bins i (e.g. Abdalla et al. 2007; Bordoloi et al. 2010). In addition, depending on the number and type of usable filters, misidentifications can cause a significant rate of catastrophic failures in the assignment of photometric redshifts (Abdalla et al. 2007). Both the assessment of constraints on cosmology by cosmic shear and the treatment of systematic effects has to cope with the implications of a complex relation between the photometric and true redshift of galaxies, see e.g. Chap. 6.

3.5 The status quo of cosmic shear

Theoretical work on the propagation of light through the inhomogeneous Universe has existed for more than four decades (Gunn 1967), with the foundations of cosmic shear laid down in the early 90's (Blandford et al. 1991; Miralda-Escudé 1991; Kaiser 1992). However, weak lensing on cosmological scales modifies the shape of galaxy images only at the per cent level, thus requiring good statistics and precise measurements. Hence it was not before the turn of the century that the first observational detections of cosmic shear were reported – independently and simultaneously – by Bacon et al. (2000), Kaiser et al. (2000), van Waerbeke et al. (2000) and Wittman et al. (2000).

Since then cosmic shear has rapidly evolved into a mature technique that produces increasingly stringent constraints on cosmological parameters, recently having become competitive to other established methods, see e.g. Hoekstra et al. (2002) for an analysis of the RCS survey, van Waerbeke et al. (2005) who worked on the VIRMOS-DESCART survey, Jarvis et al. (2006) who analysed CTIO data, and Hetterscheidt et al. (2007) for an analysis of the GaBoDS survey. The largest survey to date with which cosmic shear was studied (so far an area of $57\,\mathrm{deg}^2$ was the maximum used for weak lensing analyses) is the Canada-France-Hawaii Telescope Legacy Survey (CFHTLS), see Hoekstra et al. (2006), Semboloni et al. (2006), and Fu et al. (2008). Besides, CFHTLS, RCS, VIRMOS-DESCART, and GaBoDS data have been combined into a set covering a total of about $100\,\mathrm{deg}^2$ by Benjamin et al. (2007).

In Fig. 3.5 confidence contours for the two cosmological parameters Ω_m and σ_8, which are constrained best by cosmic shear, are shown for the state of the art of ground-based cosmic shear

[1]Note that for ease of notation we use the same symbol for redshift and comoving distance probability distributions although $p(z)$ and $p(\chi)$ are different functions.

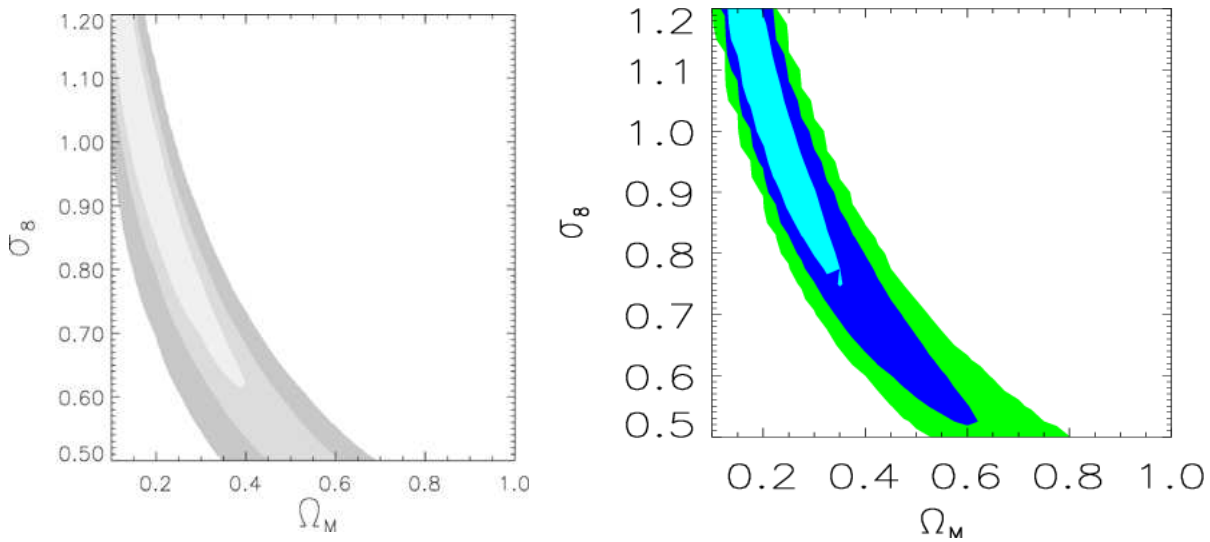

Figure 3.5: Cosmic shear constraints in the $\Omega_\mathrm{m} - \sigma_8$ plane. *Left panel*: Combined $1\,\sigma$, $2\,\sigma$, and $3\,\sigma$-contours for the current set of available ground-based wide-field surveys, i.e. CFHTLS, RCS, VIRMOS-DESCART, and GaBoDS (from Benjamin et al. 2007). *Right panel*: Same as on the left, but using only the largest cosmic shear survey to date, CFHTLS. Both the results from the wide and deep surveys are included (from Semboloni et al. 2006).

observations, i.e. the results from the combined CFHTLS wide and deep surveys (Semboloni et al. 2006) and those from the $100\,\mathrm{deg}^2$ compilation which comprises only the CFHTLS wide survey (Benjamin et al. 2007). One observes the characteristic, banana-shaped degeneracy between Ω_m and σ_8 which originates from the similar influence of these two parameters on the amplitude of the convergence power spectrum, via the prefactor containing Ω_m^2 in (3.34) and the three-dimensional matter power spectrum, see Fig. 3.3. The results from the $100\,\mathrm{deg}^2$ data set are in agreement within their $1\,\sigma$-limits with the current best-fit values given in Table 2.1, whereas the CFHTLS data alone clearly favours a higher normalisation of the matter power spectrum for a given value of Ω_m.

As demonstrated in Fig. 3.6, current cosmic shear data is already capable of placing mild constraints on the dark energy equation of state parameter w_0 (see also Jarvis et al. 2006; Schrabback et al. 2010, and Sect. 4.3). The standard ΛCDM cosmology with $w_0 = -1$ lies within the $1\,\sigma$ contours, but the constraints are heavily dependent on the prior which was chosen to be flat within $w_0 \in [-2 : 0]$ (Hoekstra et al. 2006). Cosmic shear observations from space do not suffer from the blurring by the atmosphere and can therefore enable more accurate shear measurements out to considerably higher redshifts. This makes space the preferred place for future weak lensing observations, but up to now survey areas have been very small, the largest space-based cosmic shear data set to date being COSMOS with $1.44\,\mathrm{deg}^2$ (Massey et al. 2007c; Schrabback et al. 2007, 2010).

Lensing delivers information complementary to CMB anisotropies, Type Ia supernovae, or galaxy redshift surveys (e.g. Hu 2002a; Tereno et al. 2005; Spergel et al. 2007; Das & Spergel 2009), thereby playing a crucial role in the development of precision cosmology. In particular in combination with CMB data, cosmic shear is able to break parameter degeneracies because it probes the matter distribution at lower redshifts and on smaller scales than the CMB fluctuations. Even on its own, cosmic shear surveys of the near future are regarded among the most promising probes of the properties of dark energy (see Hu 2002b; Huterer 2002; Albrecht et al. 2006; Peacock et al. 2006). In addition to its constraining power, a further strength of cosmic shear is that the underlying theory is built on few physical assumptions, especially since the

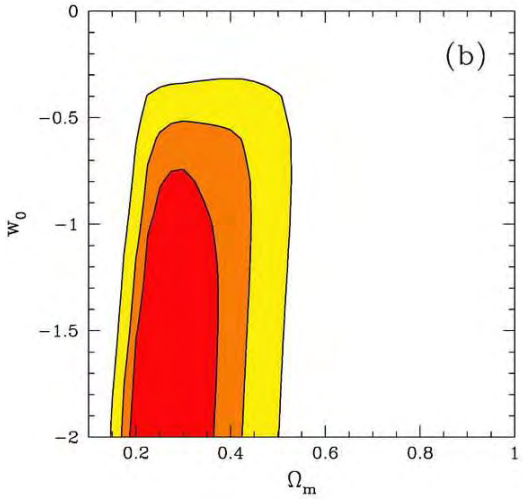

Figure 3.6: Cosmic shear constraints in the $\Omega_\mathrm{m} - w_0$ plane. Shown are the marginalised $1\,\sigma$, $2\,\sigma$, and $3\,\sigma$-contours obtained for the combination of the CFHTLS wide and deep surveys. Note that the contours depend on the prior $w_0 \in [-2 : 0]$ (from Hoekstra et al. 2006).

gravitational lensing effect does not depend on the relation between baryons and dark matter.

The resulting current prosperity in the field of weak lensing on cosmological scales is supplemented by a noticeable number of proposed or planned observational projects which feature cosmic shear as one of their primary probes. For instance, the first stage of the Pan-STARRS[2] project has recently started operations with a 1.8 m telescope. The weak lensing data is going to comprise the entire extra-galactic sky visible from Hawaii, observed down to 24th magnitude. Likewise, KIDS[3] is expected to deliver first data soon, providing imaging over 1500 deg^2 which will be about a magnitude deeper. In 2011 DES[4] is scheduled to start a 5000 deg^2 survey with similar limiting magnitude as Pan-STARRS, using a wide-field camera on a 4 m telescope.

The LSST[5] is currently in an advanced planning stage and features an 8.4 m telescope to cover the whole extra-galactic sky (20000 deg^2) down to magnitude 27.5 (LSST Science Collaborations 2009). Future space-based projects such as JDEM[6] and Euclid[7] intend to unite the advantages for shear measurement in absence of the atmosphere with large survey areas (Réfrégier et al. 2004, 2006; Laureijs et al. 2009; Réfrégier et al. 2010), thereby yielding unprecedented insight into the properties of dark matter, dark energy and gravitation. More details about the Euclid satellite and the expected performance of its cosmic shear survey will be provided in Sect. 4.2.

Finally, in about 15 years from now the SKA[8] radio interferometer is going to open up the radio regime to cosmic shear measurements. As suggested by Metcalf & White (2007), one could then use the redshifted 21cm emission line of neutral hydrogen, abundant in the Universe in the so-called dark ages between recombination and reionisation, as the background source for the lensing by the intervening large-scale structure instead of galaxies. This would provide about a thousand independent slices of 21cm brightness temperature maps, each with precisely known redshift with z exceeding 10, constituting the ultimate stage in investigating the large-scale structure via weak gravitational lensing.

With the steadily increasing accuracy of cosmic shear measurements, the understanding and elimination of systematic effects becomes more and more important. Apart from the central concerns of shear estimation from real data and the determination of redshifts from multi-

[2]Panoramic Survey Telescope & Rapid Response System, `http://pan-starrs.ifa.hawaii.edu`
[3]Kilo Degree Survey, `http://www.astro-wise.org/projects/KIDS`
[4]Dark Energy Survey, `https://www.darkenergysurvey.org`
[5]Large Synoptic Survey Telescope, `http://www.lsst.org`
[6]Joint Dark Energy Mission, `http://jdem.gdfc.nasa.gov`
[7]`http://sci.esa.int/science-e/www/area/index.cfm?fareaid=102`
[8]Square Kilometer Array, `http://www.skatelescope.org/`

colour photometry, cosmic shear is affected by the intrinsic alignment of galaxies, which is the primary astrophysical systematic. In order to prevent systematics from dominating the error budget of cosmological parameter estimates, it is hence crucial to control the effect of intrinsic alignments, which will be the topic of Chaps. 5 to 8.

Chapter 4

Optimisation of cosmic shear surveys

Weak lensing on cosmological scales has matured within the past decade into a powerful probe of cosmology. Ambitious cosmic shear surveys are planned or underway, setting new standards in the accuracy with which the cosmological model can be constrained. Accordingly, the planning stages of these new surveys require unprecedented precision on the forecasts for constraints on cosmological parameters as well as stringent treatments of potential systematic errors. These demands imply numerous optimisation steps for weak lensing surveys, a few of which will be elaborated on in this chapter.

The increased area of upcoming surveys will also allow for the fruitful investigation of higher-order weak lensing statistics, hence the need to make forecasts for the performance of these measures. To get predictions for statistical errors obtainable with three-point statistics, accurate and computationally tractable methods to determine their covariance, which is a six-point statistic, are required. In the literature formulae for covariances of three-point statistics are derived either in a spherical harmonics or a Fourier formalism, the latter directly applicable to the cosmic shear formalism introduced in Chap. 3. However, the results of these two approaches are apparently discrepant. Thus, in Sect. 4.1 we will detail the derivation of the bispectrum covariance, set the two formalisms into relation, and derive new efficient means of calculating the covariance in the Gaussian approximation (see also Joachimi et al. 2009).

With the efficient computation of bispectrum measures and their covariances at hand, we then proceed in Sect. 4.2 to make Fisher matrix forecasts for the currently most ambitious cosmic shear survey in an advanced planning stage, the Euclid satellite mission proposed to ESA (Laureijs et al. 2009; Réfrégier et al. 2010). Besides, we will outline a novel method to incorporate the effect of systematics into the total error budget of predictions on cosmological parameters. It is demonstrated that the form filling functions technique (Kitching et al. 2009) provides a robust alternative to the standard approach of marginalisation over nuisance parameters.

In Sect. 4.3 we will summarise the results of the first fully tomographic analysis of a space-based cosmic shear data, using the Hubble Space Telescope COSMOS survey (Schrabback et al. 2010). Details relevant for the interpretation of the data such as the optimisation of the information about cosmology in the data, the modelling of the dependence of the non-linear growth of structure on dark energy, and the usage of covariances are highlighted.

4.1 Bispectrum covariance in the flat-sky limit

As the concordance model of cosmology becomes more and more consolidated, the focus increasingly turns towards probing effects beyond the standard paradigm, such as non-Gaussian initial conditions or the evolution of the large-scale structure in the highly non-linear regime. To

lowest order, these effects can be measured by three-point statistics of the underlying fields, all of which are related to the bispectrum. Hence, work in both theory and observations concerning the bispectrum and its noise properties has been undertaken for CMB measurements (e.g. Hu 2000; Cooray et al. 2008), galaxy clustering surveys (e.g. Scoccimarro 2000; Scoccimarro et al. 2001; Sefusatti et al. 2006), or, more recently, weak gravitational lensing on cosmological scales (e.g. Bernardeau et al. 2002b; Jarvis et al. 2004; Takada & Jain 2004).

While theoretical computations at the bispectrum level are already considerably more demanding than for second-order statistics, this does apply even more so to the bispectrum covariance, which is a six-point statistic. On the full sky calculations are done by expanding the signal into spherical harmonics. If only small angular scales are considered, it is often more convenient to use a flat-sky approximation and work in terms of Fourier amplitudes. In the case of weak lensing the flat-sky limit is appropriate for practically all applications because signal correlations can only be measured up to separations of a few degrees.

Although other approaches exist in the literature (e.g. Matarrese et al. 1997; Sefusatti et al. 2006), a lot of work is done within a flat-sky spherical harmonic formalism (Hu 2000), which suffers – at least formally – from drawbacks. For instance, the resulting flat-sky expressions are valid only for integer arguments and thus for a bin width of unity, whereas it is desirable to evaluate the bispectrum and its covariance at real-valued angular frequencies and e.g. a logarithmic binning. The formulae still contain Wigner symbols whose physical meaning within a flat-sky consideration remains obscure. As the spherical harmonic expansion can only be done on the full unit sphere, the finite size of the survey at consideration is usually accounted for by multiplying a factor, containing the sky coverage, by hand. Moreover, the accuracy of some of the approximations in the transition between full sky and two-dimensional plane (see Hu 2000) is uncertain.

This work aims at clarifying the derivation of bispectrum covariances in the flat-sky limit. We attempt to do so by presenting a detailed calculation which is purely based on the two-dimensional Fourier formalism, followed by a comparison of this approach with the flat-sky spherical harmonic results in terms of their covariance, the behaviour under parity transformations, and the information content. Moreover, we provide further insight and illustration by establishing relations between Wigner symbols, the averaging process in the bispectrum estimator, and a geometrical view.

We begin by defining a bispectrum estimator, and showing that it is unbiased. A geometrical interpretation for the averaging processes involved is introduced, which is then applied to deal with the issue of degenerate triangle configurations. Subsequently the covariance of the estimator defined beforehand is computed. The result is compared with the spherical harmonics approach and demonstrated to be equivalent in terms of information content. To explain the differences between the covariances, we also discuss the treatment of parity in both formalisms. To avoid confusion, we refrain from using the term 'flat sky' in the following, but refer to our formalism as 'Fourier-plane' and to the approach as e.g. given in Hu (2000) as 'spherical harmonic' (both are flat-sky approximations).

4.1.1 Bispectrum estimator

We consider a continuous, two-dimensional random field g with mean zero, which is characterised by its complex Fourier amplitudes $g(\boldsymbol{\ell})$[1], where $\boldsymbol{\ell}$ denotes the angular frequency vector. Throughout, it will be assumed that this field is statistically homogeneous, i.e. invariant under

[1]Note that, contrary to the remainder of this work, we will not indicate Fourier-transformed quantities by a tilde in this section, for ease of notation. As we will exclusively work in Fourier space, there is no risk of confusion.

translations, and statistically isotropic, i.e. invariant under rotations. In a cosmological context g could for instance represent the temperature fluctuations of the CMB, the number density contrast of galaxy surveys, or the weak lensing convergence.

In what follows we will largely follow the approach of Joachimi et al. (2008), assuming likewise measurements in a compact, contiguous survey of size A. We will restrict our considerations to an angular extent much smaller than the size of the survey, i.e. to $\ell \gg \pi/\theta_{\max}$, where $\theta_{\max}$ is the maximum separation allowed by the survey geometry. Boundary effects due to the finite field size, as e.g. discussed in Joachimi et al. (2008) for the second-order level, can then be safely neglected.

Furthermore, we will not explicitly consider additional noise terms due to the discrete sampling of the continuous field g, for ease of notation. To account for these shot noise or, in the case of weak lensing, shape noise terms in the covariance, they can simply be added to the second-order measures, so in this Fourier space approach, to the power spectra (e.g. Kaiser 1998; Hu 1999). Note that the galaxy ellipticity, and not the convergence κ, is the direct observable in weak lensing. However, in absence of shape noise and for $\ell \gg 1$, the estimators in terms of the galaxy ellipticity, as given in Joachimi et al. (2008), can be re-written directly in terms of κ. Thus, one can consider the convergence as the observable that the estimator is based on without loss of generality.

For a statistically homogeneous and isotropic random field one defines the bispectrum as

$$\langle g(\boldsymbol{\ell}_1)\, g(\boldsymbol{\ell}_2)\, g(\boldsymbol{\ell}_3)\rangle = (2\pi)^2\, \delta_{\mathrm{D}}^{(2)}(\boldsymbol{\ell}_1+\boldsymbol{\ell}_2+\boldsymbol{\ell}_3)\, B(\ell_1,\ell_2,\ell_3)\;, \tag{4.1}$$

where $\delta_{\mathrm{D}}^{(2)}(\boldsymbol{\ell})$ is the two-dimensional Dirac delta-distribution. It ensures in (4.1) that the three angular frequency vectors form a triangle. For the assumed properties of g the bispectrum has three independent components, for which we have chosen the triangle side lengths $|\boldsymbol{\ell}_i| \equiv \ell_i$. For the absolute values of $\boldsymbol{\ell}$ the triangle condition translates into the requirement $|\ell_1-\ell_2| \leq \ell_3 \leq \ell_1+\ell_2$ or equivalently for any permutation of the ℓ_i.

Similarly to Joachimi et al. (2008), we construct an estimator of the bispectrum by averaging configurations over annuli, where here one has the complication of allowing only those combinations of angular frequency vectors that form a triangle. The area of an annulus with mean radius $\bar{\ell}_i$ is given by

$$A_R(\bar{\ell}_i) = 2\pi\bar{\ell}_i\Delta\ell_i \tag{4.2}$$

with the bin size $\Delta\ell_i$. Then we define the estimator

$$\begin{aligned}\hat{B}(\bar{\ell}_1,\bar{\ell}_2,\bar{\ell}_3) \;\equiv\; & \frac{(2\pi)^2}{A}\Lambda^{-1}\left(\bar{\ell}_1,\bar{\ell}_2,\bar{\ell}_3\right)\int_{A_R(\bar{\ell}_1)}\frac{\mathrm{d}^2\ell_1}{A_R(\bar{\ell}_1)}\int_{A_R(\bar{\ell}_2)}\frac{\mathrm{d}^2\ell_2}{A_R(\bar{\ell}_2)}\int_{A_R(\bar{\ell}_3)}\frac{\mathrm{d}^2\ell_3}{A_R(\bar{\ell}_3)} \\ & \times\,\delta_{\mathrm{D}}^{(2)}(\boldsymbol{\ell}_1+\boldsymbol{\ell}_2+\boldsymbol{\ell}_3)\, g(\boldsymbol{\ell}_1)\, g(\boldsymbol{\ell}_2)\, g(\boldsymbol{\ell}_3)\;,\end{aligned} \tag{4.3}$$

where Λ is a function that is related to the fraction of angular frequency combinations allowed by the triangle condition. It is defined such that (4.3) is unbiased, its explicit form being calculated below. Note that this bispectrum estimator is invariant under any permutation of its arguments since Λ is symmetric as will be shown below.

In the following we demonstrate that (4.3) is unbiased by computing the ensemble average,

$$\begin{aligned}\left\langle \hat{B}(\bar{\ell}_1,\bar{\ell}_2,\bar{\ell}_3)\right\rangle &= \frac{(2\pi)^2}{A}\Lambda^{-1}\left(\bar{\ell}_1,\bar{\ell}_2,\bar{\ell}_3\right)\int_{A_R(\bar{\ell}_1)}\frac{\mathrm{d}^2\ell_1}{A_R(\bar{\ell}_1)}\int_{A_R(\bar{\ell}_2)}\frac{\mathrm{d}^2\ell_2}{A_R(\bar{\ell}_2)}\int_{A_R(\bar{\ell}_3)}\frac{\mathrm{d}^2\ell_3}{A_R(\bar{\ell}_3)} \\ &\quad\times(2\pi)^2\left(\delta_{\mathrm{D}}^{(2)}(\boldsymbol{\ell}_1+\boldsymbol{\ell}_2+\boldsymbol{\ell}_3)\right)^2 B(\ell_1,\ell_2,\ell_3) \qquad (4.4)\\ &= (2\pi)^2\Lambda^{-1}\left(\bar{\ell}_1,\bar{\ell}_2,\bar{\ell}_3\right)\int_{A_R(\bar{\ell}_1)}\frac{\mathrm{d}^2\ell_1}{A_R(\bar{\ell}_1)}\int_{A_R(\bar{\ell}_2)}\frac{\mathrm{d}^2\ell_2}{A_R(\bar{\ell}_2)}\int_{A_R(\bar{\ell}_3)}\frac{\mathrm{d}^2\ell_3}{A_R(\bar{\ell}_3)} \\ &\quad\times\delta_{\mathrm{D}}^{(2)}(\boldsymbol{\ell}_1+\boldsymbol{\ell}_2+\boldsymbol{\ell}_3)\,B(\ell_1,\ell_2,\ell_3)\,.\end{aligned}$$

In the first step the definition of the bispectrum (4.3) was inserted. The appearance of a squared delta-distribution requires taking into account the finite survey size. As shown in Joachimi et al. (2008), one can identify

$$\left(\delta_{\mathrm{D}}^{(2)}(\boldsymbol{\ell})\right)^2 \to \frac{A}{(2\pi)^2}\,\delta_{\mathrm{D}}^{(2)}(\boldsymbol{\ell})\,, \qquad (4.5)$$

which results in the second equality of (4.4).

Since the bispectrum only depends on the magnitudes of the angular frequency vectors we can perform the integrations over the polar angles of the $\boldsymbol{\ell}$-integrals. If φ_{ℓ_i} denotes the polar angle of $\boldsymbol{\ell}_i$, one gets

$$\begin{aligned}&\int_0^{2\pi}\mathrm{d}\varphi_{\ell_1}\int_0^{2\pi}\mathrm{d}\varphi_{\ell_2}\int_0^{2\pi}\mathrm{d}\varphi_{\ell_3}\,\delta_{\mathrm{D}}^{(2)}(\boldsymbol{\ell}_1+\boldsymbol{\ell}_2+\boldsymbol{\ell}_3) \qquad (4.6)\\ =\;&\int_0^{2\pi}\mathrm{d}\varphi_{\ell_1}\int_0^{2\pi}\mathrm{d}\varphi_{\ell_2}\int_0^{2\pi}\mathrm{d}\varphi_{\ell_3}\int\frac{\mathrm{d}^2\theta}{(2\pi)^2}\,\mathrm{e}^{\mathrm{i}(\boldsymbol{\ell}_1+\boldsymbol{\ell}_2+\boldsymbol{\ell}_3)\cdot\boldsymbol{\theta}} \\ =\;&\int\frac{\mathrm{d}^2\theta}{(2\pi)^2}\,(2\pi)^3 J_0(\ell_1\theta)\,J_0(\ell_2\theta)\,J_0(\ell_3\theta) \\ =\;&(2\pi)^2\int\mathrm{d}\theta\;\theta\;J_0(\ell_1\theta)\,J_0(\ell_2\theta)\,J_0(\ell_3\theta) \\ =\;&2\pi\;\Lambda\left(\ell_1,\ell_2,\ell_3\right)\;.\end{aligned}$$

After inserting one possible representation of the delta-distribution in the first equality, we have made use of the definition of the Bessel function of the first kind of order 0, see (3.46). The result of the integral over three Bessel functions is taken from Gradshteyn et al. (2000), formula no. 6.578.9, where we have defined

$$\Lambda\left(\ell_1,\ell_2,\ell_3\right)\equiv\begin{cases}\frac{4}{\sqrt{2\ell_1^2\ell_2^2+2\ell_1^2\ell_3^2+2\ell_2^2\ell_3^2-\ell_1^4-\ell_2^4-\ell_3^4}} & \text{if}\quad |\ell_1-\ell_2|<\ell_3<\ell_1+\ell_2 \\ 0 & \text{else}\end{cases}\,, \qquad (4.7)$$

i.e. if ℓ_1,ℓ_2,ℓ_3 are chosen such that they can form the sides of a triangle, then Λ^{-1} is the area of this triangle. Hence, (4.6) represents the defining equation for Λ. The set of integrations (4.6) is also performed within the spherical harmonic approach, see the appendix of Hu (2000), with a different result, which will be investigated in Sect. 4.1.4. Note furthermore that $\Lambda\left(\ell_1,\ell_2,\ell_3\right)=0$ in case the angular frequency vectors are collinear or equivalently, if $\ell_i+\ell_j=\ell_k$ for some combination $i,j,k\in\{1,2,3\}$. At the same time, the bispectrum is non-zero for these degenerate triangle configurations, see (4.1). For the time being, we exclude degenerate triangles from the derivation, but develop a treatment for these cases in Sect. 4.1.2.

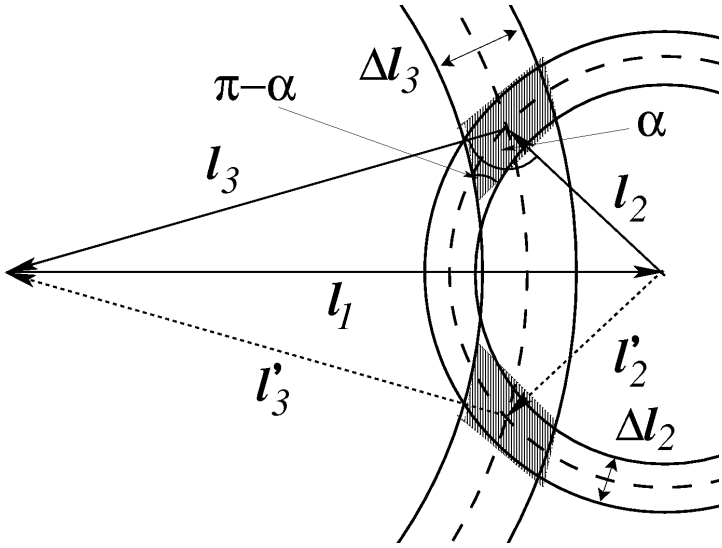

Figure 4.1: Sketch of the annuli and their overlap for fixed $\boldsymbol{\ell}_1$. The region of overlap is approximated by the shaded parallelograms. Note that due to mirror symmetry a second shaded area, related to the triangle $\boldsymbol{\ell}_1$, $\boldsymbol{\ell}'_2$, $\boldsymbol{\ell}'_3$, contributes as well.

Inserting (4.6) into (4.4), one obtains

$$\left\langle \hat{B}(\bar{\ell}_1,\bar{\ell}_2,\bar{\ell}_3)\right\rangle = (2\pi)^3\Lambda^{-1}\left(\bar{\ell}_1,\bar{\ell}_2,\bar{\ell}_3\right)\int_{\bar{\ell}_1-1/2\Delta\ell}^{\bar{\ell}_1+1/2\Delta\ell}\frac{\mathrm{d}\ell_1\ell_1}{A_R(\bar{\ell}_1)}\int_{\bar{\ell}_2-1/2\Delta\ell}^{\bar{\ell}_2+1/2\Delta\ell}\frac{\mathrm{d}\ell_2\ell_2}{A_R(\bar{\ell}_2)} \times\int_{\bar{\ell}_3-1/2\Delta\ell}^{\bar{\ell}_3+1/2\Delta\ell}\frac{\mathrm{d}\ell_3\ell_3}{A_R(\bar{\ell}_3)}\,\Lambda\left(\ell_1,\ell_2,\ell_3\right)B(\ell_1,\ell_2,\ell_3)\;. \tag{4.8}$$

Analogous to the derivation at the level of second-order statistics (Joachimi et al. 2008) we assume now that the annuli are thin enough such that Λ within the integral, evaluated at the average ℓ-values, can be taken out of the integration. Applying in addition (4.2), one arrives at

$$\begin{aligned}\left\langle \hat{B}(\bar{\ell}_1,\bar{\ell}_2,\bar{\ell}_3)\right\rangle &\approx \int_{\bar{\ell}_1-1/2\Delta\ell}^{\bar{\ell}_1+1/2\Delta\ell}\frac{\mathrm{d}\ell_1\ell_1}{\bar{\ell}_1\Delta\ell_1}\int_{\bar{\ell}_2-1/2\Delta\ell}^{\bar{\ell}_2+1/2\Delta\ell}\frac{\mathrm{d}\ell_2\ell_2}{\bar{\ell}_2\Delta\ell_2}\int_{\bar{\ell}_3-1/2\Delta\ell}^{\bar{\ell}_3+1/2\Delta\ell}\frac{\mathrm{d}\ell_3\ell_3}{\bar{\ell}_3\Delta\ell_3}\,B(\ell_1,\ell_2,\ell_3) \\ &\equiv B(\bar{\ell}_1,\bar{\ell}_2,\bar{\ell}_3)\;,\end{aligned} \tag{4.9}$$

where in the last step the bin-averaged bispectrum was defined. Hence, (4.3) defines an unbiased estimator of the bispectrum. Following the restrictions on (4.6), this estimator is non-zero if the condition $|\bar{\ell}_1-\bar{\ell}_2|<\bar{\ell}_3<\bar{\ell}_1+\bar{\ell}_2$, or likewise for all permutations, holds.

4.1.2 Averaging over triangles

A central step in the construction of the bispectrum estimator (4.3) is the correct treatment of the averaging over annuli, given the triangle condition. This section provides an illustrative, geometrical interpretation of the averaging process and applies this view to a practical treatment of degenerate triangle configurations.

Geometrical interpretation

Without loss of generality consider $\boldsymbol{\ell}_1$ to be fixed. Due to the assumed statistical isotropy of the underlying random field the angular integration over φ_{ℓ_1} is expected to simply reduce to an average over all directions of $\boldsymbol{\ell}_1$. Then the geometric situation in the Fourier plane can be seen as in Fig. 4.1. For a given triangle, composed of the mean vectors $\boldsymbol{\ell}_1$, $\boldsymbol{\ell}_2$, $\boldsymbol{\ell}_3$ with lengths $\bar{\ell}_i$ for $i=\{1,2,3\}$, the annuli for $\bar{\ell}_2$ and $\bar{\ell}_3$ are shown. Due to the triangle condition, the average is not taken over the whole area of the annuli, but merely over the region that the

annuli have in common. This area of overlap is well approximated by a parallelogram of size $A_\parallel = \Delta\ell_2\Delta\ell_3/\sin\alpha$, where α is the internal angle of the triangle opposite $\bar{\ell}_1$. This relation can readily be computed from the geometry of the sketch and by noting $\sin\alpha = \sin(\pi - \alpha)$.

The configuration is mirror-symmetric with respect to an axis through $\boldsymbol{\ell}_1$. Correspondingly, another area of overlap of the same size, which is connected to the triangle $\boldsymbol{\ell}_1$, $\boldsymbol{\ell}_2'$, $\boldsymbol{\ell}_3'$, contributes as well. Noting that axis reflection is in two dimensions equivalent to the parity transformation, the averaging is performed over triangles of both parities. A detailed discussion on this issue is given in Sect. 4.1.4.

As the angle α can also be related to the size of the triangle at consideration, $\Lambda^{-1} = (1/2)\,\bar{\ell}_2\bar{\ell}_3\sin\alpha$, one finds the following correspondence of expressions:

$$\begin{aligned} &\int_0^{2\pi}\frac{\mathrm{d}\varphi_{\ell_1}}{2\pi}\int_0^{2\pi}\frac{\mathrm{d}\varphi_{\ell_2}}{2\pi}\int_0^{2\pi}\frac{\mathrm{d}\varphi_{\ell_3}}{2\pi}\;\delta_\mathrm{D}^{(2)}(\boldsymbol{\ell}_1+\boldsymbol{\ell}_2+\boldsymbol{\ell}_3) \qquad (4.10)\\ =\;&(2\pi)^{-2}\;\Lambda\left(\bar{\ell}_1,\bar{\ell}_2,\bar{\ell}_3\right)\\ =\;&\frac{2\,A_\parallel}{A_R(\bar{\ell}_2)\;A_R(\bar{\ell}_3)}\,, \end{aligned}$$

where the first equality is an immediate consequence of (4.6). To arrive at the last expression, we used (4.2). Hence, the angular integration over the delta-distribution yields the ratio of the area of overlap A_overlap, approximated by $2\,A_\parallel$, and the product of the area of the annuli the ℓ-integrations (excluding the fixed $\boldsymbol{\ell}_1$) run over. This ratio is in turn proportional to the inverse of the area of the triangle spanned by the angular frequency vectors. Therefore, by placing a prefactor of Λ^{-1} in the estimator (4.3), one replaces the normalisation by the area of the annuli with the effective area, over which the average is actually performed.

Two approximations are involved in this picture. First, the shaded regions in Fig. 4.1 are approximated as parallelograms, which is a good assumption if the angle, at which the two annuli intersect, does not become too small. Moreover, the narrower the annuli, the less discrepancy between the area of the parallelogram and the actual overlap is expected. If the triangle approaches the degenerate case, where $\bar{\ell}_2$ and $\bar{\ell}_3$ eventually come to lie on $\bar{\ell}_1$, the area of overlap attains a more complex shape. In particular, the correspondence to the area of the triangle, whose inverse is divergent, does not hold anymore. Second, reconsidering (4.8), we have replaced the average of Λ over triangle side lengths by Λ, evaluated at the average side lengths. This approximation similarly breaks down for thick annuli and configurations in which a small change in the length of an angular frequency vector causes a strong change in the size of the overlap region, as is the case near degeneracy.

In Fig. 4.2, we have plotted the relative deviation of

$$A_\mathrm{overlap}^\mathrm{n.d.} = \bar{\ell}_2\;\bar{\ell}_3\;\Delta\ell_2\;\Delta\ell_3\;\Lambda\left(\bar{\ell}_1,\bar{\ell}_2,\bar{\ell}_3\right) \qquad (4.11)$$

from the actual area of the overlap region, which we calculated numerically. For simplicity, we assume a constant bin width $\Delta\ell_2 = \Delta\ell_3 \equiv \Delta$ for all computations related to Fig. 4.2. For a small bin width $\Delta = 0.05$, given integer steps in ℓ, we find for the two configurations considered in the top panel that the approximation of the overlap area by parallelograms is excellent for the vast majority of triangle configurations. However, as expected, the deviation rises sharply when approaching the degenerate case. Changing to $\Delta = 1$, i.e. the maximum meaningful bin width in this setup, the relative deviation is larger, but still very small except for triangles close to degeneracy.

Degenerate triangles

As discussed in the foregoing section, the approximations made in the course of the construction of the bispectrum estimator break down for degenerate triangle configurations. Equation (4.10)

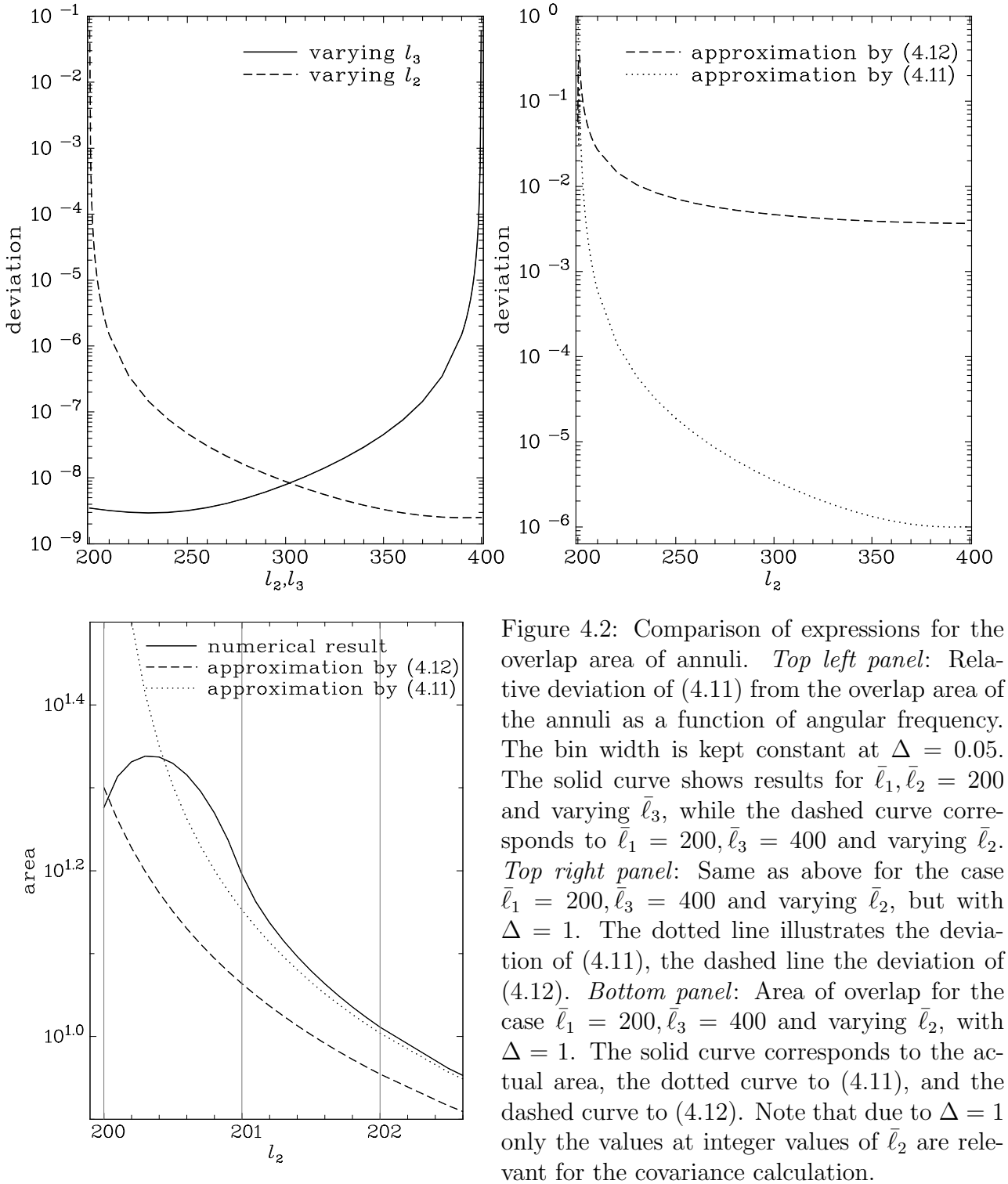

Figure 4.2: Comparison of expressions for the overlap area of annuli. *Top left panel*: Relative deviation of (4.11) from the overlap area of the annuli as a function of angular frequency. The bin width is kept constant at $\Delta = 0.05$. The solid curve shows results for $\bar{\ell}_1, \bar{\ell}_2 = 200$ and varying $\bar{\ell}_3$, while the dashed curve corresponds to $\bar{\ell}_1 = 200, \bar{\ell}_3 = 400$ and varying $\bar{\ell}_2$. *Top right panel*: Same as above for the case $\bar{\ell}_1 = 200, \bar{\ell}_3 = 400$ and varying $\bar{\ell}_2$, but with $\Delta = 1$. The dotted line illustrates the deviation of (4.11), the dashed line the deviation of (4.12). *Bottom panel*: Area of overlap for the case $\bar{\ell}_1 = 200, \bar{\ell}_3 = 400$ and varying $\bar{\ell}_2$, with $\Delta = 1$. The solid curve corresponds to the actual area, the dotted curve to (4.11), and the dashed curve to (4.12). Note that due to $\Delta = 1$ only the values at integer values of $\bar{\ell}_2$ are relevant for the covariance calculation.

becomes invalid, the inverse area of the triangle Λ diverging. Yet, to be of practical use, it is necessary to extend the validity of (4.3) to the case of degenerate triangles. We do so by making use of the geometrical interpretation of the averaging process.

Still keeping $\boldsymbol{\ell}_1$ fixed, consider the situation of a degenerate triangle as sketched in Fig. 4.3. Here, $\bar{\ell}_1 = \bar{\ell}_2 + \bar{\ell}_3$, while the depicted triangle has side lengths $\bar{\ell}_1$, $\bar{\ell}_2 + \Delta\ell_2/2$, and $\bar{\ell}_3 + \Delta\ell_3/2$. Again, we identify a parallelogram that serves as an approximation for the overlap of the annuli, although, as the sketch suggests, with considerably lower accuracy. The relation between the internal angle α of the triangle to the internal angle of the parallelogram $\pi - \alpha$ holds as before, so that one can derive an analogous formula to (4.11), but with modified triangle side lengths.

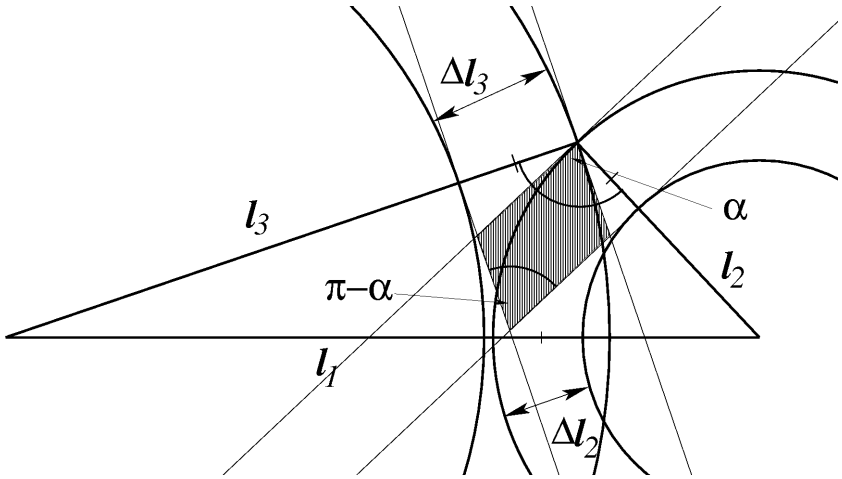

Figure 4.3: Sketch of the region averaged over in case of a degenerate triangle, again for fixed $\boldsymbol{\ell}_1$. The depicted triangle has side lengths $\bar{\ell}_1$, $\bar{\ell}_2 + \Delta\ell_2/2$, and $\bar{\ell}_3 + \Delta\ell_3/2$. The shaded parallelogram approximates the region of overlap, the mirror-symmetric counterpart not being shown.

Symmetrising this argument for all three angular frequency vectors, we propose the following formula to compute the area of overlap in the degenerate case:

$$A_{\mathrm{overlap}}^{\mathrm{deg.}} := \bar{\ell}_2\,\bar{\ell}_3\,\Delta\ell_2\,\Delta\ell_3\,\Lambda\left(\bar{\ell}_1+\frac{\Delta\ell_1}{2},\bar{\ell}_2+\frac{\Delta\ell_2}{2},\bar{\ell}_3+\frac{\Delta\ell_3}{2}\right)\,. \tag{4.12}$$

As is evident from Fig. 4.2, centre panel, the relative deviation of (4.12) from the true overlap area is still fairly small, but – unsurprisingly – noticeably stronger than for (4.11). The right-hand panel gives the size of the overlap area for values of $\bar{\ell}_2$ close to 200, which is the degenerate case. Note that since this plot was determined for $\Delta = 1$, the values relevant for the covariance calculation are only those at integer ℓ. While the true overlap area curbs down to a finite value at $\bar{\ell}_2 = 200$, (4.11) diverges. Still, for $\bar{\ell}_2 = 201$ it produces a fair and for $\bar{\ell}_2 \geq 202$ an excellent approximation. In the degenerate case (4.12) is indeed capable of reproducing the size of the overlap area to good accuracy.

Thus, we suggest to incorporate degenerate triangle configurations into our formalism by replacing $\bar{\ell}_i \to \bar{\ell}_i + \Delta\ell_i/2$ in all arguments of Λ for these cases. This way, we heuristically correct for the breakdown of approximations in the assignment of the actual area, over which triangle configurations are averaged. While the modification is at this stage only motivated by the geometrical interpretation, we will establish a more strict foundation of (4.12) by relating it to Wigner symbols in Sect. 4.1.4.

4.1.3 Bispectrum covariance

The covariance of the bispectrum is defined as

$$\begin{aligned}
&\mathrm{Cov}\left(\hat{B}(\bar{\ell}_1,\bar{\ell}_2,\bar{\ell}_3),\ \hat{B}(\bar{\ell}_4,\bar{\ell}_5,\bar{\ell}_6)\right) \\
\equiv\ &\left\langle\left(\hat{B}(\bar{\ell}_1,\bar{\ell}_2,\bar{\ell}_3)-\left\langle\hat{B}(\bar{\ell}_1,\bar{\ell}_2,\bar{\ell}_3)\right\rangle\right)\ \left(\hat{B}(\bar{\ell}_4,\bar{\ell}_5,\bar{\ell}_6)-\left\langle\hat{B}(\bar{\ell}_4,\bar{\ell}_5,\bar{\ell}_6)\right\rangle\right)\right\rangle \\
=\ &\left\langle\hat{B}(\bar{\ell}_1,\bar{\ell}_2,\bar{\ell}_3)\ \hat{B}(\bar{\ell}_4,\bar{\ell}_5,\bar{\ell}_6)\right\rangle - B(\bar{\ell}_1,\bar{\ell}_2,\bar{\ell}_3)\ B(\bar{\ell}_4,\bar{\ell}_5,\bar{\ell}_6)\,.
\end{aligned} \tag{4.13}$$

The computation of the correlator of two bispectrum estimators involves a 6-point correlator of g, which can be expanded into its connected parts as e.g. outlined in Bernardeau et al. (2002a). Denoting the connected correlators by a subscript c, which will only be done in this paragraph

to avoid confusion, we obtain

$$\begin{aligned}
&\langle g(\boldsymbol{\ell}_1)\, g(\boldsymbol{\ell}_2)\, g(\boldsymbol{\ell}_3)\, g(\boldsymbol{\ell}_4)\, g(\boldsymbol{\ell}_5)\, g(\boldsymbol{\ell}_6)\rangle \qquad (4.14)\\
=\;& \langle g(\boldsymbol{\ell}_1)\, g(\boldsymbol{\ell}_2)\rangle_\mathrm{c} \langle g(\boldsymbol{\ell}_3)\, g(\boldsymbol{\ell}_4)\rangle_\mathrm{c} \langle g(\boldsymbol{\ell}_5)\, g(\boldsymbol{\ell}_6)\rangle_\mathrm{c} + \langle g(\boldsymbol{\ell}_1)\, g(\boldsymbol{\ell}_2)\rangle_\mathrm{c} \langle g(\boldsymbol{\ell}_3)\, g(\boldsymbol{\ell}_5)\rangle_\mathrm{c} \langle g(\boldsymbol{\ell}_4)\, g(\boldsymbol{\ell}_6)\rangle_\mathrm{c}\\
&\qquad + (13 \text{ permutations})\\
+\;& \langle g(\boldsymbol{\ell}_1)\, g(\boldsymbol{\ell}_2)\, g(\boldsymbol{\ell}_3)\rangle_\mathrm{c} \langle g(\boldsymbol{\ell}_4)\, g(\boldsymbol{\ell}_5)\, g(\boldsymbol{\ell}_6)\rangle_\mathrm{c} + \langle g(\boldsymbol{\ell}_1)\, g(\boldsymbol{\ell}_2)\, g(\boldsymbol{\ell}_4)\rangle_\mathrm{c} \langle g(\boldsymbol{\ell}_3)\, g(\boldsymbol{\ell}_5)\, g(\boldsymbol{\ell}_6)\rangle_\mathrm{c}\\
&\qquad + (8 \text{ permutations})\\
+\;& \langle g(\boldsymbol{\ell}_1)\, g(\boldsymbol{\ell}_2)\, g(\boldsymbol{\ell}_3)\, g(\boldsymbol{\ell}_4)\rangle_\mathrm{c} \langle g(\boldsymbol{\ell}_5)\, g(\boldsymbol{\ell}_6)\rangle_\mathrm{c} + \langle g(\boldsymbol{\ell}_1)\, g(\boldsymbol{\ell}_2)\, g(\boldsymbol{\ell}_3)\, g(\boldsymbol{\ell}_5)\rangle_\mathrm{c} \langle g(\boldsymbol{\ell}_4)\, g(\boldsymbol{\ell}_6)\rangle_\mathrm{c}\\
&\qquad + (13 \text{ permutations})\\
+\;& \langle g(\boldsymbol{\ell}_1)\, g(\boldsymbol{\ell}_2)\, g(\boldsymbol{\ell}_3)\, g(\boldsymbol{\ell}_4)\, g(\boldsymbol{\ell}_5)\, g(\boldsymbol{\ell}_6)\rangle_\mathrm{c}\ ,
\end{aligned}$$

where the permutations are to be taken with respect to the indices of the angular frequencies such that for each correlator, no combination of indices is repeated (as the individual correlators are invariant under permutations of the indices within that correlator). The resulting connected parts are related to spectra via

$$\left\langle \prod_{i=1}^{N} g(\boldsymbol{\ell}_i) \right\rangle_\mathrm{c} = (2\pi)^2\, \delta_\mathrm{D}^{(2)}\left(\sum_{i=1}^{N} \boldsymbol{\ell}_i\right)\, P_N(\boldsymbol{\ell}_1, \ldots, \boldsymbol{\ell}_N)\ , \qquad (4.15)$$

where we identify $P_2(\boldsymbol{\ell}_1, \boldsymbol{\ell}_2) \equiv P(\ell_1)$ as the power spectrum and $P_3(\boldsymbol{\ell}_1, \boldsymbol{\ell}_2, \boldsymbol{\ell}_3) \equiv B(\ell_1, \ell_2, \ell_3)$ as the bispectrum. Note the close analogy of (4.15) to (2.32). As the random field g vanishes on average, $\langle g(\boldsymbol{\ell})\rangle = 0$, only P_4 (the trispectrum) and P_6 (the pentaspectrum) will appear in addition in the covariance formula, see (4.14).

Introducing a shorthand notation $\int_{A_R(\bar{\ell}_i)} \mathrm{d}^2\ell_i / A_R(\bar{\ell}_i) \equiv \int_i$, one can write the correlator of the bispectrum estimators by using (4.3) as

$$\begin{aligned}
\left\langle \hat{B}(\bar{\ell}_1, \bar{\ell}_2, \bar{\ell}_3)\, \hat{B}(\bar{\ell}_4, \bar{\ell}_5, \bar{\ell}_6) \right\rangle \;=\; & \frac{(2\,\pi)^4}{A^2}\, \Lambda^{-1}\left(\bar{\ell}_1, \bar{\ell}_2, \bar{\ell}_3\right) \Lambda^{-1}\left(\bar{\ell}_4, \bar{\ell}_5, \bar{\ell}_6\right) \int_1 \int_2 \int_3 \int_4 \int_5 \int_6 \qquad (4.16)\\
& \times \delta_\mathrm{D}^{(2)}(\boldsymbol{\ell}_1 + \boldsymbol{\ell}_2 + \boldsymbol{\ell}_3)\, \delta_\mathrm{D}^{(2)}(\boldsymbol{\ell}_4 + \boldsymbol{\ell}_5 + \boldsymbol{\ell}_6)\, \langle g(\boldsymbol{\ell}_1)\, g(\boldsymbol{\ell}_2)\, g(\boldsymbol{\ell}_3)\, g(\boldsymbol{\ell}_4)\, g(\boldsymbol{\ell}_5)\, g(\boldsymbol{\ell}_6)\rangle\ ,
\end{aligned}$$

which then allows us to insert (4.14) and (4.15). The resulting terms contain products of several delta-distribution. Concerning the terms containing three two-point correlators, one obtains e.g.

$$\begin{aligned}
&\delta_\mathrm{D}^{(2)}(\boldsymbol{\ell}_1 + \boldsymbol{\ell}_2 + \boldsymbol{\ell}_3)\, \delta_\mathrm{D}^{(2)}(\boldsymbol{\ell}_4 + \boldsymbol{\ell}_5 + \boldsymbol{\ell}_6)\, \delta_\mathrm{D}^{(2)}(\boldsymbol{\ell}_1 + \boldsymbol{\ell}_2)\, \delta_\mathrm{D}^{(2)}(\boldsymbol{\ell}_3 + \boldsymbol{\ell}_4)\, \delta_\mathrm{D}^{(2)}(\boldsymbol{\ell}_5 + \boldsymbol{\ell}_6) P(\ell_1)\, P(\ell_3)\, P(\ell_5)\\
=\;& \delta_\mathrm{D}^{(2)}(\boldsymbol{\ell}_3)\, \delta_\mathrm{D}^{(2)}(\boldsymbol{\ell}_4 + \boldsymbol{\ell}_5 + \boldsymbol{\ell}_6)\, \delta_\mathrm{D}^{(2)}(\boldsymbol{\ell}_1 + \boldsymbol{\ell}_2)\, \delta_\mathrm{D}^{(2)}(\boldsymbol{\ell}_3 + \boldsymbol{\ell}_4)\, \delta_\mathrm{D}^{(2)}(\boldsymbol{\ell}_5 + \boldsymbol{\ell}_6) P(\ell_1)\, P(0)\, P(\ell_5)\\
=\;& 0\ , \qquad (4.17)
\end{aligned}$$

and likewise for all other terms in which the correlators do not contain one angular frequency each out of the sets $\{\boldsymbol{\ell}_1, \boldsymbol{\ell}_2, \boldsymbol{\ell}_3\}$ and $\{\boldsymbol{\ell}_4, \boldsymbol{\ell}_5, \boldsymbol{\ell}_6\}$. A similar argument holds for the terms composed of power spectrum and trispectrum, where the trispectrum is readily shown to vanish if the two-point correlator contains both angular frequencies out of the same of the sets mentioned above. This way, the number of terms with three power spectra reduces to 6, the number of terms with trispectrum and power spectrum to 9.

To proceed, we demonstrate the treatment of some exemplary terms in the covariance, for

instance

$$\begin{aligned}
&\int_1\int_2\int_3\int_4\int_5\int_6 \delta_{\mathrm{D}}^{(2)}(\boldsymbol{\ell}_1+\boldsymbol{\ell}_2+\boldsymbol{\ell}_3)\;\delta_{\mathrm{D}}^{(2)}(\boldsymbol{\ell}_4+\boldsymbol{\ell}_5+\boldsymbol{\ell}_6)\;\langle g(\boldsymbol{\ell}_1)\;g(\boldsymbol{\ell}_4)\rangle\,\langle g(\boldsymbol{\ell}_2)\;g(\boldsymbol{\ell}_5)\rangle\,\langle g(\boldsymbol{\ell}_3)\;g(\boldsymbol{\ell}_6)\rangle \\
=\;& (2\pi)^6\int_1\int_2\int_3\int_4\int_5\int_6 \delta_{\mathrm{D}}^{(2)}(\boldsymbol{\ell}_1+\boldsymbol{\ell}_2+\boldsymbol{\ell}_3)\;\delta_{\mathrm{D}}^{(2)}(\boldsymbol{\ell}_4+\boldsymbol{\ell}_5+\boldsymbol{\ell}_6) \\
&\qquad\times\delta_{\mathrm{D}}^{(2)}(\boldsymbol{\ell}_1+\boldsymbol{\ell}_4)\;\delta_{\mathrm{D}}^{(2)}(\boldsymbol{\ell}_2+\boldsymbol{\ell}_5)\;\delta_{\mathrm{D}}^{(2)}(\boldsymbol{\ell}_3+\boldsymbol{\ell}_6)\;P(\ell_1)\;P(\ell_2)\;P(\ell_3) \\
=\;& (2\pi)^6\frac{\delta_{\bar{\ell}_1\bar{\ell}_4}\;\delta_{\bar{\ell}_2\bar{\ell}_5}\;\delta_{\bar{\ell}_3\bar{\ell}_6}}{A_R(\bar{\ell}_1)\;A_R(\bar{\ell}_2)\;A_R(\bar{\ell}_3)}\int_1\int_2\int_3\left(\delta_{\mathrm{D}}^{(2)}(\boldsymbol{\ell}_1+\boldsymbol{\ell}_2+\boldsymbol{\ell}_3)\right)^2\;P(\ell_1)\;P(\ell_2)\;P(\ell_3)\;, \qquad (4.18)
\end{aligned}$$

where the integrations over $\boldsymbol{\ell}_4$ to $\boldsymbol{\ell}_6$ only yield a non-zero result if the annuli of the angular frequencies in the corresponding delta-distributions, which are integrated over, coincide. Thus, for every such integration a Kronecker symbol is generated. The resulting expression in (4.18) can now easily be simplified by using (4.5), producing a factor of $A/(2\,\pi)^2$, and subsequently (4.6) to execute the remaining angular integrations. Note that again only the delta-distribution depends on the polar angles of the angular frequencies. Therefore, considering only the Gaussian contribution to the covariance, (4.16) turns into

$$\begin{aligned}
\left\langle\hat{B}(\bar{\ell}_1,\bar{\ell}_2,\bar{\ell}_3)\;\hat{B}(\bar{\ell}_4,\bar{\ell}_5,\bar{\ell}_6)\right\rangle_{\mathrm{Gauss}} &= \frac{(2\,\pi)^9}{A\;A_R(\bar{\ell}_1)\;A_R(\bar{\ell}_2)\;A_R(\bar{\ell}_3)}\;\Lambda^{-1}\left(\bar{\ell}_1,\bar{\ell}_2,\bar{\ell}_3\right) \qquad (4.19)\\
&\times D_{\bar{\ell}_1,\bar{\ell}_2,\bar{\ell}_3,\bar{\ell}_4,\bar{\ell}_5,\bar{\ell}_6}\int_{A_R(\bar{\ell}_1)}\frac{\mathrm{d}\ell_1\ell_1}{A_R(\bar{\ell}_1)}\;P(\ell_1)\int_{A_R(\bar{\ell}_2)}\frac{\mathrm{d}\ell_2\ell_2}{A_R(\bar{\ell}_2)}\;P(\ell_2)\int_{A_R(\bar{\ell}_3)}\frac{\mathrm{d}\ell_3\ell_3}{A_R(\bar{\ell}_3)}\;P(\ell_3)\;,
\end{aligned}$$

where we again pulled Λ, evaluated at the averaged angular frequencies, out of the radial integrations. Besides, we defined the shorthand notation

$$\begin{aligned}
D_{\ell_1,\ell_2,\ell_3,\ell_4,\ell_5,\ell_6} \;\equiv\;& \delta_{\ell_1\ell_4}\;\delta_{\ell_2\ell_5}\;\delta_{\ell_3\ell_6}+\delta_{\ell_1\ell_5}\;\delta_{\ell_2\ell_4}\;\delta_{\ell_3\ell_6}+\delta_{\ell_1\ell_4}\;\delta_{\ell_2\ell_6}\;\delta_{\ell_3\ell_5} \qquad (4.20)\\
&+\delta_{\ell_1\ell_5}\;\delta_{\ell_2\ell_6}\;\delta_{\ell_3\ell_4}+\delta_{\ell_1\ell_6}\;\delta_{\ell_2\ell_4}\;\delta_{\ell_3\ell_5}+\delta_{\ell_1\ell_6}\;\delta_{\ell_2\ell_5}\;\delta_{\ell_3\ell_4}
\end{aligned}$$

for convenience. By making use of (4.2) and defining the bin-averaged power spectrum as

$$P(\bar{\ell}_i)\equiv\int_{\bar{\ell}_i-1/2\Delta\ell}^{\bar{\ell}_i+1/2\Delta\ell}\frac{\mathrm{d}\ell_i\ell_i}{\bar{\ell}_i\Delta\ell}\;P(\ell_i)\;, \qquad (4.21)$$

see Joachimi et al. (2008), in analogy to the definition of the bin-averaged bispectrum, one obtains the expression

$$\begin{aligned}
\left\langle\hat{B}(\bar{\ell}_1,\bar{\ell}_2,\bar{\ell}_3)\;\hat{B}(\bar{\ell}_4,\bar{\ell}_5,\bar{\ell}_6)\right\rangle_{\mathrm{Gauss}} &= \frac{(2\,\pi)^3}{A\;\bar{\ell}_1\bar{\ell}_2\bar{\ell}_3\Delta\ell_1\Delta\ell_2\Delta\ell_3}\;\Lambda^{-1}\left(\bar{\ell}_1,\bar{\ell}_2,\bar{\ell}_3\right) \qquad (4.22)\\
&\times D_{\bar{\ell}_1,\bar{\ell}_2,\bar{\ell}_3,\bar{\ell}_4,\bar{\ell}_5,\bar{\ell}_6}\;P(\bar{\ell}_1)P(\bar{\ell}_2)P(\bar{\ell}_3)\;.
\end{aligned}$$

Terms composed of two three-point correlators can be processed as follows,

$$\begin{aligned}
&\int_1\int_2\int_3\int_4\int_5\int_6 \delta_{\mathrm{D}}^{(2)}(\boldsymbol{\ell}_1+\boldsymbol{\ell}_2+\boldsymbol{\ell}_3)\;\delta_{\mathrm{D}}^{(2)}(\boldsymbol{\ell}_4+\boldsymbol{\ell}_5+\boldsymbol{\ell}_6)\;\langle g(\boldsymbol{\ell}_1)\;g(\boldsymbol{\ell}_2)\;g(\boldsymbol{\ell}_4)\rangle\,\langle g(\boldsymbol{\ell}_3)\;g(\boldsymbol{\ell}_5)\;g(\boldsymbol{\ell}_6)\rangle \\
=\;& (2\pi)^4\int_1\int_2\int_3\int_4\int_5\int_6 \delta_{\mathrm{D}}^{(2)}(\boldsymbol{\ell}_1+\boldsymbol{\ell}_2+\boldsymbol{\ell}_3)\;\delta_{\mathrm{D}}^{(2)}(\boldsymbol{\ell}_4+\boldsymbol{\ell}_5+\boldsymbol{\ell}_6) \\
&\qquad\times\delta_{\mathrm{D}}^{(2)}(\boldsymbol{\ell}_1+\boldsymbol{\ell}_2+\boldsymbol{\ell}_4)\;\delta_{\mathrm{D}}^{(2)}(\boldsymbol{\ell}_3+\boldsymbol{\ell}_5+\boldsymbol{\ell}_6)\;B(\ell_1,\ell_2,\ell_4)\;B(\ell_3,\ell_5,\ell_6) \qquad (4.23)\\
=\;& (2\pi)^4\;\delta_{\bar{\ell}_3\bar{\ell}_4}\int_1\int_2\int_3\int_5\int_6 \delta_{\mathrm{D}}^{(2)}(\boldsymbol{\ell}_1+\boldsymbol{\ell}_2+\boldsymbol{\ell}_3)\;\delta_{\mathrm{D}}^{(2)}(-\boldsymbol{\ell}_1-\boldsymbol{\ell}_2+\boldsymbol{\ell}_5+\boldsymbol{\ell}_6) \\
&\qquad\times\delta_{\mathrm{D}}^{(2)}(\boldsymbol{\ell}_3+\boldsymbol{\ell}_5+\boldsymbol{\ell}_6)\;B(\ell_1,\ell_2,|\boldsymbol{\ell}_1+\boldsymbol{\ell}_2|)\;B(\ell_3,\ell_5,\ell_6) \\
=\;& A\;(2\pi)^2\;\delta_{\bar{\ell}_3\bar{\ell}_4}\int_1\int_2\int_3\int_5\int_6 \delta_{\mathrm{D}}^{(2)}(\boldsymbol{\ell}_1+\boldsymbol{\ell}_2+\boldsymbol{\ell}_3)\;\delta_{\mathrm{D}}^{(2)}(\boldsymbol{\ell}_3+\boldsymbol{\ell}_5+\boldsymbol{\ell}_6)\;B(\ell_1,\ell_2,\ell_3)\;B(\ell_3,\ell_5,\ell_6)\;,
\end{aligned}$$

where to generate the Kronecker symbol $\delta_{\bar{\ell}_3\bar{\ell}_4}$, we made use of fact that $\boldsymbol{\ell}_1 + \boldsymbol{\ell}_2 = -\boldsymbol{\ell}_3$ due to the corresponding delta-distribution. To arrive at the last equality, (4.5) has been applied after processing the arguments of the delta-distributions similar to (4.17). The remaining terms, containing four- and six-point correlators of g, can be dealt with in close analogy to (4.23). We mention the special case

$$\begin{aligned}
&\int_1\int_2\int_3\int_4\int_5\int_6 \delta_{\mathrm{D}}^{(2)}(\boldsymbol{\ell}_1+\boldsymbol{\ell}_2+\boldsymbol{\ell}_3)\;\delta_{\mathrm{D}}^{(2)}(\boldsymbol{\ell}_4+\boldsymbol{\ell}_5+\boldsymbol{\ell}_6)\;\langle g(\boldsymbol{\ell}_1)\,g(\boldsymbol{\ell}_2)\,g(\boldsymbol{\ell}_3)\rangle\,\langle g(\boldsymbol{\ell}_4)\,g(\boldsymbol{\ell}_5)\,g(\boldsymbol{\ell}_6)\rangle \\
&= (2\pi)^4\int_1\int_2\int_3\int_4\int_5\int_6 \left(\delta_{\mathrm{D}}^{(2)}(\boldsymbol{\ell}_1+\boldsymbol{\ell}_2+\boldsymbol{\ell}_3)\right)^2\;\left(\delta_{\mathrm{D}}^{(2)}(\boldsymbol{\ell}_4+\boldsymbol{\ell}_5+\boldsymbol{\ell}_6)\right)^2 B(\ell_1,\ell_2,\ell_3)\;B(\ell_4,\ell_5,\ell_6) \\
&= A^2\int_1\int_2\int_3 \delta_{\mathrm{D}}^{(2)}(\boldsymbol{\ell}_1+\boldsymbol{\ell}_2+\boldsymbol{\ell}_3)\;B(\ell_1,\ell_2,\ell_3)\int_4\int_5\int_6 \delta_{\mathrm{D}}^{(2)}(\boldsymbol{\ell}_4+\boldsymbol{\ell}_5+\boldsymbol{\ell}_6)\;B(\ell_4,\ell_5,\ell_6) \\
&= \frac{A^2}{(2\pi)^4}\,\Lambda\left(\bar{\ell}_1,\bar{\ell}_2,\bar{\ell}_3\right)\;\Lambda\left(\bar{\ell}_4,\bar{\ell}_5,\bar{\ell}_6\right)\;B(\bar{\ell}_1,\bar{\ell}_2,\bar{\ell}_3)\,B(\bar{\ell}_4,\bar{\ell}_5,\bar{\ell}_6)\;, \qquad (4.24)
\end{aligned}$$

which, after inserting this expression into (4.16), cancels the product $B(\bar{\ell}_1,\bar{\ell}_2,\bar{\ell}_3)B(\bar{\ell}_4,\bar{\ell}_5,\bar{\ell}_6)$ in the definition of the covariance (4.13).

Combining these results, we obtain the total bispectrum covariance

$$\begin{aligned}
&\mathrm{Cov}\left(B(\bar{\ell}_1,\bar{\ell}_2,\bar{\ell}_3),\;B(\bar{\ell}_4,\bar{\ell}_5,\bar{\ell}_6)\right) = \qquad (4.25)\\
&\frac{(2\,\pi)^3}{A\;\bar{\ell}_1\bar{\ell}_2\bar{\ell}_3\Delta\ell_1\Delta\ell_2\Delta\ell_3}\,\Lambda^{-1}\left(\bar{\ell}_1,\bar{\ell}_2,\bar{\ell}_3\right)\;D_{\bar{\ell}_1,\bar{\ell}_2,\bar{\ell}_3,\bar{\ell}_4,\bar{\ell}_5,\bar{\ell}_6}\;P(\bar{\ell}_1)P(\bar{\ell}_2)P(\bar{\ell}_3) \\
&+\frac{\mathcal{C}}{A}\,\delta_{\bar{\ell}_3\bar{\ell}_4}\int_1\int_2\int_3\int_5\int_6 \delta_{\mathrm{D}}^{(2)}(\boldsymbol{\ell}_1+\boldsymbol{\ell}_2+\boldsymbol{\ell}_3)\;\delta_{\mathrm{D}}^{(2)}(\boldsymbol{\ell}_3+\boldsymbol{\ell}_5+\boldsymbol{\ell}_6)\;B(\ell_1,\ell_2,\ell_3)\;B(\ell_3,\ell_5,\ell_6)+(8\text{ perm.}) \\
&+\frac{\mathcal{C}}{A}\,\delta_{\bar{\ell}_3\bar{\ell}_6}\int_1\int_2\int_3\int_4\int_5 \delta_{\mathrm{D}}^{(2)}(\boldsymbol{\ell}_1+\boldsymbol{\ell}_2+\boldsymbol{\ell}_3)\;\delta_{\mathrm{D}}^{(2)}(\boldsymbol{\ell}_4+\boldsymbol{\ell}_5-\boldsymbol{\ell}_3)\;P_4(\boldsymbol{\ell}_1,\boldsymbol{\ell}_2,\boldsymbol{\ell}_4,\boldsymbol{\ell}_5)\;P(\ell_3)+(8\text{ perm.}) \\
&+\frac{\mathcal{C}}{A}\int_1\int_2\int_3\int_4\int_5\int_6 \delta_{\mathrm{D}}^{(2)}(\boldsymbol{\ell}_1+\boldsymbol{\ell}_2+\boldsymbol{\ell}_3)\;\delta_{\mathrm{D}}^{(2)}(\boldsymbol{\ell}_4+\boldsymbol{\ell}_5+\boldsymbol{\ell}_6)\;P_6(\boldsymbol{\ell}_1,\boldsymbol{\ell}_2,\boldsymbol{\ell}_3,\boldsymbol{\ell}_4,\boldsymbol{\ell}_5,\boldsymbol{\ell}_6)\;,
\end{aligned}$$

where the prefactor reads $\mathcal{C} \equiv (2\pi)^6\,\Lambda^{-1}\left(\bar{\ell}_1,\bar{\ell}_2,\bar{\ell}_3\right)\;\Lambda^{-1}\left(\bar{\ell}_4,\bar{\ell}_5,\bar{\ell}_6\right)$.

The general form of the covariance terms is in agreement with the expressions derived in Sefusatti et al. (2006). As mentioned in Sect. 4.1.1, shot or shape noise can readily be included into this covariance by adding a corresponding noise term to the power spectra. Weak lensing or galaxy clustering surveys often have in addition tomographic information, so that the data is binned into (photometric) redshift bins. The covariance can be generalised to this case in a straightforward manner by obeying the practical rule that each photometric redshift 'sticks' to the angular frequency it is assigned to, see Takada & Jain (2004). A similar argument holds for the generalisation to CMB polarisation bispectrum covariances (Hu 2000).

4.1.4 Equivalence to spherical harmonics approach

In this section we demonstrate that both our and the spherical harmonic approach are equivalent in the sense that they measure the same information in a survey. Moreover, we investigate the behaviour with respect to parity, and the relation between the covariances of both approaches, considering for the remainder of this work only the Gaussian part of (4.25).

Comparison of covariances

On the celestial sphere one can decompose the random field g into spherical harmonics, which produces a set of coefficients $g_{\ell m}$ with ℓ, m integers and $\ell \geq 0$, $-\ell \leq m \leq \ell$. In terms of the

$g_{\ell m}$ one can define a bispectrum estimator as (e.g. Hu 2000)

$$\hat{B}_{\ell_1,\ell_2,\ell_3} = \sum_{m_1,m_2,m_3} \begin{pmatrix} \ell_1 & \ell_2 & \ell_3 \\ m_1 & m_2 & m_3 \end{pmatrix} g_{\ell_1 m_1}\, g_{\ell_2 m_2}\, g_{\ell_3 m_3}\ , \tag{4.26}$$

where the object in parentheses is the Wigner-3j symbol. Properties of the Wigner symbol are reviewed in Hu (2000); most importantly, it obeys the triangle condition, i.e. it is non-zero only for $|\ell_1 - \ell_2| \leq \ell_3 \leq \ell_1 + \ell_2$ and permutations thereof. For this estimator Hu (2000) derived the simple Gaussian covariance

$$\mathrm{Cov}\left(B_{\bar{\ell}_1,\bar{\ell}_2,\bar{\ell}_3},\ B_{\bar{\ell}_4,\bar{\ell}_5,\bar{\ell}_6}\right) = D_{\bar{\ell}_1,\bar{\ell}_2,\bar{\ell}_3,\bar{\ell}_4,\bar{\ell}_5,\bar{\ell}_6}\ P_{\bar{\ell}_1} P_{\bar{\ell}_2} P_{\bar{\ell}_3}\ , \tag{4.27}$$

where P_ℓ denotes the full-sky power spectrum, and where $D_{\bar{\ell}_1,\bar{\ell}_2,\bar{\ell}_3,\bar{\ell}_4,\bar{\ell}_5,\bar{\ell}_6}$ is used as defined in (4.20). Moreover, he gives approximate relations between the spherical harmonic and Fourier-plane spectra,

$$P_\ell \approx P(\ell)\ ; \qquad B_{\ell_1,\ell_2,\ell_3} \approx \begin{pmatrix} \ell_1 & \ell_2 & \ell_3 \\ 0 & 0 & 0 \end{pmatrix} \sqrt{\frac{(2\ell_1+1)(2\ell_2+1)(2\ell_3+1)}{4\pi}}\, B(\ell_1,\ell_2,\ell_3)\ , \tag{4.28}$$

valid for $\ell_1, \ell_2, \ell_3 \gg 1$. These equations can only hold for integer ℓ. In addition, the Wigner symbol with $m_1 = m_2 = m_3 = 0$ vanishes for $L \equiv \ell_1 + \ell_2 + \ell_3$ odd, see the following section for details. Making use of the standard procedure of multiplying (4.27) by an *ad hoc* factor of $f_{\mathrm{sky}}^{-1} = 4\pi/A$ to account for finite sky coverage of the survey, one can derive a flat-sky spherical harmonic covariance with (4.28) as (Hu 2000; Takada & Jain 2004)

$$\begin{aligned} \left\langle \hat{B}(\bar{\ell}_1,\bar{\ell}_2,\bar{\ell}_3)\ \hat{B}(\bar{\ell}_4,\bar{\ell}_5,\bar{\ell}_6) \right\rangle \ \approx\ & \frac{(4\pi)^2\ D_{\bar{\ell}_1,\bar{\ell}_2,\bar{\ell}_3,\bar{\ell}_4,\bar{\ell}_5,\bar{\ell}_6}}{A\,(2\bar{\ell}_1+1)\,(2\bar{\ell}_2+1)\,(2\bar{\ell}_3+1)} \\ & \times \begin{pmatrix} \bar{\ell}_1 & \bar{\ell}_2 & \bar{\ell}_3 \\ 0 & 0 & 0 \end{pmatrix}^{-2} P(\bar{\ell}_1)\ P(\bar{\ell}_2)\ P(\bar{\ell}_3)\ , \end{aligned} \tag{4.29}$$

where still the angular frequencies are required to be integer, and L even. As is true for our approach, (4.29) holds for $\ell \gg 1$ only. To be able to compare this widely used formula to our results, a relation between the Wigner symbol and Λ has to be found.

When comparing the spherical harmonics and the Fourier-plane approach, Hu (2000) already came across integrals of the form (4.6). We reproduce his computation,

$$\begin{aligned} & \int \mathrm{d}^2\ell_1 \int \mathrm{d}^2\ell_2 \int \mathrm{d}^2\ell_3\ \delta_{\mathrm{D}}^{(2)}(\boldsymbol{\ell}_1 + \boldsymbol{\ell}_2 + \boldsymbol{\ell}_3) \\ =\ & \int \mathrm{d}^2\ell_1 \int \mathrm{d}^2\ell_2 \int \mathrm{d}^2\ell_3 \int \frac{\mathrm{d}^2\theta}{(2\,\pi)^2}\ \mathrm{e}^{\mathrm{i}(\boldsymbol{\ell}_1+\boldsymbol{\ell}_2+\boldsymbol{\ell}_3)\cdot\boldsymbol{\theta}} \\ \approx\ & \int \mathrm{d}\ell_1\ell_1 \int \mathrm{d}\ell_2\ell_2 \int \mathrm{d}\ell_3\ell_3 \sqrt{\frac{(2\,\pi)^5}{\ell_1\ell_2\ell_3}} \int \mathrm{d}\Omega\ Y^0_{\ell_1}(\boldsymbol{n})\ Y^0_{\ell_2}(\boldsymbol{n})\ Y^0_{\ell_3}(\boldsymbol{n}) \\ \approx\ & 8\pi^2 \int \mathrm{d}\ell_1\ell_1 \int \mathrm{d}\ell_2\ell_2 \int \mathrm{d}\ell_3\ell_3 \begin{pmatrix} \ell_1 & \ell_2 & \ell_3 \\ 0 & 0 & 0 \end{pmatrix}^2\ , \end{aligned} \tag{4.30}$$

where $\int \mathrm{d}\Omega$ is the integral over the unit sphere, and where $Y^m_\ell(\boldsymbol{n})$ denotes the spherical harmonic function with $\boldsymbol{n}$ the unit normal vector on the sphere. We are concerned with the validity of this derivation for the following reasons: Terms with integer and real-valued ℓ are mixed, e.g. it remains unclear how the integration over the Wigner symbol squared is to be understood. To get from the second to the third equality, the Fourier base $\mathrm{e}^{\mathrm{i}\boldsymbol{\ell}\cdot\boldsymbol{\theta}}$ is expanded into spherical

harmonics, an approximation which Hu (2000) correctly states to be valid for small angles only. However, the integration over angles runs over the full two-dimensional plane or the unit sphere, respectively. Moreover, it is not specified how the non-trivial transition from an integral over the plane to one over the unit sphere is executed. Instead of (4.30), we propose to use (4.6), which is an exact and rigorous expression.

To allow for a comparison between (4.30) and our approach based on (4.6), we need to establish a relation between the square of the Wigner symbol and (4.7). We refer to Borodin et al. (1978, see also references therein) who compute approximation formulae of the Wigner symbol in the context of the quasi-continuous limit of quantum states with high angular momenta. The base of their derivation is formed by the exact relation

$$\begin{aligned} &\int_0^{2\pi} \mathrm{d}\varphi \int_0^{2\pi} \mathrm{d}\psi \int_0^{\pi} \mathrm{d}\theta \sin\theta \; D^{\ell_1}_{m_1 m_1'}(\varphi,\theta,\psi) \; D^{\ell_2}_{m_2 m_2'}(\varphi,\theta,\psi) \; D^{\ell_3}_{m_3 m_3'}(\varphi,\theta,\psi) \qquad (4.31) \\ = \;& 8\pi^2 \begin{pmatrix} \ell_1 & \ell_2 & \ell_3 \\ m_1 & m_2 & m_3 \end{pmatrix} \cdot \begin{pmatrix} \ell_1 & \ell_2 & \ell_3 \\ m_1' & m_2' & m_3' \end{pmatrix} , \end{aligned}$$

where $D^{\ell}_{mm'}$ denotes the $m \times m'$ element of the Wigner D matrix, which in turn is a function of the three Euler angles φ, θ, and ψ. Making use of a quasi-classical approximation of the $D^{\ell}_{mm'}$, Borodin et al. (1978) compute expressions for the general Wigner symbol in the limit of large and continuous angular frequencies. From these results we extract the approximation

$$\begin{aligned} \begin{pmatrix} \ell_1 & \ell_2 & \ell_3 \\ 0 & 0 & 0 \end{pmatrix}^2 \;\approx\; & \frac{2}{\pi} \left\{ 2 \left(\ell_1 + \frac{1}{2}\right)^2 \left(\ell_2 + \frac{1}{2}\right)^2 + 2 \left(\ell_2 + \frac{1}{2}\right)^2 \left(\ell_3 + \frac{1}{2}\right)^2 \right. \qquad (4.32) \\ & \left. + 2 \left(\ell_3 + \frac{1}{2}\right)^2 \left(\ell_1 + \frac{1}{2}\right)^2 - \left(\ell_1 + \frac{1}{2}\right)^4 - \left(\ell_2 + \frac{1}{2}\right)^4 - \left(\ell_3 + \frac{1}{2}\right)^4 \right\}^{-1/2} , \end{aligned}$$

which allows us to generalise the Wigner symbol to real-valued arguments. Equation (4.32) holds only for $\ell_1, \ell_2, \ell_3 \gg 1$, which, in the quantum-mechanical context of Borodin et al. (1978), originates from the use of expressions that are valid for large angular momenta, i.e. the quasi-classical limit, only. This condition on angular frequencies also underlies the approximations in (4.28) and (4.30) and can in our context be interpreted as a natural consequence of working in the flat-sky approximation.

As is demonstrated in Fig. 4.4, we find that (4.32) constitutes an excellent approximation, whose accuracy over a wide range of ℓ-values is orders of magnitude better than the approximation given in Takada & Jain (2004), eq. (A3),

$$\begin{aligned} \begin{pmatrix} \ell_1 & \ell_2 & \ell_3 \\ 0 & 0 & 0 \end{pmatrix}^2 \;\approx\; & \frac{\mathrm{e}^3}{\sqrt{2}\,\pi} (L+2)^{-1/2} \left(\frac{L}{2} - \ell_1 + 1\right)^{-1/2} \left(\frac{L}{2} - \ell_2 + 1\right)^{-1/2} \qquad (4.33) \\ & \times \left(\frac{L}{2} - \ell_3 + 1\right)^{-1/2} \left(\frac{L/2 - \ell_1 + 1/2}{L/2 - \ell_1 + 1}\right)^{L - 2\ell_1 + 1/2} \\ & \times \left(\frac{L/2 - \ell_2 + 1/2}{L/2 - \ell_2 + 1}\right)^{L - 2\ell_2 + 1/2} \left(\frac{L/2 - \ell_3 + 1/2}{L/2 - \ell_3 + 1}\right)^{L - 2\ell_3 + 1/2} . \end{aligned}$$

Only for triangle configurations close to degeneracy does the latter formula perform slightly better. Both approximation formulae are least accurate in the case of a degenerate triangle configuration with fractional errors around 10 % or slightly above, but improve quickly to very small percentage deviations when the configuration approaches a more equilateral form. In Fig. 4.4 we also plot the fractional errors as a function of the triangle area enclosed by the three angular frequency vectors and as a function of the internal angle Φ_3 opposite ℓ_3, being

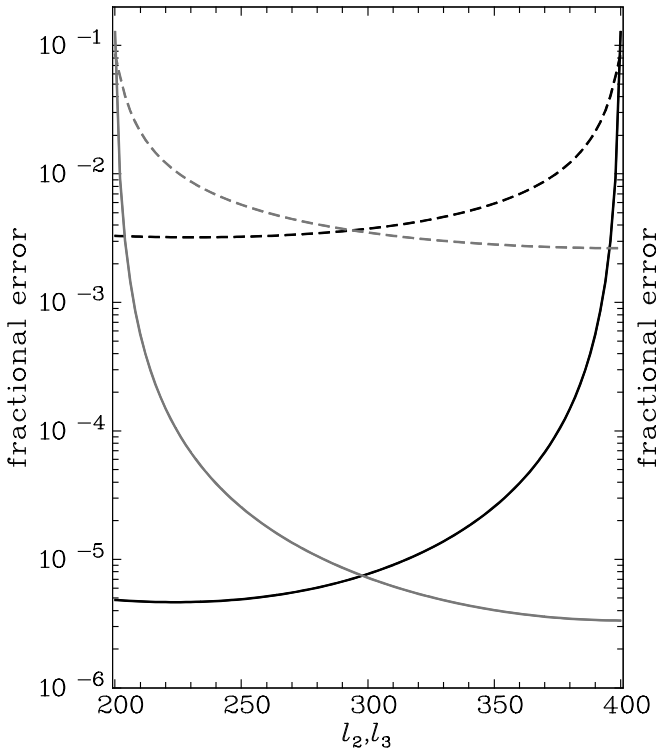

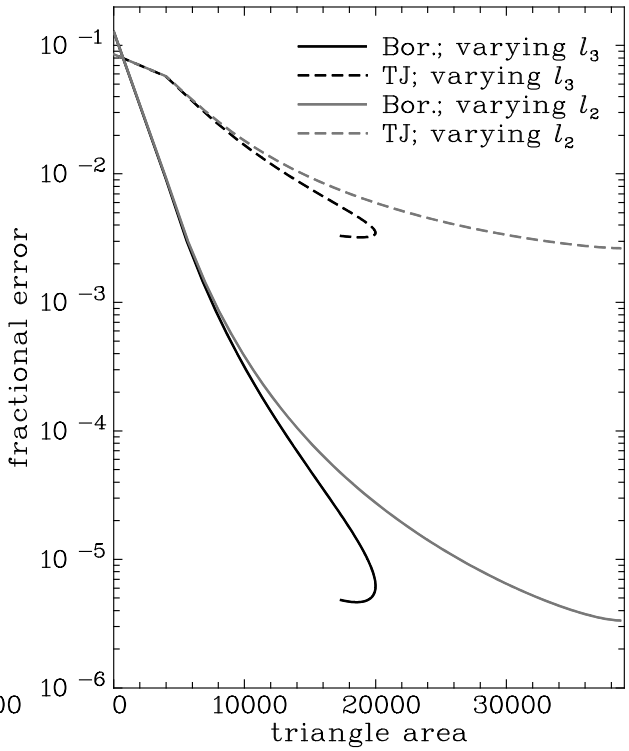

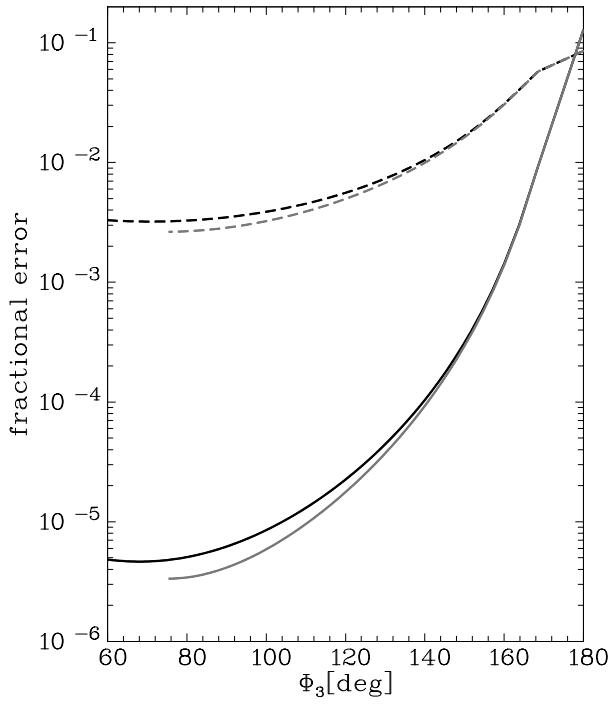

Figure 4.4: Fractional error of the approximation formulae for the Wigner symbol. *Top left panel*: Shown are the relative deviations of (4.32) and (4.33) from the true absolute value of the Wigner symbol. The same triangle configurations as in Fig. 4.2 are used. Results for $\ell_1 = 200, \ell_3 = 400$ and varying ℓ_2 are shown in gray while those corresponding to $\ell_1, \ell_2 = 200$ and varying ℓ_3 are plotted in black. Solid curves are obtained using (4.32), dashed curves by employing (4.33). *Top right panel*: Same as above, but now plotting on the abscissa the corresponding triangle area enclosed by the three angular frequency vectors. Note that before reaching the equilateral configuration, the area has a maximum and starts to decrease again. *Bottom panel*: Same as above, but now as a function of the internal angle Φ_3 opposite ℓ_3, which is the longest side of the triangle in both configurations considered. Hence, $\Phi_3 = 60°$ corresponds to the equilateral case, and $\Phi_3 = 180°$ to the degenerate case.

the longest side of the triangle in the configurations considered. In terms of these quantities we observe a more universal behaviour of the errors, in particular in the regime where the approximations are less accurate. We find to good approximation that, when approaching the degenerate case, relative errors increase exponentially with decreasing triangle area and increasing Φ_3.

For $\ell \gg 1$, and if the triangle configuration is not too close to the degenerate case, one may approximate $\ell_i + 1/2 \approx \ell_i$, so that one finds from (4.7) and (4.32)

$$\begin{pmatrix} \ell_1 & \ell_2 & \ell_3 \\ 0 & 0 & 0 \end{pmatrix}^2 \approx \frac{\Lambda\left(\ell_1, \ell_2, \ell_3\right)}{2\pi} \,. \tag{4.34}$$

Remarkably, since for integer angular frequencies we have $\Delta\ell_1 = \Delta\ell_2 = \Delta\ell_3 = 1$, (4.32) exactly reproduces our earlier conjecture (4.12), which strongly supports its validity. If one replaces the Wigner symbol in (4.30) by (4.34), however, one obtains a result which is a factor of 2 larger compared to (4.6).

Inserting (4.34) into (4.29), and using $2\ell + 1 \approx 2\ell$ for $\ell \gg 1$, we get

$$\left\langle \hat{B}(\bar{\ell}_1, \bar{\ell}_2, \bar{\ell}_3)\, \hat{B}(\bar{\ell}_4, \bar{\ell}_5, \bar{\ell}_6) \right\rangle \approx \frac{2\pi^2\, D_{\bar{\ell}_1,\bar{\ell}_2,\bar{\ell}_3,\bar{\ell}_4,\bar{\ell}_5,\bar{\ell}_6}}{A\, \bar{\ell}_1\, \bar{\ell}_2\, \bar{\ell}_3} \begin{pmatrix} \bar{\ell}_1 & \bar{\ell}_2 & \bar{\ell}_3 \\ 0 & 0 & 0 \end{pmatrix}^{-2} P(\bar{\ell}_1)\, P(\bar{\ell}_2)\, P(\bar{\ell}_3) \,, \tag{4.35}$$

which is equivalent to (4.22) if the latter equation is specified to $\Delta\ell_1 = \Delta\ell_2 = \Delta\ell_3 = 1$, and integer ℓ with L even – except for (4.35) being a factor of 2 smaller. In the following, we are going to elaborate on this apparent discrepancy.

Parity

To elucidate the different noise properties of the Fourier-plane and spherical harmonic bispectrum estimators, we investigate their behaviour with respect to parity. In two dimensions the parity transformation corresponds to an axis reflection, or equivalently, the reversal of the polar angle of all spatial vectors. To flip the parity of a triangle, one can do an odd permutation of its sides, see e.g. the two triangles sketched in Fig. 4.1. Hence, to test the behaviour of estimators for triangles of different parity, it is sufficient to flip any two of its angular frequency arguments.

Consulting (4.26), we find

$$\hat{B}_{\ell_1,\ell_3,\ell_2} = (-1)^{\ell_1+\ell_2+\ell_3}\, \hat{B}_{\ell_1,\ell_2,\ell_3} \tag{4.36}$$

because of the behaviour of the Wigner symbol under change of parity,

$$\begin{pmatrix} \ell_1 & \ell_2 & \ell_3 \\ m_1 & m_2 & m_3 \end{pmatrix} = (-1)^{\ell_1+\ell_2+\ell_3} \begin{pmatrix} \ell_1 & \ell_3 & \ell_2 \\ m_1 & m_3 & m_2 \end{pmatrix} \,, \tag{4.37}$$

and likewise for all odd permutations of the columns in the Wigner symbol. Thus, the spherical harmonics estimator is parity-invariant for L even and changes sign for L odd. Most cosmological theories predict parity-invariant large-scale structures and CMB anisotropies. If parity symmetry is built into the cosmological model at consideration, measures that vary under parity transformations do not have any predictive power, wherefore they are usually not considered in a data analysis. Accordingly, (4.26) is only used for arguments that have L even. Note that parity invariance is also incorporated into the relation between the spherical harmonics and Fourier-plane bispectra, see the second equality of (4.28), via the Wigner symbol which vanishes for L odd (this behaviour is a direct consequence of (4.37) for $m_1 = m_2 = m_3 = 0$).

The Fourier-plane estimator is by design parity-invariant, which can be seen mathematically from swapping arguments of (4.3), or illustratively by inspecting Fig. 4.1. From the sketch it is evident that triangle configurations of different parity are averaged over with equal weight. For a more formal argument, we can explicitly construct estimators that average only over triangle configurations of the same parity. To this end, consider the two-dimensional cross product

$\boldsymbol{a} \times \boldsymbol{b} = a_x b_y - a_y b_x$ (Schneider & Lombardi 2003) of the angular frequency vectors $\boldsymbol{\ell}_1, \boldsymbol{\ell}_2, \boldsymbol{\ell}_3$. If they form a triangle, one finds $\boldsymbol{\ell}_1 \times \boldsymbol{\ell}_2 = \boldsymbol{\ell}_2 \times \boldsymbol{\ell}_3 = \boldsymbol{\ell}_3 \times \boldsymbol{\ell}_1$, which follows from $\boldsymbol{\ell}_1 + \boldsymbol{\ell}_2 + \boldsymbol{\ell}_3 = 0$. A change in the parity of the triangle implies a sign flip in these cross products.

Noting that $\boldsymbol{\ell}_i \times \boldsymbol{\ell}_j = \ell_i \ell_j \sin(\varphi_{\ell_j} - \varphi_{\ell_i})$, we compute a condition on the polar angles,

$$\varphi_{\ell_2} - \varphi_{\ell_1} \in [0, \pi] \;\; ; \quad \varphi_{\ell_3} - \varphi_{\ell_2} \in [0, \pi] \;\; ; \quad \varphi_{\ell_1} - \varphi_{\ell_3} \in [0, \pi] \;\; . \tag{4.38}$$

To obtain the parity transformed triangle, swap the signs of the polar angles in (4.38). Under the premise that the vectors do form a triangle, one of the conditions in (4.38) is redundant, the remaining ones restricting the angular integrations in the averaging of (4.3). For instance, the integration ranges could be modified to $\varphi_{\ell_1} \in [0, 2\pi]$, $\varphi_{\ell_2} \in [\varphi_{\ell_1}, \pi + \varphi_{\ell_1}]$, and $\varphi_{\ell_3} \in [\varphi_{\ell_1} - \pi, \varphi_{\ell_1}]$. Due to rotational symmetry, which still holds, the inner integrals have to yield the same result for all possible values of φ_{ℓ_1}. Therefore, we can set the ranges of the inner integrals to $\varphi_{\ell_2} \in [0, \pi]$ and $\varphi_{\ell_3} \in [-\pi, 0]$ without loss of generality. To maintain the symmetry, we keep the integral over φ_{ℓ_1} in our notation. These findings are reflected in the shorthand notation

$$\int \mathrm{d}\{\varphi_1, \varphi_2, \varphi_3\} \equiv \int_0^{2\pi} \frac{\mathrm{d}\varphi_{\ell_1}}{2\pi} \int_0^{\pi} \frac{\mathrm{d}\varphi_{\ell_2}}{\pi} \int_{-\pi}^{0} \frac{\mathrm{d}\varphi_{\ell_3}}{\pi} \;, \tag{4.39}$$

which we use to define the following bispectrum estimators,

$$\begin{aligned}
\hat{B}_\Delta(\bar{\ell}_1, \bar{\ell}_2, \bar{\ell}_3) \;&=\; \frac{2\pi^2}{A} \Lambda^{-1}\left(\bar{\ell}_1, \bar{\ell}_2, \bar{\ell}_3\right) \int_{\bar{\ell}_1 - 1/2\Delta\ell}^{\bar{\ell}_1 + 1/2\Delta\ell} \frac{\mathrm{d}\ell_1 \ell_1}{\bar{\ell}_1 \Delta\ell_1} \int_{\bar{\ell}_2 - 1/2\Delta\ell}^{\bar{\ell}_2 + 1/2\Delta\ell} \frac{\mathrm{d}\ell_2 \ell_2}{\bar{\ell}_2 \Delta\ell_2} \int_{\bar{\ell}_3 - 1/2\Delta\ell}^{\bar{\ell}_3 + 1/2\Delta\ell} \frac{\mathrm{d}\ell_3 \ell_3}{\bar{\ell}_3 \Delta\ell_3} \\
&\quad \times \frac{1}{3} \left\{ \int \mathrm{d}\{\varphi_1, \varphi_2, \varphi_3\} + \int \mathrm{d}\{\varphi_2, \varphi_3, \varphi_1\} + \int \mathrm{d}\{\varphi_3, \varphi_1, \varphi_2\} \right\} \\
&\quad \times \delta_{\mathrm{D}}^{(2)}(\boldsymbol{\ell}_1 + \boldsymbol{\ell}_2 + \boldsymbol{\ell}_3)\; g(\boldsymbol{\ell}_1)\; g(\boldsymbol{\ell}_2)\; g(\boldsymbol{\ell}_3) \;; \\
\hat{B}_\nabla(\bar{\ell}_1, \bar{\ell}_2, \bar{\ell}_3) \;&=\; \frac{2\pi^2}{A} \Lambda^{-1}\left(\bar{\ell}_1, \bar{\ell}_2, \bar{\ell}_3\right) \int_{\bar{\ell}_1 - 1/2\Delta\ell}^{\bar{\ell}_1 + 1/2\Delta\ell} \frac{\mathrm{d}\ell_1 \ell_1}{\bar{\ell}_1 \Delta\ell_1} \int_{\bar{\ell}_2 - 1/2\Delta\ell}^{\bar{\ell}_2 + 1/2\Delta\ell} \frac{\mathrm{d}\ell_2 \ell_2}{\bar{\ell}_2 \Delta\ell_2} \int_{\bar{\ell}_3 - 1/2\Delta\ell}^{\bar{\ell}_3 + 1/2\Delta\ell} \frac{\mathrm{d}\ell_3 \ell_3}{\bar{\ell}_3 \Delta\ell_3} \\
&\quad \times \frac{1}{3} \left\{ \int \mathrm{d}\{\varphi_1, \varphi_3, \varphi_2\} + \int \mathrm{d}\{\varphi_2, \varphi_1, \varphi_3\} + \int \mathrm{d}\{\varphi_3, \varphi_2, \varphi_1\} \right\} \\
&\quad \times \delta_{\mathrm{D}}^{(2)}(\boldsymbol{\ell}_1 + \boldsymbol{\ell}_2 + \boldsymbol{\ell}_3)\; g(\boldsymbol{\ell}_1)\; g(\boldsymbol{\ell}_2)\; g(\boldsymbol{\ell}_3) \;.
\end{aligned} \tag{4.40}$$

Here, we have symmetrised the restricted integrations (4.39) by averaging over all either even or odd permutations of $\{\varphi_{\ell_1}, \varphi_{\ell_2}, \varphi_{\ell_3}\}$. Consequently, changing parity via any odd permutation of the angular frequencies in the arguments of (4.40) turns one estimator into the other, as demanded, for instance $\hat{B}_\Delta(\bar{\ell}_1, \bar{\ell}_3, \bar{\ell}_2) = \hat{B}_\nabla(\bar{\ell}_1, \bar{\ell}_2, \bar{\ell}_3)$.

Note that the prefactor of the estimators in (4.40) is diminished by a factor of 2 with respect to (4.3), which is necessary to keep them unbiased. This can be shown by computing the expectation value of (4.40) in close analogy to the procedure outlined in Sect. 4.1.1. However, the separate consideration of angular and radial integrals that enabled us to make use of (4.6) is not possible anymore in this non-symmetric case. For instance, given fixed $\boldsymbol{\ell}_1$, the restricted angular integrations (4.39) can still produce a triangle of opposite parity by including a triangle with $|\boldsymbol{\ell}_2'| = \ell_3$ and $|\boldsymbol{\ell}_3'| = \ell_2$. This is reflected in the fact that the integration (4.6), if properly normalised[2], still yields the same result when limiting the length of the integration range to π.

[2]In the derivation of Sect. 4.1.1 the proper normalisation of 2π for each angular integral is hidden within $A_R(\ell)$. Note that we have given (4.6) without this normalisation, whereas it is included in (4.10).

Instead, one can execute the integral over the angular frequency which is still averaged over the full two-dimensional plane, such as

$$\begin{aligned}&\int_{\bar\ell_1-1/2\Delta\ell}^{\bar\ell_1+1/2\Delta\ell}\frac{\mathrm{d}\ell_1\ell_1}{\bar\ell_1\Delta\ell_1}\int_{\bar\ell_2-1/2\Delta\ell}^{\bar\ell_2+1/2\Delta\ell}\frac{\mathrm{d}\ell_2\ell_2}{\bar\ell_2\Delta\ell_2}\int_{\bar\ell_3-1/2\Delta\ell}^{\bar\ell_3+1/2\Delta\ell}\frac{\mathrm{d}\ell_3\ell_3}{\bar\ell_3\Delta\ell_3}\\ &\qquad\times\int_0^{2\pi}\frac{\mathrm{d}\varphi_{\ell_1}}{2\pi}\int_0^{\pi}\frac{\mathrm{d}\varphi_{\ell_2}}{\pi}\int_{-\pi}^{0}\frac{\mathrm{d}\varphi_{\ell_3}}{\pi}\,\delta_\mathrm{D}^{(2)}(\boldsymbol{\ell}_1+\boldsymbol{\ell}_2+\boldsymbol{\ell}_3)\\ =\;&\frac{1}{2\pi\bar\ell_1\Delta\ell_1}\int_{\bar\ell_2-1/2\Delta\ell}^{\bar\ell_2+1/2\Delta\ell}\frac{\mathrm{d}\ell_2\ell_2}{\bar\ell_2\Delta\ell_2}\int_{\bar\ell_3-1/2\Delta\ell}^{\bar\ell_3+1/2\Delta\ell}\frac{\mathrm{d}\ell_3\ell_3}{\bar\ell_3\Delta\ell_3}\int_0^{\pi}\frac{\mathrm{d}\varphi_{\ell_2}}{\pi}\int_{-\pi}^{0}\frac{\mathrm{d}\varphi_{\ell_3}}{\pi}\,\mathbf{1}_{\boldsymbol{\ell}_1,\boldsymbol{\ell}_2,\boldsymbol{\ell}_3}\,,\end{aligned}\tag{4.41}$$

where $\mathbf{1}_{\boldsymbol{\ell}_1,\boldsymbol{\ell}_2,\boldsymbol{\ell}_3}=1$ if $\boldsymbol{\ell}_1,\boldsymbol{\ell}_2,\boldsymbol{\ell}_3$ form a triangle, and 0 else. The remaining integrations reproduce the overlapping region of the annuli for $\boldsymbol{\ell}_2$ and $\boldsymbol{\ell}_3$, as depicted in Fig. 4.1. By limiting the integration to the half plane to one side of an axis collinear to $\boldsymbol{\ell}_1$, the overlap is obviously halved. Since the area of the annuli for $\boldsymbol{\ell}_2$ and $\boldsymbol{\ell}_3$ is also reduced by half each, the value of the integration should double, see (4.10). Following the geometrical interpretation once again, we thus arrive at

$$\begin{aligned}&\int_{\bar\ell_1-1/2\Delta\ell}^{\bar\ell_1+1/2\Delta\ell}\frac{\mathrm{d}\ell_1\ell_1}{\bar\ell_1\Delta\ell_1}\int_{\bar\ell_2-1/2\Delta\ell}^{\bar\ell_2+1/2\Delta\ell}\frac{\mathrm{d}\ell_2\ell_2}{\bar\ell_2\Delta\ell_2}\int_{\bar\ell_3-1/2\Delta\ell}^{\bar\ell_3+1/2\Delta\ell}\frac{\mathrm{d}\ell_3\ell_3}{\bar\ell_3\Delta\ell_3}\\ &\qquad\times\int_0^{2\pi}\frac{\mathrm{d}\varphi_{\ell_1}}{2\pi}\int_0^{\pi}\frac{\mathrm{d}\varphi_{\ell_2}}{\pi}\int_{-\pi}^{0}\frac{\mathrm{d}\varphi_{\ell_3}}{\pi}\,\delta_\mathrm{D}^{(2)}(\boldsymbol{\ell}_1+\boldsymbol{\ell}_2+\boldsymbol{\ell}_3)\;B(\ell_1,\ell_2,\ell_3)\\ \approx\;&\frac{1}{2\pi^2}\,\Lambda(\bar\ell_1,\bar\ell_2,\bar\ell_3)\;B(\bar\ell_1,\bar\ell_2,\bar\ell_3)\;.\end{aligned}\tag{4.42}$$

Comparing this result to (4.4), the estimators (4.40) have indeed to be smaller by a factor of 2 to still be unbiased.

To obtain bispectrum estimators that are completely analogous to (4.26), we define

$$\hat B_\pm(\bar\ell_1,\bar\ell_2,\bar\ell_3)\equiv\frac{1}{2}\,\left(\hat B_\Delta(\bar\ell_1,\bar\ell_2,\bar\ell_3)\pm\hat B_\nabla(\bar\ell_1,\bar\ell_2,\bar\ell_3)\right)\;.\tag{4.43}$$

As $\left\langle\hat B_-(\bar\ell_1,\bar\ell_2,\bar\ell_3)\right\rangle=0$ for a parity symmetric random field g, and $\hat B_-(\bar\ell_1,\bar\ell_3,\bar\ell_2)=-\hat B_-(\bar\ell_1,\bar\ell_2,\bar\ell_3)$, this estimator shows identical behaviour compared to $\hat B_{\bar\ell_1,\bar\ell_2,\bar\ell_3}$ with L odd. In practice both measures could be used to assess deviations from parity symmetry. The estimators $\hat B_+(\bar\ell_1,\bar\ell_2,\bar\ell_3)$ and $\hat B_{\bar\ell_1,\bar\ell_2,\bar\ell_3}$ with L even are likewise invariant under parity transformations. After some algebra that closely follows the outline of Sect. 4.1.3 we find that the covariance of $\hat B_+$ is the same as (4.25), which is not unexpected because we already noted that (4.3) is also parity-symmetric.

With (4.43) at hand, one can readily extract the different treatment of even and odd parity measures in the spherical harmonic and Fourier-plane formalisms. Estimators (4.26) separate the set of possible arguments $\{\ell_1,\ell_2,\ell_3\}$ disjointly into parity even (L even) and parity odd (L odd), whereas $\hat B_+$ and $\hat B_-$ are defined on the same full set of angular frequency combinations[3]. In other words, when limiting $\hat B_+$ to integer angular frequencies only, the same information is contained in 'half' the number of measures in the spherical harmonics case, namely those with L even. The latter estimators have a covariance of half the size of the covariance of $\hat B_+$, so that the overall information content is the same for both approaches – as required.

[3]A similar behaviour as for the spherical harmonic estimators would have been unexpected since the possible arguments of $\hat B_\pm$ form a non-countable set.

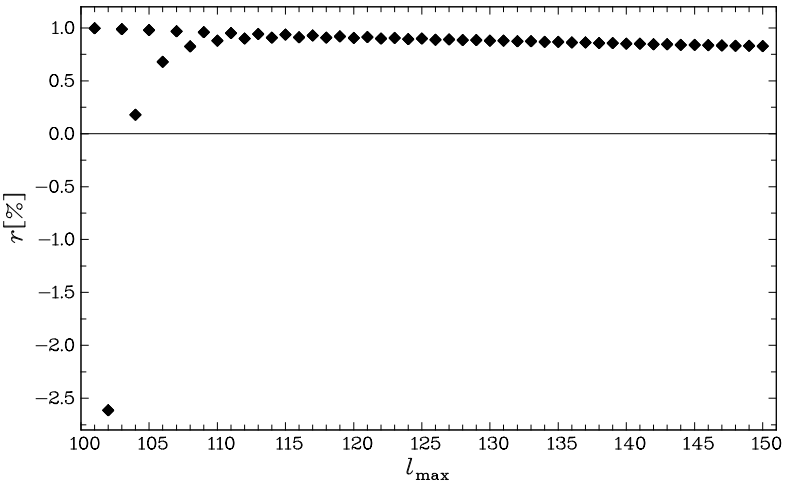

Figure 4.5: Comparison of the Fisher information as obtained by spherical harmonics and Fourier-plane approach. Given is the relative deviation r as a function of the maximum angular frequency $\ell_{\max}$ used in (4.44).

Information content

We verify the findings of the foregoing section by comparing the information contained in both approaches in terms of the Fisher matrix (Tegmark et al. 1997, see also Appendix A). For a practical implementation we specialise to a non-tomographic weak lensing survey (see e.g. Bartelmann & Schneider 2001 for an overview), assuming a cosmology-independent covariance that can be well approximated by the Gaussian approximation, i.e. using (4.22) and (4.29), respectively. To allow for direct comparison, we limit the Fourier-plane approach to integer ℓ with all bin sizes set to unity. Due to the symmetry under permutations of the arguments of the bispectra, one can impose the condition $\ell_1 \leq \ell_2 \leq \ell_3$ on both formalisms, rendering a block-wise diagonal covariance matrix. Inspecting (4.22), the only dependence on the arguments of the second bispectrum, i.e. ℓ_4 to ℓ_6, is due to the Kronecker symbols (4.20), so that the summations over ℓ_4 to ℓ_6 become trivial.

Hence, the Fisher matrix can be written as

$$F_{\mu\nu} = \sum_{l_{\min}\leq\ell_1\leq\ell_2\leq\ell_3\leq l_{\max}} D_{\bar\ell_1,\bar\ell_2,\bar\ell_3,\bar\ell_1,\bar\ell_2,\bar\ell_3} \, \frac{\partial B(\ell_1,\ell_2,\ell_3)}{\partial p_\mu} \, \frac{A\;\bar\ell_1\bar\ell_2\bar\ell_3\;\Delta\ell_1\Delta\ell_2\Delta\ell_3\;\Lambda\left(\bar\ell_1,\bar\ell_2,\bar\ell_3\right)}{(2\,\pi)^3\;P(\bar\ell_1)P(\bar\ell_2)P(\bar\ell_3)} \, \frac{\partial B(\ell_1,\ell_2,\ell_3)}{\partial p_\nu} \;, \quad (4.44)$$

where $D_{\bar\ell_1,\bar\ell_2,\bar\ell_3,\bar\ell_1,\bar\ell_2,\bar\ell_3} = 6$ for equilateral triangles, $D_{\bar\ell_1,\bar\ell_2,\bar\ell_3,\bar\ell_1,\bar\ell_2,\bar\ell_3} = 2$ for isosceles, and for general triangles $D_{\bar\ell_1,\bar\ell_2,\bar\ell_3,\bar\ell_1,\bar\ell_2,\bar\ell_3} = 1$. The derivatives are taken with respect to a set of cosmological parameters $\boldsymbol{p}$. In this toy example we use only the single parameter $\Omega_{\rm m}$, reducing the Fisher matrix to a scalar F. Besides, we restrict the angular frequency values to an unphysically small range between $l_{\min} = 100$ and $l_{\max} = 150$ for computational reasons.

Weak lensing power spectra are computed for a standard ΛCDM cosmology, including non-linear evolution via the fit formula of Smith et al. (2003). The bispectra are obtained via perturbation theory (e.g. Fry 1984), using Scoccimarro & Couchman (2001) with the definition of the non-linear wave vector by Takada & Jain (2004) to account for non-linear evolution. For the projections along the line of sight we assume a redshift probability distribution according to Smail et al. (1994) with $\beta = 1.5$ and a deep survey of 0.9 median redshift. Shape noise is incorporated by replacing the power spectra in the covariances with

$$\bar P(\ell) = P(\ell) + \frac{\sigma_\epsilon^2}{2\bar n} \;, \quad (4.45)$$

where the ellipticity dispersion $\sigma_\epsilon = 0.35$ and the galaxy number density $n = 40\,\mathrm{arcmin}^{-2}$ are set to typical values for planned space-based surveys.

We calculate the relative deviation of the Fisher information, $r \equiv F_{\text{Fourier}}/F_{\text{sph. harm.}} - 1$, as a function of $l_{\max}$. Note that, since we only consider ratios of F, the survey size A drops out. Our results are shown in Fig. 4.5. For $l_{\max}$ very close to $l_{\min}$ one sees alternating jumps in r which can mostly be traced back to the fact that, due to the condition $\ell_1 \leq \ell_2 \leq \ell_3$, the terms entering (4.44) do not always split exactly half into L even and odd. After this 'burn in' for $l_{\max} \lesssim 120$, r shows only little variation. The remaining offset from zero, which is slowly decreasing, can entirely be assigned to the different prefactors in the covariances, i.e. the terms related to the Wigner symbol and Λ, respectively. The range of angular frequencies plotted in Fig. 4.5 is still far from any physically relevant situation, but nonetheless the two approaches agree already better than 99 %.

4.1.5 Conclusions

In this section we intended to give insight into the derivation and the form of the bispectrum covariance in the flat-sky approximation, based exclusively on the two-dimensional Fourier formalism. We defined an unbiased estimator that takes the average over the overlap of annuli in Fourier space, and computed its covariance. To obtain precise normalisations, a case distinction is necessary between degenerate and non-degenerate triangle configurations. However, given that both normalisations become very similar for $\ell \gg 1$, which is assumed in the flat-sky approach anyway, we suggest as a simple and fair approximation to use the expression derived for the degenerate case. Then our result for the Gaussian part of the bispectrum covariance reads

$$\begin{aligned}\text{Cov}\left(B(\bar{\ell}_1,\bar{\ell}_2,\bar{\ell}_3),\ B(\bar{\ell}_4,\bar{\ell}_5,\bar{\ell}_6)\right)_{\text{Gauss}} &= \frac{(2\,\pi)^3\ D_{\bar{\ell}_1,\bar{\ell}_2,\bar{\ell}_3,\bar{\ell}_4,\bar{\ell}_5,\bar{\ell}_6}}{A\ \bar{\ell}_1\bar{\ell}_2\bar{\ell}_3\ \Delta\ell_1\Delta\ell_2\Delta\ell_3} \\ &\times \Lambda^{-1}\left(\bar{\ell}_1+\frac{\Delta\ell_1}{2},\bar{\ell}_2+\frac{\Delta\ell_2}{2},\bar{\ell}_3+\frac{\Delta\ell_3}{2}\right)\ P(\bar{\ell}_1)P(\bar{\ell}_2)P(\bar{\ell}_3)\ .\end{aligned} \tag{4.46}$$

This formula is readily generalised to the total covariance by modifying the arguments of Λ, appearing in the non-Gaussian terms of (4.25), accordingly. It is directly applicable to any real values of angular frequencies, to arbitrary binning, and to any compact, finite survey geometry. This formula can be modified to incorporate shot or shape noise, as well as to account for photometric redshift information or CMB polarisation in a straightforward manner.

While the general form of our result was in agreement with existing work, we found, contrary to Hu (2000), that the size of the covariance is a factor of 2 larger than the one obtained by the flat-sky spherical harmonic approach. By defining parity-sensitive bispectrum estimators, we discussed the behaviour of both formalisms with respect to parity transformations, arguing that the difference in the covariances is indeed to be expected because in the spherical harmonic framework, parity-invariant measures are restricted to a subset of the angular frequency combinations at which the bispectra are evaluated. In a practical example we demonstrated that both approaches indeed contain the same information in terms of the Fisher matrix, with a high level of agreement. As a consequence, we can confirm that studies performed in the flat-sky spherical harmonic approach, such as Takada & Jain (2004), yield correct parameter constraints as long as the analysis is restricted to integer ℓ with the sum of the three angular frequencies being even.

We established a relation between the geometrical and intuitive process of averaging over the overlapping regions of annuli in the Fourier plane and the Wigner symbol of the spherical harmonic approach. Both quantities were demonstrated to be in turn connected to a simple measure that is proportional to the size of the area enclosed by the triangle configuration for

which the bispectrum is calculated. This resulted in convenient, yet precise approximation formulae for the prefactors of the covariances of both approaches at consideration.

Under the assumption of a compact survey geometry and scales much smaller than the extent of the survey area, (4.25) provides a cleanly derived bispectrum covariance matrix that naturally incorporates the scaling with survey size, is not restricted to integer angular frequencies, and allows for any appropriate binning.

4.2 Forecasting the performance of cosmological surveys

To plan future surveys, it is crucial to compute accurate predictions for the statistical errors attainable on the physical quantities of interest, but also to provide precise estimates of the level of systematic errors that one has to expect. In the following we will present a case study of the power of two- and three-point cosmic shear statistics to constrain cosmological parameters, forecast for the Euclid weak lensing survey. Moreover we outline a novel, very general technique to quantify the degradation of statistical constraints by a systematic signal on whose form one has only limited a priori information.

4.2.1 Constraints from the Euclid imaging survey

The Euclid satellite mission is a proposal to the ESA Cosmic Visions Programme and, if selected, is scheduled to be launched around 2018. With the design of NASA's Joint Dark Energy Mission currently being uncertain, Euclid constitutes the most ambitious project to date that features weak lensing on cosmological scales as one of its primary probes. In combination with a spectroscopic galaxy redshift survey and several secondary cosmological probes, cosmic shear with Euclid is intended to address the nature of dark matter and dark energy, shed light on the initial conditions of structure formation, and test the validity of General Relativity on large scales.

Euclid is planned to observe the whole extra-galactic sky over the course of five years out to a median redshift of close to unity, using a 1.2 m Korsch telescope positioned at the L2 Lagrange point. In addition to imaging in a broad filter ranging from the R to the Z band in which the shear is measured, near infrared photometry in three filters and slitless spectroscopy will be obtained. In conjunction with supplementary ground-based multi-colour photometry in visible bands, the former will yield accurate photometric redshifts for all galaxies in the weak lensing survey. The spectroscopy primarily serves the purpose of measuring baryonic acoustic oscillations or, more generally, galaxy clustering, but also provides calibration data for photometric redshifts.

Hitherto Euclid has been rated excellently against competing missions proposed to ESA. A contributing factor to this success are accurate predictions for the performance of the survey, using the Fisher matrix formalism (see Appendix A). At the current stage the influence of the treatment of potential systematic errors is not yet incorporated into these predictions, but discussed separately and on a more qualitative basis. Thus the task reduces to calculate Fisher matrices for cosmic shear two- and three-point measures for a given set of survey parameters. These are determined such that the primary science objectives of the mission are met while staying within the allocated budget and mission duration. We will consider two sets of survey parameters, a conservative one which is capable of fulfilling the minimum requirements, and a slightly more optimistic one which meets the scientific goals of the mission. As discussed in Sect. 3.4, it is most convenient to work with Fourier-space measures, i.e. the convergence power spectrum and bispectrum, which implies the assumption that the information contained in the spectra can also be completely extracted from the data.

As the fiducial model for the Fisher matrix forecast we choose a flat CDM cosmology with variable dark energy in the parametrisation given by (2.15). We assume $\Omega_\mathrm{m} = 0.25$, $\Omega_\Lambda = 0.75$, $h = 0.7$, $w_0 = -0.95$, and $w_a = 0$. The primordial power spectrum has a Harrison-Zeldovich slope of $n_\mathrm{s} = 1$ and is normalised according to $\sigma_8 = 0.8$. We employ the transfer function given by Eisenstein & Hu (1998) with $\Omega_\mathrm{b} = 0.0445$ and the non-linear correction of Smith et al. (2003). The matter bispectrum is then calculated from the power spectrum via perturbation theory and the non-linear correction by Scoccimarro & Couchman (2001), as described in Sect. 4.1.4.

The convergence spectra are obtained via line-of-sight projection, assuming an overall redshift distribution according to Smail et al. (1994),

$$p_\mathrm{tot}(z) \propto \left(\frac{z}{z_0}\right)^2 \exp\left\{-\left(\frac{z}{z_0}\right)^\beta\right\} , \tag{4.47}$$

where $\beta = 1.5$. The characteristic redshift z_0 is related to the median redshift of the survey via $z_0 \approx z_\mathrm{med}/1.412$. The redshift distribution is cut at $z_\mathrm{max} = 3$ and normalised. It is then divided into $N_\mathrm{bin} = 5$ bins between $z_\mathrm{min} = 0$ and z_max such that each of these 'photometric redshift' bins contains the same number of galaxies. To include the effect of photometric redshift scatter, we assume the distribution of photometric redshifts for a given true redshift to be a Gaussian, centred on the true redshift and with a width of $\sigma_\mathrm{ph}(1+z)$. The distributions of true redshifts $p^{(i)}(z)$ for each of the photometric redshift bins i are then computed according to the scheme detailed in Joachimi & Schneider (2009), see also Chap. 6. For the minimally required set of Euclid survey parameters we assume $z_\mathrm{med} = 0.9$ and $\sigma_\mathrm{ph} = 0.05$. In this situation one can expect a total number density of galaxies of $n_\mathrm{g} = 30\,\mathrm{arcmin}^{-2}$ (Laureijs et al. 2009). The requirements to meet the targeted objectives demand $z_\mathrm{med} = 1.0$ and $\sigma_\mathrm{ph} = 0.03$, yielding $n_\mathrm{g} = 40\,\mathrm{arcmin}^{-2}$.

Both the power spectrum and bispectrum are evaluated at 20 logarithmic angular frequency bins spaced between $\ell_\mathrm{min} = 10$ and $\ell_\mathrm{max} = 3000$. The covariances are computed under the approximation of Gaussianity, following Joachimi et al. (2008) in the case of the power spectrum and Joachimi et al. (2009), equivalent to the results of Sect. 4.1, for the bispectra. For both sets of survey parameters, the survey area is set to $20000\,\mathrm{deg}^2$ and the dispersion of intrinsic ellipticities, incorporated via (4.45), is $\sigma_\epsilon = 0.35$. Note that the assumption of Gaussian covariances also implies that there is zero cross-correlation between two- and three-point statistics, as their covariance would be a five-point statistic. This fact and the under-estimation of statistical errors on small angular scales when neglecting the non-Gaussianity of structure evolution causes the Fisher matrix forecasts to be overly optimistic.

Assuming that the covariances do not depend on cosmological parameters, one obtains

$$F_{\mu\nu}^\mathrm{PS} = \sum_{\substack{l_\mathrm{min}\le\ell\le l_\mathrm{max}\\ 1\le i\le j\le N_\mathrm{bin},\,1\le k\le l\le N_\mathrm{bin}}} \frac{\partial P^{(ij)}(\ell)}{\partial p_\mu}\,\mathrm{Cov}^{-1}\left(P^{(ij)}(\ell),\,P^{(kl)}(\ell)\right)\frac{\partial P^{(kl)}(\ell)}{\partial p_\nu}\,; \tag{4.48}$$

$$F_{\mu\nu}^\mathrm{BS} = \sum_{\substack{l_\mathrm{min}\le\ell_1\le\ell_2\le\ell_3\le l_\mathrm{max}\\ 1\le i,j,k\le N_\mathrm{bin},\,1\le l,m,n\le N_\mathrm{bin}}} \frac{\partial B^{(ijk)}(\ell_1,\ell_2,\ell_3)}{\partial p_\mu}\,\mathrm{Cov}^{-1}\left(B^{(ijk)}(\ell_1,\ell_2,\ell_3),\,B^{(lmn)}(\ell_1,\ell_2,\ell_3)\right)\frac{\partial B^{(lmn)}(\ell_1,\ell_2,\ell_3)}{\partial p_\nu}$$

for all cosmological parameters p_μ under consideration. Since the power spectrum is invariant under permutations of the photometric redshift bins, $P^{(ij)} = P^{(ji)}$, we have imposed the condition $i \le j$ in the sum. In contrast, permutations of the redshift indices of the convergence bispectrum yield different measures as long as $\ell_1 < \ell_2 < \ell_3$, so that the summation runs over all combinations of photometric redshift bins. A more complicated case distinction to avoid counting the same bispectra twice is needed for symmetric triangle configurations in angular frequency space, i.e. for isosceles and equilateral triangles, which has not been made explicit

Table 4.1: Marginalised statistical errors from two- and three-point weak lensing statistics for the Euclid imaging survey. Given are the $1\,\sigma$ errors after marginalising over all other cosmological parameters. The second column shows constraints using the power spectrum alone, the third column those using the bispectrum alone. In both cases the minimal survey requirements were assumed to obtain these errors. The fourth and fifth column display combined two- and three-point constraints for the minimally required and targeted survey parameters, respectively.

parameter	power spectrum	bispectrum	combined (req.)	combined (goal)
Ω_m	0.005	0.003	0.002	0.001
σ_8	0.007	0.004	0.003	0.002
h	0.120	0.046	0.041	0.031
n_s	0.028	0.013	0.011	0.008
Ω_b	0.015	0.006	0.005	0.004
w_0	0.064	0.048	0.028	0.026
w_a	0.490	0.355	0.224	0.197
Ω_Λ	0.050	0.029	0.023	0.014

in (4.48). Note that due to the vanishing cross-correlation, combined constraints are obtained by simply adding the Fisher matrices of two- and three-point statistics.

In Table 4.1 the resulting marginalised $1\,\sigma$ errors are listed. While our fiducial model is spatially flat, we do not impose flatness as a general condition and use Ω_m and Ω_Λ as independent parameters, thus totalling 8 cosmological parameters in the analysis. Despite this larger flexibility in the model, the anticipated errors on Ω_m and σ_8, using two-point statistics alone from the Euclid survey with minimum requirements, are at least an order of magnitude smaller than for contemporary studies (Benjamin et al. 2007; Schrabback et al. 2010). Results from the bispectrum alone yield even tighter constraints on all parameters, with the least increase on the dark energy parameters and the highest gain on parameters that cosmic shear is not primarily sensitive to, like h and Ω_b. It should be kept in mind though that the assumption of Gaussianity of the covariance is much more simplistic for the bispectrum than at the two-point level.

Combined power spectrum and bispectrum constraints for both the minimally required and the targeted set of survey parameters are also given in Table 4.1. To better understand the gain in information when considering joint constraints, degeneracies between cosmological parameters need to be taken into account, which we illustrate by plotting two-dimensional confidence regions, marginalised over all parameters that are not shown, in Fig. 4.6. The prominent degeneracy between Ω_m and σ_8 is also present in three-point statistics, albeit with a slight tilt of the degeneracy line with respect to the two-point case. As a consequence, the strong degeneracy is partly broken when combining two- and three-point statistics, producing a decrease in marginal errors on both parameters by more than a factor of two compared to the power spectrum only analysis. Other parameter combinations profit as well from the combination of power spectrum and bispectrum statistics, in particular if the degeneracy directions differ significantly, like e.g. for Ω_Λ together with each of the two dark energy equation of state parameters, or for the near orthogonal contours in the $w_0 - \Omega_\mathrm{b}$ plane.

Switching to the Euclid target survey parameters, and thus to a deeper survey with more accurate redshift information, again increases parameter constraints considerably, especially for Ω_m and Ω_Λ. The merit on the dark energy equation of state parameters is smallest, but still we obtain a decrease in errors by more than 60 % for both parameters compared to the original analysis, using only the power spectrum and minimal requirements. The small gain due to

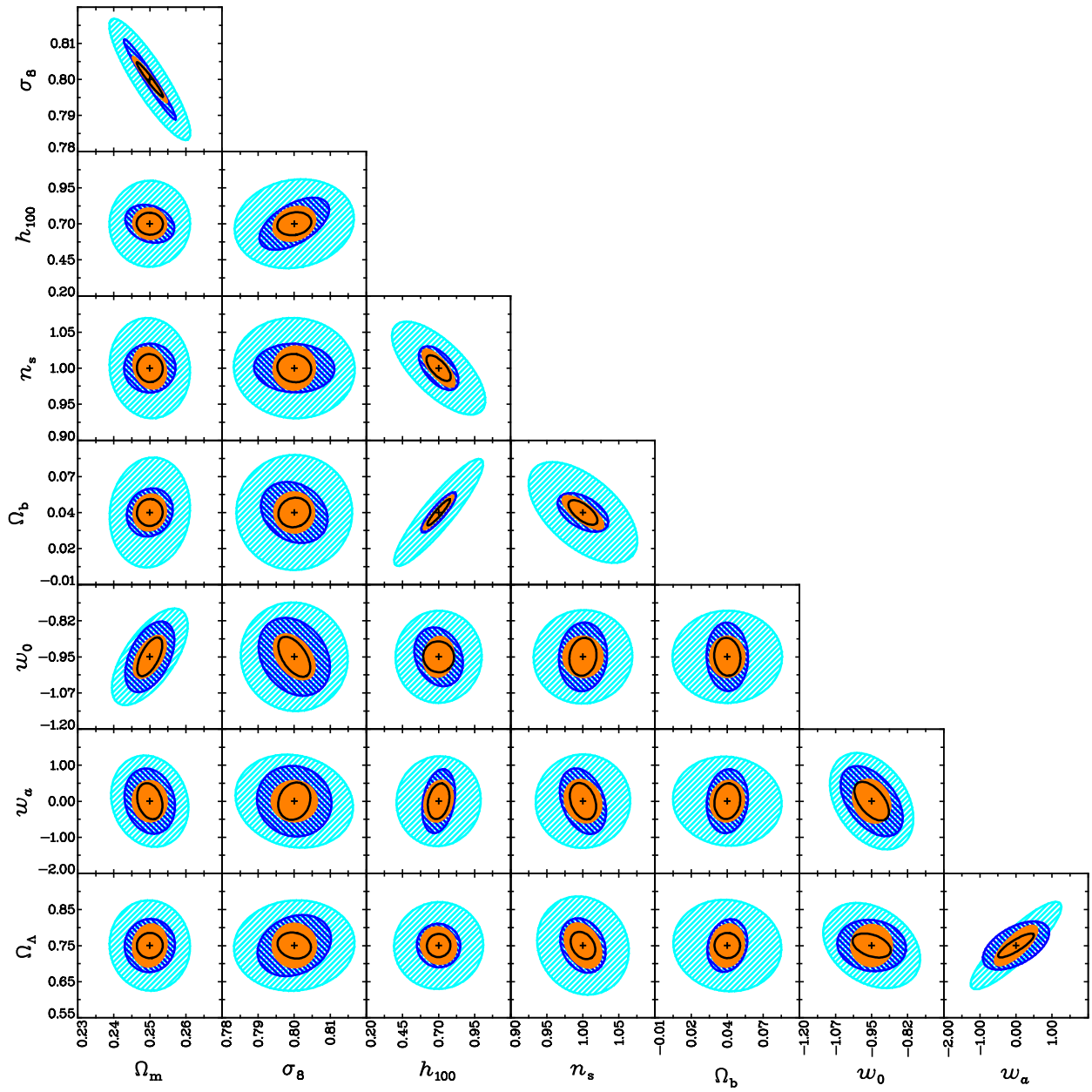

Figure 4.6: Marginalised 2D parameter constraints for the Euclid cosmic shear survey, obtained via a Fisher matrix analysis. Shown in each panel are the $2\,\sigma$ confidence contours after marginalising over all remaining parameters of the set $\{\Omega_\mathrm{m}, \Omega_\Lambda, \Omega_\mathrm{b}, w_0, w_a, \sigma_8, h, n_\mathrm{s}\}$. Light blue hatched credible regions correspond to constraints from the power spectrum and dark blue hatched regions to constraints from the bispectrum, all evaluated for the minimally required Euclid survey parameters. Orange filled regions display the results for the combined two- and three-point statistics while the black contour indicates the combined constraints when using the targeted survey parameters instead. In each panel the fiducial values of the cosmological parameters are marked by a cross.

the more ambitious survey parameters is in agreement with Amara & Réfrégier (2007) who found a weak sensitivity of the survey depth to dark energy, in contrast to the much stronger dependence on survey area.

A focus of Euclid will be to pin down the properties of dark energy. To illustrate its constraining power, we plot in Fig. 4.7 the confidence contours obtained from the Fisher matrix

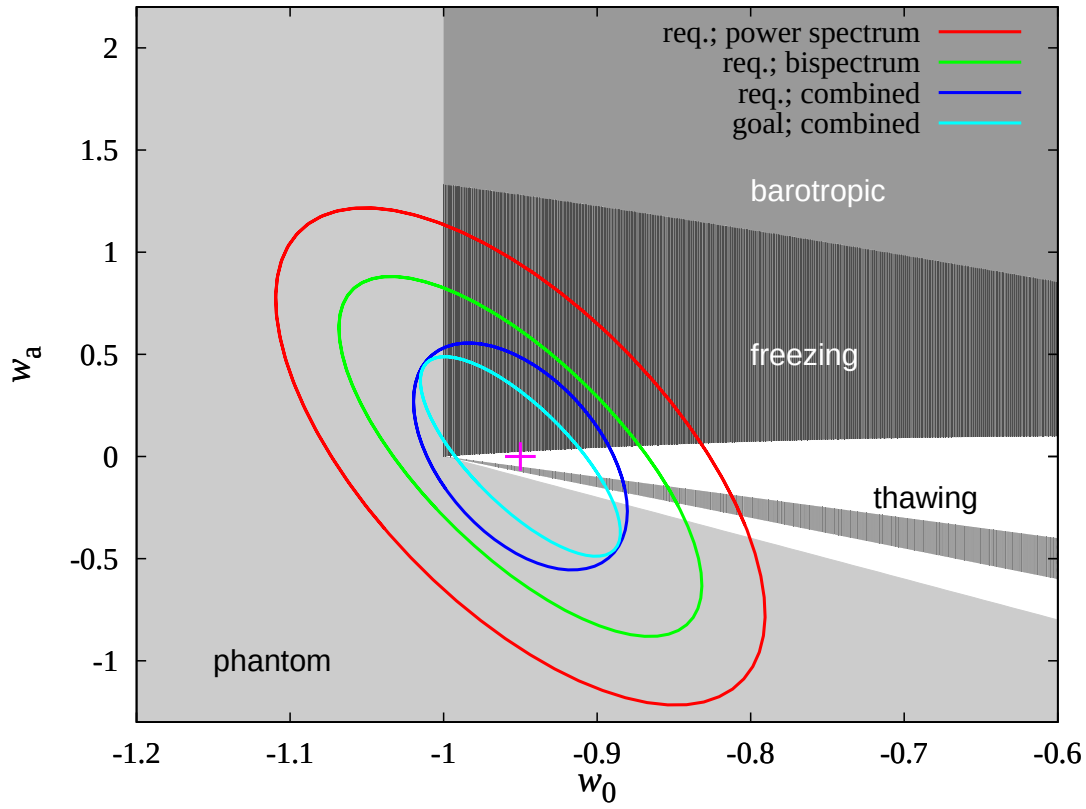

Figure 4.7: Dark energy constraints for the Euclid weak lensing survey. Shown are the $2\,\sigma$-confidence contours in the $w_0 - w_a$ plane for the same fiducial cosmology as in Fig. 4.6, including $w_0 = -0.95$ and $w_a = 0$ as marked by the pink cross. Red contours represent constraints from the power spectrum only, and green lines those from the bispectrum only, assuming the minimally required Euclid survey parameters in both cases. Dark blue contours result from combining two- and three-point statistics. The same holds for the light blue lines, but here the targeted survey parameters were used. The parameter plane is split up into regions of allowed cosmological parameter values for different classes of dark energy scenarios, see the text for details.

analysis in the $w_0 - w_a$ plane which has been divided into regions occupied by different classifications of dark energy models. The nomenclature and the definitions of these regions are adopted from Barger et al. (2006) and references therein. Phantom dark energy comprises models where $w(z) < -1$ for $z \lesssim 1$, i.e. the ratio of pressure over density for the dark energy component has been smaller, i.e. more negative, than for ΛCDM in recent times. Models that fall into the phantom category can show features like states of negative kinetic energy and are therefore often considered unphysical. The class of thawing dark energy models is defined by an equation of state parameter $w(z)$ that increases starting from an early value around -1, as is e.g. the case for theories involving axions. In contrast, for freezing models the equation of state parameter decreases from initially $w(z) > -1$. For instance, the DGP model of modified gravity (Dvali et al. 2000) belongs to the latter class. Barotropic fluids encompass models stemming from string theory, such as the Chaplygin gas for which $p_\Lambda \propto -1/\rho_\Lambda$.

Figure 4.7 demonstrates that already Euclid weak lensing constraints for two-point statistics and the minimally required survey parameters can rule out the complete class of barotropic dark energy models at more than $2\,\sigma$ if the likelihood peaks close to the ΛCDM values. The range of dark energy parameters in the remaining classes is also restrained considerably, e.g. ruling out

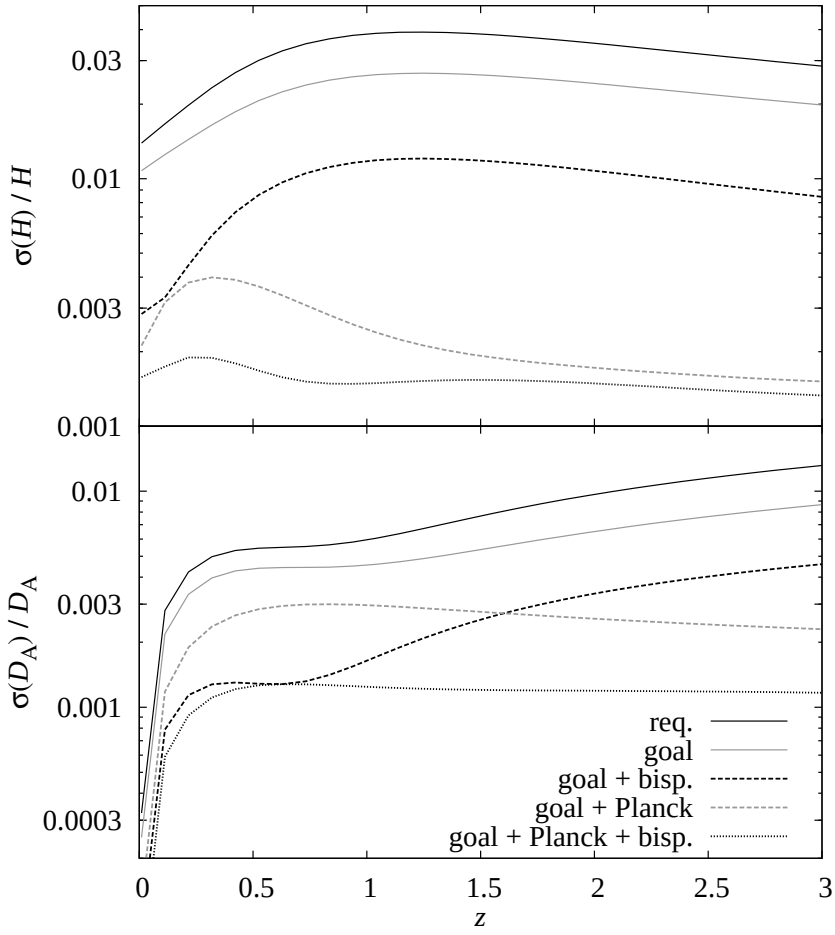

Figure 4.8: Fractional errors on the Hubble parameter H and the angular diameter distance D_A as a function of redshift. The black solid curves were obtained for cosmic shear two-point statistics with the minimum required parameters of the Euclid imaging survey, the grey solid lines for the targeted survey parameters. For the black dashed curves information from the convergence bispectrum was added, using the targeted Euclid parameters. The grey dashed curve corresponds to combining Euclid two-point cosmic shear information with the expected constraints from Planck. Euclid two- and three-point cosmic shear statistics and Planck data produce the black dotted lines.

DGP, situated in the 'freezing' class with $w_0 \gtrsim -0.8$, at more than $2\,\sigma$ as well. Combined two- and three-point statistics for the targeted Euclid survey parameters are even more stringent and could exclude ΛCDM with more than 95 % confidence if the 'true' parameter values were located at $w_0 = -0.95$ and $w_a = 0$, as assumed for this Fisher matrix analysis.

It is also instructive to consider Euclid weak lensing constraints on more physical quantities, e.g. to compare with the performance of other cosmological methods, in particular BAOs which constitute the other primary probe of Euclid. BAOs measure the expansion history via angular diameter distances D_A and the Hubble parameter H, yielding a minimal fractional error of the order 0.01 on both quantities around a redshift of about unity (Laureijs et al. 2009). To transform the statistical errors on cosmological parameters which are available from the Fisher matrix analysis to those on H and D_A at different redshifts z_μ, we make use of the law of Gaussian error propagation and obtain

$$\mathrm{Cov}\left(H(z_\mu),\ H(z_\nu)\right) = \sum_{\alpha,\,\beta} \frac{\partial H(z_\mu)}{\partial p_\alpha}\ \left(F^{-1}\right)_{\alpha\beta}\ \frac{\partial H(z_\nu)}{\partial p_\beta}\ , \tag{4.49}$$

and likewise for the angular diameter distance. Here we employed the fact that the inverse Fisher matrix is an estimate for the parameter covariance. The derivatives with respect to cosmological parameters p_μ are readily obtained via (2.19) and (2.10) in combination with $D_\mathrm{A}(z) = f_\mathrm{k}(\chi(z))/(1+z)$. The relevant cosmological parameters used for this analysis are Ω_m, Ω_Λ, w_0, w_a, and h, but note that the latter quantity cancels in the fractional error of the Hubble parameter. By densely sampling the points z_μ, we can compute the fractional errors $\sigma(H)/H$

and $\sigma(D_\mathrm{A})/D_\mathrm{A}$, which are displayed in Fig. 4.8.

We find that the constraints from two-point cosmic shear statistics alone, using the minimally required survey parameters, are compatible to those by Euclid BAO measurements, producing slightly larger fractional errors on H, especially around $z = 1$, and smaller fractional errors on D_A on all scales. Switching to the targeted Euclid survey parameters improves the constraints moderately at all redshifts. Adding information from three-point statistics decreases errors considerably, in particular at $z \lesssim 1$ where non-linear evolution shows more prominent effects.

A high level of complementarity is expected from the combination of cosmic shear, measuring the structure of the Universe between redshifts 0 and about 2 in the case of Euclid, and the CMB, which provides a snapshot of the Universe at $z \sim 1100$. Making the simplistic assumption that cosmic shear and CMB data are uncorrelated, we add in Fisher matrix forecasts for the Planck satellite, as is also shown in Fig. 4.8. In combination with cosmic shear power spectra the CMB data improves constraints especially at high redshifts, e.g. by determining the curvature, i.e. $\Omega_\mathrm{m} + \Omega_\Lambda$ to high accuracy. The overall decrease in the fractional error on H is dramatic and attains an order of magnitude for $z > 1$. Joint constraints by weak lensing two- and three-point statistics and the CMB push the fractional errors of both H and D_A down to the per mil level for all redshifts out to $z = 3$.

In summary, when applied to a Euclid-like survey, cosmic shear is indeed one of the most powerful cosmological probes, testing hypotheses about the nature of dark matter and dark energy, the initial conditions of structure formation, and the law of gravity to unprecedented precision. Moreover we find that cosmic shear yields constraints complementary to other cosmological measurement techniques, where great synergy is expected in particular with upcoming high-precision CMB data. However, it should be kept in mind that the predictions presented here are still idealistic, be it that cross-correlations are neglected when probes are combined, that cosmic shear covariances are assumed to be Gaussian, or that both the likelihood and the posterior in parameter space are assumed to be close to Gaussian form, which is inherent to the Fisher matrix formalism. To arrive at realistic forecasts, it is also essential to incorporate the effect of steps in the pipeline that control systematics such as the intrinsic alignment of galaxies.

4.2.2 Functional form filling

The near-future large cosmological surveys such as Planck and Euclid will place excellent statistical constraints on cosmological parameters. This enforces a rigorous treatment of systematic effects which could otherwise dominate the error budget and thus limit the performance of these ambitious campaigns. In other words, one aims at minimising the total mean square error on a parameter p_μ, given by

$$\sigma_\mathrm{tot}(p_\mu) = \sqrt{\sigma^2(p_\mu) + b^2(p_\mu)}\,, \tag{4.50}$$

where $b(p_\mu)$ is the systematic error, or equivalently the parameter bias. The standard approach to include the effect of a systematic into the total error budget is the assumption of a model for the systematic signal which contains a limited amount of freedom in the form of so-called nuisance parameters. The likelihood analysis is then performed simultaneously for the parameters of interest and the nuisance parameters, subsequently marginalising over the latter and thereby decreasing the statistical constraints on the cosmological information. An example can be found in Schrabback et al. (2010) where a single nuisance parameter is used to account for the uncertainty in the redshift distribution entering the cosmic shear signal.

There are both conceptual and practical concerns with this approach. If the model of the systematic is not flexible enough to represent the actual signal that contaminates the data, the parameter bias will in general not be reduced or could even increase. Moreover, should an insufficient parametrisation of the systematic be implemented such that it is not capable of mimicking the dependence of the data on a certain cosmological parameter, then the marginalisation over the nuisance parameters may largely underestimate the widening of the error bounds due to the systematic treatment. Finally, a systematic effect is not treated as such when marginalising over nuisance parameters, but instead transformed into an additional statistical uncertainty in the inference on cosmological parameters.

The aforementioned points remain unproblematic in practice if the systematic signal is well understood, so that its modelling is correct with high confidence. In that case it is justified to understand the systematic simply as a further contribution to the total signal whose model has to be incorporated into the statistical analysis. However, this does not hold true for most applications in cosmology as well as other fields of physics, prominent examples for poorly understood systematics in cosmic shear being shear measurement biases (e.g. Heymans et al. 2006a; Massey et al. 2007a) or the intrinsic alignment of galaxies, see the following chapters. At least the practical issues with marginalisation over nuisance parameters can be overcome by introducing a very general, e.g. piecewise linear, parametrisation of the systematic, and using the nodal points of this parametrisation as nuisance parameters, see e.g. Bridle & King (2007), Joachimi & Bridle (2009), and Chap. 8.

In Kitching et al. (2009) we have proposed an alternative technique for quantifying systematic effects by computing accurately and directly the contribution of the parameter bias b to (4.50), working in a more robust and efficient way than marginalisation approaches. Consider a signal $s(x)$ which has been measured in the interval $[x_{\min}; x_{\max}]$ and which is contaminated by a systematic $f(x)$. The exact form of the systematic is unknown, except that the systematic is bound by a positive function $B(x)$ such that $|f(x)| \leq B(x)$. We are going to determine the worst possible parameter bias that can result from a systematic within the region specified by $B(x)$.

For simplicity we have assumed that the bound $B(x)$ is symmetric around the abscissa, but the considerations below can be readily generalised. Note that the need to specify the bound $B(x)$ corresponds to the appropriate choice of the priors on the nuisance parameters in the marginalisation approach, although $B(x)$ generally allows for more flexibility in the bound. If $|f(x)| \leq B(x)$, one can always find a transformation of the systematic such that it is bound by ± 1 instead. Thus, we will only consider the case $B(x) \equiv 1$ in the following, to ease the notation.

The actual systematic could have any functional form that is bound by $\pm B(x) \equiv \pm 1$. The goal is to find those forms that yield the strongest bias, which is then used to compute an upper limit on the mean square error. To this end, we expand the systematic $f(x)$ into an arbitrary basis set $\Psi_n(x)$ via

$$f(x) = \sum_{n=0}^{N} a_n \, \Psi_n(x) \, , \tag{4.51}$$

where the a_n are real coefficients, and where N denotes the maximum order of the expansion. We require that the set of basis functions is complete in the interval $[x_{\min}; x_{\max}]$, so that in the limit $N \to \infty$ all possible functional forms of $f(x)$ within the region defined by $x \in [x_{\min}; x_{\max}]$ and $f(x) \in [-1; +1]$ can be represented. We will use the parametrisation (4.51) to exhaustively sample the region defined via $B(x)$ with every possible functional form of the systematic, hence the name 'functional form filling' for our technique. To keep the formalism tractable, we demand

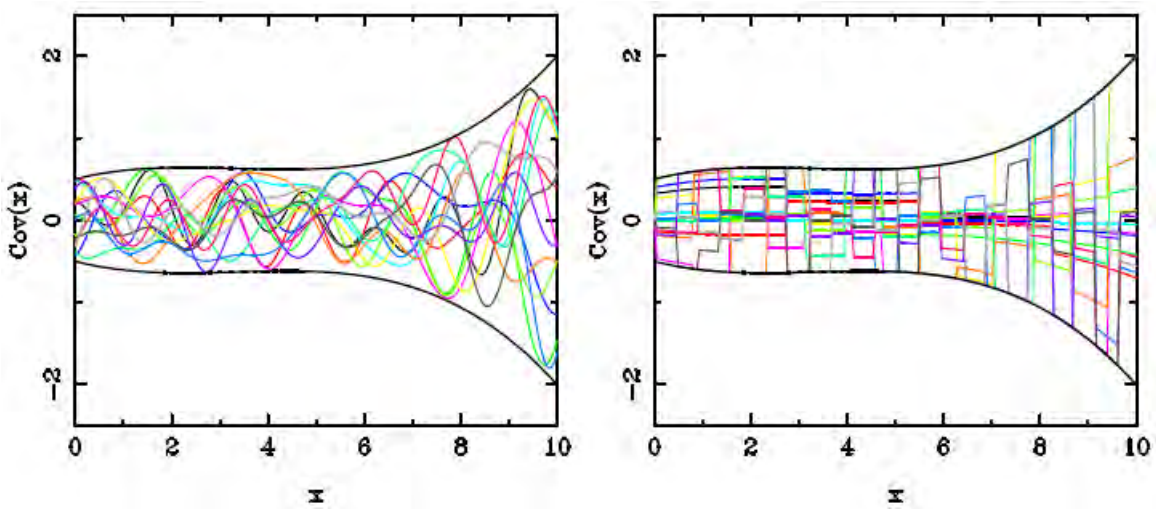

Figure 4.9: Example set of functions $f(x)$, denoted in the context of Kitching et al. (2009) by $\mathrm{Cov}(x)$, filling the region between $\pm B(x)$ as indicated by the black curves. In the left panel the Fourier basis set was used, in the right panel the top-hat basis. The functions displayed were obtained by uniform random sampling of the set of coefficients with a maximum order of $N = 15$ (from Kitching et al. 2009).

in addition orthogonality of the basis functions, i.e.

$$\int_{x_{\min}}^{x_{\max}} \mathrm{d}x\; w(x)\; \Psi_m(x)\; \Psi_n(x) = \delta_{mn}\;, \tag{4.52}$$

where $w(x)$ is a weight function in the integration that depends on the basis chosen. Two examples of basis functions which will be considered in more detail are the Fourier series

$$\Psi_n^{\mathrm{Fourier}}(x) = \begin{cases} \cos\left\{\frac{n}{2}\left(\frac{\pi(2x-x_{\max}-x_{\min})}{x_{\max}-x_{\min}}\right)\right\} & n \text{ even} \\ \sin\left\{\frac{n+1}{2}\left(\frac{\pi(2x-x_{\max}-x_{\min})}{x_{\max}-x_{\min}}\right)\right\} & n \text{ odd}\;, \end{cases} \tag{4.53}$$

and the top-hat basis

$$\Psi_n^{\mathrm{Bin}}(x) = \Theta\left(x - x_n + \frac{\Delta x}{2}\right) - \Theta\left(x - x_n - \frac{\Delta x}{2}\right)\;, \tag{4.54}$$

where $\Theta(x)$ denotes the Heaviside step function. The latter choice is equivalent to binning the support of $f(x)$ and assuming the systematic as piecewise constant. Here we have defined the bin width $\Delta x = (x_{\max} - x_{\min})/(N+1)$ and the bin centres $x_n = x_{\min} + (n+1/2)\,\Delta x$. The weight function $w(x)$ in (4.52) is unity for the top-hat basis, and for the Fourier series $w(x) = 1/\pi$.

If one requires in addition that the basis functions $\Psi_n(x)$ are bounded, one can define a finite range $[-Q_n; Q_n]$ such that every $|f(x)| \leq 1$ is represented by (4.51) with $a_n \in [-Q_n; Q_n]$ for every n, which can be seen as follows. The coefficients of the expansion are given by

$$a_n = \int_{x_{\min}}^{x_{\max}} \mathrm{d}x\; w(x)\; f(x)\; \Psi_n(x)\;, \tag{4.55}$$

which is readily verified by inserting (4.51) and applying (4.52). Making use of the generalised triangle inequality and $|f(x)| \leq 1$, one can then derive the bound

$$|a_n| \leq \int_{x_{\min}}^{x_{\max}} \mathrm{d}x\; |w(x)|\; |\Psi_n(x)| \equiv Q_n\;. \tag{4.56}$$

For the top-hat basis obviously $Q_n = \Delta x$ for all n. In case of the Fourier basis one can evaluate the integral in (4.56) explicitly by considering the intervals in which the sine and cosine are positive and negative separately, resulting in $Q_0 = 2$ and $Q_n = 4/\pi \approx 1.27$ for $n > 0$. This relation is not invertible, i.e. sampling the a_n from $[-Q_n; Q_n]$ does not guarantee $|f(x)| \leq 1$ everywhere. Thus, we sample the expansion coefficients from the interval defined by Q_n, which ensures completeness in the bounded region, and discard all functions with $|f(x)| > 1$ for any value of x.

In Fig. 4.9 exemplary functional forms have been drawn from both the basis sets (4.53) and (4.54) to sample a given region. They were obtained by uniform random sampling of the coefficients a_n, using a maximum order in the expansion of $N = 15$. Note that the generalisation to an arbitrary boundary as the one in the figure is easily achieved by multiplying (4.51) by $B(x)$.

One may be concerned whether the boundedness of the systematic signal necessarily implies that the parameter biases it causes are bounded as well. Kitching et al. (2009) prove explicitly that for $|f(x)| \leq B(x)$ the modulus of the bias on a given cosmological parameter has indeed a maximum. Here, we demonstrate for a simplified problem, but otherwise with a similar ansatz, that the modulus of the bias b_μ has a maximum for a given fixed amplitude of the systematic. Consider a discrete data set $\{s_i \equiv s(x_i)\}$ with covariance C_{ij}, where $x_i \in [x_{\min}; x_{\max}]$ for all i. The signal is contaminated by a systematic $\{f_i \equiv f(x_i)\}$ which is normalised via $\sum_i f_i^2 = \mathcal{N}^2$. By means of the Fisher matrix formalism, see Appendix A, one can then compute the extremal parameter bias under the constraint of a fixed normalisation. We consider the expression

$$\hat{b}_\mu = \sum_\nu \left(F^{-1}\right)_{\mu\nu} \sum_{i,j} f_i \left(C^{-1}\right)_{ij} \frac{\partial s_j}{\partial p_\nu} - \lambda \left\{ \sum_i f_i^2 - \mathcal{N}^2 \right\} , \tag{4.57}$$

where F is the Fisher matrix and λ a Lagrange multiplier. Note that the first term in (4.57) is just the usual bias formula, see e.g. (6.73) and Appendix A. Computing $\partial \hat{b}_\mu / \partial f_k = 0$ for every k, we determine the extremum of b_μ by varying the set of $\{f_i\}$ under the constraint that the systematic has a fixed amplitude. One arrives at

$$f_k = \frac{1}{2\lambda} \sum_\nu \left(F^{-1}\right)_{\mu\nu} \sum_j \left(C^{-1}\right)_{kj} \frac{\partial s_j}{\partial p_\nu} , \tag{4.58}$$

where the Lagrange multiplier can then be chosen such that the correct normalisation is ensured. Equation (4.58) yields the systematic signal that causes the strongest parameter bias for a given normalisation. Hence, assuming that the covariance C_{ij} is close to diagonal, i.e. $\left(C^{-1}\right)_{kj} \propto \delta_{kj}$, the maximum bias in this case is given by a systematic that is a linear combination of the derivatives of the signal with respect to the cosmological parameters under consideration. If only a single parameter is estimated from the data, the worst systematic is proportional to the derivative of the signal with respect to this parameter because it mimics exactly the effect of this parameter on the signal (as was also found by Amara & Réfrégier 2008).

In principle we are now in the position to completely sample the region of possible systematics bounded by $B(x)$, compute for every function $f(x)$ sampled the parameter bias either via the Fisher matrix formalism or a likelihood analysis, and find the strongest bias within the bounded region which can then be used to calculate (4.50). However, completeness is only guaranteed for $N \to \infty$ and infinitely many samples of the expansion coefficients a_n. In practice we have to truncate the series at some finite order N, so that features in the systematic that are on smaller scales than the variability of $\Psi_N(x)$ are not captured. This limited resolution of functional form filling is unproblematic since highly oscillatory systematics are not common in reality and behave similar to noise, which renders it unlikely that they produce a strong bias.

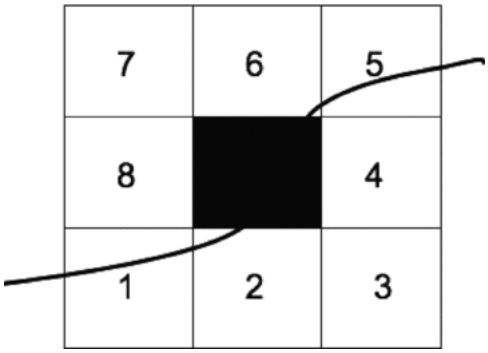

Figure 4.10: Measuring the level to which regions are filled by functions. After pixelising the region, all functions crossing a certain pixel are checked through which neighbouring pixel these functions enter, and through which they exit. Taking into account that functions cannot have multiple values (e.g. enter via 1 and exit via 8), there are in total 22 possible combinations of such enter- and exit-pixels (from Kitching et al. 2009).

It should in all cases be possible to find a physically motivated resolution of the functional form filling formalism.

The maximum order N of the expansion and the number of functions N_F for which the bias needs to be computed in order to get a complete coverage of the bounded region down to the selected resolution can then be optimised numerically. A straightforward way to assess the completeness is to pixelise the region bounded by $B(x)$, where the pixel size determines the resolution limit. For every pixel the complete coverage of functional forms is then calculated by counting possible combinations of how functions enter and exit the pixel, as is illustrated in Fig. 4.10. Taking into account that a function cannot have multiple values, i.e. that it for instance cannot enter via pixel no. 1 and exit via pixel no. 8, there are in total 22 possible combinations of neighbouring pixels through which a function can enter and exit. Completeness is achieved if all these combinations have occurred at least once during the sampling. Note that the combinations do not have equal probability as entering or exiting through the corner pixels 1, 3, 5, and 7 is far more unlikely.

In Fig. 4.11 the efficiency of functional form filling is displayed by plotting the percentage of pixel entry-exit combinations that have been realised for a given maximum order N and number N_F of functions sampled. We use a simple case with $B(x) = 0.5$ and $x \in [0; 10]$, the pixels in this region having a width of 0.5 and a height of 0.04. We find that the Fourier basis effectively samples the region as soon as both N and N_F are of moderate size, e.g. $N = 20$ and $N_\mathrm{F} = 10^3$. In stark contrast to this, the top-hat basis cannot achieve complete coverage of the region, even for large N and N_F. This inefficiency of the binning approach is paired with the fact that a physical systematic, which is usually a smooth function, is difficult to be represented by a discontinuous top-hat basis. Functional form filling using the binning scheme via (4.54) is related to the general parametrisations of the systematic employed by Bridle & King (2007) and Joachimi & Bridle (2009) in the marginalisation over nuisance parameters and may hint at the potential inefficiency of this formalism.

A 'hard' boundary $\pm B(x)$ as used in the considerations above could be motivated mathematically, e.g. a non-negative auto-correlation power spectrum, or physically, e.g. the expected non-positive contribution by shear-intrinsic shape correlations, see Sect. 5.1 (however, note that these examples only yield one-sided constraints and need to be supplemented by a second one). Often previously acquired external data from simulations or observations can put constraints on the possible range of $f(x)$, so that one could for instance choose the $3\,\sigma$ limit to take the role of $B(x)$. A more elaborate formalism was investigated in Kitching et al. (2009), where every possible functional form of the systematic was assigned a weight based on how well it fits the external data set. Every value of the bias was then assigned the weight of the best-fit $f(x)$ out of the class of systematics that produced this bias. With this procedure, e.g. a systematic with a very high amplitude which causes a strong bias is largely downweighted because it is likely to yield a bad fit to the external data set.

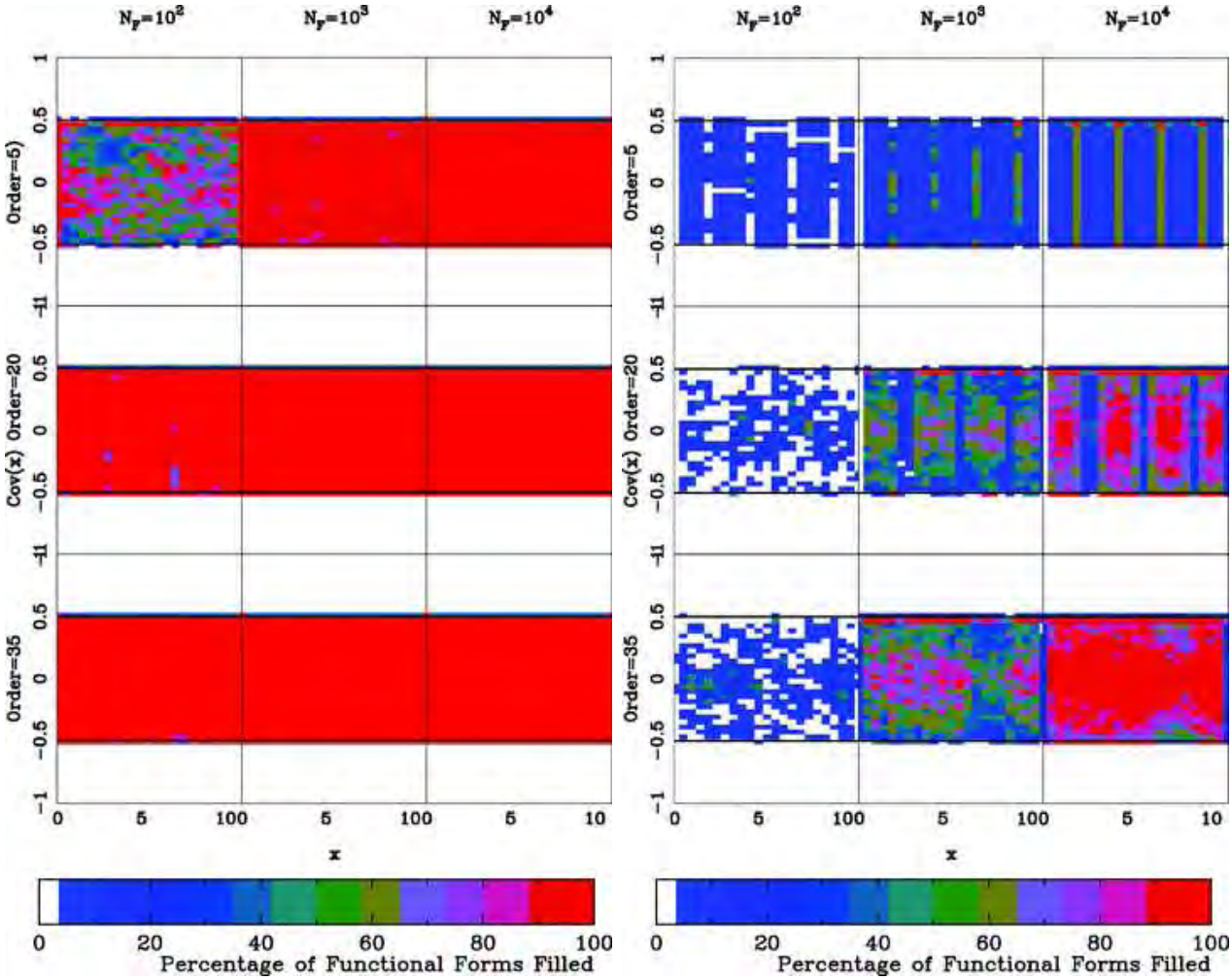

Figure 4.11: Efficiency of form filling for different numbers of sampling functions N_{F} and different maximum orders of the basis functions. The form filling is performed on a simple region with constant boundaries at -0.5 and +0.5 in the interval $x \in [0; 10]$, using the Fourier basis (left panel) and the top-hat basis (right panel). The pixels within the region have a width of 0.5 and a height of 0.04. The colour coding for each pixel corresponds to the percentage of observed enter- and exit-combinations by the sample functions out of the total of 22, see Fig. 4.10. In each panel the top row corresponds to using a maximum order of the series expansion of $N = 5$, the centre row to $N = 20$, and the bottom row to $N = 35$. From left to right column in each panel the number N_{F} of functions used to sample the region is 10^2, 10^3, and 10^4 (from Kitching et al. 2009).

Kitching et al. (2009) have shown that functional form filling and marginalisation over nuisance parameters which enter the model of the systematic yield the same mean square error if, and only if, the functional form of the systematic is known a priori. Should that not be the case, marginalisation will in general tend to underestimate the mean square error due to the limited flexibility in the model of the systematic. Furthermore the authors argue that functional form filling is competitive to marginalisation as regards computational time, in particular if more advanced techniques like Monte Carlo procedures are used instead of the current uniform sampling of the coefficients a_n to acquire a set of functional forms. Hence, the technique outlined above constitutes an efficient and effective alternative to standard marginalisation over nuisance parameters, offering the practical advantage of a robust estimation of parameter biases and the conceptual plus of treating a systematic as such.

4.3 Cosmic shear analysis of the HST COSMOS Survey

The Hubble Space Telescope (HST) COSMOS survey currently provides the largest contiguous area of space-based data suitable for weak lensing studies, thus serving as a benchmark for today's capabilities of cosmic shear analysis techniques as well as a showcase for future ambitious projects like Euclid. Schrabback et al. (2010) have undertaken the first fully tomographic cosmic shear analysis of COSMOS, including the most thorough and careful treatment of weak lensing systematics done hitherto. In the following we are going to summarise the main steps in the analysis and the results, before elaborating on a number of key points in the extraction of cosmological information, namely the effect of dynamical dark energy on the non-linear evolution of structure and analytic calculations for optimising the angular binning and the signal covariances.

4.3.1 Cosmic shear tomography with COSMOS

The COSMOS survey (Scoville et al. 2007) was observed with HST between 2003 and 2005, totalling 326 hours of exposure time and an area of $1.64\,\mathrm{deg}^2$, the largest contiguous area ever covered by HST. Images were taken in a filter centred on 814 nm, reaching a magnitude limit of 26.7 of galaxies usable for shear measurement. The shear catalogue contains in total about 450000 galaxies, corresponding to a galaxy density of $n = 76\,\mathrm{arcmin}^{-2}$ which is about twice the value anticipated for Euclid. Hence the survey is very deep with a median redshift above unity and galaxies out to $z \lesssim 5$.

The HST imaging is supplemented by a photometric catalogue in 30 optical and infrared bands (COSMOS-30, Ilbert et al. 2009), yielding high-quality photometric redshifts for a brighter subsample of galaxies with magnitude $\lesssim 24$. The scatter in photometric redshifts is as low as $\sigma_{\mathrm{ph}}(1+z)$ with $\sigma_{\mathrm{ph}} = 0.012$ for galaxies with $z < 1.25$ and reaches $\sigma_{\mathrm{ph}} = 0.06$ at $z \sim 2$. However, there are about 20 % of catastrophic failures in the assignment of photometric redshifts, governed by faint high-redshift galaxies for which the Balmer break could not be identified, and which are therefore incorrectly assigned a low redshift of less than 0.6. These undetected outliers could jeopardise the redshift scaling of the weak lensing signal, so that we exclude faint galaxies with low photometric redshifts from the cosmological analysis.

The objects in the shear catalogue with reliable photometric redshift estimates are then divided into five bins, with their boundaries chosen such that the expected overlap of the underlying redshift distributions is minimal. The remainder, which still comprises more than half of the available galaxies, constitutes a sixth broad bin, where the redshift distribution is extrapolated from the one of the brighter subset with individual redshift information. The residual uncertainty in this redshift distribution due to the extrapolation is accounted for by introducing a nuisance parameter into the likelihood analysis.

The shear is extracted from the galaxy images via the KSB+ formalism (e.g. Hoekstra et al. 1998). The known multiplicative and systematic errors of this method are corrected via the results of the STEP simulations (Heymans et al. 2006a; Massey et al. 2007a). The density of stars in COSMOS is too low to perform the usual interpolation of the PSF shape across the field of view. Instead, images of dense stellar fields are analysed, taking particular care of temporal PSF variations that could be identified as being dependent on the telescope focus and the angle between the pointing direction and the Sun. Moreover, the high level of radiation damage of the CCD detector in space causes a considerable charge transfer inefficiency, resulting in trails in read-out direction behind all objects. To avoid the introduction of spurious ellipticities, this effect is also corrected for empirically.

The statistical constraints expected for a COSMOS-type survey are too weak to allow for

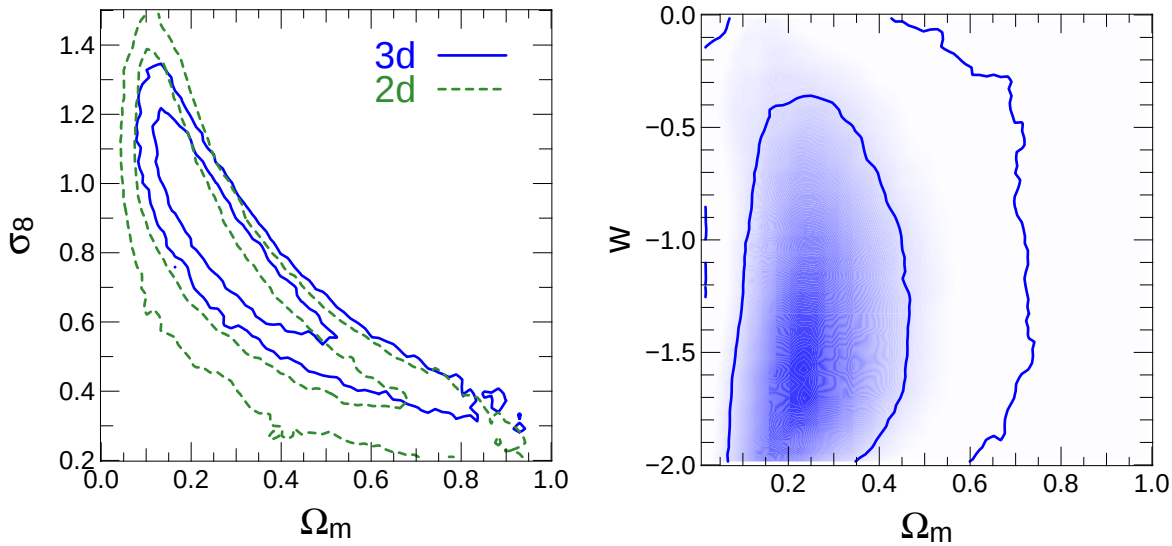

Figure 4.12: Constraints on cosmological parameters by cosmic shear tomography from the COSMOS survey. *Left panel*: $1\,\sigma$ and $2\,\sigma$-confidence contours in the $\Omega_\mathrm{m} - \sigma_8$ plane for a flat ΛCDM cosmology. The Hubble parameter h and the nuisance parameter f_z, quantifying the uncertainty in the redshift distribution of faint galaxies, have been marginalised over. Blue solid lines correspond to the results of a tomographic cosmic shear analysis, green dashed lines to those of a standard non-tomographic analysis. *Right panel*: $1\,\sigma$ and $2\,\sigma$-confidence contours in the $\Omega_\mathrm{m} - w_0$ plane for a flat wCDM cosmology. The parameters f_z, h, and σ_8 have been marginalised over. Confidence contours are shown as blue lines while the blue region indicates the highest density of the posterior probability. Note that the constraints depend considerably on the prior $w_0 \in [-2; 0]$ (from Schrabback et al. 2010).

a sophisticated treatment of a potential contamination by intrinsic alignments. However, for the same reason this contamination should not produce any significant biases on cosmological parameters. Yet, we exclude auto-correlations of the narrow redshift bins 1 to 5 to avoid potential contributions from intrinsic ellipticity correlations. Furthermore luminous red galaxies (LRGs), i.e. large elliptical galaxies that are preferentially located in regions of high matter density, are discarded from the shear catalogue for the cosmological analysis because recent work suggests that most of the intrinsic alignment signal is carried by LRGs, see Sect. 5.1. Including auto-correlations and LRGs in the parameter estimation does not change the results in a significant way, hence intrinsic alignments are not considered a relevant source of systematic errors in COSMOS.

From the shear estimates tomographic correlation functions are computed via (3.42). Both aperture mass and ring statistics are derived from $\xi_\pm$, producing B-mode signals that are consistent with zero, which suggests that the elimination of possible systematics has been successful. The angular binning of the correlation function is optimised with respect to the information content, taking into account that the smallest scales cannot be modelled accurately due to the highly non-linear density field and baryonic effects (see Sect. 4.3.3). The covariance cannot be measured from the data because of the small survey size, but is calculated via ray tracing through the Millennium simulation (Hilbert et al. 2009), see again Sect. 4.3.3 for details. Since we also aim at determining the dark energy equation of state parameter w_0, its effect on structure evolution needs to be incorporated into the modelled correlation functions, see the following section.

The subsequent likelihood analysis reveals that the constraints on the parameters Ω_m, Ω_Λ, σ_8, and w_0 are fully consistent with the ΛCDM concordance model as well as other estab-

lished cosmological probes such as WMAP 5year CMB data. As shown in Fig. 4.12, the full tomographic analysis yields significantly smaller confidence contours than the standard two-dimensional approach. While the standard and tomographic analyses are consistent at the $1\,\sigma$ level, the former slightly prefers a lower value of σ_8, which is likely due to the two-dimensional analysis effectively probing the structure at lower redshifts, while the most massive structures in COSMOS are seen at $z \sim 0.7$ (Massey et al. 2007b). Although the survey size is more than an order of magnitude smaller than current ground-based cosmic shear surveys, constraints are only moderately weaker due to the superior depth and galaxy number density of COSMOS (compare to Figs. 3.5 and 3.6).

Due to the small area of COSMOS, constraints on w_0 are still weak, see Fig. 4.12. In the implementation we used, the model correlation functions display no dependence on the equation of state parameter if $w_0 \ll -1$, so that a lower boundary on w_0 cannot be found. As a consequence, the confidence limits on w_0 are highly dependent on the prior which we choose as $w_0 \in [-2; 0]$. Although cosmic shear can place upper limits on w_0, the exact value of this limit is thus also prior-dependent, in our case $w_0 < -0.41$ with 90 % confidence. Besides, we find for the deceleration parameter

$$q_0 = -\frac{\ddot{a}a}{\dot{a}^2} = \frac{\Omega_\mathrm{m}}{2} - \Omega_\Lambda \tag{4.59}$$

that is is negative with 94.3 % confidence, using only the constraint on h by the HST key project, the constraint on Ω_b by Big Bang Nucleosynthesis, and a weak prior on n_s. Hence, cosmic shear provides independent evidence for the accelerated expansion of the Universe at the $2\,\sigma$ level.

The COSMOS survey has been subject to a cosmic shear analysis before by Massey et al. (2007c) who only used the auto-correlations between three redshift bins. Our study relies on the full cosmic shear tomography with largely improved redshift information, a simulated covariance that avoids issues with sampling noise and biases due to the covariance inversion, and a more thorough treatment of sources of systematics. The benefit of this rigorous approach can best be appreciated by considering Bean (2009) who claimed to have detected a departure from general relativity governed by cosmic shear data based on the shear catalogue by Massey et al. (2007c)[4], which can probably be traced back to residual systematics.

4.3.2 Modelling the effect of dark energy on structure evolution

Accurate measurements of cosmological parameters not only necessitate a careful processing of the data but also precise modelling on the theoretical side, in particular as regards the effects of dark energy with a non-standard equation of state. Due to the small survey size the scales probed by cosmic shear in COSMOS reach from the quasi-linear into the highly non-linear regime of structure formation. Thus it is essential to account for non-linear evolution of structure in the modelling, which cannot be computed analytically. In cosmic shear and most other cosmological methods probing the large-scale structure at low to medium redshifts the standard approach is to use fits to large sets of simulations, the most recent and widespread one provided by Smith et al. (2003).

First, when compared to more recent simulation results, the fit formula by Smith et al. (2003) slightly underestimates the non-linear corrections to the power spectrum (e.g. Hilbert et al. 2009). This systematic shift affects σ_8 strongest and has been studied in detail by Schrabback et al. (2010). Besides, the fit formula was not designed to incorporate a dependence on the

[4]This claim has been withdrawn in a corrected version, see Bean & Tangmatitham (2010).

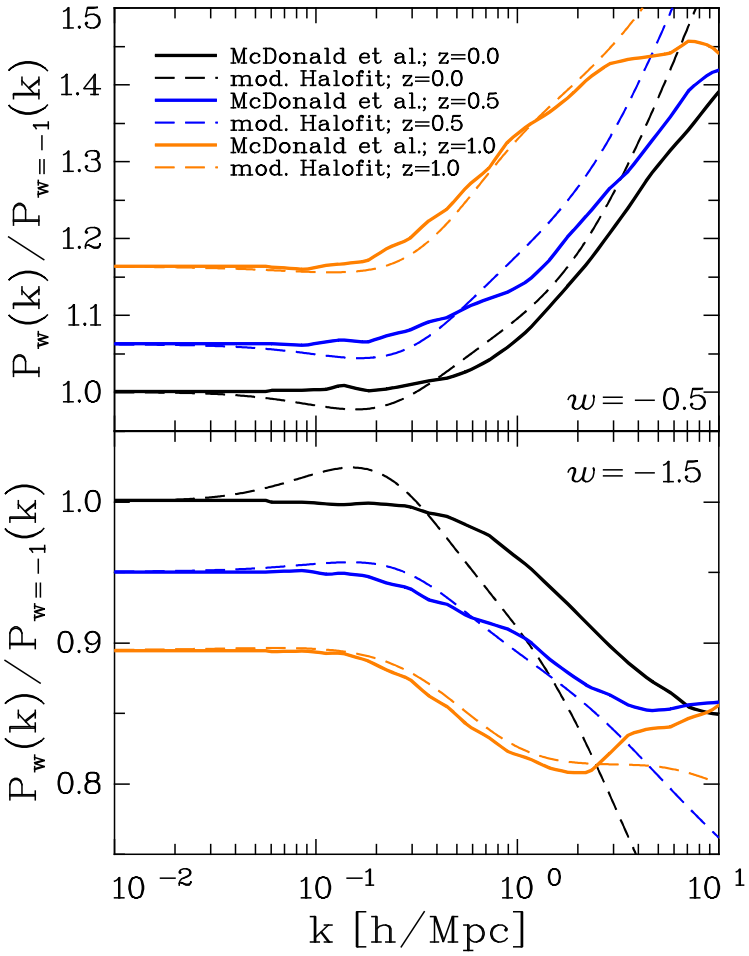

Figure 4.13: Performance of the modified halofit fitting function in presence of dynamical dark energy. Shown is the ratio of the three-dimensional matter power spectrum for $w_0 = -0.5$ (top panel) and $w_0 = -1.5$ (bottom panel) over the power spectrum computed for $w_0 = -1$, plotted as a function of wavenumber k. Solid curves correspond to the functions fit to the simulation results by McDonald et al. (2006), dashed lines to the modified halofit fitting functions. Black lines are computed for $z = 0$, blue lines for $z = 0.5$, and orange lines for $z = 1$ (as published in Schrabback et al. 2010).

dark energy equation of state parameters w_0 and w_a, but is based on the interpolation between sets of simulations for either an open universe without dark energy or a flat ΛCDM model.

As an alternative, one could resort to more recent simulations investigating non-linear structure evolution in presence of dynamical dark energy, such as McDonald et al. (2006) who also provide fits to their results. However, owing to the large number of simulations to be run to achieve good coverage of the multi-dimensional parameter space, the range of some cosmological parameters is tightly restricted. For instance, the new fit formula by McDonald et al. (2006) has been tested only for $\sigma_8 = 0.897 \pm 0.097$, which needs to be compared to the range $\sigma_8 \in [0.2; 1.5]$ used in the likelihood analysis, see Fig. 4.12. Since we prefer not to affect the parameter estimation by narrow priors which are imposed by the availability of fits for the modelling, we cannot make direct use of the formulae by McDonald et al. (2006).

Instead, we adopt the heuristic and rather simplistic approximation implemented in the publicly available `icosmo` code (Réfrégier et al. 2008). It is based upon a modification of the halofit routine of Smith et al. (2003) in which the interpolation between the open and flat cosmological models is determined by the parameter $f = \Omega_\Lambda/(1-\Omega_\mathrm{m})$, where $f = 0$ corresponds to open universes without dark energy (we assume $\Omega_\mathrm{m} < 1$), and $f = 1$ to flat ΛCDM models. We now exploit the fact that certain variable dark energy models mimic OCDM universes, see e.g. Fig. 2.3, which can be understood as follows. Inserting the dark energy equation of state (2.14) in the parametrisation (2.15) into (2.13), one obtains the evolution of the dark energy

density parameter as[5]

$$\Omega_\Lambda(z) = \Omega_{\Lambda,0}\ \exp\left\{3\left((w_0 + w_a + 1)\ \ln(1+z) - w_a\ \frac{z}{1+z}\right)\right\}\ . \tag{4.60}$$

Incorporating this equation into (2.19), it is readily seen that a flat ΛCDM model with $w_0 = -1/3$ and $w_a = 0$ has exactly the same expansion history as an OCDM universe with identical Ω_m but without dark energy, the latter taking the place of the curvature term. Motivated by this coincidence, the interpolation parameter f in the halofit routine is replaced by

$$f' \equiv -\frac{1}{2}\left(3\left[w(z)\ f - \frac{1}{3}\ (1-f)\right] + 1\right)\ , \tag{4.61}$$

where $w(z)$ is given by (2.15) and $f = \Omega_\Lambda/(1-\Omega_\mathrm{m})$ as before. If a model does not feature dark energy, $f' = f = 0$. For a flat ΛCDM model the interpolation now takes place between $w(z) = -1/3$ mimicking OCDM ($f' = 0$) and the cosmological constant $w(z) \equiv -1$ ($f' = 1$).

In Fig. 4.13 we plot the three-dimensional matter power spectrum for $w_0 = [-0.5; -1.5]$, normalised to the power spectrum in the ΛCDM model with otherwise identical parameters. To be able to compare the performance of the modified interpolation (4.61) to the fits to the simulations by McDonald et al. (2006), we choose a set of cosmological parameters that is covered by the fits, in particular $\sigma_8 = 0.9$. Generally speaking, $w_0 > -1$ leads to an increase in power, the stronger the smaller and thus more non-linear the scale, and vice versa for $w_0 < -1$. McDonald et al. (2006) hypothesise that this dependence is caused by the change in formation redshift of dark matter haloes at a given scale due to dark energy. The halofit modification is not capable of tracing the scale dependence for $w_0 = -1.5$ at $z = 0$, but provides otherwise a fair approximation to the fits extracted from the simulations. The discrepancy becomes significant again for the smallest scales, but we also find that the fits by McDonald et al. (2006) are probably dominated by numerical artefacts for $k \gtrsim 2\,\mathrm{Mpc}\,h^{-1}$. Since the lensing analysis of the deep COSMOS survey is mostly sensitive to structures at $z \gtrsim 0.4$ where the deviations of the halofit modification are small, (4.61) is used in Schrabback et al. (2010) and for all dark energy computations in this work.

While (4.61) is sufficiently accurate to avoid parameter biases to be of the same order as the statistical errors of the COSMOS analysis, future cosmic shear surveys require substantially improved models, not only for the dependence on the dark energy parametrisation, but also for per-cent precision on the non-linear evolution of structure, the dependence on further parameters that e.g. constrain modifications of the law of gravity, and baryonic effects playing a crucial role on the smallest scales. Within the coming years the computational power may increase enough to run an individual large-scale simulation for every point of interest in parameter space, but it might still be desirable to develop more elegant solutions, see e.g. Angulo & White (2010).

4.3.3 Analytic predictions for the COSMOS analysis

One of the major advancements in the COSMOS analysis by Schrabback et al. (2010) is the usage of a covariance matrix which has been obtained via ray tracing through the large-scale Millennium simulation (Hilbert et al. 2009). However, a number of issues have to be dealt with when taking this approach. First, one would ideally compute a covariance for every point

[5]Note that the corresponding equation in Joachimi & Schneider (2009) has the wrong sign in the exponential. Note furthermore that we use the term Ω_Λ for dark energy in general rather than only for the cosmological constant.

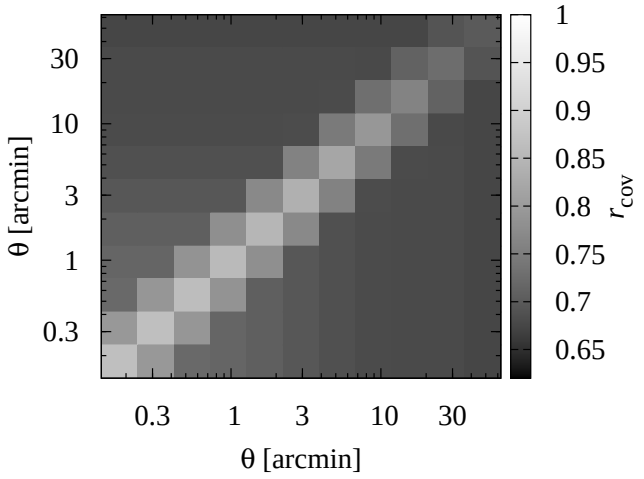

Figure 4.14: Effect on the Gaussian covariance of ξ_+ when changing the value of σ_8 from 0.8 to 0.9. Shown is the ratio of the covariance $r_{\rm cov}$ for 12 logarithmic bins between angular scales 0.1 and 60 arcmin, for the auto-variance of $\xi_+^{(11)}$. The colour coding is given alongside the panels. Note the contribution by shape noise to the diagonal.

in parameter space sampled in the likelihood analysis. Due to the additional dependence on cosmology, tighter constraints could be expected (Eifler et al. 2009), but in this case only the parameter combination used to create the Millennium simulation is available. This is unproblematic as long as the parameter set is close to the maximum likelihood point of the analysis. Unfortunately, recent studies agree that $\sigma_8 \sim 0.8$ (this also holds for weak lensing with COSMOS, see Schrabback et al. 2010), whereas for the Millennium simulation $\Omega_{\rm m} = 0.25$ and $\sigma_8 = 0.9$.

A computationally cheap and purely analytic way to determine covariances of second-order cosmic shear measures was derived by Joachimi et al. (2008) in the limit of Gaussian density fluctuations. Under this assumption, and for a contiguous survey aperture of size A, the covariance for tomography convergence power spectra reads

$$\mathrm{Cov}\left(P_\kappa^{(ij)}(\bar{\ell}),\ P_\kappa^{(kl)}(\bar{\ell}')\right) = \frac{2\pi}{A\bar{\ell}\Delta\ell}\left(\bar{P}_\kappa^{(ik)}(\bar{\ell})\bar{P}_\kappa^{(jl)}(\bar{\ell}) + \bar{P}_\kappa^{(il)}(\bar{\ell})\bar{P}_\kappa^{(jk)}(\bar{\ell})\right)\ \delta_{\bar{\ell}\bar{\ell}'}\ , \tag{4.62}$$

where $\Delta\ell$ is the width of the angular frequency bin. We have defined

$$\bar{P}_\kappa^{(kl)} = P_\kappa^{(kl)} + \delta_{kl}\,\frac{\sigma_\epsilon^2}{2\bar{n}^{(k)}}\ , \tag{4.63}$$

where the second term, containing the intrinsic ellipticity dispersion σ_ϵ and average number density of galaxies in bin i, $\bar{n}^{(i)}$, accounts for galaxy shape noise. As the errors on the power spectra are uncorrelated at different angular frequencies in the Gaussian limit, see the Kronecker symbol $\delta_{\bar{\ell}\bar{\ell}'}$ in (4.62), one can easily derive the covariance of the shear correlation functions from (4.62) by means of (3.45) and (3.47), resulting in

$$\begin{aligned}\mathrm{Cov}\left(\xi_\pm^{(ij)}(\theta_1),\ \xi_\pm^{(kl)}(\theta_2)\right) \ &= \ \frac{1}{2\pi A}\int_0^\infty \mathrm{d}\ell\ \ell\ J_{0/4}(\ell\theta_1)\ J_{0/4}(\ell\theta_2) \\ &\times\left\{\left(\bar{P}_\kappa^{(ik)}(\ell)\bar{P}_\kappa^{(jl)}(\ell) + \bar{P}_\kappa^{(il)}(\ell)\bar{P}_\kappa^{(jk)}(\ell)\right) + \frac{\sigma_\epsilon^4}{4\bar{n}^{(i)}\bar{n}^{(j)}}\left(\delta_{ik}\delta_{jl} + \delta_{il}\delta_{jk}\right)\right\}\ ,\end{aligned} \tag{4.64}$$

see Joachimi et al. (2008) for details and an expression for the cross-variance between ξ_+ and ξ_-. However, due to the small scales probed by COSMOS, non-Gaussianity produces significant contributions to the covariance (e.g. Semboloni et al. 2007), so that (4.64) cannot be used for the analysis. Still, the analytic covariance calculations provide helpful consistency checks during the complex production of covariance estimates from simulations.

For instance, as can directly be seen from (4.62) and (4.64), one expects in the Gaussian case that the covariance for a default value of $\sigma_8 = 0.8$ compared to the slightly offset value of

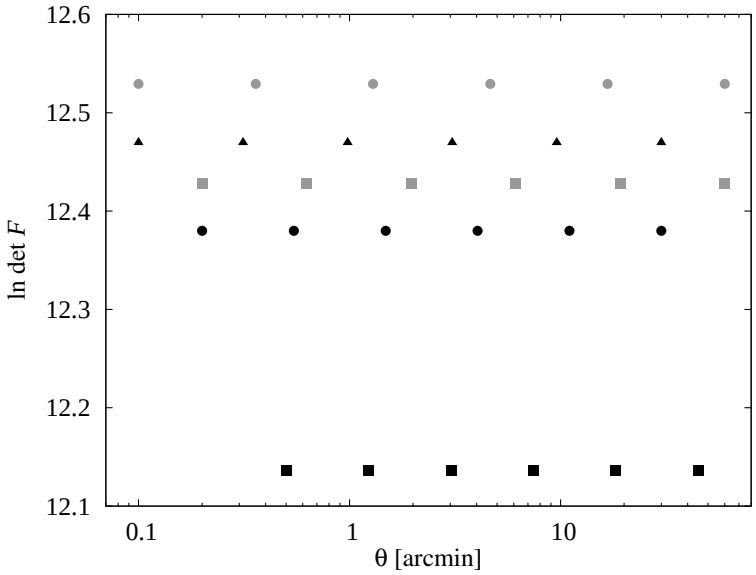

Figure 4.15: Information content of COSMOS cosmic shear data for different angular binning of the correlation functions. Shown is the logarithm of the determinant of the Fisher matrix, calculated for the cosmological parameters Ω_m, σ_8, and w_0. In each case the points are plotted at the positions of the bin boundaries. Throughout, 5 logarithmically spaced bins are used. The minimum and maximum available angular scale is $\theta = 0.1$ arcmin and $\theta = 60$ arcmin, respectively.

$\sigma_8 = 0.9$ of the Millennium data causes a constant suppression of the entries of the covariance matrix by $(0.8/0.9)^4 \approx 0.624$ if shape noise can be neglected. In Fig. 4.14 we show the ratio of the Gaussian covariances of the correlation function ξ_+ for $\sigma_8 = 0.8$ over $\sigma_8 = 0.9$, and otherwise identical parameters. Indeed the ratio is close to 0.62 on larger scales while on the smallest scales the limited numerical accuracy of the computation produces higher values. On the diagonal shape noise dominates, and as it is independent of σ_8, the ratio is close to unity. Since the entries of the simulated covariance with $\sigma_8 = 0.9$ are thus expected to be larger or of similar size as the real ones, Schrabback et al. (2010) by default use the Millennium covariance as a conservative estimate for the true errors.

Moreover, simulations can only provide a finite number of realisations n which renders the covariance noisy and in addition limits the dimension d of the data vector usable for the analysis. As was demonstrated in Hartlap et al. (2007), an unbiased estimator for the inverse of the covariance, needed to compute likelihoods, is given by

$$\widehat{(\mathrm{Cov})^{-1}} = \frac{n-d-2}{n-1}\,\left(\widehat{\mathrm{Cov}}\right)^{-1} \equiv \mathcal{F}\,\left(\widehat{\mathrm{Cov}}\right)^{-1}\,, \tag{4.65}$$

where $\widehat{\mathrm{Cov}}$ denotes an estimator for the (non-inverted) covariance. If $d \lesssim n$, the inverse covariance computed from (4.65) will be close to zero and the corresponding errors large. In case the prefactor $\mathcal{F}$ is ignored, a bias is introduced, not on the parameter estimates themselves but on their errors. Hence, $d \ll n$ is desirable, where $n = 288$ realisations were obtained for COSMOS-like survey patches from the Millennium data.

Again relying on the analytic covariance formulae (4.64), we perform Fisher matrix predictions (for details see Appendix A) on the confidence regions of the parameters Ω_m, σ_8, and w_0 for different angular binnings. We use the determinant of the Fisher matrix as a measure for the size of the error ellipsoid in parameter space, the results shown in Fig. 4.15. For a given number of 5 logarithmically spaced θ-bins the results obviously indicate that a wide coverage of angular scales is desirable, with more information originating from the smaller, sub-arcminute scales. The resulting tendency to prefer small angular scales is counteracted by the limited validity of the modelling at the smallest scales due to baryonic effects and the interpolation of non-linear power for $w_0 \neq -1$, see the foregoing section. We decide to use 5 logarithmically spaced angular bins between $\theta \approx 0.5$ and $\theta = 30$ arcmin. The COSMOS analysis uses all correlations between 6 redshift bins for both ξ_+ and ξ_-, excluding the auto-correlations of the first 5 bins to avoid

intrinsic alignment systematics, rendering 32 entries in the data vector per angular frequency bin. This yields $p = 160$ and consequently a reasonable value of $\mathcal{F} = 0.439$.

Similar to the case of modelling the dependence on dark energy parameters, we are confident that the measures taken to determine covariances of the correlation functions were of sufficient accuracy to produce unbiased parameter estimates with realistic error bounds. Future surveys require more elaborate approaches, employing either large suites of simulations or more precise models and fits of non-Gaussian contributions. In this sense COSMOS does not only provide the first competitive space-based cosmic shear data set, but is also likely to be the last survey which can be studied with first-generation shear measurement techniques, simple approximations in the modelling, and rather small computational efforts in estimating the covariance of the signals.

Chapter 5

The intrinsic alignment of galaxies

It is a key assumption in the analysis of cosmic shear statistics that the intrinsic ellipticity of one galaxy is neither correlated with the intrinsic shape of, nor the gravitational shear acting on, another galaxy. However, the formation and evolution of galaxies is closely connected to the matter distribution that surrounds them, implying correlations of galaxy properties such as shapes and spins with those of the large-scale structure, as well as of other galaxies in the vicinity. As a consequence, the intrinsic ellipticities do exhibit correlations, summarised under the term 'intrinsic alignments'. These correlations prove to be the major astrophysical systematic in cosmic shear statistics, but in principle contain also valuable information about the properties and interactions of galaxies well worth exploring.

The investigation of intrinsic alignments is a fairly recent development, the first studies roughly coinciding with the first detections of cosmic shear at the turn of the century. The more subtle effect of cross-correlations between gravitational shear and intrinsic ellipticities was not identified as a potential contaminant of lensing measurements before the work by Hirata & Seljak (2004). In Sect. 5.1 we summarise the current state of knowledge about intrinsic alignments, including measurements from observations and simulations, modelling efforts, and methods suggested to avoid systematic errors due to intrinsic alignments in cosmic shear analyses.

As we will argue below, the theoretical understanding of intrinsic alignments, and hence the accuracy of models, is still crude at present. Therefore it is paramount to accumulate as many observational constraints on properties of the intrinsic alignment signals as possible. We present new measurements of gravitational shear-intrinsic ellipticity correlations among red galaxies, using the MegaZ LRG (luminous red galaxy) and further SDSS samples. With MegaZ LRG, we include for the first time a data set which features only photometric instead of spectroscopic redshift information into such an analysis.

In Sect. 5.3 the correlation function model, which is later fit to the observed correlations, is derived from first principles, incorporating the effect of photometric redshift uncertainty, and assessing the relevance of contributions by other signals. We give a summary of the analysed galaxy samples as well as the measurement and analysis methods applied to them in Sects. 5.2 and 5.4. The observed correlation functions, the corresponding best-fit models, and the resulting constraints on intrinsic alignment model parameters are presented in Sect. 5.5. We use our best-fit model to estimate the contamination of cosmological constraints for a present-day cosmic shear survey by means of a Fisher matrix prediction in Sect. 5.6, specifying the possible ranges of parameter biases still allowed by our intrinsic alignment constraints. Finally, we conclude on our findings about the intrinsic alignment measurements in MegaZ LRG and SDSS samples in Sect. 5.7.

The observed correlation functions including covariances and further quantities characteris-

ing the SDSS galaxy samples such as redshift and luminosity distributions were kindly provided by Rachel Mandelbaum. The 2SLAQ redshift data used to assess the photometric redshift accuracy were kindly made available by Filipe Abdalla.

5.1 Introduction to intrinsic alignments

In this section an overview over the research on intrinsic alignments is provided, covering the underlying physical processes, modelling, findings from simulations and observations, and a summary of methods designed to suppress biases on cosmological parameters due to intrinsic alignments in weak lensing studies.

5.1.1 The origin of intrinsic correlations

The intrinsic alignment of galaxies potentially causes a serious systematic modification of the cosmic shear signal because it mimics shear correlations. Consider a correlator of the ellipticities of two galaxy populations i and j, which forms the basis of all second-order cosmic shear measures. As was demonstrated in Sect. 3.2, in the regime of very weak lensing the measured ellipticity ϵ can be written as the sum of the intrinsic ellipticity ϵ^{s} of the galaxy and the gravitational shear γ acting on it. Then the correlator reads

$$\left\langle \epsilon_i \epsilon_j^* \right\rangle = \underbrace{\left\langle \gamma_i \gamma_j^* \right\rangle}_{\mathrm{GG}} + \underbrace{\left\langle \epsilon_i^{\mathrm{s}} \epsilon_j^{\mathrm{s}*} \right\rangle}_{\mathrm{II}} + \underbrace{\left\langle \gamma_i \epsilon_j^{\mathrm{s}*} \right\rangle + \left\langle \epsilon_i^{\mathrm{s}} \gamma_j^* \right\rangle}_{\mathrm{GI}} . \tag{5.1}$$

The first term on the right-hand side is the desired cosmic shear signal, where we introduced the shorthand notation 'GG' for this term. The standard approach to cosmic shear would now ignore the remaining three correlators, assuming that the intrinsic ellipticity of a galaxy is correlated neither with the shear nor with the intrinsic ellipticity of other galaxies.

However, the second term on the right-hand side in (5.1) might be non-vanishing if the galaxies correlated were subject to the same tidal gravitational forces during their formation or evolution, for instance if they reside in regions which are connected by a filament of the large-scale structure, if they have a common dark matter halo, or if they approach each other in the course of a merger. In general, the intrinsic ellipticities can only be correlated if the galaxies are physically close, i.e. have both a small angular and line-of-sight separation, except for rare situations in which large-scale filaments may induce long-distance correlations. Henceforth we will use the name 'intrinsic ellipticity correlations', or II correlations in short, for this effect. Due to the alignment in the same tidal field, galaxies are preferentially oriented in parallel, so that the II signal is expected to be positive.

The remaining terms in (5.1) describe correlations between intrinsic ellipticity and gravitational shear. Suppose that the galaxies of sample i are located at lower redshift than those of sample j. As the lensing effect is generated by the matter structure between $z = 0$ and the redshift of the source galaxy, one does not expect any correlation between a lensed galaxy in the foreground and the intrinsic ellipticity of a background object in absence of long-term correlations induced by filaments. Thus $\left\langle \gamma_i \epsilon_j^{\mathrm{s}*} \right\rangle = 0$ should hold unless e.g. photometric redshift errors cause a significant overlap of the redshift distributions of samples i and j, such that galaxies from the background population j could in reality be situated in front of galaxies from the foreground population i.

In case a matter structure generates a tidal gravitational field in which a close-by galaxy is aligned and by which at the same time a background object is gravitationally lensed, intrinsic

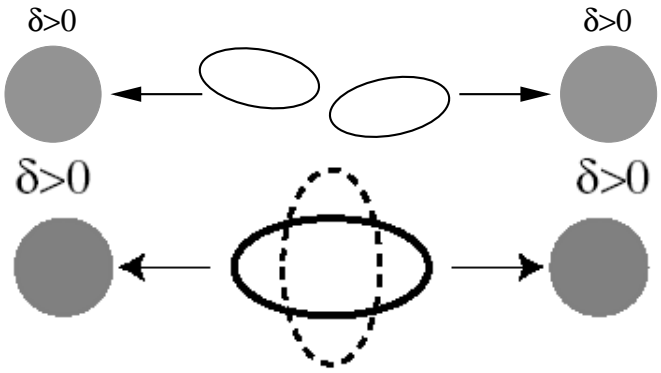

Figure 5.1: Sketch of intrinsic alignments as seen on the sky. Arrows indicate gravitational forces. *Top panel*: Generation of intrinsic ellipticity correlations between two physically close galaxies subject to the same tidal gravitational field. *Bottom panel*: Generation of shear-intrinsic ellipticity correlations between a foreground galaxy (solid line) which is aligned in the tidal gravitational field of the surrounding matter and the image of a background galaxy (dashed line), tangentially stretched due to the lensing by the same foreground structures (bottom panel from Hirata & Seljak 2004).

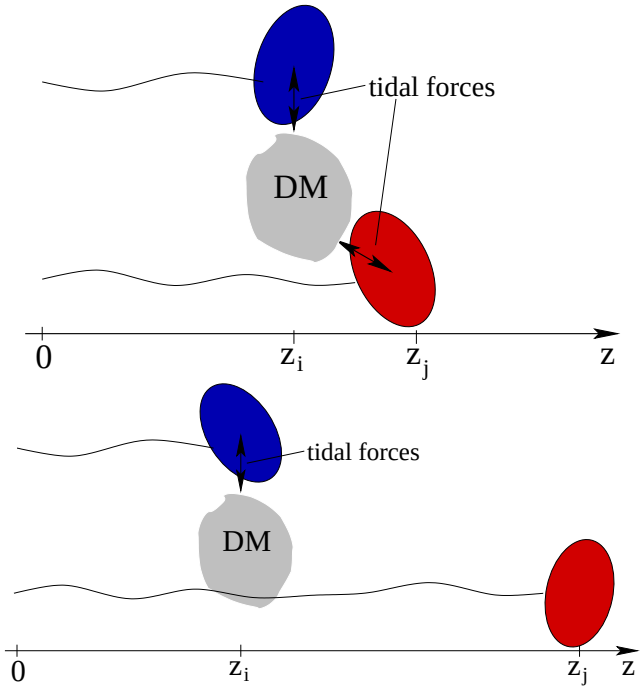

Figure 5.2: Sketch of intrinsic alignments as seen along the line of sight. Wavy lines represent the lensing signal. *Top panel*: To become intrinsically aligned, both galaxies have to be subject to tidal gravitational forces exerted by the same matter structures, hence $z_i \approx z_j$ is required. *Bottom panel*: Shear-intrinsic ellipticity correlations are generated if a matter structure tidally aligns a nearby galaxy at redshift z_i and contributes to the lensing signal of a background galaxy at $z_j > z_i$.

ellipticity-gravitational shear correlations (GI correlations henceforth)[1], as first identified by Hirata & Seljak (2004), will result. Due to the contribution by gravitational lensing, GI correlations are neither restricted to pairs of galaxies close on the sky nor to pairs with similar redshifts. Lensed background galaxies are preferentially aligned tangentially with respect to foreground matter overdensities, while foreground galaxies point towards the overdensity on average, so that a net anti-correlation of the ellipticities and hence a negative GI signal is expected. On the smallest scales, correlations might even arise from the alignment of a foreground galaxy with its own halo, the latter contributing to the shear of background galaxies (Bridle & Abdalla 2007). Figures 5.1 and 5.2 illustrate the generation of intrinsic alignments, sketching the correlation between a pair of galaxies as seen on the sky, and along the line of sight.

Analytic progress in modelling intrinsic alignments is difficult even for relatively simple

[1]Note that for both intrinsic alignment contributions a variety of names exists in the literature, although the abbreviations II and GI are used in most cases.

situations, but the correlation properties of the dark matter structure can at least in principle be studied to high accuracy by means of N-body simulations (for results but also caveats see Sect. 5.1.3). However, the correlations that are observed and that contaminate cosmic shear measurements are those of the visible baryonic matter. Thus the relation between correlations of dark matter and those of the baryons residing in the galaxies is of paramount importance, but calculations and simulations are far from reaching the necessary precision, postponing the advent of accurate models into the more distant future. In addition, this missing link between dark and baryonic matter implies that intrinsic alignments are expected to depend on various galaxy properties such as their mass and luminosity, their environment, their merger history, and hence their type and colour.

5.1.2 Models of intrinsic alignments

The lack of precise intrinsic alignment models hampers the simple removal of the intrinsic alignment contamination from the cosmic shear signal as well as the straightforward deduction of properties of galaxies from intrinsic correlations. A coarse yet reliable model for intrinsic alignments would be helpful to assess the importance of the systematic error induced on cosmic shear constraints. Moreover, based on this model, one could acquire a robust parametrisation with nuisance parameters (or a region to sample with form filling functions, see Sect. 4.2.2) in order to marginalise over the intrinsic alignment effects in the course of parameter estimation.

Practically all attempts at constructing a physical prescription for intrinsic alignments are based on the linear alignment model originally suggested by Catelan et al. (2001). They assumed that the shape of the luminous part of a galaxy follows exactly the shape of its host halo, and that the ellipticity of the latter is determined by the local tidal gravitational field of the large-scale structure. We now write $\epsilon^{\mathrm{s}} = \gamma_{\mathrm{I}} + \epsilon_{\mathrm{rnd}}$, i.e. we split the intrinsic ellipticity of a galaxy into a correlated part, the intrinsic shear γ_{I}, and a purely random contribution ϵ_{rnd} which is neither correlated with the gravitational nor the intrinsic shear. Note that an intrinsic shear field γ_{I} is a hypothetical construct, but it could be uniquely defined if γ_{I} was indeed completely specified in terms of the tidal field of the large-scale structure.

The simplest possible form allowed by the assumptions made above is a linear relation between the intrinsic shear and the gravitational field, given by (Catelan et al. 2001)

$$\begin{aligned} \gamma_{\mathrm{I},1}(\boldsymbol{x}) &= -\frac{C_1'}{4\pi G}\left(\frac{\partial^2}{\partial x_1^2} - \frac{\partial^2}{\partial x_2^2}\right)\Phi_{\mathrm{p}}(\boldsymbol{x})\,; \\ \gamma_{\mathrm{I},2}(\boldsymbol{x}) &= -\frac{C_1'}{4\pi G}\,2\,\frac{\partial}{\partial x_1}\frac{\partial}{\partial x_2}\,\Phi_{\mathrm{p}}(\boldsymbol{x})\,, \end{aligned} \tag{5.2}$$

where we wrote the normalisation in the notation of Hirata & Seljak (2004) in which C_1' is an arbitrary constant. The partial derivatives are with respect to comoving coordinates, and $\Phi_{\mathrm{p}}(\boldsymbol{x}) \equiv \Phi(\boldsymbol{x}, z_{\mathrm{p}})$ denotes the so-called 'primordial' potential, i.e. the linear gravitational potential evaluated at the epoch of galaxy formation, at a redshift z_{p} well within the matter-dominated era. Hirata & Seljak (2004) used the relations (5.2) to derive the intrinsic alignment power spectra for the linear alignment model.

In a first step the primordial potential is related to the matter density contrast via the Poisson equation (2.28). This expression is then Fourier-transformed, yielding

$$\tilde{\Phi}(\boldsymbol{k}, z) = -\frac{3}{2}\,H_0^2\Omega_{\mathrm{m}}(1+z)\,k^{-2}\,\tilde{\delta}(\boldsymbol{k}, z) = -4\pi G\,\rho_{\mathrm{m}}(z)\,(1+z)^{-2}\,k^{-2}\,\tilde{\delta}(\boldsymbol{k}, z)\,, \tag{5.3}$$

where (2.17) was inserted to obtain the second equality. The growth factor introduced in Sect. 2.4 quantifies the dependence of the matter density contrast on redshift in the limit of

linear structure formation and is normalised to unity at $z = 0$. Therefore one can write

$$\tilde{\delta}_{\rm lin}(\boldsymbol{k}, z = 0) = \frac{\tilde{\delta}_{\rm lin}(\boldsymbol{k}, z)}{D(z)} = \frac{\tilde{\delta}_{\rm lin}(\boldsymbol{k}, z_{\rm p})}{D(z_{\rm p})} \,, \tag{5.4}$$

where we omitted the subscript of $D(z)$ for ease of notation. Restricting (5.3) to linear scales and employing (5.4), one obtains the ratio

$$\frac{\tilde{\Phi}(\boldsymbol{k}, z)}{\tilde{\Phi}(\boldsymbol{k}, z_{\rm p})} = \frac{(1+z)\,D(z)}{(1+z_{\rm p})\,D(z_{\rm p})} = K_D^{-1}\,(1+z)\,D(z) \,. \tag{5.5}$$

In the last step we made use of the fact that $z_{\rm p}$ lies in the matter-dominated era during which $D(z) \propto 1/(1+z)$, where the constant of proportionality K_D is independent of both z and $z_{\rm p}$ (see Dodelson 2004, or Sect. 2.4). Inserting (5.5) into (5.3), one arrives at the desired relation,

$$\tilde{\Phi}_{\rm p}(\boldsymbol{k}) = -K_D\,\frac{4\pi G\,\rho_{\rm m}(z)}{D(z)\,(1+z)^3}\,k^{-2}\,\tilde{\delta}_{\rm lin}(\boldsymbol{k}, z) \,. \tag{5.6}$$

This expression differs from the result given in Hirata & Seljak (2004), eq. (14), by an additional factor $(1+z)^{-2}$ in (5.6). This discrepancy was also found in other re-derivations (R. Bean, S. Bridle, D. Kirk, I. Laszlo; private communication), leaving it an open issue which of the formulae is the correct one (C. Hirata, private communication). In addition we have obtained an additional constant K_D in (5.6) which stems from the normalisation of the growth factor. Since the intrinsic shear has an arbitrary normalisation C_1' in (5.2), this term is irrelevant and absorbed by defining $C_1 \equiv C_1'\,K_D$.

The remainder of this work relies on eq. (14) in Hirata & Seljak (2004), i.e. uses (5.6) with only a factor $(1+z)$ in the denominator. In Chaps. 6 and 8 the linear alignment model will either be used as an exemplary contamination of the cosmic shear signal or as the fiducial model in a very general parametrisation, so that a modification of the model will only marginally affect the results presented in these chapters. The signal-to-noise achieved with the method presented in Chap. 7 depends on the amplitude of the intrinsic alignment correlations which we do not expect to change dramatically with the different redshift evolutions found above and by Hirata & Seljak (2004) though. In contrast, the analysis presented below is strongly dependent on the actual form of the intrinsic alignment signals, and a change in the $(1+z)$-terms in (5.6) would clearly alter the inference made on the redshift dependence of intrinsic alignments, see Sect. 5.5.3.

Equation (5.2) defines a spin-2 intrinsic shear field $\gamma_{\rm I} = \gamma_{\rm I,\,1} + {\rm i}\gamma_{\rm I,\,2}$ which gives the expectation value of the ellipticity of a galaxy in the absence of gravitational lensing. If the intrinsic shear field is given by (5.2) or a related prescription, then the average intrinsic shear signal for a population i of galaxies is given by (Hirata & Seljak 2004)

$$\bar{\gamma}_{\rm I}^{(i)}(\boldsymbol{\theta}) = \int_0^{\chi_{\rm hor}} {\rm d}\chi\; p^{(i)}(\chi)\;\gamma_{\rm I}\left(f_{\rm k}(\chi)\boldsymbol{\theta}, \chi\right) \,, \tag{5.7}$$

where $p^{(i)}(\chi)$ denotes as before the probability distribution of comoving distances for galaxy sample i. Analogously to the lensing case, one can then define a convergence of the intrinsic shear field $\kappa_{\rm I}^{(i)}(\boldsymbol{\theta})$, which is directly related to the intrinsic shear via $\tilde{\kappa}_{\rm I}(\boldsymbol{\ell}) = \tilde{\bar{\gamma}}_{\rm I}(\boldsymbol{\ell})\;{\rm e}^{-2{\rm i}\beta}$, see (3.14). This intrinsic convergence can be written as the projection of a three-dimensional intrinsic convergence $\delta_{\rm I}$, which can be understood as the analogue of the matter density contrast for the intrinsic shear field,

$$\kappa_{\rm I}^{(i)}(\boldsymbol{\theta}) = \int_0^{\chi_{\rm hor}} {\rm d}\chi\; p^{(i)}(\chi)\;\delta_{\rm I}\left(f_{\rm k}(\chi)\boldsymbol{\theta}, \chi\right) \,. \tag{5.8}$$

Alternatively, we could have directly obtained δ_I from the three-dimensional intrinsic shear field via $\tilde{\delta}_\mathrm{I}(\boldsymbol{k}) = \tilde{\gamma}_\mathrm{I}(\boldsymbol{k})\ \mathrm{e}^{-2\mathrm{i}\varphi_{k_\perp}}$, where $\varphi_{k_\perp}$ is the azimuthal angle of the wave vector $\boldsymbol{k}$ (e.g. Schneider & Bridle 2010), and where the Fourier transform has only been applied to the two dimensions perpendicular to the line of sight.

Here we have assumed that the intrinsic shear field is – like the gravitational shear field – curl-free to good approximation, as holds for instance for the linear alignment model. One can now define intrinsic alignment power spectra in terms of the quantities constructed above as

$$\left\langle \tilde{\delta}_\mathrm{I}(\boldsymbol{k},\chi)\ \tilde{\delta}_\mathrm{I}^*(\boldsymbol{k'},\chi) \right\rangle = (2\pi)^3\ \delta_\mathrm{D}^{(3)}(\boldsymbol{k}-\boldsymbol{k'})\ P_\mathrm{II}(k,\chi)\ ; \tag{5.9}$$

$$\left\langle \tilde{\delta}(\boldsymbol{k},\chi)\ \tilde{\delta}_\mathrm{I}^*(\boldsymbol{k'},\chi) \right\rangle = (2\pi)^3\ \delta_\mathrm{D}^{(3)}(\boldsymbol{k}-\boldsymbol{k'})\ P_{\delta\mathrm{I}}(k,\chi)\ . \tag{5.10}$$

In analogy to (5.9) a B-mode intrinsic shear power spectrum can be defined as well (Schneider & Bridle 2010). Note that the cross-power spectra between intrinsic shear E- and B-mode and between matter and intrinsic shear B-mode should vanish if one demands parity invariance of the intrinsic shear field (see Schneider 2003).

Hirata & Seljak (2004) inserted their eq. (14) into (5.2) and then computed the three-dimensional intrinsic shear power spectrum, resulting in

$$P_\mathrm{II}\,(k,z) = C_1^2\ \rho_\mathrm{cr}^2\ \frac{\Omega_\mathrm{m}^2\ (1+z)^4}{D^2(z)}\ P_\delta\,(k,z)\ , \tag{5.11}$$

where (5.6) demands that the linear matter power spectrum is to be employed, but note that we will use the full power spectrum instead (see also Bridle & King 2007). If (5.6) were used instead, the term $(1+z)^4$ in (5.11) would be absent. Similarly, the power spectrum of the cross-correlation between the tangential component of the intrinsic shear and the matter density contrast reads

$$P_{\delta\mathrm{I}}\,(k,z) = -C_1\ \rho_\mathrm{cr}\ \frac{\Omega_\mathrm{m}\ (1+z)^2}{D(z)}\ P_\delta\,(k,z)\ . \tag{5.12}$$

Note that Hirata & Seljak (2004) consider in addition source clustering effects whose contributions were not included in (5.11) and (5.12). If source clustering is neglected, the linear alignment model does not produce any B-mode signals because a tidal quadrupole field as defined via (5.2) is purely E-mode, and the intrinsic shear is assumed to be linearly related to this pattern.

The normalisation of the power spectra is in principle arbitrary, as it is determined by the unknown strength of the response of the intrinsic shear γ_I to the tidal field. In practice C_1 was fixed by comparison with observations. For this purpose Hirata & Seljak (2004) used the ellipticity dispersion at a pair separation of $\theta \approx 1.5\,\mathrm{deg}$ from SuperCOSMOS data, assuming that this dispersion is dominated by intrinsic ellipticity correlations. Their result can be expressed as $C_1\,\rho_\mathrm{cr} \approx 0.0134$ (Bridle & King 2007). As mentioned before, the intrinsic alignment signal is expected to depend on the properties of the galaxy sample under consideration, and thus it is likely that the value of C_1 features additional redshift, galaxy type, or luminosity dependencies, even if the linear alignment model correctly accounted for the underlying processes. We will extend the model (5.12) accordingly in Sect. 5.5.3.

The linear alignment model may provide a realistic description of the intrinsic alignment of elliptical galaxies on large scales for which tidal stretching by the large-scale gravitational field is probably the dominant mechanism that determined galaxy shapes. For all other cases, in particular small scales, the model is simplistic in the assumptions that the linear density contrast can be used, that the galaxy shape is homologous with the shape of the host halo, and

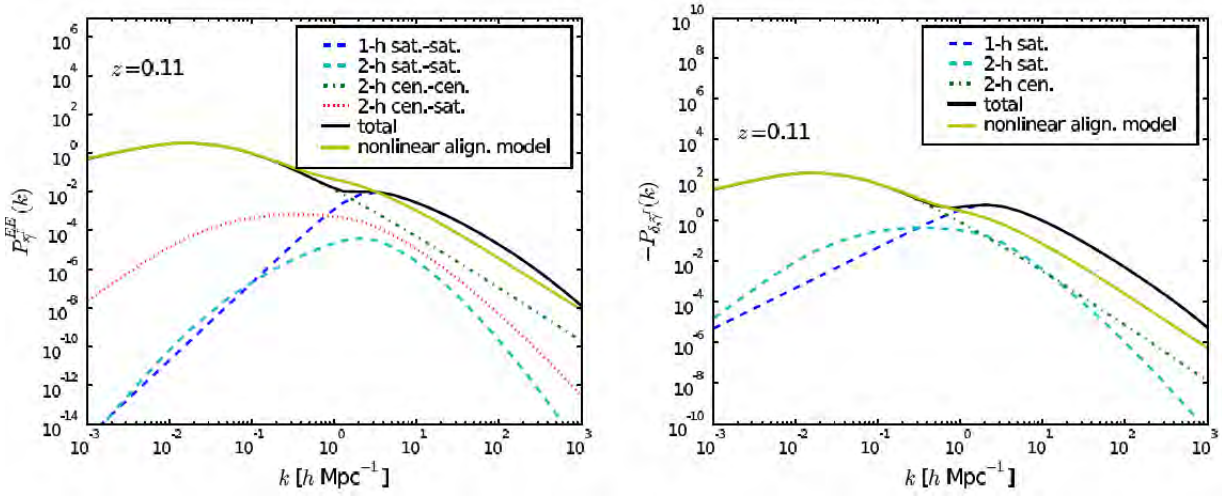

Figure 5.3: Contributions to the intrinsic alignment halo model power spectra. *Left panel*: E-mode intrinsic ellipticity (II) power spectrum at $z = 0.11$. The 1-halo satellite-satellite term is shown as dark blue dashed line, the 2-halo satellite-satellite term as light blue dashed line, the 2-halo central-central term as green dotted line, and the 2-halo central-satellite term as red dotted line (for details see Schneider & Bridle 2010). The black solid curve represents the total halo model power spectrum. For reference the non-linear version of the linear alignment model is plotted as olive curve. *Right panel*: Gravitational shear-intrinsic ellipticity (GI) power spectrum at $z = 0.11$. The coding of the curves is the same as above, but note that there is no satellite-central cross-term in this case (from Schneider & Bridle 2010).

that the intrinsic shear depends linearly on the tidal gravitational field. Bridle & King (2007) suggested an ad-hoc extension to smaller scales by using the full matter power spectrum in (5.11) and (5.12) instead of the linear one, a modification which lacks physical justification but provides reasonable fits to current data (see Fig. 5.6 below). By default we are going to employ this non-linear version of the linear alignment model (NLA model henceforth).

Recent progress in the modelling of linear alignments was presented by Schneider & Bridle (2010) who used a halo model approach to improve the linear alignment model on small scales. Their calculations are based on the still very simplistic assumptions that the galaxy at the centre of a halo has an intrinsic ellipticity according to the intrinsic alignment model, whereas the satellite galaxies are represented by sticks pointing towards the centre of the halo. As can be seen in Fig. 5.3, the resulting intrinsic alignment power spectra are dominated on large scales by correlations between central galaxies in different haloes, reproducing just the linear alignment power spectrum as given in Hirata & Seljak (2004). On small scales the correlations between satellite galaxies within the same halo provide the strongest contribution. Since both the change in amplitude due to the satellite term and the scale at which it becomes important roughly agree with the non-linear modification of the linear alignment model, we consider the latter as sufficiently accurate.

While the knowledge about the form of the three-dimensional power spectra (5.11) and (5.12) underlying the intrinsic alignment signal is poor, the projection of these power spectra along the line of sight, and hence the redshift dependence of the resulting two-point II and GI contributions, is well understood, as will be demonstrated in the following. Just like in the case

of the cosmic shear signal, the projected intrinsic alignment power spectra can be defined via

$$\left\langle \tilde{\kappa}_{\mathrm{I}}^{(i)}(\boldsymbol{\ell})\ \tilde{\kappa}_{\mathrm{I}}^{(j)\,*}(\boldsymbol{\ell'})\right\rangle = (2\pi)^2\ \delta_{\mathrm{D}}^{(2)}(\boldsymbol{\ell}-\boldsymbol{\ell'})\ C_{\mathrm{II}}^{(ij)}(\ell)\ ; \tag{5.13}$$

$$\left\langle \tilde{\kappa}^{(i)}(\boldsymbol{\ell})\ \tilde{\kappa}_{\mathrm{I}}^{(j)\,*}(\boldsymbol{\ell'}) + \tilde{\kappa}_{\mathrm{I}}^{(i)}(\boldsymbol{\ell})\ \tilde{\kappa}^{(j)\,*}(\boldsymbol{\ell'})\right\rangle = (2\pi)^2\ \delta_{\mathrm{D}}^{(2)}(\boldsymbol{\ell}-\boldsymbol{\ell'})\ C_{\mathrm{GI}}^{(ij)}(\ell)\ . \tag{5.14}$$

Note that, contrary to the remainder of this thesis, we denote projected power spectra by C in order to avoid confusion with the various three-dimensional power spectra used here and in the following. Moreover we have symmetrised the GI signal, taking into account that the intrinsic contribution might stem from both the galaxy samples i and j. Repeating the derivation outlined in Sect. 3.3, where (5.8) plays the role of (3.24) for the intrinsic shear field, one arrives at the following Limber equations,

$$C_{\mathrm{II}}^{(ij)}(\ell) = \int_0^{\chi_{\mathrm{hor}}} \mathrm{d}\chi\ \frac{p^{(i)}(\chi)\ p^{(j)}(\chi)}{f_{\mathrm{k}}^2(\chi)}\ P_{\mathrm{II}}\left(\frac{\ell}{f_{\mathrm{k}}(\chi)},\chi\right)\ ; \tag{5.15}$$

$$C_{\mathrm{GI}}^{(ij)}(\ell) = \frac{3H_0^2\Omega_{\mathrm{m}}}{2c^2}\int_0^{\chi_{\mathrm{hor}}} \mathrm{d}\chi\ \frac{p^{(i)}(\chi)\ g^{(j)}(\chi)+g^{(i)}(\chi)\ p^{(j)}(\chi)}{a(\chi)\ f_{\mathrm{k}}(\chi)}\ P_{\delta\mathrm{I}}\left(\frac{\ell}{f_{\mathrm{k}}(\chi)},\chi\right)\ . \tag{5.16}$$

Note that a unified formalism for the derivation of the cosmic shear, intrinsic alignment, and further signals will be provided in Chap. 8. For examples of the projected intrinsic alignment power spectra as calculated from the non-linear version of the intrinsic alignment model we refer the reader to Figs. 5.6, 6.12, and 8.3. Real-space statistics for the II and GI signals can be obtained in exact analogy to the lensing case.

5.1.3 Evidence for intrinsic alignments

Both simulations and observations indicate that correlations due to the intrinsic alignment of galaxies are indeed non-zero and suggest that they are likely to constitute the major astrophysical source of systematic errors for cosmic shear surveys. For instance, Bridle & King (2007) find that intrinsic alignments lead to a biased estimation of the dark energy equation of state parameter w_0 by up to 50 % (relative to a fiducial value of $w_0 = -1$) for a Euclid-like survey, using the NLA model with SuperCOSMOS normalisation.

As a consequence, various publications have dealt with this possible contaminant of cosmic shear. The alignment of dark matter haloes, resulting from external tidal forces, has been subject to extensive study, both analytic and numerical (Croft & Metzler 2000; Heavens et al. 2000; Lee & Pen 2000; Catelan et al. 2001; Crittenden et al. 2001; Jing 2002; Mackey et al. 2002; Hirata & Seljak 2004; Bridle & Abdalla 2007; Hahn et al. 2007). The galaxies in turn are assumed to align with the angular momentum vector (in the case of spiral galaxies) or the shape (in the case of elliptical galaxies) of their host halo, which is suggested by the observed correlations of galaxy spins (e.g. Pen et al. 2000) and galaxy ellipticities (e.g. Brainerd et al. 2009). However, this alignment is not perfect – see for instance van den Bosch et al. (2002), Okumura et al. (2009), and Okumura & Jing (2009). Schäfer (2009) provides a review on the current knowledge about galaxy spin correlations. Recently, hydrodynamic simulations have reached the volume and the accuracy to yield first predictions on the alignment of galaxy disks within their immediate dark matter environment and the local filamentary structure (Bett et al. 2010; Hahn et al. 2010).

While the results of theoretical approaches vary significantly in their details, they all agree insofar as they predict intrinsic ellipticity (II) correlations of $1-10$ % of the lensing signal for non-tomographic surveys with a median redshift around unity, whereas the effect may even dominate the cosmic shear signal for shallow surveys. This behaviour is expected because a

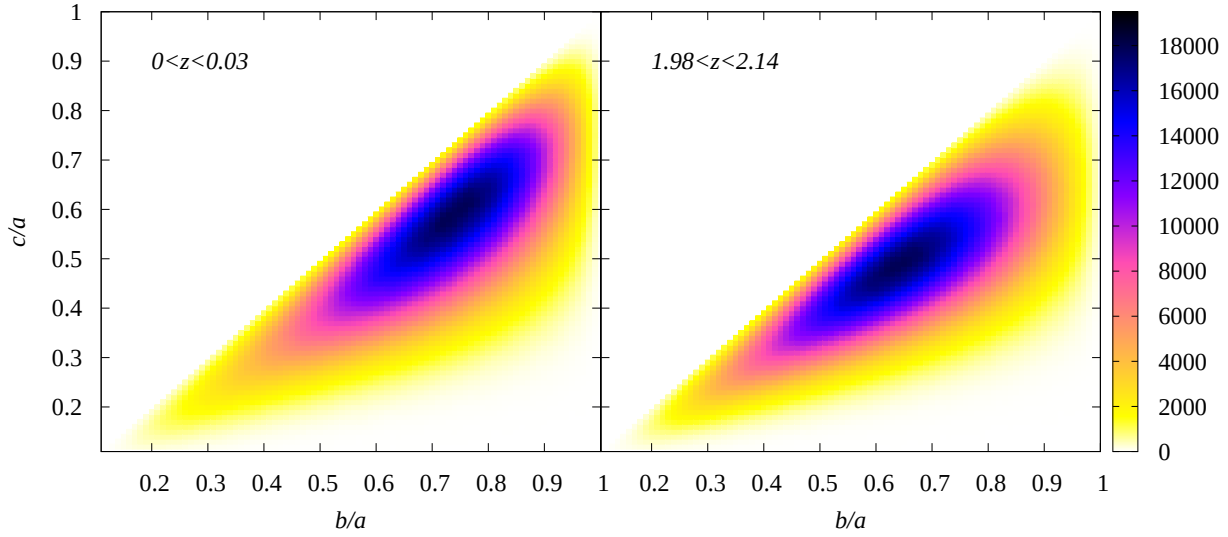

Figure 5.4: Distribution of the principal axes of dark matter haloes in the Millennium intrinsic alignment catalogue. Shown is the distribution of haloes as a function of the axis ratios b/a and c/a, where the ordering of the principal axes is $c \leq b \leq a$. The number of haloes in each bin is colour-coded as given on the right-hand side. The left panel depicts the distribution for haloes with redshifts less than 0.03 while the right panel shows the distribution of haloes at redshifts in the range $1.98 < z < 2.14$. Note that in these plots haloes in the upper right corner are spherical, haloes along the main diagonal are prolate, and haloes located towards the right margin are oblate.

high median redshift corresponds to a broad redshift distribution of galaxies, which decreases the probability of finding two galaxies at similar redshifts. Likewise, the contamination by an II signal is expected to be strong for auto-correlations in a survey that has been divided into narrow redshift bins.

N-body simulations yield an upper limit of about 10 % for shear-intrinsic ellipticity (GI) correlations (Heymans et al. 2006b), in agreement with the analytical prediction of the linear alignment model in combination with SuperCOSMOS observations (Hirata & Seljak 2004). Such a contamination causes an underestimation (due to the anti-correlation of shear and intrinsic ellipticity) of σ_8 of about 5 % and a bias on the parameters of the dark energy equation of state by up to 50 % from a fiducial value of -1 if acting together with II correlations (Bridle & King 2007). Based on the simulations and intrinsic alignment modelling by Heymans et al. (2006b), Semboloni et al. (2008) predict that cosmic shear three-point statistics are affected even stronger by intrinsic alignments, finding a 15 % contamination for medium-deep surveys, and that the III correlation could be an order of magnitude larger than the shear signal in shallow lensing data.

It should be noted that the direct simulation of intrinsic alignment effects is still at a very crude level, using dark matter-only simulations which are subsequently populated via ad-hoc descriptions of how to place galaxies into dark matter haloes. Heymans et al. (2006b) chose elliptical galaxies to have the same ellipticity as their host haloes, while the disks of spiral galaxies were positioned such that their angular momenta are aligned with the angular momentum of the halo. In the latter case a random misalignment of the angular momentum vectors was allowed which is described by a Gaussian probability distribution with a dispersion of 20 deg (van den Bosch et al. 2002). With these prescriptions Heymans et al. (2006b) found negligible intrinsic alignments for spiral galaxies, translating into an expected low intrinsic alignment signal for late-type galaxies, as is indeed found observationally (see below).

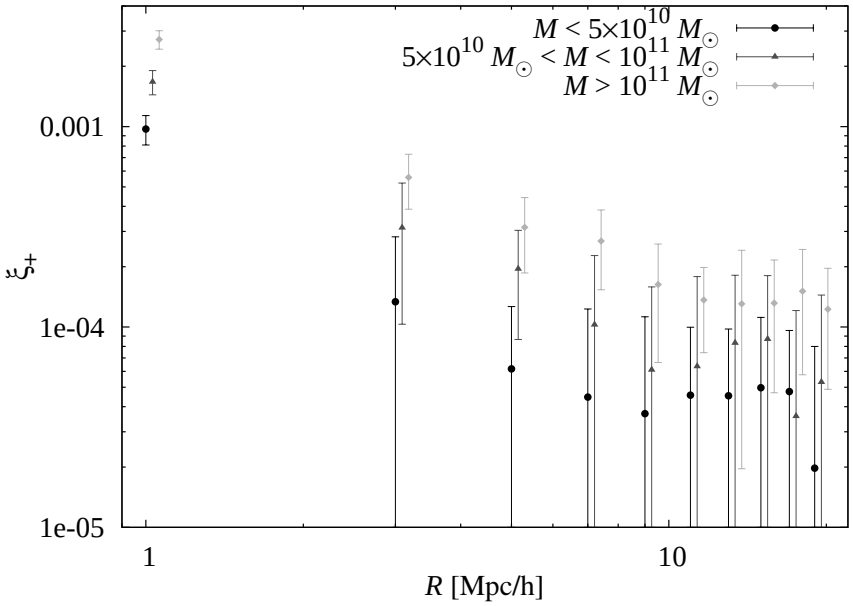

Figure 5.5: Correlation function ξ_+ of projected halo intrinsic ellipticities as a function of comoving transverse separation R. This signal corresponds to II correlations if all galaxies have the same ellipticities as their host haloes. Results are shown for three different bins in halo mass, with cuts at $5 \times 10^{10} M_\odot$ and $10^{11} M_\odot$. Error bars are $1\,\sigma$. (Correlation functions courtesy of E. Semboloni.)

To improve on the precision of intrinsic alignment simulations, a new study with the Millennium simulation (Springel et al. 2005) is underway (Semboloni et al., in prep.), which is going to update foregoing studies in several ways. First, the superior size of the Millennium simulation will yield unprecedented statistical constraints, enabling e.g. to split the data into various subsets. Moreover we use semi-analytic models (Bower et al. 2006) to populate the haloes with galaxies, adding galaxy properties such as luminosities that the intrinsic alignment signal might also depend on to the intrinsic shear catalogue. The intrinsic alignment modelling is updated, e.g. concerning the misalignment angles of spiral angular momentum vectors. Besides, the effect of satellite galaxies can be included, although only their positions and no shape or angular momentum information are available, so that strong assumptions have still to be made about their alignment properties.

Presumably the most important improvement is the reduction of the particle mass by about a factor of 20 compared to the simulations of Heymans et al. (2006b). For a given dark matter halo the mass resolution thus increases, allowing for more precise measurements of the halo shape and its angular momentum, whose importance we will highlight in the following. In Fig. 5.4 we have plotted the distribution of halo shapes for all objects in the Millennium catalogue that have shape information (for details concerning the selection of these haloes and the computation of shapes see Bett et al. 2010), in terms of the ratios of the principal axes a, b, and c. We have chosen the ordering $c \leq b \leq a$, so that $c = b = a$ corresponds to a spherical halo, $c \approx b < a$ to a prolate halo, and $c < b \approx a$ to an oblate halo. It is evident from the figure that in general dark matter haloes are preferentially prolate, and that the deviation from sphericity is significantly larger at higher redshift.

This evolution of halo shape with redshift can be ascribed to a high merger rate of dark matter haloes at $z \sim 2$. A subhalo that has recently been accreted creates an elongation of the host halo along the direction of the infall, leading to a prolate halo. Since the preferred direction of infalling subhaloes is closely related to the large-scale filamentary structure, one expects also stronger correlations among the haloes due to this effect. At low redshift the large number of mergers in the past has led to a thermalisation of the halo, so that its shape should be more spherical on average. However, one also has to take into account a measurement bias with a very similar mechanism. As soon as the friends-of-friends algorithm, which is used to identify bound halo structures, assigns an infalling 'particle', i.e. a subhalo, to the host halo, the asphericity of this halo largely increases. We expect this systematic effect to be the more

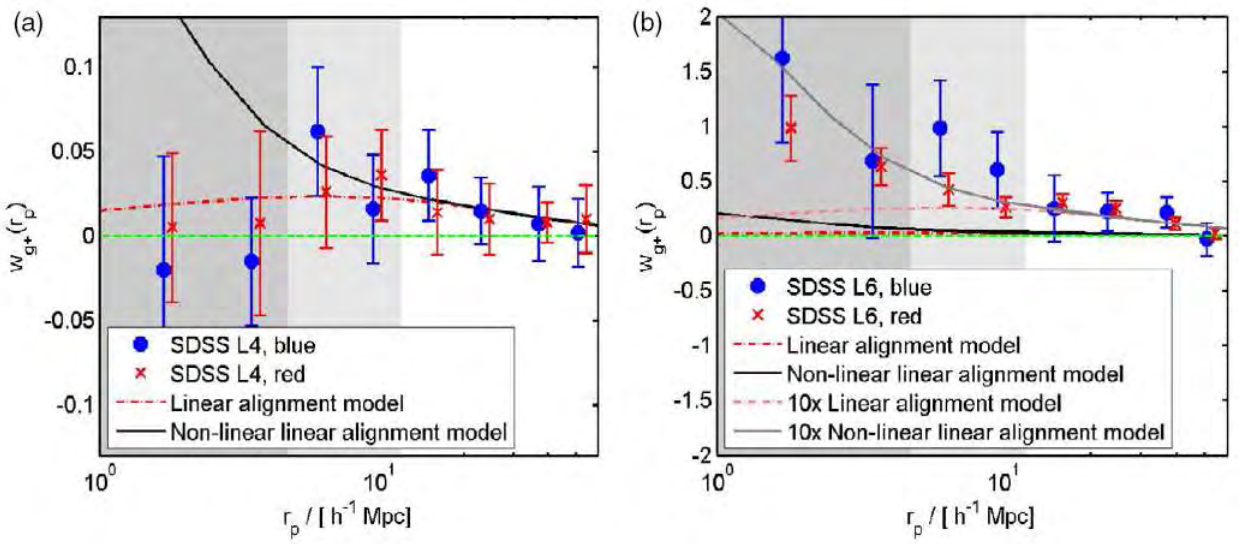

Figure 5.6: GI correlations in the SDSS spectroscopic sample (for the precise definition of the correlation function $w_{\mathrm{g+}}$ see Sect. 5.3) as a function of comoving transverse separation r_{p} (R in our notation). *Left panel*: For galaxies with absolute r-band magnitudes $-21 \leq M_r \leq -20$, centred on L^*. The GI signal for blue galaxies is shown as blue circles, the one for red galaxies as red crosses. For reference, a signal calculated from the linear alignment model is plotted as red dashed line while the black solid curve results from using the non-linear version of the linear alignment model. The grey areas indicate regions excluded from the model fits in Hirata et al. (2007). *Right panel*: Same as above, but for the brightest galaxies in the sample with absolute magnitudes $-23 \leq M_r \leq -22$. The additional light-coloured curves correspond to 10 times the linear alignment model signals with SuperCOSMOS normalisation, indicating the strong signal for bright red galaxies (from Bridle & King 2007).

important the lower the mass resolution of the simulation.

Furthermore high resolution allows us to measure intrinsic alignments for less massive haloes than foregoing work. Using again all haloes with shape information and assuming that all these haloes are populated by elliptical galaxies which are homologous with their host halo, we obtain the correlations shown in Fig. 5.5, plotted as a function of the comoving transverse separation R of the haloes. Split into three mass bins, we see a trend of increased correlations with higher halo mass which becomes more evident at small scales, mostly due to smaller statistical errors. This tendency is in agreement with the observation that the intrinsic alignment signal becomes stronger for more luminous and redder galaxies (see below), where both the brighter and the more early-type galaxies are the more massive ones. Note that the full range of redshifts between $z = 0$ and $z \approx 2$ was used to calculate these correlation functions.

A low-resolution simulation is only capable of measuring intrinsic alignments for the most massive haloes and is prone to over-estimating the asphericity and shape correlations for haloes that contain a small number of simulation particles. Both effects artificially boost the intrinsic alignment signal, leading us to the hypothesis that Heymans et al. (2006b) and Semboloni et al. (2008) possibly may have over-predicted the amplitude of the intrinsic alignment terms. Whether this can be verified, or even quantified in more detail, by means of the Millennium simulation data is currently under investigation.

Observationally, it is challenging to shed light on the nature of intrinsic alignments since usually the cosmic shear signal clearly dominates the ellipticity correlations, hence rendering it impossible to directly study the II and GI signals by those galaxy samples which are rele-

vant for cosmic shear (see Chap. 7 though). Intrinsic ellipticity correlations have either been analysed in shallow data in which the measured ellipticity correlation cannot originate from a gravitational shear signal, or by exploiting that the II signal is restricted to physically close pairs of galaxies. Cross-correlations between the galaxy number density distribution and ellipticities have been used to infer the GI contribution, assuming that galaxies trace the underlying matter distribution in a simple form, an approach which we will also apply in this chapter.

Brown et al. (2002) tentatively detected intrinsic ellipticity correlations in the shallow SuperCOSMOS field. Heymans et al. (2004) analysed the COMBO-17, RCS and VIRMOS-DESCART surveys by comparing signals from close and distant pairs of galaxies separately, finding a relatively weak effect due to an II contribution, modifying their estimate for σ_8 by less than a third of the statistical errors. Mandelbaum et al. (2006) did not find intrinsic ellipticity correlations in a sample of galaxies from the Sloan Digital Sky Survey (SDSS) with spectroscopic redshifts, whereas Brainerd et al. (2009) report a clear II signal in photometric redshift data from the same survey. A null detection also resulted from the combination of blue galaxy samples from SDSS and the WiggleZ Survey, where the latter is at a higher redshift of $z \sim 0.5$ (Mandelbaum et al. 2009).

Mandelbaum et al. (2006) reported the first observational verification of shear-ellipticity correlations in SDSS and estimated an upper limit of 20 % contamination for cosmic shear surveys, while Hirata et al. (2007) found a best-fit intrinsic alignment model with data from SDSS and the 2SLAQ survey, which predicts 6.5 % contamination to the cosmic shear signal. The latter study also suggested an increase in the intrinsic alignment amplitude with the luminosity of the sample, as well as a dependence on the galaxy type, finding no significant signal for blue galaxies; see Fig. 5.6 for a synopsis of these results. This was confirmed by Mandelbaum et al. (2009) who did not detect a GI signal in the WiggleZ Survey which is dominated by late-type galaxies.

A small amplitude of the intrinsic alignment signal for blue, rather faint galaxies alleviates the threat for the integrity of cosmic shear studies because this type of galaxies dominates cosmic shear catalogues. Nonetheless a small number of red galaxies that display strong intrinsic alignments could jeopardise unbiased cosmological parameter estimates, so that their signal needs to be well understood. Below we will present a novel analysis of shear-intrinsic ellipticity correlations among luminous red galaxies in several SDSS and the MegaZ LRG samples, providing a study for early-type galaxies that is complementary to Mandelbaum et al. (2009).

5.1.4 Control of intrinsic alignment contamination

As was demonstrated in the foregoing sections, the intrinsic alignment of galaxies is very likely to constitute a serious contaminant of cosmic shear surveys if left untreated. Since our knowledge about the underlying processes of galaxy formation and evolution is limited, detailed modelling of the intrinsic alignment power spectra (5.9) and (5.10) is to date beyond question. However, the projection of these power spectra along the line of sight, as given by (5.15) and (5.16), can be computed from first principles. Thus, provided that the redshift probability distributions $p^{(i)}(z)$ of the bins i in a tomographic cosmic shear survey are sufficiently narrow that the redshift evolution of the three-dimensional intrinsic alignment power spectra within them is negligible, the redshift dependence of the projected II and GI signals is known to high accuracy.

In Fig. 5.7 we have illustrated the scaling of the II, GI, and cosmic shear (GG) signals with redshift. We used a Euclid-like redshift distribution of the form (4.47) with $z_{\mathrm{med}} \approx 0.9$. The distribution was cut into 20 bins such that each one contains the same number of galaxies, adding a Gaussian scatter with dispersion $0.05(1+z)$ to simulate photometric redshift uncertainty. Then tomography convergence power spectra were computed for a flat ΛCDM

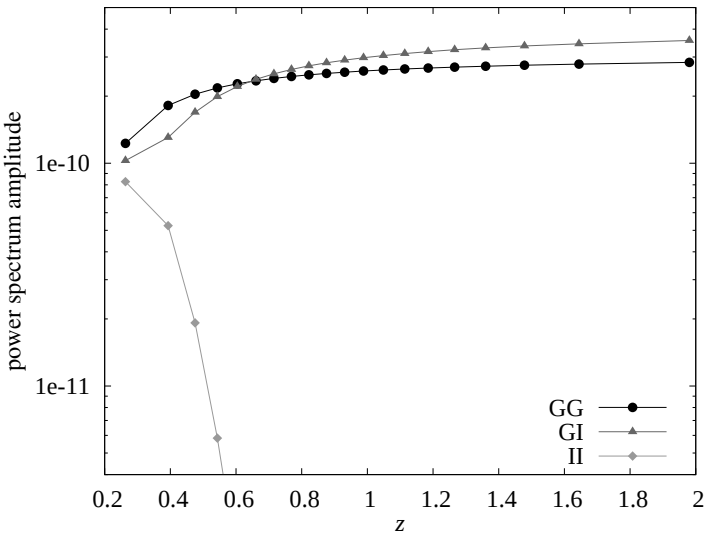

Figure 5.7: Redshift dependence of the GG, GI, and II signals. Shown is the amplitude of the power spectra $P^{(i=1,j)}(\ell)$ at $\ell \approx 200$ as a function of the median redshift of galaxy sample j. The power spectra were computed for a ΛCDM cosmology and a Euclid-like redshift distribution divided into 20 bins containing an equal number of galaxies, and using a photometric redshift dispersion of $0.05(1+z)$. The GI and II terms were obtained from the non-linear version of the intrinsic alignment model. The GG signal is shown as black circles, the GI signal as dark grey triangles, and the II signal as light grey diamonds.

cosmology with $\Omega_\mathrm{m} = 0.25$, $\sigma_8 = 0.8$, $h = 0.7$, and $n_\mathrm{s} = 1$, using the transfer function by Eisenstein & Hu (1998) with $\Omega_\mathrm{b} = 0.05$ and non-linear corrections via Smith et al. (2003). The II and GI terms were obtained from the non-linear version of the intrinsic alignment model, see (5.11) and (5.12), assuming the SuperCOSMOS normalisation, i.e. $C_1\,\rho_\mathrm{cr} \approx 0.0134$. We have plotted the power spectrum amplitude at a fixed angular frequency of $\ell \approx 200$ as a function of the median redshift of the redshift distribution in each bin, correlating the first bin $i = 1$ with all background bins j.

Obviously, the II term has a distinctively different redshift dependence than the other two contributions, quickly dropping as the difference in redshift between the correlated redshift distribution increases. As is also evident from (5.15), the signal would decrease even stronger if the width and hence the overlap of the redshift distributions were smaller. This scaling with redshift is explained by the need for galaxies to be physically close in order to mutually align. As a consequence, intrinsic ellipticity correlations are relatively easy to remove from the cosmic shear signal if redshift information is available.

King & Schneider (2002) and Heymans & Heavens (2003) used different approaches to downweighting galaxy pairs that are close in redshift, making use of redshift information for individual galaxies but otherwise assuming non-tomographic cosmic shear data. The method by Heymans & Heavens (2003) removes the II contamination with a marginal loss of statistical power, but it partly relies on a priori information about intrinsic alignments. For an application of this technique to the COMBO-17 survey see Heymans et al. (2004). Fine tomographic slices in redshift were used by King & Schneider (2003) to project the II signal into a set of template functions. If the photometric redshift scatter is not significantly larger than the width of the photometric redshift bins a survey is divided into, the exclusion of redshift auto-correlations effectively removes II correlations with a moderate increase in error on cosmological parameters (Takada & White 2004). Besides, intrinsic ellipticity correlations can generate B-modes (Hirata & Seljak 2004; Heymans et al. 2006b), which could in principle be used for its identification if alternative sources of a curl-component could safely be excluded.

In contrast to the II term, cross-correlations between gravitational shear and intrinsic ellipticity produce a signal that displays a very similar redshift dependence compared to cosmic shear, as Fig. 5.7 suggests. This behaviour is caused by the lensing contribution to the GI term, see (5.16), so that the signal is not restricted to physically close objects, but increases for larger

separations of galaxies in redshift. The increase of the power spectrum amplitude with redshift is slightly more pronounced for the GI than for the GG signal. This can be understood by noting that gravitational lensing is most effective if the lens is positioned at half the distance to the source, see the dependence of (3.28) on distance. Hence, the lensing signal of the foreground bin i is effectively generated by the matter distribution at $z_i/2$ in cosmic shear, whereas the GI signal stems from correlations with the intrinsic shapes directly at z_i. Increasing the redshift z_j of the background bin thus implies a more pronounced increase for the GI term in the difference between the redshifts at which the galaxy shears are effectively correlated, leading to a stronger rise in signal amplitude according to (3.28).

The similarity in the redshift dependencies of the GI and GG signals complicates the control of the GI contamination without making strong assumptions about an underlying intrinsic alignment model. First ideas how to control the GI signal were already put forward in the initiating work of Hirata & Seljak (2004). King (2005) used again sets of template functions to fit the lensing and intrinsic alignment signals simultaneously, albeit with limited freedom in the template models and thus a significant model dependence. In a purely geometric approach Joachimi & Schneider (2008, 2009) presented a technique to remove the GI signal from cosmic shear data which relies exclusively on the characteristic dependence on redshift; see Chap. 6 for details. However, the robustness of this method entails a considerable loss of information on cosmology which is intolerable for future cosmic shear surveys. Although Heymans et al. (2006b) reported the detection of weak B-modes caused by shear-intrinsic ellipticity correlations in their simulations, it is questionable whether this effect is strong enough to be unambiguously measured and therefore apt to remove the GI contamination.

Bridle & King (2007) investigated the effect of both the GI and II terms on cosmological parameter constraints by binning the systematic signals in wavenumber and redshift with nuisance parameters at each node of the grid which are then marginalised over. Increasing freedom in the representation of the GI signal is achieved at the cost of a bigger number of nuisance parameters, which dilutes the cosmological information that can be extracted from the data down to a similar level found for the nulling technique.

Additional information on intrinsic alignments can in principle be obtained from the galaxy distribution, which comes for free from cosmic shear surveys. This further set of correlations is then used to self-calibrate systematic effects of weak lensing (e.g. Hu & Jain 2004; Bernstein 2009). Zhang (2008) applied the self-calibration technique to the GI contamination, deriving an approximate relation between the GI and the galaxy number density-intrinsic ellipticity correlations. Joachimi & Bridle (2009) combined the general self-calibration ansatz by Bernstein (2009) with the formalism of Bridle & King (2007) to construct a comprehensive self-calibration treatment of intrinsic alignments, see Chap. 8 for details about this technique. For a first benchmark test of this approach see the recent application of self-calibration to the 100 deg^2 Survey by Kirk et al. (2010).

5.2 The MegaZ LRG and spectroscopic SDSS samples

We now turn to the analysis of GI correlations in three SDSS galaxy samples, providing the most comprehensive study of intrinsic alignments among red galaxies to date. The MegaZ LRG sample (Collister et al. 2007) is based on SDSS five-band ($ugriz$) imaging data and used for the first time for intrinsic alignment studies. It contains more than a million luminous red galaxies at intermediate redshifts between 0.4 and 0.7, i.e. beyond the redshifts of the LRGs already targeted with the SDSS spectrograph ($z \lesssim 0.45$, Eisenstein et al. 2001). While the original catalogue was selected from the 4th SDSS data release, we use an updated version based on

Table 5.1: Overview of the galaxy samples analysed, including the sample name employed in the following, the number of galaxies $N_{\rm gal}$ used to measure the galaxy number density and the galaxy shapes, the mean redshift $\langle z \rangle$, and the mean luminosity $\langle L \rangle$ in terms of the fiducial luminosity L_0 corresponding to $M_r = -22\,{\rm mag}$.

sample	$N_{\rm gal}$ (density)	$N_{\rm gal}$ (shape)	$\langle z \rangle$	$\langle L \rangle / L_0$
MegaZ, all z	863813	427604	0.56	1.07
MegaZ, $z < 0.529$	434321	214660	0.50	0.83
MegaZ, $z > 0.529$	429492	212944	0.59	1.22
SDSS LRG, faint, $z < 0.27$	16701	7030	0.21	1.06
SDSS LRG, faint, $z > 0.27$	19397	9038	0.32	1.07
SDSS LRG, medium, $z < 0.27$	16701	6139	0.22	1.50
SDSS LRG, medium, $z > 0.27$	19397	6700	0.31	1.50
SDSS LRG, bright, $z < 0.27$	16701	3532	0.22	2.13
SDSS LRG, bright, $z > 0.27$	19397	3659	0.31	2.12
SDSS L4 red	280000	26872	0.10	0.25

data release 6 (Adelman-McCarthy et al. 2008).

The photometry in five bands is used to determine photometric redshifts for the MegaZ LRG sample. For a subset of the galaxies, spectroscopic redshift information is required for calibration and cross-checking, which is provided by the 2dF-SDSS LRG and Quasar Survey (2SLAQ, Cannon et al. 2006). Consequently, the selection criteria of MegaZ LRG have been designed to match those of 2SLAQ, using a series of magnitude and colour cuts (for details see Cannon et al. 2006; Collister et al. 2007). These criteria have an efficiency of 95 % in detecting LRGs in the redshift range $0.4 \leq z \leq 0.7$, the failures being almost entirely due to M-type stars. For details on the photometric redshift measurement see Sect. 5.4.1.

As shown in Table 5.1, we arrive at about 860000 galaxies with a mean redshift of 0.56 in the full MegaZ LRG sample which will be used to compute galaxy number densities and hence trace the matter density field. The total number of galaxies is less than that of the full MegaZ LRG catalogue by Collister et al. (2007) because a fraction of the area was discarded for which galaxy shapes could not be measured. As will be discussed in Sect. 5.4.2, accurate shape measurements could be obtained for about 50 % of these galaxies, used to trace the intrinsic shear field.

We also compute r-band luminosities taking into account dust extinction, the shift of the spectrum to the rest frame at $z = 0$ (k-correction), and the evolution of the spectral energy distribution (e-correction), following Wake et al. (2006). Luminosities are given in terms of a fiducial luminosity L_0, corresponding to a k+e-corrected absolute magnitude of $M_r = -22\,{\rm mag}$. Due to this procedure, the corrected luminosity acts as a tracer for the total stellar mass, and consequently also for the total mass, of the galaxy. Throughout, we do not use the actual magnitudes and luminosities from MegaZ LRG but from the 2SLAQ galaxies, which should be a good approximation due to the identical selection criteria.

In addition, with a cut at photometric redshift $z = 0.529$, we split the sample into two redshift bins, each containing roughly the same number of galaxies. We show the redshift and luminosity distributions of both MegaZ LRG subsamples in Fig. 5.8, where we only plot the histogram of about 5000 galaxies that have spectroscopic redshift information from 2SLAQ; see Chap. 5.4.1. As is evident from the figure, the redshift cut for the MegaZ LRG sample also segregates the galaxies in luminosity.

Besides MegaZ LRG we also consider the spectroscopic SDSS LRG sample (Eisenstein et al.

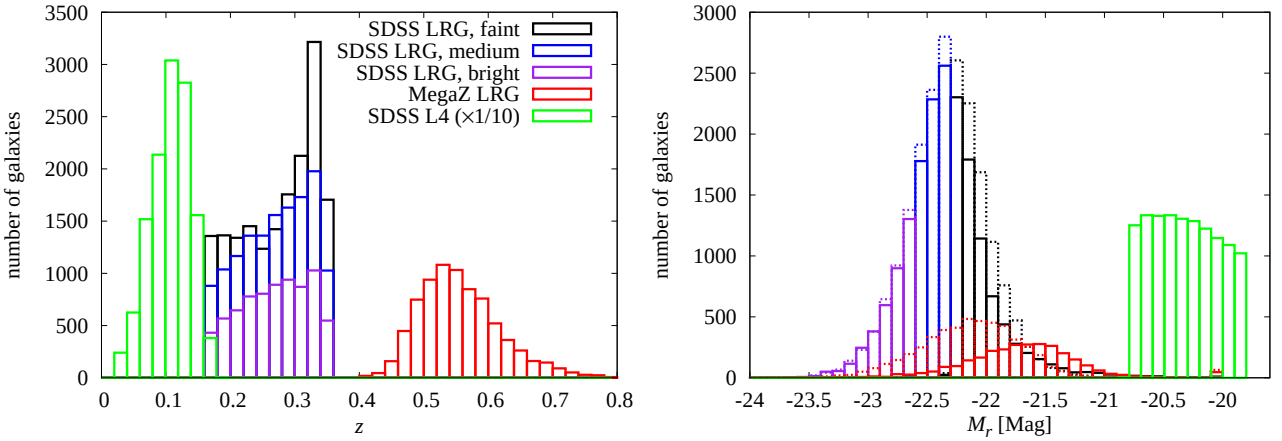

Figure 5.8: *Left panel*: Redshift distributions of the galaxy samples under consideration. Shown are the histograms for the SDSS LRG samples in black (faint, $M_r > -22.3$), blue (medium, $-22.6 < M_r < -22.3$), and purple (bright, $M_r < -22.6$), and for the galaxies in the MegaZ LRG sample with spectroscopic redshifts in red. Note that both SDSS and MegaZ samples are split into two redshift bins each, the SDSS samples at $z = 0.27$ and the MegaZ sample at $z = 0.529$. The histogram for the SDSS L4 sample of red galaxies is shown in green, downscaled by a factor of 10 for easier comparison. *Right panel*: Distribution of $k+e$-corrected absolute magnitudes M_r. The colour coding of the histograms is the same as in the left panel. Solid lines correspond to the low redshift bin, dotted lines to the high redshift bin for the two LRG samples.

2001) and the red L4 SDSS main sample (defined by Mandelbaum et al. 2006), adopting the data already used by Hirata et al. (2007). The SDSS LRG sample was derived from the 4th data release (Adelman-McCarthy et al. 2006), using a flux limit of $r < 19$ and colour cuts to isolate the LRGs. The sample we employ includes galaxies in the redshift range $0.16 < z < 0.35$ for which the sample is approximately volume-limited and contains in total about 36000 galaxies. Magnitudes are extinction- and $k+e$-corrected to $z = 0$ (Wake et al. 2006). The SDSS LRG sample is then divided into subsamples according to the criteria given in Hirata et al. (2007). First, two redshift bins are created by splitting the sample at $z = 0.27$. Each of the redshift bins is then further divided into three luminosity subsamples with cuts in absolute r-band magnitude at -22.3 and -22.6.

We also incorporate the SDSS main sample into our analysis, further extending the baseline in redshift and luminosity. The complete number of approximately 280000 galaxies in the main sample is used to trace the density field, whereas the galaxies with shape information are divided into four luminosity subsamples (Mandelbaum et al. 2006). These subsamples are called L3 to L6 and were originally defined by Seljak et al. (2005), each comprising one magnitude in M_r, where L6 contains the brightest galaxies. Hirata et al. (2007) introduced in addition a colour cut to separate early- and late-type galaxies. We use the largest subsample of red galaxies, L4, which contains nearly 27000 galaxies with shape information at a luminosity of about L^* at $z \sim 0.1$. This sample can also readily be combined with the LRG data, whilst the brighter subsamples L5 and L6 would partially overlap with the LRG samples. In the case of the L4 sample, magnitudes were corrected for extinction, and $k+e$-corrected by means of the software described in Blanton et al. (2003). Redshift and luminosity distributions for the SDSS LRG and main samples are also shown in Fig. 5.8.

Hirata et al. (2007) used an empirical colour cut at $u - r = 2.1 + 4.2\,z$ for observer-frame colours to separate the red and blue subsamples. For the total number of galaxies with

luminosities corresponding to L4 they determined a red galaxy fraction of 0.52 although one would expect early-type galaxies to be clearly subdominant. It is possible that the colour cut does not optimally separate the blue cloud and the red sequence in the galaxy colour-magnitude diagram, but allows for blue galaxies to leak into the regime of the red subsample (R. Mandelbaum, private communication). Assuming that blue galaxies carry a negligible intrinsic alignment signal (see Mandelbaum et al. 2009), this leakage could cause an underprediction of the gI correlations of the galaxies belonging to the red sequence within the L4 sample, as well as an underestimation of the mean luminosity of these red sequence galaxies. We note this as a caveat for the interpretation of constraints by the L4 sample, but defer a new calculation and analysis of the red L4 sample to future work.

To maximise the signal-to-noise of the observed correlations while still being able to measure the dependence of intrinsic alignments on luminosity, we follow the strategy of Hirata et al. (2007) by using all available galaxies for galaxy number density measurements, irrespective of their luminosity, for both the SDSS LRG and L4 samples. As a consequence, the samples used to trace the matter density and the intrinsic shear are different, especially concerning their size, see Table 5.1. The cross-correlations between number density and shape are then computed by finding pairs of one galaxy from the density sample and one from the shape sample, see Sect. 5.4.2. Since for both the SDSS LRG and main samples the galaxies used to compute number densities are not split into luminosity bins, it is also sufficient to determine only the global galaxy bias, and not a luminosity-dependent one.

Note that the MegaZ LRG, SDSS LRG, and the main red L4 sample each cover in excess of a thousand square degrees of effective survey area. In combination these samples cover the widest ranges of redshifts and luminosities to date on which one can study intrinsic alignments of early-type galaxies.

5.3 Modelling galaxy number density-shape correlations

While the methodology for spectroscopic samples is already well established (Mandelbaum et al. 2006; Hirata et al. 2007), we consider for the first time a galaxy sample which features only photometric redshift information, obtained from the MegaZ LRG catalogue. In this section we derive the models which are later compared to the observational data, beginning with the three-dimensional correlation functions of galaxy number density-ellipticity correlations, and then incorporating photometric redshift uncertainty. For reasons of optimum signal-to-noise and a simplified physical interpretation, the observations come in terms of line-of-sight projected correlation functions as a function of comoving transverse separation between galaxy pairs, and we transform the model accordingly.

5.3.1 Three-dimensional correlation functions

Cross-correlations between galaxy number densities and galaxy shapes at the same redshift are dominated by number density-intrinsic ellipticity correlations (gI henceforth; note that we follow the notation of Joachimi & Bridle 2009 in this chapter) if the redshift distributions of the samples considered are sufficiently compact such that gravitational lensing is negligible. Restricting the analysis to the linear and quasi-linear regime of structure evolution, one can assume that the galaxy distribution is linearly related to the underlying matter distribution, which allows one to infer the matter-intrinsic power spectrum $P_{\delta\mathrm{I}}$ and thus constrain GI models. Note that throughout we will work under the assumption of a spatially flat universe.

We define the three-dimensional correlation function between the galaxy number density

contrast δ_g and the tangential intrinsic shear $\gamma_{\mathrm{I},+}$ as

$$\xi_\mathrm{gI}(R,\Pi,z) \equiv \left\langle \delta_\mathrm{g}\left(0,\chi(z)-\frac{x_\parallel}{2},z\right)\ \gamma_{\mathrm{I},+}\left(\boldsymbol{x}_\perp,\chi(z)+\frac{x_\parallel}{2},z\right)\right\rangle\ , \tag{5.17}$$

for a given mean redshift z of the galaxy pairs correlated. Here we introduced a three-dimensional comoving separation vector $\boldsymbol{x}$ which has a line-of-sight component $\Pi \equiv x_\parallel$. Its transverse components are denoted by $\boldsymbol{x}_\perp$, with modulus $R \equiv |\boldsymbol{x}_\perp|$. The first argument of both δ_g and $\gamma_{\mathrm{I},+}$ denotes the position on the sky, the second the position along the line of sight, and the third quantifies the epoch, given in terms of the redshift. Note that a line-of-sight separation $\Pi \neq 0$ implies that δ_g and $\gamma_{\mathrm{I},+}$ are not measured at precisely the same epoch, contrary to what we have written in (5.17). However, as Π is small compared to the comoving distance $\chi(z)$ to the galaxies under consideration, this approximation holds to good accuracy.

Following Hirata & Seljak (2004), the radial component of the intrinsic shear is measured with respect to $\boldsymbol{x}_\perp$, and without loss of generality we can choose the coordinate system such that $\gamma_{\mathrm{I},+} = \gamma_{\mathrm{I},1}$. Note that usually, and also in the remainder of this work, γ_+ is defined as the tangential component of the shear. Measuring radial instead of tangential alignment implies a change of sign, so that e.g. the galaxy-galaxy lensing signal which we calculate below is negative. Denoting again Fourier variables by a tilde, one can write the relation between convergence and 1-component of the shear as

$$\tilde{\gamma}_\mathrm{I}(\boldsymbol{k}) = \ \mathrm{e}^{2\mathrm{i}\beta}\ \tilde{\kappa}_\mathrm{I}(\boldsymbol{k})\ , \tag{5.18}$$

where β is the polar angle of $\boldsymbol{k}_\perp$, i.e. the projection of the wave vector onto the plane of the sky. We will denote the line-of-sight component of $\boldsymbol{k}$ by $k_\parallel$. Then one can write the three-dimensional correlation function by Fourier transforming (5.17) as

$$\begin{aligned}\xi_\mathrm{gI}(R,\Pi,z) &= \int\frac{\mathrm{d}^3k}{(2\,\pi)^3}\int\frac{\mathrm{d}^3k'}{(2\,\pi)^3}\ \mathrm{e}^{-\mathrm{i}\boldsymbol{k}\cdot\boldsymbol{x}}\left\langle\tilde{\delta}^*_\mathrm{g}(\boldsymbol{k'},z)\ \tilde{\gamma}_{\mathrm{I},+}(\boldsymbol{k},z)\right\rangle \\ &= \int\frac{\mathrm{d}^3k}{(2\,\pi)^3}\int\frac{\mathrm{d}^3k'}{(2\,\pi)^3}\ \mathrm{e}^{-\mathrm{i}\boldsymbol{k}\cdot\boldsymbol{x}}\ \mathrm{e}^{2\mathrm{i}\beta}\ \left\langle\tilde{\delta}^*_\mathrm{g}(\boldsymbol{k'},z)\ \tilde{\kappa}_\mathrm{I}(\boldsymbol{k},z)\right\rangle\ .\end{aligned} \tag{5.19}$$

Inserting the definition of the three-dimensional gI power spectrum,

$$\left\langle\tilde{\delta}^*_\mathrm{g}(\boldsymbol{k'},z)\ \tilde{\kappa}_\mathrm{I}(\boldsymbol{k},z)\right\rangle = (2\,\pi)^3\ \delta_\mathrm{D}^{(3)}\left(\boldsymbol{k}-\boldsymbol{k'}\right)\ P_\mathrm{gI}(k,z)\ , \tag{5.20}$$

and subsequently executing the integration of (5.19) over $\boldsymbol{k'}$ yields

$$\begin{aligned}\xi_\mathrm{gI}(R,\Pi,z) &= \int\frac{\mathrm{d}^3k}{(2\,\pi)^3}\ \mathrm{e}^{-\mathrm{i}\boldsymbol{k}\cdot\boldsymbol{x}}\ \mathrm{e}^{2\mathrm{i}\beta}\ P_\mathrm{gI}(k,z) \\ &= \int\frac{\mathrm{d}^3k}{(2\,\pi)^3}\ \mathrm{e}^{-\mathrm{i}k_\parallel\Pi}\ \mathrm{e}^{-\mathrm{i}\boldsymbol{k}_\perp\cdot\boldsymbol{x}_\perp}\ \mathrm{e}^{2\mathrm{i}\beta}\ P_\mathrm{gI}\left(\sqrt{k_\perp^2+k_\parallel^2},z\right) \\ &= -\int\frac{\mathrm{d}k_\parallel}{2\,\pi}\ \mathrm{e}^{-\mathrm{i}k_\parallel\Pi}\int_0^\infty\frac{\mathrm{d}k_\perp k_\perp}{2\,\pi}\ J_2(k_\perp R)\ P_\mathrm{gI}\left(\sqrt{k_\perp^2+k_\parallel^2},z\right)\ ,\end{aligned} \tag{5.21}$$

where in order to arrive at the third equality, the definition of the second-order Bessel function of the first kind was used, see (3.46). In this derivation it was implicitly assumed that the intrinsic shear field does not feature B-modes, as is for instance the case for the linear alignment paradigm.

One can now integrate over the line of sight, making use of the definition of the Dirac delta-distribution, to obtain the projected gI correlation function as employed by Mandelbaum et al. (2006), Hirata et al. (2007), and Mandelbaum et al. (2009),

$$w_\mathrm{g+}(R,z) \equiv \int_{-\infty}^{\infty}\mathrm{d}\Pi\ \xi_\mathrm{gI}(R,\Pi,z) = -\int_0^\infty\frac{\mathrm{d}k_\perp\,k_\perp}{2\,\pi}\ J_2(k_\perp R)\ P_\mathrm{gI}(k_\perp,z)\ . \tag{5.22}$$

Real data cannot provide the correlation function for arbitrarily large line-of-sight separations, so that a truncation of the integral in (5.22) is necessary. This formula is still applicable if one can stack observations for all values of Π for which galaxy pairs carry a signal. While this can easily be achieved for spectroscopic observations, photometric redshift scatter smears the signal in Π such that a cut-off $\Pi_{\max}$ needs to be taken into account explicitly in the modelling. Of course it would be possible to compute the observed correlations out to very large $\Pi_{\max}$, but this way many uncorrelated galaxy pairs would enter the correlation function, thereby decreasing the signal-to-noise dramatically.

Instead, we proceed from (5.21) by noting that ξ_{gI} is real, so that

$$\xi_{\mathrm{gI}}(R,\Pi,z) = -\int_0^\infty \frac{\mathrm{d}k_\parallel}{\pi} \int_0^\infty \frac{\mathrm{d}k_\perp k_\perp}{2\,\pi}\; J_2(k_\perp R)\; P_{\mathrm{gI}}\left(\sqrt{k_\perp^2+k_\parallel^2}, z\right)\; \cos(k_\parallel \Pi)\;. \tag{5.23}$$

As can be seen from this equation, ξ_{gI} is an even function in both R and Π, so that it is sufficient to compute just one quadrant. Note that by definition $R \geq 0$, whereas Π can also attain negative values.

Equation (5.23) yields the three-dimensional gI correlation function for exact or, to good approximation, spectroscopic redshifts whose very small uncertainties we are going to neglect. For the model of $P_{\delta\mathrm{I}}$ given by (5.12) with SuperCOSMOS normalisation and $b_{\mathrm{g}} = 1$, we plot $\xi_{\mathrm{gI}}(R,\Pi,z)$ for $z \approx 0.5$ in Fig. 5.9, bottom panel. As expected, the correlation is strongest for small separations, in particular for $|\Pi|$ close to zero. If spectroscopic data is available, essentially all information is captured when a cut-off $\Pi_{\max} = 60\,\mathrm{Mpc}\,h^{-1}$ is used in the integration (5.22), as done e.g. in Mandelbaum et al. (2009) and also in this work. Due to the definition (5.17), the gI correlation function measures the radial alignment of the galaxy shape with respect to the separation vector of the galaxy pair considered. Therefore the correlation function vanishes for all Π at $R = 0$ since then the separation vector points along the of sight. Note that the contours do not approach the $\Pi = 0$-axis asymptotically, but cross this line at some value of R, as expected for a differentiable correlation function.

Photometric redshift errors cause the observed correlation function to be a 'smeared' version of (5.23), introducing a spread especially along the line of sight but to a lesser extent also in transverse separation. If we denote quantities determined via photometric redshifts by a bar, the actually measured 3D correlation function reads

$$\xi_{\mathrm{gI}}^{\mathrm{phot}}(\bar{R},\bar{\Pi},\bar{z}_{\mathrm{m}}) = \int \mathrm{d}z_{\mathrm{m}} \int \mathrm{d}R \int \mathrm{d}\Pi\; p\left(R,\Pi,z_{\mathrm{m}} \,|\, \bar{R},\bar{\Pi},\bar{z}_{\mathrm{m}}\right)\; \xi_{\mathrm{gI}}(R,\Pi,z_{\mathrm{m}})\;, \tag{5.24}$$

where z_{m} denotes the mean redshift of the galaxy samples used for the number density and the shape measurement. Here, p is the probability distribution of the true values of R, Π, and z_{m}, given photometric redshift estimates of these quantities. In words, (5.24) means that in order to obtain the observed correlation function, we integrate over ξ_{gI} as given in (5.23), weighted by the probability that the true values for separations and redshift actually correspond to the estimates based on photometric redshifts.

The direct observables for this measurement are the redshifts of the two galaxy samples under consideration, z_1 and z_2, and their angular separation θ. The sets of variables (z_1, z_2, θ) and (R, Π, z_{m}) are related via a bijective transformation. Writing (5.24) in terms of (z_1, z_2, θ),

one obtains

$$\begin{aligned}
\xi_{\rm gI}^{\rm phot}(\bar{R},\bar{\Pi},\bar{z}_{\rm m}) &= \int {\rm d}z_1 \int {\rm d}z_2 \int {\rm d}\theta\; p\left(z_1,z_2,\theta \,|\, \bar{z}_1\left\{\bar{z}_{\rm m},\bar{\Pi}\right\},\bar{z}_2\left\{\bar{z}_{\rm m},\bar{\Pi}\right\},\bar{\theta}\left\{\bar{z}_{\rm m},\bar{R}\right\}\right) \\
&\qquad \times \xi_{\rm gI}\left(R\left\{z_1,z_2,\theta\right\},\Pi\left\{z_1,z_2\right\},z_{\rm m}\left\{z_1,z_2\right\}\right) \\
&= \int {\rm d}z_1 \int {\rm d}z_2 \int {\rm d}\theta\; p_n(z_1|\bar{z}_1\left\{\bar{z}_{\rm m},\bar{\Pi}\right\})\; p_\epsilon(z_2|\bar{z}_2\left\{\bar{z}_{\rm m},\bar{\Pi}\right\})\; \delta_{\rm D}\left(\theta-\bar{\theta}\left\{\bar{z}_{\rm m},\bar{R}\right\}\right) \\
&\qquad \times \xi_{\rm gI}\left(R\left\{z_1,z_2,\theta\right\},\Pi\left\{z_1,z_2\right\},z_{\rm m}\left\{z_1,z_2\right\}\right) \\
&= \int {\rm d}z_1 \int {\rm d}z_2\; p_n\left(z_1|\bar{z}_1\left\{\bar{z}_{\rm m},\bar{\Pi}\right\}\right)\; p_\epsilon\left(z_2|\bar{z}_2\left\{\bar{z}_{\rm m},\bar{\Pi}\right\}\right) \\
&\qquad \times \xi_{\rm gI}\left(R\left\{z_1,z_2,\bar{\theta}(\bar{z}_{\rm m},\bar{R})\right\},\Pi\left\{z_1,z_2\right\},z_{\rm m}\left\{z_1,z_2\right\}\right)\;.
\end{aligned} \tag{5.25}$$

In the second step it was assumed that the probability distributions of z_1, z_2, and θ are mutually independent, and that θ is exactly known. We have introduced the option of different redshift probability distributions for the galaxy sample with number density information p_n and the one with shape information p_ϵ. In the last equality all photo-z-related quantities have been expressed in terms of the arguments of the correlation function on the left-hand-side.

We make use of the following approximate relations between the two triples of variables,

$$\begin{aligned}
z_{\rm m} &= \frac{1}{2}\left(z_1+z_2\right)\;; \\
R &\approx \theta\,\chi(z_{\rm m})\;; \\
\Pi &\approx \frac{c}{H(z_{\rm m})}\left(z_2-z_1\right)\;,
\end{aligned} \tag{5.26}$$

where $H(z)$ is the Hubble parameter. The last expression follows from (2.10). Note that the same transformations have been used to bin the observational data in terms of redshift, transverse and line-of-sight separation. With this equation for Π, in combination with the assignment of probability distributions in (5.25), we have introduced the convention that $\Pi > 0$ means that the galaxy from the density sample is at lower redshift than the galaxy from the shape sample. If and only if the distributions for the density and the shape sample are identical, which we shall assume throughout this work, the correlation function remains symmetric with respect to Π, i.e. $\xi_{\rm gI}^{\rm phot}(\bar{R},\bar{\Pi},\bar{z}_{\rm m}) = \xi_{\rm gI}^{\rm phot}(\bar{R},-\bar{\Pi},\bar{z}_{\rm m})$.

With these equations at hand, one can also write down the inverse transformation of (5.26), which is needed to evaluate (5.25),

$$\begin{aligned}
\theta &= R\,\chi^{-1}(z_{\rm m})\;; \\
z_1 &= z_{\rm m}-\frac{\Pi\,H(z_{\rm m})}{2c}\;; \\
z_2 &= z_{\rm m}+\frac{\Pi\,H(z_{\rm m})}{2c}\;.
\end{aligned} \tag{5.27}$$

Then (5.25) can be expressed as

$$\begin{aligned}
\xi_{\rm gI}^{\rm phot}(\bar{R},\bar{\Pi},\bar{z}_{\rm m}) &= \int {\rm d}z_1 \int {\rm d}z_2\; p_n\left(z_1 \mid \bar{z}_{\rm m}-\frac{\bar{\Pi}\,H(\bar{z}_{\rm m})}{2c}\right)\; p_\epsilon\left(z_2 \mid \bar{z}_{\rm m}+\frac{\bar{\Pi}\,H(\bar{z}_{\rm m})}{2c}\right) \\
&\qquad \times \xi_{\rm gI}\left(\bar{R}\,\frac{\chi\left(\frac{1}{2}(z_1+z_2)\right)}{\chi\left(\bar{z}_{\rm m}\right)},\frac{c\,|z_2-z_1|}{H\left(\frac{1}{2}(z_1+z_2)\right)},\frac{1}{2}(z_1+z_2)\right)\;.
\end{aligned} \tag{5.28}$$

Note that the absolute value for z_2-z_1 has been introduced in the second argument of $\xi_{\rm gI}$, which is possible since it is an even function in this argument. The integrals in (5.28) run over the

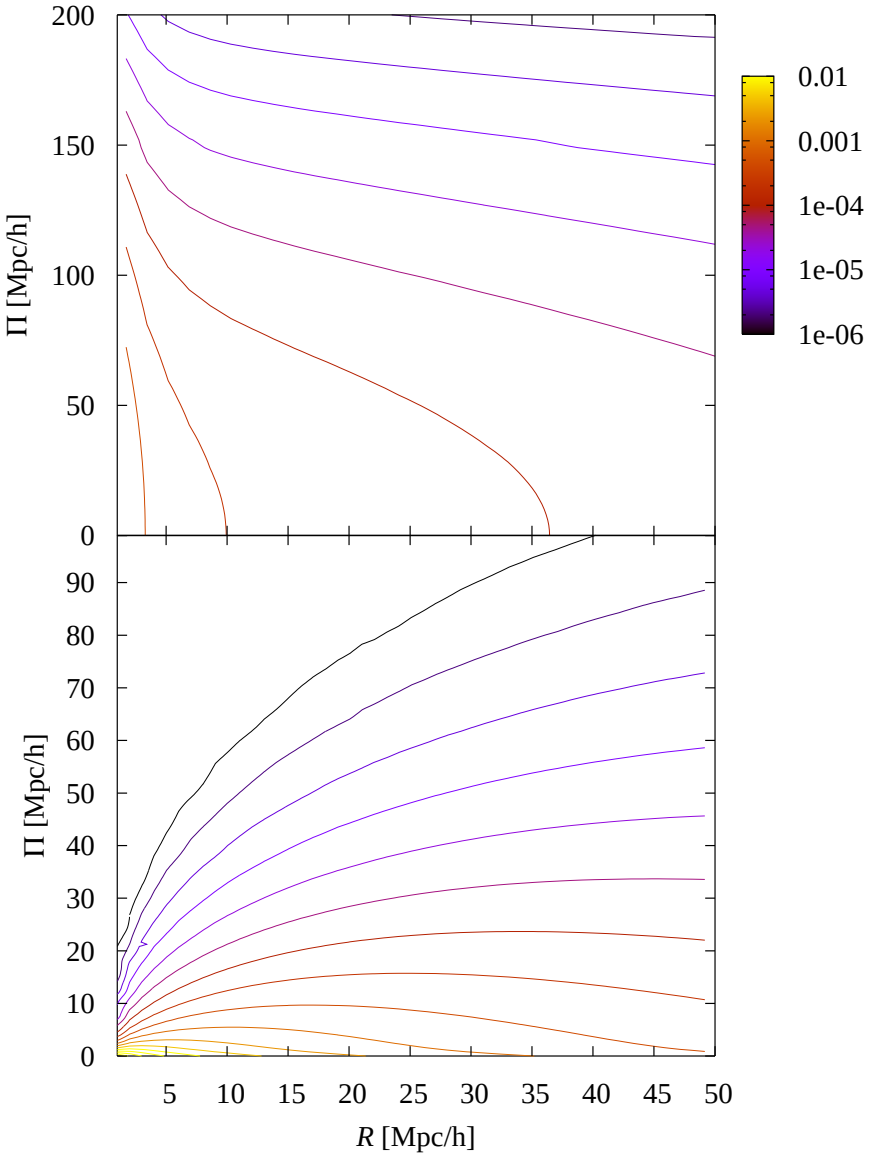

Figure 5.9: Three-dimensional gI correlation function as a function of comoving line-of-sight separation Π and comoving transverse separation R at $z \approx 0.5$. Contours are logarithmically spaced between 10^{-2} (yellow) and 10^{-6} (black). *Top panel*: Applying a Gaussian photometric redshift scatter of width 0.02. *Bottom panel*: Assuming exact redshifts. Note the largely different scaling of the ordinate axes. The galaxy bias has been set to unity and (5.12) with SuperCOSMOS normalisation has been used to model $P_{\delta\mathrm{I}}$ in both cases. Redshift-space distortions have not been taken into account.

full range of spectroscopic (exact) redshifts. As a consequence, $|z_2 - z_1|$ in the second argument of ξ_{gI} can obtain relatively large values, leading to very large $\Pi \gg 100\,\mathrm{Mpc}\,h^{-1}$. However, the spectroscopic correlation function ξ_{gI} becomes very small for large Π, so that the integrand in (5.28) can safely be set to zero in this case.

Still, any sizeable photometric redshift scatter leads to a considerable spread of the three-dimensional correlation function in Π, as can be seen in Fig. 5.9, top panel. Assuming a Gaussian photometric redshift scatter with width 0.02 around every true redshift, the strong signal concentrated at small Π and $R \lesssim 10\,\mathrm{Mpc}\,h^{-1}$ in the spectroscopic case is scattered along the line of sight, so that the values of ξ_{gI} at $\Pi > 200\,\mathrm{Mpc}\,h^{-1}$ are still more than a per cent of those at $\Pi = 0$ for any R. In contrast, we find that the net scatter of signal between different transverse separations is negligible. Hence, in principle the projected correlation function (5.22) does not change when using photometric instead of spectroscopic redshift information as long as the complete range of Π for which a signal is measured enters the line-of-sight integration. However, in practice the line-of-sight integral has to be truncated for reasons of a good signal-to-noise ratio, so that in the case of photometric redshifts part of the signal is lost. Therefore it is crucial to repeat the same steps applied to the data also to the model and use the same cut-off Π_{max} in (5.22).

We now derive a relation between the three-dimensional gI correlation function in the presence of photometric redshift scatter and the angular power spectrum, which proves most convenient to compute $\xi_{\rm gI}^{\rm phot}$ in practice. Inserting (5.21) into (5.28), one can write

$$\begin{aligned}\xi_{\rm gI}^{\rm phot}(\bar{R},\bar{\Pi},\bar{z}_{\rm m}) &= -\int {\rm d}z_1 \int {\rm d}z_2\; p_n\left(z_1 \mid \bar{z}_{\rm m}-\frac{\bar{\Pi}\,H(\bar{z}_{\rm m})}{2c}\right)\; p_\epsilon\left(z_2 \mid \bar{z}_{\rm m}+\frac{\bar{\Pi}\,H(\bar{z}_{\rm m})}{2c}\right) \\ &\times \int\frac{{\rm d}k_\parallel}{2\,\pi}\int_0^\infty \frac{{\rm d}k_\perp k_\perp}{2\,\pi}\; J_2\left(k_\perp \bar{R}\,\frac{\chi\,(z_{\rm m})}{\chi(\bar{z}_{\rm m})}\right)\; P_{\rm gI}\left(\sqrt{k_\perp^2+k_\parallel^2},z_{\rm m}\right)\; \exp\left\{-{\rm i}\,k_\parallel\,\frac{c\,(z_2-z_1)}{H\,(z_{\rm m})}\right\}\;. \end{aligned} \tag{5.29}$$

where we employed $z_{\rm m}=(z_1+z_2)/2$ as a shorthand notation. Making use of $\theta=\bar{R}/\chi(\bar{z}_{\rm m})$, see (5.27), and defining the angular frequency $\ell=k_\perp\chi\,(z_{\rm m})$, one obtains

$$\begin{aligned}\xi_{\rm gI}^{\rm phot}(\bar{R},\bar{\Pi},\bar{z}_{\rm m}) &= -\int {\rm d}z_1 \int {\rm d}z_2\; p_n\left(z_1 \mid \bar{z}_{\rm m}-\frac{\bar{\Pi}\,H(\bar{z}_{\rm m})}{2c}\right)\; p_\epsilon\left(z_2 \mid \bar{z}_{\rm m}+\frac{\bar{\Pi}\,H(\bar{z}_{\rm m})}{2c}\right) \\ &\times \int\frac{{\rm d}k_\parallel}{2\,\pi}\int_0^\infty \frac{{\rm d}\ell\;\ell}{2\,\pi}\;\frac{J_2\left(\ell\theta(\bar{R},\bar{z}_{\rm m})\right)}{\chi^2(z_{\rm m})}\; P_{\rm gI}\left(\sqrt{\left(\frac{\ell}{\chi(z_{\rm m})}\right)^2+k_\parallel^2},z_{\rm m}\right)\; \exp\left\{-{\rm i}\,k_\parallel\,\frac{c\,(z_2-z_1)}{H\,(z_{\rm m})}\right\}\;. \end{aligned} \tag{5.30}$$

We then transform the integration variables $\{z_1,z_2\}$ to $\{z_m,\Delta z\equiv z_2-z_1\}$. Note that the determinant of the Jacobian of this transformation is unity. We apply Limber's approximation, which in this case can be written as

$$\begin{aligned}& p_n\left(z_{\rm m}-\frac{\Delta z}{2}\mid \bar{z}_{\rm m}-\frac{\bar{\Pi}\,H(\bar{z}_{\rm m})}{2c}\right)\; p_\epsilon\left(z_{\rm m}+\frac{\Delta z}{2}\mid \bar{z}_{\rm m}+\frac{\bar{\Pi}\,H(\bar{z}_{\rm m})}{2c}\right) \\ \approx\;& p_n\left(z_{\rm m}|\bar{z}_1(\bar{z}_{\rm m},\bar{\Pi})\right)\; p_\epsilon\left(z_{\rm m}|\bar{z}_2(\bar{z}_{\rm m},\bar{\Pi})\right)\;. \end{aligned} \tag{5.31}$$

Here we have assumed that the two redshift probability distributions are sufficiently broad and have similar forms, so that an evaluation at $z_{\rm m}$ instead of $z_{\rm m}\pm\Delta z/2$ does not change the results significantly. Since the photometric redshifts on which the distributions are conditional encapsulate the dependence of $\xi_{\rm gI}^{\rm phot}$ on the line-of-sight separation Π, we do not extend this approximation to the second argument. Equation (5.30) thereby simplifies to

$$\begin{aligned}\xi_{\rm gI}^{\rm phot}(\bar{R},\bar{\Pi},\bar{z}_{\rm m}) &\approx -\int {\rm d}z_{\rm m}\int {\rm d}\Delta z\;\frac{p_n\left(z_{\rm m}|\bar{z}_1(\bar{z}_{\rm m},\bar{\Pi})\right)\; p_\epsilon\left(z_{\rm m}|\bar{z}_2(\bar{z}_{\rm m},\bar{\Pi})\right)}{\chi^2(z_{\rm m})} \\ &\times \int\frac{{\rm d}k_\parallel}{2\,\pi}\int_0^\infty \frac{{\rm d}\ell\;\ell}{2\,\pi}\; J_2\left(\ell\theta(\bar{R},\bar{z}_{\rm m})\right)\; P_{\rm gI}\left(\sqrt{\left(\frac{\ell}{\chi(z_{\rm m})}\right)^2+k_\parallel^2},z_{\rm m}\right)\; \exp\left\{-{\rm i}\,k_\parallel\,\frac{c\,\Delta z}{H\,(z_{\rm m})}\right\} \\ &= -\int {\rm d}z_{\rm m}\;\frac{H\,(z_{\rm m})}{c}\;\frac{p_n\left(z_{\rm m}|\bar{z}_1(\bar{z}_{\rm m},\bar{\Pi})\right)\; p_\epsilon\left(z_{\rm m}|\bar{z}_2(\bar{z}_{\rm m},\bar{\Pi})\right)}{\chi^2(z_{\rm m})} \\ &\qquad\times\int_0^\infty\frac{{\rm d}\ell\;\ell}{2\,\pi}\; J_2\left(\ell\theta(\bar{R},\bar{z}_{\rm m})\right)\; P_{\rm gI}\left(\frac{\ell}{\chi(z_{\rm m})},z_{\rm m}\right)\;, \end{aligned} \tag{5.32}$$

where in order to arrive at the second equality, we integrated over Δz. The resulting Dirac delta-distribution renders the $k_\parallel$ integration trivial. Making use of the expressions ${\rm d}z_{\rm m}={\rm d}\chi H\,(z_{\rm m})\,/c$ and $p(z)=p(\chi)\,{\rm d}\chi/{\rm d}z$, one obtains the result

$$\begin{aligned}&\xi_{\rm gI}^{\rm phot}(\bar{R},\bar{\Pi},\bar{z}_{\rm m}) \\ =\;& -\int_0^\infty\frac{{\rm d}\ell\;\ell}{2\,\pi}\; J_2\left(\ell\theta(\bar{R},\bar{z}_{\rm m})\right)\;\int_0^{\chi_{\rm hor}}{\rm d}\chi\;\frac{p_n\left(\chi|\chi(\bar{z}_1(\bar{z}_{\rm m},\bar{\Pi}))\right)\,p_\epsilon\left(\chi|\chi(\bar{z}_2(\bar{z}_{\rm m},\bar{\Pi}))\right)}{\chi^2}\; P_{\rm gI}\left(\frac{\ell}{\chi},z(\chi)\right) \\ =\;& -\int_0^\infty\frac{{\rm d}\ell\;\ell}{2\,\pi}\; J_2\left(\ell\theta(\bar{R},\bar{z}_{\rm m})\right)\; C_{\rm gI}\left(\ell;\bar{z}_1(\bar{z}_{\rm m},\bar{\Pi}),\bar{z}_2(\bar{z}_{\rm m},\bar{\Pi})\right)\;, \end{aligned} \tag{5.33}$$

where in the last step we introduced the projected gI auto-correlation power spectrum C_{gI}, given by the Limber equation

$$C_{\mathrm{gI}}\left(\ell;\bar{z}_1,\bar{z}_2\right)=\int_0^{\chi_{\mathrm{hor}}}\mathrm{d}\chi'\,\frac{p_n\left(\chi'|\chi(\bar{z}_1)\right)\;p_\epsilon\left(\chi'|\chi(\bar{z}_2)\right)}{\chi'^2}\;P_{\mathrm{gI}}\left(\frac{\ell}{\chi'},z(\chi')\right)\;. \tag{5.34}$$

In addition to the angular frequency, we have written the photometric redshifts $\bar{z}_1$ and $\bar{z}_2$, which characterise the redshift distributions entering C_{gI}, explicitly as arguments. We will give more formal insight into this relation in Chap. 8. Note that Limber equations, such as (5.34) or those introduced in Sect. 5.3.2 and Chap. 8, in general hold only approximately, the range of validity being the more limited the narrower the kernels in the line-of-sight integration (e.g. Simon 2007).

We have verified that the calculations of the three-dimensional gI correlation function according to (5.28) and (5.33) agree within the numerical accuracy. The latter can be determined much more efficiently by computing the angular power spectrum via Limber's equation (5.34) and then using Hankel transformations to obtain the correlation function $\xi_{\mathrm{gI}}^{\mathrm{phot}}(\bar{R},\bar{\Pi},\bar{z}_{\mathrm{m}})$ via (5.33), employing the transformation (5.26). Note that the probability distributions of comoving distances are related to those of redshifts via $p_x\left(\chi|\chi(\bar{z}_i)\right)=p_x\left(z|\bar{z}_i\right)\mathrm{d}z/\mathrm{d}\chi$. We will provide details about the latter distributions in Sect. 5.4.1.

One can proceed likewise to obtain analogous expressions for the galaxy clustering signal (gg hereafter) which is also relevant to our investigation. Galaxy-galaxy lensing, which will be considered in more detail in the following subsection, vanishes if the density field probed by the galaxy distribution and the source galaxies on whose images the gravitational shear is measured are located at exactly the same redshift. Thus one cannot proceed with the same formalism as used to derive the gI contribution, see the assumptions underlying the definition (5.17), but has to incorporate redshift probability distributions from the start, again arriving at an expression analogous to (5.33).

Throughout, we will assume that the galaxy bias b_{g} is constant with scale for each galaxy sample considered. Then P_{gI} can be related to the matter-intrinsic power spectrum via $P_{\mathrm{gI}}\left(k,z\right)=b_{\mathrm{g}}\,P_{\delta\mathrm{I}}\left(k,z\right)$, where we calculate $P_{\delta\mathrm{I}}$ according to the non-linear version of the linear alignment model (NLA model hereafter; see Catelan et al. 2001; Hirata & Seljak 2004; Bridle & King 2007) according to (5.12). Note that Hirata & Seljak (2004) and Bridle & King (2007) matched the amplitude of the linear alignment model to SuperCOSMOS observations at low redshift. This choice is common in the literature but of no particular relevance for our study, and we emphasise that the normalisation is in principle arbitrary. Since it is already known that luminous red galaxies carry a significant intrinsic alignment signal (Hirata et al. 2007), we will use the SuperCOSMOS normalisation for the remainder of this section as a conservative estimate for the amplitude of $P_{\delta\mathrm{I}}$. The matter power spectrum entering (5.12) is computed as described in Sect. 5.1.4.

Note that throughout this work we do not include redshift-space distortions into our modelling. Since for both spectroscopic and photometric data we integrate the correlation functions over the line-of-sight separation out to at least $60\,\mathrm{Mpc}\,h^{-1}$ and $90\,\mathrm{Mpc}\,h^{-1}$, respectively, redshift-space distortions should have a negligible influence on the integrated signals (see also the discussion in Mandelbaum et al. 2009).

5.3.2 Contribution by other signals

Due to the photometric redshift scatter, contributions to galaxy number density-shape correlations other than the gI term may become important. In the weak lensing limit the measured ellipticity of a galaxy image is the sum of the intrinsic ellipticity and the gravitational shear,

while the galaxy number density is determined by a large intrinsic term plus modifications by lensing magnification effects. Hence, in terms of angular power spectra one can write (for details see Bernstein 2009; Joachimi & Bridle 2009)

$$C_{n\epsilon}(\ell; z_1, z_2) = C_{\mathrm{gG}}(\ell; z_1, z_2) + C_{\mathrm{gI}}(\ell; z_1, z_2) + C_{\mathrm{mG}}(\ell; z_1, z_2) + C_{\mathrm{mI}}(\ell; z_1, z_2) \;, \tag{5.35}$$

for each set of galaxy samples that is correlated. Apart from the gI signal, contributions from galaxy-galaxy lensing (gG), magnification-shear correlations (mG), and magnification-intrinsic correlations (mI) occur.

If $z_1 \approx z_2$, the gI term is expected to dominate whereas galaxy-galaxy lensing governs $C_{n\epsilon}(\ell; z_1, z_2)$ in case a number density and a shape sample at largely different redshifts are correlated. In addition, correlations between lensing magnification and gravitational shear can have a contribution, e.g. if a matter overdensity causes both tangential shear alignment and an apparent boost in the number density of background galaxies. Likewise this overdensity could tidally align surrounding galaxies and thus create correlations between magnification and the intrinsic galaxy shapes.

All these additional signals are related to the three-dimensional correlation function via relations of the form (5.33), so that, in order to assess the importance of their contributions, it is sufficient to compare the angular power spectra. The corresponding Limber equations of the additional signals read

$$\begin{aligned}
C_{\mathrm{gG}}(\ell; \bar{z}_1, \bar{z}_2) &= b_{\mathrm{g}} \int_0^{\chi_{\mathrm{hor}}} \mathrm{d}\chi \, \frac{p_n(\chi|\chi(\bar{z}_1)) \; q_\epsilon(\chi, \chi(\bar{z}_2))}{\chi^2} \, P_\delta\left(\frac{\ell}{\chi}, z(\chi)\right) \;; \\
C_{\mathrm{mG}}(\ell; \bar{z}_1, \bar{z}_2) &= 2(\alpha - 1) \int_0^{\chi_{\mathrm{hor}}} \mathrm{d}\chi \, \frac{q_n(\chi, \chi(\bar{z}_1)) \; q_\epsilon(\chi, \chi(\bar{z}_2))}{\chi^2} \, P_\delta\left(\frac{\ell}{\chi}, z(\chi)\right) \;; \\
C_{\mathrm{mI}}(\ell; \bar{z}_1, \bar{z}_2) &= 2(\alpha - 1) \int_0^{\chi_{\mathrm{hor}}} \mathrm{d}\chi \, \frac{q_n(\chi, \chi(\bar{z}_1)) \; p_\epsilon(\chi|\chi(\bar{z}_2))}{\chi^2} \, P_{\delta\mathrm{I}}\left(\frac{\ell}{\chi}, z(\chi)\right) \;,
\end{aligned} \tag{5.36}$$

where α is the power-law exponent of the cumulative galaxy luminosity function of the density sample at its faint end (e.g. Bartelmann & Schneider 2001), and where we again assumed a linear galaxy bias. Moreover we have defined

$$q_x(\chi, \chi_1) = \frac{3H_0^2\Omega_{\mathrm{m}}}{2\,c^2} \frac{\chi}{a(\chi)} \int_\chi^{\chi_{\mathrm{hor}}} \mathrm{d}\chi' \, p_x(\chi'|\chi_1) \, \frac{\chi' - \chi}{\chi'} \tag{5.37}$$

for $x = \{n, \epsilon\}$, in close analogy to (3.28). For a formal treatment and derivation of the signals (5.36) see Chap. 8.

To get an estimate for the value of α, we make use of the findings by Mandelbaum et al. (2005) who studied a high-redshift LRG sample with characteristics similar to the MegaZ LRG data. They obtained $s = 0.27$, where s is the logarithmic slope of the galaxy magnitude distribution, which translates into $\alpha = 2.5\,s = 0.675$ (see Narayan 1989; Bartelmann & Schneider 2001). We note in passing that α could in principle be estimated from the MegaZ data itself from a histogram of the magnitudes of the sample. We defer this determination to future work. The MegaZ LRG sample has a significantly higher luminosity than the LRG sample considered by Mandelbaum et al. (2005), so that one would expect a larger α and thus stronger magnification signals. However, as will be demonstrated below, we also find stronger intrinsic alignment amplitudes for MegaZ LRG than for SuperCOSMOS, where we will assume the latter here, so that our findings on the importance of the different contributions should still be representative for this analysis.

Furthermore we choose the normalisation of the NLA model given by SuperCOSMOS, as well as a galaxy bias $b_{\mathrm{g}} = 1.9$, which is roughly in agreement with the findings by Blake et al. (2007)

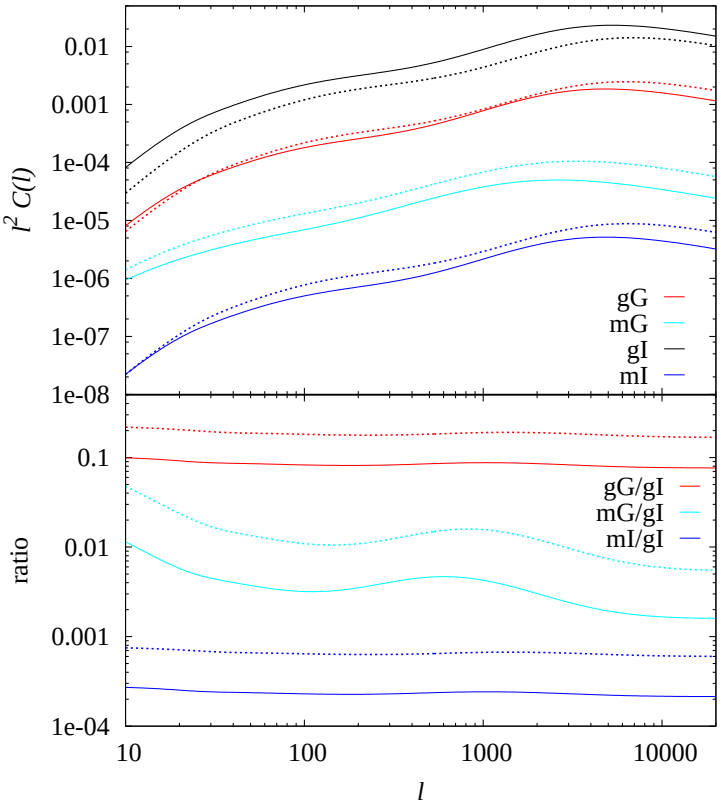

Figure 5.10: *Top panel*: Modulus of the angular power spectra of the different signals contributing to galaxy number density-shape correlations. Number density-intrinsic correlations (gI) are shown in black, galaxy-galaxy lensing (gG) in red, magnification-shear correlations (mG) in light blue, and magnification-intrinsic correlations (mI) in dark blue. Solid curves correspond to the auto-correlation at $z = 0.4525$, dotted curves to the one at $z = 0.6025$. We have used the MegaZ LRG redshift distribution shown in Fig. 5.12. *Bottom panel*: Ratio of the aforementioned signals over the gI correlations, with the same coding of the curves as above.

and also turns out to be close to the actual fit results, see Sect. 5.5.2. We employ the redshift distribution for the MegaZ LRG sample as determined from 2SLAQ spectroscopic redshifts; for details see Sect. 5.4.1. The resulting angular power spectra for all four contributions to (5.35) are shown in Fig. 5.10. We plot auto-correlations which should yield the main contribution to $\xi_{\rm gI}^{\rm phot}(\bar{R}, \bar{\Pi}, \bar{z}_{\rm m})$ if $|\Pi|$ does not become too large, using $\bar{z}_1 = \bar{z}_2 = 0.4525$ and $\bar{z}_1 = \bar{z}_2 = 0.6025$ as representative values in the range of MegaZ LRG photometric redshifts.

For the photometric redshift accuracy of the MegaZ LRG sample the gI signal still clearly dominates the number density-shape correlations. It has a lower amplitude at $\bar{z} = 0.6025$ than at $\bar{z} = 0.4525$ due to the significantly broader redshift distribution at the higher photometric redshift. To verify that it is indeed the width of the distribution, and not the shift of its mean redshift, that causes the depletion, we shift the redshift distribution at $\bar{z} = 0.4525$ to a mean of 0.6 and re-compute the gI signal which then has a similar, slightly higher amplitude compared to the gI correlations at $\bar{z} = 0.4525$. The other signals are less affected by the width of the contributing redshift distributions since they depend on lensing and thus have a much broader kernel in the line-of-sight integration, see (5.36).

The mI signal never attains more than a per mil of the gI term and is hence irrelevant for our purposes. Magnification-shear (mG) correlations can contribute more than a per cent of the gI term at small angular frequencies. However, due to the Bessel function J_2 in the kernel of (5.33) and the fact that angular scales larger than about 3 deg are not probed by our observations, contributions from $\ell \lesssim 50$ are largely suppressed in $\xi_{\rm gI}^{\rm phot}(\bar{R}, \bar{\Pi}, \bar{z}_{\rm m})$, so that the mG term should not add more than a few per cent to the total signal, which is considerably smaller than the expected parameter errors. It may become necessary to consider the mG signal for analyses of larger surveys with less accurate photometric redshifts though.

Galaxy-galaxy lensing has a scale dependence that is similar to the gI term, thereby yielding a nearly constant contribution of $10 - 20\,\%$. Therefore we need to incorporate the gG term

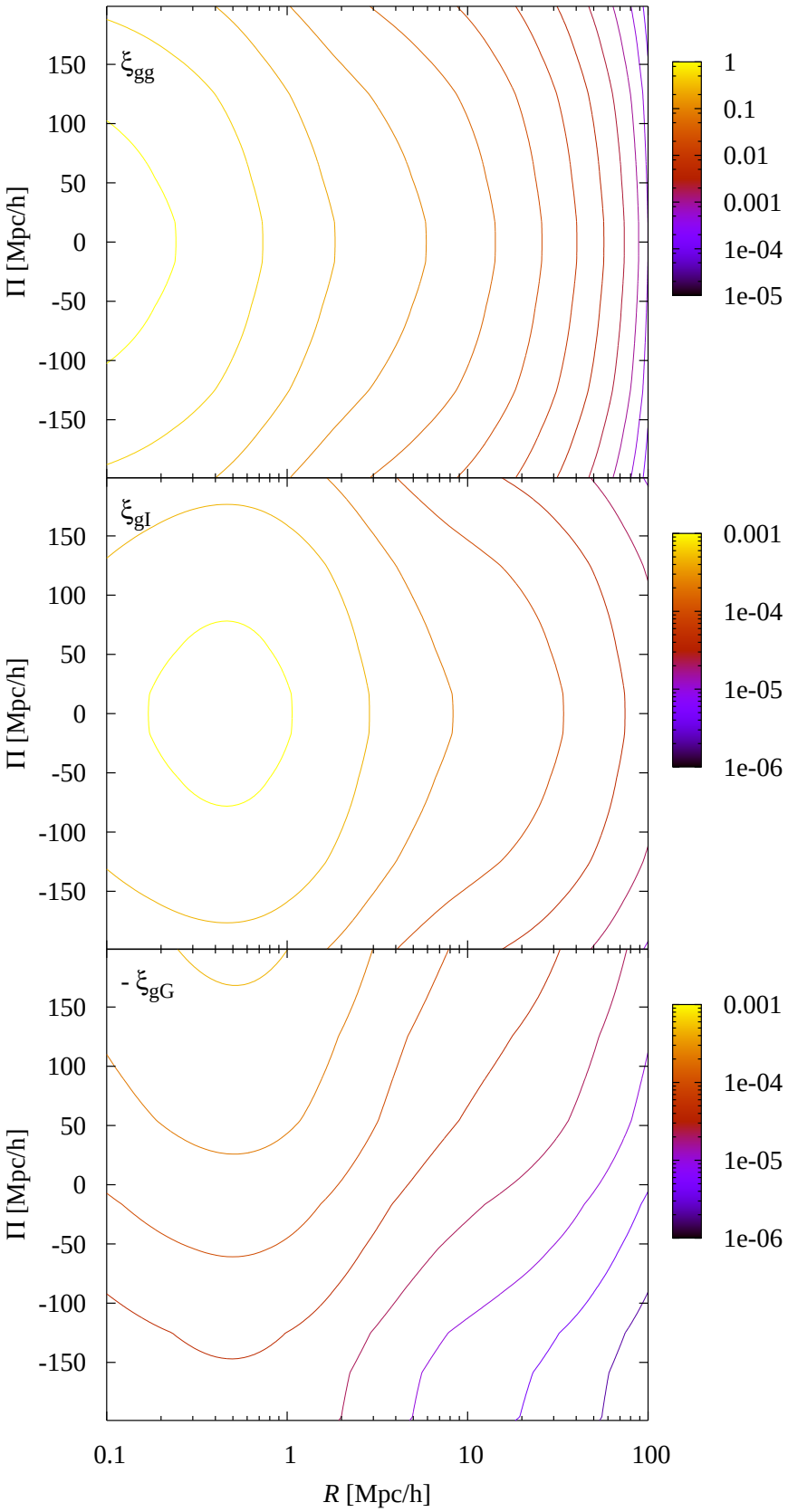

Figure 5.11: Three-dimensional correlation functions $\xi^{\rm phot}$ as a function of comoving line-of-sight separation Π and comoving transverse separation R at $z_{\rm m} \approx 0.5$. The galaxy bias was set to 1.9 in all panels, and (5.12) with SuperCOSMOS normalisation was used for modelling the intrinsic alignment signals. *Top panel*: Galaxy clustering correlation (gg). Contours are logarithmically spaced between 1 (yellow) and 10^{-5} (violet). *Centre panel*: Galaxy number density-intrinsic shape correlation (gI). Contours are logarithmically spaced between 10^{-3} (yellow) and 10^{-6} (violet). *Bottom panel*: Galaxy-galaxy lensing (gG). For ease of direct comparison the contours are encoded exactly like in the centre panel. Note that the galaxy-galaxy lensing signal is not symmetric around $\Pi = 0$, in contrast to the gg and gI terms. Besides, it is negative, so that the modulus is plotted.

into our model, mainly affecting the amplitude of the model correlation function due to the almost constant ratio gG/gI. Note again that, contrary to the usual approach to galaxy-galaxy lensing studies, we have defined the correlation function such that radial alignment produces a positive signal. Hence, the inclusion of the gG term into the model decreases its amplitude. The

modulus of the three-dimensional gG corelation function is shown in Fig. 5.11, bottom panel, for $z_\mathrm{m} \approx 0.5$, and again assuming $b_\mathrm{g} = 1.9$. Due to the lensing contribution, the gG correlation is not symmetric with respect to the line with $\Pi = 0$, even if the redshift distributions of the galaxy shape and density samples are identical.

In Fig. 5.11, centre panel, the predicted gI correlation function for the MegaZ LRG sample (assuming alignments consistent with those in SuperCOSMOS, and including photometric redshift errors) is plotted. The signal is strongest around $\Pi = 0$, but extends far out along the line-of-sight direction due to the photometric redshift scatter. The correlations have a maximum at $R \sim 0.5\,\mathrm{Mpc}\,h^{-1}$ and decrease for larger R due to the diminishing physical interaction between galaxies at large separation, and for small R since the separation vector between pairs of galaxies gets close to the line-of-sight direction, see also Fig. 5.9.

The above statements hold only if the amplitude of the intrinsic alignment signal is of the order found in the SuperCOSMOS survey. If the contribution by intrinsic alignments were weaker, the importance of the gG and mG signals would further increase. However, Hirata et al. (2007) have demonstrated that LRGs show a strong intrinsic alignment signal at $z \sim 0.3$, so unless we find a strong decline of intrinsic alignments with redshift, the SuperCOSMOS normalisation should be a conservative assumption.

We also consider galaxy clustering (gg) which is obtained from galaxy number density autocorrelations and will be used to determine the galaxy bias of the different samples. Since the gg signal is affected in the same way by the photometric redshift scatter as number density-shape cross-correlations, we proceed in exact analogy and compute the three-dimensional correlation function $\xi_\mathrm{gg}(\bar{R}, \bar{\Pi}, \bar{z}_\mathrm{m})$ from (e.g. Hu & Jain 2004)

$$\xi_\mathrm{gg}^\mathrm{ang}\,(\theta; \bar{z}_1, \bar{z}_2) = \int_0^\infty \frac{\mathrm{d}\ell\;\ell}{2\,\pi}\; J_0\,(\ell\theta)\;\; C_\mathrm{gg}\,(\ell; \bar{z}_1, \bar{z}_2) \tag{5.38}$$

by means of (5.27), where the angular power spectrum is related to the matter power spectrum via

$$C_\mathrm{gg}\,(\ell; \bar{z}_1, \bar{z}_2) = b_\mathrm{g}^2 \int_0^{\chi_\mathrm{hor}} \mathrm{d}\chi\; \frac{p_n\,(\chi|\chi(\bar{z}_1))\;\; p_\epsilon\,(\chi|\chi(\bar{z}_2))}{\chi^2}\; P_\delta\left(\frac{\ell}{\chi}, z(\chi)\right)\;. \tag{5.39}$$

We show the three-dimensional correlation function of galaxy clustering in the top panel of Fig. 5.11. The strong spread of the gg signal along the line of sight demonstrates that in the case of the MegaZ LRG sample, photometric redshift scatter and the corresponding effect of a truncation at large Π when computing the projected correlation function has to be modelled with similar care as for the gI term. Since galaxy clustering produces a strong signal, we can safely neglect potential contributions by lensing magnification effects in this case.

5.3.3 Projected correlation functions

As in the spectroscopic case, the quantity that is actually compared to the data is the projected gI correlation function $w_\mathrm{g+}$, obtained by integrating the three-dimensional correlation function $\xi_\mathrm{gI}^\mathrm{phot}(\bar{R}, \bar{\Pi}, \bar{z}_\mathrm{m})$ over Π. In addition we take the average over a range of photometric redshifts $\bar{z}_\mathrm{m}$ which e.g. corresponds to the two redshift bins defined for the MegaZ LRG sample, resulting in

$$w_\mathrm{g+}(\bar{R}) = \int_{-\bar{\Pi}_\mathrm{max}}^{\bar{\Pi}_\mathrm{max}} \mathrm{d}\bar{\Pi} \int \mathrm{d}\bar{z}_\mathrm{m}\; \mathcal{W}(\bar{z}_\mathrm{m})\; \xi_\mathrm{gI}^\mathrm{phot}(\bar{R}, \bar{\Pi}, \bar{z}_\mathrm{m})\;, \tag{5.40}$$

where the truncation at Π_max, taken to be the same as for the data, has now been written explicitly.

The average over $\bar{z}_\mathrm{m}$ contains the weighting $\mathcal{W}(z)$ of redshifts for a flux-limited sample as derived by Mandelbaum et al. (2009), which is given by

$$\mathcal{W}(z) = \frac{p^2(z)}{\chi^2(z)\,\chi'(z)} \left[\int \mathrm{d}z\, \frac{p^2(z)}{\chi^2(z)\,\chi'(z)}\right]^{-1} , \tag{5.41}$$

where $p(z)$ is in this case the unconditional probability distribution of photometric redshifts for the MegaZ LRG sample (or its redshift-binned subsamples). As before, $\chi'(z)$ denotes the derivative of comoving distance with respect to redshift. Note that the denominator $\chi^2(z)\,\chi'(z)$ in (5.41) is proportional to the derivative of the comoving volume V_com with respect to redshift at z. Equation (5.41) can be illustrated by considering a volume-limited sample for which $p(z) = \mathrm{d}V_\mathrm{com}/\mathrm{d}z$ holds. Then $\mathcal{W}(z) = p(z)$, as expected for a simple average over redshift in (5.40). A flux-limited sample like MegaZ LRG misses faint galaxies at high redshifts compared to a volume-complete sample, and these redshifts are downweighted accordingly by (5.41) in the averaging process.

In the case of galaxy clustering, the projected correlation function $w_\mathrm{gg}(\bar{R})$ is determined in exact analogy to (5.40). In addition to the photometric MegaZ LRG sample, we will also reconsider spectroscopic samples from SDSS. As discussed before, the line-of-sight truncation can be ignored in the case of spectroscopic data, so that the projected correlation function is simply given by

$$w_\mathrm{g+}(R) = -b_\mathrm{g} \int \mathrm{d}z\, \mathcal{W}(z) \int_0^\infty \frac{\mathrm{d}k_\perp\, k_\perp}{2\,\pi}\, J_2(k_\perp R)\, P_{\delta\mathrm{I}}(k_\perp, z) , \tag{5.42}$$

where (5.22) and the same redshift averaging procedure as in (5.40) were used. Similarly, one obtains for the spectroscopic galaxy clustering signal (e.g. Hirata et al. 2007)

$$w_\mathrm{gg}(R) = b_\mathrm{g}^2 \int \mathrm{d}z\, \mathcal{W}(z) \int_0^\infty \frac{\mathrm{d}k_\perp\, k_\perp}{2\,\pi}\, J_0(k_\perp R)\, P_\delta(k_\perp, z) . \tag{5.43}$$

For a consistency check on the modelling of the line-of-sight truncation of the correlation functions in case of the MegaZ LRG sample, we compute the model and the observed correlation functions for $\bar{\Pi}_\mathrm{max} = 90\,\mathrm{Mpc}\,h^{-1}$ and $\bar{\Pi}_\mathrm{max} = 180\,\mathrm{Mpc}\,h^{-1}$. For the number density-shape correlations as well as the galaxy clustering signal, we compare the ratios of the correlation functions with these two cut-offs in Sect. 5.5.1, finding good agreement between model and observational data. We use cut-offs in the signal integration along the line-of-sight at either $180\,\mathrm{Mpc}\,h^{-1}$ or $90\,\mathrm{Mpc}\,h^{-1}$ for the fits to the full MegaZ sample and find consistent results with errors of the same order, see below. The signals for w_gg and $w_\mathrm{g+}$ both have similar signal-to-noise when truncating at these two values of $\bar{\Pi}_\mathrm{max}$. The correlation functions for the two MegaZ redshift bins have been truncated at $\bar{\Pi}_\mathrm{max} = 90\,\mathrm{Mpc}\,h^{-1}$ throughout.

5.4 Measurement details

In the following we provide details about different steps in the analysis of the galaxy samples leading to the correlations functions w_gg and $w_\mathrm{g+}$, and the subsequent parameter constraints. We concentrate on the new MegaZ LRG sample, presenting the determination and quality of photometric redshifts, the measurement of galaxy shapes and the correlation functions, as well as the routine used to fit the models of Sect. 5.3 to the data.

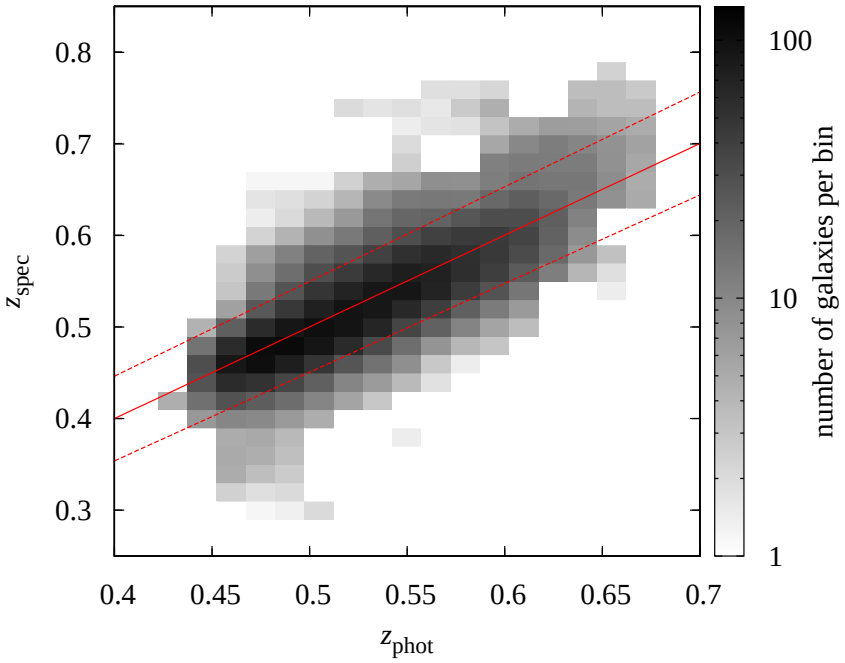

Figure 5.12: Binned histogram of spectroscopic redshifts from 2SLAQ and photometric redshift estimates from the MegaZ LRG catalogue. We used about 5000 galaxies contained in the verification sample from 2SLAQ. Note that the shading of the bins is logarithmic. The solid line indicates a one-to-one relation between spectroscopic and photometric redshifts, coinciding with the mean trend to high accuracy. The dotted lines correspond to the $\pm 1\sigma$ scatter.

5.4.1 Photometric redshifts

The MegaZ LRG sample relies on photometric redshift information obtained from the SDSS *ugriz* photometric bands, using the spectroscopic calibration from the 2SLAQ survey (Cannon et al. 2006) which overlaps with SDSS on a number of patches around the celestial equator. In the overlap region about 13000 galaxies were identified as LRGs in the redshift range $0.4 \leq z \leq 0.7$. This sample could then be used to both calibrate and test the photometric redshift estimation (Collister et al. 2007; Abdalla et al. 2008).

About 8000 galaxies were used to train the neural network photometric redshift code ANNz (Collister & Lahav 2004), leaving approximately 5100 galaxies to verify the estimates (Collister et al. 2007; Abdalla et al. 2008). We use this latter subset to assess the quality of photometric redshifts, as shown in Fig. 5.12. Due to the homogeneity of the population and the strong Balmer break, LRGs are particularly suited for accurate photometric redshift estimation (Eisenstein et al. 2003), so that a small scatter of photometric redshifts around the spectroscopically determined values can be expected. Accurate photometric redshifts are paramount for our analysis in order to guarantee that the gI contribution dominates galaxy number density-shape correlations, see Sect. 5.3.2.

We indeed find excellent photometric redshifts for the MegaZ LRG data, with the distribution of the differences between photometric redshift estimate and spectroscopic redshift having a mean of zero. As a consequence, the mean trend of the photometric redshift distribution, given a spectroscopic redshift, is indistinguishable from a one-to-one relation, see Fig. 5.12. The number of outliers, i.e. galaxies with a difference between photometric redshift $\bar{z}$ and spectroscopic redshift z largely exceeding the typical scatter, is always less than 3 % for a given photometric redshift bin in the range $0.45 < \bar{z} < 0.65$. The distribution of differences between photometric and spectroscopic redshift is well fit by a Gaussian with width $0.024(1 + z)$ (corresponding to the dotted lines in the figure), in good agreement with the results by Collister et al. (2007) who find a very similar scatter in the range $0.45 < \bar{z} < 0.50$ in which most galaxies of our sample reside. Their scatter increases by up to 50 % for higher photometric redshifts in the range $0.60 < \bar{z} < 0.65$.

To compute the model correlation function for the MegaZ LRG sample, we require the probability of a redshift z given the photometric redshift estimate $\bar{z}_i$, entering the probability distributions in (5.34), (5.36), and (5.39). These conditional distributions are extracted from the two-dimensional histogram shown in Fig. 5.12 by a vertical section at $\bar{z}_i$. The unconditional distribution of photometric redshifts entering (5.40), (5.42), and (5.43) via (5.41) is obtained by summing the entries of each column in the histogram.

Note that we use the redshift distribution of Fig. 5.12 for both the shape-selected and the full number density sample as we find that their redshift distributions agree to good accuracy. This is not obvious because the images of the galaxies selected for shape measurement need to have a certain minimum angular size. We trace the agreement of the two redshift distributions for the MegaZ sample back to a rough balance between the effect that galaxies at higher redshift, i.e. at larger distance, appear smaller and the counter-acting effect that for a given range of apparent magnitudes galaxies at higher redshift are on average intrinsically brighter and thus have larger physical sizes.

5.4.2 Galaxy shape and correlation function measurement

In addition to the data provided by the MegaZ LRG and SDSS catalogues we require galaxy ellipticities to infer the intrinsic and gravitational shear. Like Mandelbaum et al. (2006), Hirata et al. (2007), and Mandelbaum et al. (2009) we make use of the measurements by Mandelbaum et al. (2005) who obtained the shapes of more than 30 million galaxies with a limiting magnitude of $r = 21.8$ from SDSS imaging data. The shape measurement pipeline is described in detail in Mandelbaum et al. (2005), with marginal modifications as summarised in Mandelbaum et al. (2006).

The 'Reglens' pipeline fits Gaussian profiles with elliptical isophotes to galaxy images in the r and i filters from SDSS atlas images, i.e. highly resolved postage stamp images of SDSS objects (Stoughton et al. 2002). The components of the galaxy ellipticity are then given by

$$e_1 = \frac{1-r^2}{1+r^2}\,\cos 2\phi\,; \qquad e_2 = \frac{1-r^2}{1+r^2}\,\sin 2\phi\,, \tag{5.44}$$

where r is the ratio of the semi-axes of the ellipse and ϕ the position angle of the major axis. In practice a number of corrections have to be applied to the images to obtain this ellipticity, most importantly to mitigate the effects of the smearing and circularisation of galaxy images by the PSF and the introduction of spurious ellipticities due to optical distortions in the instrument (see Mandelbaum et al. 2006 for details). As a consequence of these effects the ellipticity (5.44) is not an unbiased estimate of the total shear, but one needs to take into account the response of the image ellipticity to a shear via $\gamma_i = \langle e_i \rangle / (2\mathcal{R})$ with $\mathcal{R} \approx 0.87$ (Kaiser et al. 1995; Bernstein & Jarvis 2002).

Only galaxies with high-quality shape measurements enter the correlation functions, which amounts to about half the total number of galaxies in MegaZ LRG, see Table 5.1. The fraction of galaxies with shape information is almost independent of redshift, but depends strongly on galaxy magnitudes and observing conditions. The variation of the fraction of galaxies with shapes due to the latter effects is accounted for in the random galaxy catalogues needed for the computation of the correlation functions.

We use the Landy-Szalay estimator (Landy & Szalay 1993) to compute the three-dimensional galaxy clustering correlation function. It is given by

$$\hat{\xi}_{\mathrm{gg}}(R, \Pi, z) = \frac{DD - 2DR + RR}{RR}\,, \tag{5.45}$$

where DD denotes the number of galaxy pairs in the MegaZ LRG catalogue, RR is the number of galaxy pairs in a random catalogue, and DR is the number of pairs with one galaxy in the MegaZ LRG sample and one in the random catalogue. All these pair counts are done for galaxies at redshift z, with transverse comoving separation R and comoving line-of-sight separation Π. In the case of the MegaZ LRG samples, R and Π are determined from the photometric redshift estimates (and hence correspond to $\bar{R}$ and $\bar{\Pi}$ in the notation of the foregoing section). For details on the random catalogue generation and treatment see Mandelbaum et al. (2006).

The Landy-Szalay estimator is particularly robust because any additive bias in the data is cancelled to first order. To keep this property, Mandelbaum et al. (2006) generalised (5.45) to number density-shape cross-correlations by defining the estimator

$$\hat{\xi}_{\mathrm{g}+}(R,\Pi,z) = \frac{S_+D - S_+R}{R_SR}\,, \tag{5.46}$$

where S_+D stands for the correlation between all galaxies in the catalogue, tracing the density field, and those from the subset with shape information in MegaZ LRG, given by

$$S_+D = \sum_{i\neq j|R,\Pi,z} \frac{e_+(j|i)}{2\mathcal{R}}\,. \tag{5.47}$$

Here, $e_+(j|i)$ denotes the radial component of the ellipticity of galaxy j measured with respect to the direction towards galaxy i out of the number density sample. A similar equation holds for S_+R, but in this case the galaxy of the number density sample is taken from the random catalogue. Since the shape and number density samples have different properties, we also use different random catalogues R_S and R, respectively, so that the denominator of (5.47) is given by the number of pairs R_SR with one galaxy from catalogue R_S and one from R. Again, all galaxies are selected from bins in R, Π, and z.

We use 10 logarithmically spaced bins in transverse separation in the range $0.3-60\,\mathrm{Mpc}\,h^{-1}$ for the MegaZ LRG data and re-bin the existing correlation function for the SDSS LRG and L4 samples accordingly. Bins in line-of-sight separation have a width of $\Delta\Pi = 10\,\mathrm{Mpc}\,h^{-1}$. The projected correlation functions are computed by summing the three-dimensional correlation functions over Π and multiplying by $\Delta\Pi$, i.e. using a Riemannian sum to approximate (5.40), (5.42), and (5.43). The cut-off in this stacking process is $\Pi_{\max} = 60\,\mathrm{Mpc}\,h^{-1}$ for the spectroscopic data sets, capturing virtually all of the signal (Mandelbaum et al. 2006; Hirata et al. 2007; Mandelbaum et al. 2009). MegaZ LRG correlation functions are computed for $\Pi_{\max} = 90\,\mathrm{Mpc}\,h^{-1}$ and $\Pi_{\max} = 180\,\mathrm{Mpc}\,h^{-1}$, where we will investigate the effect of these truncations in more detail in Sect. 5.5.1.

5.4.3 Fitting routine

We perform the fits to the data via weighted least squares minimisation, using the reduced χ^2 at the minimum to quantify the goodness of fit. To obtain confidence regions, we compute the likelihood according to $L \propto \exp(-\chi^2/2)$, i.e. assuming Gaussianity. The posterior probability in parameter space is computed via Bayes' theorem, using a top-hat prior that is truncated far outside the regime where the likelihood deviates substantially from zero. When doing three-parameter fits, we marginalise in each case over the hidden parameter. $1\,\sigma$- and $2\,\sigma$ confidence contours are then defined by the regions containing 68.3 % or 95.4 % of the (marginalised) posterior.

Covariances of the correlation functions are determined from the data using a jackknife with 256 regions, thereby accounting for shape noise, shot noise, cosmic variance, and shape

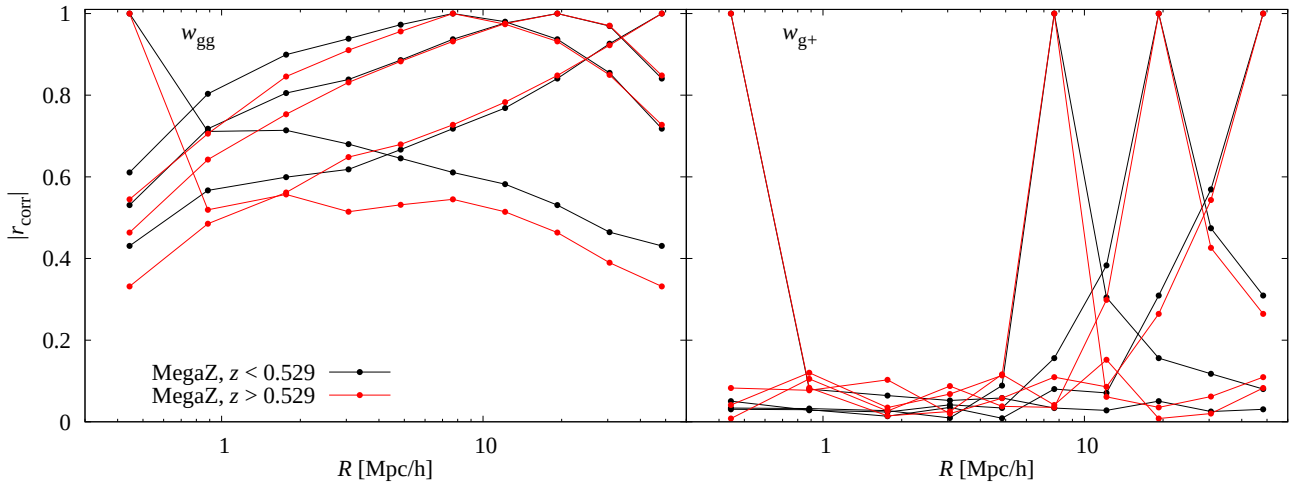

Figure 5.13: Correlation coefficients $r_{\rm corr}$ of the correlation functions $w_{\rm gg}$ (left panel) and $w_{\rm g+}$ (right panel) for the redshift-binned MegaZ samples. Shown is the modulus of $r_{\rm corr}$ for the 10 R bins correlated with the bin at the smallest transverse separation R considered ($R = 0.44\,{\rm Mpc}\,h^{-1}$), the bin at the smallest R used for the fits ($R = 7.67\,{\rm Mpc}\,h^{-1}$), the centre bin used for the fits ($R = 19.25\,{\rm Mpc}\,h^{-1}$), and the bin at the largest R ($R = 48.30\,{\rm Mpc}\,h^{-1}$). Black curves correspond to the low-redshift bin, red curves to the high-redshift bin. Note that the black and red lines for the correlations of $w_{\rm g+}$ with $R = 0.44\,{\rm Mpc}\,h^{-1}$ nearly coincide.

measurement errors. Since these jackknife covariances, obtained from a finite number of realisations, are noisy, their direct inverse required for the χ^2 is biased (Hirata et al. 2004; Hartlap et al. 2007). We employ the corrected estimator for the inverse covariance presented in Hartlap et al. (2007) given by (4.65). We again denote the dimension of the data vector by d and the number of realisations used to estimate the covariance by n. For the SDSS samples ($d = 10$, $n = 50$) we find $\mathcal{F} \approx 0.776$, and for MegaZ ($d = 10$, $n = 256$) $\mathcal{F} \approx 0.957$, the latter result being in excellent agreement with the simulations described in Appendix D of Hirata et al. (2004).

To study the characteristics of the covariances, we compute the correlation coefficient between different transverse separation bins,

$$r_{\rm corr}(R_i, R_j) = \frac{{\rm Cov}(R_i, R_j)}{\sqrt{{\rm Cov}(R_i, R_i)\,{\rm Cov}(R_j, R_j)}}\,, \tag{5.48}$$

where ${\rm Cov}(R_i, R_j)$ is the covariance of the projected correlation functions between different transverse separations. In Fig. 5.13 we have plotted $r_{\rm corr}$ for the covariances of both $w_{\rm gg}$ and $w_{\rm g+}$ for the two MegaZ LRG samples at low and high redshift. While $w_{\rm g+}$ decorrelates quickly with only moderate correlation between neighbouring bins on the largest scales, $w_{\rm gg}$ features strong positive, long-range correlations particularly on the larger scales used for the fits. The correlation coefficients have similar values for the two redshift bins, the bin for $z < 0.529$ showing generally slightly higher correlation. For the spectroscopic SDSS samples we find a similar correlation structure for $w_{\rm g+}$, but much weaker correlations in $w_{\rm gg}$.

The difference in correlation length between $w_{\rm gg}$ and $w_{\rm g+}$ is caused by the different kernels in the Hankel transformation between power spectrum and correlation function, see (5.33) and (5.38). Since $J_2(x)$ decreases faster than $J_0(x)$ for increasing x, we expect $w_{\rm gg}$ to generally feature stronger correlations. A given transverse separation R between galaxies is observed under a smaller angle if these galaxy pairs are located at higher redshift, and it is this angle which enters the argument of the Bessel functions. Therefore the correlation present in $w_{\rm gg}$ is more pronounced in the MegaZ LRG samples, which are at considerably higher redshift than the other SDSS samples.

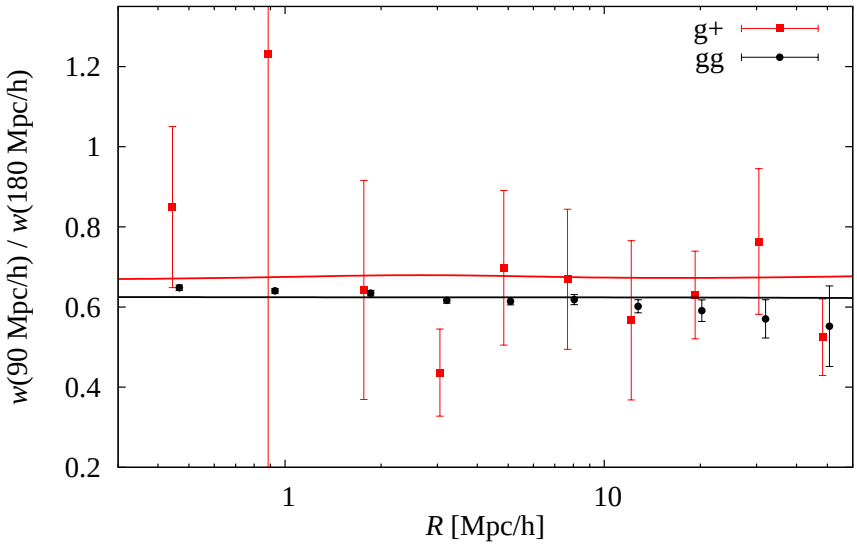

Figure 5.14: Effect of the cut-off in Π in the projection of the three-dimensional correlation functions along the line of sight. Shown is the ratio of the projected correlation function computed for $\bar{\Pi}_{\max} = 90\,\mathrm{Mpc}\,h^{-1}$ over the correlation function obtained with $\bar{\Pi}_{\max} = 180\,\mathrm{Mpc}\,h^{-1}$, for both the galaxy clustering signal (gg, in black) and number density-shape correlations (g+, in red). Points are computed from the MegaZ LRG data, using the full range in redshifts. Note that the black points have been slightly offset horizontally for clarity. The lines are obtained from the model, including a contribution by galaxy-galaxy lensing. Fair agreement between data and model on these ratios is found for both the gg and g+ terms. Note that the error bars at different transverse separations are strongly correlated.

5.5 Results

In this section we present the resulting projected correlation functions for the different galaxy samples. We verify that our modelling correctly takes the line-of-sight truncation of the correlation functions into account, determine the galaxy bias from the galaxy clustering signals, and place constraints on an intrinsic alignment model using number density-shape correlations.

5.5.1 Scaling with line-of-sight truncation

To test whether both the data and the model show the same behaviour when varying $\bar{\Pi}_{\max}$, we compute both $w_{\mathrm{g+}}$ and w_{gg} for the MegaZ LRG sample according to (5.40) for $\bar{\Pi}_{\max} = 90\,\mathrm{Mpc}\,h^{-1}$ and $\bar{\Pi}_{\max} = 180\,\mathrm{Mpc}\,h^{-1}$. Then we compare the ratio of $w_{\mathrm{g+}}$ with cut-off $\bar{\Pi}_{\max} = 90\,\mathrm{Mpc}\,h^{-1}$ over $w_{\mathrm{g+}}$ with cut-off $\bar{\Pi}_{\max} = 180\,\mathrm{Mpc}\,h^{-1}$ (and likewise for w_{gg}) obtained from the model to the corresponding ratio computed from the observations. Since the projected correlation functions with the different cut-offs are strongly correlated, we compute the errors on the ratio again via jackknifing. Note that due to these correlations the actual errors on the ratio are significantly smaller than if one assumed them to be independent. Note furthermore that the ratio also inherits a significant correlation between different transverse separations from the individual projected correlation functions, in particular for w_{gg}, see Fig. 5.13.

In Fig. 5.14 we have plotted the ratios of the projected correlation functions with the different cut-offs. The model prediction for this ratio is in good agreement with the data, yielding a loss of about 40 % for galaxy clustering and $\sim 1/3$ for number density-shape correlations (including the gG contribution) when reducing $\bar{\Pi}_{\max}$ from $180\,\mathrm{Mpc}\,h^{-1}$ to $90\,\mathrm{Mpc}\,h^{-1}$. Furthermore, both model and data are consistent with the fact that the loss of signal due to the smaller cut-off in

Table 5.2: Galaxy bias b_g for the different galaxy samples used. Given is the $1\,\sigma$-error on b_g, marginalised over C, and the reduced χ^2 for 3 degrees of freedom. The value for the SDSS L4 sample has been derived from the results by Hirata et al. (2007).

sample	b_g	χ^2_red
MegaZ, all z, $\Pi_\mathrm{max} = 90\,\mathrm{Mpc/h}$	$1.89^{+0.05}_{-0.05}$	0.15
MegaZ, all z, $\Pi_\mathrm{max} = 180\,\mathrm{Mpc/h}$	$1.85^{+0.05}_{-0.05}$	0.40
MegaZ, $z < 0.529$, $\Pi_\mathrm{max} = 90\,\mathrm{Mpc/h}$	$1.82^{+0.06}_{-0.06}$	0.01
MegaZ, $z > 0.529$, $\Pi_\mathrm{max} = 90\,\mathrm{Mpc/h}$	$2.05^{+0.06}_{-0.06}$	2.45
SDSS LRG, $z < 0.27$	$1.88^{+0.10}_{-0.10}$	0.82
SDSS LRG, $z > 0.27$	$1.89^{+0.07}_{-0.07}$	0.97
SDSS L4 red	1.04	–

Π is roughly constant in transverse separation.

The gg ratio, which has significantly smaller errors than the g+ ratio, may favour a gentle decrease with R contrary to the model. However, we do not consider this tendency as significant because at a transverse pair separation of $R \lesssim 1\,\mathrm{Mpc}\,h^{-1}$ clustering is non-linear, and non-linear galaxy bias effects may not cancel in the ratio anymore. Moreover, keep in mind the strong correlation of the errors at different transverse separations.

5.5.2 Galaxy bias

To relate the observed galaxy number density-intrinsic correlations (plus the corrections due to galaxy-galaxy lensing) to the matter-intrinsic correlations which generate intrinsic alignments, the galaxy bias b_g needs to be measured. We compute b_g from the galaxy clustering signal, assuming a linear bias model, but using the full matter power spectrum which should extend the validity of the fits into the quasi-linear regime (see also Hirata et al. 2007 who test several methods to determine the galaxy bias in a similar context). Note that all our considerations rely on the hypothesis that we have assumed the correct cosmological model.

The redshift averaging and the projection along the line of sight of w_gg is performed according to (5.40) for the photometric MegaZ LRG samples and following (5.43) for the SDSS LRG samples. We do not repeat the bias measurement for the SDSS L4 sample but adopt the value determined by Hirata et al. (2007), rescaled to our value of σ_8 by employing $b_\mathrm{g} \propto \sigma_8^{-1}$, which results in $b_\mathrm{g} = 1.04$. To all model projected correlation functions w_gg we add a constant C as a further fit parameter to account for the undetermined integral constraint on the numerator of the Landy-Szalay estimator (Landy & Szalay 1993; see also Hirata et al. 2007) due to the unknown mean galaxy number density. For the fit we discard scales $R < 6\,\mathrm{Mpc}\,h^{-1}$, i.e. the five data points at the smallest R where the assumption of a linear bias is expected to break down (Tasitsiomi et al. 2004; Mandelbaum et al. 2006).

In Fig. 5.15 the projected correlation functions w_gg for the two MegaZ LRG redshift bins and the two SDSS LRG redshift bins are shown. Note that the SDSS LRG samples have not been split further into luminosity bins because the full SDSS LRG sample, divided into the two redshift bins, is used to trace the galaxy number density field. In each case we also plot the best-fit models, indicating that the model is a good description of the data on scales where non-linear bias is not important. At smaller transverse separation, which have been excluded from the fits as marked by the grey region, the data have increasingly larger positive offsets with respect to the model, caused by non-linear clustering effects.

The best-fit values for b_g, marginalised over C, are listed in Table 5.2. We find good

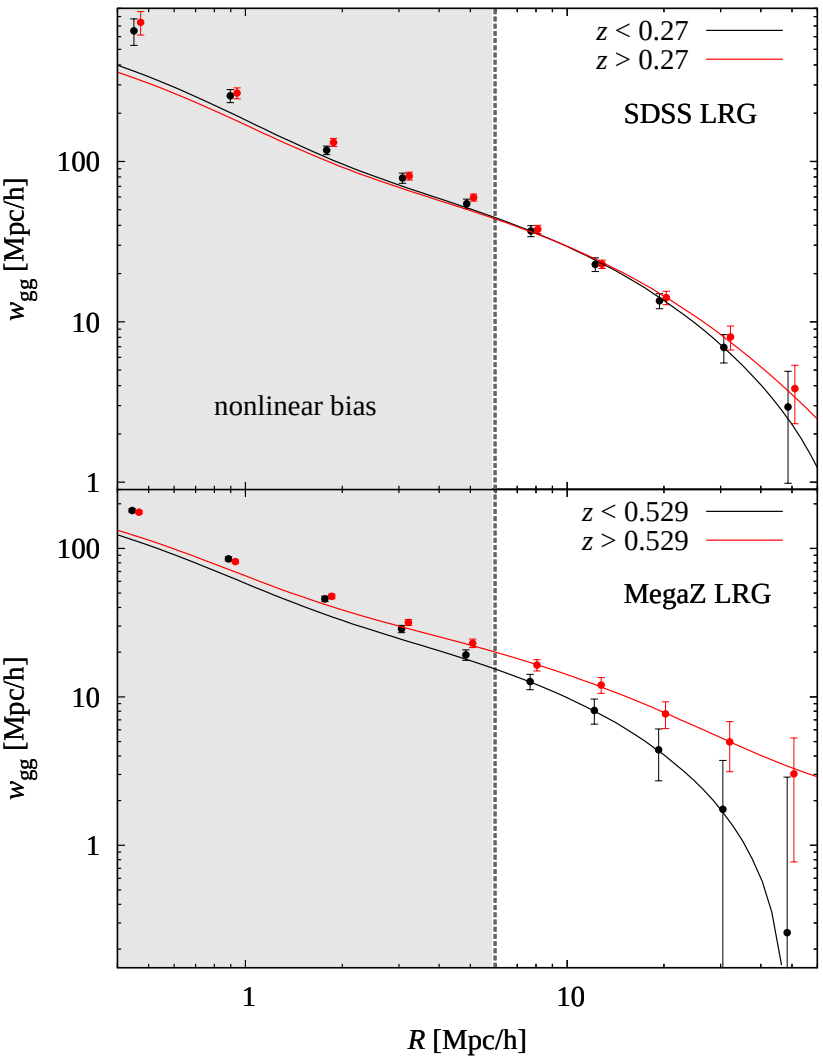

Figure 5.15: Projected correlation function $w_{\rm gg}$ as a function of comoving transverse separation R. *Top panel*: For the SDSS LRG sample with redshifts smaller than 0.27 (black) and with redshifts larger than 0.27 (red). *Bottom panel*: For the MegaZ LRG sample with photometric redshifts smaller than 0.529 (black) and with photometric redshifts larger than 0.529 (red). Note that the red points have been slightly offset horizontally for clarity, and that the error bars are strongly correlated. In addition we show the best-fit models as black and red curves, respectively. Only the data points outside the grey region have been used for the fits to avoid the region with non-linear bias.

agreement for the best-fit galaxy bias, determined for the different $\Pi_{\rm max}$ in the MegaZ LRG data, again confirming that we are correctly modelling the truncation in the line-of-sight projection. Splitting the MegaZ LRG data into two redshift bins at $z = 0.529$, we obtain a stronger bias for the bin at higher redshift. This is expected as the bin with $z > 0.529$ contains on average significantly more luminous galaxies which are more strongly biased, see Fig. 5.8. Only the high-redshift MegaZ LRG sample yields a reduced χ^2 that significantly exceeds unity which we trace back to the strong correlations between errors as the plot in Fig. 5.15 suggests a good fit. For the low-redshift bin of the MegaZ LRG sample we obtain a very small reduced χ^2 of 0.01, but cannot identify any sources of an over-estimation of the errors. The SDSS LRG samples yield a similar galaxy bias compared to the full MegaZ sample, with no significant evolution in redshift.

Using again that the bias scales as $b_{\rm g} \propto \sigma_8^{-1}$, our findings for the SDSS LRG samples can be compared to the results for the equivalent bias model in Hirata et al. (2007) who use $\sigma_8 = 0.751$. Rescaling the values of Table 5.2 to this value of σ_8, we get $b_{\rm g} = 2.00 \pm 0.11$ for the low-redshift sample and $b_{\rm g} = 2.01 \pm 0.07$ for the high-redshift sample. These values agree comfortably within $1\,\sigma$, with $b_{\rm g} = 2.01 \pm 0.12$ for $z < 0.27$ and $b_{\rm g} = 1.97 \pm 0.07$ for $z > 0.27$ as found by Hirata et al. (2007). Note that the latter analysis used a narrower range in transverse separation with $R = 7.5 - 47\,{\rm Mpc}\,h^{-1}$ compared to $R = 6 - 60\,{\rm Mpc}\,h^{-1}$ considered in this work.

5.5.3 Intrinsic alignment fits

With the galaxy bias at hand we can now proceed to fit models of intrinsic alignments via $w_{\mathrm{g+}}$. The NLA model (5.12) features in principle no free parameters, apart from the overall amplitude. Within the physical picture of this model the amplitude quantifies how the shape of a galaxy responds to the presence of a tidal gravitational field. It is likely that this response depends on the galaxy population under consideration, and thus possibly features an additional evolution with time and hence redshift dependence (on top of the one inherent to the NLA model), as well as a variation with galaxy luminosity.

Therefore we will use a more flexible prescription for the gI power spectrum which we set to

$$P_{\mathrm{gI}}^{\mathrm{model}}(k,z,L) = A\; b_{\mathrm{g}}\; P_{\delta\mathrm{I}}(k,z)\; \left(\frac{1+z}{1+z_0}\right)^{\eta_{\mathrm{other}}} \left(\frac{L}{L_0}\right)^{\beta}\,, \tag{5.49}$$

where $z_0 = 0.3$ is an arbitrary pivot redshift, and L_0 a pivot luminosity which corresponds as before to an absolute r-band magnitude of -22. The matter-intrinsic power spectrum $P_{\delta\mathrm{I}}$ is given by (5.12), including the normalisation to SuperCOSMOS. This model contains the three free parameters $\{A, \beta, \eta_{\mathrm{other}}\}$, and it has a fixed dependence on transverse scales.

The additional amplitude parameter A and the luminosity term can be taken out of all integrations leading to $w_{\mathrm{g+}}$ because they neither depend on redshift nor comoving distance, so that they can be varied in the likelihood analysis with low computational cost. The additional redshift term containing η_{other} depends on the integration variable in (5.34) though. To facilitate the likelihood analysis for the MegaZ LRG samples with photometric redshifts, we assume that this term can be taken out of the integration and is evaluated at the mean photometric redshift $\bar{z}_{\mathrm{m}}$ of the two galaxy samples in (5.34). This approximation should hold to fair accuracy if the corresponding redshift probability distributions are sufficiently narrow, i.e. for a small photometric redshift uncertainty.

The additional redshift dependence is then integrated over in the averaging process in (5.40) and (5.42) for photometric and spectroscopic samples, respectively. Since the assumption of a linear bias also enters the model (5.49), we again limit the parameter estimation to scales $R > 6\,\mathrm{Mpc}\,h^{-1}$. Note that we do not explicitly propagate the errors on the galaxy bias determined in the foregoing section through to the uncertainty on intrinsic alignment parameters as we find them to be marginal compared to the measurement error in $w_{\mathrm{g+}}$.

In Fig. 5.16, the projected correlation functions for the full MegaZ LRG sample as well as for the two MegaZ LRG redshift bins, split at $z = 0.529$, are plotted. We first fit the data using only A as a free parameter and keeping $\beta = \eta_{\mathrm{other}} = 0$ fixed, with the fit results on A presented in Table 5.3. On the scales usable for the fit, the best-fit gI model, which is also plotted in Fig. 5.16, traces the data points well, whereas for $R \lesssim 1\,\mathrm{Mpc}\,h^{-1}$ points lie several σ above and below the model curve, possibly indicating strongly non-linear effects. The nature of these deviations is unknown, but since they occur on scales whose order corresponds to the virial radius of LRGs, one may hypothesise that at these ranges of R complicated dependencies on the tidal field or a change in the intrinsic alignment mechanism play a role.

By default we include the galaxy-galaxy lensing term in the modelling for the photometric redshift data, but the table also lists results for A when discarding the gG term. Since the gG signal yields a negative contribution to $w_{\mathrm{g+}}$, a lower amplitude A than in the case including galaxy-galaxy lensing is needed to get a good fit to the data. The change in amplitude ranges between 6 % for the low redshift MegaZ sample and 10 % for the high redshift sample. Given that we obtain $A \sim 2$, i.e. about twice the value of the intrinsic alignment amplitude than assumed for Fig. 5.10, which suppresses the gG/gI ratio by a factor of 2, good agreement is

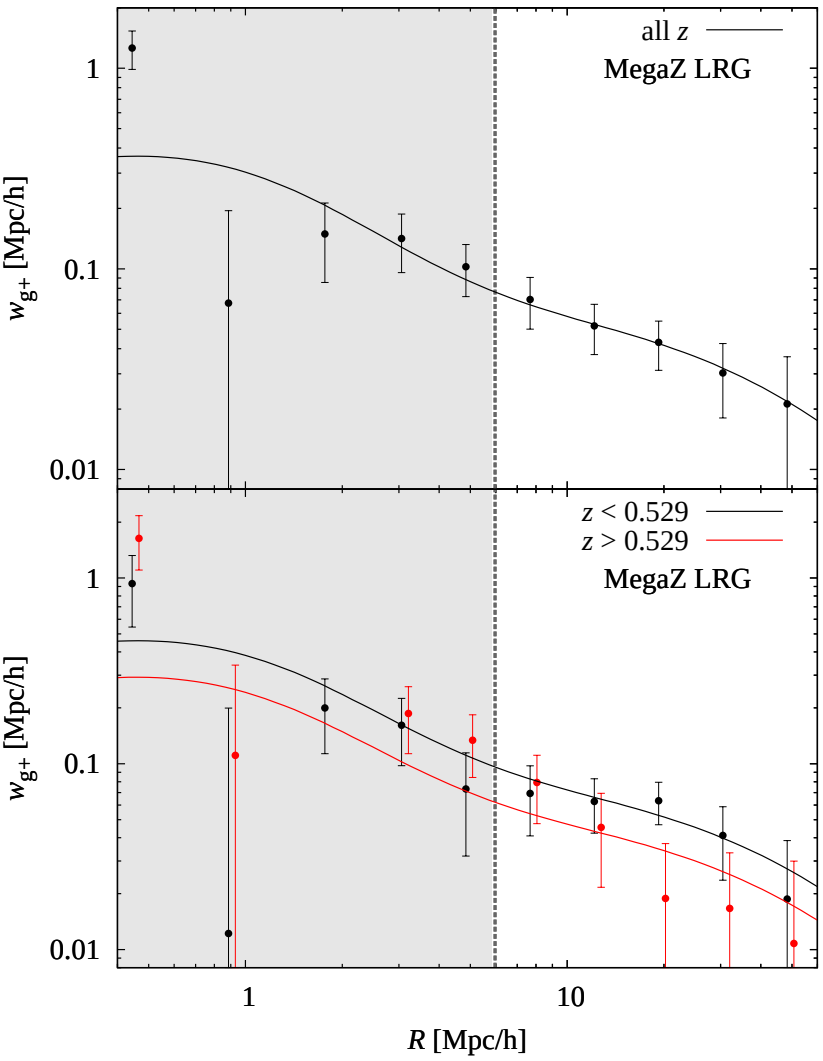

Figure 5.16: Projected correlation function w_{g+} as a function of comoving transverse separation R for different MegaZ LRG subsamples. *Top panel*: Shown is w_{g+} for the MegaZ sample with the full range in redshifts. The black curve corresponds to the best-fit model when only varying the amplitude A, without contributions by galaxy-galaxy lensing. *Bottom panel*: Same as above, but for the MegaZ sample split into two photometric redshift bins, where results for $z < 0.529$ are shown in black, and for $z > 0.529$ in red. Note that the red points have been slightly offset horizontally for clarity, and that the error bars are correlated. Only the data points outside the grey region have been used for the fits.

found with the prediction of that figure. Also, we find again good agreement between the fits for the full MegaZ samples with different $\Pi_{\max}$.

We also perform the analysis on w_{g+} for the SDSS LRG and L4 data, which Hirata et al. (2007) have done before, but using only a generic power-law dependence for the dependence on R. The LRG data are divided into three luminosity bins, all of which are in addition split into two redshift bins at $z = 0.27$, see Table 5.1. As redshifts are determined spectroscopically in this case, we use (5.42) to compute w_{g+}. The resulting correlation functions and their best-fit models are shown in Fig. 5.17, the resulting parameter constraints on A listed as well in Table 5.3.

In general, the dependence on R given by the NLA model describes the data reasonably well, yielding reduced χ^2 values of order unity. Only the high-redshift SDSS LRG samples tend to a χ^2 that significantly exceeds unity which is caused by an excess signal around $R = 10\,\mathrm{Mpc}\,h^{-1}$ of unknown origin, as can be seen in Fig. 5.17, bottom panel. In all cases the amplitude A is higher than the original SuperCOSMOS normalisation, which would correspond to $A = 1$. As is obvious from the exemplary posterior probabilities for A shown in Fig. 5.18, the results for the different galaxy samples are clearly inconsistent for an intrinsic alignment model that has only A as a free parameter.

The SDSS LRGs span a very similar and relatively short range in redshifts, so that no strong evolution with redshift is expected in these subsamples. Then it is evident from the fit

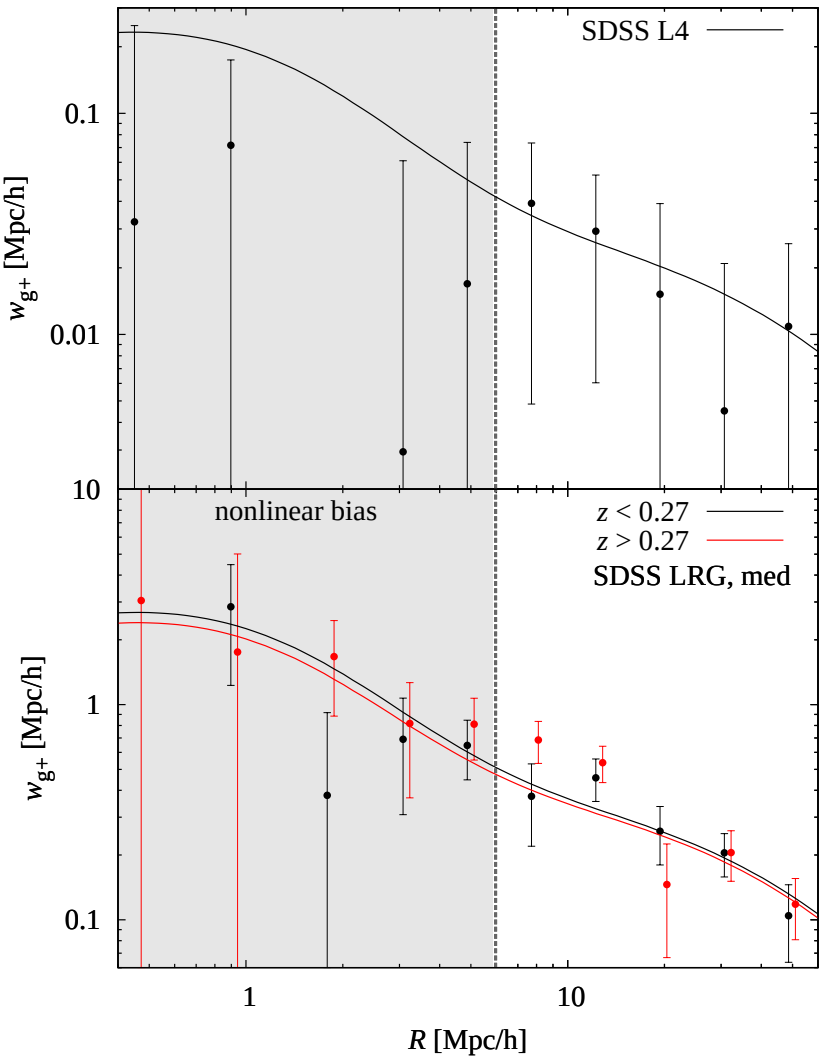

Figure 5.17: Projected correlation function w_{g+} as a function of comoving transverse separation R for different SDSS samples. *Top panel*: Shown is w_{g+} for the SDSS L4 sample. The black curve corresponds to the best-fit model when only varying the amplitude A. *Bottom panel*: Same as above, but for the SDSS LRG medium brightness sample split into two redshift bins, where results for $z < 0.27$ are shown in black, and for $z > 0.27$ in red. Note that the red points have been slightly offset horizontally for clarity, and that the error bars are correlated. Only the data points outside the grey region have been used for the fits.

results in Table 5.3 that the intrinsic alignment amplitude increases with galaxy luminosity, with the brightest sample attaining a high amplitude roughly ten times the one found for SuperCOSMOS. These findings are compatible with the results of the power-law fits to the SDSS samples by Hirata et al. (2007). Despite a mean luminosity which is 50 % higher than that of the low-redshift MegaZ LRG sample, the high-redshift sample has a smaller amplitude parameter A, indicative of a decrease of the intrinsic alignment amplitude with redshift beyond the redshift evolution in the NLA model.

Therefore we repeat the fits to w_{g+} for different combinations of samples, now allowing for an additional redshift and luminosity dependence according to (5.49). The resulting two-dimensional marginalised confidence contours and marginal one-dimensional posterior distributions for the parameter set $\{A, \beta, \eta_{\text{other}}\}$ are shown in Fig. 5.19. The corresponding marginal $1\,\sigma$ errors on these parameters and the goodness of fit are given in Table 5.4. In the computation of marginalised constraints we assumed flat priors in the ranges $A \in [0; 10]$, $\eta_{\text{other}} \in [-10 : 10]$, and $\beta \in [-5 : 5]$.

Combining all SDSS LRG samples we can constrain β well, i.e. the power-law slope of the luminosity evolution of the intrinsic alignment amplitude, while the errors on η_{other} remain large, as expected from the considerations made above. Adding in the two redshift-binned MegaZ LRG samples greatly improves constraints on the extra redshift evolution and also narrows down the possible values of A. The marginalised $1\,\sigma$ contours for the SDSS LRG only

Table 5.3: $1\,\sigma$ confidence limits on the amplitude A of the gI power spectrum, assuming no extra evolution with redshift or luminosity, i.e. fixing $\eta_{\rm other} = 0$ and $\beta = 0$. We also give the mean redshift and the mean luminosity $\langle L\rangle / L_0$ for each sample, as well as the reduced χ^2 of the fit for 4 degrees of freedom. The last column contains the fit results when the galaxy-galaxy lensing signal is not taken into account for the modelling. We find that the χ^2 does not change significantly in this case due to the very similar R-dependence of the gI and gG signals.

sample	$\langle z\rangle$	$\langle L\rangle / L_0$	A	$\chi^2_{\rm red}$	A (w/o gG)
MegaZ, all z, $\Pi_{\rm max} = 90\,$Mpc/h	0.56	1.07	$1.88^{+0.33}_{-0.30}$	0.02	$1.73^{+0.32}_{-0.30}$
MegaZ, all z, $\Pi_{\rm max} = 180\,$Mpc/h	0.56	1.07	$1.81^{+0.38}_{-0.31}$	0.25	$1.66^{+0.31}_{-0.38}$
MegaZ, $z < 0.529$, $\Pi_{\rm max} = 90\,$Mpc/h	0.50	0.83	$2.34^{+0.51}_{-0.53}$	0.32	$2.19^{+0.51}_{-0.53}$
MegaZ, $z > 0.529$, $\Pi_{\rm max} = 90\,$Mpc/h	0.59	1.22	$1.51^{+0.45}_{-0.45}$	0.40	$1.36^{+0.45}_{-0.48}$
SDSS LRG, $z < 0.27$, faint	0.21	1.06	$3.02^{+1.19}_{-1.13}$	1.30	
SDSS LRG, $z > 0.27$, faint	0.32	1.07	$4.45^{+0.98}_{-0.99}$	1.82	
SDSS LRG, $z < 0.27$, med	0.22	1.50	$6.78^{+1.03}_{-1.06}$	0.51	
SDSS LRG, $z > 0.27$, med	0.31	1.50	$5.80^{+0.89}_{-0.83}$	2.03	
SDSS LRG, $z < 0.27$, bright	0.22	2.13	$8.74^{+1.43}_{-1.38}$	1.15	
SDSS LRG, $z > 0.27$, bright	0.31	2.12	$9.35^{+1.88}_{-1.88}$	2.07	
SDSS L4	0.10	0.25	$1.13^{+0.62}_{-0.68}$	0.14	

Table 5.4: $1\,\sigma$ marginalised confidence limits on the amplitude A, the slope of the additional redshift dependence $\eta_{\rm other}$, and the luminosity dependence β of the intrinsic alignment model (5.49). Flat priors in the ranges $A \in [0; 10]$, $\eta_{\rm other} \in [-10 : 10]$, and $\beta \in [-5 : 5]$ have been applied. In addition we list the number of samples $N_{\rm sample}$ used in joint fit and the reduced χ^2. The number of the degrees of freedom is given by $5\,N_{\rm sample} - 3$.

sample	$N_{\rm sample}$	A	$\eta_{\rm other}$	β	$\chi^2_{\rm red}$
SDSS LRG	6	$3.69^{+0.68}_{-0.59}$	$0.20^{+2.14}_{-2.00}$	$1.20^{+0.30}_{-0.39}$	1.37
SDSS LRG + MegaZ LRG	8	$3.39^{+0.53}_{-0.44}$	$-3.60^{+0.80}_{-0.83}$	$1.00^{+0.30}_{-0.27}$	1.27
SDSS LRG + MegaZ LRG + SDSS L4	9	$3.24^{+0.38}_{-0.34}$	$-3.40^{+0.80}_{-0.65}$	$1.10^{+0.20}_{-0.14}$	1.13

and the SDSS + MegaZ LRG fits are marginally consistent, and the reduced χ^2 improves by 7 % when adding the MegaZ LRG data. Incorporating in addition the SDSS L4 sample at low redshift and with low mean luminosity, constraints on all parameters, in particular β and A, tighten further. The inclusion of the L4 sample yields largely consistent confidence regions and decreases the reduced χ^2 close to unity.

The joint fit of all considered samples clearly favours an increase of the intrinsic alignment signal with galaxy luminosity. Indeed we find that $\beta < 0.5$ is excluded at the $4\,\sigma$ level. The data also prefer a decrease of intrinsic alignments with redshift, excluding positive $\eta_{\rm other}$ with similarly high confidence when using our default NLA model following Hirata & Seljak (2004). However, as was discussed in Sect. 5.1.2, we have found a different redshift evolution based on the linear alignment assumption. Our findings for $P_{\delta \rm I}$ differ by a factor of $(1+z)^{-2}$ from (5.12), which translates into a shift of $\eta_{\rm other}$ by $+2$ for the corrected version of the NLA model. Hence, no redshift evolution beyond the latter, new version of NLA model, i.e. $\eta_{\rm other} = -2$ in the units of Fig. 5.19 and Table 5.4, is still consistent with our fits within the $2\,\sigma$ contours. We find an overall intrinsic alignment normalisation $A = 3.2^{+0.4}_{-0.3}$, which e.g. translates into an amplitude of 43 % of the standard NLA model by Hirata & Seljak (2004) with SuperCOSMOS normalisation for a typical red galaxy with $L = L_0/4$ at redshift $z = 0.5$.

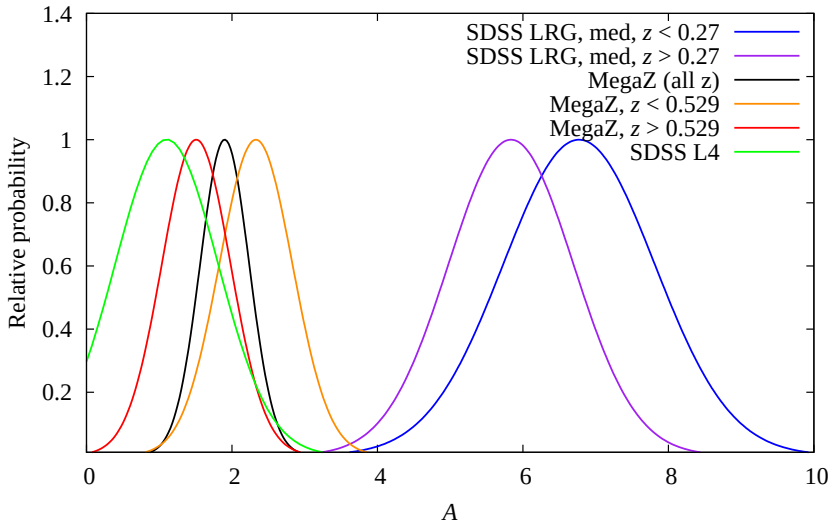

Figure 5.18: Constraints on the amplitude A of the intrinsic alignment model, keeping all other parameters fixed at their fiducial values $\beta = \eta_{\rm other} = 0$. The black curve corresponds to using the full MegaZ LRG sample. The constraints from the individual MegaZ LRG redshift bins are shown as red lines ($z > 0.529$) and orange lines ($z < 0.529$). For comparison we also show the constraints on A for the SDSS L4 sample as green line and for the SDSS LRG medium luminosity samples with $z < 0.27$ (blue line) and $z > 0.27$ (purple line).

As a measure for residual systematics in the projected correlation functions, we also consider $w_{g\times}$ for the full as well as the high- and low-redshift MegaZ LRG samples. This correlation measures a net curl in the galaxy ellipticities around the positions of other galaxies which is expected to vanish for both the intrinsic and gravitational shear due to parity invariance. Any significant signal in $w_{g\times}$ would thus be an indicator for residual systematics as for instance induced by imperfect PSF corrections. We find reduced χ^2 values smaller than unity for fits of a zero signal to $w_{g\times}$ on all available scales $R \in [0.3; 60]$ Mpc h^{-1}, for all MegaZ LRG samples. Hirata et al. (2007) have performed similar checks on the SDSS samples used in this work and similarly find no evidence for residual systematics.

5.6 Implications for cosmology

Intrinsic alignments constitute the major astrophysical source of systematic uncertainties for cosmic shear surveys. If left untreated, they can severely bias cosmological parameters estimates (e.g. Bridle & King 2007). If the contamination by intrinsic alignments is well known, it can ideally be incorporated into the modelling by subtracting the mean intrinsic alignment signal from the lensing term and accounting for the residual uncertainty in the systematic by introducing nuisance parameters over which one can then marginalise. To elucidate the implications for cosmological constraints from cosmic shear surveys by our constraints on intrinsic alignments, we will optimistically assume that the mean systematic signal is given by our best-fit model. In this approach, the decisive quantity is then not the mean value of the bias on cosmological parameters, which can be easily corrected for by subtracting the mean intrinsic alignment signal, but the uncertainty in the bias, which directly affects the accuracy with which the cosmological model can be constrained when taking the systematics into account.

We assess the range of possible biases on cosmological parameters which originate from intrinsic alignment signals using the constraints obtained from the foregoing investigation. Since

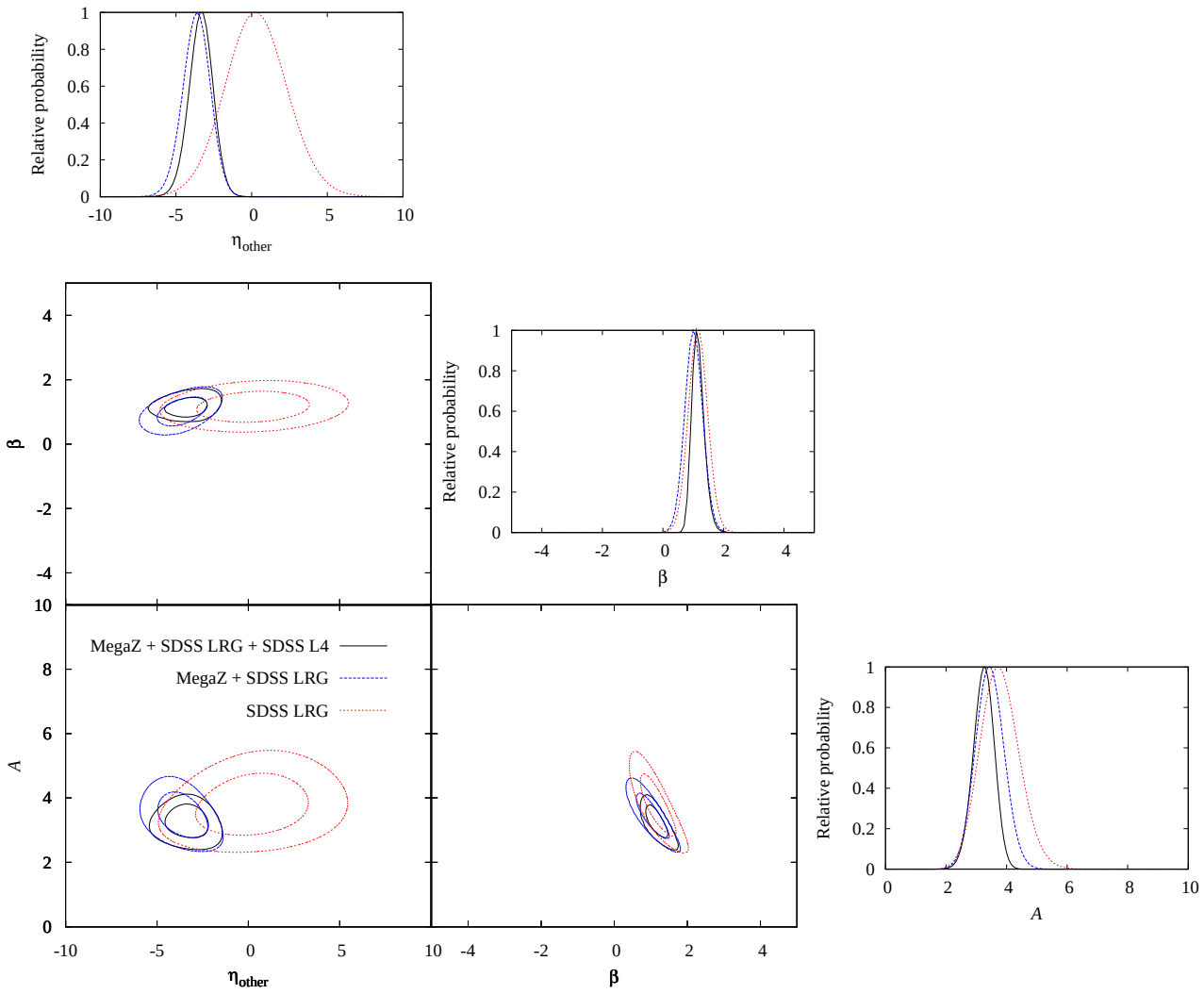

Figure 5.19: Constraints by the joint fit to MegaZ LRG and SDSS samples on the amplitude A of the intrinsic alignment model, the extra redshift dependence with power-law index $\eta_{\rm other}$, and the index β of the luminosity dependence. In the lower left panels the two-dimensional $1\,\sigma$ and $2\,\sigma$ contours are given, marginalised in each case over the parameter not shown with flat priors over the ranges used in this plot. The upper right panels display the constraints on A, $\eta_{\rm other}$, and β, each marginalised over the two remaining parameters. Red lines are obtained via fits to the six SDSS LRG samples, blue lines via fits to the MegaZ LRG and SDSS LRG samples combined, and black lines result for the joint fit to the MegaZ LRG, SDSS LRG, and SDSS L4 samples.

the SDSS L4 sample proved to be consistent with the results for the two LRG samples, we conclude that our intrinsic alignment model should also be valid for typical, less luminous early-type galaxies predominantly found in a cosmic shear survey.

By means of a Fisher matrix analysis we compute the effect on a present-day cosmic shear survey which roughly follows CFHTLS (Hoekstra et al. 2006; Semboloni et al. 2006; Fu et al. 2008) parameters. To calculate the matter power spectrum, we use the same cosmology, transfer function, and non-linear correction as outlined in Sect. 5.3.1. For computational simplicity we use the convergence power spectrum (the GG signal henceforth) as the observable cosmic shear two-point statistic, which is given by the Limber equation (3.34) or, in the notation of this

chapter,

$$C_{\mathrm{GG}}^{(ij)}(\ell) = \int_0^{\chi_{\mathrm{hor}}} \mathrm{d}\chi \, \frac{q_\epsilon^{(i)}(\chi) \, q_\epsilon^{(j)}(\chi)}{\chi^2} \, P_\delta\left(\frac{\ell}{\chi}, \chi\right) \, , \tag{5.50}$$

where $q_\epsilon^{(i)}$ is given by (5.37). Instead of specifying a photometric redshift for a redshift probability distribution, we switch here to the usual notation of using an index i that characterises a (broad) distribution $p^{(i)}(z)$ entering (5.37). The corresponding Limber equations for the GI and II signals can readily be re-formulated accordingly, see (5.15) and (5.16).

We employ an overall redshift distribution according to (4.47) with parameters $\alpha_z = 0.836$, $\beta_z = 3.425$, and $z_0 = 1.171$, yielding a median redshift of 0.78 (Benjamin et al. 2007). We slice this distribution into 5 'photometric' redshift bins such that every bin contains the same number of galaxies. The corresponding redshift distribution for each bin is then computed via the formalism detailed in Joachimi & Schneider (2009), see also Chap. 6, assuming a photometric redshift uncertainty of $0.05(1 + z)$. We compute Gaussian covariances for the power spectra (following Joachimi et al. 2008), assuming a survey size of $A_{\mathrm{survey}} = 100\,\mathrm{deg}^2$. Shape noise is incorporated with an overall galaxy number density of $12\,\mathrm{arcmin}^{-2}$ and a dispersion of the absolute value of the intrinsic ellipticity of 0.35.

We consider a parameter vector $\boldsymbol{p} = \{\Omega_{\mathrm{m}}, \sigma_8, h, n_{\mathrm{s}}, \Omega_{\mathrm{b}}, w_0\}$ in the cosmological analysis, for a flat universe with dark energy equation-of-state parameter w_0. Assuming that the covariance is not dependent on these parameters, one obtains the Fisher matrix (Tegmark et al. 1997, Appendix A)

$$F_{\mu\nu} = \sum_{\ell, i\le j, k\le l} \frac{\partial C_{\mathrm{GG}}^{(ij)}(\ell)}{\partial p_\mu} \, \mathrm{Cov}^{-1}\left(C_{\mathrm{GG}}^{(ij)}(\ell), \, C_{\mathrm{GG}}^{(kl)}(\ell)\right) \frac{\partial C_{\mathrm{GG}}^{(kl)}(\ell)}{\partial p_\nu} \, , \tag{5.51}$$

where we use 40 logarithmically spaced angular frequency bins between $\ell = 10$ and $\ell = 10^4$. With the Fisher matrix, one can calculate the bias on a cosmological parameter via (e.g. Kim et al. 2004; Huterer & Takada 2005; Huterer et al. 2006; Taylor et al. 2007; Amara & Réfrégier 2008; Kitching et al. 2009; Joachimi & Schneider 2009)

$$b(p_\mu) = \sum_\nu \left(F^{-1}\right)_{\mu\nu} \sum_{\ell, i\le j, k\le l} \left[C_{\mathrm{II}}^{(ij)}(\ell) + C_{\mathrm{GI}}^{(ij)}(\ell)\right] \, \mathrm{Cov}^{-1}\left(C_{\mathrm{GG}}^{(ij)}(\ell), \, C_{\mathrm{GG}}^{(kl)}(\ell)\right) \frac{\partial C_{\mathrm{GG}}^{(kl)}(\ell)}{\partial p_\nu} \, , \tag{5.52}$$

where the systematic is given by the sum of II and GI power spectra. Note that the parameter bias is independent of the survey size while the statistical errors obtained from $F_{\mu\nu}$ are proportional to $1/\sqrt{A_{\mathrm{survey}}}$.

The intrinsic alignment analysis presented above only dealt with red galaxies, whereas a typical galaxy population in cosmic shear surveys is dominated by blue galaxies for which Mandelbaum et al. (2009) reported a null detection using a galaxy sample spanning a range of redshifts compatible to MegaZ LRG. Thus we assume that only the red fraction f_r of galaxies in the survey carries an intrinsic alignment signal. Consequently the II power spectrum is multiplied by a factor f_r^2, and the GI power spectrum by f_r, resulting in the same model used by Kirk et al. (2010).

We make the further assumption that the survey contains a fraction $f_r = 0.15$ of red galaxies with a luminosity of $L/L_0 = 0.25$, both numbers being constant as a function of redshift. This implies that f_r and the luminosity term in (5.49) only affect the intrinsic alignment amplitude and do not produce an additional dependence on redshift. While these values for f_r and L/L_0 are realistic on average for a cosmic shear galaxy sample, one expects a considerable

Table 5.5: Range of possible parameter biases due to intrinsic alignments for a CFHTLS-like survey. We have listed the $1\,\sigma$ statistical error $\sigma_{\rm stat}$ resulting from the Fisher matrix analysis after marginalising over all remaining parameters in the second column, as well as the range of biases we obtained by sampling from the $2\,\sigma$ region of $\{A, \beta, \eta_{\rm other}\}$ from the fits to the three sets of galaxy samples given in Table 5.4, given in the third to fifth column. The range of biases is defined as the length of the interval containing 99 % of the one-dimensional distribution of biases.

parameter	$\sigma_{\rm stat}$	SDSS LRG	SDSS LRG + MegaZ	SDSS LRG + MegaZ + L4
$\Omega_{\rm m}$	0.07	0.38	0.08	0.04
σ_8	0.12	0.50	0.06	0.04
w_0	0.59	1.95	0.54	0.26

dependence on redshift, i.e. a decrease of f_r and increase of mean luminosity with redshift for a flux-limited survey. These assumptions should not have a decisive influence on the spread of biases in the cosmological parameter plane though. Note that, as before, we take the additional redshift dependence of the intrinsic alignment model (5.49) out of the line-of-sight integrations in (5.15) and (5.16), using the mean of the median redshifts of the two photometric redshift bins correlated in the extra term.

The II and GI signals are then computed via (5.49) where the free intrinsic alignment parameters $\{A, \beta, \eta_{\rm other}\}$ are determined as follows. We overlay the three-dimensional $2\,\sigma$ volume of the fits to the sample combinations shown in Table 5.4 and Fig. 5.19 with a square grid, containing N nodes in total. For the combination of $\{A, \beta, \eta_{\rm other}\}$ on each grid node we compute the projected intrinsic alignment power spectra according to (5.15) and (5.16) and subsequently the parameter biases via (5.52). This way we obtain a bias vector $\boldsymbol{b} = \{b(p_1), .., b(p_{N_{\rm D}})\}$, where $N_{\rm D}$ is the number of cosmological parameters under consideration, for every grid node sampled within the $2\,\sigma$ volume in intrinsic alignment parameter space.

We convert the ensemble of N parameter bias vectors $\{\boldsymbol{b}_1, .., \boldsymbol{b}_N\}$ into a distribution of bias values via Gaussian kernel density estimation, i.e. we approximate this distribution by

$$p(\boldsymbol{x}|\,\{\boldsymbol{b}_i\}) = \frac{1}{N}\,\sum_{i=1}^{N}\prod_{j=1}^{N_{\rm D}}\,\frac{1}{\sqrt{2\pi}h_j}\,\exp\left\{-\frac{(x_j - b_{i,\,j})^2}{2h_j^2}\right\}\,, \tag{5.53}$$

where we use $N_{\rm D} = 2$ when considering the distribution in a two-dimensional parameter plane, and $N_{\rm D} = 1$ when computing the one-dimensional distribution. The widths $\boldsymbol{h}$ of the Gaussians in every dimension of cosmological parameter space are free parameters, and we choose them to take the minimum values which still produce a smooth distribution. While we use six cosmological parameters to compute the biases on cosmology, we focus in our presentation of the uncertainty in the biases on a subset with the most interesting cosmological parameters in cosmic shear analyses, $\{\Omega_{\rm m}, \sigma_8, w_0\}$. For the tightly constrained parameters $\Omega_{\rm m}$ and σ_8 we use $h = 0.002$ and in the dimension corresponding to w_0 we set $h = 0.01$. Note that we use the same widths for all sample combinations considered in order not to distort the comparison between the resulting bias distributions.

In Fig. 5.20 we show the contours comprising 99 % of the distribution (5.53) in the two-dimensional parameter planes spanned by all pairs from the set $\{\Omega_{\rm m}, \sigma_8, w_0\}$, sampling from the posteriors of the intrinsic alignment parameters obtained for the three sample combinations given in Table 5.4. In this figure we have written the parameter biases (and not parameter values) on the axes such that in absence of any intrinsic alignment contamination the contours should be centred around $(0; 0)$ in each panel.

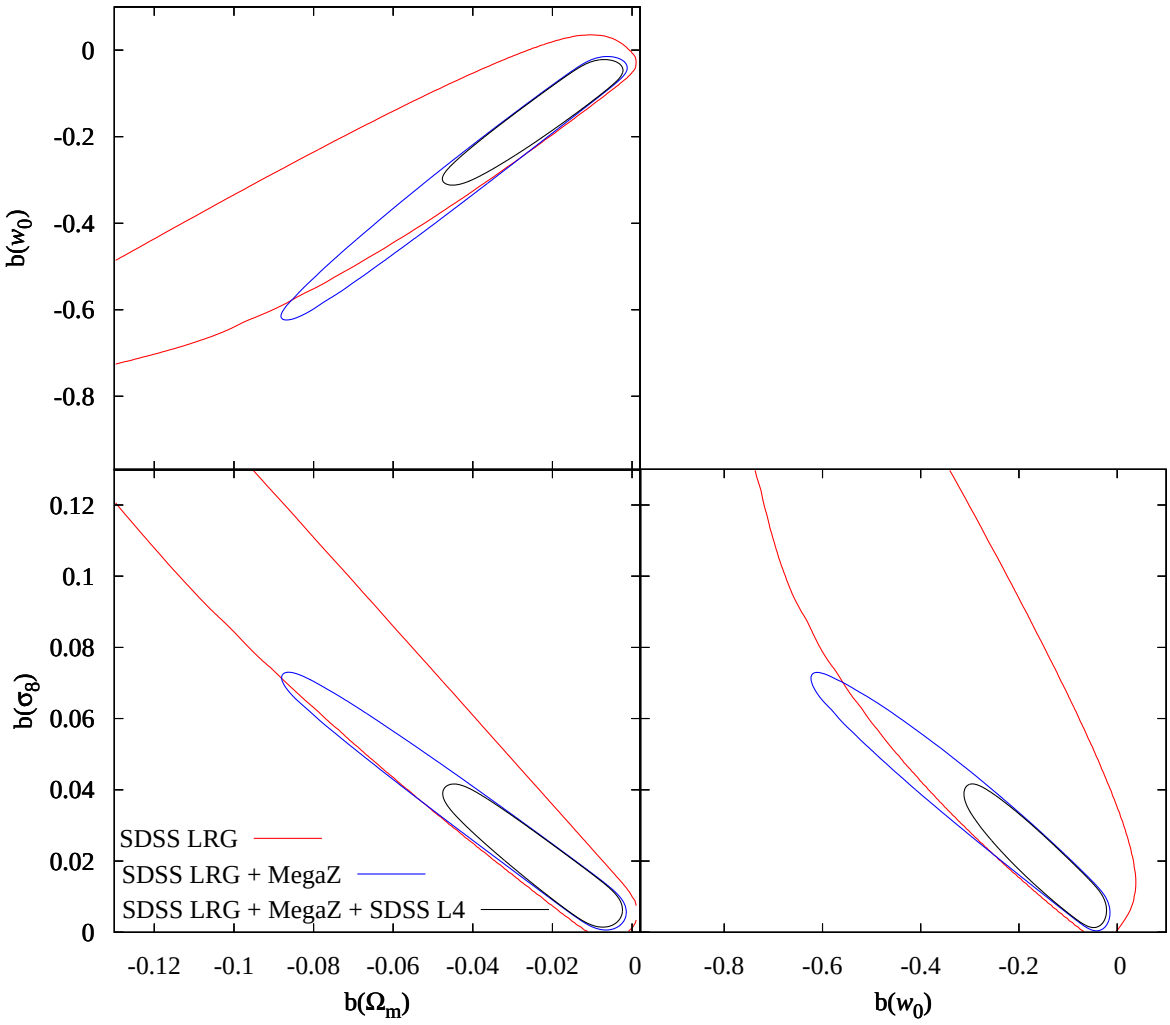

Figure 5.20: Bias on cosmological parameters due to intrinsic alignments for a CFHTLS-like weak lensing survey. Shown are the regions in which 99 % of the possible biases on the parameters $\{\Omega_\mathrm{m}, \sigma_8, w_0\}$ are located when the parameters $\{A, \beta, \eta_\mathrm{other}\}$ in the intrinsic alignment model are sampled from the $2\,\sigma$ confidence region. The region resulting from the SDSS LRG constraints is shown in red, the one from the MegaZ + SDSS LRG constraints in blue, and the region from the joint constraints by the MegaZ, SDSS LRG and L4 samples in black. For this analysis the 6 parameters $\{\Omega_\mathrm{m}, \sigma_8, h, n_\mathrm{s}, \Omega_\mathrm{b}, w_0\}$ were varied. We assumed a constant fraction $f_r = 0.15$ of red galaxies and a constant luminosity of $L/L_0 = 0.25$ for the red galaxies in the shear catalogue. Note that the region corresponding to the SDSS LRG only fits extends far beyond the plot boundaries.

The general direction of parameter biases, for instance along the $\Omega_\mathrm{m} - \sigma_8$ degeneracy, is in agreement with other predictions on biases due to intrinsic alignments, see for instance Fig. 6.24. As is evident from (5.52), if the GI term dominates which is expected for deep cosmic shear surveys, the bias is proportional to the amplitude parameter A of the intrinsic alignment model. Thus the remaining uncertainty in A explains the degeneracy in the contours, pointing approximately radially away from $(0; 0)$. The large errors on intrinsic alignment parameters, in particular on η_other, in the case of using the SDSS LRG samples alone allow for a vast region of possible parameter biases. The contours tighten dramatically when adding in the MegaZ LRG data, fixing also the redshift dependence to good accuracy. The additional information provided by the SDSS L4 sample constrains the total amplitude of the intrinsic alignment

signal still better, thereby reducing the extent of the contours by about a factor of two along the degenerate direction.

In Table 5.5 we list the $1\,\sigma$ marginalised statistical errors for the three cosmological parameters of interest, obtained from (5.51) via $\sigma_{\rm stat}(p_\mu) = \sqrt{(F^{-1})_{\mu\mu}}$. Moreover we give the size of the interval that contains 99 % of the one-dimensional distribution (5.53), again as a measure for the spread of biases on cosmology. In agreement with the two-dimensional plots of Fig. 5.20 we find that adding the MegaZ LRG samples to the SDSS LRG data considerably shrinks the range of biases, e.g. by more than a factor eight in the case of σ_8. In combination with the L4 sample the intervals decrease in size by roughly another factor of two, reaching values which are significantly smaller than the $1\,\sigma$ statistical errors. Hence, under the assumptions made above and provided that the mean intrinsic alignment signal were accurately known, the uncertainty in the knowledge about the free parameters of (5.49) would be subdominant to the statistical errors in a CFHTLS-like survey.

5.7 Conclusions

In this chapter we have investigated the intrinsic alignment of galaxies which has recently attracted considerable interest as a severe contaminant of cosmic shear data. We presented an overview of the current picture of intrinsic alignments, measurements from simulations and observations, suggested removal techniques, and modelling attempts. Our re-derivation of the linear alignment model, which has served as the base for most intrinsic alignment parametrisations to date (e.g. Bridle & King 2007; Schneider & Bridle 2010), leads to the claim that its redshift dependence may need to be modified.

Then we proceeded to the measurement of intrinsic alignments, or more precisely the correlations between the matter distribution and the intrinsic shear field generating a gravitational shear-intrinsic ellipticity (GI) signal, in MegaZ LRG, a sample of more than 860000 galaxies at intermediate redshifts. MegaZ LRG relies on high-quality photometric redshift information, calibrated via the 2SLAQ catalogue, and hence constitutes the first sample without spectroscopic redshifts used for intrinsic alignment studies. We developed a formalism that incorporates photometric redshift uncertainty into the computation of correlation function models, and demonstrated explicitly the effect of photometric redshift scatter on the modelling. The contamination by other signals to galaxy number density-shape correlations was assessed, finding that the galaxy-galaxy lensing signals needs to be taken into account while magnification effects remain negligible.

In combination with data from the SDSS LRG and the red SDSS L4 samples which had been previously measured by Hirata et al. (2007), the MegaZ LRG sample provides an excellent data set for investigating intrinsic alignments of early-type galaxies, with unprecedented baselines in redshift and galaxy luminosity. We verified that both our model and the MegaZ LRG correlation functions display a consistent behaviour with respect to the truncation of the line-of-sight projection. We also determined galaxy biases in linear theory for the MegaZ and SDSS LRG samples from galaxy clustering correlation functions and found good agreement with the previous analysis by Hirata et al. (2007) in the latter case.

We clearly detected an intrinsic alignment signal in $w_{\rm g+}$ for both the low- and high-redshift bin MegaZ LRG samples. Using the non-linear version of the linear alignment (NLA) model supplemented by power-law terms for a luminosity and an extra redshift dependence, we obtained good individual fits to all subsamples with reduced χ^2 not exceeding unity in most cases. If only the overall amplitude A of the model is a free parameter, the results for the different subsamples are not consistent with each other, A differing by up to a factor of about 8. Includ-

ing an extra redshift and luminosity dependence, the SDSS LRG, MegaZ LRG, and SDSS L4 samples yield consistent constraints with reduced χ^2 close to unity.

The redshift evolution of the NLA model based on Hirata & Seljak (2004) without extra terms is inconsistent with the combined fits, yielding a slope of the extra redshift dependence $\eta_{\rm other} = -3.4^{+0.8}_{-0.7}$. Employing the modified linear alignment version as derived in Sect. 5.1 corresponds to a shift in $\eta_{\rm other}$ by $+2$, so that this model is in agreement with the joint fit of all samples at the $2\,\sigma$-level. Moreover the data clearly favours an increase of the intrinsic alignment amplitude with the luminosity of the galaxy, excluding a power-law slope of the luminosity term $\beta < 0.5$ at the $4\,\sigma$-level.

We found a best-fit overall model amplitude of $A = 3.2^{+0.4}_{-0.3}$ in terms of the SuperCOSMOS normalisation, translating into a GI signal with an amplitude which is 43 % of the standard NLA model by Hirata & Seljak (2004) with $A = 1$ for a red galaxy at $z = 0.5$ and an absolute r-band magnitude of -20.5. Hence, although we apparently determined a high intrinsic alignment amplitude $A > 1$, the constraints on redshift and luminosity evolution obtained by this analysis suggest that the GI term for galaxies, at redshifts and with luminosities typically found in cosmic shear surveys, may be smaller by a factor of two compared to the widely used z- and L-independent SuperCOSMOS normalisation.

The consistency of the SDSS L4 sample demonstrates that our model does not only hold for luminous red galaxies but can be extended to fainter early-type galaxies which populate cosmic shear surveys in significant numbers. However, we noted that the red L4 sample as defined by Hirata et al. (2007) is likely to be contaminated by a fraction of galaxies from the blue cloud, which could potentially have affected the intrinsic alignment signal and also the mean luminosity. This issue is currently under investigation.

To elucidate the potential of our novel intrinsic alignment constraints, we considered the bias due to intrinsic ellipticity and GI correlations on cosmological parameters, assuming a typical present-day cosmic shear survey. In a Fisher matrix calculation we sampled intrinsic alignment signals from the parameter regions allowed by our fits and determined the regions in cosmological parameter space in which the corresponding biases on cosmology are located. We found that the constraints by the MegaZ LRG sample, in particular on the redshift evolution of intrinsic alignments, dramatically reduce the range of possible biases. Under the assumption that the mean of the systematic is known and can be subtracted from the lensing signal, the joint intrinsic alignment constraints from all galaxy samples can diminish the scatter in cosmological parameter biases significantly below the statistical uncertainty of a CFHTLS-like survey.

The comparatively tight intrinsic alignment parameter constraints and the mutual consistency of galaxy samples with vastly different mean redshifts and luminosities should be encouraging enough to add further data and improve constraints on this intrinsic alignment model which has at least to some extent a physical grounding. The generalisation of the formalism introduced by Mandelbaum et al. (2006) to photometric redshift data has opened up the possibility to include a large amount of galaxy samples into the analysis, especially those which are at higher redshift and contain fainter galaxies, thus being closer to typical cosmic shear survey samples.

The main requirement on these samples is that the photometric redshift scatter is sufficiently small in order to avoid the contributions by galaxy-galaxy lensing and magnification effects becoming too strong. We note however that the contribution by galaxy-galaxy lensing could in principle be obtained from the same data by correlating subsamples which are clearly separated in redshift, so that matter-intrinsic shear correlations vanish. For instance, the COSMOS survey with its excellent photometric redshifts (Ilbert et al. 2009) and galaxy shape catalogues (Schrabback et al. 2010) could provide intrinsic alignment measurements out to very high redshift. Furthermore, the analysis performed in this work could also be directly applied to

cosmic shear surveys, or at least to subsamples in them, such as CFHTLS, Pan-STARRS, or DES.

However, one should keep in mind that both the modelling and the observations presented above are subject to strict limitations. The intrinsic alignment model which we applied has a fixed dependence on transverse separation. While the still considerable error bars enabled good fits of our model in R, modifications might be necessary when using richer data sets. Other factors, like e.g. a dependence on the galaxy environment (see Hirata et al. 2007), could also become relevant. Yet, advances in theory towards a more detailed and realistic physical model of intrinsic alignments cannot be expected in the foreseeable future, so that better constraints by the data may not evolve in parallel with a better physical understanding of intrinsic alignments.

Moreover we have limited our analysis to scales larger than about $6\,\mathrm{Mpc}\,h^{-1}$, which corresponds to an angular scale of 15 arcmin at the mean redshift of the MegaZ LRG sample. Although cosmic shear surveys extract a major part of the cosmological information from smaller scales, we have to date no reliable observations of matter-intrinsic shear correlations in this regime and can only suspect that non-linear evolution and tidal fields on the scales of galaxy haloes produce a complex behaviour of the correlations. We cannot use the formalism of this work to go to these small scales since the assumption of a linear bias breaks down. The only way forward is to introduce general, very flexible parametrisations of both the galaxy bias and the intrinsic alignment model and simultaneously analyse galaxy clustering, number density-shape cross-correlations, and cosmic shear. We will investigate this so-called self-calibration ansatz of intrinsic alignments in full detail in Chap. 8.

Chapter 6

The nulling technique

Intrinsic alignments constitute the major astrophysical source of systematic error for cosmic shear studies, their consequences being the more serious the more accurate the surveys can pin down the cosmological model. Therefore it is vital to come up with analysis techniques that effectively control the bias on cosmological parameters induced by intrinsic alignments and that will thus form an integrative part of future cosmic shear data analysis pipelines.

As already discussed in the foregoing chapter, the mechanisms creating intrinsic alignments are complex, so that models currently are, and are likely to remain, too crude to simultaneously estimate cosmological parameters and the free parameters of an intrinsic alignment model from cosmic shear data, without risking the introduction of new biases e.g. due to ignoring additional dependencies on galaxy properties such as colour and luminosity. Hence, model-independent methods are required which necessarily have to rely on the well-known redshift dependence of the intrinsic alignment signals.

Correlations between the intrinsic ellipticities of galaxies (II correlations henceforth) can only occur between physically close pairs of galaxies, causing a distinct redshift dependence of the signal (see Fig. 5.7) which can be exploited to remove the II signal (e.g. King & Schneider 2002, 2003; Takada & White 2004). Cross-correlations between intrinsic ellipticity and gravitational shear (GI correlations hereafter) show a very similar behaviour with redshift compared to the cosmic shear signal (GG in the following), rendering the GI term a more serious concern.

Following the original proposal of Hirata & Seljak (2004), Joachimi & Schneider (2008, 2009) developed and investigated the nulling technique, a purely geometrical approach to eliminate the GI systematic from tomographic cosmic shear surveys. In Sect. 6.1 we will outline the principle of nulling by constructing certain linear combinations of tomographic second-order cosmic shear measures. Several implementations to determine the weights entering these linear combinations are then discussed in Sect. 6.2. Due to the similarity between the GI and GG terms, the elimination of GI correlations inevitably also affects the cosmic shear signal which causes an increase in the errors on cosmological parameters. This loss of information is studied by means of a likelihood analysis as presented in Sect. 6.3.

Slightly re-formulating the nulling transformation, one can understand it as a rotation and subsequent truncation of the cosmic shear data vector, yielding further insight and leading to a more efficient nulling procedure, see Sect. 6.4. By means of this new procedure and a Fisher matrix analysis, we then proceed to asses the dependence of nulling on the quality of redshift information provided by future cosmic shear surveys, based on the realistic modelling detailed in Sect. 6.5. After optimising the nulling weights in Sect. 6.6, we provide a comprehensive analysis of how nulling is affected by different parameters characterising photometric redshifts in cosmic shear galaxy samples in Sects. 6.7 and 6.8. Finally, in Sect. 6.9 we present a summary and conclusions on this novel intrinsic alignment removal technique.

6.1 Principle of nulling

Consider a tomographic cosmic shear signal from pairs of galaxies in two redshift bins i and j, obtained via a second-order cosmic shear measure such as the correlation functions $\xi_\pm^{(ij)}(\theta)$, see Sect. 3.4. Note that for the remainder of this chapter the Universe is assumed to be spatially flat to ease the notation, and that furthermore we assume for the following derivation that the redshift distributions of the galaxy samples considered are disjoint, i.e. we neglect the errors due to photometric redshifts. From Sect. 6.4 onwards we will then explicitly take into account photometric redshift uncertainty and study its effect on nulling.

The contamination by gravitational shear-intrinsic ellipticity correlations is caused by the matter distribution within the redshift slice situated closer to the observer, see (5.1) and the discussion thereafter. If one cannot rely on a model governing the statistical properties of this contamination, it is necessary to eliminate the contribution of the matter within the lower redshift bin to the cosmic shear signal completely because only then can one ensure that GI correlations are not present anymore. One way to illustrate the modification of the cosmic shear signal that this requirement entails is a change in the weighting of the projection of the matter density contrast along the line of sight, usually given by (3.22). Instead of using (3.23), we now define a new convergence

$$\bar{\kappa}^{(i)}(\boldsymbol{\theta}) \equiv \int_0^{\chi_\mathrm{hor}} \mathrm{d}\chi \; B^{(i)}(\chi) \; \kappa(\boldsymbol{\theta}, \chi) \; , \tag{6.1}$$

where $B^{(i)}(\chi)$ denotes the new weight function, measured in units of inverse length like the comoving distance distribution $p^{(i)}(\chi)$. After inserting (3.22) into (6.1) and rearranging the integrations, the relation of $\bar{\kappa}^{(i)}(\boldsymbol{\theta})$ to the density contrast reads

$$\bar{\kappa}^{(i)}(\boldsymbol{\theta}) = \frac{3H_0^2\Omega_\mathrm{m}}{2c^2} \int_0^{\chi_\mathrm{hor}} \mathrm{d}\chi \; \frac{\bar{g}^{(i)}(\chi) \; \chi}{a(\chi)} \; \delta\left(\chi\boldsymbol{\theta}, \chi\right) \; , \tag{6.2}$$

with the modified lensing efficiency

$$\bar{g}^{(i)}(\chi) = \int_\chi^{\chi_\mathrm{hor}} \mathrm{d}\chi' \, B^{(i)}(\chi') \left(1 - \frac{\chi}{\chi'}\right) \; . \tag{6.3}$$

The lensing efficiency determines the amplitude by which the density contrast at the corresponding distance contributes to the convergence. Thus, demanding that the matter structure at a comoving distance $\hat{\chi}_i$, to be chosen appropriately within bin i, does not yield any contribution to the cosmic shear signal is equivalent to the constraint

$$\bar{g}^{(i)}(\hat{\chi}_i) = \int_{\hat{\chi}_i}^{\chi_\mathrm{hor}} \mathrm{d}\chi \; B^{(i)}(\chi) \left(1 - \frac{\hat{\chi}_i}{\chi}\right) = 0 \; . \tag{6.4}$$

Equation (6.4) ensures the elimination of the contribution of matter at $\hat{\chi}_i$ to the shear signal, and consequently of the GI correlations, motivating the name 'nulling' for this method. It makes use of the characteristic dependence on distance, $1 - \hat{\chi}_i/\chi$, which corresponds to the ratio $D_\mathrm{ds}/D_\mathrm{s}$ of the angular diameter distance between lens and source and the one between observer and source.

Note that a nulling technique has been applied before in the context of cosmic shear by Huterer & White (2005) who aimed at nulling small-scale information influenced by poorly determined baryonic physics. As $D_\mathrm{ds}/D_\mathrm{s}$ is a smooth function of both the lens and the source position, the integration in (6.4) is rather insensitive to small changes in the distances of the

mass distribution, acting as the lens. Consequently, the contributions from distances slightly smaller or larger than $\hat{\chi}_i$ are also strongly downweighted by $B^{(i)}(\chi)$, provided that the weight function is also smooth. This leads to the near cancellation of the signal from the whole bin i if $\hat{\chi}_i$ is chosen to be the distance corresponding to the centre of the bin.

Motivated by the considerations given above, we define a new second-order cosmic shear measure in terms of the tomographic correlation functions as

$$\Xi_\pm^{(i)}(\theta) \equiv \int_0^{\chi_\mathrm{hor}} \mathrm{d}\chi \; B^{(i)}(\chi) \; \xi_\pm(z(\hat{\chi}_i), z(\chi), \theta) \; , \tag{6.5}$$

where the correlation functions $\xi_\pm(z_1, z_2, \theta)$ are – formally – evaluated at the exact, e.g. spectroscopically determined, redshifts z_1 and z_2. So far, $B^{(i)}(\chi)$ is only constrained for $\hat{\chi}_i < \chi \leq \chi_\mathrm{hor}$ by (6.4). We set $B^{(i)}(\chi) \equiv 0$ for $0 \leq \chi \leq \hat{\chi}_i$ because otherwise correlation functions with $z(\chi) < z(\hat{\chi}_i)$, which can be contaminated by intrinsic alignments at $z(\chi)$, would contribute to (6.5). Through this, no information is discarded since the correlation functions are symmetric in their first and second arguments, so that, swapping the redshifts, they enter other measures, constructed like in (6.5) but with smaller $\hat{\chi}_i$.

Now assume that $\xi_\pm(z(\hat{\chi}_i), z(\chi), \theta)$ is contaminated by GI correlations. Since $B^{(i)}(\chi)$ vanishes for $\chi < \hat{\chi}_i$, it is sufficient to consider $z(\chi) > z(\hat{\chi}_i)$ in the integral. Then intrinsic alignment has to be generated by the matter structure at $\hat{\chi}_i$. However, the contribution of matter at $\hat{\chi}_i$ to the convergence and subsequently to the shear entering the correlation function is eliminated by the weight function when chosen according to (6.4), so that the $\Xi_\pm^{(i)}(\theta)$ are free of GI correlations.

In practice distance information is obtained in terms of redshift rather than comoving distance. Moreover only photometric redshift data will be available for the large number of galaxies in cosmic shear surveys, so that redshift information is given in the form of discrete redshift bins. To arrive at a practical measure, we first transform (6.5) to z as the integration variable and subsequently approximate the integral as a Riemannian sum,

$$\Xi_\pm^{(i)}(\theta) \approx \sum_{j=1}^{N_z} B^{(i)}(\chi(z_j)) \; \xi_\pm^{(ij)}(\theta) \; \chi'(z_j) \; \Delta z \; , \tag{6.6}$$

where N_z is the number of redshift bins and $\chi'(z)$ the derivative of the comoving distance with respect to z, calculated from (2.10). The distance-redshift relation enters into many of the following equations since (3.22) and related equations are formulated in terms of comoving distance, whereas the binning is performed in redshift. Again for reasons of simplicity, we have assumed in (6.6) that the binning in redshift is equidistant with width Δz. The subsequent equations can also be readily expressed using variable bin sizes, and we will generalise the nulling formalism in Sect. 6.4.

Henceforth, we refer to the first bin of the tomography correlation functions entering (6.6), i.e. the bin where the signal is nulled, as the 'initial bin'. In (6.6) z_j denotes the lower boundary redshift of bin j, implying that in the sum the correlation function $\xi_\pm^{(ij)}(\theta)$ is registered onto the lower boundary of bin j. We will optimise the choice of redshifts which the redshift bins (or more generally the redshift distributions) are registered onto in Sect. 6.6.1. To render (6.6) a good approximation, the redshift binning has to be sufficiently narrow. In addition, it is assumed that the redshift bins cover the total galaxy population almost completely, so that on discretising (6.5), the upper boundary of the integral can be reduced to the upper boundary of the highest redshift bin, denoted by z_max.

For the sake of lower computational efforts, the further investigation of nulling is performed

in Fourier space, by defining the new power spectrum

$$\begin{aligned}\Pi^{(i)}(\ell) &\equiv \int_0^{\chi_{\rm hor}} \mathrm{d}\chi\ B^{(i)}(\chi)\ P_\kappa(z(\hat{\chi}_i), z(\chi), \ell) \\ &\approx \sum_{j=1}^{N_z} B^{(i)}(\chi(z_j))\ P_\kappa^{(ij)}(\ell)\ \chi'(z_j)\ \Delta z\ , \end{aligned} \tag{6.7}$$

where $P_\kappa(z_1, z_2, \ell)$ denotes the convergence power spectrum for exactly known redshifts, and the angular frequency ℓ is the Fourier variable on the sky. The quantity $P_\kappa^{(ij)}(\ell)$ constitutes the corresponding tomographic measure, related to the three-dimensional power spectrum of matter density fluctuations P_δ via Limber's equation (3.34). Note that in (3.34) the lensing efficiency $g^{(i)}(\chi)$ in its original form, i.e. with $p^{(i)}(\chi)$ as the weight, enters. Since the nulling technique requires detailed redshift information, $\Delta z \ll 1$. The weighted convergence in (3.23) can then be written as $\kappa^{(i)}(\boldsymbol{\theta}) \approx \kappa(\boldsymbol{\theta}, \hat{\chi}_i)$, or equivalently $p^{(i)}(\chi) \approx \delta_{\rm D}(\chi - \hat{\chi}_i)$ to good approximation, where $\delta_{\rm D}$ is the Dirac delta distribution. In our case the dependence of the tomography power spectra on the probability distribution of galaxy distances is only marginal.

From the $N_z(N_z+1)/2$ tomography power spectra, which are in principle available, only N_z power spectra $\Pi^{(i)}(\ell)$ are constructed via (6.7). However, we can determine more than just one weight function $B^{(i)}(\chi)$ per initial bin. Thus, as will be explained in Sects. 6.2.5 and 6.3, the number of new power spectra is equal to the number of input $P_\kappa^{(ij)}(\ell)$. Note that, after the explicit computation of weight functions, we are going to show newly constructed power spectra and discuss their features in Sect. 6.2.5.

As the weighting by $B^{(i)}(\chi)$ does not depend on angular scales, the considerations made above for $\Xi_\pm^{(i)}(\theta)$ also hold for $\Pi^{(i)}(\ell)$ as well as any other second-order cosmic shear measure. The weight functions, once obtained, can be applied directly to measures accessible to observations, constructed in analogy to (6.6), by means of the transformations between convergence power spectra and real-space measures, as given in Schneider et al. (2002b) and Sect. 3.4. Hence, (6.5) and (6.7) are related via

$$\Xi_\pm^{(i)}(\theta) = \int_0^\infty \frac{\mathrm{d}\ell\ \ell}{2\pi} J_{0/4}(\ell\theta)\ \Pi^{(i)}(\ell)\ , \tag{6.8}$$

where J_μ denotes the Bessel function of the first kind of order μ as given by (3.46).

In terms of power spectra we can also explicitly demonstrate how the nulling technique removes the GI signal in the limit of a very fine redshift binning. In reality the power spectra $\Pi^{(i)}(\ell)$ will not have contributions from the lensing power spectra alone, as written in (6.7), but of the observed signal $P_{\rm obs}^{(ij)}(\ell) = P_{\rm GG}^{(ij)}(\ell) + P_{\rm GI}^{(ij)}(\ell)$, where the latter term is unknown. Assuming narrow redshift bins and hence $p^{(i)}(\chi) \approx \delta_{\rm D}(\chi - \chi(\hat{z}_i))$, (5.16) is transformed as follows,

$$\begin{aligned} P_{\rm GI}^{(ij)}(\ell) &\approx \frac{3H_0^2\Omega_{\rm m}}{2c^2}\ g^{(j)}(\chi(\hat{z}_i))\ \frac{1+\hat{z}_i}{\chi(\hat{z}_i)}\ P_{\delta{\rm I}}\left(\frac{\ell}{\chi(\hat{z}_i)}, \chi(\hat{z}_i)\right) \\ &\approx \frac{3H_0^2\Omega_{\rm m}}{2c^2}\ \left(1 - \frac{\chi(\hat{z}_i)}{\chi(z_j)}\right)\ \frac{1+\hat{z}_i}{\chi(\hat{z}_i)}\ P_{\delta{\rm I}}\left(\frac{\ell}{\chi(\hat{z}_i)}, \chi(\hat{z}_i)\right)\ , \end{aligned} \tag{6.9}$$

where the approximation has been applied to distribution i in the first step and to distribution j in the second equality. The latter transformation only affects the lensing efficiency and is readily seen by inserting the approximated distance distribution into (3.25). Note that the second term in (5.16), containing $g^{(i)}(\chi)\ p^{(j)}(\chi)$, vanishes if the redshift distributions do not overlap. This does not hold anymore for more realistic, broader distributions, the consequences

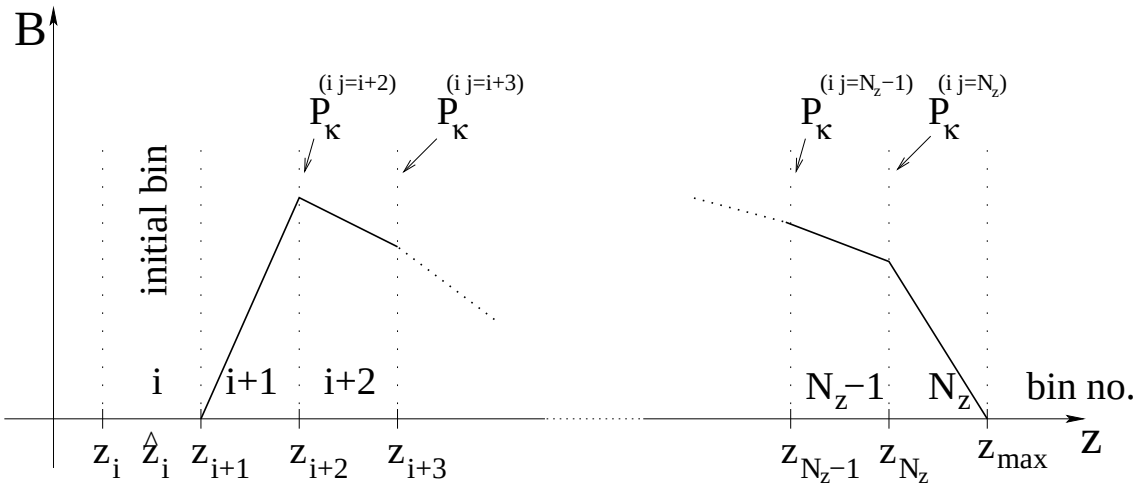

Figure 6.1: Sketch illustrating the conventions made for the construction of weight functions. The redshift z_j denotes the lower boundary of bin j; the tomography power spectrum $P_\kappa^{(ij)}(\ell)$ (or the corresponding real space measure) is registered onto this redshift in (6.7). With respect to these boundary redshifts, $B^{(i)}(\chi(z_{i+2}))$ is the first and $B^{(i)}(\chi(z_{N_z}))$ the last non-zero value of the weight function. The upper boundary redshift of the highest bin is denoted by $z_{\max}$. The initial bin is located between z_i and z_{i+1} with a central redshift of $\hat{z}_i$, so that $\hat{\chi}_i = \chi(\hat{z}_i)$.

being discussed in Sect. 6.7.3. Writing the GI power spectrum as a continuous function of the redshifts, one finds

$$P_{\rm GI}(z(\hat{\chi}_i), z(\chi), \ell) = \frac{3H_0^2\Omega_{\rm m}}{2c^2} \left(1 - \frac{\hat{\chi}_i}{\chi}\right) \frac{1 + z(\hat{\chi}_i)}{\hat{\chi}_i} P_{\delta{\rm I}}\left(\frac{\ell}{\hat{\chi}_i}, \hat{\chi}_i\right) . \tag{6.10}$$

Note that only the term $1 - \hat{\chi}_i/\chi$ depends on the second argument of $P_{\rm GI}(z(\hat{\chi}_i), z(\chi), \ell)$ which is integrated over in (6.7). It is then readily seen that the nulling transformation according to (6.7) eliminates the GI signal if (6.4) is fulfilled.

In (6.7) it is sufficient to let the sum over redshift bins start only at $i + 2$ because all other function values of $B^{(i)}(\chi)$ vanish. First, we demanded that $B^{(i)}(\chi) \equiv 0$ for $0 \leq \chi \leq \hat{\chi}_i$. In addition, to avoid contamination by intrinsic ellipticity correlations, we force the weight function to vanish within bin i completely, implying that $B^{(i)}(\chi)$ departs from zero only from the upper boundary of bin i, i.e. from redshift z_{i+1}, onwards, so that the first non-vanishing value of the weight function in (6.7) is $B^{(i)}(\chi(z_{i+2}))$. For further details about the downweighting of II correlations in conjunction with nulling the GI signal see Sect 6.7.3.

Consequently, $P_\kappa^{(ij)}(\ell)$ with $|j - i| \leq 1$, i.e. power spectra which auto-correlate redshift bins or cross-correlate adjacent bins, are removed from the new measure (6.7), securing the downweighting of II correlations. Takada & White (2004) demonstrate that errors on inferred parameters degrade by only about 10 % for 5 or more redshift bins if the auto-correlation power spectra are simply excluded from the analysis in shear tomography, which constitutes a simple and efficient method. Due to the narrow redshift binning that our method requires, the contamination by intrinsic alignment may extend to neighbouring bins, see e.g. Bridle & King (2007) and Sect. 6.7.3 for details. Since we assume a choice of the redshift bins such that the number of galaxies with $z > z_{\max}$ is negligible, we set $B^{(i)}(\chi) \equiv 0$ for $\chi \geq \chi(z_{\max})$. The conventions concerning the construction of weight functions made in this section are summarised in Fig. 6.1.

6.2 Determination of nulling weight functions

To show the feasibility of the nulling technique, it is important to know to what extent and how efficiently the weight function $B^{(i)}(\chi)$ can be constructed in practice. As a basic condition, $B^{(i)}(\chi)$ has to obey the constraint (6.4). In addition, it is required that the weight function should be optimised in the sense that, when aiming at constraining cosmological parameters, the information content in the new power spectrum $\Pi^{(i)}(\ell)$ attains a maximum. This condition is quantified in terms of the Fisher matrix (for details see Appendix A), which reads, when measuring the power spectrum in N_ℓ angular frequency bins,

$$F^{(i)}_{\mu\nu} = \sum_{\alpha,\,\beta=1}^{N_\ell} \left.\frac{\partial\Pi^{(i)}(\ell_\alpha)}{\partial p_\mu}\right|_{\rm f} \left(C_\Pi^{(ii)\,-1}\right)_{\alpha\beta} \left.\frac{\partial\Pi^{(i)}(\ell_\beta)}{\partial p_\nu}\right|_{\rm f} . \tag{6.11}$$

The vector $\boldsymbol{p}$ is composed of the cosmological parameters that are considered. Its size N_p implies the dimension $N_p \times N_p$ for the Fisher matrix. The index f is assigned to the power spectrum $\Pi^{(i)}(\ell)$, indicating that it is evaluated at the parameters of the fiducial cosmological model. The covariance $C_\Pi^{(ii)}$ measures the correlation of $\Pi^{(i)}$ between different angular frequency bins. From the definition (6.7) one finds

$$\left(C_\Pi^{(ij)}\right)_{\alpha\beta} = \sum_{k=i+2,\,l=j+2}^{N_z} \left(C_P^{(ikjl)}\right)_{\alpha\beta} B^{(i)}(\chi(z_k))\; B^{(j)}(\chi(z_l))\; \chi'(z_k)\; \chi'(z_l)\; \Delta z^2 , \tag{6.12}$$

where the covariance of the convergence power spectra is given by (see Joachimi et al. 2008 for details)

$$\begin{aligned}\left(C_P^{(ijkl)}\right)_{\alpha\beta} &= \frac{2\pi}{A\ell_\alpha\Delta\ell_\alpha}\left\{\bar{P}_\kappa^{(ik)}(\ell_\alpha)\bar{P}_\kappa^{(jl)}(\ell_\alpha) + \bar{P}_\kappa^{(il)}(\ell_\alpha)\bar{P}_\kappa^{(jk)}(\ell_\alpha)\right\}\delta_{\alpha\beta} \\ &\quad \text{with} \quad \bar{P}_\kappa^{(kl)} \equiv P_\kappa^{(kl)} + \delta_{kl}\,\frac{\sigma_\epsilon^2}{2\bar{n}^{(k)}} ,\end{aligned} \tag{6.13}$$

where A denotes the size of the survey and $\Delta\ell$ the width of the angular frequency bins. The shape noise contribution is governed by the intrinsic galaxy ellipticity dispersion σ_ϵ, i.e. $\sigma_\epsilon^2 = \langle\epsilon^{\rm s}\epsilon^{\rm s*}\rangle$ and by the mean number density of galaxies $\bar{n}^{(i)}$ in bin i. Note that for (6.13) to be valid, we have assumed that the shear field is Gaussian and that the survey geometry is simple. Consequently, the power spectrum covariance is diagonal in angular frequency space, so that (6.12) is diagonal as well, rendering the inversion needed for (6.11) trivial.

Besides, in (6.13) it is assumed that any B-mode contribution to the power spectrum vanishes, which is expected for a pure lensing signal and which was already implicitly assumed throughout the preceding derivations. As a side remark, if there was a B-mode contribution due to GI correlations, the nulling technique could eliminate it as long as the B-mode signal has the same characteristic redshift dependence as the E-modes. However, though seen in simulations (Heymans et al. 2006b), B-mode GI correlations are not expected from theory (Hirata & Seljak 2004), so that the scaling with redshift is unknown.

As the actual quantity that is maximised, we choose the trace of the Fisher matrix because of its simple functional form, with the Fisher matrix elements entering $\mathrm{tr}(F^{(i)})$ linearly. Actually, the determinant of the Fisher matrix would be a more natural choice since its inverse is a measure of the volume of the error ellipsoid in parameter space, the inverse Fisher matrix being an estimate of the corresponding covariance matrix. However, due to the non-linearity of the determinant the numerical treatment is considerably less stable. As we demonstrate in Sect. 6.3, the trace fulfils the demand of concentrating the bulk of information into the power spectrum

constructed out of the optimised weight function well enough. Exemplary, lower-dimensional calculations show that the difference in the form of the weight functions, using the trace or the determinant, is marginal.

Considering the continuous limit of $\Pi^{(i)}(\ell)$ in (6.7) for a moment, one arrives at a problem of variational calculus, determining the maximum of $\mathrm{tr}(F^{(i)})$ with respect to the function $B^{(i)}(\chi)$ under the constraint (6.4). However, due to the binned redshift information, $B^{(i)}(\chi)$ only enters the equations in the form of discrete function values, turning the problem into a maximisation with respect to these function values. The complete weight function is then constructed by either interpolation or in parametrised form. Plugging (6.12) and (6.13) into (6.11) yields

$$\begin{aligned}\mathrm{tr}(F^{(i)}) &= \frac{A}{2\pi}\sum_{\alpha=1}^{N_\ell}\ell_\alpha\,\Delta\ell_\alpha\left[\sum_{\mu=1}^{N_p}\left(\sum_{j=i+2}^{N_z}\left\{\frac{\partial P_\kappa^{(ij)}(\ell_\alpha)}{\partial p_\mu}\chi'(z_j)+P_\kappa^{(ij)}(\ell_\alpha)\frac{\partial\chi'(z_j)}{\partial p_\mu}\right\}B(\chi(z_j))\right)^2\right] \\ &\times\left[\sum_{j,\,k=i+2}^{N_z}B(\chi(z_j))\;B(\chi(z_k))\;\chi'(z_j)\;\chi'(z_k)\;\left\{\bar{P}_\kappa^{(ij)}(\ell_\alpha)\bar{P}_\kappa^{(ik)}(\ell_\alpha)+\bar{P}_\kappa^{(ii)}(\ell_\alpha)\bar{P}_\kappa^{(jk)}(\ell_\alpha)\right\}\right]^{-1}. \quad (6.14)\end{aligned}$$

All power spectra and derivatives thereof are evaluated at the fiducial values of the cosmological model. Note that $\mathrm{tr}(F^{(i)})$ is independent of the overall amplitude of $B^{(i)}(\chi)$, as must be the case. The function values of $B^{(i)}(\chi)$ enter $\mathrm{tr}(F^{(i)})$ non-linearly, so that analytical progress is hampered in the general case. Both numerical approaches and analytical approximations are investigated in the following.

6.2.1 Piecewise linear approach

First, we consider a piecewise linear ansatz and write

$$B^{(i)}(\chi(z)) \equiv B_j + \frac{z-z_j}{\Delta z}\left\{B_{j+1}-B_j\right\} \quad \text{for} \quad z\in[z_j,z_{j+1}]\ , \quad (6.15)$$

where the notation $B_j \equiv B^{(i)}(\chi(z_j))$ was introduced for convenience. Moreover, we identify $B_{N_z+1} \equiv B^{(i)}(\chi(z_{\max})) = 0$. The superscript (i) of the weight function is dropped when using this shorthand notation. As before, z_j denotes the lower boundary redshift of bin j, whereas we denote the central redshift of the initial bin, entering the constraint (6.4), as $\hat{z}_i$. With the weight function in the form of (6.15), the constraint reads

$$\sum_{j=i+1}^{N_z}\int_{z_j}^{z_{j+1}}\mathrm{d}z\left[B_j+\frac{z-z_j}{\Delta z}\left\{B_{j+1}-B_j\right\}\right]\;\chi'(z)\left(1-\frac{\chi(\hat{z}_i)}{\chi(z)}\right)=0\ . \quad (6.16)$$

Due to the conditions imposed on $B^{(i)}(\chi)$, as mentioned in Sect. 6.1, $B_{i+1}=0$ holds, so that the constraint assumes the compact form

$$\sum_{j=i+2}^{N_z}B_j\left(I_j^0-I_j^1+I_{j-1}^1\right)=0\ , \quad (6.17)$$

where the quantities

$$\begin{aligned}I_j^0 &= \int_{z_j}^{z_{j+1}}\mathrm{d}z\;\chi'(z)\left(1-\frac{\chi(\hat{z}_i)}{\chi(z)}\right)=\chi(z_{j+1})-\chi(z_j)-\chi(\hat{z}_i)\;\ln\left(\frac{\chi(z_{j+1})}{\chi(z_j)}\right)\ ; \quad (6.18)\\ I_j^1 &= \int_{z_j}^{z_{j+1}}\mathrm{d}z\;\frac{z-z_j}{\Delta z}\;\chi'(z)\left(1-\frac{\chi(\hat{z}_i)}{\chi(z)}\right)\end{aligned}$$

were introduced. Fixing one of the function values via (6.17), the remaining B_j are varied to obtain a maximum of the trace of the Fisher matrix, using a Nelder-Mead simplex algorithm, which is robust and does not require partial derivatives. However, this type of maximisation routine easily gets stuck in local extrema, which in this case are caused by single outliers among the B_j. These are considered unrealistic since $B^{(i)}(\chi)$ is expected to be smooth, but the piecewise linear ansatz does not put any constraints on the derivatives of the weight function.

To avoid the false maxima due to outliers, we subtract the regularisation term

$$U \equiv \Lambda \sum_{j=i+1}^{N_z} \left(B_{j+1} - 2B_j + B_{j-1}\right)^{2\eta} \tag{6.19}$$

from (6.14), summing the differences in slopes at the nodes, thereby disfavouring solutions with abrupt changes in the first derivative. The fudge factor $\Lambda > 0$ can be chosen arbitrarily, while η denotes a small, positive integer. The larger η, the more weight is given to large changes in slope in U, where we found a suitable value of $\eta = 2$. If a value of Λ is chosen such that U and $\mathrm{tr}(F^{(i)})$ are roughly the same order of magnitude, the resulting weight functions are very smooth. By gradually lowering Λ, less smooth $B^{(i)}(\chi)$ with a more pronounced maximum are obtained. In case an outlier B_j occurs, the initial values of the simplex algorithm are altered, until a stable solution with $\Lambda = 0$ results.

The weight functions of this section are hardly susceptible to false maxima due to their smoothness, so that mostly we can set $\Lambda = 0$ from the beginning. However, the procedure outlined here is necessary for the more oscillatory weight functions that will be computed in Sect. 6.2.5. Still, the final results presented in this work have been obtained with $\Lambda = 0$ throughout. As can be seen from (6.14), the maximum of $\mathrm{tr}(F^{(i)})$ does not depend on the overall amplitude of $B^{(i)}(\chi)$, leading to a degeneracy in the maximised B_j, which will be lifted by a normalisation, see Sect. 6.2.4.

6.2.2 Chebyshev series approach

The second numerical approach assumes that $B^{(i)}(\chi)$ is composed of a finite series of ansatz functions with a set of free parameters. In this case, we choose Chebyshev polynomials of the first kind T_μ, which already lead to good approximations for low polynomial orders and yield evenly distributed errors. The weight function is expanded as

$$B^{(i)}(\chi) \equiv \left\{\chi - \chi(z_{i+1})\right\} \left\{\chi - \chi(z_{\max})\right\} \sum_{\mu=0}^{N_\mathrm{c}} b_\mu \, T_\mu \left(\frac{2\chi - \left\{\chi(z_{i+1}) + \chi(z_{\max})\right\}}{\chi(z_{\max}) - \chi(z_{i+1})} \right) , \tag{6.20}$$

where the b_μ denote the $N_\mathrm{c} + 1$ free coefficients. The argument of T_μ is chosen such that it takes on values in the interval $[-1, 1]$. Plugging this definition into (6.4), one gets

$$\sum_{\mu=0}^{N_\mathrm{c}} b_\mu Q^1_\mu = 0 \tag{6.21}$$

with the definition

$$\begin{aligned} Q^1_\mu \;\equiv\; & \int_{z_{i+1}}^{z_{\max}} \mathrm{d}z \left\{\chi(z) - \chi(z_{i+1})\right\} \left\{\chi(z) - \chi(z_{\max})\right\} \\ & \times T_\mu \left(\frac{2\chi(z) - \left\{\chi(z_{i+1}) + \chi(z_{\max})\right\}}{\chi(z_{\max}) - \chi(z_{i+1})} \right) \left(1 - \frac{\chi(\hat{z}_i)}{\chi(z)}\right) \chi'(z) \, . \end{aligned} \tag{6.22}$$

Again, one of the parameters is fixed by (6.21), while N_c parameters are used for the multi-dimensional maximisation of the trace of the Fisher matrix with the simplex algorithm. If the number of free parameters is chosen to be more than about 5, the resulting weight functions are prone to significant oscillations, generated by the response of the ansatz polynomials to the steep rise in $B^{(i)}(\chi)$ for $\chi(z) - \chi(z_{i+1}) \ll 1$. These unphysical features, corresponding to shallow maxima in parameter space, are readily detected by visual inspection of the resulting weight functions and avoided by altering the – in this approach low-dimensional – set of initial values b_μ. As for the piecewise linear ansatz, we observe the degeneracy in the parameters yielding the maximum due to the free scaling of the weight function.

6.2.3 Simplified analytical approach

We elaborate on an analytical approach that is computationally fast and can provide an important consistency check for the preceding numerical methods. However, as stated above, the non-linearity hinders the analytical treatment of the full problem; instead, we confine ourselves in the following to considering a single angular frequency bin and only one element of the Fisher matrix, i.e. a single cosmological parameter. A vector notation is introduced as follows.

Let the non-vanishing values of the weight function B_j, given in their shorthand notation of Sect. 6.2.1, form a vector $\boldsymbol{B}$. Note that in the vector notation we again drop the superscript (i) since the initial bin that $\boldsymbol{B}$ refers to will be clear from the context. By defining another vector $\boldsymbol{f}$ with components

$$f_j \equiv \left(1 - \frac{\chi(\hat{z}_i)}{\chi(z_j)}\right) \chi'(z_j) \quad \text{for} \quad j = i+2, .., N_z \,, \tag{6.23}$$

the constraint (6.4) simply turns in its discretised version into

$$(\boldsymbol{B} \cdot \boldsymbol{f}) = 0 \,. \tag{6.24}$$

Note that the constant bin width Δz is not included in $\boldsymbol{f}$, as it drops out when setting the discrete constraint expression to zero. The covariance of $\Pi^{(i)}$, given by (6.12), reduces to a scalar quantity due to the single angular frequency bin ℓ under consideration. Defining a matrix $\bar{C}$ with elements

$$\bar{C}_{kl} \equiv \left(C_P^{(ikil)}\right)_\ell \, \chi'(z_k) \, \chi'(z_l) \,, \tag{6.25}$$

the covariance can be written as

$$C_\Pi^{(ii)} = \boldsymbol{B}^\tau \bar{C} \boldsymbol{B} \, \Delta z^2 \,. \tag{6.26}$$

The Fisher matrix element, now indicated by a subscript o, reads as

$$F_o^{(i)} = \frac{(\boldsymbol{B} \cdot \boldsymbol{\rho})^2}{\boldsymbol{B}^\tau \bar{C} \boldsymbol{B}} \tag{6.27}$$

with a further vector defined for convenience,

$$\rho_j \equiv \frac{\partial P_\kappa^{(ij)}(\ell)}{\partial p} \chi'(z_j) + P_\kappa^{(ij)}(\ell) \frac{\partial \chi'(z_j)}{\partial p} \,. \tag{6.28}$$

By means of this vector, one is able to rewrite the derivative of the power spectrum with respect to the remaining cosmological parameter p as $\partial \Pi^{(i)}(\ell)/\partial p = (\boldsymbol{B} \cdot \boldsymbol{\rho}) \, \Delta z$, which can be seen by

taking the derivative of (6.7). The bin widths Δz cancel in $F_o^{(i)}$, so that they do not need to appear in the definitions of $\bar{C}$ and $\boldsymbol{\rho}$. The constraint is incorporated by means of a Lagrange multiplier λ, leading to the quantity $G \equiv F_o^{(i)} + \lambda\,(\boldsymbol{B}\cdot\boldsymbol{f})$, which is to be maximised with respect to the components of the vector $\boldsymbol{B}$. One obtains

$$\nabla_B\, G = 2\boldsymbol{\rho}\,\frac{(\boldsymbol{B}\cdot\boldsymbol{\rho})}{\boldsymbol{B}^\tau\bar{C}\boldsymbol{B}} - 2\,\bar{C}\boldsymbol{B}\,\left(\frac{(\boldsymbol{B}\cdot\boldsymbol{\rho})}{\boldsymbol{B}^\tau\bar{C}\boldsymbol{B}}\right)^2 + \lambda\boldsymbol{f} = 0\;, \tag{6.29}$$

which can be formally solved for $\boldsymbol{B}$, resulting in

$$\boldsymbol{B} = \mathcal{N}\bar{C}^{-1}\left\{\boldsymbol{\rho}\,\frac{\boldsymbol{B}^\tau\bar{C}\boldsymbol{B}}{(\boldsymbol{B}\cdot\boldsymbol{\rho})} + \frac{\lambda}{2}\,\boldsymbol{f}\,\left(\frac{\boldsymbol{B}^\tau\bar{C}\boldsymbol{B}}{(\boldsymbol{B}\cdot\boldsymbol{\rho})}\right)^2\right\}\;, \tag{6.30}$$

where the free normalisation $\mathcal{N}$ of $\boldsymbol{B}$ has been introduced.

An overall scaling factor in $\boldsymbol{B}$ neither modifies the information content of $\Pi^{(i)}$ nor does it alter the constraint (6.4), which illustrates that the conditions stated above do not fix the normalisation. The formal solution is plugged into (6.24), which is then solved for the Lagrange multiplier,

$$\frac{\lambda}{2} = -\,\frac{(\boldsymbol{B}\cdot\boldsymbol{\rho})}{\boldsymbol{B}^\tau\bar{C}\boldsymbol{B}}\,\frac{\boldsymbol{f}^\tau\bar{C}^{-1}\boldsymbol{\rho}}{\boldsymbol{f}^\tau\bar{C}^{-1}\boldsymbol{f}}\;. \tag{6.31}$$

Replacing $\lambda/2$ in (6.30) subsequently yields

$$\begin{aligned}\boldsymbol{B} &= \mathcal{N}\,\frac{\boldsymbol{B}^\tau\bar{C}\boldsymbol{B}}{(\boldsymbol{B}\cdot\boldsymbol{\rho})}\left\{\bar{C}^{-1}\boldsymbol{\rho} - \frac{\boldsymbol{f}^\tau\bar{C}^{-1}\boldsymbol{\rho}}{\boldsymbol{f}^\tau\bar{C}^{-1}\boldsymbol{f}}\,\bar{C}^{-1}\boldsymbol{f}\right\} \\ &= \mathcal{N}'\left\{\bar{C}^{-1}\boldsymbol{\rho} - \frac{\boldsymbol{f}^\tau\bar{C}^{-1}\boldsymbol{\rho}}{\boldsymbol{f}^\tau\bar{C}^{-1}\boldsymbol{f}}\,\bar{C}^{-1}\boldsymbol{f}\right\}\;,\end{aligned} \tag{6.32}$$

where the scalar quantity $(\boldsymbol{B}\cdot\boldsymbol{\rho})\,/\boldsymbol{B}^\tau\bar{C}\boldsymbol{B}$ was absorbed into the normalisation $\mathcal{N}'$, so that now the righthand side depends no longer on $\boldsymbol{B}$. Optimised analytical weight functions can be calculated by means of (6.32), interpolating linearly between the values of the components of $\boldsymbol{B}$. In order to achieve results as close to the non-simplified, numerical approaches as possible, the employed element $F_o^{(i)}$ is chosen to be the diagonal element of the Fisher matrix that yields the largest contribution to the trace. Afterwards $\boldsymbol{B}$ is determined on a grid of ℓ-values within the range considered in the numerical approaches, the solution vector resulting in the largest $F_o^{(i)}$ being taken as the 'optimal' weight function. As long as this term, which is supposed to be the strongest contribution to the sum in (6.14), dominates the trace of the Fisher matrix, we expect this procedure to yield a reasonably good approximation to the numerical results.

6.2.4 Resulting nulling weights

To construct actual weight functions $B^{(i)}(\chi)$, a fictive tomographic cosmic shear survey with a comparatively large number of narrow redshift bins is needed. Due to the choice of $\Pi^{(i)}(\ell)$ as the quantity considered, the necessary input data comprises a set of tomographic power spectra, which are obtained for a ΛCDM universe with fiducial parameters $\Omega_\mathrm{m} = 0.3$, $\Omega_\Lambda = 0.7$, and $H_0 = 100\,h\,\mathrm{km/s/Mpc}$ with $h = 0.7$. The three-dimensional power spectrum of density fluctuations is specified by the primordial slope $n_\mathrm{s} = 1$, the normalisation $\sigma_8 = 0.9$ and the shape parameter Γ, calculated according to Sugiyama (1995) with $\Omega_\mathrm{b} = 0.04$. The linear power spectrum is given by the fit formula of Bardeen et al. (1986), while the non-linear evolution is

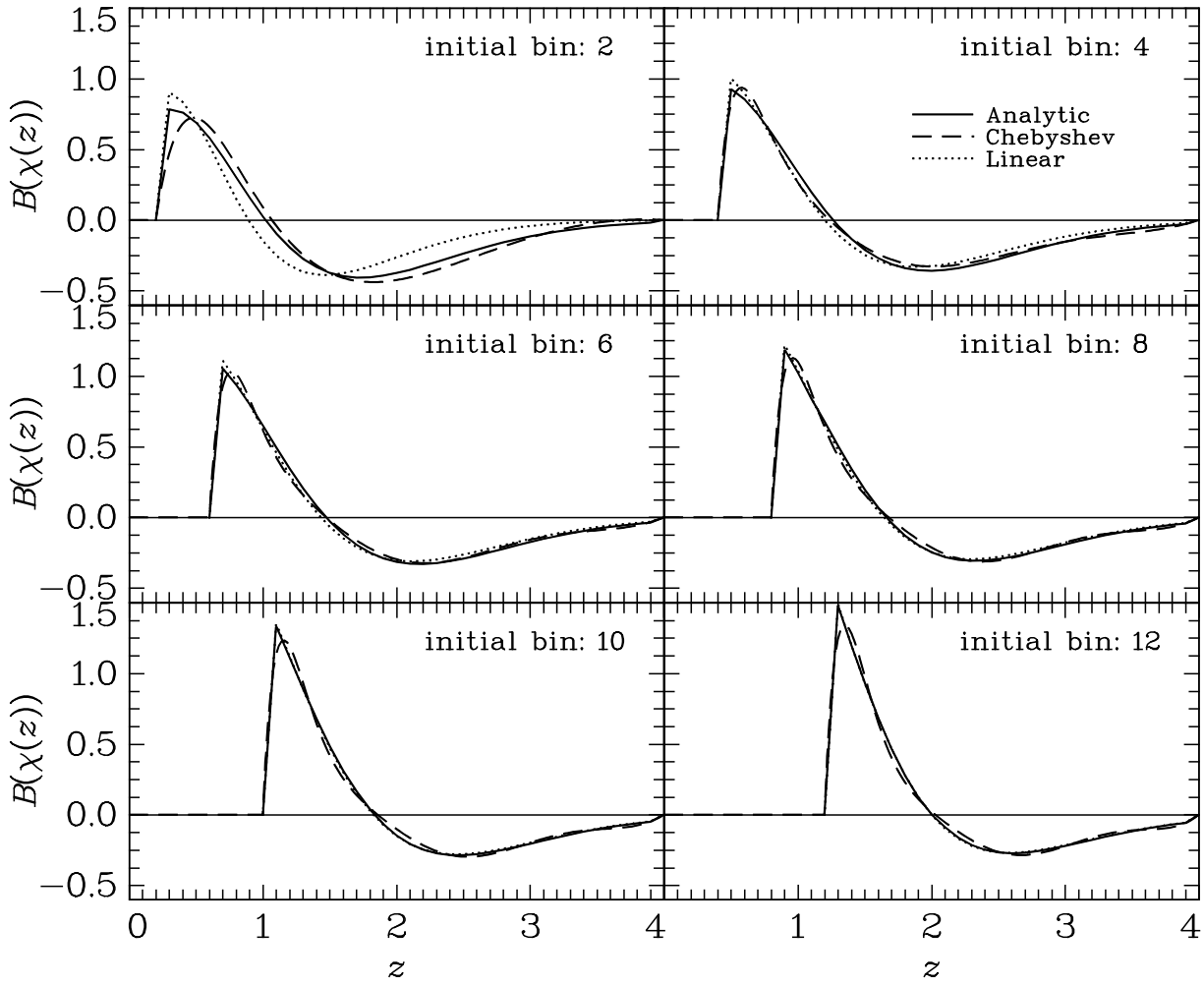

Figure 6.2: Nulling weights $B^{(i)}(\chi(z))$ as a function of redshift for $N_z = 40$ bins. The initial bin numbers i are given in the respective panels, the corresponding bins being located directly below the redshift where the weight functions drop to zero. Plotted are the simplified analytical solution as solid curve, the Chebyshev series solution as dashed line, and the piecewise linear solution as dotted curve.

included via the prescription of Smith et al. (2003). The tomography power spectra are then determined for $N_\ell = 75$ logarithmic angular frequency bins between $\ell = 50$ and $\ell = 10^4$.

Furthermore, we specify survey properties that enter (6.14) via the power spectrum covariance (6.13). For this a normalised galaxy redshift probability distribution of the form (4.47) with $z_0 = 1.0$ and $\beta = 1.5$ is assumed. The redshift distribution is cut off at $z_\mathrm{max} = 4$, requiring a renormalisation, which leads to the modified distribution $p_\mathrm{cut}(z)$. However, due to the large cut-off redshift the modification is marginal. The dependence of the covariance on the survey size A is trivial, its value being irrelevant for the determination of the weight functions. For later calculations of likelihoods, we set A to a fiducial size of $1\,\mathrm{deg}^2$. Moreover, we set the intrinsic ellipticity dispersion to $\sigma_\epsilon = 0.4$ and choose a mean galaxy number density of $\bar{n} = 30\,\mathrm{arcmin}^{-2}$. The bin-wise number densities are obtained by

$$\bar{n}^{(i)} = \bar{n} \int_{z_i}^{z_{i+1}} \mathrm{d}z \; p_\mathrm{cut}(z) \; . \tag{6.33}$$

The derivatives of the power spectra with respect to cosmological parameters in (6.14) are obtained via finite differencing, while $\partial\chi'(z_j)/\partial p_\mu$ is calculated from (2.10) in analytical form.

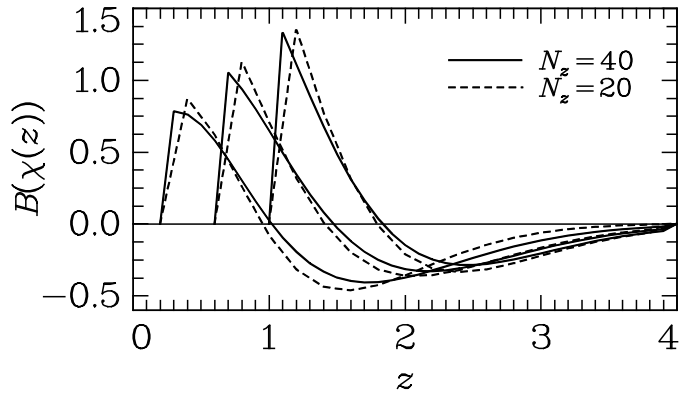

Figure 6.3: Nulling weight functions as a function of redshift for two different redshift binnings. Solid curves were obtained with $N_z = 40$; dashed lines with $N_z = 20$. Plotted are the simplified analytical solutions for initial bins 2, 6, and 10 in the case of 40 bins, and 1, 3, and 5 in the case of 20 bins.

To determine the Fisher information, we consider the set of cosmological parameters $\boldsymbol{p} = (\Omega_\mathrm{m}, \Omega_\Lambda, \sigma_8, h)$. Aiming at smooth weight functions, we use a large number of redshift bins, i.e. $N_z = 40$, corresponding to $\Delta z = 0.1$. As mentioned in the foregoing section, the normalisation of the weight functions is not yet fixed. To allow for direct comparison of the three approaches, we impose the condition

$$\int_{\hat{\chi}_i}^{\chi_\mathrm{hor}} \mathrm{d}\chi \, |B^{(i)}(\chi)|^2 = 1 \, . \tag{6.34}$$

Furthermore, the free sign of $B^{(i)}(\chi)$ is chosen such that the weight function first assumes positive values when departing from zero at the upper boundary of the initial bin.

In Fig. 6.2 the resulting weight functions of all three approaches under consideration are shown for varying initial bin i. All methods are in very good agreement; only in the upper left panel are larger deviations visible. A close inspection reveals that the weight functions constructed by means of the Chebyshev series suffer from slight oscillations that can rapidly increase in amplitude in some cases if N_c is chosen too large. These can presumably be explained by the steep rise of $B^{(i)}(\chi)$ near the initial bin.

Generally speaking, the agreement justifies the assumptions made in the different approaches. In particular, the results of the relatively crude approximations of the analytical approach are compatible with the numerical calculations, so that it is well-suited to further investigation. The weight functions have a zero-crossing, which is expected due to (6.4), where the term $1 - \hat{\chi}_i/\chi$ is non-negative throughout the integration interval. The largest weight is assigned to those redshifts that are located directly above the initial bin, respectively, because the efficiency of the lensing of a source in this range of redshifts by the mass distribution within the initial bin is low or, in other words, $D_\mathrm{ds}/D_\mathrm{s}$ is small, which decreases the contribution by GI correlations.

The division of a cosmic shear survey into 40 redshift bins is realistic in the near future. However, the bin size would not be chosen constant as in this study, but probably scale with $1 + z$. Mainly for computational reasons, we reduce the number of redshift bins used in the following likelihood analysis to 20, a number which could be achieved by some of the upcoming wide-field projects such as Pan-STARRS, KIDS, or the Dark Energy Survey. We compare the form of the weight functions obtained above with an analogous set, determined for $N_z = 20$. Figure 6.3 illustrates for a sample of analytical solutions for $B^{(i)}(\chi)$ that the sets for both redshift binnings agree well. The higher density of sampling points in the case of $N_z = 40$ enables a steeper rise of the weight functions at the upper boundary of the initial bin, leading to deviations in similar magnitude in the tail of $B^{(i)}(\chi)$. These results also suggest that the effects due to the discretisation of the weight functions are negligible as long as the number of redshift bins is not chosen too small.

6.2.5 Higher order weights

The power spectrum $\Pi^{(i)}(\ell)$, given by (6.7), is a linear combination of the observed power spectra, with the weighting determined by the function $B^{(i)}(\chi)$, as calculated in the foregoing section. More such linear combinations can be constructed with differing weight functions that still obey the constraint equation, resulting in further power spectra free of GI correlations. If one retains the condition of maximising the Fisher matrix and, in addition, demands that the weight functions should be orthogonal with respect to each other in a suitably defined sense, one arrives at higher-order measures that have the second-most, third-most, etc., information content.

Since in (6.7) the first term that yields a contribution is for $j = i + 2$ (see also Fig. 6.1), $N_z - i - 1$ convergence power spectra are used to form $\Pi^{(i)}(\ell)$ in the implementation presented above. As a consequence, one is able to construct $N_z - i - 2$ mutually orthogonal power spectra $\Pi^{(i)}(\ell)$ from this data set. The additional combination that could be built furthermore with linear independence from the set of convergence power spectra then necessarily violates (6.4) and consequently contains GI correlations.

Denoting the order of the weight function by a subscript in square brackets, the condition of mutual orthogonality between weight functions of order q and r can be formulated as

$$\int_{\hat{\chi}_i}^{\chi(z_{\max})} \mathrm{d}z \; B^{(i)}_{[q]}(\chi(z)) \; B^{(i)}_{[r]}(\chi(z)) \; w(z) = 0 \tag{6.35}$$

for all orders $q > r$, where $w(z)$ is an arbitrary weight function. As far as the two numerical approaches are concerned, the higher order weight functions are obtained by fixing one further free parameter for every orthogonality condition. In the case of the piecewise linear ansatz, one obtains by plugging the ansatz functions (6.15) into (6.35)

$$\sum_{j=i+1}^{N_z} \int_{z_j}^{z_{j+1}} \mathrm{d}z \left[B_{[q],j} + \frac{z - z_j}{\Delta z} \left\{ B_{[q],j+1} - B_{[q],j} \right\} \right] \; B^{(i)}_{[r]}(\chi(z)) \; w(z) = 0 \tag{6.36}$$

for every $r = 1, .., q - 1$. The lower order weight functions have been determined in advance and are known. Defining

$$\begin{aligned} I^2_{r,j} &= \int_{z_j}^{z_{j+1}} \mathrm{d}z \; B^{(i)}_{[r]}(\chi(z)) \; w(z) \; ; \\ I^3_{r,j} &= \int_{z_j}^{z_{j+1}} \mathrm{d}z \; \frac{z - z_j}{\Delta z} \; B^{(i)}_{[r]}(\chi(z)) \; w(z) \; , \end{aligned} \tag{6.37}$$

one can write (6.36) in analogy to (6.17) as

$$\sum_{j=i+2}^{N_z} B_{[q],j} \left(I^2_{r,j} - I^3_{r,j} + I^3_{r,j-1} \right) = 0 \; . \tag{6.38}$$

The Chebyshev approach yields, inserting (6.20) into (6.35),

$$\sum_{\mu=0}^{N_\mathrm{c}} b_\mu Q^2_{r,\mu} = 0 \; , \tag{6.39}$$

again for $r = 1, .., q - 1$, where we have defined

$$\begin{aligned} Q^2_{r,\mu} \equiv & \int_{z_{i+1}}^{z_{\max}} \mathrm{d}z \left\{ \chi(z) - \chi(z_{i+1}) \right\} \left\{ \chi(z) - \chi(z_{\max}) \right\} \\ & \times T_\mu \left(\frac{2\chi(z) - \left\{ \chi(z_{i+1}) + \chi(z_{\max}) \right\}}{\chi(z_{\max}) - \chi(z_{i+1})} \right) B^{(i)}_{[r]}(\chi(z)) \; w(z) \; . \end{aligned} \tag{6.40}$$

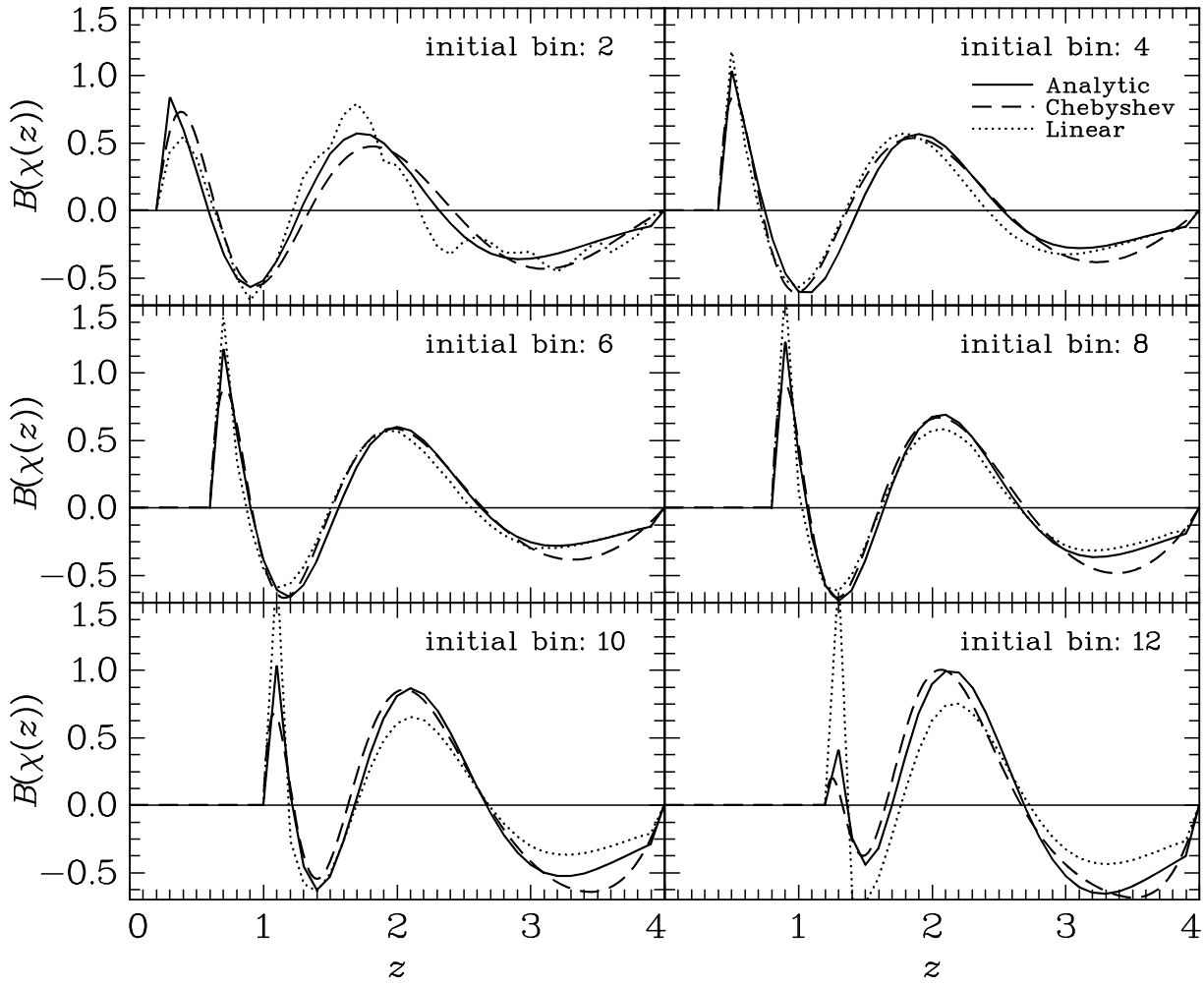

Figure 6.4: Second-order nulling weight functions as a function of redshift for $N_z = 40$. The initial bins are given in the respective panels. The coding of the curves is the same as in Fig. 6.2.

Besides, higher order weight functions can be constructed with the analytical ansatz, again considering only a single angular frequency bin and solely one component of the Fisher matrix, optimising it subsequently as outlined in Sect. 6.2.3. To clarify the notation, we rewrite the result for the first-order weight function (6.32) as

$$\boldsymbol{B}_{[1]} = \mathcal{N}' \bar{C}^{-1} \boldsymbol{\rho}^{\{1\}} \quad \text{with} \quad \boldsymbol{\rho}^{\{1\}} \equiv \boldsymbol{\rho} - \frac{\boldsymbol{f}^\tau \bar{C}^{-1} \boldsymbol{\rho}}{\boldsymbol{f}^\tau \bar{C}^{-1} \boldsymbol{f}} \, \boldsymbol{f} \; . \tag{6.41}$$

As in Sect. 6.2.3 we perform the derivation for an initial bin i, where the index does not explicitly appear in the formulae, but enters the quantities $\boldsymbol{f}$, $\bar{C}$, and $\boldsymbol{\rho}$. In this context the condition of orthogonality can be implemented as

$$\left(\boldsymbol{B}_{[q]} \cdot \widetilde{\boldsymbol{B}}_{[r]} \right) = 0 \tag{6.42}$$

for all orders $q > r$, where $\widetilde{B}_j \equiv B^{(i)}(\chi(z_j))w(z_j)$ was defined. This condition is incorporated into the maximisation by more Lagrange multipliers, the expression to be maximised for order q turning into

$$G_{[q]} = F_o^{(i)} + \lambda_{[q]} \left(\boldsymbol{B}_{[q]} \cdot \boldsymbol{f} \right) + \sum_{r=1}^{q-1} \mu_{[q]}^r \left(\boldsymbol{B}_{[q]} \cdot \widetilde{\boldsymbol{B}}_{[r]} \right) \; , \tag{6.43}$$

where the $\mu^r_{[q]}$ are the Lagrange multipliers for the respective orthogonality conditions. The Fisher matrix element $F_o^{(i)}$ is still given by (6.27), now with weight functions $\boldsymbol{B}_{[q]}$. After taking the gradient with respect to the components of $\boldsymbol{B}_{[q]}$ in analogy to the first-order calculation, one arrives at the formal solution

$$\boldsymbol{B}_{[q]} = \mathcal{N}\bar{C}^{-1}\left\{\boldsymbol{\rho}\,\frac{\boldsymbol{B}^\tau_{[q]}\bar{C}\boldsymbol{B}_{[q]}}{\left(\boldsymbol{B}_{[q]}\cdot\boldsymbol{\rho}\right)} + \frac{\lambda_{[q]}}{2}\,\boldsymbol{f}\,\left(\frac{\boldsymbol{B}^\tau_{[q]}\bar{C}\boldsymbol{B}_{[q]}}{\left(\boldsymbol{B}_{[q]}\cdot\boldsymbol{\rho}\right)}\right)^2 + \sum_{r=1}^{q-1}\frac{\mu^r_{[q]}}{2}\,\widetilde{\boldsymbol{B}}_{[r]}\,\left(\frac{\boldsymbol{B}^\tau_{[q]}\bar{C}\boldsymbol{B}_{[q]}}{\left(\boldsymbol{B}_{[q]}\cdot\boldsymbol{\rho}\right)}\right)^2\right\}\,. \tag{6.44}$$

The Lagrange multipliers are successively replaced by inserting this solution into the corresponding constraint equations. As a first step, from $\left(\boldsymbol{f}\cdot\boldsymbol{B}_{[q]}\right)=0$ one obtains

$$\frac{\lambda_{[q]}}{2} = -\frac{\left(\boldsymbol{B}_{[q]}\cdot\boldsymbol{\rho}\right)}{\boldsymbol{B}^\tau_{[q]}\bar{C}\boldsymbol{B}_{[q]}}\,\frac{\boldsymbol{f}^\tau\bar{C}^{-1}\boldsymbol{\rho}}{\boldsymbol{f}^\tau\bar{C}^{-1}\boldsymbol{f}} - \sum_{r=1}^{q-1}\frac{\mu^r_{[q]}}{2}\,\frac{\boldsymbol{f}^\tau\bar{C}^{-1}\widetilde{\boldsymbol{B}}_{[r]}}{\boldsymbol{f}^\tau\bar{C}^{-1}\boldsymbol{f}}\,. \tag{6.45}$$

Plugging in this expression, (6.44) turns into

$$\boldsymbol{B}_{[q]} = \mathcal{N}'\bar{C}^{-1}\left\{\boldsymbol{\rho}^{\{1\}} + \sum_{r=1}^{q-1}\frac{\mu^r_{[q]}}{2}\,\widetilde{\boldsymbol{B}}^{\{1\}}_{[r]}\,\frac{\boldsymbol{B}^\tau_{[q]}\bar{C}\boldsymbol{B}_{[q]}}{\left(\boldsymbol{B}_{[q]}\cdot\boldsymbol{\rho}\right)}\right\} \tag{6.46}$$

with the definition

$$\boldsymbol{x}^{\{1\}} \equiv \boldsymbol{x} - \frac{\boldsymbol{f}^\tau\bar{C}^{-1}\boldsymbol{x}}{\boldsymbol{f}^\tau\bar{C}^{-1}\boldsymbol{f}}\,\boldsymbol{f}\,, \tag{6.47}$$

where $\boldsymbol{x}\in\left\{\boldsymbol{\rho},\boldsymbol{B}_{[q]}\right\}$. Again, multiplicative scalars have been absorbed into the normalisation. In a similar manner, inserting (6.46) into (6.42) for $r=1$ leads to

$$\boldsymbol{B}_{[q]} = \mathcal{N}'\bar{C}^{-1}\left\{\boldsymbol{\rho}^{\{2\}} + \sum_{r=2}^{q-1}\frac{\mu^r_{[q]}}{2}\,\widetilde{\boldsymbol{B}}^{\{2\}}_{[r]}\,\frac{\boldsymbol{B}^\tau_{[q]}\bar{C}\boldsymbol{B}_{[q]}}{\left(\boldsymbol{B}_{[q]}\cdot\boldsymbol{\rho}\right)}\right\}\,, \tag{6.48}$$

where we set

$$\boldsymbol{x}^{\{2\}} \equiv \boldsymbol{x}^{\{1\}} - \frac{\widetilde{\boldsymbol{B}}^\tau_{[1]}\bar{C}^{-1}\boldsymbol{x}^{\{1\}}}{\widetilde{\boldsymbol{B}}^\tau_{[1]}\bar{C}^{-1}\widetilde{\boldsymbol{B}}^{\{1\}}_{[1]}}\,\widetilde{\boldsymbol{B}}^{\{1\}}_{[1]}\,. \tag{6.49}$$

If one continues likewise for the remaining constraint equations, one obtains in accordance with (6.41) the compact result

$$\boldsymbol{B}_{[q]} = \mathcal{N}\bar{C}^{-1}\boldsymbol{\rho}^{\{q\}} \tag{6.50}$$

for all orders q, where the redefined normalisation is denoted by just $\mathcal{N}$ again. Here we made use of the recursion relation

$$\boldsymbol{x}^{\{r\}} = \boldsymbol{x}^{\{r-1\}} - \frac{\widetilde{\boldsymbol{B}}^\tau_{[r-1]}\bar{C}^{-1}\boldsymbol{x}^{\{r-1\}}}{\widetilde{\boldsymbol{B}}^\tau_{[r-1]}\bar{C}^{-1}\widetilde{\boldsymbol{B}}^{\{r-1\}}_{[r-1]}}\,\widetilde{\boldsymbol{B}}^{\{r-1\}}_{[r-1]}\,, \tag{6.51}$$

supplemented by the initial step (6.47). Consequently, a recursion relation for the vectors $\boldsymbol{B}_{[q]}$, corresponding to the higher order weight functions, can be derived, which reads

$$\boldsymbol{B}_{[q]} = \mathcal{N}\left\{\boldsymbol{B}_{[q-1]} - \frac{\widetilde{\boldsymbol{B}}^\tau_{[q-1]}\,\boldsymbol{B}_{[q-1]}}{\widetilde{\boldsymbol{B}}^\tau_{[q-1]}\bar{C}^{-1}\widetilde{\boldsymbol{B}}^{\{q-1\}}_{[q-1]}}\,\bar{C}^{-1}\widetilde{\boldsymbol{B}}^{\{q-1\}}_{[q-1]}\right\} \tag{6.52}$$

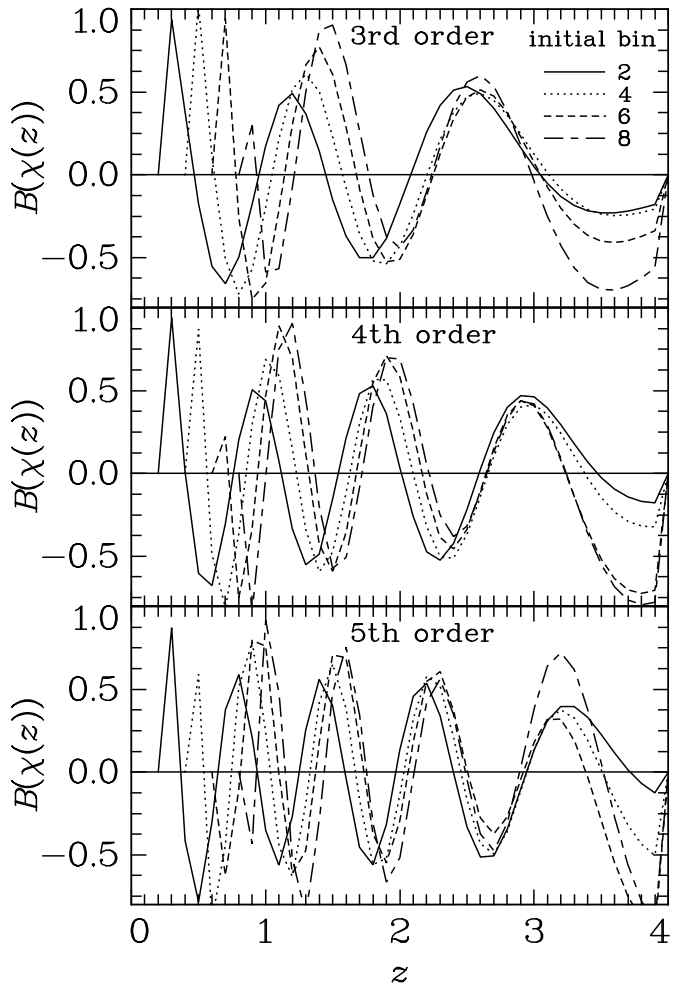

Figure 6.5: Higher-order nulling weight functions as a function of redshift for $N_z = 40$. From top to bottom the third to fifth order analytical solutions are shown. Solid curves correspond to initial bin $i = 2$, dotted curves to $i = 4$, short-dashed curves to $i = 6$, and long-dashed curves to $i = 8$.

for $q \geq 2$, the vector $\boldsymbol{B}_{[1]}$ as the starting point for this recursion being given by (6.41).

The weight function $w(z)$ could for instance be chosen, such that it scales with the redshift probability distribution $p_{\rm cut}(z)$, assigning a larger weight to well-sampled redshift ranges. However, we set $w(z) \equiv 1$ in the following for reasons of simplicity. In addition, (6.42) then turns into an orthogonality relation also for the vectors $\boldsymbol{B}_{[q]}$.

In Fig. 6.4 the results for second-order weight functions $B^{(i)}_{[2]}(\chi)$ are plotted, for all three methods considered in this work and using the same setup as described in Sect. 6.2.4. Apart from slight numerical instabilities, as can be seen for the linear approach in the upper left panel, and the differing response to sharp peaks in the weight functions, most prominent in the lower right panel, the curves largely agree. Again, the simplified analytical ansatz proves to be compatible, being computationally advantageous to a large extent due to its recursive form (6.52). For all curves the number of zeros has increased by two compared to the first-order results, a trend that continues for higher orders. A sample of analytical solutions for third- to fifth-order weight functions is given in Fig. 6.5.

Adopting the notation introduced for the weight functions, the new power spectra can be generalised to higher orders as

$$\Pi^{(i)}_{[q]}(\ell) \approx \sum_{j=1}^{N_z} B^{(i)}_{[q]}(\chi(z_j))\; P^{(ij)}_{\kappa}(\ell)\; \chi'(z_j)\; \Delta z \tag{6.53}$$

for initial bin i and order q. Employing analytically determined weight functions, we compute these power spectra for different initial bins and orders, the resulting graphs shown in Fig. 6.6.

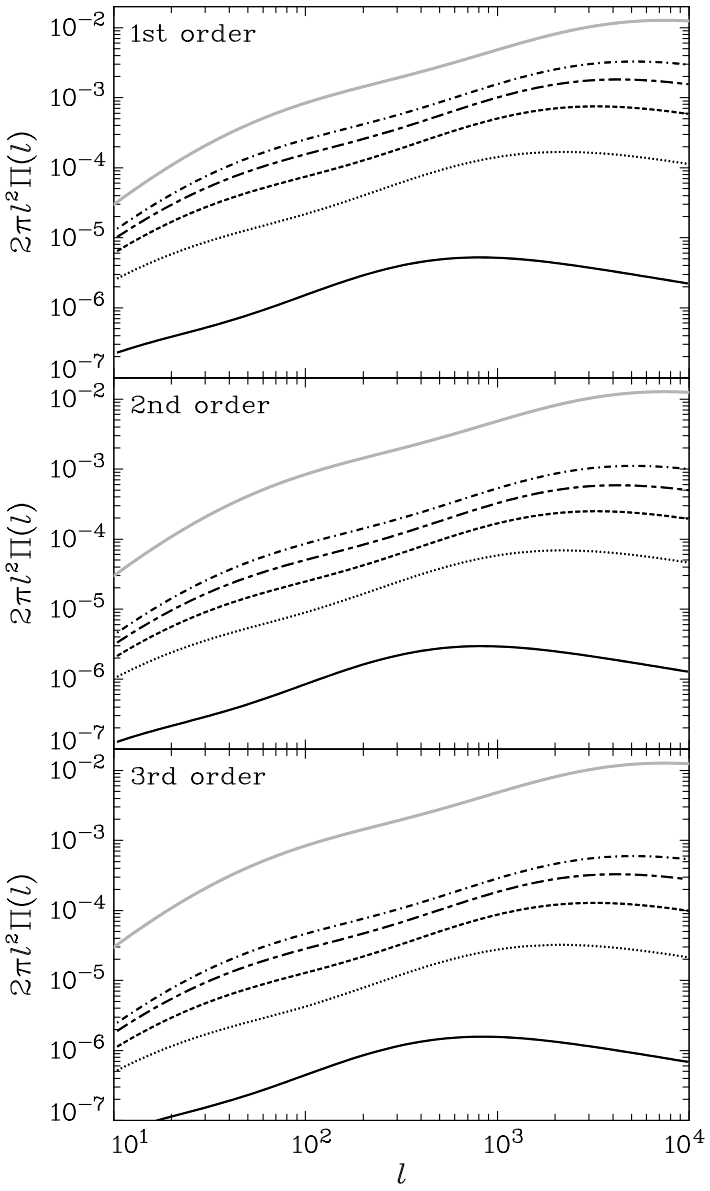

Figure 6.6: Transformed power spectra as a function of angular frequency, making use of the analytically determined nulling weight functions. The power spectra $\Pi^{(i)}_{[q]}(\ell)$ are given as black curves, their order q ranging from 1 in the top panel to 3 in the bottom panel. Within each panel the power spectra for initial bins $i = 1, .., 5$ are plotted in the following sequence of line types: solid, dotted, dashed, chain-dashed, and dot-dashed. In addition, the convergence power spectrum $P_\kappa(\ell)$, integrated over the full redshift distribution (4.47), is shown for reference as grey curve.

For reference the convergence power spectrum $P_\kappa(\ell)$, integrated over the full redshift distribution as given by (4.47), is plotted in addition. It is important to note that $\Pi^{(i)}_{[q]}(\ell)$ and $P_\kappa(\ell)$ can only be compared with difficulty in terms of the overall amplitude, since for the newly constructed power spectra, the amplitude can be chosen arbitrarily due to the free normalisation of the $B^{(i)}_{[q]}(\chi)$. In Fig. 6.6 it is fixed by (6.34), so that the weights are of order unity. Therefore it is evident that the $\Pi^{(i)}_{[q]}(\ell)$ have considerably lower amplitude than the reference power spectrum since to obtain the former quantities, power spectrum signals are partially subtracted.

Concerning shape, the $\Pi^{(i)}_{[q]}(\ell)$ show a largely similar behaviour with respect to the convergence power spectrum, the latter peaking at higher values of ℓ. This can be understood by taking into account that the tomography power spectrum with the smallest difference between bins i and j contributes most to the respective $\Pi^{(i)}_{[q]}(\ell)$, as can be concluded from the form of the first-order weight functions, its pronounced peak being located just above the initial bin, see Fig. 6.2. Thus, the new power spectra receive their signal preferentially from less distant galaxies, so that they probe smaller physical separations for fixed angular scale or ℓ, respectively. On small scales non-linear structure evolution sets in, enhancing the signal. Consequently, the characteristic bump caused by non-linearity is visible for smaller ℓ, i.e. larger angles, in the

transformed power spectra in comparison with $P_\kappa(\ell)$, leading also to the shift of the peak.

6.3 Information loss

By eliminating contributions to the cosmic shear signal at certain distances from the observer, one necessarily reduces the information content of the data set, so that the desired constraints on cosmological parameters are less stringent. A more technical way to understand the information loss associated with the nulling transformation is the fact that when stacking lensing power spectra according to (6.7), one necessarily also has negative contributions due to the form of the nulling weights (e.g. Fig. 6.2), thereby reducing the total signal amplitude. Thus, to judge the practical value of the nulling technique, we are going to quantify the accuracy with which cosmological parameters can be determined by the newly constructed power spectra (6.7) in this section.

If one considers the set of $N_z - i - 1$ tomography power spectra used to construct $\Pi^{(i)}_{[q]}(\ell)$ as the components of a data vector, then nulling is equivalent to a rotation of this vector such that all but one component of the resulting vector are free of GI correlations. The 'cleaned' components correspond to the $N_z - i - 2$ new power spectra (6.53) for $q = 1, .., N_z - i - 2$, whereas the last component must contain a weight function that is collinear to $\boldsymbol{f}$, or simply

$$\Pi^{(i)}_{[N_z-i-1]}(\ell) \approx \sum_{j=1}^{N_z} P_\kappa^{(ij)}(\ell) \left(1 - \frac{\chi(\hat{z}_i)}{\chi(z_j)}\right) \chi'(z_j)\, \Delta z\,; \tag{6.54}$$

i.e., $\boldsymbol{f}$ itself is chosen as the weight, see (6.23). The vector rotation mentioned above is invertible, so that, illustratively, it is obvious that using the new, full data vector instead of the one containing the convergence power spectra for the data analysis, one should obtain the same results. This statement is equivalent to the Fisher matrix, as a measure of the information content, being invariant under such orthogonal transformations of the data vector (see Tegmark et al. 1997). We will return to this point in the following section.

Let the complete data vectors forming the basis of this analysis be $\boldsymbol{D}$ for the original set and $\boldsymbol{D'}$ for the transformed one, which can be written in the convenient form

$$\begin{aligned}
\boldsymbol{D} &= \Big(P_\kappa^{(13)}(\ell_1),\ ..\ , P_\kappa^{(1N_z)}(\ell_1), P_\kappa^{(24)}(\ell_1),\ ..\ , P_\kappa^{(2N_z)}(\ell_1), \\
&\quad P_\kappa^{(35)}(\ell_1),\quad ..\quad , P_\kappa^{(N_z-3\,N_z-1)}(\ell_1), P_\kappa^{(N_z-3\,N_z)}(\ell_1), P_\kappa^{(N_z-2\,N_z)}(\ell_1), \\
&\qquad P_\kappa^{(13)}(\ell_2),\quad ..\quad , P_\kappa^{(13)}(\ell_{N_\ell}),\quad ..\quad , P_\kappa^{(N_z-2\,N_z)}(\ell_{N_\ell})\Big)\,; \\
\boldsymbol{D'} &= \Big(\Pi^{(1)}_{[1]}(\ell_1),\ ..\ , \Pi^{(1)}_{[N_z-2]}(\ell_1), \Pi^{(2)}_{[1]}(\ell_1),\ ..\ , \Pi^{(2)}_{[N_z-3]}(\ell_1), \\
&\quad \Pi^{(3)}_{[1]}(\ell_1),\quad ..\quad , \Pi^{(N_z-3)}_{[1]}(\ell_1), \Pi^{(N_z-3)}_{[2]}(\ell_1), \Pi^{(N_z-2)}_{[1]}(\ell_1), \\
&\qquad \Pi^{(1)}_{[1]}(\ell_2),\quad ..\quad , \Pi^{(1)}_{[1]}(\ell_{N_\ell}),\quad ..\quad , \Pi^{(N_z-2)}_{[1]}(\ell_{N_\ell})\Big)\,.
\end{aligned} \tag{6.55}$$

We refer to $\boldsymbol{D}$ as containing the full information although the vector is not composed of all tomography power spectra; however, as already discussed above, these entries would most probably have to be discarded anyway to avoid intrinsic ellipticity correlations. With the choice (6.55), both vectors have the same dimension $N_\mathrm{D} = N_\ell(N_z - 1)(N_z - 2)/2$. Their components are ordered such that the corresponding covariance matrices obtain a block-diagonal structure because the power spectra evaluated at different angular frequencies are not correlated due to

	p_f	p_min	p_max	p_l	p_u
Ω_m	0.3	0.10	0.70	0.20	0.40
Ω_Λ	0.7	0.40	1.00	0.58	0.82
σ_8	0.9	0.40	1.40	0.80	1.00
h	0.7	0.30	1.05	0.60	0.80

Table 6.1: Set of cosmological parameters used for the analysis. The columns indicate the parameter values of the fiducial model p_f, limiting values p_min and p_max of the parameter plane considered, and lower (p_l) and upper limits (p_u) of the prior applied in the marginalisation.

the assumption of Gaussianity. Hence, the covariance C_D of the data vector $\boldsymbol{D}$ reads

$$C_\mathrm{D} = \begin{pmatrix} \langle \Delta\boldsymbol{d}_1 \, \Delta\boldsymbol{d}_1^\tau \rangle & 0 & ... & 0 \\ 0 & \langle \Delta\boldsymbol{d}_2 \, \Delta\boldsymbol{d}_2^\tau \rangle & ... & 0 \\ ... & ... & ... & 0 \\ 0 & 0 & 0 & \left\langle \Delta\boldsymbol{d}_{N_\ell} \, \Delta\boldsymbol{d}_{N_\ell}^\tau \right\rangle \end{pmatrix} , \tag{6.56}$$

where for the sake of a compact notation, the vector

$$\boldsymbol{d}_i \equiv \left(P_\kappa^{(13)}(\ell_i), \; .. \, , P_\kappa^{(1N_z)}(\ell_i), P_\kappa^{(24)}(\ell_i), \quad .. \quad , P_\kappa^{(N_z-2\,N_z)}(\ell_i) \right) \tag{6.57}$$

was introduced, so that $\boldsymbol{D} = (\boldsymbol{d}_1, \; .. \, , \boldsymbol{d}_{N_\ell})$. The remaining non-trivial blocks $\langle \Delta\boldsymbol{d}_i \, \Delta\boldsymbol{d}_i^\tau \rangle$ for the angular frequency bin ℓ_i with dimension $(N_z-1)(N_z-2)/2 \times (N_z-1)(N_z-2)/2$ each are computed by means of (6.13) and can then readily be inverted numerically. The covariance of $\boldsymbol{D'}$ is dealt with analogously.

Since the set of $\Pi_{[q]}^{(i)}(\ell)$ with $q = 1, \, .. \, , N_z - i - 1$ contains the full information, the optimisation of the weight functions with respect to the trace of the Fisher matrix becomes superfluous in this situation. Instead, one can construct the $\boldsymbol{B}^{[q]}$ simply as a set of orthogonal vectors, starting with $\boldsymbol{f}$, for instance by means of the Gram-Schmidt algorithm. This way the vectors corresponding to the weight functions still fulfil the constraint equation (6.24).

To calculate credible regions, the likelihood function in parameter space has to be evaluated, which reads under the assumption of a Gaussian probability distribution function

$$L(\boldsymbol{D}|\boldsymbol{p}) = \frac{1}{(2\pi)^{\frac{N_D}{2}} \sqrt{\det C_D}} \; \exp\left\{ -\frac{1}{2} \left[\boldsymbol{D}(\boldsymbol{p}) - \boldsymbol{D}_\mathrm{f}\right]^\tau {C_D}^{-1} \left[\boldsymbol{D}(\boldsymbol{p}) - \boldsymbol{D}_\mathrm{f}\right] \right\} \tag{6.58}$$

and likewise for $\boldsymbol{D'}$, where $\boldsymbol{D}_\mathrm{f}$ stands for the data vector, as obtained for the fiducial model, and $\boldsymbol{p}$ again denotes the set of varied cosmological parameters. The covariance matrices are only evaluated at the fiducial cosmology, as well as the set of weight functions $B_{[q]}^{(i)}(\chi)$ entering the measures in $\boldsymbol{D'}$. We assume flat priors on the whole range of parameters considered, leading to a posterior likelihood

$$L_\mathrm{post}(\boldsymbol{p}|\boldsymbol{D}) = \frac{L(\boldsymbol{D}|\boldsymbol{p})}{\sum_{\boldsymbol{p}} L(\boldsymbol{D}|\boldsymbol{p})} \; . \tag{6.59}$$

The boundaries of the four-dimensional grid in parameter space over which the sum in the equation above runs and the fiducial cosmological parameters are summarised in Table 6.1. Otherwise the setup described in Sect. 6.2.4 is kept, except for a number of adjustments owing to the restrictions in computational power. The power spectra are now calculated for $N_\ell = 30$ bins in the range between $\ell = 50$ and $\ell = 10^4$, making use of the fit formula for the non-linear structure evolution by Peacock & Dodds (1996). In addition, the number of redshift bins is reduced to $N_z = 20$, still ranging from $z = 0$ to $z = 4$.

If all entries in $\boldsymbol{D'}$ of the form $\Pi_{[N_z-i-1]}^{(i)}(\ell)$ are removed, only components free of GI correlations remain. The loss of information caused by this removal is illustrated in Fig. 6.7 where

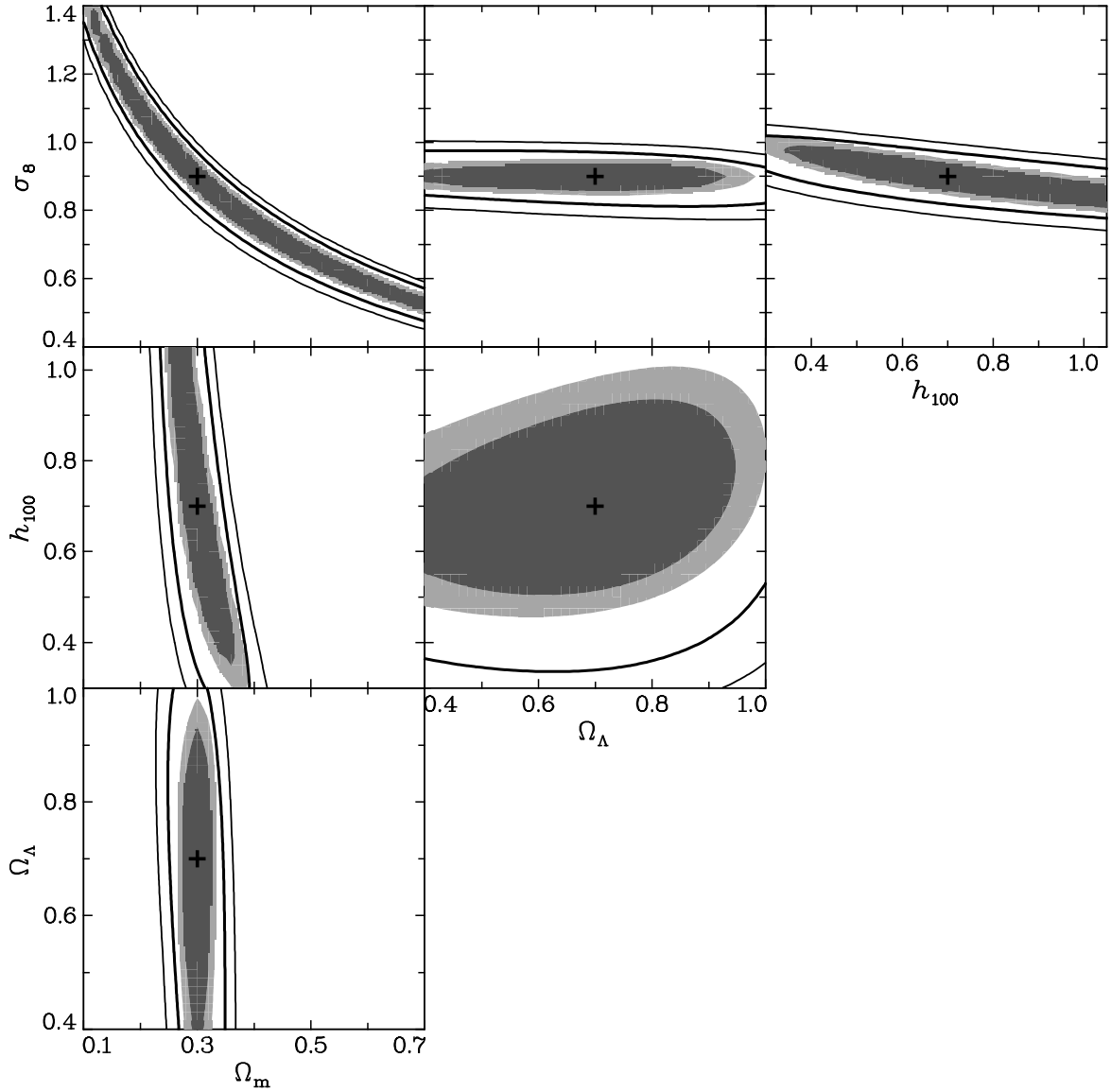

Figure 6.7: Contours of posterior likelihood before and after nulling. Shown are all possible two-dimensional cuts through parameter space. Note that we used a fiducial survey size of $1\,\mathrm{deg}^2$. The cosmological parameters that are not given on the axes are evaluated at their fiducial values. In each panel the cross indicates the fiducial set of parameters. The results for the data vector $\boldsymbol{D}$, i.e. the set of tomography power spectra before nulling, are given as shaded contours, where the dark-grey area contains 60 % and the light-grey area 80 % of the posterior likelihood. The contour lines indicate the corresponding areas after nulling, using the full set, i.e. the maximum number of uncontaminated components in $\boldsymbol{D'}$. Thick lines correspond to the 60 % and thin lines to the 80 % credible region.

two-dimensional cuts through the credible regions in parameter space, resulting before and after nulling, are given. The parameters not shown are evaluated at their fiducial values, so that the cross in each panel marks the fiducial model, in this case coinciding with the point of maximum likelihood. In the $\Omega_\mathrm{m} - \sigma_8$ plane, one recognises the typical banana shape, while the Hubble parameter and the density of dark energy are only poorly constrained by our setup. As expected, the contours after the application of the nulling technique have widened throughout. The inner contour line remains outside the light-cray area, implying that the probability that

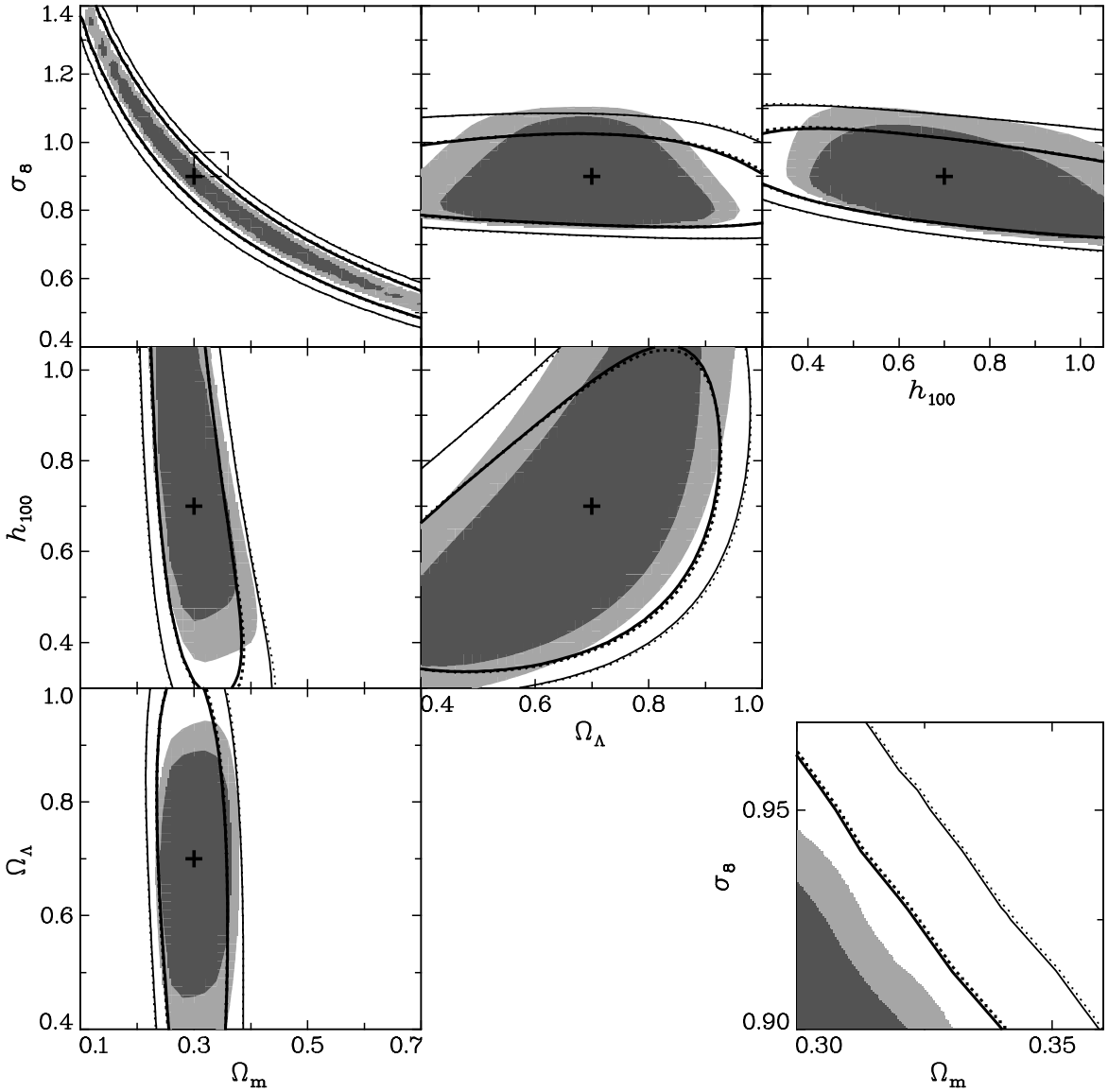

Figure 6.8: Contours of posterior likelihood before and after nulling. Shown are the contours for all combinations of cosmological parameters out of the set $(\Omega_\mathrm{m}, \Omega_\Lambda, \sigma_8, h)$, the remaining two parameters being marginalised over. The coding of areas and curves is the same as in Fig. 6.7. In addition, the dotted curves enclose the credible regions resulting from using only the single optimised weight function as determined in Sect. 6.2.4, i.e. power spectra of the form $\Pi^{(i)}_{[1]}(\ell)$, in $\boldsymbol{D'}$. As before, thick lines correspond to the 60 % and thin lines to the 80 % credible region, while in each panel the cross indicates the fiducial pair of parameters. The lower right panel is a detail of the upper left diagram, as outlined by the dashed box. As can be seen here, solid and dotted curves nearly coincide.

a range of parameters contains the true cosmological model decreases from 80 % to less than 60 % after the removal of contamination by intrinsic alignment. It is interesting to note that the ratio of the χ^2, i.e. the argument of the exponential in (6.58), before and after nulling is roughly constant over the whole range of parameters considered.

In Fig. 6.8 the same set of credible regions is plotted, but here the hidden parameters have been marginalised over with flat priors within the range indicated in Table 6.1. The appearance of the contours in the $\Omega_\mathrm{m} - \sigma_8$ plane remains similar due to the small influence

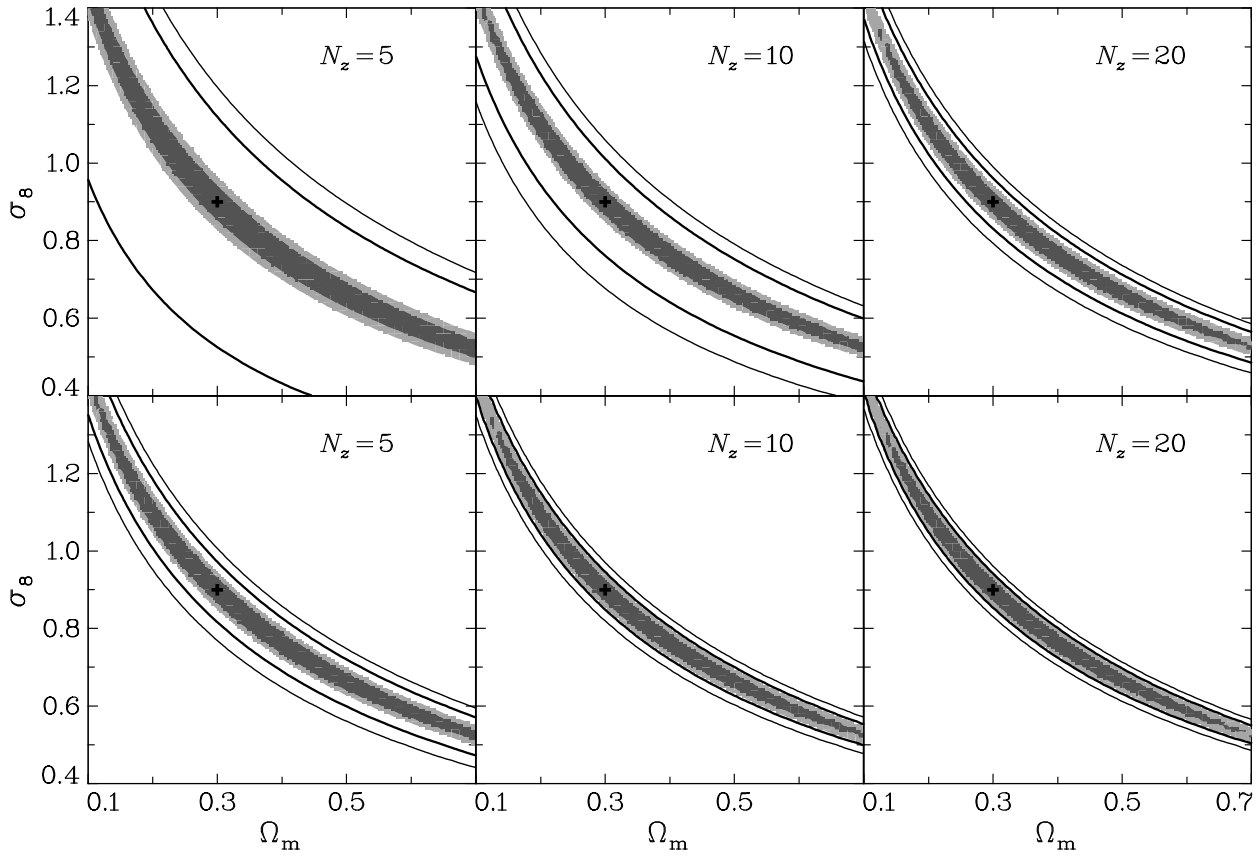

Figure 6.9: Credible regions in the $\Omega_m - \sigma_8$ plane for different redshift binning, before and after nulling, and using the full set of transformed cosmic shear measures. In the upper panels the data vectors as given in (6.55) are used, while for the results shown in the lower panels the cross-correlation power spectra of adjacent bins were also incorporated into both $\boldsymbol{D}$ and $\boldsymbol{D'}$. The data sets used are otherwise identical, except for the number of redshift bins, which is $N_z = 5$ in the left panels, $N_z = 10$ in the centre panels, and $N_z = 20$ in the right panels. The coding of areas and curves is the same as in Fig. 6.7. Again, the crosses indicate the fiducial set of cosmological parameters.

of h and Ω_Λ. However, the characteristic banana-like shape causes the area of maximum likelihood to be shifted away from the fiducial model in panels where one of the parameters Ω_m or σ_8 is marginalised over. Consequently, the posterior likelihood peaks at lower values of σ_8 in the top centre and right panel, while L_{post} obtains its maximum at lower values than $\Omega_m = 0.3$ in the central left and lower left panel. Besides that, the nulling implies that the degeneracy in h and Ω_Λ even increases, see Fig. 6.7, which leads to a significant elongation of the credible regions along these parameters in the panels of Fig. 6.8 mentioned above. Although this stretching causes lines of equal likelihood to even intersect, thereby apparently improving parameter constraints in one dimension, it is expected that the total area of a credible region increases by nulling, which corresponds to an overall decrease in constraints. This is indeed the case as will be shown below.

In addition, we have computed the posterior likelihood for nulling with first-order measures alone, i.e. for a vector $\boldsymbol{D'}$ with all components apart from those with a subscript [1] removed. The resulting contours are also presented in Fig. 6.8. Within the resolution of the graphics and the grid we employed to cover the parameter space, the contours for the first-order nulling

p_1	p_2	$\Delta q_{\rm tot}$ [%]	Δq_1 [%]
$\Omega_{\rm m}$	σ_8	29.2	30.3
$\Omega_{\rm m}$	h	45.6	48.3
$\Omega_{\rm m}$	Ω_Λ	50.3	52.5
Ω_Λ	σ_8	36.4	37.5
Ω_Λ	h	21.2	21.7
h	σ_8	26.4	27.3

Table 6.2: Increase in q-values for the marginalised credible regions shown in Fig. 6.8. The relative change in q is given for nulling with the full set ($\Delta q_{\rm tot}$) and with first-order measures only (Δq_1).

N_z	Δq [%]	$\Delta q'$ [%]
5	192.5	35.5
10	92.7	17.2
20	28.9	15.6

Table 6.3: Increase in q-values for credible regions, resulting from different redshift binning of the survey. The values Δq correspond to the regions shown in the upper panels, the values $\Delta q'$ to the regions in the lower panels of Fig. 6.9.

coincide with the results for the full set[1]. Only for the more concentrated likelihood in the $\Omega_{\rm m} - \sigma_8$ plane are the first-order contours located distinctly farther outside, as can be seen in the inlet of Fig. 6.8. The values where the contours are drawn for the two setups deviate by less than 3 % in the latter case; for all other parameter planes, the deviation of the contour values is approximately 1 %.

We quantify the widening of contours in terms of the quadrupole moments of the likelihood function, employing q-values as introduced by Kilbinger & Schneider (2004). For any two-dimensional likelihood analysis, one defines

$$Q_{\mu\nu} = \sum_{\boldsymbol{p}} L_{\rm post}(\boldsymbol{D}|\boldsymbol{p}) \left(p_\mu - p_{{\rm f},\mu}\right) \left(p_\nu - p_{{\rm f},\nu}\right) \tag{6.60}$$

for $\mu, \nu = 1, 2$. Then the quantity

$$q = \sqrt{\det Q} = \sqrt{Q_{11}\ Q_{22} - Q_{12}^2} \tag{6.61}$$

scales with the area of the credible region. Hence, an increase in q-value corresponds to a degradation of parameter constraints. We compute the relative change in q due to nulling, using both the full set and only first-order measures. The results, listed in Table 6.2, confirm the only marginally weaker performance of the first-order-only configuration. Depending on the combination of parameters, the increase in q ranges between 20 % and about 50 %.

To assess the importance of a large number of redshift bins, we considered a further setup with only two varied parameters $(\Omega_{\rm m}, \sigma_8)$, but otherwise identical with respect to the foregoing implementation. We used 5, 10, and 20 redshift bins to cover the range between $z = 0$ and $z = 4$. The resulting credible regions before and after nulling, using the full set of measures, are given in Fig. 6.9, upper panels. Concerning the original set of tomography power spectra, the increase in the number of redshift bins does not improve the parameter constraints appreciably, as already discussed for instance by Hu (1999). In contrast to this, the loss of information due to the removal of potentially contaminated components of the data vector is dramatic for $N_z = 5$ and still considerable for $N_z = 10$, see Table 6.3 for the corresponding changes in q-values. In the lower panels of Fig. 6.9 the credible regions, resulting from the inclusion of the cross-correlation power spectra of adjacent bins into the data vectors (6.55), are shown (see also Table 6.3). The contours tighten substantially, in particular in the case $N_z = 5$, where the probability of a contamination by intrinsic alignment of cross-correlations between

[1]Note that 'full set' means the use of the maximum number of new power spectra that are not contaminated.

neighbouring bins is low anyway due to the large bin size. With this setup, a number of 10 redshift bins already ensures that parameters are still well-constrained after nulling.

6.4 Towards an efficient nulling transformation

In the foregoing section it was established that the nulling transformation can be interpreted as a rotation of the data vector. Here we will exploit this fact to create a more compact formalism and an efficient means to calculating nulling weights. While it was demonstrated that, by optimising the weights, the bulk of the cosmological information can be concentrated in the first-order nulling modes, we will use all orders in the following, thereby avoiding additional optimisation procedures. The new formalism is apt to an arbitrary binning of photometric redshifts and to the incorporation of photometric redshift errors.

Since distance information is in practice given in terms of redshift and only available in discretised form, it is convenient to re-write the central nulling condition (6.4) as

$$\sum_{j=i+1}^{N_z} B^{(i)}(\chi(z_j))\ \chi'(z_j)\ \Delta z_j\ \left(1-\frac{\chi(\hat{z}_i)}{\chi(z_j)}\right)=0\ , \tag{6.62}$$

where we now allow for an arbitrary bin width Δz_j. In analogy to (6.7) the transformed power spectra are given by

$$\Pi^{(i)}(\ell)=\sum_{j=i+1}^{N_z} B^{(i)}(\chi(z_j))\ P_{\rm obs}^{(ij)}(\ell)\ \chi'(z_j)\ \Delta z_j\ , \tag{6.63}$$

where $P_{\rm obs}^{(ij)}(\ell)=P_\kappa^{(ij)}(\ell)+P_{\rm GI}^{(ij)}(\ell)+P_{\rm II}^{(ij)}(\ell)$, i.e. we assume in the most general case that the observed signal is contaminated by both GI and II correlations. In both cases $B^{(i)}(\chi)\equiv 0$ for $\chi\le\hat{\chi}_i$ was assumed, as before. For the sake of a compact notation we define the vectors

$$\begin{aligned}
\boldsymbol{T}^{(i)}_{[0]} &\equiv \frac{\boldsymbol{T'}^{(i)}_{[0]}}{|\boldsymbol{T'}^{(i)}_{[0]}|} \quad \text{with} \quad T'^{(i)}_{[0]\,j}=\left(1-\frac{\chi(\hat{z}_i)}{\chi(z_j)}\right)\ ; \qquad (6.64)\\
\boldsymbol{T}^{(i)}_{[1]} &\equiv \frac{\boldsymbol{T'}^{(i)}_{[1]}}{|\boldsymbol{T'}^{(i)}_{[1]}|} \quad \text{with} \quad T'^{(i)}_{[1]\,j}=B^{(i)}(\chi(z_j))\ \chi'(z_j)\ \Delta z_j\ ,
\end{aligned}$$

so that the constraint (6.62) turns into an orthogonality relation, $(\boldsymbol{T}^{(i)}_{[0]}\cdot\boldsymbol{T}^{(i)}_{[1]})=0$. We now compute weights $\boldsymbol{T}^{(i)}_{[q]}$ of higher 'order' $q\ge 2$ by requiring that they be normalised and obey

$$\left(\boldsymbol{T}^{(i)}_{[q]}\cdot\boldsymbol{T}^{(i)}_{[r]}\right)=0 \quad \text{for all} \quad 0\le r<q\ . \tag{6.65}$$

From (6.63) it follows that the transformed power spectra of order q are then given by

$$\Pi^{(i)}_{[q]}(\ell)=\sum_{j=i+1}^{N_z} T^{(i)}_{[q]\,j}\ P_{\rm obs}^{(ij)}(\ell)\ . \tag{6.66}$$

In the discretised version given by (6.62) the weight function has N_z-i free parameters, namely the function values $B^{(i)}(\chi(z_j))$. For fixed initial bin i these free parameters translate into the N_z-i-dimensional vectors $\boldsymbol{T}^{(i)}_{[q]}$. Since (6.62) does not restrict the overall amplitude, we fix

the normalisation by assigning unit length to the vectors $\boldsymbol{T}^{(i)}_{[q]}$. In total, one can thus construct $N_z - i$ new power spectra per bin i, but since the additional constraint (6.62) reduces the degrees of freedom by one, one new power spectrum cannot be freed from the GI contamination. It is the zeroth-order power spectrum, also constructed via (6.66) for $q = 0$, which obviously cannot fulfil the nulling constraint.

By defining vectors that contain the cosmic shear observables, i.e. in our case the power spectra,

$$\begin{aligned} \boldsymbol{P}^{(i)}(\ell) &\equiv \left\{ P^{(i,j=i+1)}_{\rm obs}(\ell),\ \ldots\ , P^{(i,j=N_z)}_{\rm obs}(\ell) \right\}^{\tau} ; \\ \boldsymbol{\Pi}^{(i)}(\ell) &\equiv \left\{ \Pi^{(i)}_{[0]}(\ell),\quad \ldots\quad , \Pi^{(i)}_{[N_z-i-1]}(\ell) \right\}^{\tau} \end{aligned} \tag{6.67}$$

and composing the transformation matrix

$$\boldsymbol{T}^{(i)} \equiv \left(\boldsymbol{T}^{(i)}_{[0]}, ..., \boldsymbol{T}^{(i)}_{[N_z-i-1]} \right) \tag{6.68}$$

for every photometric redshift bin i and angular frequency ℓ, the new power spectra are given by $\boldsymbol{\Pi}^{(i)}(\ell) = \boldsymbol{T}^{(i)} \boldsymbol{P}^{(i)}(\ell)$. Due to the construction of the weights $\boldsymbol{T}^{(i)}_{[q]}$ the transformation matrix is orthogonal with $\det \boldsymbol{T}^{(i)} = 1$, and so is the transformation of the full data set. Therefore the nulling technique can be interpreted as a rotation of the cosmic shear data vector such that in the rotated set the GI contamination is restricted to certain elements, namely those with a subscript $[q = 0]$. By removing these, one loses part of the lensing signal and hence statistical power, but eliminates the GI systematic within the limits of the approximations made in the foregoing derivation.

Performing a rotation, the dimension of the nulled data vector, which is composed of the $\boldsymbol{\Pi}^{(i)}(\ell)$ for every i and ℓ, is exactly the same as for the original data set. For the data analysis one removes the contaminated nulled power spectra with subscript [0], i.e. one entry per initial bin. This is the step that actually does the nulling and modifies both statistical and systematic error budgets. In this work, we are going to use all remaining nulled power spectra with $q \geq 1$ throughout. Since they are merely specified by being composed of mutually orthogonal weights, there is no ordering among different q. In particular, it is impossible to make a priori statements about the information content of different orders q.

It should be noted, however, that one can combine the formalism outlined above with a data compression algorithm, based on Fisher information. As investigated above (see also Joachimi & Schneider 2008), nearly all information about cosmological parameters can be concentrated in a limited set of nulled power spectra, constructed from the first-order weights $\boldsymbol{T}^{(i)}_{[1]}$. The additional requirement that a suitable combination of Fisher matrix elements is to be maximised introduces a strong hierarchy in terms of information content into the sequence of $\boldsymbol{\Pi}^{(i)}(\ell)$ with $q \geq 1$. We will not consider such an optimisation in this work.

We will employ the Fisher matrix formalism (see Appendix A for details) to determine both statistical and systematic errors before and after applying the nulling technique. In the following we discuss a few caveats when using Fisher matrices to assess the performance of nulling. We assume a Gaussian likelihood of the form

$$L_x(\boldsymbol{x}|\boldsymbol{p}) = \frac{1}{(2\pi)^{\frac{N_d}{2}} \sqrt{\det C_x(\boldsymbol{p})}} \exp\left\{ -\frac{1}{2} \left[\boldsymbol{x} - \bar{\boldsymbol{x}}(\boldsymbol{p})\right]^{\tau} C_x(\boldsymbol{p})^{-1} \left[\boldsymbol{x} - \bar{\boldsymbol{x}}(\boldsymbol{p})\right] \right\} , \tag{6.69}$$

for a data vector $\boldsymbol{x}$ with expectation value $\bar{\boldsymbol{x}}(\boldsymbol{p})$ and covariance $C_x(\boldsymbol{p})$, where N_d is the dimension of the full data vector. Now consider an invertible linear transformation $\boldsymbol{T}$ of the data vector,

$$\boldsymbol{y} \equiv \boldsymbol{T}\, \boldsymbol{x} ; \qquad C_y = \boldsymbol{T}\, C_x\, \boldsymbol{T}^{\tau} . \tag{6.70}$$

In the context of nulling $\boldsymbol{x}$ corresponds to the data vector $\boldsymbol{P}^{(i)}(\ell)$, and $\boldsymbol{y}$ to the data vector of transformed power spectra $\boldsymbol{\Pi}^{(i)}(\ell)$, while the transformation is given by (6.66). Plugging the relations (6.70) into (6.69), one finds that the exponential remains unchanged, while the prefactor gets an additional term $|\det \boldsymbol{T}|^{-1}$, using $\det(\boldsymbol{T}C_x\boldsymbol{T}^\tau) = \det C_x\,(\det \boldsymbol{T})^2$. This modification merely leads to a rescaling of the likelihood values, and thus likelihood contours in parameter space remain unchanged. Since $\boldsymbol{T}$ is invertible, the data in $\boldsymbol{x}$ and $\boldsymbol{y}$ contains the same amount of information about the parameters. Accordingly, the Fisher matrix is also invariant under this transformation (Tegmark et al. 1997), which is easily demonstrated by inserting (6.70) into (A.10).

However, in the case of nulling the transformation (6.66) to the new data vector $\boldsymbol{\Pi}^{(i)}(\ell)$ depends on the cosmological parameters one aims at determining because the elements of $\boldsymbol{T}$ are composed of comoving distances. Hence, the likelihood is now parameter-dependent in both arguments,

$$L_y(\boldsymbol{y}|\boldsymbol{p}) = (\det \boldsymbol{T}(\boldsymbol{p}))^{-1}\; L_x(\boldsymbol{x}|\boldsymbol{p})\;, \tag{6.71}$$

where we omitted the modulus of $\det \boldsymbol{T}$ as this expression can always be turned positive by swapping two entries of either the original or the transformed data vector. The prefactor in (6.71) acts like a prior on the original likelihood of $\boldsymbol{x}$. In Sect. 6.3 an example of the magnitude of the effect of this prior was assessed unintentionally by not taking into account the prefactor although $\det \boldsymbol{T}$ differed from unity due to the different normalisation (6.34). As stated in this section, however, the likelihood values of both data sets were checked to be identical to the level of numerical accuracy. We conclude that the effect of the prior due to the data transformation must have been considerably weaker than the one of the flat prior imposed in the analysis. As far as nulling is concerned, the prior of (6.71) only acts on the cosmological parameters Ω_m, Ω_Λ, w_0, and w_a which enter the comoving distance (2.10) in a non-trivial way.

We intend to compute the Fisher matrix for the original and the transformed data set, in both cases at the point of maximum likelihood, i.e. for the fiducial set of parameters. At this point in parameter space we expect the derivative with respect to parameters to vanish on average, $\langle \partial L/\partial p_\mu \rangle = 0$. If the relation holds for $L_x(\boldsymbol{x}|\boldsymbol{p})$, it is clear from (6.71) that this is generally not the case for $L_y(\boldsymbol{y}|\boldsymbol{p})$. Therefore we set the requirement that $\det \boldsymbol{T} = 1$, which is fulfilled by the orthogonal transformation constructed in the foregoing section. Then one can show that the Fisher matrices of both data vectors are equivalent, even for a parameter-dependent data transformation, as is detailed in Appendix B.

Furthermore, we assume that the original covariance C_x does not depend on cosmological parameters. Since an additional cosmology dependence would lead to tighter constraints, this is a conservative assumption (see e.g. Eifler et al. 2009). Using the equivalence of the Fisher matrices, and returning to the notation in the context of the nulling technique, we then arrive at the following expression for the original (index 'orig') and the nulled (index 'null') data vector (see Appendix B),

$$\begin{aligned} F_{\mu\nu}^\mathrm{orig} &= \sum_{\alpha,\,\beta=1}^{N_\mathrm{d}} \frac{\partial P_{\mathrm{GG}\alpha}}{\partial p_\mu} \left(C_P^{-1}\right)_{\alpha\beta} \frac{\partial P_{\mathrm{GG}\beta}}{\partial p_\nu} \\ &= \sum_{\alpha,\,\beta,\,\gamma,\,\delta=1}^{N_\mathrm{d}} T_{\alpha\gamma}\, \frac{\partial P_{\mathrm{GG}\gamma}}{\partial p_\mu} \left(C_\Pi^{-1}\right)_{\alpha\beta} T_{\beta\delta}\, \frac{\partial P_{\mathrm{GG}\delta}}{\partial p_\nu} \equiv F_{\mu\nu}^\mathrm{null}\;, \end{aligned} \tag{6.72}$$

where $\boldsymbol{P_{\mathrm{GG}}}$ and $\boldsymbol{T}$ are the lensing power spectrum data vector and the nulling transformation matrix of the full data set, respectively. The data vectors of the full set have the dimension $N_\mathrm{d} = N_\ell N_z\,(N_z-1)\,/2$ if N_ℓ angular frequency bins are considered. The covariance matrices

of the original and nulled power spectra are denoted by C_P and C_Π. The equality of original and nulled Fisher matrix, i.e. the Fisher matrix after performing the nulling rotation, directly follows from (6.70), second equation. However, the actual nulling step removes elements from the transformed data vector, thereby reducing the dimension of the nulled data vector to $N_\ell\,(N_z-1)\,(N_z-2)\,/2$ and causing $F_{\mu\nu}^{\mathrm{null,red}} \leq F_{\mu\nu}^{\mathrm{orig}}$, where $F_{\mu\nu}^{\mathrm{null,red}}$ denotes the Fisher matrix, computed from the nulled data vector after the removal of the contaminated power spectra with $q = 0$.

To assess the effect of the systematic, we furthermore calculate the bias on every parameter by means of the bias formalism (Kim et al. 2004; Huterer & Takada 2005; Huterer et al. 2006; Taylor et al. 2007; Amara & Réfrégier 2008; Kitching et al. 2009). Assuming a systematic P_{GI} that is subdominant with respect to the signal and causes only small systematic errors, the bias b on a parameter p_μ can be calculated by

$$b(p_\mu) = \sum_\nu \left(F_{\mu\nu}^{\mathrm{orig}}\right)^{-1} \sum_{\alpha,\,\beta=1}^{N_\mathrm{d}} P_{\mathrm{GI}\alpha} \left(C_P^{-1}\right)_{\alpha\beta} \frac{\partial P_{\mathrm{GG}\beta}}{\partial p_\nu}\,, \tag{6.73}$$

and likewise for the nulled data set. A formal derivation of the bias formalism, including the discussion of its limitations can be found in Appendix C.

6.5 Modelling cosmic shear data

6.5.1 Redshift distributions

To model realistic redshift probability distributions of galaxies in the presence of photometric redshift errors, we keep close to the formalisms used in Ma et al. (2006) and Amara & Réfrégier (2007). We assume survey parameters that should be representative of any future space-based mission aimed at precision measurements of cosmic shear, such as the Euclid satellite proposed to ESA (Laureijs et al. 2009). Note that the probability distributions of comoving distances and redshift, used in parallel in this work, are related via $p_z(z) = p_\chi(\chi)\,\chi'(z)$.

According to Smail et al. (1994), we again assume an overall redshift probability distribution of the form (4.47) with $\beta = 1.5$. To get a median redshift of $z_{\mathrm{med}} = 0.9$, we choose $z_0 = 0.64$. The distribution is cut at $z_{\mathrm{max}} = 3$ and then normalised to unity. The total distribution of galaxies per unit survey area is then $n_{\mathrm{tot}}(z) = n\,p_{\mathrm{tot}}(z)$, where n is the total number density of galaxies. The choice of photometric redshift bin boundaries for the tomography is in principle arbitrary. Here, we divide $p_{\mathrm{tot}}(z)$ into N_z photometric redshift bins such that every bin contains the same number of galaxies, i.e.

$$\int_{z_{i-1}}^{z_i} \mathrm{d}z\; p_{\mathrm{tot}}(z) = \frac{1}{N_z} \quad \text{for every} \quad i = 1,\,\ldots,\,N_z\,, \tag{6.74}$$

where the z_i mark the redshifts of the bin boundaries, and where $z_0 = 0$ and $z_{N_z} = z_{\mathrm{max}}$. This choice of binning is solely for computational convenience and to allow for easy comparisons of setups with a different number of bins. The nulling technique as such does not rely on any particular choice of photometric redshift binning.

Our model for photometric redshift errors accounts for two effects, a statistical uncertainty characterised by the redshift dispersion $\sigma_{\mathrm{ph}}(1+z)$, and misidentifications of a fraction f_{cat} of galaxies with offsets from the centre of the distribution of $\pm\Delta_z$. We write the conditional probability of obtaining a photometric redshift z_{ph} given the true, spectroscopic redshift z as

$$\begin{aligned} p(z_{\mathrm{ph}}\,|\,z) \;\propto\; & (1-f_{\mathrm{cat}})\; G\left(z_{\mathrm{ph}};\; z,\, \sigma_{\mathrm{ph}}\,(1+z)\right) + \frac{f_{\mathrm{cat}}}{2} \\ & \times\; \left\{G\left(z_{\mathrm{ph}};\; z_+,\, \sigma_{\mathrm{ph}}\,(1+z_+)\right) + G\left(z_{\mathrm{ph}};\; z_-,\, \sigma_{\mathrm{ph}}\,(1+z_-)\right)\right\}\,, \end{aligned} \tag{6.75}$$

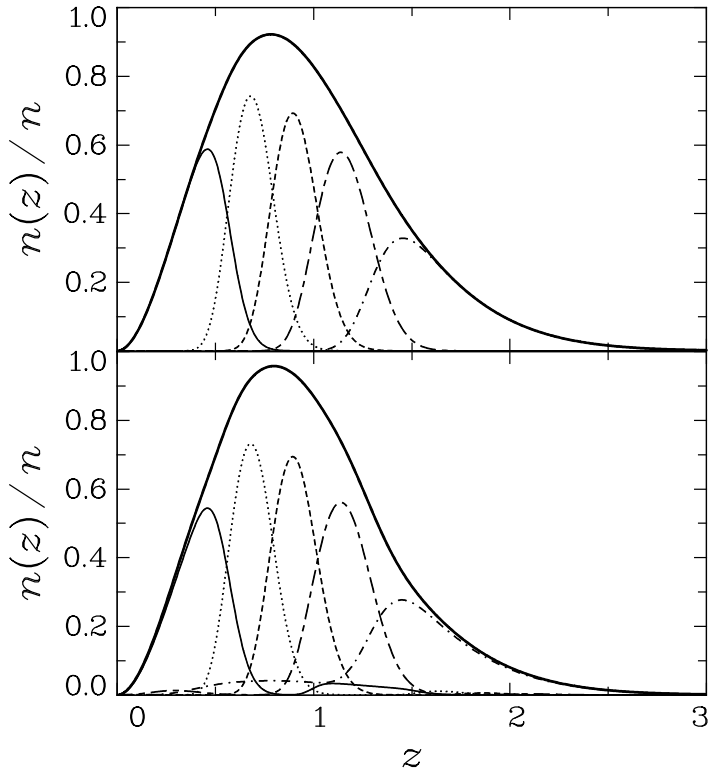

Figure 6.10: Number density distribution of galaxies for a division into $N_z = 5$ redshift bins, rendered dimensionless through dividing by the total number density n. The thick solid line corresponds to the overall galaxy number density distribution, normalised to unity. The thin curves represent the distributions corresponding to the five photometric redshift bins, normalised to $1/N_z$. The original bin boundaries are chosen according to (6.74). Note that the sum of the individual distributions adds up to the total distribution for every z. *Top panel*: Resulting distributions for $\sigma_{\rm ph} = 0.05$ and no catastrophic outliers. *Bottom panel*: Resulting distributions for $\sigma_{\rm ph} = 0.05$, $f_{\rm cat} = 0.1$, and $\Delta_z = 1.0$.

where $G\,(z_{\rm ph};\ z,\,\sigma)$ is a Gaussian with mean z and dispersion σ, and where $z_+ = z + \Delta_z$ and $z_- = z - \Delta_z$. When integrating (6.75) over $z_{\rm ph}$ with infinite range, it yields unity for every z. However, since we consider a finite redshift range, the distributions corresponding to the lowest and highest photometric redshift bins and those with significant outlier population will be cut at 0 and $z_{\rm max}$, so that we normalise $p(z_{\rm ph}\,|\,z)$ by demanding $\int_0^{z_{\rm max}} {\rm d}z_{\rm ph}\; p(z_{\rm ph}\,|\,z) = 1$ for every z. Multiplying $p(z_{\rm ph}\,|\,z)$ with the overall redshift probability distribution of galaxies $p_{\rm tot}(z)$ yields the two-dimensional probability of obtaining a pair of redshift measurements $\{z_{\rm ph}, z\}$. When integrating this probability over photometric redshift within the bin boundaries defined above, one arrives at the true probability distribution of galaxies for every photometric redshift bin i,

$$p^{(i)}(z) = \frac{p_{\rm tot}(z)\int_{z_{i-1}}^{z_i}{\rm d}z_{\rm ph}\; p(z_{\rm ph}\,|\,z)}{\int_0^{z_{\rm max}}{\rm d}z'\; p_{\rm tot}(z')\int_{z_{i-1}}^{z_i}{\rm d}z_{\rm ph}\; p(z_{\rm ph}\,|\,z')}\;. \tag{6.76}$$

Due to the multiplication by $p_{\rm tot}(z)$ these distributions are limited to the interval $[0, z_{\rm max}]$ although (6.75) is non-vanishing outside that range. To ensure that the dispersions of the Gaussians in (6.75) are positive, $\Delta_z \leq 1$ is required. In this work we set $\Delta_z = 1$ fixed since this choice produces outlier distributions that are well separated from the central peak, as also found in realistic situations, see below.

The number density of galaxies located in photometric redshift bin i as a function of spectroscopic redshift is given by

$$n^{(i)}(z) = n_{\rm tot}(z)\int_{z_{i-1}}^{z_i}{\rm d}z_{\rm ph}\; p(z_{\rm ph}\,|\,z)\;, \tag{6.77}$$

so that evidently $\sum_i n^{(i)}(z) = n_{\rm tot}(z)$ for every redshift z. Using this last equation and multiplying (6.74) by n, one sees that the sum of the number densities of galaxies, having their true redshifts between the bin boundaries defined by (6.74), is the same for all bins, namely

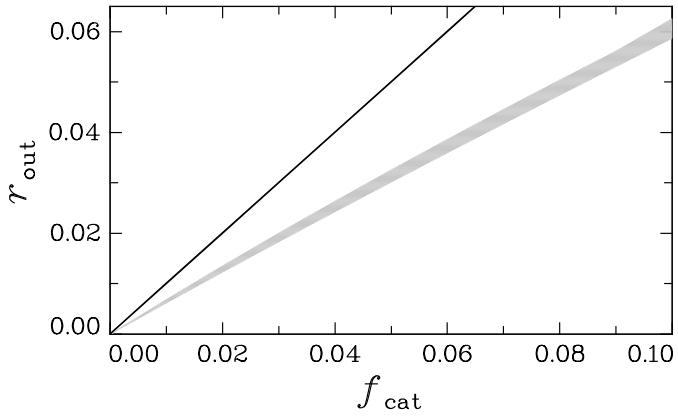

Figure 6.11: Relation between $f_{\rm cat}$ and the true fraction of outliers in the redshift distributions $r_{\rm out}$. The grey area marks the range of possible values of $r_{\rm out}$ if $\sigma_{\rm ph}$ lies in the interval [0.01; 0.1], where $\sigma_{\rm ph} = 0.01$ produces the upper limit and $\sigma_{\rm ph} = 0.1$ the lower limit of the grey region. A one-to-one relation is indicated by the solid black line.

n/N_z, as requested. However, the number densities of galaxies per photometric redshift bin, i.e. $n^{(i)} = \int_0^{z_{\rm max}} {\rm d}z\, n^{(i)}(z)$, are generally not identical. The photometric redshift errors lead to a redistribution of galaxies, which will in our model cause the outermost galaxy distributions to contain slightly more objects than n/N_z.

Two examples for galaxy distributions $n^{(i)}(z)$ obtained via this formalism are shown in Fig. 6.10, one without outliers and with a dispersion of $\sigma_{\rm ph} = 0.05$, and one where outliers with $f_{\rm cat} = 0.1$ at an offset $\Delta_z = 1$ have been added. As is evident from the plot in the lower panel, the outlier Gaussians are modified by (6.76) into elongated bumps, which are well separated from the central peak. They are most prominent as a distribution with $z \gtrsim 1$, being part of the lowest photometric bin, and a broad distribution at low redshifts, belonging to the highest photometric bin. This behaviour is qualitatively in good agreement with the characteristic shape of the scatter plots in the spectroscopic redshift - photometric redshift plane, as for instance analysed in Abdalla et al. (2007), which also justifies our choice of $\Delta_z = 1$.

To judge the performance of nulling in the presence of catastrophic outliers in the redshift distributions, it is important to note that $f_{\rm cat}$ does not equal the true fraction of outliers, primarily because of the subsequent multiplication of (6.75) by the overall redshift distribution $p_{\rm tot}(z)$, see (6.76). We compute the true fraction of outliers, denoted by $r_{\rm out}$, as the part of a redshift distribution that is contained in the two outlier Gaussians of our model. A quantity $p_{\rm cat}(z_{\rm ph}\,|\,z)$ is defined identically to (6.75), but with the first term, i.e. the central Gaussian, removed. Then we define the outlier fraction as

$$r_{\rm out} \equiv \frac{1}{N_z} \sum_{i=1}^{N_z} \frac{\int_0^{z_{\rm max}} {\rm d}z\; p_{\rm tot}(z) \int_{z_{i-1}}^{z_i} {\rm d}z_{\rm ph}\; p_{\rm cat}(z_{\rm ph}\,|\,z)}{\int_0^{z_{\rm max}} {\rm d}z\; p_{\rm tot}(z) \int_{z_{i-1}}^{z_i} {\rm d}z_{\rm ph}\; p(z_{\rm ph}\,|\,z)}\;, \tag{6.78}$$

where $r_{\rm out}$ is averaged over all photometric redshift bins.

In Fig. 6.11 the relation between $r_{\rm out}$ and $f_{\rm cat}$ for fixed $\Delta_z = 1.0$ is plotted. The grey region comprises the results for the range from $\sigma_{\rm ph} = 0.01$ to $\sigma_{\rm ph} = 0.1$. Evidently, the true fraction of outliers is smaller than $f_{\rm cat}$, reaching up to about 6 % for $f_{\rm cat} \leq 0.1$. The strongest contribution to $r_{\rm out}$ originates from the bins at the lowest and highest redshifts, where the outlier distributions are enhanced because one of the outlier Gaussians is located in a redshift regime where $p_{\rm tot}(z)$ obtains high values. The redshift distributions centred at medium redshifts have their central Gaussian at $z \sim 1$ where $p_{\rm tot}(z)$ peaks, so that the outlier fraction in the corresponding bins is small.

In the following, we will consider the range $0 \leq f_{\rm cat} \leq 0.1$, which yields outlier fractions that should comprise realistic limits of catastrophic failures in the photometric redshift determination of surveys aimed at measuring cosmic shear tomography (see Abdalla et al. 2007). For the COSMOS field Ilbert et al. (2009) found photometric redshift dispersions in the range

between 0.007 for the brightest galaxies and 0.06 for fainter objects up $z \sim 2$. Taking these values as a reference, we are going to consider the range $0 \leq \sigma_{\rm ph} \leq 0.1$.

6.5.2 Lensing power spectra

As the basis for our analysis we use sets of tomographic cosmic shear power spectra which are computed for a wCDM universe with fiducial parameters $\Omega_{\rm m} = 0.25$, $\Omega_{\Lambda,0} = 0.75$, and $H_0 = 100\,h\,{\rm km/s/Mpc}$ with $h = 0.7$. Throughout, the spatial geometry of the Universe is assumed to be flat. We incorporate a variable dark energy scenario by parametrising its equation of state via (2.15), where the cosmological constant is chosen as the fiducial model, i.e. $w_0 = -1$ and $w_a = 0$. Then the dark energy density parameter is then given by (4.60).

The three-dimensional power spectrum of matter density fluctuations P_δ is further specified by the primordial slope $n_{\rm s} = 1$, the normalisation $\sigma_8 = 0.9$ and the shape parameter Γ, calculated according to Sugiyama (1995) with $\Omega_{\rm b} = 0.05$. Using the transfer function of Eisenstein & Hu (1998) (without baryonic wiggles), the non-linear power spectrum is computed by means of the fit formula of Peacock & Dodds (1996). The tomography power spectra are then determined via (3.34), incorporating the photometric redshift models of the foregoing section, for $N_\ell = 100$ logarithmic angular frequency bins between $\ell = 10$ and $\ell = 2 \cdot 10^4$.

The nulled power spectra $\Pi^{(i)}_{[q]}(\ell)$ are then calculated via (6.66). The nulling weights $\boldsymbol{T}^{(i)}_{[0]}$, see (6.64), are computed for the fiducial cosmology, while the higher orders are obtained by Gram-Schmidt ortho-normalisation. The Gram-Schmidt procedure does not uniquely define the order of the orthogonal vectors, so that no particular ordering is assigned to q, as opposed to the approach in Sect. 6.2.5, where a higher order q corresponded to a lower information content in $\Pi^{(i)}_{[q]}(\ell)$.

On applying nulling to a real data set, one has to assume the values of the relevant parameters $\Omega_{\rm m}$, Ω_Λ, w_0, and w_a to obtain $\boldsymbol{T}^{(i)}_{[0]}$. Whilst it is a realistic premise that these parameters are approximately known, slightly incorrect assumptions may degrade the downweighting of the GI signal, but do not introduce a new bias to the parameter estimation, as will be assessed in detail in Sect. 6.6.2. A sample of both original and nulled tomography power spectra are plotted in Fig. 6.12. For this sample the nulling has been performed following variant (C), which will be discussed in detail in Sect. 6.6.1.

As regards the calculation of the power spectrum covariance (Joachimi et al. 2008, and references therein), entering the Fisher matrix, we have to specify further survey characteristics in addition to the aforementioned redshift probability distribution. We assume a survey size of $20,000\,{\rm deg}^2$ and a total number density of galaxies of $n = 35\,{\rm arcmin}^{-2}$, resulting in approximately $35/N_z\,{\rm arcmin}^{-2}$ galaxies per photometric redshift bin. To compute shape noise, the dispersion of intrinsic ellipticities is set to $\sigma_\epsilon = 0.35$. These survey parameters correspond to those representative of future cosmic shear satellite missions such as Euclid, see Sect. 4.2.1.

6.5.3 Intrinsic alignment signal

To quantify the bias on cosmological parameters before and after nulling, a GI systematic power spectrum is added to the data vector. We adopt the non-linear version of the linear alignment model of Bridle & King (2007), employing (5.11) and (5.12) with the full matter power spectrum including non-linear corrections. Originating from analytical considerations by Hirata & Seljak (2004), the linear alignment model in the form employed here lacks solid physical motivation, but fits within the error bars of Mandelbaum et al. (2006). It also provides reasonable fits to the results of the halo model considerations by Schneider & Bridle (2010).

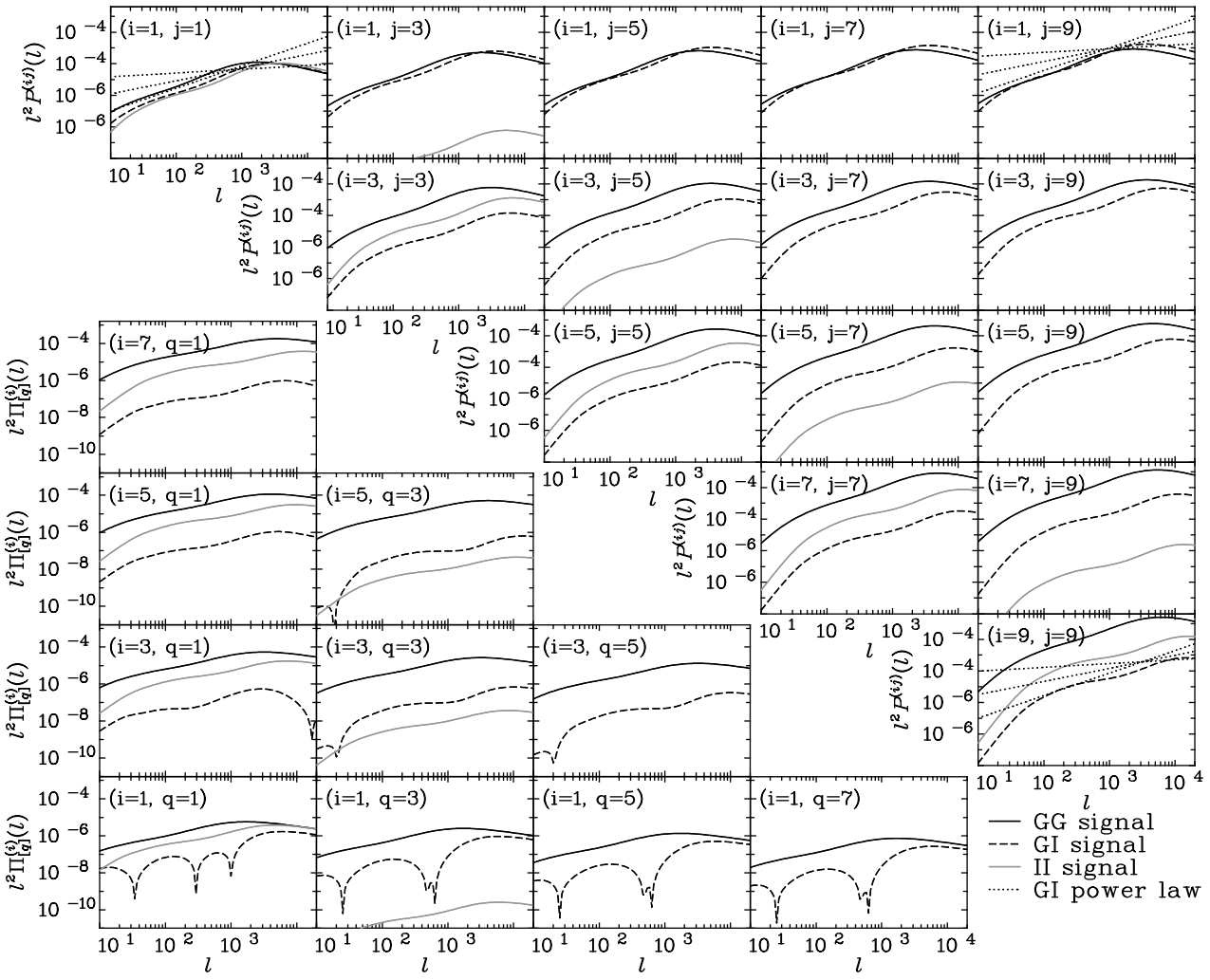

Figure 6.12: Original and nulled tomography power spectra as a function of angular frequency. The survey has been divided into $N_z = 10$ photometric redshift bins with dispersion $0.03(1+z)$. *Top right panels*: Lensing power spectra $P_{\rm GG}^{(ij)}(\ell)$ are shown as solid lines. The modulus of linear alignment model GI power spectra $P_{\rm GI}^{(ij)}(\ell)$ is given by dashed lines, the corresponding II signal by grey curves. In each panel the redshift bins i and j are plotted. In the panels with the combinations $i, j \in \{1, 9\}$ the absolute values of the power law GI models have been added for reference as dotted curves. Note that the II power spectrum becomes very small if i and j are largely different. *Bottom left panels*: The absolute values of the nulled lensing and linear alignment model systematic power spectra are shown as solid (GG), dashed (GI), and grey (II) curves, respectively. In each panel the corresponding redshift bin i and the order q are given. The nulled measures do not have a particular ordering in q, see text for details. For the lower redshift bins the GI signal is oscillating around zero. The II signal becomes very small for higher orders q.

While the nulling technique as such is completely independent of the actual functional form of the systematic, the residual bias does depend on the GI signal. Thus, we consider an additional set of simplistic power-law GI power spectra for reference. They are given by

$$P_{\delta\rm I}^{\rm p.l.}(k,z) = -A_{\rm GI}\left(\frac{k}{k_{\rm ref}}\right)^{s_{\rm GI}-2}(1+z)\,, \tag{6.79}$$

where $k_{\rm ref} = 1\,h/\mathrm{Mpc}$. As is evident from (6.73), the produced bias is simply proportional to

initial bin i	$s = 3$	$s = 5$
1	1170	20
2	3420	1470
3	5420	2330
4	7960	3170
5	11680	4310
6	none	5860
7	none	7960
8	none	13620

Table 6.4: Upper limits on the allowed angular frequency range if the II contamination in the nulled data shall be suppressed by at least a factor of s with respect to the nulled GG term. These limitations apply only for orders $q = 1$, and only if nulling is not preceded by a suitable II removal technique, as we advocate. The parameters are the same as in Fig. 6.12. Note that in a narrow range around $\ell \sim 100$ the II signal can be close to or slightly above the limit imposed by s.

the amplitude of the systematic, so that we do not need to investigate variations of the overall magnitude of the GI term. Hence, we relate the normalisation of (6.79) to the linear alignment model (5.12), and set $A_{\rm GI} = |P_{\delta{\rm I}}^{\rm l.a.}(k_{\rm ref}, z_{\rm med})|(1 + z_{\rm med})^{-1}$. For the power law slope we use the values $s_{\rm GI} = \{0.1, 0.4, 0.7\}$, where the central value best reproduces the average slope of the linear alignment model power spectra. The tomography power spectra are then obtained via (5.16).

The resulting power spectra are also shown in Fig. 6.12. As already mentioned in Bridle & King (2007), the linear alignment model produces a strong systematic, partially surpassing the lensing signal in amplitude for cross-correlations of largely different redshift bins. Since the GI term is negative, the sum of lensing and intrinsic alignment power spectrum can become negative in the corresponding ℓ-range in these cases[2]. Due to our choice of normalisation, the power-law toy GI signal can dominate the lensing power spectrum on even larger angular frequency intervals.

After nulling, the systematic is largely suppressed, oscillating around zero for the lower redshift bins. Still, significant residual signals remain because the finite extent of the redshift probability distributions has been neglected in the derivation of nulling. In particular, the systematic signal is eliminated only at a single redshift within each bin, thus being merely downweighted in neighbouring redshift ranges. A detailed discussion about the sources of the residual bias will follow in Sect. 6.7. We note that nulling works independently of the strength of the systematic; it can even be applied to data in which the GI term surpasses the cosmic shear signal.

We have also added II power spectra to Fig. 6.12 in order to judge in how far our assumption of dropping the II signal in our considerations is valid. The original II power spectra yield a strong contribution for auto-correlations, but drop off quickly if the correlated redshift distributions have less overlap. In the transformed data set, the II contamination is smaller than the residual GI signal and thus negligible for power spectra with $q > 1$. For $q = 1$ however, the II signal is significant such that in this case nulling would have to be preceded by an II removal technique. In the limit of completely disjoint photometric bins, the II signal would be confined to auto-correlations in the original data set. Since these are not included into the construction of the nulled power spectra, the latter would be completely free of II terms in this idealised case.

To ensure that the II term remains sufficiently small compared to the GG signal, one could restrict the subsequent analysis partly to larger angular scales. For instance, to achieve a minimum suppression by a factor s of the II signal with respect to the lensing signal, we determine maximum allowed ℓ-values, given in Table 6.4. These upper bounds would only have to be applied to orders $q = 1$, and are valid in the case of the setup used to produce Fig. 6.12.

[2]Note however that the total power spectrum of auto-correlations of ellipticities, i.e. GG+GI+II, always has to be positive by definition.

The limitations due to the II contamination are expected to become more restrictive as the photometric redshift scatter increases.

Alternatively, our findings suggest that, due to the confinement of the II term to a limited set of nulled power spectra, a treatment of the II signal *after* nulling may also provide a promising ansatz. In the current implementation the nulled power spectra of order $q = 1$ have a dominating contribution from original power spectra $P^{ij}(\ell)$ with $j = i + 1$, which contain the bulk of the II signal after the removal of auto-correlations from the analysis. Hence, the residual II terms accumulate within the measures of order $q = 1$. The freedom to choose the weights of (6.66) in the subspace orthogonal to $\boldsymbol{T}^{(i)}_{[0]}$ allows for a more specific treatment of the II signal in the nulled data. We emphasise that the final goal is a simultaneous removal of all intrinsic alignment contributions, but this is beyond the scope of this paper and subject to future work.

As the GI contamination has a large amplitude, the question is raised whether the bias formalism still yields accurate results. The effect of a large systematic is investigated in detail in Appendix C. We conclude from our findings that even for a strong GI term the bias is obtained with good accuracy whereas the statistical errors, which are also affected by a strong systematic, can deviate more significantly. To guarantee results that are as close as possible to a full likelihood analysis, we downscale all GI signals by a factor of five throughout the subsequent sections. Since the bias is proportional to the overall amplitude of the systematic, and since we are mostly going to consider ratios of biases, the rescaling does not have an influence on the statements concerning the performance of nulling. Merely the mean square error (4.50) is affected because the systematic error becomes less dominant. A lower systematic amplitude slightly disfavours nulling as it lowers the bias while causing an increase in statistical errors. Besides, limiting the strength of biases avoids unphysical parameter estimates as for instance $\Omega_\mathrm{m} < 0$. Such effects are normally avoided by priors, which have not been included in our Fisher matrix analysis though.

In surveys with a significant GI systematic, intrinsic ellipticity correlations are likely to affect parameter estimation, too. To restrict our considerations to the GI contamination, we follow Takada & White (2004), excluding auto-correlations from both original and nulled data vectors, and assuming that the remaining measures do not have an II signal. Note that due to the exclusion of auto-correlation power spectra the statistical errors on cosmological parameters in this work are larger than those of other cosmic shear tomography analyses, even for our original data sets.

Excluding auto-correlations is of limited accuracy to control the II signal since we use a relatively dense binning, partially with large photometric errors, so that cross-correlations of adjacent photometric redshift bins would contain significant II terms as well. With realistic data one could in principle let the nulling be preceded by an II removal technique such as King & Schneider (2002) who also take a purely geometric approach. However, the redshift-dependent weighting of galaxy pairs, on which the II removal is based, modifies the calculation of the projected cosmic shear measures such as (3.34), which in turn entails a modification of the nulling weights. The improvements of the nulling technique we investigate in Sect. 6.7.3 will also constitute an efficient tool to control the II term.

6.6 Improving the nulling performance

6.6.1 Optimising the nulling weights

In the composition of the nulling weights (6.64) one has the freedom to choose the specific redshift $\hat{z}_i$ within the initial bin at which the GI contribution is eliminated, as well as the

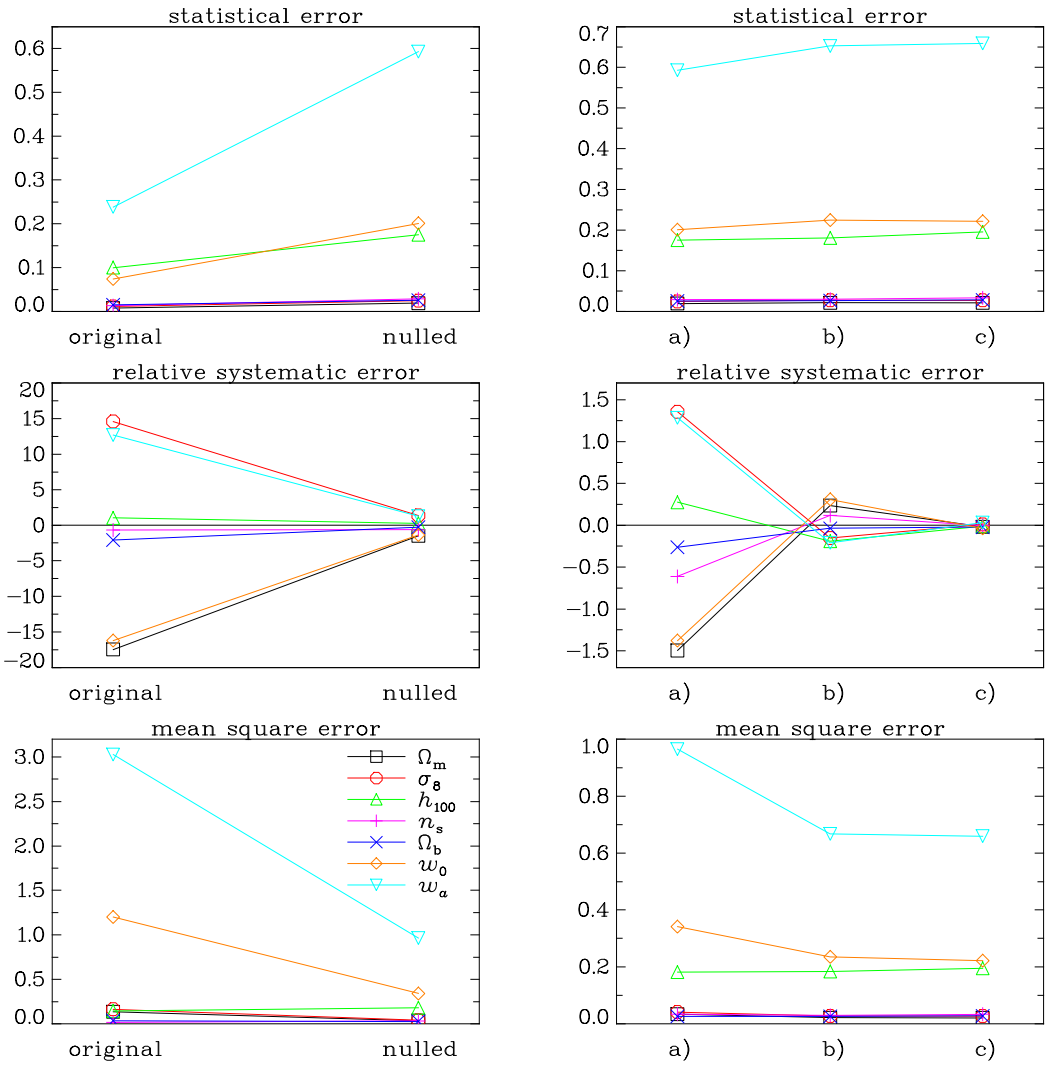

Figure 6.13: Comparison of the performance of the different nulling weights. Shown are marginalised statistical errors σ in the top panels, relative systematic errors $b_{\rm rel}$ in the centre panels, and mean square errors $\sigma_{\rm tot}$ in the bottom panels. For the correspondence between considered parameters and line colours/symbols see the legend. *Left column*: Change in errors from original to nulled data set, using the referencing to bin boundaries, i.e. variant (A). *Right column*: Residual errors using the different nulling weights. (A) Referencing to bin boundaries; (B) Referencing to bin centres; (C) Nulling including detailed redshift information.

referencing of redshifts z_j to the background redshift bins. For convenience we placed $\hat{z}_i$ in Sects. 6.1 to 6.3 at the centre of the initial bin and identified z_j with the lower boundary of bin j. Since this choice was fairly arbitrary, we seek to find a more appropriate referencing that leads to a minimum residual GI contamination.

A more natural choice is to position both the redshift of the initial bin $\hat{z}_i$ and the reference redshifts of the background bins at the centre between the photometric redshift bin boundaries, denoted by $z_{\rm c}^{(i)}$. This setup does not require knowledge about the redshift probability distribution of each bin, although this information has to be available at high precision for future cosmic shear surveys. Hence, we furthermore define nulling weights that take redshift information into account. Re-examining (6.9), one can drop the approximation of narrow redshift/distance probability distributions for the background bins, keeping the first equality of

Table 6.5: Overview on nulling variants considered. The variants differ by the redshifts assigned to the foreground and background photometric redshift bins, and by the form of the zeroth-order weight function.

variant	foreground	background	0^{th} order weights
(A)	bin centre	lower boundary	$1-\chi(\hat{z}_i)/\chi(z_j)$
(B)	bin centre	bin centre	$1-\chi(\hat{z}_i)/\chi(z_j)$
(C)	median redshift	bin centre	$g^{(j)}\left(\chi(\hat{z}_i)\right)$

(6.9). Thereby, instead of the comoving distance ratio $(1-\chi(\hat{z}_i)/\chi(z_j))$, one directly uses the lensing efficiency, which is the average of this ratio, weighted by the redshift/distance probability distribution of the background photometric redshift bin. The zeroth-order nulling weight in (6.64) is then given by $T'^{(i)}_{[0]_j} = g^{(j)}\left(\chi(\hat{z}_i)\right)$. For the remaining free redshift of the initial bin $\hat{z}_i$ we choose the median redshift of distribution i, a measure that contains information about the form of the distribution, but is robust against outliers.

Hence, in total we are going to consider three different versions of nulling: (A) the 'old' version of nulling with referencing to the lower boundaries of the background bins, a variant (B) where the background bins are identified with the bin centres $z_{\text{c}}^{(i)}$ instead, and (C) the nulling that includes detailed redshift information via assigning the foreground bins to their median redshifts and using the comoving distance ratio, weighted by $p^{(j)}(\chi)$, as the zeroth-order nulling weight. The properties of these variants are summarised in Table 6.5.

In Fig. 6.13 the performance of nulling with different nulling weights is shown. We plot the marginalised statistical error $\sigma(p_\mu) = \sqrt{(F^{-1})_{\mu\mu}}$ and the relative bias

$$b_{\text{rel}}(p_\mu) \equiv b(p_\mu)/\sigma_{\text{orig}}(p_\mu)\ , \tag{6.80}$$

where σ_{orig} denotes the statistical error before nulling, for every cosmological parameter. Note that if we referred the bias after nulling to the statistical error after nulling, the usual loss of information due to nulling could cause a decrease in b/σ even if the GI contamination remained completely unmodified. With the definition (6.80), b_{rel} is an unambiguous measure of the relative importance of systematic errors in the data. Moreover, the mean square error (4.50) is given in the figure. Here and in the following, the seven parameters $\boldsymbol{p} = \{\Omega_{\text{m}}, \sigma_8, h, n_{\text{s}}, \Omega_{\text{b}}, w_0, w_a\}$ are considered in the Fisher matrix analysis. The data set is composed of power spectra for $N_z = 10$ bins without photometric redshift errors, where the systematic stems from the linear alignment model, downscaled by a factor of five.

The left column of Fig. 6.13 illustrates the change in errors due to nulling with the referencing used hitherto, i.e. variant (A). While the marginalised statistical errors increase by up to a factor of about three for the weakly constrained dark energy parameters, the bias drops from values of up to $17\,\sigma$ to numbers that are of the same order of magnitude as the original statistical errors, i.e. $b_{\text{rel}} \approx 1$. For parameters that were strongly biased this leads to a considerable decrease in the mean square error, but σ_{tot} may also slightly increase if the systematic was subdominant already before nulling as is the case for the Hubble parameter.

In the right column of Fig. 6.13 resulting errors for all three nulling variants are given. It is evident that the newly introduced versions (B) and (C) of nulling perform significantly better in removing the systematic. Variant (B) decreases the bias by at least a factor of three with respect to (A), reversing the sign of the bias for almost all parameters. This hints at using the reference redshifts of the nulling weights as free parameters to control the amount of bias allowed in the data, as will be further discussed in Sect. 6.9. Variant (C) nearly perfectly eliminates the GI contamination. Although the underlying data lacks photometric redshift errors, knowledge

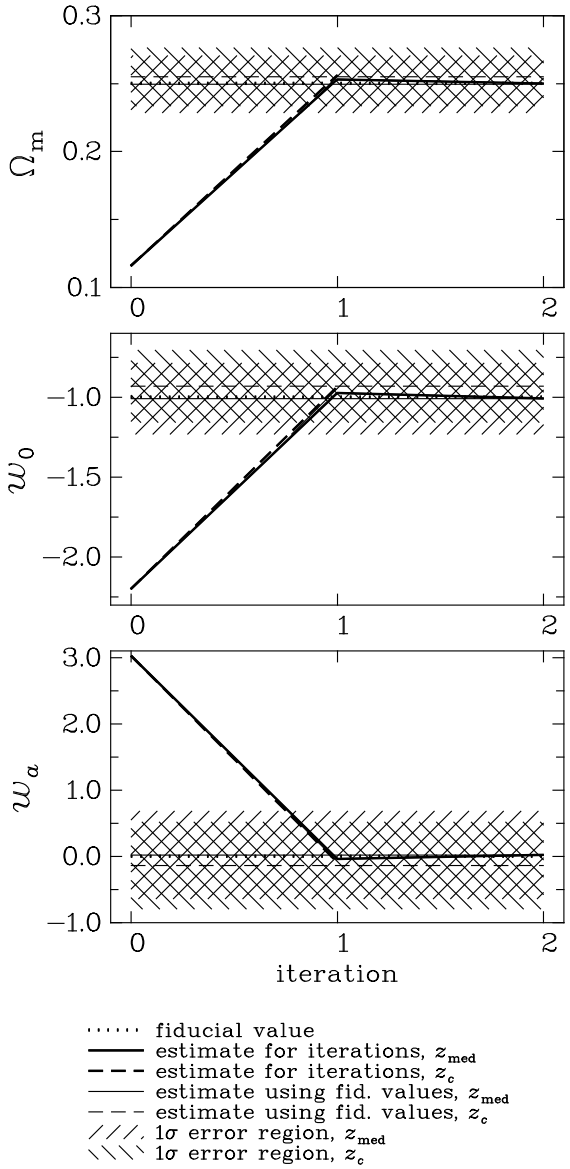

Figure 6.14: Cosmology dependence of the nulling weights. The change in estimates for the cosmological parameters, entering the distance-redshift relation non-trivially, is plotted for different iteration steps. The estimates resulting from using variant (C) are shown as solid lines, those for variant (B) as dashed lines. Iteration 0 corresponds to the initial values for the parameters, in this case the results of the analysis of the unmodified data set. For reference, the estimates obtained by using the true underlying cosmology to compute the nulling weights are plotted as thin lines. The hatched regions around these lines signify the 1σ error region. Note that variant (B) reaches an accuracy compatible to using the true cosmology already after one iteration while variant (C) takes two iterations.

about the distributions $p^{(i)}(z)$ is still advantageous as e.g. the lowest and highest redshift bin are broad and largely asymmetric. Regarding statistical errors, the better a version is capable of removing the systematic, the less stringent parameter constraints become. However, the improved bias reduction clearly outweighs the marginal increase in statistical errors.

In summary, we propose to henceforth use nulling with referencing to the centres of photometric redshift bin divisions, i.e. variant (B), in absence of detailed information about redshift distributions, and else version (C) which exploits this knowledge. Both approaches will be considered in the following analyses.

6.6.2 Cosmology dependence of the nulling weights

The nulling weights $T^{(i)}_{[q]\,j}$ depend on those parameters of the cosmological model that enter the comoving distance in a non-trivial way, i.e. for our model assumptions Ω_m, w_0, and w_a. Since only ratios of comoving distances enter the nulling weights, there is no dependence on h which enters the prefactor of (2.10). If the relevant cosmological parameters chosen to compute the nulling weights are different from the true parameters of the data set, the performance of nulling may deteriorate. A grossly incorrect choice of nulling weights could in principle

affect the lensing signal more than the GI term, which could then even cause a larger bias on parameters in the transformed data than in the original one.

Avoiding any a priori guesses of the true values of the relevant cosmological parameters, we explore the cosmology dependence of the nulling weights by taking the estimates from the analysis of the original data set as input cosmology for the computation of the $T^{(i)}_{[q]\,j}$. As we use the linear alignment model (5.12), the estimates $p_\mathrm{b} = p_\mathrm{f} + b$, where p_f is the true parameter value and b is the bias, are far from the true values and beyond any decent a priori guess, so that this setup can be understood as a worst-case scenario. With the weights obtained this way, the nulled data can be analysed, yielding another set of parameter estimates. This can then be taken as input for a refined set of nulling weights, thereby creating an iterative process which can be terminated when successive iterations yield stable parameter estimates.

In Fig. 6.14 the results of this iteration process are shown for nulling variants (B) and (C), both showing a very similar behaviour. The parameter estimates for iteration 0 correspond to the estimates of the analysis of the original data set. Given these largely incorrect input parameters, nulling is still able to reduce the bias due to intrinsic alignment to a level close to the one when using the true cosmology as input. Already after the first iteration step the residual bias is considerably smaller than the statistical errors. After at most two iterations, the results for the residual bias are indistinguishable from those with the correct input parameters.

Hence, the dependence of the nulling weights on cosmology is only weak, being solely due to geometrical terms. Consequently, nulling is robust against an incorrect initial guess for cosmological parameters needed to compute the nulling weights. For a consistency check, the iterative procedure outlined above can be performed on the data. In the remainder of this work we will use the true cosmology to calculate the nulling weights for reasons of simplicity.

6.7 Influence of redshift information on nulling

6.7.1 Redshift binning

First, we investigate the performance of nulling as a function of the number of photometric redshift bins the survey is divided into. The larger N_z, the better (6.62) is an approximation of (6.4), so that the GI removal is expected to work more efficiently. Furthermore, since nulling eliminates the contribution to the lensing signal of the background objects only at a single redshift, more concentrated redshift probability distributions are nulled more accurately, given an appropriately chosen redshift $\hat{z}_i$ within the initial bin. At the same time, less statistical information is lost because the entries of the transformed data vector, which are removed in the process of nulling, contain less independent information if the redshift distributions have a smaller spacing.

In search for a single quantity that measures an overall power of a data set to constrain cosmological parameters we define the average statistical power as

$$\bar{F} \equiv \left\{\det\left(F_{\mu\nu}\right)\right\}^{\frac{1}{2\,N_p}} \,, \tag{6.81}$$

where N_p is the number of parameters considered, i.e. the dimension of the Fisher matrix. This measure is motivated by the fact that the determinant of the Fisher matrix is inversely proportional to the volume of the N_p-dimensional error ellipsoid in parameter space. If errors are not correlated, $\bar{F}^2$ reduces to the geometric mean of the inverse square errors. In addition,

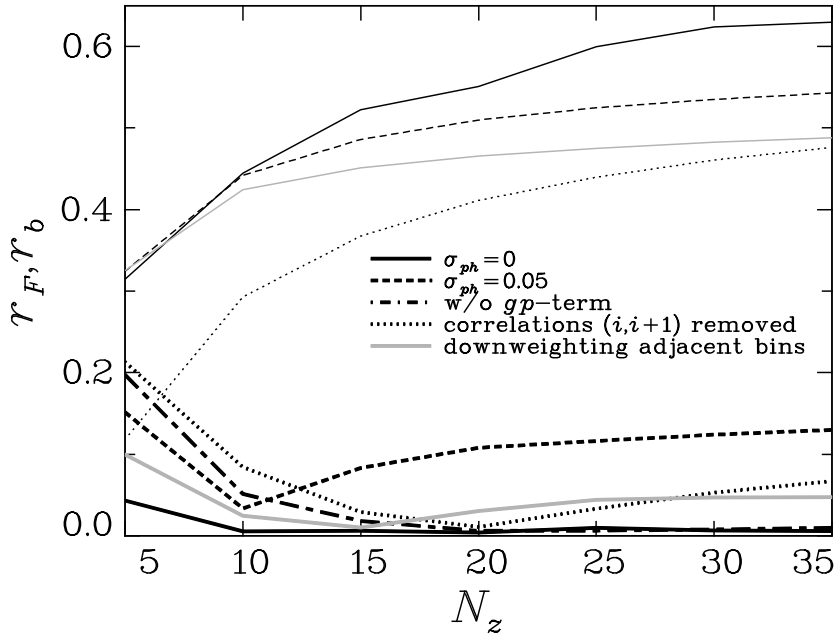

Figure 6.15: Ratios r_F and r_b as a function of the number of photometric redshift bins N_z. Thin curves represent r_F, thick curves r_b. Results for zero photometric redshift error are given as solid black lines; results for $\sigma_{\rm ph} = 0.05$ are plotted as dashed lines. For the case $\sigma_{\rm ph} = 0.05$, r_b is also plotted without the gp-term included in the calculation of the systematic, see the dot-dashed line. Since only the systematic signal is manipulated, the statistical signal in this case is still given by the dashed line. Dotted lines represent r_F and r_b if correlations of adjacent bins, i.e. bin combinations (ij) with $j = i + 1$, are excluded. Incorporating the downweighting scheme for correlations of adjacent bins introduced in Sect. 6.7.3 produces the grey solid curves. The two latter sets of curves were also obtained for $\sigma_{\rm ph} = 0.05$. Note that the black solid and the dot-dashed lines are very close to zero for $N_z > 10$ and $N_z > 20$, respectively.

we introduce an average relative bias

$$\bar{b} \equiv \sqrt{\frac{1}{N_p}\sum_{\mu=1}^{N_p}\frac{b^2(p_\mu)}{\sigma^2_{\rm orig}(p_\mu)}} = \sqrt{\frac{1}{N_p}\sum_{\mu=1}^{N_p} b^2_{\rm rel}(p_\mu)}\,, \tag{6.82}$$

which is the root mean square of the ratio of the systematic over the statistical error before nulling over all considered parameters. We refer to the performance of nulling via the ratios

$$r_F \equiv \frac{\bar{F}_{\rm null}}{\bar{F}_{\rm orig}}\,; \qquad r_b \equiv \frac{\bar{b}_{\rm null}}{\bar{b}_{\rm orig}} \tag{6.83}$$

of $\bar{F}$ and $\bar{b}$ after ('null') and before ('orig') nulling, respectively. For a good performance of nulling, r_F should tend to one, i.e. the nulled data constrains parameters as well as the original one, whereas r_b tends to zero, which corresponds to a complete elimination of the systematic.

Figure 6.15 shows results for the ratios r_F and r_b for different N_z, both without photometric redshift errors and for $\sigma_{\rm ph} = 0.05$. In this section the linear alignment model is used as the systematic, downscaled by a factor of five. For five redshift bins $\bar{F}_{\rm null}$ is only about a third of $\bar{F}_{\rm orig}$, but r_F rises, first strongly and then with an increasingly shallow slope for larger N_z. This development is mostly based on the improving performance of nulling since for a cosmic shear tomography data set statistical errors only marginally decrease for $N_z \geq 5$ (see e.g. Hu 1999; Simon et al. 2004; Ma et al. 2006; Bridle & King 2007; Joachimi & Schneider 2008).

Introducing a photometric redshift dispersion of $\sigma_{\rm ph} = 0.05$, one finds that, for small N_z, r_F increases in the same way as in the case without photometric redshift errors. As soon as the size of the redshift bins attains the same order as the width of the dispersion $\sigma_{\rm ph}(1+z)$, less additional redshift information becomes available to constrain parameters. Since nulling, like other techniques that deal with the control of intrinsic alignments (e.g. Bridle & King 2007), requires more precise redshift information, the curve for r_F levels off.

Even for only five bins in redshift, nulling is capable of reducing the average bias $\bar{b}$ by more than 95 % for perfect redshift information. For $N_z \geq 10$, less than 1 % of the average bias remains. If a more realistic photometric redshift dispersion is present in the data, r_b significantly degrades to approximately 0.15 for $N_z = 5$. For ten photometric redshift bins a minimum value of $r_b \approx 3.5\,\%$ is achieved before this ratio increases again for more bins, meaning that the treatment of the systematic worsens in spite of the improvement of redshift information due to the finer division of photometric redshifts. This apparent contradiction requires a more thorough investigation and will be addressed in Sect. 6.7.3.

6.7.2 Minimum information loss

Given ideal spectroscopic redshift information, equivalent to considering the limit $N_z \to \infty$, it would be possible to precisely eliminate the GI contamination at a given redshift, see (6.9), so that r_b tends to zero in absence of photometric redshift errors, as is indeed the case. However, the curves for r_F in Fig. 6.15 apparently indicate that the full statistical information is not regained in this limit, i.e. r_F does not tend to unity. We investigate this further by calculating r_F out to larger N_z, assuming a simplified model with infinitesimally narrow redshift bins, $p^{(i)}(z) = \delta_{\rm D}(z - z_i)$, and a covariance that contains only shot noise. The resulting curve, shown in Fig. 6.16, increases slower than logarithmically as a function of N_z, so that one can expect that indeed nulling inevitably reduces the statistical power of a data set, even when spectroscopic redshifts would be available.

To illustrate this effect, consider again the continuous, integral version of (6.64), still in the limit of perfect redshift information. Choosing the zeroth-order nulling weight proportional to $1 - \chi_i/\chi_j$, see (6.64), one can write the corresponding transformed power spectrum as

$$\begin{aligned}\Pi_{[0]}(\ell,\chi_i) &\propto \int_{\chi_i}^{\chi_{\rm hor}} {\rm d}\chi_j \left(1-\frac{\chi_i}{\chi_j}\right) P_{\rm GG}(\ell,\chi_i,\chi_j) \qquad (6.84)\\ &\propto \int_{\chi_i}^{\chi_{\rm hor}} {\rm d}\chi_j \left(1-\frac{\chi_i}{\chi_j}\right) \int_0^{\chi_i} {\rm d}\chi \left(1-\frac{\chi}{\chi_i}\right)\left(1-\frac{\chi}{\chi_j}\right) \{1+z(\chi)\}^2 P_\delta\left(\frac{\ell}{\chi},\chi\right) ,\end{aligned}$$

where in order to arrive at the second equality, the lensing power spectrum for spectroscopic redshifts has been obtained by inserting $p^{(i)}(z) = \delta_{\rm D}(z - z_i)$ into (3.34). Note that the upper limit in the integration over χ changes from $\chi_{\rm hor}$ to χ_i because the lensing efficiency, here written as $1 - \chi/\chi_i$, vanishes for $\chi > \chi_i$. Rearranging the terms, one arrives at

$$\begin{aligned}\Pi_{[0]}(\ell,\chi_i) &\propto \int_0^{\chi_i} {\rm d}\chi \left(1-\frac{\chi}{\chi_i}\right) g'(\chi)\{1+z(\chi)\}^2 P_\delta\left(\frac{\ell}{\chi},\chi\right) \qquad (6.85)\\ &\text{with} \quad g'(\chi) \equiv \int_{\chi_i}^{\chi_{\rm hor}} {\rm d}\chi_j \left(1-\frac{\chi_i}{\chi_j}\right)\left(1-\frac{\chi}{\chi_j}\right) .\end{aligned}$$

Comparing (6.85) to (3.34), one finds that the term $g'(\chi)$ is formally equivalent to the lensing efficiency of the background distribution[3], the term $1 - \chi_i/\chi_j$ acting analogously to a distance

[3]For perfect correspondence the lower limit of the integral over χ_j should be χ instead of χ_i. However, the nulling weight given as $1 - \chi_i/\chi_j$ has to vanish for $\chi_j < \chi_i$, and at the same time the outer integral ensures $\chi < \chi_i$.

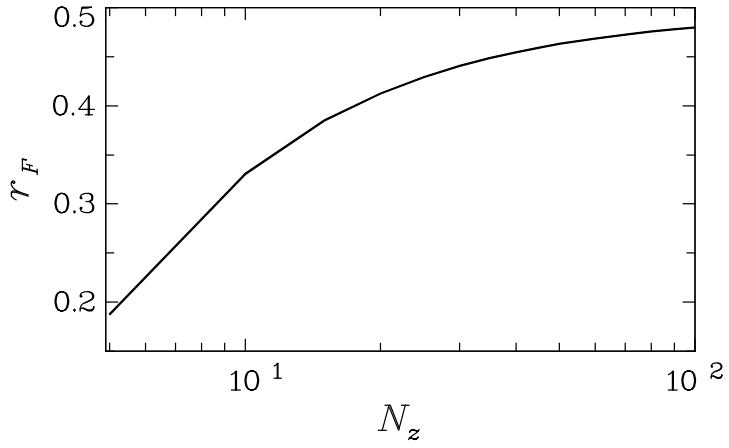

Figure 6.16: Ratio r_F as a function of the number of photometric redshift bins N_z. This result has been obtained by means of a simplified Fisher matrix calculation, placing galaxies at fixed redshifts and neglecting cosmic variance in the covariance. For large N_z the increase in r_F is slower than logarithmic.

probability distribution of galaxies. Thus, this 'background distribution' of the transformed power spectrum is broad, extending from the position of the foreground bin at χ_i to the maximum distance $\chi_{\rm hor}$. Since the zeroth-order nulled power spectra are removed from the data set, it is this integrated redshift information for all foreground bin positions χ_i that is necessarily lost due to nulling.

6.7.3 Intrinsic alignment contamination from adjacent bins

The increase in r_b for large N_z in the case $\sigma_{\rm ph} = 0.05$, as seen in Fig. 6.15, can be explained by inspecting (5.16). To produce a GI effect, the intrinsic alignment has to act on the foreground galaxy while the background galaxy is lensed. Hence, the GI signal should stem from the first term in (5.16), whereas the second term that contains $g^{(i)}(\chi)\ p^{(j)}(\chi)$ with $i < j$ vanishes if the redshift probability distributions are disjoint, see (6.9). We refer to the latter expression as the *gp*-term hereafter. This term can yield a contribution to the systematic in case the distributions overlap such that the true position of a galaxy from the background population is in front of galaxies from the foreground distribution. The contribution to the GI signal by swapped galaxy positions is not accounted for by nulling and produces a residual systematic.

To quantify the effect caused by the *gp*-term, we compute the average bias for the same model of the three-dimensional GI power spectrum, but now with the *gp*-term removed from (5.16). The resulting ratio r_b is plotted in Fig. 6.15 as well. While this curve shows a similar behaviour than the one for the systematic with *gp*-term for $N_z \leq 10$, it does not follow the turnaround and continues to decrease for larger N_z down to values of r_b obtained for data without photometric redshift errors, as expected. Thus, the increase in r_b of the data with $\sigma_{\rm ph} = 0.05$ for $N_z > 10$ can indeed be explained by the contamination due to the *gp*-term.

The *gp*-term cannot be quantified in detail as it depends explicitly on the form of the matter-intrinsic shear power spectrum, see (5.16). However, it is produced by an overlap of the redshift distributions of foreground and background distributions, so that the *gp*-term can be controlled by removing or downweighting bin combinations with a large overlap in redshift, in particular adjacent photometric redshift bins. For instance, one can simply exclude power spectra for bins (ij) with $j = i + 1$ from the analysis, which results in the dotted curves given in Fig. 6.15. Indeed the contamination by the *gp*-term is suppressed, producing merely a less significant increase in r_b for $N_z > 20$, but the statistical power decreases dramatically due to the removal of all power spectra with $j = i + 1$.

To alleviate this effect, we propose to downweight adjacent redshift bin combinations. According to (6.65), increasing an entry in the zeroth-order nulling weight implies a lower value in the corresponding entries of the higher-order weights. Hence, a manipulation of the zeroth-

order weights can be used to downweight certain power spectra in the process of nulling. We introduce the following modified weights

$$T'^{\mathrm{w},(i)}_{[0]\,j} \equiv w_{ij}\, T'^{(i)}_{[0]\,j} \quad \text{with} \quad w_{ij} = 1 + \exp\left\{ -\left(\frac{\hat{z}_j - \hat{z}_i}{\sigma_{\mathrm{ph}}\,(1+\hat{z}_i)} \right)^2 \right\} . \tag{6.86}$$

To motivate this choice, consider that for $j \gg i$ one gets $w_{ij} \approx 1$, so that in the regime where the *gp*-term is unimportant the original weights are reproduced. Moreover, $w_{ii} = 2$, which is in agreement with the fact that the *gp*-term is equal to the first term in (5.16) for auto-correlations (note however that auto-correlations are excluded from the analysis anyway). The width of the Gaussian in (6.86) is in principle arbitrary, but here conveniently chosen to scale with the width of the photometric redshift bins.

Therefore, the w_{ij} are expected to follow the redshift dependence of the *gp*-term, so that the higher-order nulling weights $\boldsymbol{T}^{\mathrm{w},(i)}_{[q]}$ with $q \geq 1$ efficiently downweight its contribution. Note that the modification of the nulling weights is done before normalisation such that the vectors $\boldsymbol{T}^{\mathrm{w},(i)}_{[q]}$ still have unit length. As an aside, the weighting scheme (6.86) would also contribute to the downweighting of contaminations by the II term.

Applying this Gaussian weighting scheme to the nulling procedure, one obtains the grey curves of Fig. 6.15. While for a small number of redshift bins r_F is similar to the case where all power spectra except auto-correlations were used, the curve approaches the results for the case with power spectra of adjacent bins removed for large N_z. This means that for small N_z the overlap between redshift bins is marginal, so that the weighting has only little effect, whereas for many bins power spectra with $j = i + 1$ are largely downweighted such that removing them produces similar results. The Gaussian weighting ensures that $r_b \lesssim 5\,\%$ for all $N_z > 10$. We will further consider the performance of this weighting scheme in Sect. 6.8.3.

The best binning in photometric redshifts in terms of nulling performance does not only depend on the number of bins N_z, but to a certain extent also on the choice of bin boundaries. The optimal positions of bin boundaries are determined by the detailed form of the relation between photometric and true, spectroscopic redshifts, which is specific to each survey and thus shall not be further assessed here.

6.8 Influence of photometric redshift uncertainty

6.8.1 Photometric redshift errors

This section deals with the dependence of nulling on the photometric redshift dispersion σ_{ph}, in absence of catastrophic outliers. The number of photometric redshift bins is kept at $N_z = 10$ for the remainder of this work, mainly for computational reasons. Future cosmic shear surveys, relying on precise redshift information and a large number of galaxy detections, will allow for considerably more photometric redshift bins, which may be advantageous in terms of nulling, see the foregoing section.

In Fig. 6.17 r_F is plotted as a function of σ_{ph} while in Fig. 6.18, upper panel, the ratios of the marginalised statistical errors before and after nulling are given for the parameters Ω_{m} and σ_8 individually. The curves for the other cosmological parameters vary considerably in magnitude, but otherwise show the same characteristics as the ones depicted. The ratio r_F decreases only very weakly with increasing σ_{ph} for both nulling variants (B) and (C), taking values between 0.44 and 0.48, because splitting the range of redshifts between 0 and 3 into 10 photometric redshift bins does not lead to a significant degrading of redshift information, even for $\sigma_{\mathrm{ph}} = 0.1$. In contrast to this, the ratio of the marginalised errors of individual cosmological parameters

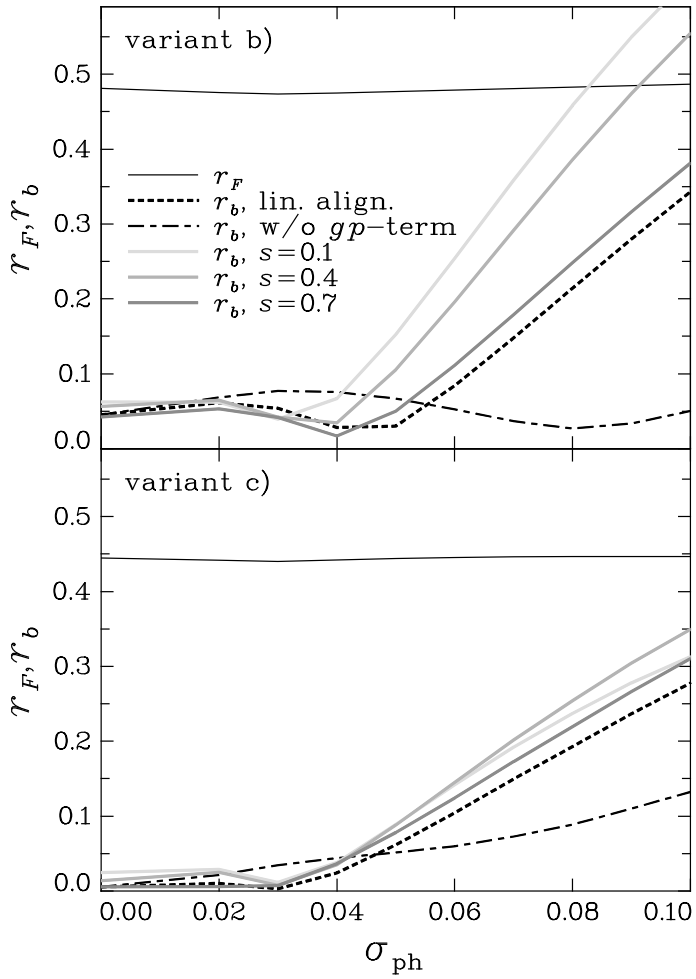

Figure 6.17: *Top panel*: Ratios r_F and r_b as a function of photometric redshift dispersion $\sigma_{\rm ph}$. The nulling has been performed by using variant (B), and the linear alignment model, downscaled by a factor of five, has been employed as systematic. Solid black curves correspond to r_F while r_b for the linear alignment model as systematic is given as black dashed curve. The values of r_b for the same model, but with the *gp*-term removed from the GI power spectrum calculation, is given as dot-dashed line. The grey curves show r_b for the GI power-law models, where the different grey-scales stand for different slopes s as given in the legend. *Bottom panel*: Same as above, but using nulling variant (C).

does vary with $\sigma_{\rm ph}$, but changes are smaller than about 10 %. The statistical errors of both the original and the nulled data set increase for larger photometric redshift errors similarly, but the error of the nulled set starts to do so already at smaller $\sigma_{\rm ph}$, thereby producing a peak at $\sigma_{\rm ph} \approx 0.03$ in both curves in Fig. 6.18. Marginalised errors for each of the seven considered parameters are a factor of roughly two to three larger for the nulled data.

As is evident from Fig. 6.17, lower panel, nulling using variant (C) is capable of reducing the average bias caused by the linear alignment model by more than a factor of 50 for $\sigma_{\rm ph} \lesssim 0.04$. Looking at the effect on the bias of individual parameters in Fig. 6.18, lower panel, one sees that the systematic is suppressed by more than 2 orders of magnitude for small $\sigma_{\rm ph}$. In spite of the strong intrinsic alignment signal, the bias is kept subdominant up to $\sigma_{\rm ph} \approx 0.05$. The drop in r_b at $\sigma_{\rm ph} \sim 0.03$ is also visible in Fig. 6.17 and can be traced back to a sign change in the residual bias for several parameters, among them $\Omega_{\rm m}$ and σ_8.

For larger redshift dispersions, r_b shows an approximately linear increase, which can only partially be ascribed to the contamination by the *gp*-term as can be concluded from comparing with the curve for the linear alignment model without *gp*-term. The rise in r_b is caused by two effects that are visible in Fig. 6.18. First, the strong relative bias in $\Omega_{\rm m}$ and σ_8 for the original data set starts to slowly decrease for $\sigma_{\rm ph} \gtrsim 0.02$, predominantly because the statistical errors rise due to the degrading information content in the line-of-sight direction. Second, the residual bias after nulling increases as a function of $\sigma_{\rm ph}$ and starts to attain values of the same order as the statistical errors, i.e. $|b_{\rm rel}| \sim 1$, at just about $\sigma_{\rm ph} \approx 0.05$. The part of this degradation that cannot be traced back to the effect by the *gp*-term has to stem from the incorrect assessment

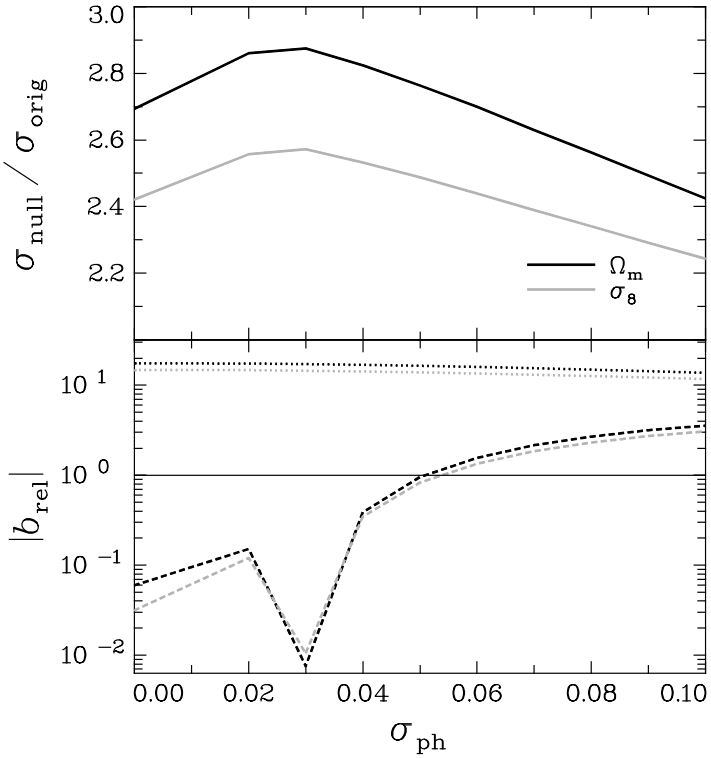

Figure 6.18: Performance of nulling as a function of photometric redshift dispersion $\sigma_{\rm ph}$. The nulling has been done using variant (C), and the linear alignment model, downscaled by a factor of five, has been employed as systematic. Shown are the results for the parameters $\Omega_{\rm m}$ as black curves, and for σ_8 as grey curves. *Top panel*: Ratio of the marginalised statistical errors after and before nulling. *Bottom panel*: Relative bias $b_{\rm rel}$. Dotted curves correspond to $b_{\rm rel}$ before nulling; dashed curves to $b_{\rm rel}$ after nulling. The solid line marks values of $b_{\rm rel}$ for which the marginalised statistical errors equal the bias. Note the logarithmic scaling of the ordinate axis.

of the redshift dependence of the GI signal, either due to the approximations inherent to the derivations of nulling or the suboptimal placement of the redshift at which the signal is nulled.

Figure 6.17 also shows r_b for the power-law GI model with varying slopes. The behaviour of r_b as a function of $\sigma_{\rm ph}$ is in very good agreement with the results for the linear alignment model, r_b reaching about 0.03 for $\sigma_{\rm ph} \lesssim 0.04$, and up to 30 % higher values for $\sigma_{\rm ph} = 0.1$ in comparison with the linear alignment model. This suggests that at least the orders of magnitude of our results as well as the general conclusions drawn from a particular GI model used in this work can be taken to robustly estimate the effects of a realistic GI contamination.

Moreover, Fig. 6.17, upper panel, illustrates the performance of nulling using variant (B), i.e. renouncing on information about the form of the redshift probability distributions, and placing the redshift at which the signal is nulled at the centres of the photometric redshift bins $z_{\rm c}^{(i)}$, respectively. This version of nulling is capable of retaining marginally more information in the data, in particular for small $\sigma_{\rm ph}$. For high quality redshift information the reduction in bias is worse, r_b doubling approximately compared to variant (C). Again at $\sigma_{\rm ph} \sim 0.04$, r_b starts to increase, but more steeply, so that for $\sigma_{\rm ph} > 0.04$ nulling quickly becomes rather inefficient. As for variant (C), the curves for r_b of the different GI models agree well in their functional form, but yield largely different amplitudes. It is striking that the curve calculated without the *gp*-term does not feature a distinct increase for large $\sigma_{\rm ph}$. This suggests that variant (B), when combined with the weighting scheme of Sect. 6.7.3, could perform well also for larger photometric redshift errors, as we will investigate in Sect. 6.8.3.

6.8.2 Analysing optimal nulling redshifts

The construction of nulling weights allows for a certain freedom in the choice of redshifts, which the photometric redshift bins are assigned to. We wish to investigate which choice of redshifts $\hat{z}_i$, i.e. those redshifts where the signal is nulled, is optimal in the sense that the resulting zeroth-order nulling weights (6.64) best reproduce the redshift dependence of the GI

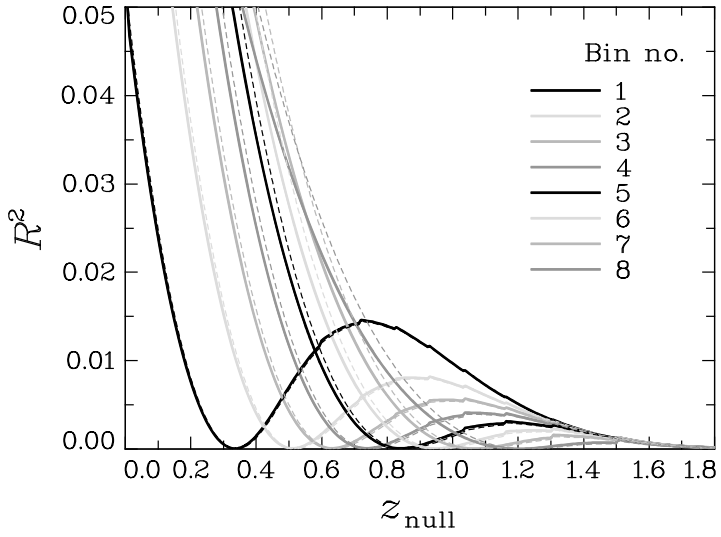

Figure 6.19: Least squares sum R^2 as a function of nulling redshift $z_{\rm null}$. The results for photometric redshift bins one to eight correspond to the suite of grey-scale curves as given in the legend. Thin dashed lines represent the results for R^2 obtained when calculating the power spectrum without *gp*-term. Since we used $\sigma_{\rm ph} = 0.05$ to produce this data, the minima of the latter curves are slightly offset. The local minima of these curves correspond to the optimal nulling redshifts $z_{\rm null}$ plotted in Fig. 6.21. Note that R^2 at the local minima is close to, but always larger than zero.

signal, and thus effectively remove the systematic. The procedure to find such optimal nulling redshifts, denoted by $z_{\rm null}$, is outlined in the following. We emphasise that the calculation of $z_{\rm null}$ merely constitutes a diagnostic tool, inapplicable to data, since the GI systematic has to be known exactly to do this.

Judging from (6.9) and the considerations in Sect. 6.6.1, using the lensing efficiency $g^{(j)}\left(\chi(\hat{z}_i)\right)$ as zeroth-order nulling weight is most effective in case of precise redshift information. In fact, in the limit of spectroscopic redshifts $g^{(j)}\left(\chi(\hat{z}_i)\right)$ matches the redshift dependence of the GI signal perfectly. In the approximation of infinitesimally narrow redshift probability distributions for the photometric redshift bins with lower median redshift, i.e. the initial bins, the redshifts $\hat{z}_i$ would mark the position, at which the GI signal would be perfectly removed. In reality, the photometric redshift bins i have finite size as do the corresponding distributions of true redshifts $p^{(i)}(z)$. The nulling redshift $\hat{z}_i$ is not fully specified anymore and has to be chosen appropriately. One reasonable choice is the median redshift of bin i, which corresponds to nulling variant (C). In this section we treat the $\hat{z}_i$ as free parameters and determine an optimal value $z_{\rm null}$.

Hence, we aim at determining $\hat{z}_i$ such that $g^{(j)}\left(\chi(\hat{z}_i)\right)$ fits $P_{\rm GI}^{(ij)}(\ell)$ best since then nulling completely removes the intrinsic alignment signal with $g^{(j)}\left(\chi(\hat{z}_i)\right)$ as zeroth-order weight. To this end, we compute the best fitting lensing efficiency, using the least squares sum of all background bins j,

$$R^2\left(A_P, \hat{z}_i\right) = \sum_{j=i+1}^{N_z} \left(A_P P_{\rm GI}^{(ij)}(\ell) - g^{(j)}\left(\chi(\hat{z}_i)\right)\right)^2 , \tag{6.87}$$

where the initial bin i and the angular frequency ℓ are fixed. As default, we employ the values of $P_{\rm GI}^{(ij)}(\ell)$ for the central angular frequency bin, i.e. the bin with index $N_\ell/2$, which corresponds to $\ell \approx 414$. We warn that this is a crude approximation as the three-dimensional intrinsic alignment power spectrum varies significantly over the range of the integral in (5.16). The redshift-independent part of the dependence of the GI power spectrum on ℓ can be absorbed into the free scaling A_P. The remaining ℓ-dependence is accounted for by determining $z_{\rm null}$ for different angular frequencies, see Fig. 6.21 below.

Since differences in the amplitude of $P_{\rm GI}^{(ij)}(\ell)$ and $g^{(j)}\left(\chi(\hat{z}_i)\right)$ are not of interest, the dependence of R^2 on the scaling is eliminated by calculating the extremal A_P from the condition

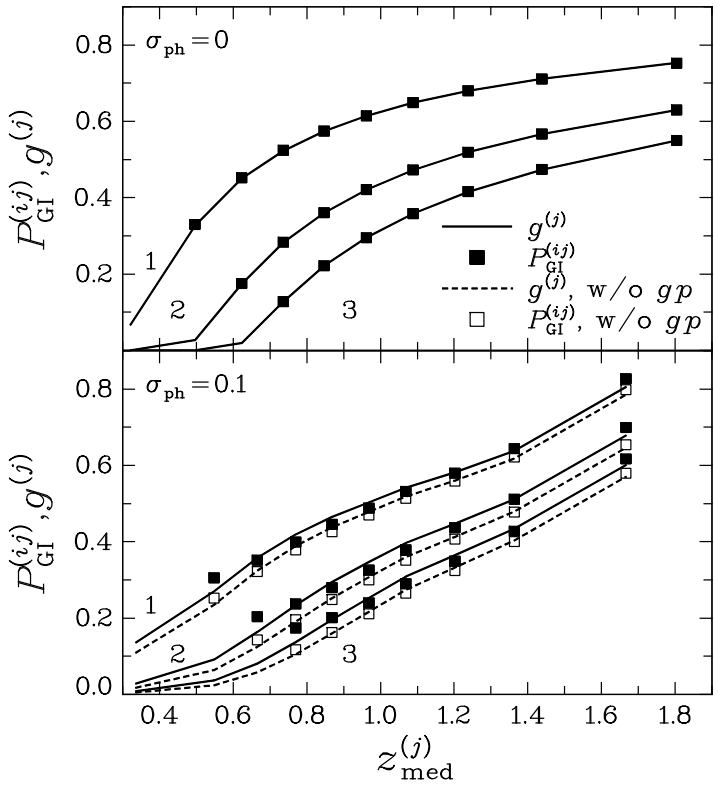

Figure 6.20: Determination of the optimal nulling redshift. *Top panel*: Results for $\sigma_{\rm ph} = 0$. The filled squares display the redshift dependence of the GI power spectrum, i.e. $A_P P_{\rm GI}^{(ij)}(\ell)$ are plotted for different background bins j and fixed i and ℓ. The lines correspond to the lensing efficiencies $g^{(j)}\left(\chi(\hat{z}_i)\right)$ for the best-fitting $\hat{z}_i$, respectively. The values for bin j of both lensing efficiencies and power spectra have been assigned to the median redshift of this bin, linearly interpolating in between for $g^{(j)}\left(\chi(\hat{z}_i)\right)$. The numbers alongside the curves mark the initial bin number i. *Bottom panel*: Same as above, but for $\sigma_{\rm ph} = 0.1$. Here we plot in addition the results obtained by excluding the gp-term from the calculation of the GI signal as dashed curves and open squares, respectively.

$\partial R^2/\partial A_P = 0$, yielding

$$A_P = \frac{\sum_{j=i+1}^{N_z} g^{(j)}\left(\chi(\hat{z}_i)\right) P_{\rm GI}^{(ij)}(\ell)}{\sum_{j=i+1}^{N_z} \left(P_{\rm GI}^{(ij)}(\ell)\right)^2} \,. \tag{6.88}$$

Now R^2 is computed for a wide range of $\hat{z}_i$, making use of the fact that (6.88) reduces the problem to a one-dimensional minimisation. The value of $\hat{z}_i$ that corresponds to the minimum least squares is then set as the optimal nulling redshift $z_{\rm null}$.

In Fig. 6.19 the least squares sum R^2 is plotted as a function of the $\hat{z}_i$ for a data set with $\sigma_{\rm ph} = 0.05$, using the downscaled linear alignment model to compute the GI power spectrum. Note that for high redshifts $\hat{z}_i$, the lensing efficiency tends to zero, thereby implying an extremal value of $A_P = 0$. Thus, the least squares go to zero for high redshifts because a GI power spectrum, scaled to zero, fits a vanishing lensing efficiency perfectly. The optimal nulling redshift is therefore extracted from the well-defined local minima of R^2, which can be clearly seen in Fig. 6.19.

The procedure to compute $z_{\rm null}$ is illustrated by Fig. 6.20. The redshift dependence of the GI power spectra for initial bins 1 to 3, and the corresponding best-fit lensing efficiencies are plotted, referring the values for bin j of both quantities to the median redshift of distribution $p^{(j)}(z)$.[4] The curves corresponding to the lensing efficiency are obtained via linear interpolation of the set of $g^{(j)}\left(\chi(\hat{z}_i)\right)$ with $j = i+1, .., N_z$. For the case without photometric redshift errors, nulling redshifts can be found such that the resulting lensing efficiencies almost exactly fit the redshift dependence of the GI power spectrum, so that in this case the approximation of infinitesimally narrow initial bins has little negative influence on the nulling performance.

[4]This referring is merely for illustrative purposes and not part of the procedure outlined above.

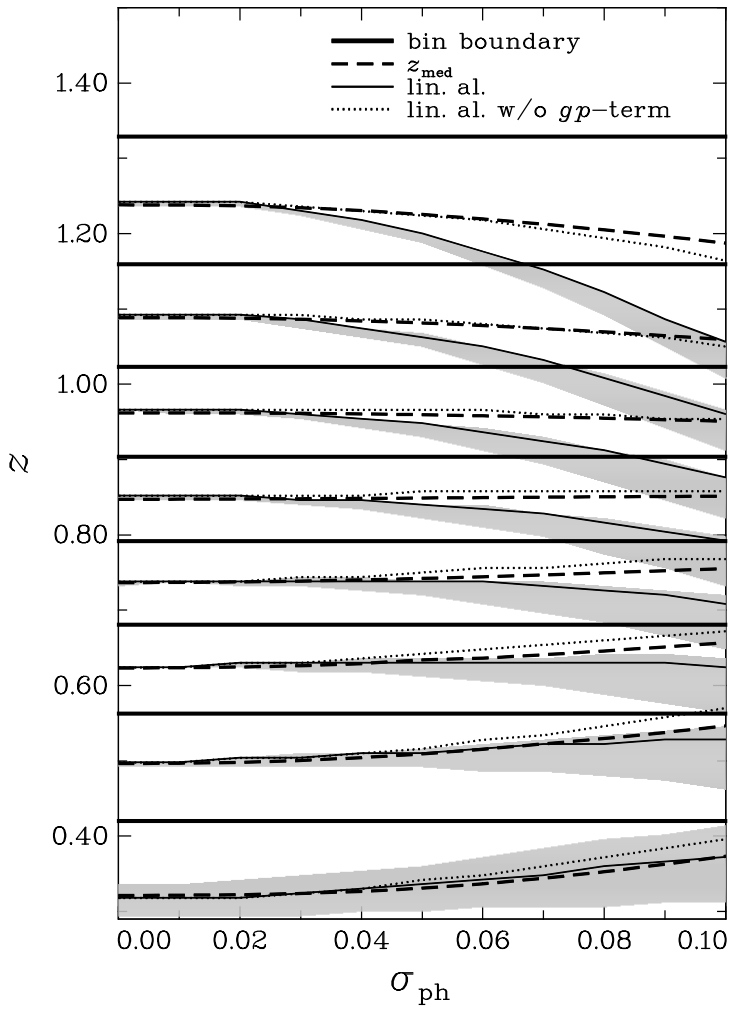

Figure 6.21: Optimal nulling redshift $z_{\rm null}$ as a function of photometric redshift dispersion $\sigma_{\rm ph}$. Plotted are the results for different GI signals, including the linear alignment model with and without *gp*-term, and the power law model with slopes $s_{\rm GI} = \{0.1, 0.4, 0.7\}$. Solid curves correspond to $z_{\rm null}$ for the linear alignment model, evaluated at the central angular frequency bin. Excluding the *gp*-term for this setup results in the dotted line. The grey areas indicate the range of $z_{\rm null}$ for all intrinsic alignment models considered, evaluated at the lowest and highest angular frequency bin each. In addition, the bin boundaries are shown as thick solid lines, while the median redshifts of the redshift probability distributions are represented by thick dashed curves.

In the bottom panel of Fig. 6.20 we plot results for a large redshift uncertainty of $\sigma_{\rm ph} = 0.1$. Deviations of the redshift dependence of the GI signal from the best-fitting $g^{(j)}\left(\chi(\hat{z}_i)\right)$ are visible particularly for the lowest bin considered, i.e. for $j = i+1$, and the bin at the highest redshift. The latter effect can be ascribed to the large width and asymmetry of the corresponding redshift probability distribution, see Fig. 6.10. The GI power spectrum shifts to higher values for bins $j = i+1$ and $\sigma_{\rm ph} \gg 0$ because of the *gp*-term, which has the strongest contribution for adjacent photometric redshift bins. Accordingly, the GI signal is significantly smaller for bins $j = i+1$ if calculated without the *gp*-term, and a lensing efficiency that fits the GI term much better, i.e. with smaller $R^2(A_P, z_{\rm null})$, can be found. Since $P_{\rm GI}^{(ij)}(\ell)$ without the *gp*-term is generally best-fit by lensing efficiencies with higher $\hat{z}_i$ than the power spectrum with *gp*-term, R^2 attains its minimum at higher $\hat{z}_i$, as is also evident from Fig. 6.19.

We repeat the determination of $z_{\rm null}$ for all relevant initial bins, for the GI power spectrum at the lowest and highest angular frequency bin in addition to the central one, and varying $\sigma_{\rm ph}$, our findings being depicted in Fig. 6.21. The grey regions cover the range of resulting curves for all four considered GI models (linear alignment; power law with $s_{\rm GI} = \{0.1, 0.4, 0.7\}$), evaluated at the lowest, central, and highest angular frequency bin each. Hence, these regions should mark to good accuracy the possible range of $z_{\rm null}$ for any GI signal. In addition, curves representing the photometric redshift bin boundaries, the median redshifts of the distributions, and $z_{\rm null}$ for the linear alignment model, computed for the central angular frequency bin with and without the *gp*-term are shown.

In the regime of $\sigma_{\rm ph}$ in which nulling performs excellently, i.e. $\sigma_{\rm ph} \lesssim 0.04$ (Fig. 6.17), we

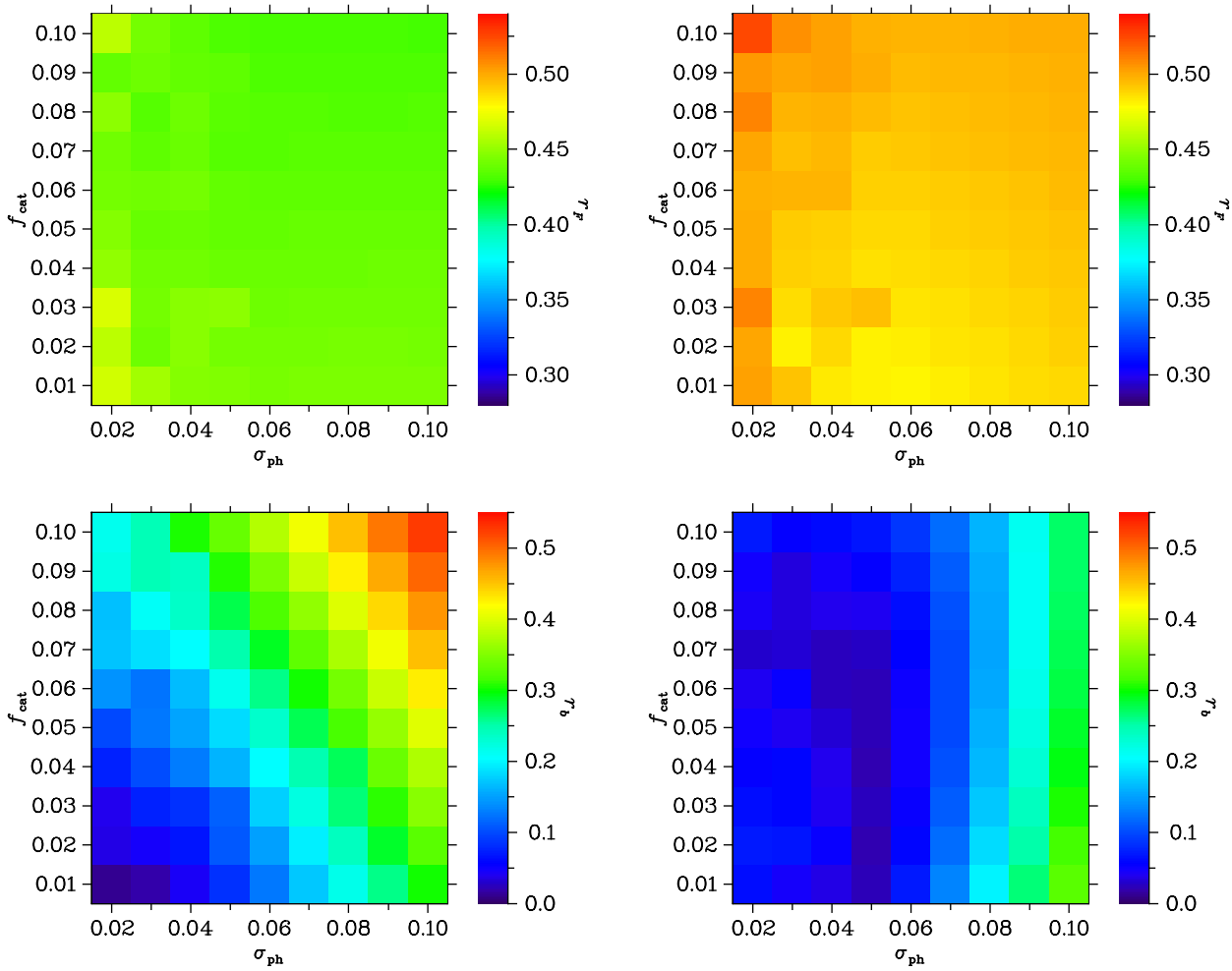

Figure 6.22: Ratios of average statistical and systematic errors r_F and r_b as a function of photometric redshift dispersion $\sigma_{\rm ph}$ and outlier fraction $f_{\rm cat}$. The offset of the outlier distributions has been fixed at $\Delta_z = 1$. As systematic the linear intrinsic alignment model, downscaled by a factor of five, has been employed. *Left*: Results for nulling which takes into account knowledge of the redshift probability distributions, i.e. variant (C). In the upper panel r_F is shown, and in the lower one r_b. *Right*: Same as before, but for nulling with referencing to the centres of the photometric redshift bins, i.e. variant (B).

find that the median redshifts are very close to the optimal nulling redshifts. Only for the lowest initial bin the allowed region of $z_{\rm null}$ is broader, but still well-fit by the median redshift. Using the central redshifts $z_{\rm c}^{(i)}$ as nulling redshifts proves to be a fair approximation if the underlying redshift probability distributions are not too asymmetric, as is for instance the case in our model of redshift distributions except for the distributions at the lowest and highest median redshift. These results confirm that variant (C) with nulling at the median redshifts yields indeed the best performance for a survey with small redshift dispersion. As can also be concluded from Fig. 6.21, variant (B) works only slightly less effectively in this case.

Regarding the behaviour of the curves for large $\sigma_{\rm ph}$, $z_{\rm null}$ considerably deviates from its values at small redshift errors, partially crossing the original photometric redshift bin boundaries. While the median redshifts at least qualitatively follow the change in $z_{\rm null}$ with increasing $\sigma_{\rm ph}$ by trend, the $z_{\rm c}^{(i)}$ of nulling variant (B) represent the actual $z_{\rm null}$ even worse, as the results of Fig. 6.17 verify. The drop of $z_{\rm null}$ for the higher initial bins can almost entirely be explained by

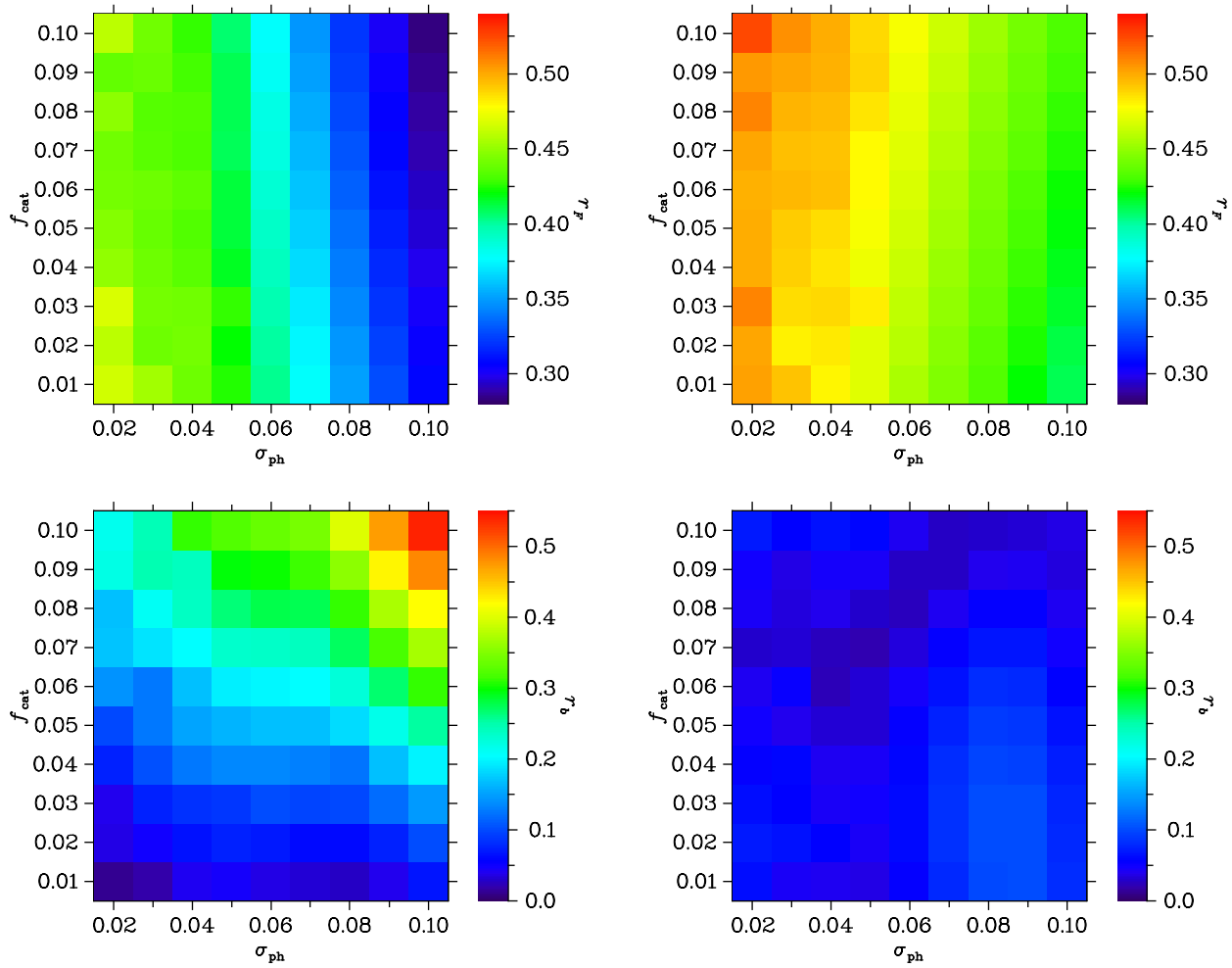

Figure 6.23: Same as in Fig. 6.22, but now including the weighting scheme outlined in Sect. 6.7.3. As expected the residual bias is further reduced while losing still more cosmological information.

the *gp*-term contribution. Its removal produces curves that keep close to the median redshifts, see Fig. 6.21. The remaining offsets of $z_{\rm null}$ from the median redshifts presumably originate from the variation of the integrand in (5.16) across the broad distribution of the initial bins. However, since we compute the GI power spectrum only for single ℓ-bins, the accuracy in the calculation of $z_{\rm null}$ is limited. This holds true in particular for broad redshift distributions, as the widening of the grey regions, which is dominated by the scatter of the curves computed for different angular frequency bins, indicates.

6.8.3 Catastrophic outliers

Future cosmic shear data, in particular for space-based surveys incorporating infrared bands (Abdalla et al. 2007), will be able to rely on exquisite multi-band photometry, so that the fraction of catastrophic failures in the assignment of photometric redshifts will be kept at a very low level. A significant fraction of outliers in the redshift probability distributions would have a devastating effect on the removal of intrinsic alignment. For instance, consider a photometric redshift bin i at relatively high redshift. If it mistakenly contains galaxies whose true redshift is low, these would produce a strong GI signal when correlated with another high redshift background bin j.

Table 6.6: Errors on cosmological parameters for three exemplary data sets with different photometric redshift errors. *Top*: Ratios r_F and r_b for the three data sets considered. Moreover, the parameters specifying the photometric redshift errors and the nulling variant used are given. The offset of outliers is fixed at $\Delta_z = 1.0$ for all sets. The linear alignment model has been used throughout as systematic, as well as the weighting scheme of Sect. 6.7.3. Note that set no. 2 is the underlying data for the results of Fig. 6.24. *Bottom*: Marginalised statistical errors σ, biases b, total errors $\sigma_{\rm tot}$, and $b_{\rm rel}$ for every cosmological parameter, shown for both original and nulled data sets. Besides, the ratios of statistical errors and biases before and after nulling are given.

set	$\sigma_{\rm ph}$	$f_{\rm cat}$	$r_{\rm out}$	nulling	r_F	r_b
1	0.03	0.01	0.007	(C)	0.438	0.026
2	0.05	0.05	0.032	(B)	0.475	0.039
3	0.07	0.10	0.060	(B)	0.465	0.028

set	par.	original data				nulled data				ratios	
		σ	b	$\sigma_{\rm tot}$	$b_{\rm rel}$	σ	b	$\sigma_{\rm tot}$	$b_{\rm rel}$	$\frac{\sigma_{\rm null}}{\sigma_{\rm orig}}$	$\left\lvert\frac{b_{\rm null}}{b_{\rm orig}}\right\rvert$
1	$\Omega_{\rm m}$	0.008	-0.137	0.137	-16.921	0.023	-0.003	0.023	-0.137	2.849	0.023
	σ_8	0.012	0.166	0.167	14.290	0.030	0.004	0.030	0.125	2.557	0.022
	h	0.104	0.109	0.151	1.042	0.213	-0.001	0.213	-0.003	2.043	0.006
	$n_{\rm s}$	0.014	-0.012	0.018	-0.882	0.036	-0.001	0.036	-0.029	2.615	0.086
	$\Omega_{\rm b}$	0.015	-0.032	0.035	-2.032	0.031	-0.001	0.031	-0.045	1.989	0.044
	w_0	0.078	-1.231	1.233	-15.845	0.247	-0.034	0.249	-0.136	3.173	0.027
	w_a	0.250	3.123	3.133	12.486	0.737	0.097	0.743	0.132	2.946	0.031
2	$\Omega_{\rm m}$	0.009	-0.136	0.136	-15.674	0.025	0.003	0.025	0.140	2.830	0.025
	σ_8	0.012	0.165	0.166	13.316	0.031	-0.002	0.031	-0.057	2.510	0.011
	h	0.109	0.095	0.145	0.871	0.203	-0.042	0.207	-0.209	1.859	0.447
	$n_{\rm s}$	0.014	-0.014	0.020	-0.973	0.033	0.003	0.033	0.075	2.352	0.181
	$\Omega_{\rm b}$	0.016	-0.034	0.038	-2.101	0.030	-0.002	0.030	-0.084	1.831	0.073
	w_0	0.085	-1.225	1.228	-14.486	0.262	0.067	0.270	0.254	3.094	0.054
	w_a	0.271	3.132	3.143	11.559	0.765	-0.109	0.773	-0.143	2.825	0.035
3	$\Omega_{\rm m}$	0.010	-0.135	0.135	-14.090	0.026	-0.002	0.026	-0.075	2.758	0.015
	σ_8	0.014	0.164	0.164	12.066	0.033	0.005	0.034	0.145	2.466	0.030
	h	0.116	0.079	0.140	0.676	0.218	-0.042	0.222	-0.194	1.879	0.538
	$n_{\rm s}$	0.015	-0.016	0.022	-1.100	0.037	-0.002	0.037	-0.065	2.458	0.145
	$\Omega_{\rm b}$	0.017	-0.038	0.041	-2.157	0.032	-0.005	0.032	-0.168	1.828	0.142
	w_0	0.095	-1.211	1.215	-12.773	0.283	0.021	0.284	0.073	2.986	0.017
	w_a	0.302	3.127	3.142	10.360	0.832	0.042	0.833	0.050	2.755	0.013

We compute the ratios r_F and r_b now as functions of both $\sigma_{\rm ph}$ and $f_{\rm cat}$, keeping the offset fixed at $\Delta_z = 1.0$. To judge the effect of outliers, it is important to note that $f_{\rm cat}$ is not the true fraction of catastrophics, but $r_{\rm out}$ as given by Fig. 6.11. Results for r_F and r_b are given in Fig. 6.22 for the linear intrinsic alignment model as the systematic, again downscaled by a factor of five. The left column shows results for nulling variant (C), the right column for variant (B). In Fig. 6.23 the weighting scheme (6.86) has been applied in addition.

Inspecting the plots obtained without the weighting scheme first, one sees that as before, r_F varies only little with the parameters of photometric redshift, varying around 45 % for variant (C). Variant (B) retains slightly more information than (C), i.e. around 50 %, which is in

accordance with Figs. 6.13 and 6.17. Moreover, the fraction of catastrophic outliers indeed has a strong effect on the ability of nulling to remove the GI systematic. Variant (C) performs well for high quality redshifts, but r_b increases significantly when increasing both $\sigma_{\rm ph}$ and $f_{\rm cat}$, reaching $r_b \approx 0.5$ for $\sigma_{\rm ph} = 0.1$ and $f_{\rm cat} = 0.1$. Contrary to this, variant (B) proves to be much more robust against catastrophic outliers, still reducing the average bias by about a factor of ten for $\sigma_{\rm ph} \leq 0.05$ and any outlier fraction considered here. The performance merely degrades for large $\sigma_{\rm ph}$, but remains below $r_b \approx 0.3$ in the case of the linear alignment model, see also Fig. 6.17.

Introducing the weighting scheme for adjacent photometric redshift bins to the nulling technique modifies its performance substantially. For $\sigma_{\rm ph} \lesssim 0.05$ the changes are small, as expected. The larger $\sigma_{\rm ph}$, the more adjacent bin combinations are downweighted, the larger the decrease in r_F. The ratio r_F drops by up to 0.15 in the case of variant (C). At the same time the region in which r_b is desirably small extends significantly towards larger $\sigma_{\rm ph}$. While this improvement is mostly relevant in the regime of low outlier rates for variant (C), variant (B) achieves $r_b \lesssim 0.1$ across the full range of $\sigma_{\rm ph}$ and $f_{\rm cat}$ considered. In other words, nulling can reduce the GI contamination by at least a factor of 10 for all realistic configurations of redshift errors, given that the GI systematics we consider should be close to a worst case. The even stronger biases caused by the power law models (Fig. 6.17) are mostly due to the *gp*-term and can thus also be expected to curb down on applying the weighting scheme.

To summarise our findings, we present our different error measures for three exemplary models in Table 6.6. The three sets represent surveys with high (set 1), medium (set 2), and low (set 3) quality redshift information, with parameters $\sigma_{\rm ph}$ and $f_{\rm cat}$ as given in the table. According to the results of the foregoing sections we use variant (C) for the high-quality set 1, and variant (B) for the other configurations, always including the weighting scheme for adjacent photometric redshift bins. For all sets, the survey is divided into $N_z = 10$ redshift bins, the downweighted linear alignment model is used as GI signal, and $\Delta_z = 1.0$ is fixed. For all these models nulling retains about 45 % of the statistical power in terms of r_F and depletes the GI contamination by about a factor of 30. Figure 6.24 shows two-dimensional marginalised 2σ-error contours before and after nulling for set 2. Note that since we did not add any priors to the Fisher matrix calculation, negative values for e.g. $\Omega_{\rm b}$ are not excluded.

6.8.4 Uncertainty in redshift distribution parameters

The parameters characterising the redshift distributions are determined from data, for instance by making use of a spectroscopic subsample of galaxies. Hence, there is also uncertainty in the shape of the $p^{(i)}(z)$, or equivalently, in the parameters describing the redshift distributions such as $z_{\rm med}$, or $\sigma_{\rm ph}$. The performance of variant (C), which explicitly takes into account information about the redshift distributions, will clearly be affected by this uncertainty, as shall be investigated in the following.

We quantify the uncertainty in the redshift distributions in terms of the median redshift, allowing for a Gaussian scatter with width $\sigma_{z_{\rm med}}$ around the true value of $z_{\rm med}$ for every redshift bin. Then Monte-Carlo samples of sets of $z_{\rm med}$ are drawn from these distributions and used to subsequently compute nulling weights, do the Fisher analysis of the nulled data set, and obtain the ratio r_b. As input we use a set of power spectra calculated for $N_z = 10$ bins with $\sigma_{\rm ph} = 0.03$ and without catastrophic outliers. For high-quality redshift information that nulling variant (C) is suited for one can adopt the requirements on $\sigma_{z_{\rm med}}$ of planned satellite missions like Euclid, targeting $\sigma_{z_{\rm med}} = 0.001$ and demanding at least $\sigma_{z_{\rm med}} = 0.002$. Drawing 5000 Monte-Carlo samples each for both of these values of $\sigma_{z_{\rm med}}$ produces the distributions of r_b displayed in Fig. 6.25.

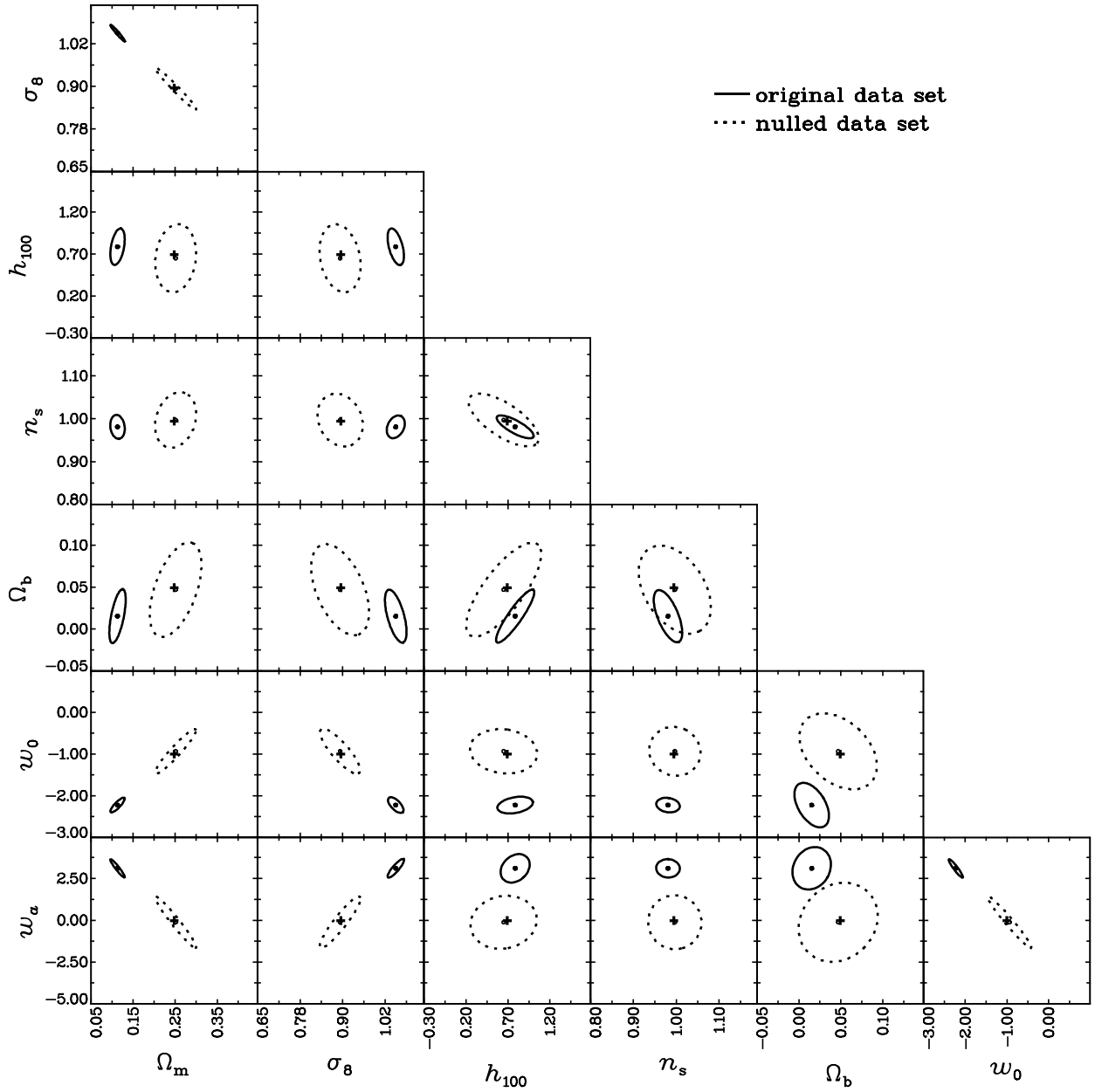

Figure 6.24: Parameter constraints before and after nulling. Shown are the two-dimensional marginalised 2σ-errors for the original data set as solid curves and for the nulled data set as dotted curves. The fiducial parameter values are marked by the crosses. The survey has been divided into $N_z = 10$ photometric redshift bins. Photometric redshift errors are characterised by $\sigma_{\rm ph} = 0.05$, $f_{\rm cat} = 0.05$, and $\Delta_z = 1.0$. As systematic the linear alignment model, downscaled by a factor of five, has been employed. The nulling was done using variant (B), including the weighting scheme outlined in Sect. 6.7.3.

For each histogram a value $\bar{r}_b$ is marked, defined such that $r_b < \bar{r}_b$ for 90 % of all samples. We find $\bar{r}_b \approx 0.010$ for $\sigma_{z_{\rm med}} = 0.001$ and $\bar{r}_b \approx 0.019$ for $\sigma_{z_{\rm med}} = 0.002$. The distributions peak at the value $r_b \approx 0.003$, which results from using the $z_{\rm med}$ as nulling redshifts (see Fig. 6.17). Given a non-vanishing photometric redshift error, $z_{\rm med}$ is not necessarily the optimal choice, and indeed samples with $r_b < 0.003$ exist, although the histograms decline rapidly for small r_b. The distribution for $\sigma_{z_{\rm med}} = 0.002$ is much shallower and decreases only slowly for $r_b > 0.003$, resulting in a $\bar{r}_b$ about twice as big as for $\sigma_{z_{\rm med}} = 0.001$. Hence, nulling variant (C) requires

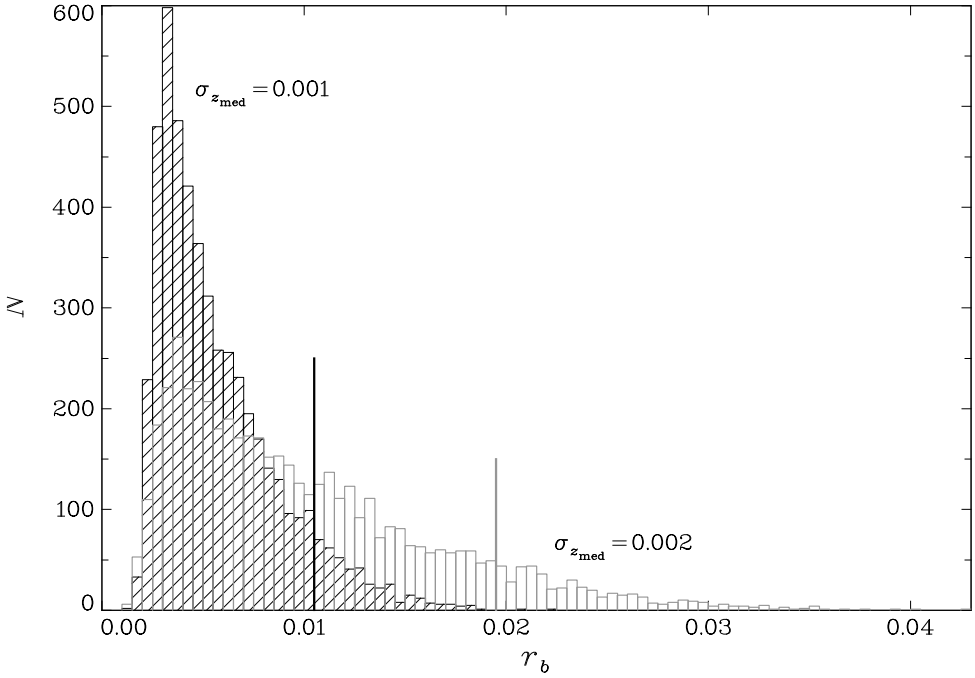

Figure 6.25: Distribution of r_b for 5000 Monte-Carlo samples of the set of $z_{\rm med}$, using a model with $\sigma_{\rm ph} = 0.03$ and no catastrophic outliers. The black hatched distribution was obtained for a scatter of $\sigma_{z_{\rm med}} = 0.001$, the grey distribution for $\sigma_{z_{\rm med}} = 0.002$. The vertical lines mark the limit $\bar{r}_b$, which is chosen such that $r_b < \bar{r}_b$ for 90 % of all samples.

knowledge of the form of the redshift distribution comparable to the planned goals of future satellite missions to fully demonstrate its potential. Any moderate deviation of the nulling redshifts from its optimum, approximated by the $z_{\rm med}$, results in a significant increase in residual bias.

On the other hand, nulling variant (B) does not rely on detailed knowledge about the $p^{(i)}(z)$ and performed well over a wide range of redshift distribution characteristics, but only when including the Gaussian weighting scheme of adjacent redshift bins. The latter procedure does depend on the form of the redshift distributions to a certain extent as the width of the weight should be chosen such that the Gaussian covers the range of overlap between the redshift distributions, which in turn depends on $\sigma_{\rm ph}$. However, general information about the width of redshift distribution is mandatory for all upcoming cosmic shear surveys. Since the width of the Gaussian in (6.86) can in principle be chosen arbitrarily, one can always adjust this width to safely suppress the *gp*-term.

6.9 Conclusions

In this chapter we elaborated on a purely geometrical method to eliminate gravitational shear-intrinsic ellipticity (GI) correlations, which constitute a source of severe contamination to the cosmic shear signal. Using a nulling technique, new observables free of this contamination were constructed by suitably weighting tomographic cosmic shear power spectra. The weighting was determined such that the contribution to the cosmic shear signal from matter structures potentially causing GI correlations is removed by exploiting the characteristic dependence of these correlations on redshift.

Three approaches to obtaining weight functions were investigated, which in addition opti-

mise the information content of the new observables in terms of the Fisher matrix. The results for both analytical and numerical methods are in good agreement, also for higher orders that are constructed by imposing a suitably defined condition of orthogonality. Most notably, the analytical ansatz, being computationally simple, is compatible in spite of several simplifications.

Using a set of tomographic power spectra with 20 redshift bins in a likelihood analysis, we computed credible regions in a four-dimensional parameter space to assess the loss of information due to nulling. The contours widen significantly with an increase in q-values of up to 50 % although reasonably stringent constraints on cosmological parameters are still possible. Besides, it was demonstrated that the use of a smaller subset of power spectra, excluding those constructed by means of higher-order weight functions, yields a practically identical performance, compared to the full set.

Data with a small number of redshift bins could be shown to almost completely lose its ability to constrain cosmological parameters when intrinsic alignment is taken into account (see also Bridle & King 2007). The requirement on the density of photometric redshift bins is relaxed if the contamination by II correlations of power spectra cross-correlating adjacent bins is safely under control. Hence, a large number of redshift bins is desirable for cosmic shear studies, in spite of the fact that, without the effects of intrinsic galaxy alignment, constraints on cosmological parameters are not appreciably improved once $N_z \gtrsim 5$. These results underline once more the need for both precise and detailed redshift information to control systematics in cosmic shear.

We emphasise that, using the full set of new power spectra, a maximisation of the information content in the weight functions is not necessary. In particular, this means that nulling as such does not rely on the Fisher matrix formalism and the determination of optimal weight functions, nor do the credible regions that result from applying the nulling. If only the first-order power spectra are employed, parameter constraints do depend on the optimisation of weight functions. However, the first-order results agree well for the three considered approaches, so that the change of the likelihood contours due to the use of these different methods is expected to be only marginal.

The moderate change in q-values indicates that this method is in principle suited to inferring cosmological parameters with fair precision. It is currently the only truly secure means of safely eliminating GI – and in addition, by construction, II – correlations since no assumptions are made about the still uncertain models of these systematic effects. An improvement in the performance of nulling could be achieved by taking advantage of the intrinsic ellipticity correlations not being only restricted to galaxy pairs which are close in redshift, but also close on the sky, thereby allowing for keeping part of the signal from correlations of adjacent redshift bins.

As soon as reliable data exists for modelling the intrinsic alignment of galaxies, an intermediate approach between strict nulling and the full reliance on the GI power spectrum could be developed. Since the tidal forces acting on a galaxy are caused by the surrounding matter-density distribution, correlations between the galaxy number density and intrinsic ellipticity can be used to determine the tidal field and, consequently, the expectation value of the orientation of the intrinsic ellipticity, see Sect. 5.3 for details. This additional information, appropriately incorporated into the nulling technique, may improve parameter constraints, while keeping the influence of model uncertainties at a low level.

Moreover we investigated the performance of the nulling technique in presence of realistic photometric redshift information and errors. We considered both the information loss due to nulling and the amount of residual bias due to GI correlations. Several modifications and improvements to the original nulling technique were suggested, which we summarise by providing a recipe on how to apply nulling to a cosmic shear tomography data set.

(1) Decide on which variant of nulling is best suited for the data set. If the data has precise information about the redshift distributions, and if these distributions have a small scatter and negligible outlier fraction, then variant (C), which takes into account this information, should be chosen. Otherwise variant (B) is preferable, if combined with a Gaussian downweighting of combinations of adjacent photometric redshift bins. This weighting scheme is necessary since overlapping redshift distributions can cause a swap of foreground and background galaxies, which produces a GI signal that cannot be controlled by means of nulling. Both variants perform considerably better than the original referencing suggested by Joachimi & Schneider (2008).

(2) Calculate the nulling weights, depending on the variant chosen. This work defines these weights such that nulling can be interpreted as an orthonormal transformation of the cosmic shear data vector. Since the weights are composed of comoving distances, one has to assume a cosmology to compute them. An incorrect choice of parameters affects the GI removal and could in principle cause an even stronger bias on parameter estimates. We showed that any reasonable choice of cosmological parameters will produce equally suited nulling weights – one could even start with the resulting, largely biased parameters of the analysis of the original data set. Iteratively using the parameter estimates as input for a renewed nulling analysis renders the final results independent of any initial assumptions.

(3) Compute nulled cosmic shear measures from the nulling weights and the tomography measures available. As nulling does not depend on angular scales, any measure such as the shear correlation functions or the aperture mass dispersion is suited. The number and size of photometric redshift bins should be chosen such that the overlap of the corresponding redshift distributions is kept at a minimum. Although nulling reduces the GI signal also for a division into 5 bins, we found that $N_z \geq 10$ is required to achieve good performance. Auto-correlations should be excluded from the analysis because of the potential contamination by an II signal. Applying the Gaussian weighting scheme will also reduce the II contamination in shear measures of adjacent photometric redshift bins.

Performing a likelihood analysis with the nulled data should then yield parameter constraints that have a low residual bias due to intrinsic alignment contributions. However, we outlined that nulling inevitably reduces the information content in the data, even if spectroscopic redshifts were available. Note that, even for very accurate redshifts the determination of distance in terms of redshift would still be limited by redshift space distortions, i.e. the peculiar velocities of the observed galaxies, which therefore provide an upper limit to the number of usable redshift bins.

We demonstrated that lensing information, integrated over wide redshift ranges, is eliminated together with the GI term, which can be traced back to the distinct, but still similar dependence on redshift of the lensing and GI signal. In terms of our figure of merit r_F we found that of the order 50 % of the statistical power is lost. The loss affects those cosmological parameters most which rely on the redshift dependence of the lensing signal, in particular w_0 and w_a. The Dark Energy Task Force Figure of Merit (Albrecht et al. 2006) decreases by roughly an order of magnitude.

In this study we have not exploited any feature of intrinsic alignments apart from its dependence on redshift. However, observations suggest that the strongest intrinsic alignment signal stems from luminous galaxies (Mandelbaum et al. 2006; Hirata et al. 2007). Photometric redshift estimates for these bright galaxies usually have a much smaller scatter (Ilbert et al. 2009), so that nulling may work better on this important subset. Thus, our conclusions on the performance of the nulling technique should be conservative.

Given excellent redshift information, nulling variant (C) reduces the bias, averaged over all parameters considered as defined in (6.82), by at least a factor of 100. To achieve this

goal, stringent conditions like $\sigma_{\rm ph} \lesssim 0.03$, a negligible fraction of catastrophic outliers, and an uncertainty in the median redshift $\sigma_{z_{\rm med}} \lesssim 0.001$ hold. Even future space-based surveys will fulfil these requirements only for a brighter subsample of galaxies (which are expected to have the strongest intrinsic alignment signal though), but still this nulling version could serve as a valuable consistency check. To suppress the GI signal by a factor of about 20, the conditions are moderately released, in particular on $\sigma_{\rm ph}$, in case the Gaussian weighting is used. Moreover, we determined optimal nulling redshifts, demonstrating that for accurate redshift information variant (C) is close to the best configuration possible in this geometric approach.

Throughout the considered parameter plane, spanned by $f_{\rm cat} \leq 0.1$ (corresponding to a true outlier fraction of $\leq 6\,\%$) and $\sigma_{\rm ph} \leq 0.1$, the nulling version based on variant (B) was capable of reducing the average bias by at least a factor of 10. Consequently, the requirements on photometric redshift parameters are low in this case. Merely a number $N_z \geq 10$ of photometric redshift bins, for which the width of the underlying redshift distributions should be known, is demanded, which is readily achieved by the majority of future cosmic shear surveys. Although we showed that the functional behaviour of the residual bias is similar for all considered models, the values of the residual bias depend on the actual form of the GI signal. Since all models considered in this work produce severe parameter biases, we have further reason to believe that the numbers for the performance of the nulling technique given above should be understood as conservative.

We have neglected the contamination by the II signal in all our considerations, arguing that the nulling could be preceded by an appropriate II removal technique. While for disjoint photometric redshift bins the II signal does not appear in the transformed data at all, it was demonstrated that, for realistic situations, ignoring the II term may cause a significant contamination of a subset of the nulled power spectra. On the other hand, this restriction of the II signal to certain nulled power spectra only could also allow for a removal of II after nulling. In any case, the ultimate goal is a combined geometrical treatment of all intrinsic alignment contributions, which is subject to forthcoming work.

Although we sampled only a fraction of the huge parameter space spanned by the various photometric redshift parameters, GI models, and nulling variants, it should be possible to draw a wide range of conclusions from this work. For instance, a relevant question is how a cosmic shear data set should be binned in order to remove intrinsic alignment and keep a maximum of information. The bin boundaries should be chosen such that the overlap of the corresponding redshift distributions is minimal, as long as the distributions do not become too asymmetric. Re-inspecting Fig. 6.15, the number of bins should be as big as the photometric redshift scatter allows, i.e. the width of the bins should not become smaller than about $\sigma_{\rm ph}(1+z)$ since otherwise no more information is added. As our results show, the photometric redshift scatter does not necessarily limit the level to which the GI signal can be eliminated, but then it places strong bounds on the remaining power to constrain cosmological parameters in the nulled data set, see Figs. 6.22 and 6.23.

We emphasise that, in spite of defining GI signals to quantify the bias removal, the nulling technique itself does not rely on any information about intrinsic alignment except for the well-known redshift dependence of the GI term. In principle, nulling is also applicable to data sets in which the GI contribution dominates over lensing. Provided a sufficient suppression, it would be possible to recover the cosmic shear signal by nulling the data. Besides, nulling is not restricted to cosmic shear at the two-point level.

Concerning three-point statistics, gravitational shear-intrinsic ellipticity cross terms, GII and GGI, may constitute an even more serious contamination (Semboloni et al. 2008). The geometric principle of nulling can be applied to tomography bispectra and related real-space measures in a straightforward manner (Shi et al. 2010). The performance as regards both the

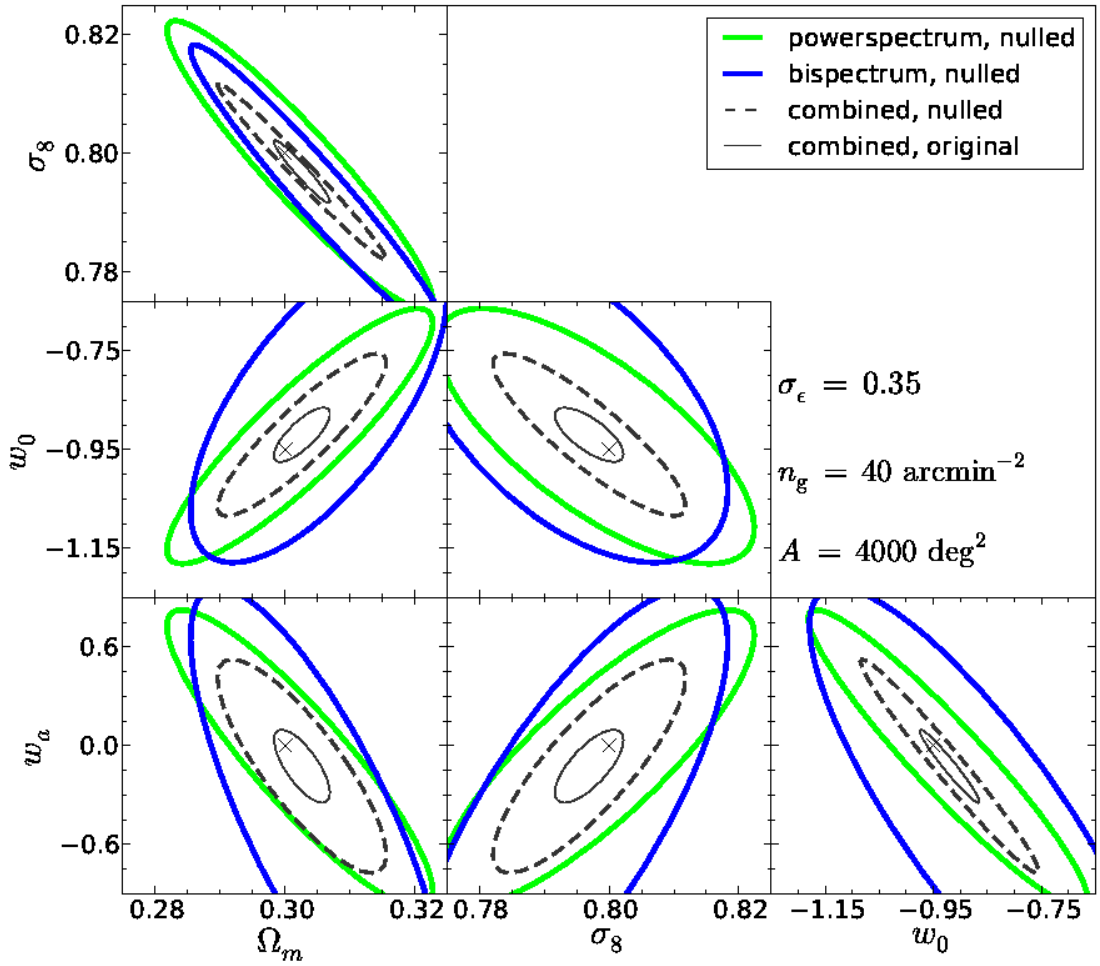

Figure 6.26: Performance of nulling for combined two- and three-point statistics. Shown are the marginalised $1\,\sigma$ constraints after nulling, obtained by a Fisher matrix analysis using two-point statistics only (green contours), three-point statistics only (blue contours), and the combination thereof (black dashed contours). For reference the constraints from the combined statistics before nulling are also shown as black solid lines, centred on the 'best-fit' parameter values determined from the nulled measures. A DES-like survey with survey parameters as indicated in the figure and a toy power-law intrinsic alignment model was used. Note that the covariances were assumed to follow Gaussian statistics, so that there is no cross-correlation between two- and three-point statistics. The fiducial parameter values are marked by a cross in each panel, implying that nulling reduces the intrinsic alignment contamination such that the true values are located even within the $1\,\sigma$ regions of the original data set (from Shi et al. 2010).

intrinsic alignment bias reduction and the information loss is similar to the two-point level, as can be seen in Fig. 6.26. There are indications that the increase in statistical errors due to nulling is slightly less severe for tomography bispectra than power spectra because more redshift combinations can be kept; compare the reduction of bin combinations from order N_z^3 to N_z^2 for bispectra, and N_z^2 to N_z for power spectra.

Due to the significant information loss of nulling, this technique is most probably not desirable as the standard GI removal tool for ambitious future surveys, so that the need for both an improved understanding of intrinsic alignments and high-performance removal techniques that take knowledge about the GI models into account persists. Still, with its very low level of input assumptions, nulling serves as a valuable cross-check for these model-dependent techniques yet

to be developed and as such can contribute to the credibility of cosmic shear as a powerful and robust cosmological probe. In Chap. 8 we will propose an alternative method that is capable of mitigating the loss of information by incorporating additional information via correlations of the galaxy distribution.

Chapter 7

Intrinsic alignment boosting

Geometrical transformations of second-order cosmic shear measures can not only be used to eliminate gravitational shear-intrinsic ellipticity (GI henceforth) correlations from the measured signal, but also to extract intrinsic alignments, as will be detailed in this chapter. This is desirable because firstly, intrinsic alignments constitute an interesting cosmological signal worth investigating but usually subdominant to the lensing contribution. It sheds light onto the interaction between galaxies, their haloes, and the large-scale structure, and thereby provides insight into the formation and evolution of galaxies. Secondly, the GI signal strongly depends on the redshift, colour, and luminosity distribution of the galaxy sample (see Chap. 5), so that the blind extrapolation in one or more of these quantities, in order to describe the actual sample in which cosmic shear is observed, is fraught with uncertainty. Therefore, observational data are highly requested which can put limits on the possible range of intrinsic alignment signals directly for the relevant galaxy samples.

GI correlations have been subject to several observational studies (Mandelbaum et al. 2006; Hirata et al. 2007; Mandelbaum et al. 2009), but none of these observations were direct measurements of intrinsic alignments for the galaxy populations and redshifts which are most interesting for future cosmic shear surveys because the galaxy samples selected for these surveys are obviously selected such that the shear signal clearly dominates the correlations of galaxy ellipticities. The GI signal is usually inferred from cross-correlations between galaxy number densities and ellipticities in samples with spectroscopic redshifts, see Chap. 5. This approach requires the assumption of a simple form of the galaxy bias, usually a constant bias for each galaxy sample, which is of limited accuracy and inapplicable on small scales. If one wishes to analyse larger galaxy samples for which only photometric redshift information is available, further signals such as galaxy-galaxy lensing contribute and need to be modelled carefully, see Sect. 5.3.2, but also Bernstein (2009), Joachimi & Bridle (2009), and Sect. 8 for an overview on the types of signals contributing to correlations between galaxy number density and ellipticity.

In the following we will develop a model-independent technique to extract the GI signal from a cosmic shear data set, thereby allowing for direct measurements of GI correlations on the most relevant galaxy samples. This 'GI boosting' approach can be regarded as complementary to the nulling technique dealt with in the foregoing chapter, both in its purpose and in its implementation. Analogous to the nulling technique, we will construct linear combinations of second-order cosmic shear measures, making only use of the well-known characteristic redshift dependence of the GI and lensing (GG hereafter) signals.

In Sect. 7.1 we present the principle of GI boosting and derive general conditions, which are used in Sect. 7.2 to explicitly construct weight functions for the boosting transformation of the cosmic shear signal. Section 7.3 details the modelling which we apply in Sect. 7.4 to assess the performance of the boosting technique. In Sect. 7.5 we construct a method to remove GI

correlations based on the GI boosting technique and investigate the relation between the new approach and the standard nulling method of Joachimi & Schneider (2008, 2009), before we summarise and conclude on our findings about the boosting technique in Sect. 7.6.

7.1 Principle of boosting

7.1.1 Basic relations

We will base our technique on a tomographic cosmic shear data set, i.e. correlations of galaxy ellipticities which are in addition split into subsamples according to the available redshift information. Analogous to the nulling technique the method outlined in the following does not affect angular scales, so that we can without loss of generality use tomographic power spectra as our two-point cosmic shear measures. For an overview on the basics of cosmic shear see e.g. Schneider (2006) whose notation we mostly follow.

The convergence power spectrum of cosmic shear, correlating two galaxy samples i and j, reads

$$P_{\mathrm{GG}}^{(ij)}(\ell) = \frac{9H_0^4\Omega_{\mathrm{m}}^2}{4c^4}\int_0^{\chi_{\mathrm{hor}}} \mathrm{d}\chi\; g^{(i)}(\chi)\, g^{(j)}(\chi)\; \{1+z(\chi)\}^2\, P_\delta\left(\frac{\ell}{\chi},\chi\right)\;, \tag{7.1}$$

where P_δ is the three-dimensional matter power spectrum, ℓ the angular frequency, and z the redshift. The integration runs over all comoving distances χ up to the comoving distance horizon χ_{hor}. Note that this equation is equivalent to (3.34). We have made use of the lensing efficiency (3.25) and the probability distribution of comoving distances $p^{(i)}(\chi)$ for galaxy sample i. Note that we assume a spatially flat universe throughout. The tomographic power spectrum of shear-ellipticity correlations (for details see e.g. Hirata & Seljak 2004, and Sect. 5.1.1),

$$P_{\mathrm{GI}}^{(ij)}(\ell) = \frac{3H_0^2\Omega_{\mathrm{m}}}{2c^2}\int_0^{\chi_{\mathrm{hor}}} \mathrm{d}\chi\; \left\{p^{(i)}(\chi)\; g^{(j)}(\chi) + g^{(i)}(\chi)\; p^{(j)}(\chi)\right\}\; \frac{1+z(\chi)}{\chi}\; P_{\delta\mathrm{I}}\left(\frac{\ell}{\chi},\chi\right)\;, \tag{7.2}$$

where $P_{\delta\mathrm{I}}$ denotes the three-dimensional cross-power spectrum between matter density contrast and intrinsic shear field. As a reminder, the intrinsic shear is defined as the correlated part of the intrinsic ellipticity of a galaxy image (e.g. Hirata & Seljak 2004). One can then proceed to construct an intrinsic shear field by assigning to every point in space the intrinsic shear a galaxy would have at this position. For instance, if the intrinsic alignment model of Catelan et al. (2001) held true, this could simply be done by computing the quadrupole of the local gravitational field, see Sect. 5.1 for details. Only one of the terms in (7.2) is non-vanishing unless the probability distributions overlap. As intrinsic ellipticity correlations (II hereafter) can readily be removed before applying a treatment of the GI signal, we neglect them in this work, so that the total power spectrum, i.e. the actual observable in our study, is given by

$$P_{\mathrm{obs}}^{(ij)}(\ell) = P_{\mathrm{GG}}^{(ij)}(\ell) + P_{\mathrm{GI}}^{(ij)}(\ell)\;. \tag{7.3}$$

A discussion on how II correlations affect the boosting technique is provided in Sect. 7.6.

To derive expressions for the transformed signals, we assume that precise redshift, or equivalently distance, information is available, so that the survey can be sliced into thin tomographic bins. One can then approximate $p^{(i)}(\chi) \approx \delta_{\mathrm{D}}(\chi-\chi_i)$, where χ_i is an appropriately chosen comoving distance in bin i. Here δ_{D} denotes the Dirac delta distribution. The lensing efficiency (3.25) can then be written in the form

$$g^{(j)}(\chi_i) \to g(\chi_j,\chi_i) \equiv \begin{cases} 1-\frac{\chi_i}{\chi_j} & \text{if } \chi_i < \chi_j \\ 0 & \text{else}\;. \end{cases} \tag{7.4}$$

With these approximations the power spectra (7.1) and (7.2) turn into

$$P_{\rm GG}(\chi_i,\chi_j,\ell) = \frac{9H_0^4\Omega_{\rm m}^2}{4c^4}\int_0^{\min(\chi_i,\chi_j)}{\rm d}\chi\; g(\chi_i,\chi)\;g(\chi_j,\chi)\left\{1+z(\chi)\right\}^2 P_\delta\left(\frac{\ell}{\chi},\chi\right)\;; \tag{7.5}$$

$$\begin{aligned} P_{\rm GI}(\chi_i,\chi_j,\ell) &= \frac{3H_0^2\Omega_{\rm m}}{2c^2}\left\{g(\chi_j,\chi_i)\,\frac{1+z(\chi_i)}{\chi_i}\,P_{\delta{\rm I}}\left(\frac{\ell}{\chi_i},\chi_i\right)\right. \\ &\qquad \left. + g(\chi_i,\chi_j)\,\frac{1+z(\chi_j)}{\chi_j}\,P_{\delta{\rm I}}\left(\frac{\ell}{\chi_j},\chi_j\right)\right\}, \end{aligned} \tag{7.6}$$

where the dependence of the power spectra on the comoving distances of the two galaxy samples involved was made explicit. Note that if $\chi_i<\chi_j$, only the first term contributes to $P_{\rm GI}(\chi_i,\chi_j,\ell)$ whereas for $\chi_i>\chi_j$ only the second term is non-zero.

7.1.2 Signal transformation

We seek to find linear combinations of tomographic second-order cosmic shear measures such that in the resulting measures the cosmic shear signal is largely suppressed with respect to the GI signal. The starting point is analogous to the nulling technique as outlined by Joachimi & Schneider (2008). We define transformed power spectra as

$$\Pi_{\rm obs}^{(i)}(\ell)\equiv\int_{\chi_{\rm min}}^{\chi_{\rm hor}}{\rm d}\chi\;B^{(i)}(\chi)\;P_{\rm obs}(\chi_i,\chi,\ell)\;, \tag{7.7}$$

where $B^{(i)}(\chi)$ is a weight function yet to be determined. Note that (7.7) holds also for both the GG and GI contributions individually as the observed power spectrum is a linear superposition of the two, see (7.3). We will investigate two different choices for the lower boundary of the integration $\chi_{\rm min}$ in this work. To construct the boosting technique, we choose the maximum range $\chi_{\rm min}=0$ whereas in Sect. 7.5.1 we will set $\chi_{\rm min}=\chi_i$ instead.

Inserting (7.6) into the definition (7.7), one finds that

$$\begin{aligned} \Pi_{\rm GI}^{(i)}(\ell) &= \frac{3H_0^2\Omega_{\rm m}}{2c^2}\int_0^{\chi_{\rm hor}}{\rm d}\chi\;B^{(i)}(\chi)\left\{g(\chi,\chi_i)\,\frac{1+z(\chi_i)}{\chi_i}\,P_{\delta{\rm I}}\left(\frac{\ell}{\chi_i},\chi_i\right)\right. \\ &\qquad \left. + g(\chi_i,\chi)\,\frac{1+z(\chi)}{\chi}\,P_{\delta{\rm I}}\left(\frac{\ell}{\chi},\chi\right)\right\} \\ &= \frac{3H_0^2\Omega_{\rm m}}{2c^2}\,G^{(i)}(\chi_i)\,\frac{1+z(\chi_i)}{\chi_i}\,P_{\delta{\rm I}}\left(\frac{\ell}{\chi_i},\chi_i\right)+\int_0^{\chi_i}{\rm d}\chi\;B^{(i)}(\chi)\,P_{\rm GI}(\chi,\chi_i,\ell)\;, \end{aligned} \tag{7.8}$$

where we defined the function

$$G^{(i)}(\chi)\equiv\int_\chi^{\chi_{\rm hor}}{\rm d}\bar\chi\;B^{(i)}(\bar\chi)\left(1-\frac{\chi}{\bar\chi}\right)\;. \tag{7.9}$$

Note that the integration absorbed into $G^{(i)}(\chi)$ starts at χ, which corresponds to a lower boundary of χ_i in the integral over the first term in (7.8). This can be done because $g(\chi,\chi_i)$ vanishes for $\chi<\chi_i$, see (7.4). Likewise, $\chi<\chi_i$ holds for the second term in (7.8) to be non-zero, so that the upper boundary of this integration is changed to χ_i. In addition (7.6), with only its first term non-vanishing, can be inserted. The first term in the final expression of (7.8) is generated by GI correlations originating from matter at the distance χ_i. Note that in the approximation of thin redshift slices which we are working in this term is just a rescaled version

of (7.6). Due to our choice $\chi_{\min} = 0$, the transformed GI signal receives a further contribution from shear-ellipticity correlations generated at $\chi < \chi_i$, collected into the second term of (7.8).

Transforming the lensing signal analogously by plugging (7.5) into (7.7), one arrives at

$$\begin{aligned}\Pi^{(i)}_{\mathrm{GG}}(\ell) &= \frac{9H_0^4\Omega_{\mathrm{m}}^2}{4c^4}\int_0^{\chi_i}\mathrm{d}\chi\int_\chi^{\chi_{\mathrm{hor}}}\mathrm{d}\bar{\chi}\;B^{(i)}(\bar{\chi})\left(1-\frac{\chi}{\bar{\chi}}\right)\left(1-\frac{\chi}{\chi_i}\right)\{1+z(\chi)\}^2\,P_\delta\left(\frac{\ell}{\chi},\chi\right) \qquad (7.10)\\ &= \frac{9H_0^4\Omega_{\mathrm{m}}^2}{4c^4}\int_0^{\chi_i}\mathrm{d}\chi\left(1-\frac{\chi}{\chi_i}\right)G^{(i)}(\chi)\,\{1+z(\chi)\}^2\,P_\delta\left(\frac{\ell}{\chi},\chi\right)\;.\end{aligned}$$

Again, (7.9) was used to produce the final expression. The conditions $\chi < \chi_i$ and $\bar{\chi} > \chi$, imposed by (7.4), result in the upper boundary of the first and the lower boundary of the second integral, respectively. The transformed cosmic shear signal thus depends on the form of $G^{(i)}(\chi)$ in the interval between 0 and χ_i. To suppress the GG signal, $G^{(i)}(\chi)$ should be chosen such that the integral in the final expression of (7.10) is close to zero while at the same time $G^{(i)}(\chi_i)$ has to be comparatively large to boost the GI contribution, see (7.8).

In reality line-of-sight information will not be available in terms of comoving distances, but rather in terms of the observable redshift. Furthermore the galaxy redshift distributions will have a finite width and also overlap due to scatter, in particular if only photometric redshift information is available as will be the case for the vast majority of galaxies in future cosmic shear surveys. To arrive at a practical prescription for constructing the transformed power spectra, we therefore change the integration variable in (7.7) to redshift and subsequently discretise the integral, yielding

$$\Pi^{(i)}_{\mathrm{obs}}(\ell) \approx \sum_{j=j_{\min}}^{N_z} B^{(i)}(\chi(z_j))\;P^{(ij)}_{\mathrm{obs}}(\ell)\;\chi'(z_j)\;\Delta z_j\;, \qquad (7.11)$$

where $\chi'(z)$ is the derivative of comoving distance with respect to redshift, and Δz_j is the width of redshift bin j. In total N_z galaxy samples are available for study. Here and in the following we identify $z_i \equiv z(\chi_i)$. The condition $\chi_{\min} = 0$ used for the boosting technique translates into $j_{\min} = 1$. Note that (7.11) is of the same form as (6.63) which defines the transformed power spectrum for nulling.

7.1.3 Solving for the weight function

In the foregoing section we saw that the GI signal can be boosted, and the GG signal at the same time suppressed, by formulating conditions on the function $G^{(i)}(\chi)$. Via its defining equation (7.9) it is related to the weight function $B^{(i)}(\chi)$ that enters the transformation (7.7). Hence, to obtain a boosting transformation, one has to solve (7.9) for $B^{(i)}(\chi)$ for a given function $G^{(i)}(\chi)$.

We begin by noting that (7.9) is a Volterra integral equation of the first kind. It has a kernel that is linear in the integration variable, so that one can readily solve for the weight function by differentiating twice, resulting in

$$B^{(i)}(\chi) = \chi\,\frac{\mathrm{d}^2G^{(i)}(\chi)}{\mathrm{d}\chi^2}\;. \qquad (7.12)$$

We have found the solution of the inhomogeneous Volterra equation (7.9) under the premises that $G^{(i)}(\chi)$ is twice continuously differentiable, $G^{(i)}(\chi_{\mathrm{hor}}) = 0$ and $\mathrm{d}G^{(i)}/\mathrm{d}\chi|_{\chi_{\mathrm{hor}}} = 0$. If one specifies $G^{(i)}(\chi)$ down to a value $\chi_{\min}$, then $B^{(i)}(\chi)$ is well-defined in the range $[\chi_{\min}, \chi_{\mathrm{hor}}]$ by (7.9). Note that if we dropped the assumption of a flat universe, (7.9) would still be solvable, but analytical progress would be hampered.

To find the solution of the homogeneous equation, obtained from (7.9) by setting $G^{(i)}(\chi) \equiv 0$, we define

$$b(\chi) \equiv \frac{B^{(i)}(\chi)}{\chi}\, H(\chi_{\rm hor} - \chi)\;; \quad f(\chi) \equiv \chi H(\chi)\;, \tag{7.13}$$

where $H(\chi)$ denotes the Heaviside step function. Then (7.9) can be re-written as a cross-correlation,

$$G^{(i)}(\chi) = \int_{-\infty}^{\infty} \mathrm{d}\bar{\chi}\; b(\bar{\chi})\; f(\bar{\chi} - \chi) = \{b * f\}\,(\chi)\;. \tag{7.14}$$

The introduction of the Heaviside functions in (7.13) was used to extend the integration to zero and infinity. If we denote Fourier transforms by a tilde, the convolution theorem yields $\tilde{G}^{(i)} = \tilde{b}\,\tilde{f}$. From this equation is it readily seen that for $G^{(i)}(\chi) \equiv 0$ it follows $B^{(i)}(\chi) \equiv 0$ in the interval $[\chi, \chi_{\rm hor}]$. Hence the solution of the homogeneous Volterra equation consists only of the trivial one and (7.12) constitutes the full, unique solution of (7.9). In summary, for a given $G^{(i)}(\chi)$ that fulfils the conditions imposed by (7.8) and (7.10), we can calculate the corresponding weight function via (7.12) and use the result to construct transformed power spectra (7.7).

Note the analogy between (7.9) and the definition of the lensing efficiency (3.25). This can be interpreted as $G^{(i)}(\chi)$ being a modified lensing efficiency, which is then used to construct an alternative lensing convergence with desired properties chosen via $G^{(i)}(\chi)$. For details on this view see the motivation of the nulling technique given in Joachimi & Schneider (2008).

7.2 Construction of weights

Apart from the requirements formulated in Sect. 7.1.2 to ensure a boosting of the GI signal with respect to cosmic shear, the choice of $G^{(i)}(\chi)$ is arbitrary. In the following we choose a specific parametrisation of $G^{(i)}(\chi)$ which is convenient and intuitive, but not necessarily optimal. Its base is a Gaussian that is peaked at χ_i, which fosters a strong contribution of GI correlations via the first term of (7.8). Some additional flexibility is needed at $\chi < \chi_i$, allowing for sign changes of $G^{(i)}(\chi)$ to downweight the lensing signal. We define

$$G^{(i)}(\chi) \equiv \mathcal{N}\; \exp\left\{-\frac{(\chi - \chi_{\rm m})^2}{\sigma^2}\right\} (\chi - b)\;, \tag{7.15}$$

where $\mathcal{N}$, σ, b, and $\chi_{\rm m}$ are free parameters. All four parameters depend on the choice of galaxy sample i, but we do not specify this dependence for reasons of better readability. The first derivative of $G^{(i)}(\chi)$ with respect to comoving distance reads

$$\frac{\partial G^{(i)}}{\partial \chi}(\chi) = \mathcal{N}\; \exp\left\{-\frac{(\chi - \chi_{\rm m})^2}{\sigma^2}\right\} \left[1 - 2\,(\chi - b)\;\frac{\chi - \chi_{\rm m}}{\sigma^2}\right]\;. \tag{7.16}$$

From this result and by means of (7.12) one readily obtains the weight function

$$B^{(i)}(\chi) = \mathcal{N}\,\frac{2\chi}{\sigma^2}\; \exp\left\{-\frac{(\chi - \chi_{\rm m})^2}{\sigma^2}\right\} \left[2\,(\chi - b)\;\frac{(\chi - \chi_{\rm m})^2}{\sigma^2} - 3\chi + 2\chi_{\rm m} + b\right]\;. \tag{7.17}$$

The normalisation of $G^{(i)}(\chi)$ is related to the one of $B^{(i)}(\chi)$ via (7.9), but is otherwise irrelevant to the problem. We fix $\mathcal{N}$ by requiring

$$\int_{\chi_{\rm min}}^{\chi_{\rm hor}} \mathrm{d}\chi\; \left\{B^{(i)}(\chi)\right\}^2 \approx \sum_{j=j_{\rm min}}^{N_z} \left\{B^{(i)}(\chi(z_j))\right\}^2 \chi'(z_j)\;\Delta z_j = 1\;. \tag{7.18}$$

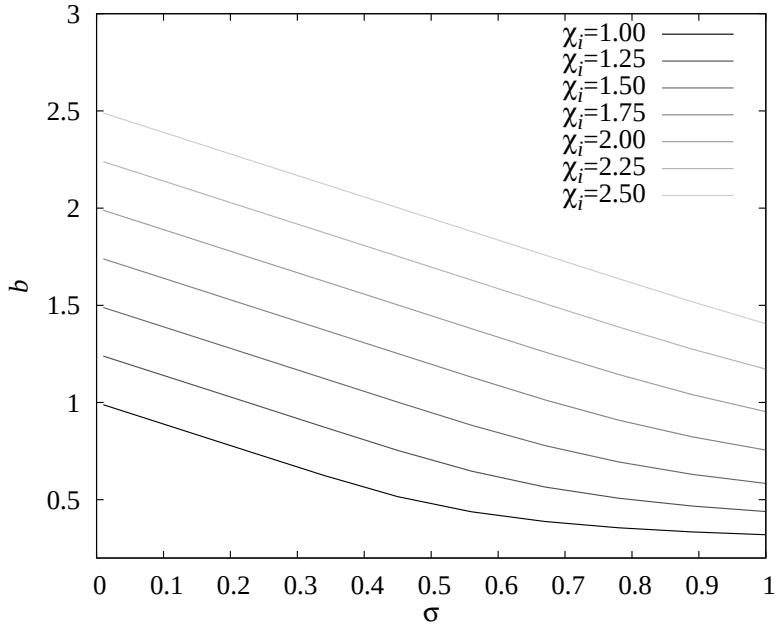

Figure 7.1: Parameter b as a function of σ, i.e. the width of the Gaussian in $G^{(i)}(\chi)$. Plotted are the results for different peak positions χ_i as indicated in the legend. For most of the considered range, (7.22) provides an excellent approximation. Only for small χ_i in combination with large σ do the curves start to level off. Note that b, σ, and χ_i are given in abstract units of 1 in this plot.

Note that since $\mathcal{N}$ depends on the other free parameters, e.g. σ, a consistent normalisation is actually important when studying $G^{(i)}(\chi)$ as a function of these parameters, as we will do in Sects. 7.4 and 7.5.

Two of the remaining three free parameters of (7.15) will now be used to boost (7.8) and suppress (7.10). First, we demand that (7.15) is peaked at χ_i, i.e. $\partial G^{(i)}/\partial\chi\,|_{\chi_i} = 0$. Using (7.16), we obtain

$$\chi_\mathrm{m} = \chi_i - \frac{\sigma^2}{2}\,(\chi_i - b)^{-1} \ . \tag{7.19}$$

The second condition should render the integral in (7.10) close to zero. While it is possible to numerically determine for instance the parameter b such that this condition is fulfilled for every angular frequency individually, we prefer to proceed in a way that does not rely on a model of cosmic shear power spectra at all. We note that if the width of the Gaussian σ is relatively small, the support of the integral in (7.10) has a small range and hence P_δ can be well approximated as only varying slowly. The dependence on redshift should be roughly $P_\delta(k,z) \propto D(z)^2 \propto (1+z)^{-2}$, where $D(z)$ is the linear growth factor for which we assumed $D(z) \propto (1+z)^{-1}$ as holds true in the matter-dominated epoch. This redshift dependence then cancels the $(1+z)^2$ term in (7.10), so that we consider the condition

$$\int_0^{\chi_i} \mathrm{d}\chi \left(1 - \frac{\chi}{\chi_i}\right) G^{(i)}(\chi) = 0 \ . \tag{7.20}$$

Inserting (7.15) together with (7.19), and making the further definitions $y \equiv (\chi - \chi_i)/\sigma$ and $m \equiv (\chi_i - b)/\sigma$, we transform this integral as follows,

$$\begin{aligned} & \int_0^{\chi_i} \mathrm{d}\chi \left(1 - \frac{\chi}{\chi_i}\right) G^{(i)}(\chi) \qquad (7.21) \\ \approx\ & -\frac{\mathcal{N}\,\sigma^3}{\chi_i} \int_{-\infty}^{0} \mathrm{d}y\ y\,(y+m)\ \exp\left\{-\left(y + \frac{1}{2m}\right)^2\right\} \\ =\ & -\frac{\mathcal{N}\,\sigma^3}{8m^2\chi_i}\left\{2m\,(1-2m^2)\ \mathrm{e}^{-1/(4m)^2} + \sqrt{\pi}\left[1 + \mathrm{Erf}\left(\frac{1}{2m}\right)\right]\right\} \ . \end{aligned}$$

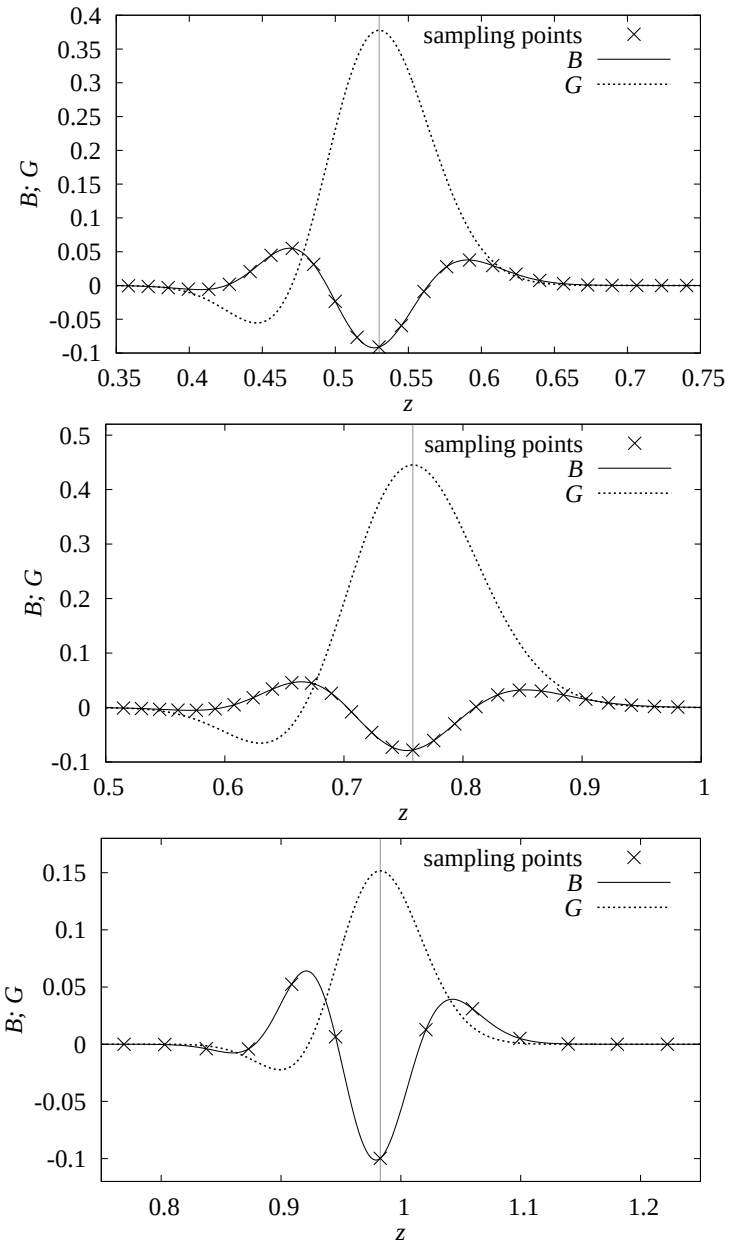

Figure 7.2: Functions $G^{(i)}(\chi(z))$ and $B^{(i)}(\chi(z))$ for different z_i, as indicated by the vertical grey lines, and redshift binnings, using the width σ_z determined via (7.24) in each case. In addition the sampling points corresponding to the median redshifts of the bins are shown for $B^{(i)}(\chi(z))$. The normalisation has been chosen according to (7.18). See Table 7.1 for an overview on the survey models referred to in the following. *Top panel*: For the spectroscopic survey S and $z_i = 0.53$; $\sigma_z = 0.055$. *Centre panel*: For the survey with good photometric redshifts P1 and $z_i = 0.76$; $\sigma_z = 0.085$. *Bottom panel*: For the survey with standard photometric redshifts P2 and $z_i = 0.98$; $\sigma_z = 0.055$.

The approximation in the first equality refers to replacing the lower boundary of the integral $-\chi_i/\sigma$ by $-\infty$, which is valid if $\chi_i/\sigma \gg 1$, i.e. if $G^{(i)}(\chi)$ is compact ($\sigma \ll 1$) and peaks not too close to zero ($\chi_i \gg 0$). The root of the term in curly brackets can be found numerically, resulting in

$$b(\sigma, \chi_i) = \chi_i - m\,\sigma \quad \text{with} \quad m \approx 1.10687\,. \tag{7.22}$$

We have solved (7.20) directly and plot the resulting b in Fig. 7.1. We find excellent agreement with the approximate solution (7.22) as long as the assumption discussed above is fulfilled. Significant deviations from the linear behaviour of b as a function of σ are only found for $\chi_i/\sigma \lesssim 2$. For reasons of simplicity we will restrict ourselves to cases where the approximation (7.22) holds. This means in particular that we will not consider signals at very small redshifts, where χ_i is necessarily small. In practice we use the condition $G^{(i)}(\chi(z_{\min})) \approx 0$ with $z_{\min}$ the minimum redshift used in the survey as a simple cross-check to ensure that this approximation is sufficiently accurate.

The conditions specified above are strictly fulfilled only for continuous χ or z. However, we

will in practice use the discretised transformation (7.11) and thus have to make sure that GI boosting and GG suppression work accurately also in this case. Via a procedure outlined in the following, we optimise the remaining free parameter σ to guarantee a good sampling of $G^{(i)}(\chi)$ by the discrete set of weights $B^{(i)}(\chi(z_j))$ with $j = 1, .., N_z$, thereby fulfilling $\partial G^{(i)}/\partial\chi\,|_{\chi_i} = 0$ and (7.20) to good accuracy.

As the sampling points of (7.11) we choose the medians of the redshift distributions of the galaxy samples employed. It is expected that the optimal choice of the parameter σ, denoted by $\sigma_{\rm opt}$ in the following, will depend intricately on the positions of these sampling points and hence on the redshift distributions of the different galaxy samples in the cosmic shear data, in particular if the number of sampling points is small, e.g. if the distributions have a large scatter. Since the binning is done in terms of redshift, it is convenient to work with the quantity $\sigma_z \equiv \{\chi'(z_i)\}^{-1}\,\sigma$ instead of σ. We will also give our choices of $\sigma_{\rm opt}$ in terms of σ_z throughout.

We introduce the discrete version of the function $G^{(i)}(\chi)$,

$$G'^{(i)}(\chi(z_k)) \equiv \sum_{j=k}^{N_z} B^{(i)}(\chi(z_j))\ \left(1 - \frac{\chi(z_k)}{\chi(z_j)}\right)\ \chi'(z_j)\,\Delta z_j\ . \tag{7.23}$$

Then we consider the root mean square deviation of all function values $G'^{(i)}(\chi(z_k))$ used,

$$\zeta(\sigma_z) \equiv \sqrt{\frac{1}{N_z}\sum_{k=1}^{N_z}\left|G'^{(i)}(\chi(z_k),\sigma_z) - G^{(i)}(\chi(z_k),\sigma_z)\right|^2}\ , \tag{7.24}$$

as a criterion for how well $G^{(i)}(\chi)$ is sampled by the discrete set of function values $B^{(i)}(\chi(z_j))$ entering (7.23). In the equation above we have made the dependence on σ_z explicit in the arguments. We emphasise that the determination of σ_z via the diagnostic ζ is optimal only in the sense that it allows us to find a representative sampling of $G^{(i)}(\chi)$ such that $\partial G^{(i)}/\partial\chi\,|_{\chi_i} = 0$ and (7.20) hold to good accuracy. It will in general not yield an optimal amplification of the GI signal over the lensing signal, which depends on the explicit form of both signals.

In Fig. 7.2 we have plotted a selection of typical results for $G^{(i)}(\chi)$ and the corresponding weight function $B^{(i)}(\chi)$. As common features of $G^{(i)}(\chi)$ a distinct peak at z_i and a negative dip at $z < z_i$, the latter necessary to fulfil (7.20), are discernible. The weight function $B^{(i)}(\chi)$ has three pronounced extrema of which the central one is located at z_i, plus a shallow fourth one at low redshift.

Note that the method laid out here is completely independent of any assumptions about the angular dependence of both the underlying lensing and intrinsic alignment signals. To determine the weights entering (7.11), we only make use of the well-known redshift dependence of the GI and GG signals, plus the redshift binning of the survey to be analysed. We note that the weights $B^{(i)}(\chi(z_j))$ depend on $\Omega_{\rm m}$ and possibly further cosmological parameters via the distance-redshift relation. However, the same applies to the weights used in the standard nulling technique, and from the investigation by Joachimi & Schneider (2009) we conclude that this dependence is weak and that the assumption of an incorrect cosmology when constructing the weights is uncritical.

7.3 Modelling the boosting transformation

To assess the performance of the boosting technique, we need to model both the cosmic shear and the intrinsic alignment signals. To this end, we assume a spatially flat ΛCDM universe with matter density parameter $\Omega_{\rm m} = 0.25$ and Hubble parameter $h = 0.7$. The matter power

identifier	redshifts	bin width	$\sigma_{\rm ph}$	$n_{\rm g}\,[\mathrm{arcmin}^{-2}]$
S	spectroscopic	$0.01(1+z)$	0	1
P1	good photo-z	$0.01(1+z)$	0.03	10
P2	standard photo-z	$0.02(1+z)$	0.05	40

Table 7.1: Overview on the different survey models used.

spectrum has a primordial slope $n_{\rm s} = 1.0$ and normalisation $\sigma_8 = 0.8$. The transfer function is computed according to Eisenstein & Hu (1998), using a baryon density parameter of $\Omega_{\rm b} = 0.05$, while the non-linear evolution of the power spectrum is determined by the fit formula of Smith et al. (2003). We use the linear alignment model (Catelan et al. 2001; Hirata & Seljak 2004) which is given by (5.12) to calculate the matter density-intrinsic power spectrum.

A cosmic shear survey is modelled by assuming an overall galaxy redshift distribution according to (4.47) with $z_0 = 0.64$ and $\beta = 1.5$, corresponding to a median redshift of $z_{\rm med} = 0.9$. We cut the distribution below $z_{\rm min} = 0.2$ and above $z_{\rm max} = 2.0$ and normalise (4.47) in that interval. The overall redshift distribution is then sliced into disjoint bins. In those cases where a scatter due to photometric redshift estimates is present, we assume the distribution of photometric redshifts for a given true redshift to be a Gaussian, centred on the true redshift and with a width of $\sigma_{\rm ph}(1+z)$. The distributions of true redshifts $p^{(i)}(z)$ for each photometric redshift bin i are then computed according to a scheme detailed in Joachimi & Schneider (2009).

We consider three different survey models which are summarised in Table 7.1. All of these surveys are assumed to cover the whole extragalactic sky, i.e. $A_{\rm survey} = 20,000\,\mathrm{deg}^2$. To calculate shape noise, we use an intrinsic ellipticity dispersion of $\sigma_\epsilon = 0.35$ throughout.

First, we construct a 'spectroscopic' survey S for which redshift bins are assigned with width $0.01(1+z)$ and no scatter. In this case the signals are calculated to excellent approximation not over the complete bin width, but at the median redshifts of each bin. Whilst it is in principle possible to achieve such a dense redshift binning and small scatter with photometric redshifts (see e.g. Ilbert et al. 2009), it is more likely that future large-area spectroscopic surveys fit into this category. In any case the number of available galaxies will be small. Taking the wide spectroscopic survey of the Euclid mission as reference (Laureijs et al. 2009), we set the overall galaxy number density to $n_{\rm g} = 1\,\mathrm{arcmin}^{-2}$.

Second, we create a survey that features high-quality photometric redshift data, termed P1. We choose the same binning scheme as for the first case, but introduce a photometric redshift scatter of $\sigma_{\rm ph} = 0.03$, corresponding to the target value of the Euclid imaging survey. To be conservative, we assume that this photometric redshift quality is only attainable for a subset of galaxies and set $n_{\rm g} = 10\,\mathrm{arcmin}^{-2}$. Finally, we make use of a setup P2 with redshift binning in steps of $0.02(1+z)$ and scatter $\sigma_{\rm ph} = 0.05$, which can be regarded as representative of a standard future imaging survey designed to do cosmic shear. Again referring to Laureijs et al. (2009), we adopt $n_{\rm g} = 40\,\mathrm{arcmin}^{-2}$ in this case.

The photometric redshift bin widths are chosen such that the associated distributions of neighbouring bins can still be well distinguished. We have found that narrowing the bin widths substantially below about $1/3\,\sigma_{\rm ph}$ deteriorates the performance of the boosting technique. It should be noted that spectroscopic redshifts as well as photometric redshifts of high quality are usually limited to a brighter subset of galaxies, therefore altering the overall redshift distribution of galaxies. However, to facilitate the comparison between the three survey models under scrutiny, we keep $p_{\rm tot}(z)$ as specified above.

With the three-dimensional GG and GI power spectra and the redshift distributions $p^{(i)}(\chi) = p^{(i)}(z)/\chi'(z)$ at hand, one can calculate the tomographic power spectra according to (7.1) and (7.2). For the further analysis we divide the angular frequency range into $N_\ell = 200$ logarithmic bins between $\ell = 10$ and $\ell = 20000$.

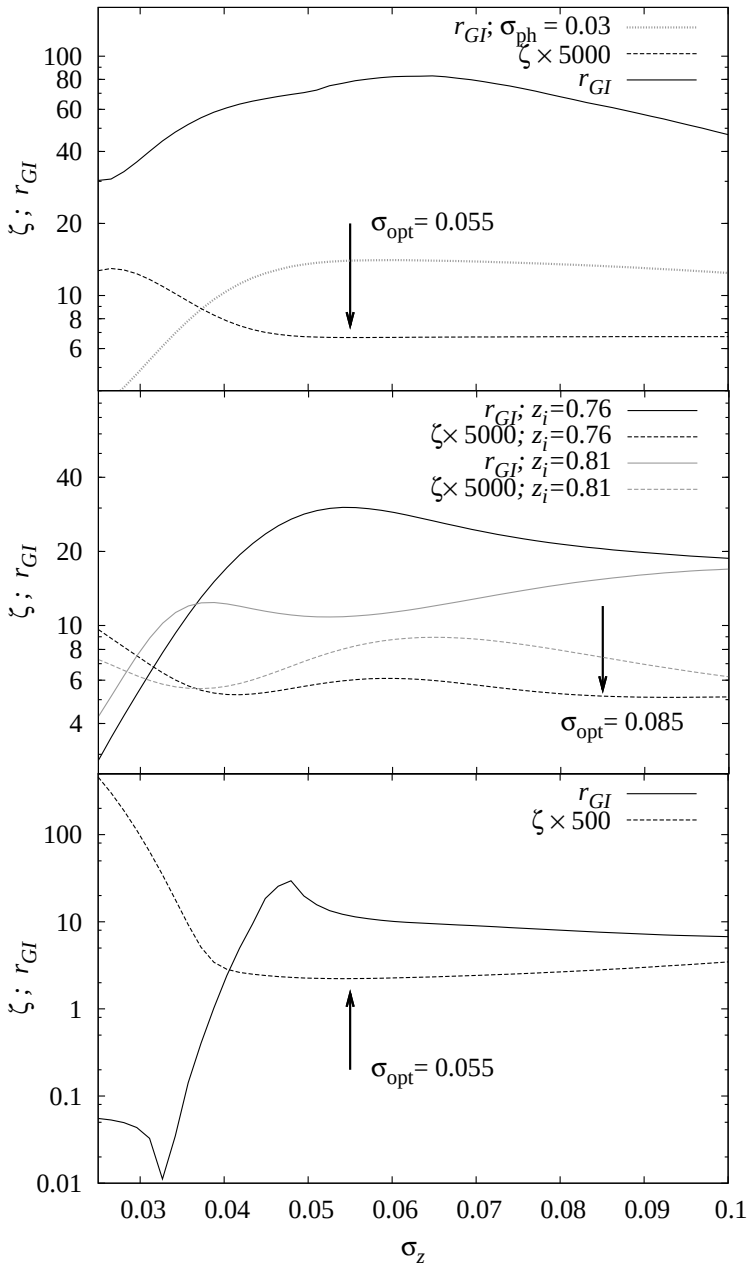

Figure 7.3: Diagnostic ζ, see (7.24), and GI over GG ratio $r_{\rm GI}$, see (7.25), as a function of σ_z. Shown is $r_{\rm GI}$ as solid curve and ζ as dashed curve. Since the normalisation of ζ is arbitrary, we have rescaled ζ for easier inspection. In each panel the choice of $\sigma_{\rm opt}$ is marked with an arrow. Note that this choice was made without resorting to $r_{\rm GI}$ which is not measurable from real data. *Upper panel*: For the spectroscopic survey S at $z_i = 0.53$. In addition we have plotted $r_{\rm GI}$ for the case $\sigma_{\rm ph} = 0.03$. Note that ζ remains the same in both cases. *Centre panel*: For the survey P1 ($\sigma_{\rm ph} = 0.03$) at $z_i = 0.76$. Note the dip of ζ at $\sigma_z \sim 0.04$ which is caused by the weight function $B^{(i)}(\chi)$ being sampled close to its extrema. We have added the curves for $z_i = 0.81$ as grey lines, where $B^{(i)}(\chi)$ is sampled almost exactly at its extrema, leading to a local maximum in $r_{\rm GI}$ at $\sigma_z = 0.038$, traced well by a corresponding minimum in ζ. *Lower panel*: For the survey P2 ($\sigma_{\rm ph} = 0.05$) at $z_i = 0.98$.

7.4 Performance of intrinsic alignment boosting

7.4.1 Boosted signals

To condense the performance of the boosting technique into a single number, we define the median with respect to angular frequency of the ratio of GI over GG signal,

$$r_{\rm GI} \equiv \text{median}\left\{\left|\frac{X_{\rm GI}(\ell_i)}{X_{\rm GG}(\ell_i)}\right|\right\}_{i=1,..,N_\ell}\,, \tag{7.25}$$

where X can be replaced by any tomography power spectrum $P^{(ij)}(\ell)$ or the transformed power spectra $\Pi^{(i)}(\ell)$. Note that this quantity is not available from a real survey because we are not able to separate the GG and GI signals, but only extract their sum from the data. We have chosen the median in (7.25) since we find that the mean is not a robust measure for two reasons.

Table 7.2: Summary of $r_{\rm GI}$ for different values of z_i and the three survey models. Given are values of $r_{\rm GI}$ of the original power spectra for the auto-correlation ('auto'), the cross-correlation between bin i and the background bin with index $(i + N_z)/2$ ('mid'), and the cross-correlation between bin i and the most distant bin with index N_z at $z \lesssim 2$ ('far'). The tag 'boost' stands for the transformed signals. In addition $\sigma_{\rm opt}$ is listed for every considered case.

survey	z_i	$\sigma_{\rm opt}$	$r_{\rm GI}$(auto)	$r_{\rm GI}$(mid)	$r_{\rm GI}$(far)	$r_{\rm GI}$(boost)
S	0.53	0.055	0.04	0.47	0.56	78.26
	0.76	0.085	0.02	0.25	0.32	415.79
	0.96	0.095	0.01	0.16	0.22	62.10
P1	0.53	0.055	0.12	0.46	0.54	13.56
	0.76	0.085	0.06	0.24	0.31	20.49
	0.96	0.095	0.04	0.16	0.21	25.86
P2	0.52	0.045	0.19	0.47	0.55	5.97
	0.74	0.050	0.10	0.26	0.32	7.75
	0.98	0.055	0.06	0.15	0.20	11.63

First, if the GG signal is suppressed by several orders of magnitude, numerical noise stemming from the computation of the power spectra can become important, leading to unphysical dips in the residual power spectrum. Second, the residual GG signal may have sign changes close to which $r_{\rm GI}$ becomes very large, thus dominating the mean. Both effects would mimic a stronger boosting than is actually observed.

In Fig. 7.3 we show $r_{\rm GI}$, together with the diagnostic ζ as defined in (7.24), as a function of σ_z for one z_i per survey model. Overall we find that small values of ζ indeed indicate regimes of σ_z in which the GI signal is well boosted. It is important to note that the absolute value of ζ is meaningless due to the arbitrariness in the overall amplitude of $G^{(i)}(\chi)$. When $G^{(i)}(\chi)$ is no longer well sampled for small σ_z, ζ features a clear increase. Sometimes secondary minima in ζ can be observed, see the centre panel of Fig. 7.3, which is caused by the sampling points being consecutively placed at the extrema of $B^{(i)}(\chi)$. Thereby, although only sparsely sampled, the discrete form (7.23) captures the main characteristics of $B^{(i)}(\chi)$ and hence can well represent $G^{(i)}(\chi)$, yielding a small value of ζ.

In the top panel of Fig. 7.3 $r_{\rm GI}$ for both surveys S and P1 is given. Since the binning scheme is identical for both surveys, ζ is the same. This example demonstrates that $r_{\rm GI}$ depends considerably on the details of the actual signals, in this case a change from $\sigma_{\rm ph} = 0$ to $\sigma_{\rm ph} = 0.03$. The diagnostic ζ does not trace the boosting of the actual signals and can consequently not be exploited to find the maximum $r_{\rm GI}$. However, for both surveys ζ identifies the regime of small σ_z in which the boosting performs worse and which thus should be avoided. In the case $\sigma_{\rm ph} = 0.05$ the sampling in redshift becomes fully insufficient for small σ_z. Accordingly, ζ rises sharply, and the GG signal starts to dominate again.

The optimal width of $G^{(i)}(\chi)$ can be chosen freely in the interval where ζ is stable and small. If there is a clear minimum, we place $\sigma_{\rm opt}$ there; otherwise we set $\sigma_{\rm opt}$ to a small value in the interval where ζ is small, see e.g. the centre panel of Fig. 7.3. This assignment of $\sigma_{\rm opt}$ may not be unique, but it is uncritical. Note that the weight functions corresponding to the optimum cases of the examples shown in Fig. 7.3 are those depicted in Fig. 7.2. We emphasise again that $r_{\rm GI}$ cannot be measured from real data, and accordingly we do not use this quantity to determine $\sigma_{\rm opt}$.

One might expect that the denser the sampling points of $G^{(i)}(\chi)$ and $B^{(i)}(\chi)$ can be placed, the more sharply peaked weight functions can be well represented by the discrete sampling, and

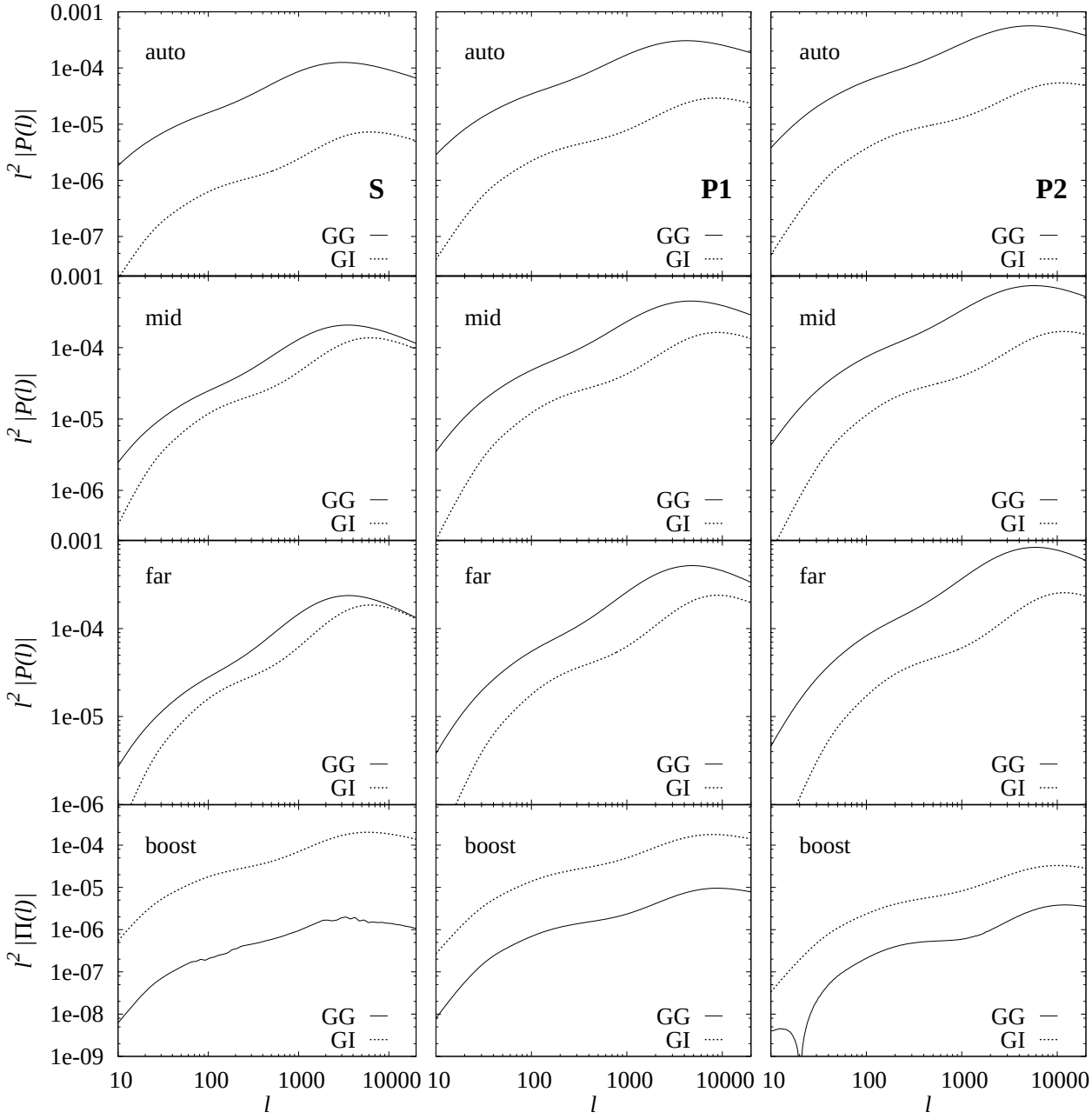

Figure 7.4: *Left column*: Example set of lensing (GG) and intrinsic alignment (GI) tomography power spectra for the spectroscopic survey S and $z_i = 0.53$. The GG signal is shown as solid line, the GI signal as dotted line. The upper three panels show power spectra for different background bins j, i.e. auto-correlations ($j = i$, 'auto'), cross-correlations with a bin at intermediate redshift ($j = (i + N_z)/2$, 'mid'), and cross-correlations with the most distant bin ($j = N_z$, 'far'). In the bottom panel the transformed GG and GI signals are plotted ('boost'). Note that absolute values of the power spectra are shown throughout. *Centre column*: Same as above, but for the survey P1 ($\sigma_{\rm ph} = 0.03$) and $z_i = 0.76$. *Right column*: Same as above, but for the survey P2 ($\sigma_{\rm ph} = 0.05$) and $z_i = 0.98$.

thus smaller values of σ_z could be chosen. However, consider the case $\sigma_{\rm ph} = 0.05$ and $z_i = 0.98$ which is shown in the bottom panels of both Figs. 7.2 and 7.3. Although $\sigma_{\rm opt}$ is small compared to e.g. our findings for survey P1, the sparse sampling obviously captures the main features of the weight function and hence results in a small ζ.

In Fig. 7.4 we have plotted example sets of original and transformed power spectra, the latter each computed for the optimal values of σ_z. Table 7.2 lists the corresponding values of $r_{\rm GI}$ and $\sigma_{\rm opt}$ for the three survey models and three redshifts z_i each, including the cases depicted in the figure. The GI over GG ratio $r_{\rm GI}$ for the original power spectra ranges from about 1 % to 50 %. For a correlation between galaxy samples i and j with $z_i < z_j$, $r_{\rm GI}$ increases strongly with the separation between z_j and z_i. Both the GI and GG signals show this behaviour due to (3.25). Since the cosmic shear signal is generated by all the matter between $z = 0$ and z_i with the highest efficiency at $z_i/2$, whereas the intrinsic alignment contribution stems form matter around z_i, the GI signal has the stronger dependence on redshift, causing the increase in $r_{\rm GI}$. For the non-linear version of the linear alignment model this effect can lead to a GI signal whose absolute value can come close to or even surpass the cosmic shear signal for large $z_j - z_i$, see e.g. also Bridle & King (2007).

It is evident from Table 7.2 that the better resolved the redshift information is, the more can the GI signal be boosted. For quasi-spectroscopic data, the residual GG contribution is well below the 2 %-level and hence expected to be negligible. In the case $z_i = 0.76$ we find by chance a near-total cancellation of the cosmic shear signal. For good photo-z data with $\sigma_{\rm ph} = 0.03$ the method is also effective, yielding $r_{\rm GI}$ well in excess of 10, so that any biases due to the residual GG contribution are likely to remain below the statistical errors of intrinsic alignment parameters. For survey P2 it is still possible to produce a dominating GI signal, with $r_{\rm GI}$ between approximately 6 and 12, but a GG residual exceeding 10 % may require further treatment to avoid a significant bias.

7.4.2 Parameter constraints

The boosted GI signal has the potential use of directly constraining models of intrinsic alignments, provided that the statistical power is sufficiently high and that systematics due to residual GG contributions are under control. We set up a simple intrinsic alignment model and use the Fisher matrix formalism (Tegmark et al. 1997) to forecast expected errors and biases on its free parameters. We define

$$P_{\delta{\rm I}}^{\rm model}\,(k,z) = A\;P_{\delta{\rm I}}\,(k,z)\;\left(\frac{1+z}{1+z_{\rm piv}}\right)^{\gamma}\;, \tag{7.26}$$

where $P_{\delta{\rm I}}$ is given by the linear alignment model (5.12). The free parameters are A and γ, i.e. we allow for an arbitrary signal amplitude and an additional redshift dependence. The fiducial model is (5.12), so $A = 1$ and $\gamma = 0$, and we set $z_{\rm piv} = 0.3$. The same parametrisation was e.g. used by Mandelbaum et al. (2009).

Assuming that the signal covariance is itself not parameter-dependent, which holds to very good accuracy for the large survey we consider (Eifler et al. 2009), the Fisher matrix reads

$$F_{\mu\nu} = \sum_{\ell}\sum_{i,j}\frac{\partial\Pi_{\rm GI}^{(i)}(\ell)}{\partial p_\mu}\;{\rm Cov}^{-1}\left(\Pi_{\rm GI}^{(i)}(\ell),\Pi_{\rm GI}^{(j)}(\ell)\right)\;\frac{\partial\Pi_{\rm GI}^{(j)}(\ell)}{\partial p_\nu}\;, \tag{7.27}$$

for a parameter vector $\boldsymbol{p} = \{A,\gamma\}$. Using (7.11), one can readily relate the covariance of the transformed power spectra to that of the original power spectra,

$$\begin{aligned}{\rm Cov}\left(\Pi_{\rm GI}^{(i)}(\ell),\Pi_{\rm GI}^{(j)}(\ell)\right) \;&=\; \sum_{k,l=0}^{N_z} B^{(i)}(\chi(z_k))\;B^{(j)}(\chi(z_l)) \\ &\quad\times{\rm Cov}\left(P_{\rm GI}^{(ik)}(\ell),\;P_{\rm GI}^{(jl)}(\ell)\right)\;\chi'(z_k)\;\chi'(z_l)\;\Delta z_k\;\Delta z_l\;.\end{aligned} \tag{7.28}$$

Table 7.3: Statistical errors $\sigma_{\rm stat}$ and residual biases $b_{\rm sys}$ for the different survey models used. The left column shows marginalised $1\,\sigma$ errors on the amplitude A of the GI signal and on γ, quantifying an additional redshift dependence. In the right column results obtained for only varying A are listed.

survey	parameter	γ varied		γ fixed	
		$\sigma_{\rm stat}$	$b_{\rm sys}$	$\sigma_{\rm stat}$	$b_{\rm sys}$
S	A	2.885	-0.009	0.827	-0.004
	γ	7.356	0.012		
P1	A	0.712	-0.081	0.172	-0.046
	γ	1.776	0.090		
P2	A	0.697	-0.181	0.272	-0.171
	γ	2.017	0.031		

The power spectrum covariance in turn is given by (see Joachimi et al. 2008, and references therein)

$$\mathrm{Cov}\left(P_{\rm GI}^{(ij)}(\ell),\,P_{\rm GI}^{(kl)}(\ell)\right) \;=\; \frac{2\pi}{A_{\rm survey}\ell\Delta\ell}\,\left(\bar{P}_{\rm GI}^{(ik)}(\ell)\bar{P}_{\rm GI}^{(jl)}(\ell)+\bar{P}_{\rm GI}^{(il)}(\ell)\bar{P}_{\rm GI}^{(jk)}(\ell)\right) \qquad (7.29)$$

$$\text{with}\quad \bar{P}_{\rm GI}^{(ij)}=P_{\rm GI}^{(ij)}+\delta_{ij}\frac{\sigma_\epsilon^2}{2\bar{n}^{(i)}}\,,$$

where $\Delta\ell$ is the width of the angular frequency bins and $\bar{n}^{(i)}$ the number of galaxies belonging to sample i. Equation (7.29) holds under the assumptions of Gaussian density fluctuations, a uniform sampling of galaxies, and a simple survey geometry where the scales considered are much smaller than the extent of the survey.

The bias formalism (e.g. Huterer et al. 2006; Amara & Réfrégier 2008; Joachimi & Schneider 2009) allows us to compute the bias on the intrinsic alignment parameters due to the residual GG signal in the transformed power spectra via

$$b_{\rm sys}(p_\mu)=\sum_\nu\left(F^{-1}\right)_{\mu\nu}\sum_\ell\sum_{i,j}\Pi_{\rm GG}^{(i)}(\ell)\;\mathrm{Cov}^{-1}\left(\Pi_{\rm GI}^{(i)}(\ell),\Pi_{\rm GI}^{(j)}(\ell)\right)\;\frac{\partial\Pi_{\rm GI}^{(j)}(\ell)}{\partial p_\nu}\,. \qquad (7.30)$$

Note that, contrary to works focusing on cosmic shear analyses and treating intrinsic alignments as the systematic, we use the GI contribution in (7.27) and insert the transformed GG signal into (7.30) such that it plays the role of a systematic. We make the assumption that, given $z_i < z_j$, the galaxy redshift distribution $p^{(i)}(z)$ entering (7.2) is sufficiently compact that we can take the term $[(1+z_i)/(1+z_{\rm piv})]^\gamma$ out of the comoving distance integration. Then both parameter derivatives needed for (7.27) and (7.30) are readily calculated analytically.

Since at this point we merely seek to demonstrate the concept of boosting, we limit the set of $\Pi^{(i)}(\ell)$ entering (7.27) to those bins i which fulfil $z_i \in [0.4; 1.4]$. This ensures that the approximation (7.21) can be used throughout and that it is straightforward to assign $\sigma_{\rm opt}$. Besides, we avoid issues at high z_i with non-zero $G^{(i)}(\chi(z_{\rm max}))$, which could possibly violate the basic condition $G^{(i)}(\chi_{\rm hor})=0$, see Sect. 7.1.3. We determine $\sigma_{\rm opt}$ by computing the diagnostic ζ given by (7.24) for all z_i and devising simple, piecewise linear formulae which yield a $\sigma_{\rm opt}$ in the regime of small ζ for every z_i. For survey P2 (standard photo-z) we use $\sigma_{\rm opt}=0.02\,z_i+0.035$. The two other surveys have the same redshift binning and hence identical ζ. We set $\sigma_{\rm opt}=0.13\,z_i-0.014$ for $z_i\le 1$ and $\sigma_{\rm opt}=-0.057\,z_i+0.173$ for $z_i>1$ in these cases.

Now we are in the position to compute the boosting transformation for power spectra with $z_i \in [0.4; 1.4]$. By means of (7.27) and (7.30) we obtain statistical and systematic error estimates

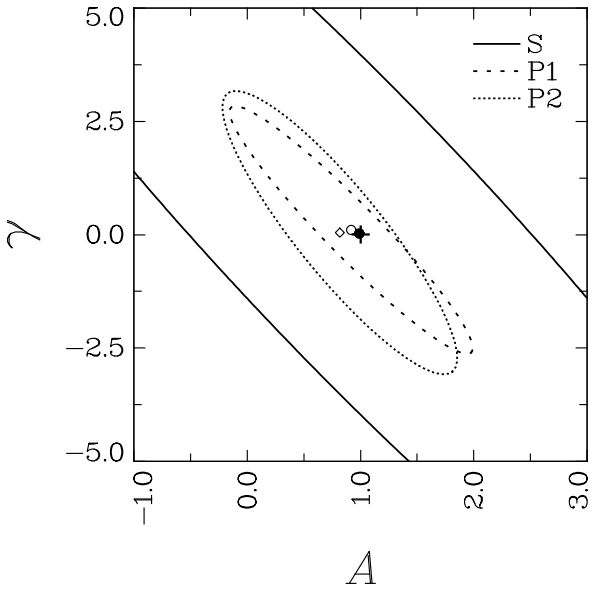

Figure 7.5: Constraints on the free parameters of the GI model. Shown are the $1\,\sigma$ confidence contours for the different survey models used. The solid ellipse with its centre indicated by a filled circle corresponds to the spectroscopic survey S, the long-dashed ellipse and open circle to survey P1, and the short-dashed ellipse with diamond to survey P2. Note that the centres of the contours are offset due to the bias by the residual GG signal. The cross marks the fiducial values of $A = 1$ and $\gamma = 0$.

for both intrinsic alignment parameters for all three survey models, summarised in Table 7.3. When varying both parameters, we find marginalised $1\,\sigma$ errors of approximately 2.9 for A and 7.4 for γ in case of survey S. The two surveys with photometric redshift data produce errors around 0.7 on A and of the order 2 for γ. As expected, the bias due to the remaining cosmic shear signal is negligible in the case of the spectroscopic survey S and clearly subdominant in the case of survey P1. Even for the standard photo-z setup P2 biases remain within the statistical $1\,\sigma$ errors, reaching up to $|b_{\rm sys}/\sigma_{\rm stat}| \approx 1/4$ for A.

In Fig. 7.5 the corresponding $1\,\sigma$ confidence contours in the parameter plane $A-\gamma$ are given for the three survey models. As we have chosen a pivot redshift which is below the minimum redshift of GI signals that enter the analysis, a positive γ leads to an increase in the amplitude of the GI model, which can be compensated by a smaller A. Hence, A and γ are anti-correlated, leading to the degeneracy as indicated by the error ellipses. The bias acts mainly on A because a residual GG signal will to zeroth order affect the overall amplitude of the signal. In all three cases the $1\,\sigma$ contours comfortably enclose the fiducial, true parameter values.

Due to the low number density of galaxies, survey S is clearly not competitive in constraints on intrinsic alignment properties. The results from the two other surveys are not capable of pinning down the intrinsic alignment model with high precision, but their bounds are comparable to current constraints by analyses of spectroscopic measurements of galaxy number density-shape cross-correlations (Mandelbaum et al. 2009). Note that the weights used for this analysis may still have considerable room for optimisation, and that we only used a limited range of z_i.

Table 7.3 also lists the resulting errors when only A is varied and no additional redshift dependence of the intrinsic alignment model is assumed. Constraints improve significantly when lifting the degeneracy with γ such that A is determined to better than ± 0.3 ($1\,\sigma$) for the survey models with photometric redshifts while constraints by survey S are about three times weaker. The bias is still negligible for the spectroscopic survey model, and clearly subdominant for survey P1 ($\sigma_{\rm ph} = 0.03$). The residual systematic affects the error budget noticeably for the analysis of survey P2 ($\sigma_{\rm ph} = 0.05$) with $|b_{\rm sys}/\sigma_{\rm stat}| \approx 63\,\%$. Again, optimisation of the boosting procedure may further decrease the residual cosmic shear signal well below the statistical $1\,\sigma$-limit.

The errors for the good photo-z and in particular the spectroscopic survey models are

dominated by shape noise due to the low number density of galaxies in each tomographic galaxy sample, apart from only the smallest angular frequencies. As can be seen from (7.29), the errors scale inversely with the total number of galaxies in the survey if cosmic variance is negligible. Thus, if in the future larger number densities of galaxies with highly accurate photometric redshifts than assumed in this work are attainable, the constraints on GI correlations via the boosting technique will improve accordingly. If we re-run the analysis for survey S with the galaxy number density assumed for survey P1, i.e. a factor of 10 higher, all the statistical errors indeed decrease by almost an order of magnitude.

7.5 Relation to the nulling technique

If one is able to extract the GI signal from cosmic shear data, the question arises whether this could also be used to remove the GI contamination from the data and thus make cosmic shear analyses robust against biases due to intrinsic alignments. Intuitively, one can simply subtract an isolated GI signal from the original measures, and indeed we are going to devise such a procedure. Afterwards we will again propose a simple, parametric weight function to construct a boosting method, whose outcome will then be used to eliminate the GI signal. These steps are not optimised and merely serve to demonstrate the link between GI boosting and its removal, as well as to compare the performance of the latter to the standard nulling technique of Joachimi & Schneider (2008, 2009) in a simple scenario.

7.5.1 Signal transformation

As an alternative to the procedure in Sect. 7.1.2, one can choose the lower integration boundary in (7.7) as $\chi_{\min} = \chi_i$. As is evident from (7.8), in this case only the first term of the transformed GI signal remains. Hence, it is likely that $\chi_{\min} = 0$ produces a larger amplitude of the modified GI power spectrum, but $\chi_{\min} = \chi_i$ results in a cleaner signal insofar as it contains only contributions from intrinsic alignments generated by matter at distance χ_i. Consequently, we are going to use the latter choice of $\chi_{\min}$ for constructing a method to remove the GI signal at χ_i. The transformed lensing signal for $\chi_{\min} = \chi_i$ is derived in analogy to (7.10) and reads

$$\Pi_{\mathrm{GG}}^{(i)}(\ell) \;=\; \frac{9H_0^4\Omega_{\mathrm{m}}^2}{4c^4}\int_0^{\chi_i}\mathrm{d}\chi\int_{\chi_i}^{\chi_{\mathrm{hor}}}\mathrm{d}\bar{\chi}\;B^{(i)}(\bar{\chi})\left(1-\frac{\chi}{\bar{\chi}}\right)\left(1-\frac{\chi}{\chi_i}\right)\{1+z(\chi)\}^2\,P_\delta\left(\frac{\ell}{\chi},\chi\right)\;. \quad (7.31)$$

Now suppose we are able to construct a boosting technique with a significant signal $\Pi_{\mathrm{GI}}^{(i)}(\ell)$ while $\Pi_{\mathrm{GG}}^{(i)}(\ell) \approx 0$. Noting again that the remaining first term in (7.8) is a rescaled version of the original GI signal (7.6), we define a further set of power spectra

$$Q_{\mathrm{obs}}^{(ij)}(\ell) \equiv P_{\mathrm{obs}}^{(ij)}(\ell) - f_{ij}\,\Pi_{\mathrm{obs}}^{(i)}(\ell) \qquad \text{with} \quad f_{ij} = \frac{g^{(j)}(\chi_i)}{G^{(i)}(\chi_i)}\;, \quad (7.32)$$

and likewise for the individual GG and GI signals. This definition holds for all $i < j$. The auto-correlations $Q^{(ii)}(\ell)$ would simply correspond to the original auto-correlation power spectra $P^{(ii)}(\ell)$. As we are still working in the approximation of very narrow redshift bins, auto-correlations are hardly affected by GI correlations at all. In practice, auto-correlations are likely to be excluded or specially treated anyway due to the presence of intrinsic ellipticity correlations, see the discussion in Sect. 7.6.

Assuming that the GI boosting works effectively, $\Pi_{\mathrm{GG}}^{(i)}(\ell) \approx 0$, so that one expects that $Q_{\mathrm{GG}}^{(ij)}(\ell) \approx P_{\mathrm{GG}}^{(ij)}(\ell)$, i.e. the transformed cosmic shear signal is close to the original GG term.

Switching to the notation of narrow redshift bins again, we find for the transformed GI signal

$$Q_{\rm GI}(\chi_i,\chi_j,\ell) = \frac{3H_0^2\Omega_{\rm m}}{2c^2}\,g(\chi_j,\chi_i)\frac{1+z(\chi_i)}{\chi_i}\,P_{\delta{\rm I}}\left(\frac{\ell}{\chi_i},\chi_i\right) - f_{ij}\,\frac{3H_0^2\Omega_{\rm m}}{2c^2}\,G^{(i)}(\chi_i)\,\frac{1+z(\chi_i)}{\chi_i}\,P_{\delta{\rm I}}\left(\frac{\ell}{\chi_i},\chi_i\right) = 0\;, \tag{7.33}$$

where we have inserted (7.6) and the first term of (7.8), and made use of the transition $g^{(j)}(\chi_i) \to g(\chi_j,\chi_i)$, see (7.4). As a consequence, $Q^{(ij)}_{\rm obs}(\ell) \approx P^{(ij)}_{\rm GG}(\ell) - f_{ij}\,\Pi^{(i)}_{\rm GG}(\ell) \approx P^{(ij)}_{\rm GG}(\ell)$. Hence, if we can devise an effective boosting technique using $\chi_{\rm min} = \chi_i$, we immediately have a means of GI removal at our disposal via (7.32).

Note that the standard nulling technique as presented in Joachimi & Schneider (2008) also makes use of the definition (7.7) with $\chi_{\rm min} = \chi_i$. The central condition in their approach is recovered in our formalism by requiring $G^{(i)}(\chi_i) = 0$, which eliminates the GI signal under the same assumption of narrow redshift bins, see (7.8). For practical purposes we also switch to the discretised form of the signal transformation (7.11), using now $j_{\rm min} = i$.

7.5.2 Construction of weights

We begin by developing again a boosting technique, now for the changed condition $\chi_{\rm min} = \chi_i$. Due to the associated change in the lower boundary of integration in (7.7), the condition to remove the GG signal is altered as well. Keeping the same approximations as used to derive (7.20), we now obtain from (7.31)

$$\int_0^{\chi_i}{\rm d}\chi\int_{\chi_i}^{\chi_{\rm hor}}{\rm d}\bar{\chi}\;B^{(i)}(\bar{\chi})\left(1-\frac{\chi}{\bar{\chi}}\right)\left(1-\frac{\chi}{\chi_i}\right) = \frac{\chi_i}{2}\left(\mathcal{M}_1 - \mathcal{M}_2\,\frac{\chi_i}{3}\right) = 0\;, \tag{7.34}$$

where we executed the integration over χ and defined

$$\mathcal{M}_\mu \equiv \int_{\chi_i}^{\chi_{\rm hor}}{\rm d}\chi\;B^{(i)}(\chi)\;\chi^{1-\mu}\;;\quad \mu = 1,2\;. \tag{7.35}$$

Inserting (7.12) into the foregoing definition and integrating by parts, one arrives at the useful relations

$$\mathcal{M}_1 = G^{(i)}(\chi_i) - \chi_i\,\frac{\partial G^{(i)}}{\partial\chi}(\chi_i)\;;\qquad \mathcal{M}_2 = -\frac{\partial G^{(i)}}{\partial\chi}(\chi_i)\;. \tag{7.36}$$

When these are plugged into (7.34), we obtain a condition which is the equivalent of (7.20), i.e. which ensures the suppression of the GG signal in the transformed power spectra (7.7),

$$\frac{\partial G^{(i)}}{\partial\chi}(\chi_i) = \frac{3}{2\,\chi_i}\,G^{(i)}(\chi_i)\;. \tag{7.37}$$

In contrast to (7.20), which is an integral condition on $G^{(i)}(\chi)$ and in its discrete form involves all sampling points between $z_{\rm min}$ and z_i, (7.37) is local and even contains a derivative of $G^{(i)}(\chi)$. Hence, we suspect that (7.37) is less robust against the inevitable discretisation of the weight function. As a cross-check for the accuracy of (7.34), and equivalently (7.37), we define the additional diagnostic

$$\eta \equiv \left|\mathcal{M}_1 - \mathcal{M}_2\,\frac{\chi_i}{3}\right| \approx \left|\sum_{j=i}^{N_z} B^{(i)}(\chi(z_j))\;\chi'(z_j)\;\Delta z_j\left(1-\frac{\chi(z_i)}{3\chi(z_j)}\right)\right|\;, \tag{7.38}$$

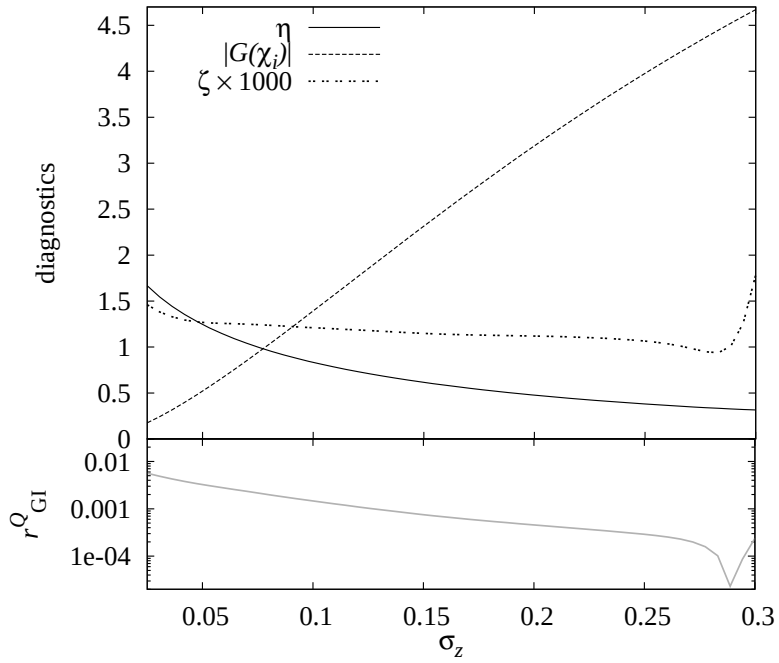

Figure 7.6: Determination of $\sigma_{\rm opt}$ for the spectroscopic survey S at $z_i = 0.53$. *Top panel*: Diagnostics ζ (dotted line), η (solid line), and $|G_Q^{(i)}(\chi_i)|$ (dashed line) as a function of σ_z. Larger σ_z yield the desired small values of η and larger $|G_Q^{(i)}(\chi_i)|$, in agreement with the minimum of ζ which is found at $\sigma_z \approx 0.28$. Note that we have rescaled ζ for convenience. *Bottom panel*: GI over GG ratio $r_{\rm GI}^Q$ as a function of σ_z. The diagnostics indeed hint at a regime of σ_z where $r_{\rm GI}^Q$ is smallest.

where the integrals (7.35) were transformed to redshift and discretised in analogy to (7.11).

Moreover, (7.37) hinders us to impose the condition $\partial G^{(i)}/\partial\chi|_{\chi_i} = 0$ again, which boosted the GI term, see (7.8). We define

$$G_Q^{(i)}(\chi) \equiv \mathcal{N}\ \exp\left\{-\frac{(\chi-\chi_i)^2}{\sigma^2}\right\}(\chi - b)\ , \tag{7.39}$$

which has one free parameter less than (7.15). To avoid any confusion with foregoing usage, we will add a sub- or superscript Q to indicate quantities which are used in this section for devising a nulling procedure. The condition (7.37) readily implies $b = \chi_i/3$. As long as $\sigma/\chi_i \ll 1$, (7.39) has an extremum in the vicinity of χ_i, located at

$$\chi_{\rm extr} = \frac{2}{3}\,\chi_i + \frac{1}{3}\,\chi_i\,\sqrt{1+\frac{9\sigma^2}{2\chi_i^2}}\ . \tag{7.40}$$

Therefore $G_Q^{(i)}(\chi)$ as defined in (7.39) should nonetheless boost the transformed GI signal fairly well. In complete analogy to the derivation in Sect. 7.2, one obtains the weight function

$$B_Q^{(i)}(\chi) = \mathcal{N}\,\frac{2\chi}{\sigma^2}\ \exp\left\{-\frac{(\chi-\chi_i)^2}{\sigma^2}\right\}\left[2\,(\chi-\frac{\chi_i}{3})\,\frac{(\chi-\chi_i)^2}{\sigma^2} - 3\chi + \frac{7}{3}\chi_i\right]\ . \tag{7.41}$$

The normalisation $\mathcal{N}$ is again given by (7.18). As before, this weight function still has one free parameter σ which will be used to optimise the representations of the continuous functions (7.39) and (7.41) by the discrete set of sampling points entering (7.7). The weights derived from (7.41) yield GI-boosted power spectra $\Pi_Q^{(k)}(\ell)$ via (7.7), which in turn produce GI-nulled measures via (7.32).

7.5.3 Nulled signals

Again we study a set of diagnostics as a function of σ_z to identify regimes of σ_z where the GI nulling performs well. In Fig. 7.6 we plot ζ as defined in (7.24), η which assesses how (7.37) is

affected by the discretisation, and $|G_Q^{(i)}(\chi_i)|$ as an indicator of the boosting of the GI signal in the $\Pi_Q^{(i)}(\ell)$[1], for the spectroscopic survey S at $z_i = 0.53$. Furthermore we show the GI over GG ratio $r_{\rm GI}^Q$, which is given by (7.25) when replacing X by the nulled power spectra (7.32). Note that small values of $r_{\rm GI}^Q$ are indicative of an effective removal of the GI signal.

One might expect that $|G_Q^{(i)}(\chi_i)|$ is largest for small σ_z because $G_Q^{(i)}(\chi)$ is sharply peaked with a large maximum value. However, this effect is counteracted by the normalisation of the weight function. Large values of σ_z cause $G_Q^{(i)}(\chi)$ to be smoother, i.e. to have smaller curvature. Due to (7.12) the amplitude of $B_Q^{(i)}(\chi)$ would thus decrease for fixed normalisation. Since we normalise $B_Q^{(i)}(\chi)$ according to (7.18) for every σ_z individually, large σ_z yield a higher normalisation relative to small σ_z, implying also larger values of $G_Q^{(i)}(\chi)$. Hence, one observes an increase in $|G_Q^{(i)}(\chi_i)|$ as a function of σ_z.

The diagnostic η has relatively large values for strongly peaked $G_Q^{(i)}(\chi)$ and decreases slowly for larger σ_z. A small change in the weight function $B_Q^{(i)}(\chi)$ due to the discretisation can induce significant changes in $G_Q^{(i)}(\chi)$, and its slope close to χ_i, which are the stronger the more sharply peaked $G_Q^{(i)}(\chi)$ is. Therefore (7.37) is more difficult to fulfil at small σ_z. Both $|G_Q^{(i)}(\chi_i)|$ and η prefer larger σ_z, in agreement with ζ, which we thus continue to use for the determination of $\sigma_{\rm opt}$. As ζ clearly disfavours $\sigma_z \gtrsim 0.3$, we choose as the optimum the minimum of ζ at about 0.28. Considering the lower panel of Fig. 7.6, this value is in very good agreement with small and hence close to optimal values of $r_{\rm GI}^Q$. Generally, we find that $\sigma_{\rm opt}$ is considerably larger for this approach, compared to the variant analysed in Sect. 7.4.

With this finding at hand, we can compute GI-boosted power spectra according to (7.7), and from these sets of nulled power spectra via (7.32), results for both being shown in Fig. 7.7. The GI term is significantly less boosted than in the version studied in Sect. 7.4.1 with $r_{\rm GI}$ less than 10 (see Table 7.2 for comparison). Still, the intrinsic alignment suppression works excellently with $r_{\rm GI}^Q \lesssim 5 \times 10^{-4}$ for all background redshift bins and angular frequencies.

In Table 7.4 values of $r_{\rm GI}^Q$ for other z_i and in addition for the good photo-z survey P1 are listed. The downweighting of the GI signal quickly deteriorates with the increase in photometric redshift uncertainty, being more than two orders of magnitude larger for survey P1. For the standard photo-z case we find that the boosting as implemented in this section is ineffective, so that we do not consider it here. As shown in Sect. 7.5.1, under idealistic circumstances one expects the signal in the nulled power spectra $Q^{(ij)}(\ell)$ to be close to the one in the original power spectra $P^{(ij)}(\ell)$. Hence, we calculate the quantity

$$\Delta_{\rm GG} \equiv \frac{Q_{\rm GG}^{(ij)}(\ell)}{P_{\rm GG}^{(ij)}(\ell)} - 1 \,, \tag{7.42}$$

which is also given in Fig. 7.7 and Table 7.4. The deviation from the original signal is at the per cent level for close foreground and background redshift bins with $z_i \lesssim z_j$, and increases to about 20 % if bins i and j are far apart, irrespective of the photometric redshift quality.

7.5.4 Information content

How does the nulling technique as outlined above perform in comparison with the standard nulling approach? For a very dense binning in redshift both methods evidently remove the GI contamination of the cosmic shear signal to high accuracy, see for instance the recent findings

[1]Note that since we have normalised $G_Q^{(i)}(\chi)$, $|G_Q^{(i)}(\chi_i)|$ is a meaningful measure of the size of $G_Q^{(i)}(\chi)$ at χ_i, relative to its overall amplitude.

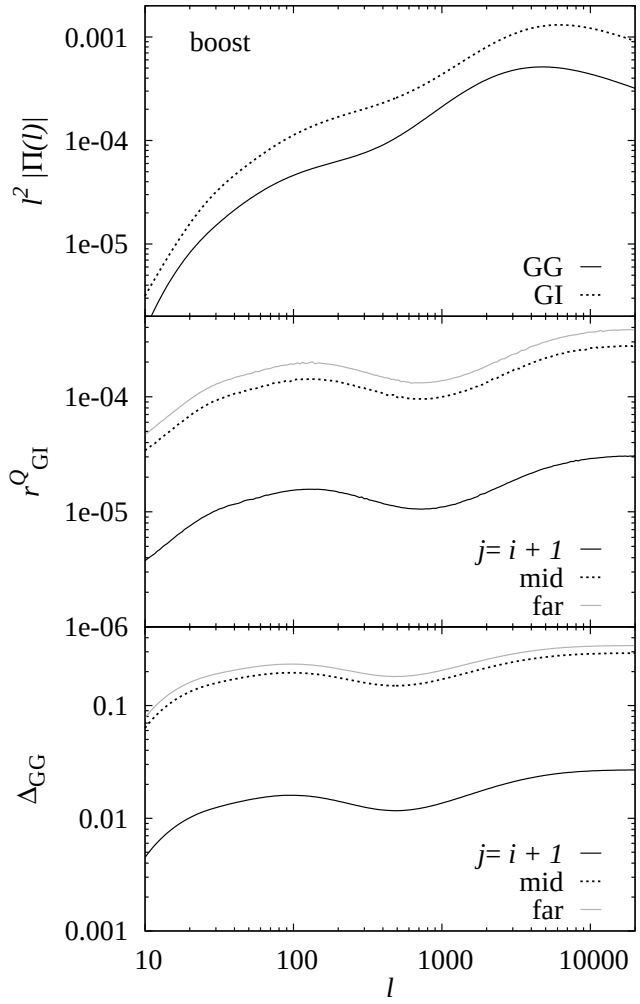

Figure 7.7: Nulling performance for the spectroscopic survey S at $z_i = 0.53$. *Top panel*: Transformed GG (solid curve) and GI (dotted curve) power spectra, computed according to (7.7). *Centre panel*: GI over GG ratio $r^Q_{\rm GI}$ as a function of angular frequency for the same parameters as above. The background redshift bin j is set to $j = i + 1$ (solid black curve), $j = (i + N_z)/2$ ('mid'; dotted black curve), and $j = N_z$ ('far'; solid grey curve). *Lower panel*: Relative deviation $\Delta_{\rm GG}$ as a function of angular frequency for the same parameters as above. The coding of the curves is identical to the foregoing case.

by Shi et al. (2010). However, Joachimi & Schneider (2009) have shown that, even in idealistic situations comparable to our spectroscopic survey, a substantial loss of cosmological information is inherent to standard nulling. We assess the information content in both nulling approaches in a simple case study.

We restrict ourselves to the spectroscopic survey model S and consider again only $z_i \in [0.4; 1.4]$, for the same reasons as discussed in Sect. 7.4.2. Again, we compute ζ for all z_i to find a simple prescription for $\sigma_{\rm opt}$; in this case we use $\sigma_{\rm opt} = -0.131\,z_i + 0.346$. The information content is quantified in terms of the cumulative signal-to-noise (S/N), defined as

$$\frac{\rm S}{\rm N} = \sum_\ell \sum_{j>i,\,l>k} Q^{(ij)}_{\rm GG}(\ell)\ {\rm Cov}^{-1}\left(Q^{(ij)}_{\rm GG}(\ell), Q^{(kl)}_{\rm GG}(\ell)\right)\ Q^{(kl)}_{\rm GG}(\ell)\ , \tag{7.43}$$

where the covariance of the nulled power spectra can be derived from (7.32),

$$\begin{aligned}{\rm Cov}\left(Q^{(ij)}(\ell), Q^{(kl)}(\ell)\right) \ &= \ {\rm Cov}\left(P^{(ij)}(\ell),\ P^{(kl)}(\ell)\right) - f_{ij}\ {\rm Cov}\left(\Pi^{(i)}_Q(\ell),\ P^{(kl)}(\ell)\right) \\ &\quad - f_{kl}\ {\rm Cov}\left(P^{(ij)}(\ell),\ \Pi^{(k)}_Q(\ell)\right) + f_{ij}\ f_{kl}\ {\rm Cov}\left(\Pi^{(i)}_Q(\ell),\ \Pi^{(k)}_Q(\ell)\right)\ .\end{aligned} \tag{7.44}$$

The S/N for data sets of original power spectra $P^{(ij)}(\ell)$ and of nulled power spectra obtained via the Joachimi & Schneider (2009) formalism are calculated in analogy to (7.43). For this setup it is safe to assume that (7.29) has only contributions from shape noise. Even with this simplification, the inversion of the covariance is computationally expensive for the total of 65

Table 7.4: Summary of the nulling performance for two survey models and different values of z_i. Given are the median values of the GI over GG ratio of the power spectra $Q^{(ij)}(\ell)$, $r^Q_{\rm GI}$, and the relative deviation of $Q^{(ij)}(\ell)$ from the original power spectra, $\Delta_{\rm GG}$, for the correlation of adjacent bins ('i+1'), the cross-correlation between bin i and the background bin with index $(i+N_z)/2$ ('mid'), and the cross-correlation between bin i and the most distant bin with index N_z at $z \lesssim 2$ ('far'). In addition $\sigma_{\rm opt}$ as determined from ζ is listed for every case considered.

survey	z_i	$\sigma_{\rm opt}$	$r^Q_{\rm GI}(i{+}1)$	$r^Q_{\rm GI}$(mid)	$r^Q_{\rm GI}$(far)	$\Delta_{\rm GG}(i{+}1)$	$\Delta_{\rm GG}$(mid)	$\Delta_{\rm GG}$(far)
S	0.53	0.280	0.1×10^{-4}	1.3×10^{-4}	1.7×10^{-4}	0.01	0.19	0.22
	0.76	0.255	0.4×10^{-4}	1.2×10^{-4}	1.6×10^{-4}	0.01	0.11	0.15
	0.96	0.235	0.3×10^{-4}	0.9×10^{-4}	1.4×10^{-4}	0.00	0.05	0.07
P1	0.53	0.280	7.9×10^{-2}	2.4×10^{-2}	3.2×10^{-2}	0.02	0.19	0.23
	0.76	0.255	4.2×10^{-2}	2.3×10^{-2}	3.0×10^{-2}	0.01	0.12	0.15
	0.96	0.235	2.9×10^{-2}	2.1×10^{-2}	2.8×10^{-2}	0.00	0.05	0.08

bins between $z_i = 0.4$ and $z_i = 1.4$. Thus we include by default only tomographic measures for every fifth bin i, but all $j > i$, in the S/N. The absolute value of the S/N depends of course on how many power spectra are incorporated, but we are only interested in the ratio of S/N for the nulled data sets over the set of original power spectra.

Note that for every z_i one can make use of $N_z - i$ power spectra $Q^{(ij)}(\ell)$. The very same number of modes is available in the standard nulling approach although one mode is discarded to perform the actual nulling (for details see Joachimi & Schneider 2009). Transformed auto-correlation power spectra with $i = j$ do not enter the S/N, but by construction the $P^{(ii)}(\ell)$ do contribute to all $Q^{(ij)}(\ell)$ via the $\Pi^{(i)}_Q(\ell)$, whereas in standard nulling auto-correlations are completely discarded. However, due to the dense redshift binning, we expect the amount of independent information contained in auto-correlation power spectra to be small.

We have given the resulting ratios of the S/N for the nulled data set over the S/N for the original one in Table 7.5. The considerable loss of information can be confirmed, the S/N for both nulling methods yielding less than 20 % of the original S/N. We find that these numbers are very robust against changes in the number and values of redshift bins i included in the S/N by varying the size of steps in bin numbers i and the range of redshifts considered. It is quite remarkable that the ratios for both nulling methods are very similar. The slightly bigger number for the nulling as devised in this work could be related to the inclusion of auto-correlation power spectra, but is not very significant anyway.

In the standard nulling case the information loss is caused by discarding part of the signal, namely one mode per bin i whereas the variant suggested here features a signal that deviates by at most about 20 % from the untransformed one. In the latter case the loss is caused by an increase in the covariance due to the subtraction of signals in (7.32). We conjecture at this point that the agreement in the amount of information lost, in spite of the largely different mechanisms of the two methods, hints at a fundamental limit of how far GI and GG signals can be distinguished by only relying on the redshift dependence of the two contributions.

7.6 Conclusions

In this chapter we presented a method which extracts gravitational shear-intrinsic ellipticity correlations (the GI signal) from a tomographic cosmic-shear data set. The approach relies neither on models of intrinsic alignments nor on knowledge of the cosmological parameters that characterise the cosmic shear (GG) signal, making only use of the typical and well-understood

Table 7.5: Ratio of cumulative signal-to-noise of the nulled set of power spectra over the original set of power spectra (SNR). The results for the nulling method devised in this work and the standard nulling technique (Joachimi & Schneider 2009) are compared. The default SNR shown is computed for a step size in foreground redshift bin index i of 5 and in the redshift range $[0.4; 1.4]$. In addition the moduli of the fractional deviation of the SNR from the default when using a step size of 3, i.e. every third bin i (third column), a step size of 7 (fourth column), and the default step size but a different redshift range $[0.5; 1.3]$ (fifth column) are given.

nulling type	SNR	step 3	step 7	$z \in [0.5; 1.3]$
this work	0.179	0.76 %	2.75 %	1.96 %
standard	0.163	0.59 %	2.32 %	1.45 %

redshift dependencies of both the GI and GG term. We derived constraints which a linear transformation of second-order cosmic shear measures has to fulfil in order to boost the GI signal and simultaneously suppress the lensing contribution. We studied in depth a particular parametrisation of the weights entering this transformation and analysed the performance of the resulting GI boosting technique for three representative survey models.

Applying the GI boosting to future all-sky cosmic shear surveys, it should be possible to isolate the GI signal with subdominant biases due to a residual GG term, and with constraints that are comparable to current results from indirect measurements of shear-ellipticity correlations (Mandelbaum et al. 2009). If one restricts the analysis to galaxies with photometric redshift information of good quality, i.e. a redshift scatter of not more than $\sigma_{\rm ph}(1+z)$ with $\sigma_{\rm ph} = 0.03$, one can achieve $1\,\sigma$-errors on the GI signal amplitude A in the parametrisation of (7.26) of better than 0.2 when varying only the amplitude, and a marginalised error of approximately 0.7 when fitting an additional redshift dependence.

Using all galaxies from a survey fulfilling $\sigma_{\rm ph} \leq 0.05$, the statistical constraints degrade only marginally but the parameter bias due to the residual GG contribution can attain more significant values of up to $b_{\rm sys}/\sigma_{\rm stat} \lesssim 2/3$. We also considered a survey with high-quality photometric or spectroscopic redshifts. However, the expected low number density of galaxies of $n_{\rm g} = 1\,\mathrm{arcmin}^{-2}$, even for future surveys, does not permit us to place competitive constraints on intrinsic alignment models. In this case of highly accurate redshift information the residual bias on parameters is negligible.

Although we have modelled scatter in photometric redshifts for our investigations, we did not consider other effects affecting the accuracy of redshift information, such as an error in the median of the galaxy redshift distributions or catastrophic failures in the determination of photometric redshifts. As several studies of intrinsic alignment removal techniques have demonstrated (e.g. Bridle & King 2007; Joachimi & Schneider 2009; Joachimi & Bridle 2009), the ability to separate the GI from the GG signal depends vitally on these parameters characterising the accuracy of and knowledge about redshifts.

The same can be expected for the GI boosting technique, possibly to an even larger extent since in this case one attempts to suppress the originally strongest contribution to ellipticity correlations, the GG signal. Hence, we hypothesise that the requirements of future ambitious weak lensing surveys, like a negligible fraction of catastrophic failures and an error in the mean of each redshift distribution of not more than $0.002(1+z)$ (Laureijs et al. 2009), are both necessary and sufficient for a success of GI boosting. We leave a detailed assessment of the requirements on the quality of redshift information to future work.

Moreover, we did not yet include intrinsic ellipticity correlations (II) into our considerations. Since the II signal is generated by physically close pairs of galaxies, it has a redshift

dependence that is clearly distinct from the GI and GG terms, and can thus be removed relatively easily (King & Schneider 2002, 2003; Heymans & Heavens 2003; Takada & White 2004). In tomographic cosmic shear data it mainly affects auto-correlations and cross-correlations of adjacent photometric redshift bins with significant overlap of their corresponding distributions of true redshifts. One of the aforementioned II removal techniques could precede the GI boosting, causing an increased shape noise contribution in particular in the auto-correlations due to the reduced number of available galaxy pairs. Alternatively, the downweighting of the II signal could also be readily incorporated into the boosting technique by introducing the additional condition $\partial^2 G^{(i)}/\partial\chi^2|_{\chi_i} = 0$, implying $B^{(i)}(\chi_i) = 0$ and therefore a downweighting of auto-correlations as well as cross-correlations of adjacent redshift distributions, see (7.7).

Our findings still have the potential for significant improvement because we have only considered one specific parametrisation of the weight function that governs the boosting transformation. While this choice is intuitive and allows analytical progress, a more versatile approach could be to assume the weight function $B^{(i)}(\chi)$ as piecewise linear, with nodes placed at the median redshift of every galaxy redshift sample. The constraints on GI boosting and GG suppression could then be directly imposed on the discretised version of the boosting transformation, thereby fixing a subset of the values of $B^{(i)}_Q(\chi)$ at its nodes. The remaining freedom in the weight function could for instance be used to maximise the signal-to-noise of the expected transformed GI signal.

We also constructed a method of GI removal, directly based on a slightly modified version of the GI boosting technique. In principle, we showed that if one is able to isolate the GI signal via boosting, one can simply subtract a rescaled version of the GI term from the original cosmic shear measures to eliminate the intrinsic alignment systematic. We find that the residual contamination of the cosmic shear signal by GI correlations is indeed small, and that the cumulative signal-to-noise of the thus treated cosmic shear signal decreases by about a factor of 6. This value is remarkably close to the result for the standard GI nulling technique as introduced by Joachimi & Schneider (2008, 2009), in spite of the differing approaches. The underlying reason for this agreement may be due to a fundamental limit in the ability to separate GI and GG signals relying only on the dependence on redshift, which is worth to be addressed in future investigations. Of course, such a limit would also imply a maximum accuracy with which parameters of intrinsic alignments can be constrained via GI boosting.

Like the method devised in this work, the standard nulling technique is also a purely geometrical method. Hence, a combined application of GI boosting and nulling to a cosmic shear data set would still be based on a minimum of assumptions about the actual forms of signals or the values of model parameters. For instance one could use an initial analysis based on nulling to yield robust estimates of the cosmic shear signal and the corresponding cosmological model. This could then be used to construct weights for the GI boosting transformation such that even in the case of standard photometric redshift quality (which we assumed to be $\sigma_{\rm ph} = 0.05$ in this paper) the bias due to the residual GG signal would be negligible, thereby enabling an equally robust estimate of the GI signal.

Ultimately, the cosmic shear analysis, the treatment of intrinsic alignments, and the inclusion of additional information from galaxy number density correlations (as in Mandelbaum et al. 2006; Hirata et al. 2007; Mandelbaum et al. 2009) will all be efficiently combined into a simultaneous analysis of the form presented in Bernstein (2009) and Joachimi & Bridle (2009), provided one can summon the computational power (see the following chapter for details). Yet the model-independent, direct, and robust boosting technique, as well as nulling and the combination of the two, will prove useful e.g. to provide reliable priors on the large set of parameters entering the integrative approaches and in addition serve as a valuable consistency check in cosmic shear analyses.

Chapter 8

Self-calibration of intrinsic alignments

In absence of a compelling model for the intrinsic alignment of galaxies, future weak gravitational lensing surveys are under threat to miss their ambitious goals on precision measurements of cosmological parameters. As demonstrated in the foregoing chapters, geometrical and model-independent methods are capable of robustly eliminating both intrinsic ellipticity (II) and gravitational shear-intrinsic ellipticity (GI) correlations, albeit with a considerable loss of cosmological information which, for instance, amounts to an order of magnitude for the Dark Energy Task Force Figure of Merit. Therefore it is crucial to develop other techniques that process the data available from cosmic shear surveys, such that intrinsic alignments are removed using a minimum level of assumptions about the form of the intrinsic alignment signals, but that guarantee at the same time a minimal loss of information about cosmology.

Deep imaging surveys not only provide information about the shape of galaxies, but allow in addition for a measurement of galaxy number densities, as well as cross-correlations between shape and number density information. This substantial extension of the set of observables increases the cosmological information to be extracted and, more importantly, enables one to internally calibrate systematic effects (Hu & Jain 2004; Bernstein 2009). By adding galaxy number density information one adds signals that are capable of pinning down the functional form of intrinsic alignments, but one also introduces as another systematic, the galaxy bias, which quantifies the lack of knowledge about how galaxies, i.e. the visible baryonic matter, follow the underlying dark matter distribution.

It is the scope of this chapter to elucidate the performance of a joint analysis of galaxy shape and number density information as regards the ability to constrain cosmological parameters when using general and flexible parametrisations of intrinsic alignments and galaxy bias. In doing so we incorporate several cosmological signals which have been considered before as promising probes of cosmology themselves, including galaxy clustering from photometric redshift surveys (Blake & Bridle 2005; Dolney et al. 2006; Zhan 2006; Blake et al. 2007; Padmanabhan et al. 2007), galaxy-galaxy lensing (e.g. Schneider & Rix 1997; Guzik & Seljak 2001, 2002; Seljak 2002; Seljak et al. 2005; Yoo et al. 2006; Johnston et al. 2007; Cacciato et al. 2009) and lensing magnification (Broadhurst et al. 1995; Zhang & Pen 2005, 2006; van Waerbeke 2010). We follow the ansatz outlined in Bernstein (2009) and extend the investigation by Bridle & King (2007) who considered the residual information content in galaxy shape correlations after marginalising over the parameters of two log-linear grid models representing the II and GI terms. We quantify the cross-calibration properties of the joint set of observables and determine the requirements on cosmological surveys to efficiently apply this joint approach, dubbed self-calibration of intrinsic alignments.

This chapter is organised as follows: In Sect. 8.1 we give an overview on the two-point correlations that form part of the galaxy shape and number density observables, and we derive their

explicit form. Section 8.2 demonstrates how we model the different signals and their dependence on cosmology. We introduce a general grid parametrisation for the intrinsic alignments and the galaxy bias. Furthermore we summarise our Fisher matrix formalism and the figures of merit we employ. In Sect. 8.3 we present our results on the dependence of the parameter constraints on the freedom in the model of intrinsic alignments and galaxy bias, the characteristics of the redshift distributions, and the priors on the different sets of nuisance parameters. Finally, in Sect. 8.4 we summarise our findings about the self-calibration of intrinsic alignments and provide conclusions.

8.1 Two-point correlations from cosmological surveys

Cosmological imaging surveys observe the angular positions and the projected shapes of huge numbers of galaxies over increasingly large areas on the sky. In addition, by means of multi-colour photometry, it is possible to perform a tomographic analysis, i.e. obtain coarse information about the line-of-sight dimension in terms of photometric redshifts (photo-z). From the galaxy shapes in a given region of space, one can infer the ellipticity

$$\epsilon^{(i)}(\boldsymbol{\theta}) = \gamma_{\mathrm{G}}^{(i)}(\boldsymbol{\theta}) + \gamma_{\mathrm{I}}^{(i)}(\boldsymbol{\theta}) + \epsilon_{\mathrm{rnd}}^{(i)}(\boldsymbol{\theta}) \;, \tag{8.1}$$

where the superscript in parentheses assigns a photo-z bin i. The observed ellipticity ϵ has contributions from the gravitational shear γ_{G} and an intrinsic shear γ_{I}, which is caused by the alignment of a galaxy in its surrounding gravitational field. Moreover, ϵ is assumed to have an uncorrelated component ϵ_{rnd}, which accounts for the purely random part of the intrinsic orientations and shapes of galaxies. Note that (8.1) is only valid if the gravitational shear is weak, see e.g. Seitz & Schneider (1997); Bartelmann & Schneider (2001) and for certain definitions of ellipticity.

Likewise, the positions of galaxies can be used to construct an estimate of the number density contrast

$$n^{(i)}(\boldsymbol{\theta}) = n_{\mathrm{m}}^{(i)}(\boldsymbol{\theta}) + n_{\mathrm{g}}^{(i)}(\boldsymbol{\theta}) + n_{\mathrm{rnd}}^{(i)}(\boldsymbol{\theta}) \;, \tag{8.2}$$

which is determined by the intrinsic number density contrast of galaxies n_{g} and the alteration of galaxy counts due to lensing magnification n_{m}. An uncorrelated shot noise contribution is added via n_{rnd}. In contrast to $\epsilon^{(i)}(\boldsymbol{\theta})$ the number density contrast $n^{(i)}(\boldsymbol{\theta})$ can obviously not be estimated from individual galaxies. One can understand $n_{\mathrm{m}}^{(i)}(\boldsymbol{\theta})+n_{\mathrm{g}}^{(i)}(\boldsymbol{\theta})$ as the ensemble average over a hypothetical, Poisson-distributed random field of which the observed galaxy distribution is one particular representation. The formal relation between the projected number density contrast as used in (8.2) and the three-dimensional galaxy number density fluctuations will be provided below, see (8.12).

As was already noted in Bernstein (2009), (8.1) and (8.2) are symmetric in the sense that they both contain an intrinsic contribution and a term caused by gravitational lensing effects. Under usual circumstances the correlated part of the ellipticity is dominated by the gravitational shear, whereas the largest term in (8.2) is due to the intrinsic number density contrast.

Both ellipticity and number density contrast vanish if averaged over sufficiently large scales. Thus, one considers to lowest order two-point statistics of these quantities. Since all real-space two-point measures are related to the power spectrum (see e.g. Kaiser 1992), we can work in terms of power spectra without loss of generality, which is desirable in particular due to a simpler structure of the signal covariances in Fourier space. Denoting the Fourier transform by

Table 8.1: Overview on the two-point correlations considered in this work. Listed are the symbols for the two-dimensional projected power spectra and the underlying three-dimensional power spectra.

measured correlation	2D PS	3D PS
shear	C_{GG}	$P_{\delta\delta}$
intrinsic-shear	C_{IG}	$P_{\delta\mathrm{I}}$
intrinsic	C_{II}	P_{II}
galaxy clustering	C_{gg}	P_{gg}
clustering-magnification	C_{gm}	$P_{\mathrm{g}\delta}$
magnification	C_{mm}	$P_{\delta\delta}$
clustering-shear	C_{gG}	$P_{\mathrm{g}\delta}$
clustering-intrinsic	C_{gI}	P_{gI}
magnification-shear	C_{mG}	$P_{\delta\delta}$
magnification-intrinsic	C_{mI}	$P_{\delta\mathrm{I}}$
galaxy ellipticity (observable)	$C_{\epsilon\epsilon}$	
galaxy number density (observable)	C_{nn}	
number density-ellipticity (observable)	$C_{n\epsilon}$	

a tilde, the power spectrum $C_{\mathrm{ab}}^{(ij)}(\ell)$[1] between redshift bins i and j can then be defined by

$$\left\langle \tilde{x}_{\mathrm{a}}^{(i)}(\boldsymbol{\ell})\, \tilde{x}_{\mathrm{b}}^{(j)}(\boldsymbol{\ell'}) \right\rangle = (2\pi)^2\, \delta_{\mathrm{D}}^{(2)}(\boldsymbol{\ell} - \boldsymbol{\ell'})\, C_{\mathrm{ab}}^{(ij)}(\ell)\,, \tag{8.3}$$

where $\delta_{\mathrm{D}}^{(2)}$ is the two-dimensional Dirac delta-distribution, and where $\boldsymbol{\ell}$ denotes the angular frequency, the Fourier variable on the sky. The measures x_{a} and x_{b} can correspond to any of the set $\{\gamma_{\mathrm{G}}, \gamma_{\mathrm{I}}, n_{\mathrm{g}}, n_{\mathrm{m}}\}$. The random contributions in (8.1) and (8.2) are not correlated with any of the other measures and only yield a contribution to the noise, see Sect. 8.2.4.

Inserting (8.1) and (8.2) into (8.3), one obtains the complete set of tomographic two-point observables which are available from shape and number density information

$$C_{\epsilon\epsilon}^{(ij)}(\ell) = C_{\mathrm{GG}}^{(ij)}(\ell) + C_{\mathrm{IG}}^{(ij)}(\ell) + C_{\mathrm{IG}}^{(ji)}(\ell) + C_{\mathrm{II}}^{(ij)}(\ell)\,; \tag{8.4}$$

$$C_{nn}^{(ij)}(\ell) = C_{\mathrm{gg}}^{(ij)}(\ell) + C_{\mathrm{gm}}^{(ij)}(\ell) + C_{\mathrm{gm}}^{(ji)}(\ell) + C_{\mathrm{mm}}^{(ij)}(\ell)\,; \tag{8.5}$$

$$C_{n\epsilon}^{(ij)}(\ell) = C_{\mathrm{gG}}^{(ij)}(\ell) + C_{\mathrm{gI}}^{(ij)}(\ell) + C_{\mathrm{mG}}^{(ij)}(\ell) + C_{\mathrm{mI}}^{(ij)}(\ell)\,, \tag{8.6}$$

see Bernstein (2009). We name signals stemming from galaxy shape information by capital letters ('G' for gravitational shear, 'I' for intrinsic shear) and signals related to galaxy number densities by small letters ('g' for intrinsic number density fluctuations, 'm' for lensing magnification). An overview of the nomenclature of the correlations in (8.4) to (8.6) is provided in Table 8.1. Note that (8.4) and (8.5) are symmetric with respect to their photo-z bin arguments. Hence, if N_{zbin} denotes the number of available photo-z bins, one has $N_{\mathrm{zbin}}(N_{\mathrm{zbin}}+1)/2$ observables for every considered angular frequency. In contrast, one can exploit N_{zbin}^2 ellipticity-number density cross-correlation power spectra (8.6) per ℓ.

The set of observables in (8.4) is the one that cosmic shear analyses are based on. The shear correlation signal (GG) is a clean probe of the underlying matter power spectrum and is thus powerful in constraining cosmological parameters (e.g. Hu 1999). However, shape measurements incorporate further terms stemming from correlations of intrinsic ellipticities (II) and shear-intrinsic cross-correlations (IG, or equivalently GI) whose contribution can be substantial, but

[1] Contrary to the foregoing chapters, and like in Chap. 5, we here use the symbol C for projected power spectra to avoid confusion with the various three-dimensional power spectra.

is to date poorly known (Hirata & Seljak 2004). These terms exist because the shapes and orientations of galaxies are influenced via the tidal gravitational fields of the matter structures in their surrounding, which firstly induce correlations between neighbouring galaxies, and secondly cause correlations by determining the intrinsic shape of a foreground object and adding to the shear signal of a background galaxy.

Intrinsic galaxy clustering (gg) adds a strong signal to the correlations of galaxy number densities (8.5), but its use to obtain cosmological parameter estimates is limited due by poor knowledge of the galaxy bias (e.g. Lahav & Suto 2004). Gravitational lensing modifies the flux of objects and thus reduces or increases number counts of galaxies above a certain limiting magnitude, depending on the form of the galaxy luminosity function close to the limiting magnitude. This produces magnification correlations (mm) and intrinsic number density-magnification cross-correlations (gm). The gm correlations occur when a foreground mass overdensity (underdensity) contains an overdensity (underdensity) of galaxies and (de)-magnifies background objects along the same line of sight causing an apparent over- or underdensity of galaxies at higher redshift.

Cross-correlations between galaxy number densities and ellipticities (8.6) contain contributions from cross terms between intrinsic clustering and shear (gG), intrinsic clustering and intrinsic shear (gI), magnification and shear (mG), and magnification and intrinsic shear (mI). For instance, one expects to find gI and gG signals when a mass structure leads to an overdensity in the local galaxy distribution and influences the intrinsic shape of galaxies at the same redshift or contributes to the shear of background objects. The latter is the usual galaxy-galaxy lensing signal. Because a foreground overdensity can in addition enhance galaxy counts due to lensing magnification, the mG and mI signals will also be non-vanishing. The form of all these correlations will be further discussed in Sect. 8.2.

All non-random terms in (8.1) and (8.2), for a given photometric redshift bin i, can be related to a source term $\mathcal{S}$, which is a function of spatial coordinates, i.e.

$$x_{\rm a}^{(i)}(\boldsymbol{\theta}) = \int_0^{\chi_{\rm hor}} {\rm d}\chi \; w^{(i)}(\chi) \; \mathcal{S}_{\rm a}\left(f_{\rm k}(\chi)\boldsymbol{\theta}, \chi\right) \; , \tag{8.7}$$

where we defined a weight function w that depends on the photo-z bin i (for a similar approach see Hu & Jain 2004). Here, χ denotes comoving distance, and $f_{\rm k}(\chi)$ is the comoving angular diameter distance. If (8.7) holds for two quantities $x_{\rm a}^{(i)}$ and $x_{\rm b}^{(j)}$, their projected power spectrum is given by the line-of-sight integral of the three-dimensional source power spectrum $P_{\mathcal{S}_a\mathcal{S}_b}$ via Limber's equation in Fourier space (Kaiser 1992),

$$C_{\rm ab}^{(ij)}(\ell) = \int_0^{\chi_{\rm hor}} {\rm d}\chi \; \frac{w^{(i)}(\chi) \; w^{(j)}(\chi)}{f_{\rm k}^2(\chi)} \; P_{\mathcal{S}_a\mathcal{S}_b}\left(\frac{\ell}{f_{\rm k}(\chi)}, \chi\right) \; . \tag{8.8}$$

By identifying weights and source terms for gravitational and intrinsic shear, as well as intrinsic clustering and magnification, we can derive Limber equations for all power spectra entering (8.4)-(8.6), see e.g. Sect. 3.3.

To compute the specialisation of (8.7) to the cosmic shear case, we first note that in Fourier space the shear and the convergence are related by the simple equation $\tilde{\kappa}_{\rm G}(\boldsymbol{\ell}) = \tilde{\gamma}_{\rm G}(\boldsymbol{\ell}) \; {\rm e}^{-2{\rm i}\varphi_\ell}$, where φ_ℓ is the polar angle of $\boldsymbol{\ell}$. As a consequence, the power spectra of shear and convergence are identical. Therefore, we can equivalently use the convergence $\kappa^{(i)}(\boldsymbol{\theta})$ as the cosmic shear observable. It is related to the three-dimensional matter density contrast δ via

$$\kappa_{\rm G}^{(i)}(\boldsymbol{\theta}) = \int_0^{\chi_{\rm hor}} {\rm d}\chi \; q^{(i)}(\chi) \; \delta\left(f_{\rm k}(\chi)\boldsymbol{\theta}, \chi\right) \; , \tag{8.9}$$

where the weight is given by

$$q^{(i)}(\chi) = \frac{3H_0^2\Omega_\mathrm{m}}{2\,c^2}\frac{f_\mathrm{k}(\chi)}{a(\chi)}\int_\chi^{\chi_\mathrm{hor}} \mathrm{d}\chi'\; p^{(i)}(\chi')\;\frac{f_\mathrm{k}(\chi'-\chi)}{f_\mathrm{k}(\chi')}\;, \tag{8.10}$$

see (3.28) for the equivalent expression in Sect. 3.3, and Bartelmann & Schneider (2001); Schneider (2006) for further details. Here a denotes the scale factor and $p^{(i)}(\chi)$ the comoving distance probability distribution of those galaxies in bin i for which shape information is available.

Analogously to the lensing case, one can define a convergence of the intrinsic shear field $\kappa_\mathrm{I}^{(i)}(\boldsymbol{\theta})$, which is directly related to the intrinsic shear via $\tilde{\kappa}_\mathrm{I}(\boldsymbol{\ell}) = \tilde{\gamma}_\mathrm{I}(\boldsymbol{\ell})\;\mathrm{e}^{-2\mathrm{i}\varphi_\ell}$, see Chap. 5 for details. This intrinsic convergence is a projection of the three-dimensional intrinsic shear field $\bar{\kappa}_\mathrm{I}$, which can be written as

$$\kappa_\mathrm{I}^{(i)}(\boldsymbol{\theta}) = \int_0^{\chi_\mathrm{hor}} \mathrm{d}\chi\; p^{(i)}(\chi)\;\bar{\kappa}_\mathrm{I}\left(f_\mathrm{k}(\chi)\boldsymbol{\theta},\chi\right)\;, \tag{8.11}$$

see e.g. Hirata & Seljak (2004) for the analogous expression in terms of intrinsic shear. Here we have assumed that the intrinsic shear field is – like the gravitational shear field – curl-free to good approximation. This holds for instance for the linear alignment model developed in Hirata & Seljak (2004). Then $\bar{\kappa}_\mathrm{I}$ corresponds to the Fourier transform of $\bar{\gamma}_\mathrm{E}^\mathrm{I}(\boldsymbol{k})$ as defined in Schneider & Bridle (2010).

Likewise, angular galaxy number density fluctuations $n_\mathrm{g}^{(i)}(\boldsymbol{\theta})$ are given by the line-of-sight projection of three-dimensional number density fluctuations δ_g as (e.g. Hu & Jain 2004)

$$n_\mathrm{g}^{(i)}(\boldsymbol{\theta}) = \int_0^{\chi_\mathrm{hor}} \mathrm{d}\chi\; p^{(i)}(\chi)\;\delta_\mathrm{g}\left(f_\mathrm{k}(\chi)\boldsymbol{\theta},\chi\right)\;. \tag{8.12}$$

It is important to note that $p^{(i)}(\chi)$ is chosen to be the same as in (8.10) and (8.11), i.e. the number counts are restricted to those galaxies with shape measurements, which require a higher signal-to-noise than the position determination. In principle, number density information could be obtained for a larger number of galaxies, in particular fainter ones. But, to determine the contribution to number density correlations by magnification, it is necessary to measure the slope of the luminosity function $\alpha^{(i)}$ at the faint end of the used galaxy distribution. We will detail the exact definition and the determination of $\alpha^{(i)}$ in Sect. 8.2.2. Since it is desirable to extract the values of the $\alpha^{(i)}$ internally from the survey, one needs to be able to measure fluxes down to values slightly below the magnitude limit of the galaxies included in $p^{(i)}(\chi)$.

Moreover galaxy number density measurements may require photometric redshifts which are of the same or better quality than for cosmic shear studies, limiting the number of faint usable galaxies. Hence, we argue that the choice of identical distance probability distributions for both shape and number density signals is a fair assumption. We add the warning that one may have to account for selection biases, for instance if one investigates cosmic shear and magnification effects with the same galaxy sample (e.g. Schmidt et al. 2009; Krause & Hirata 2009).

We now turn to the derivation of the enhancement or depletion of projected galaxy counts $n_\mathrm{m}^{(i)}(\boldsymbol{\theta})$ due to lensing magnification. The number density of galaxies n, counted above a flux threshold S at angular position $\boldsymbol{\theta}$ and comoving distance χ, is altered by gravitational lensing according to

$$n(>S, f_\mathrm{k}(\chi)\boldsymbol{\theta},\chi) = \frac{1}{\mu(\boldsymbol{\theta},\chi)}\;n_0\left(>\frac{S}{\mu(\boldsymbol{\theta},\chi)}, f_\mathrm{k}(\chi)\boldsymbol{\theta},\chi\right)\;, \tag{8.13}$$

where n_0 is the original galaxy number density, and where μ denotes the magnification (Bartelmann & Schneider 2001); see also (3.16). One assumes that the galaxy luminosity function close

to the flux limit of the survey can locally be written as a power law, $n(>S, f_\mathrm{k}(\chi)\boldsymbol{\theta}, \chi) \propto S^{-\alpha(\chi)}$. The slope α depends on the line-of-sight distance, or equivalently, redshift, but should not depend on angular dimensions due to isotropy. However, it is a function of the magnitude limit in the observed filter, in this work denoted by r_lim. This dependence is dealt with in Sect. 8.2.2, but for ease of notation we drop r_lim as an argument of α for the remainder of this section. Plugging the power-law form of the luminosity function into (8.13) yields

$$\frac{n(>S, f_\mathrm{k}(\chi)\boldsymbol{\theta}, \chi)}{n_0(>S, f_\mathrm{k}(\chi)\boldsymbol{\theta}, \chi)} = \mu(\boldsymbol{\theta}, \chi)^{\alpha(\chi)-1} \,. \tag{8.14}$$

Again following Bartelmann & Schneider (2001), one can approximate the magnification in the weak lensing regime as $\mu \approx 1 + 2\kappa_\mathrm{G}$. Since $\kappa_\mathrm{G} \ll 1$, we can in addition do a Taylor approximation to arrive at

$$\begin{aligned} \frac{n(>S, f_\mathrm{k}(\chi)\boldsymbol{\theta}, \chi)}{n_0(>S, f_\mathrm{k}(\chi)\boldsymbol{\theta}, \chi)} &\approx [1 + 2\,\kappa_\mathrm{G}(\boldsymbol{\theta}, \chi)]^{\alpha(\chi)-1} \\ &\approx 1 + 2\,\left[\alpha(\chi) - 1\right]\,\kappa_\mathrm{G}(\boldsymbol{\theta}, \chi) \,. \end{aligned} \tag{8.15}$$

Defining the excess galaxy density contrast due to magnification effects as

$$\delta_\mathrm{g}^\mathrm{m}(f_\mathrm{k}(\chi)\boldsymbol{\theta}, \chi) \equiv \frac{n(>S, f_\mathrm{k}(\chi)\boldsymbol{\theta}, \chi)}{n_0(>S, f_\mathrm{k}(\chi)\boldsymbol{\theta}, \chi)} - 1 = 2\,\left[\alpha(\chi) - 1\right]\,\kappa_\mathrm{G}(\boldsymbol{\theta}, \chi) \,, \tag{8.16}$$

one obtains for the corresponding projected density contrast

$$\begin{aligned} n_\mathrm{m}^{(i)}(\boldsymbol{\theta}) &= \int_0^{\chi_\mathrm{hor}} \mathrm{d}\chi\, p^{(i)}(\chi)\, \delta_\mathrm{g}^\mathrm{m}\left(f_\mathrm{k}(\chi)\boldsymbol{\theta}, \chi\right) \\ &= \int_0^{\chi_\mathrm{hor}} \mathrm{d}\chi\, p^{(i)}(\chi)\, 2\,\left[\alpha(\chi) - 1\right]\,\kappa_\mathrm{G}(\boldsymbol{\theta}, \chi) \,. \end{aligned} \tag{8.17}$$

In exact analogy to the standard derivation of (8.9) one can now insert the relation between the convergence and the three-dimensional matter density contrast (3.22) which, after swapping the order of integration and the names of the integration variables, yields

$$n_\mathrm{m}^{(i)}(\boldsymbol{\theta}) = \int_0^{\chi_\mathrm{hor}} \mathrm{d}\chi\, \bar{q}^{(i)}(\chi)\, \delta\left(f_\mathrm{k}(\chi)\boldsymbol{\theta}, \chi\right) \,. \tag{8.18}$$

Here, we have defined the weight

$$\bar{q}^{(i)}(\chi) = \frac{3H_0^2\Omega_\mathrm{m}}{2\,c^2}\frac{f_\mathrm{k}(\chi)}{a(\chi)}\int_\chi^{\chi_\mathrm{hor}} \mathrm{d}\chi'\, p^{(i)}(\chi')\,\frac{f_\mathrm{k}(\chi'-\chi)}{f_\mathrm{k}(\chi')}\,2\,\left[\alpha(\chi') - 1\right] \,. \tag{8.19}$$

Given that the slope of the luminosity function should be a smooth function of comoving distance, $\alpha(\chi)$ varies only weakly over the range of the integration in (8.19), being determined by the distribution $p^{(i)}(\chi)$, which has relatively compact support. Hence, the mean value theorem constitutes a good approximation, so that we can write

$$\bar{q}^{(i)}(\chi) \approx 2\,(\alpha^{(i)} - 1)\, q^{(i)}(\chi) \,, \tag{8.20}$$

where we define $\alpha^{(i)}$ to be the slope of the luminosity function, evaluated at the median redshift of the photometric bin i. Inserting (8.20) into (8.18) results in

$$\begin{aligned} n_\mathrm{m}^{(i)}(\boldsymbol{\theta}) &= 2\,(\alpha^{(i)} - 1)\int_0^{\chi_\mathrm{hor}} \mathrm{d}\chi\, q^{(i)}(\chi)\, \delta\left(f_\mathrm{k}(\chi)\boldsymbol{\theta}, \chi\right) \\ &= 2\,(\alpha^{(i)} - 1)\,\kappa_\mathrm{G}^{(i)}(\boldsymbol{\theta}) \,. \end{aligned} \tag{8.21}$$

Comparing the projection equations (8.9), (8.11), (8.12), and (8.21) to the general form (8.7), one can derive all possible cross- and auto-power spectra in the form of the general Limber equation (8.8). These read

$$C^{(ij)}_{\rm GG}(\ell) = \int_0^{\chi_{\rm hor}} {\rm d}\chi \, \frac{q^{(i)}(\chi)\, q^{(j)}(\chi)}{f_{\rm k}^2(\chi)} \, P_{\delta\delta}\left(\frac{\ell}{f_{\rm k}(\chi)}, \chi\right) ; \tag{8.22}$$

$$C^{(ij)}_{\rm IG}(\ell) = \int_0^{\chi_{\rm hor}} {\rm d}\chi \, \frac{p^{(i)}(\chi)\, q^{(j)}(\chi)}{f_{\rm k}^2(\chi)} \, P_{\delta{\rm I}}\left(\frac{\ell}{f_{\rm k}(\chi)}, \chi\right) ; \tag{8.23}$$

$$C^{(ij)}_{\rm II}(\ell) = \int_0^{\chi_{\rm hor}} {\rm d}\chi \, \frac{p^{(i)}(\chi)\, p^{(j)}(\chi)}{f_{\rm k}^2(\chi)} \, P_{\rm II}\left(\frac{\ell}{f_{\rm k}(\chi)}, \chi\right) ; \tag{8.24}$$

$$C^{(ij)}_{\rm gg}(\ell) = \int_0^{\chi_{\rm hor}} {\rm d}\chi \, \frac{p^{(i)}(\chi)\, p^{(j)}(\chi)}{f_{\rm k}^2(\chi)} \, P_{\rm gg}\left(\frac{\ell}{f_{\rm k}(\chi)}, \chi\right) ; \tag{8.25}$$

$$C^{(ij)}_{\rm gm}(\ell) = \int_0^{\chi_{\rm hor}} {\rm d}\chi \, \frac{p^{(i)}(\chi)\, \bar{q}^{(j)}(\chi)}{f_{\rm k}^2(\chi)} \, P_{{\rm g}\delta}\left(\frac{\ell}{f_{\rm k}(\chi)}, \chi\right) ; \tag{8.26}$$

$$C^{(ij)}_{\rm mm}(\ell) = \int_0^{\chi_{\rm hor}} {\rm d}\chi \, \frac{\bar{q}^{(i)}(\chi)\, \bar{q}^{(j)}(\chi)}{f_{\rm k}^2(\chi)} \, P_{\delta\delta}\left(\frac{\ell}{f_{\rm k}(\chi)}, \chi\right) ; \tag{8.27}$$

$$C^{(ij)}_{\rm gG}(\ell) = \int_0^{\chi_{\rm hor}} {\rm d}\chi \, \frac{p^{(i)}(\chi)\, q^{(j)}(\chi)}{f_{\rm k}^2(\chi)} \, P_{{\rm g}\delta}\left(\frac{\ell}{f_{\rm k}(\chi)}, \chi\right) ; \tag{8.28}$$

$$C^{(ij)}_{\rm gI}(\ell) = \int_0^{\chi_{\rm hor}} {\rm d}\chi \, \frac{p^{(i)}(\chi)\, p^{(j)}(\chi)}{f_{\rm k}^2(\chi)} \, P_{\rm gI}\left(\frac{\ell}{f_{\rm k}(\chi)}, \chi\right) ; \tag{8.29}$$

$$C^{(ij)}_{\rm mG}(\ell) = \int_0^{\chi_{\rm hor}} {\rm d}\chi \, \frac{\bar{q}^{(i)}(\chi)\, q^{(j)}(\chi)}{f_{\rm k}^2(\chi)} \, P_{\delta\delta}\left(\frac{\ell}{f_{\rm k}(\chi)}, \chi\right) ; \tag{8.30}$$

$$C^{(ij)}_{\rm mI}(\ell) = \int_0^{\chi_{\rm hor}} {\rm d}\chi \, \frac{\bar{q}^{(i)}(\chi)\, p^{(j)}(\chi)}{f_{\rm k}^2(\chi)} \, P_{\delta{\rm I}}\left(\frac{\ell}{f_{\rm k}(\chi)}, \chi\right) . \tag{8.31}$$

The terminology of both projected and three-dimensional power spectra is summarised in Table 8.1. The weights that enter the foregoing equations are the probability distribution of galaxies with comoving distance $p^{(i)}(\chi)$, and the ones defined in (8.10), and (8.19).

Good models of the three-dimensional source power spectra in the Limber equations (see also the right hand column of Table 8.1) are unknown except for the non-linear theory matter power spectrum $P_{\delta\delta}$. The distribution of galaxies is expected to follow the distribution of dark matter, so that the galaxy clustering power spectra should be related to $P_{\delta\delta}$. However, to date it is unknown how much the galaxy clustering deviates from dark matter clustering, in particular on small scales. This is usually expressed in terms of the galaxy bias $b_{\rm g}$, which is a function of both wavenumber k and redshift or line-of-sight distance χ. Hence, one can write

$$\begin{aligned} P_{\rm gg}(k,\chi) &= b_{\rm g}^2(k,\chi)\, P_{\delta\delta}(k,\chi) ; \\ P_{{\rm g}\delta}(k,\chi) &= b_{\rm g}(k,\chi)\, r_{\rm g}(k,\chi)\, P_{\delta\delta}(k,\chi) , \end{aligned} \tag{8.32}$$

where to describe the cross-correlation between matter and galaxy clustering, we introduced a correlation coefficient $r_{\rm g}$ in the second equality.

The intrinsic alignment power spectra depend on the intricacies of galaxy formation and evolution within their dark matter environment. Again, precise models of the intrinsic alignment have to rely on baryonic physics and are currently not available. For symmetry reasons we parametrise our lack of knowledge about the intrinsic alignment power spectra similarly to the galaxy bias as

$$\begin{aligned} P_{\rm II}(k,\chi) &= b_{\rm I}^2(k,\chi)\, P_{\delta\delta}(k,\chi) ; \\ P_{\delta{\rm I}}(k,\chi) &= b_{\rm I}(k,\chi)\, r_{\rm I}(k,\chi)\, P_{\delta\delta}(k,\chi) \end{aligned} \tag{8.33}$$

with the intrinsic alignment bias $b_{\rm I}$ and correlation coefficient $r_{\rm I}$ (following Bernstein 2009). Although the power spectrum $P_{\rm gI}$ could in principle contain a third, independent correlation coefficient, we assume that it is sufficient to write

$$P_{\rm gI}(k,\chi) = b_{\rm I}(k,\chi)\; r_{\rm I}(k,\chi)\; b_{\rm g}(k,\chi)\; r_{\rm g}(k,\chi)\; P_{\delta\delta}(k,\chi)\;, \tag{8.34}$$

i.e. we hypothesise that correlations between intrinsic number density fluctuations and intrinsic alignments can entirely be traced back to the effects of the intrinsic alignment bias and the galaxy bias. This is a strong assumption since instead of introducing a fifth completely unconstrained bias term, (8.34) establishes a link between the galaxy bias and intrinsic alignment biases.

We note that (8.34) is effectively included within the last term in curly brackets of Bernstein (2009), eq. (19). Bernstein (2009) uses a global unknown scalar $s^{g\kappa}$ to model an additional uncertainty in the cross-correlation between galaxy number density and intrinsic shear field, stating that this type of cross-correlation is expected to have a minimal effect on cosmological constraints. The parametrisation of (8.34) corresponds to $s^{g\kappa} = 0$ in the Bernstein (2009) notation.

Since it is realistic to assume that the galaxy distribution traces the matter distribution as well as that the intrinsic shear field is determined by the matter distribution, additional interplay between galaxy positions and intrinsic shapes should indeed be unimportant. Still the validity of (8.34) requires observational verification which can best be done by the simultaneous analysis of gravitational lensing and galaxy clustering studies as put forward in this chapter. The further consideration of the effects of an additional freedom in $P_{\rm gI}(k,\chi)$ is left to future work.

We will not limit the values of the correlation coefficients to the interval $[-1;+1]$. It is formally possible that $|r| > 1$ if our assumption about the statistics of the galaxy distribution, usually taken to be Poissonian, is incorrect (Bernstein 2009). Treating the correlation coefficients as completely free parameters, our choice of parametrisation in (8.32) and (8.33) is equivalent to modelling $P_{\rm gg}$ and $P_{{\rm g}\delta}$, or likewise $P_{\rm II}$ and $P_{\delta{\rm I}}$, independently.

We insert the parametrisations (8.32), (8.33), and (8.34) into the set of Limber equations and can this way relate all power spectra entering (8.4)-(8.6) to the three-dimensional matter power spectrum:

$$C^{(ij)}_{\rm GG}(\ell) = \int_0^{\chi_{\rm hor}} {\rm d}\chi\; \frac{q^{(i)}(\chi)\; q^{(j)}(\chi)}{f_{\rm k}^2(\chi)}\; P_{\delta\delta}\left(\frac{\ell}{f_{\rm k}(\chi)},\chi\right)\;; \tag{8.35}$$

$$C^{(ij)}_{\rm IG}(\ell) = \int_0^{\chi_{\rm hor}} {\rm d}\chi\; \frac{p^{(i)}(\chi)\; q^{(j)}(\chi)}{f_{\rm k}^2(\chi)}\; b_{\rm I}\left(\frac{\ell}{f_{\rm k}(\chi)},\chi\right)\; r_{\rm I}\left(\frac{\ell}{f_{\rm k}(\chi)},\chi\right)\; P_{\delta\delta}\left(\frac{\ell}{f_{\rm k}(\chi)},\chi\right)\;; \tag{8.36}$$

$$C^{(ij)}_{\rm II}(\ell) = \int_0^{\chi_{\rm hor}} {\rm d}\chi\; \frac{p^{(i)}(\chi)\; p^{(j)}(\chi)}{f_{\rm k}^2(\chi)}\; b_{\rm I}^2\left(\frac{\ell}{f_{\rm k}(\chi)},\chi\right)\; P_{\delta\delta}\left(\frac{\ell}{f_{\rm k}(\chi)},\chi\right)\;; \tag{8.37}$$

$$C^{(ij)}_{\rm gg}(\ell) = \int_0^{\chi_{\rm hor}} {\rm d}\chi\; \frac{p^{(i)}(\chi)\; p^{(j)}(\chi)}{f_{\rm k}^2(\chi)}\; b_{\rm g}^2\left(\frac{\ell}{f_{\rm k}(\chi)},\chi\right)\; P_{\delta\delta}\left(\frac{\ell}{f_{\rm k}(\chi)},\chi\right)\;; \tag{8.38}$$

$$C^{(ij)}_{\rm gm}(\ell) = 2\,(\alpha^{(j)}-1)\; C^{(ij)}_{\rm gG}(\ell)\;; \tag{8.39}$$

$$C^{(ij)}_{\rm mm}(\ell) = 4\,(\alpha^{(i)}-1)\;(\alpha^{(j)}-1)\; C^{(ij)}_{\rm GG}(\ell)\;; \tag{8.40}$$

$$C_{\mathrm{gG}}^{(ij)}(\ell) = \int_0^{\chi_{\mathrm{hor}}} \mathrm{d}\chi \, \frac{p^{(i)}(\chi)\, q^{(j)}(\chi)}{f_{\mathrm{k}}^2(\chi)} \, b_{\mathrm{g}}\left(\frac{\ell}{f_{\mathrm{k}}(\chi)}, \chi\right) \, r_{\mathrm{g}}\left(\frac{\ell}{f_{\mathrm{k}}(\chi)}, \chi\right) \, P_{\delta\delta}\left(\frac{\ell}{f_{\mathrm{k}}(\chi)}, \chi\right) \, ; \tag{8.41}$$

$$C_{\mathrm{gI}}^{(ij)}(\ell) = \int_0^{\chi_{\mathrm{hor}}} \mathrm{d}\chi \, \frac{p^{(i)}(\chi)\, p^{(j)}(\chi)}{f_{\mathrm{k}}^2(\chi)} \, b_{\mathrm{g}}\left(\frac{\ell}{f_{\mathrm{k}}(\chi)}, \chi\right) \, r_{\mathrm{g}}\left(\frac{\ell}{f_{\mathrm{k}}(\chi)}, \chi\right) \times b_{\mathrm{I}}\left(\frac{\ell}{f_{\mathrm{k}}(\chi)}, \chi\right) \, r_{\mathrm{I}}\left(\frac{\ell}{f_{\mathrm{k}}(\chi)}, \chi\right) \, P_{\delta\delta}\left(\frac{\ell}{f_{\mathrm{k}}(\chi)}, \chi\right) \, ; \tag{8.42}$$

$$C_{\mathrm{mG}}^{(ij)}(\ell) = 2\,(\alpha^{(i)} - 1)\, C_{\mathrm{GG}}^{(ij)}(\ell) \, ; \tag{8.43}$$

$$C_{\mathrm{mI}}^{(ij)}(\ell) = 2\,(\alpha^{(i)} - 1)\, C_{\mathrm{IG}}^{(ji)}(\ell) \, . \tag{8.44}$$

The matter power spectrum and the distances $f_{\mathrm{k}}(\chi)$, which also enter $q^{(i)}(\chi)$, depend on cosmology and can therefore be exploited to constrain cosmological parameters. While distances and $P_{\delta\delta}$ are well known from theory, the probability distribution of galaxies $p^{(i)}(\chi)$ has to be measured by using additional spectroscopic redshift information (e.g. Huterer et al. 2006; Ma et al. 2006; Abdalla et al. 2007; Bridle & King 2007; Bernstein & Huterer 2010) with a certain level of uncertainty. It may also be possible to infer some additional information from the cosmic shear data itself (Newman 2008; Schneider et al. 2006; Zhang et al. 2010). The same holds for the slopes of the luminosity function $\alpha^{(i)}$, which can be determined from the survey by studying the flux of galaxies close to the magnitude limit. The least known quantities in the equations above are the bias terms $\{b_{\mathrm{g}}, b_{\mathrm{I}}, r_{\mathrm{g}}, r_{\mathrm{I}}\}$, for which we will thus introduce a very general parametrisation in Sect. 8.2.3.

8.2 Modelling two-point statistics in cosmological surveys

In this section we detail the modelling of the terms entering (8.35) to (8.44). We specify how we parametrise the uncertainty in the galaxy redshift distributions, the slope of the luminosity function, and the bias terms. Moreover we describe our Fisher matrix approach and the way we infer the resulting errors on cosmological parameters.

8.2.1 Matter power spectrum & survey characteristics

As the basis for our analysis we compute matter power spectra for a spatially flat CDM universe with fiducial parameters $\Omega_{\mathrm{m}} = 0.25$, $\Omega_\Lambda = 0.75$, and $H_0 = 100\,h_{100}\,\mathrm{km/s/Mpc}$ with $h_{100} = 0.7$. We incorporate a variable dark energy model by parametrising its equation of state, relating pressure p_Λ to density ρ_Λ as outlined in Sect 2.2 via

$$p_\Lambda(z) = \left(w_0 + w_a \frac{z}{1+z}\right) \, \rho_\Lambda(z)\, c^2 \, , \tag{8.45}$$

where the ΛCDM Universe is chosen as the fiducial model, i.e. $w_0 = -1$ and $w_a = 0$. The dark energy density parameter is then given by (4.60). The primordial power spectrum of matter density fluctuations is assumed to be a power law with fiducial slope $n_{\mathrm{s}} = 1$. We employ the fiducial normalisation $\sigma_8 = 0.8$. The transfer function of Eisenstein & Hu (1998) is used without baryonic wiggles, computing the shape parameter with a fiducial value of $\Omega_{\mathrm{b}} = 0.05$.

The non-linear corrections to the power spectrum are computed by means of the fit formula by Smith et al. (2003). We account for the influence of dark energy on structure growth by modifying the halo model fitting routine of Smith et al. (2003) following the approach of Réfrégier et al. (2008). We provide a summary of this modification in Appendix 4.3.2.

The survey characteristics follow the rough specifications of a Stage IV experiment (Albrecht et al. 2006) such as the ESA Euclid satellite mission. To compute the noise properties, we assume the maximum extragalactic sky coverage of $A = 20000\,\mathrm{deg}^2$ and a total number density of galaxies $n = 35\,\mathrm{arcmin}^{-2}$. Shape noise is characterised by a total dispersion of intrinsic ellipticities of $\sigma_\epsilon = 0.35$. We refer to this survey as Euclid-like in the remainder of this chapter.

According to Smail et al. (1994) we assume an overall number of galaxies per unit redshift, per square arcminute

$$n_{\mathrm{tot}}(z) = \Sigma_0 \left(\frac{3z^2}{2\bar{z}^3}\right) \exp\left\{-\left(\frac{z}{\bar{z}}\right)^\beta\right\} \tag{8.46}$$

with the galaxy surface density Σ_0 and $\beta = 1.5$. The probability distribution over all the galaxies $p_{\mathrm{tot}}(z)$ is proportional to the number density $n_{\mathrm{tot}}(z)$. We set $\bar{z} = 0.64$, which produces a distribution with median redshift $z_{\mathrm{med}} = 0.9$. The distribution is cut at $z_{\mathrm{max}} = 3$ and then normalised to unity. For the tomography we define photometric bins by dividing the distribution (8.46) such that every bin contains the same number of galaxies. This choice is merely for computational convenience and to allow for an easy comparison between results with a different number of bins. As default we will use $N_{\mathrm{zbin}} = 10$ bins.

To account for photometric redshift errors, we assume that the fraction of catastrophic failures in the assignment of photometric redshifts is negligible, but include the spread of the true redshifts in the bin-wise distributions by writing the conditional probability of obtaining a photometric redshift z_{ph} given the true redshift z as

$$p(z_{\mathrm{ph}} \,|\, z) \propto \exp\left\{-\frac{(z_{\mathrm{ph}} - z)^2}{2\sigma_{\mathrm{ph}}^2\,(1+z)^2}\right\}\,, \tag{8.47}$$

where σ_{ph} denotes the photometric redshift dispersion. The redshift distribution of an individual photo-z bin $p^{(i)}(z)$ is then obtained by integrating (8.47) over the bin width and by weighting the result by the overall redshift distribution (8.46), see Chap. 6 for details. We use $\sigma_{\mathrm{ph}} = 0.05$ as our default value. This also follows the fiducial Model 1 of Ma et al. (2006).

Since the underlying redshift distributions $p^{(i)}(z)$ are determined by measurement, they are not perfectly known, but introduce further uncertainty into the analysis. A detailed analysis of the dependence of the joint analysis of galaxy shape and number density information on redshift parameters, and also the potential of calibrating these errors internally, will be investigated elsewhere (e.g. Zhang et al. 2010). Bridle & King (2007) have undertaken a more detailed study of the effect of redshift errors in the case of ellipticity correlations only. For the purpose of this work we assume that the value of σ_{ph} is unknown, i.e. we use it as a single, global parameter to account for the uncertainty in the redshift distributions. We employ a wide Gaussian prior on σ_{ph} of 10 for reasons of numerical stability.

8.2.2 Galaxy luminosity function

In order to calculate power spectra which include the lensing magnification signal, we need to model the slope of the cumulative galaxy luminosity function at the magnitude limit of the galaxy number density catalogue. In the following we extend observational results for the normalisation and redshift scaling of the galaxy redshift distribution (8.46) by Blake & Bridle (2005) to provide a fitting formula for the luminosity function slope as a function of redshift and survey magnitude limit.

Blake & Bridle (2005) have determined galaxy redshift distributions for a given magnitude limit, using COMBO-17 luminosity functions for the SDSS r filter (Wolf et al. 2003). They fitted

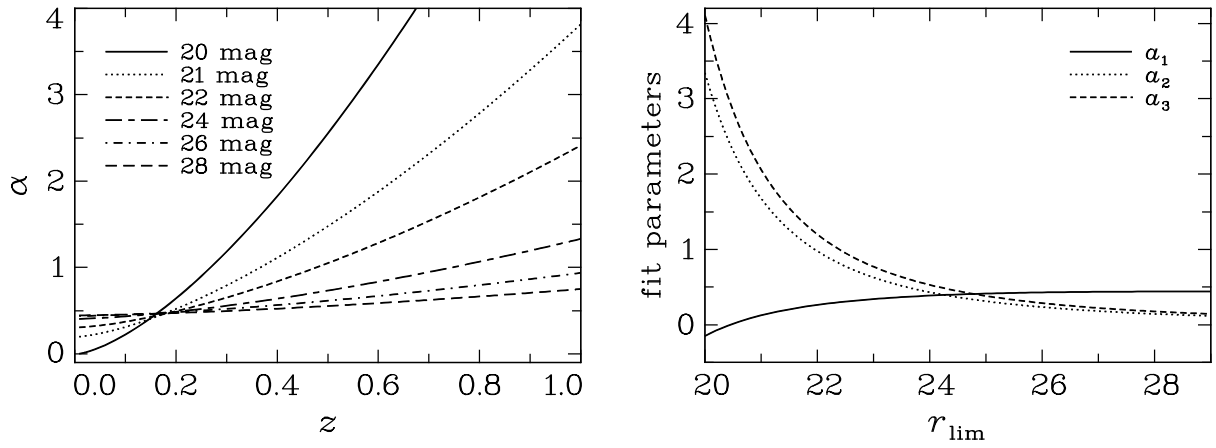

Figure 8.1: *Left panel*: Slope of the galaxy luminosity function α as a function of redshift, shown for different magnitude limits $r_{\rm lim}$ as indicated in the legend. *Right panel*: Fit parameters a_1 (solid), a_2 (dotted), and a_3 (dashed) as a function of $r_{\rm lim}$. These parameters are obtained from the polynomial fit in (8.49).

these distributions with functions of the form (4.47) with $\beta = 1.5$, using two free parameters, the redshift scaling $\bar{z}$ and the normalisation given by the galaxy surface density Σ_0. We set Σ_0 and $\bar{z}$ as a function of survey depth making use of Table 1 of Blake & Bridle (2005) and fit a power law to each quantity as a function of the limiting magnitude $r_{\rm lim}$,

$$\begin{aligned} \Sigma_0 &= \Sigma_{0,\,c}\left(\frac{r_{\rm lim}}{24}\right)^{\eta_\Sigma} \\ \bar{z} &= \bar{z}_c + \bar{z}_m\,(r_{\rm lim} - 24) \end{aligned} \tag{8.48}$$

where we find good fits using $\Sigma_{0,\,c} = 9.83$, $\eta_\Sigma = 19$, $\bar{z}_c = 0.39$ and $\bar{z}_m = 0.055$. This allows us to extrapolate beyond the range of their Table, which stops at $r_{\rm lim} = 24$.

We emphasise that in this work α denotes the negative slope of the cumulative luminosity function, and not the exponent of the Schechter function for faint galaxies which is also sometimes denoted by α (e.g. Wolf et al. 2003). Using our formalism, the slope of the Schechter function at the faint end is $-\alpha - 1$, so that the typical values of $\alpha \sim 0.5$ we find are consistent with the results of e.g. Liu et al. (2008) who find Schechter function exponent values between -1 and -2 depending on the spectral type for COSMOS.

We are interested in the slope of the luminosity function $\alpha(z, r_{\rm lim})$ at the cosmic shear survey magnitude limit. This slope is a function of redshift and magnitude limit. From (4.47) and (8.48) we have the number of galaxies as a function of redshift and magnitude limit. We convert each magnitude limit into a flux limit S and set the number of galaxies above the flux limit equal to $S^{-\alpha}$. The resulting curves for $\alpha(z, r_{\rm lim})$ are shown in Fig. 8.1, left panel.

For convenience, and to extrapolate the slope $\alpha(z, r_{\rm lim})$ to values $z > 1$, we now provide a fitting formula . First we expand the slope using a polynomial in redshift, with coefficients that depend on the limiting magnitude. Then we find an approximate equation for these coefficients as a function of limiting magnitude. This results in equations for the slope as a function of redshift and magnitude limit in terms of 15 numbers given in Table 8.2.

We fit the slope of the luminosity function as a function of redshift with a second-order polynomial

$$\alpha(z, r_{\rm lim}) = a_1(r_{\rm lim}) + a_2(r_{\rm lim})\,z + a_3(r_{\rm lim})\,z^2\ . \tag{8.49}$$

j	$b_{1\,j}$	$b_{2\,j}$	$b_{3\,j}$
1	0.44827	0	0
2	−1	+1	+1
3	0.05617	0.19658	0.18107
4	0.07704	3.31359	3.05213
5	−11.3768	−2.5028	−2.5027

Table 8.2: Fit parameters for the slope of the luminosity function as a function of limiting magnitude $r_{\rm lim}$ and redshift, see (8.49) and (8.50).

The polynomial coefficients a_i are functions of the limiting magnitude, and are shown in Fig. 8.1, right panel. We find that these coefficients are in turn well fit by a function of the form

$$a_i(r_{\rm lim}) = b_{i\,1} + b_{i\,2}\ (b_{i\,3}\, r_{\rm lim} - b_{i\,4})^{b_{i\,5}}\ , \tag{8.50}$$

with parameters $b_{i\,j}$ given in Table 8.2. We chose not to use $b_{i\,2}$ as a free parameter for the fit, but set it as $b_{i\,2} = \pm 1$, to determine the sign of the term in parentheses. By means of (8.49) and (8.50) we have condensed the dependence of α on redshift and $r_{\rm lim}$ into the 15 parameters summarised in Table 8.2.

In Fig. 8.2 we plot the relative accuracy of this set of fit formulae with respect to $\alpha(z, r_{\rm lim})$ as given in Fig. 8.1, lower panel. Over the dominant part of the considered parameter space the fit formulae provide an excellent approximation, which deviates less than 1 % from the original fits (8.48). Thus one can expect that within the framework of this approach (8.49) and (8.50) extrapolate $\alpha(z, r_{\rm lim})$ reasonably well to $z > 1$. Significantly larger deviations can only be found for the brightest limiting magnitudes at redshifts $z \lesssim 0.1$, a region of the parameter plane which is irrelevant for a competitive cosmological survey.

We use the fit given by (8.49) and (8.50) with the parameters listed in Table 8.2 to compute the slope of the luminosity function at $r_{\rm lim} = 24$. The discussion in this work applies to ground-based surveys because the COMBO-17 luminosity functions are calculated for the SDSS r filter as observed from the ground. A space mission to a depth of $r_{\rm lim} = 24$ will have a different luminosity function slope, corresponding more closely to a deeper ground-based survey, depending on the resolution of the space-based survey. We use results for $r_{\rm lim} = 24$ throughout this chapter for both ground and space surveys. We note that from Fig. 8.1, top panel, the slope of the luminosity function is changed little on increasing the survey depth beyond $r_{\rm lim} = 24$. This procedure could be improved by using deeper data which additionally feature infrared observations, for instance COSMOS ground- and space-based data or CFHTLS-Wide. However, since we use the slopes obtained this way only as fiducial values for our analysis, we do not expect the limited accuracy of this part of our modelling to have a significant impact on the analysis.

The fiducial slope in a photo-z bin i is defined as $\alpha^{(i)} \equiv \alpha(z^{(i)}_{\rm med}, r_{\rm lim} = 24)$, where $z^{(i)}_{\rm med}$ is the median redshift of bin i, see Sect. 8.1. We assume $\alpha^{(i)}$ is also measured from the survey itself, and therefore adds another source of uncertainty to the analysis which we account for by setting $\alpha^{(i)}$ to be free parameters for all $i = 1, .., N_{\rm zbin}$. Again we apply a wide Gaussian prior of 10 on every slope parameter, which does not have a measurable influence on our results, but merely ensures numerical stability.

8.2.3 Galaxy and intrinsic alignment bias

As already outlined in Sect. 8.1, the bias terms $b_X = \{b_{\rm g}, b_{\rm I}, r_{\rm g}, r_{\rm I}\}$ encoding the galaxy bias and intrinsic alignments are the least accurately known contributions to (8.35) to (8.44). We parametrise each of these terms on a grid in k and z, following Bridle & King (2007) whose ansatz is in turn similar to the recommendations by the Dark Energy Task Force (Albrecht et al.

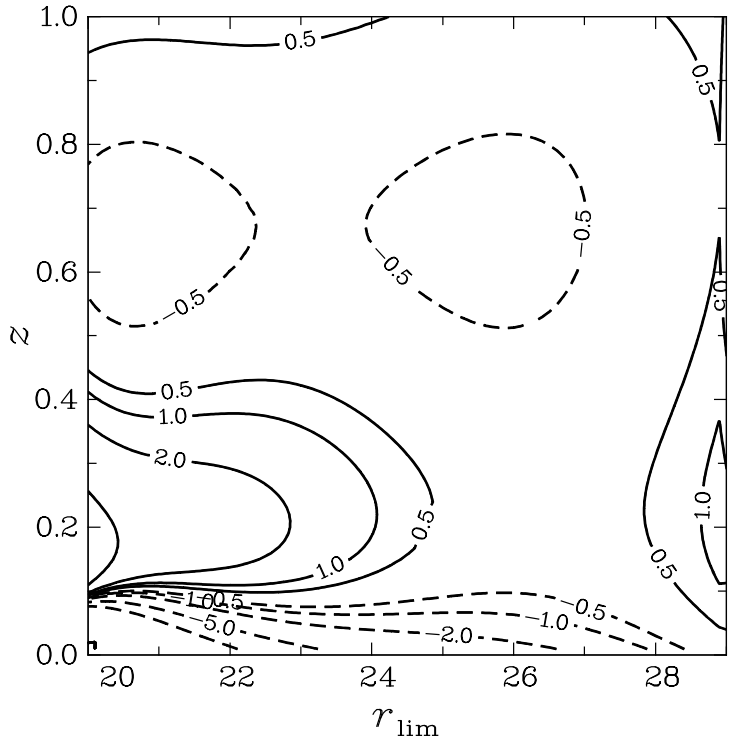

Figure 8.2: Percentage deviation of the simplified fit as defined in (8.49) and (8.50) from the original fits described by (8.48) and shown in the upper panel of Fig. 8.1. The contour levels correspond to the percentages given on the curves. Negative deviations are indicated by dashed contours. Note that across most of the parameter plane the modulus of the deviation is less than 1 %.

2006) and Bernstein (2009). Every bias term is assumed to vary around a fiducial functional form $b_X^{\rm base}$ as

$$b_X(k,\chi) = A_X\ Q_X\left(k, z(\chi)\right)\ b_X^{\rm base}(k,\chi)\ , \tag{8.51}$$

where $Q_X\left(k, z(\chi)\right)$ is an unknown two-dimensional function which comprises the aforementioned grid, and where A_X denotes an additional free overall amplitude. We use N_K bins in k and N_Z bins in redshift for each bias term and linearly interpolate in the logarithms of Q_X, k, and $1+z$, so that Q_X is given by

$$\begin{aligned}\ln Q_X\left(k,z\right) \;=\;& K_i(k)\ Z_j(z)\ B^X_{ij} + \left[1-K_i(k)\right]\ Z_j(z)\ B^X_{(i+1)\,j} \\ &+K_i(k)\ \left[1-Z_j(z)\right]\ B^X_{i\,(j+1)} + \left[1-K_i(k)\right]\ \left[1-Z_j(z)\right]\ B^X_{(i+1)\,(j+1)}\end{aligned} \tag{8.52}$$

for $k_i < k \le k_{i+1}$ and $z_j < z \le z_{j+1}$, where we defined

$$\begin{aligned}K_i(k) \;&\equiv\; \frac{\ln(k)-\ln(k_i)}{\ln(k_{i+1})-\ln(k_i)}\ ; \\ Z_j(z) \;&\equiv\; \frac{\ln(1+z)-\ln(1+z_j)}{\ln(1+z_{j+1})-\ln(1+z_j)}\ .\end{aligned} \tag{8.53}$$

The free parameters are the grid nodes B^X_{ij}. Since Q_X is a multiplicative function, one reproduces the base model $b_X^{\rm base}$ if $A_X = 1$ and if all B^X_{ij} vanish. The effect of this parametrisation on the observable projected power spectra is illustrated in Bridle & King (2007) for the case of intrinsic alignments.

The indices in (8.52) run from $i = 0, .., N_K+1$ and $0 = 1, .., N_Z+1$. We fix all parameters at the edge of the grid by setting the parameters with indices $i, j = 0$; $i = N_K+1$ or $j = N_Z+1$ to $B^X_{ij} = 0$, so that we have $N_K \times N_Z$ free grid parameters per bias term. We place the lowest and highest grid nodes at the limits of our integration ranges, so $k_0 = 3.3 \times 10^{-7} h\,{\rm Mpc}^{-1}$ and $k_{N_K+1} = 3.3 \times 10^{4} h\,{\rm Mpc}^{-1}$ in k, and in the redshift dimension $z_0 = 0$ and $z_{N_Z+1} = 19$. The grid nodes, which are free to vary, are log-linearly spaced in a smaller range, respectively. We

$N_K \times N_Z$	$\epsilon\epsilon$	nn	all
2×2	11	21	31
2×4	19	29	47
10×2	43	53	95
10×4	83	93	175
3×3	21	31	51
5×5	53	63	115
7×7	101	111	211

Table 8.3: Overview on the total number of nuisance parameters used for different setups. The label $\epsilon\epsilon$ corresponds to using ellipticity correlations only as the observables. Likewise, nn corresponds to using galaxy number density correlations only, and 'all ' to using all available correlations. For all entries we have assumed ten photometric redshift bins used for the tomography, $N_{\rm zbin} = 10$.

use $k_1 = 10^{-3} h\,\mathrm{Mpc}^{-1}$ and $k_{N_K} = 2h\,\mathrm{Mpc}^{-1}$, and for the redshift range $z_1 = z_0$ and $z_{N_Z} = 3$. In the special case of $N_K = 1$ we position the only free parameter in the k dimension at the centre between k_1 and k_{N_K}, and proceed likewise for redshifts.

It is important to note that while Bridle & King (2007) limit the flexible grid parametrisation to the non-linear regime of the power spectra, we attempt to cover all k ranges which substantially contribute to the observable power spectra. As we fix the grid values on the edges, the overall scaling of the bias terms is not free, so that we use the amplitude A_X as a further varying parameter throughout. To all bias term parameters we add a very wide Gaussian prior of standard deviation 50 to ensure numerical stability. Together with the global uncertainty on the redshift distributions, expressed in terms of $\sigma_{\rm ph}$, and the values of the slope of the galaxy luminosity function per photo-z bin, we obtain a large number of nuisance parameters that we determine simultaneously with the cosmological parameters of interest.

For later reference, we have summarised the total number of nuisance parameters for different setups in Table 8.3. While our parametrisation is fairly general and should capture most of the variability, it is of course possible that the bias terms depend on more parameters than k and z. For instance, it is well known that both intrinsic alignments and galaxy bias are a function of galaxy colour and luminosity which could be incorporated into our approach in the future. For observational constraints on this effect using intrinsic alignments see Mandelbaum et al. (2006); Hirata et al. (2007) and in galaxy biasing see McCracken et al. (2008); Swanson et al. (2008); Simon et al. (2009); Cresswell & Percival (2009); Wang et al. (2007) for recent examples.

To compute the fiducial models for all the power spectra entering the observables (8.4) to (8.6), we set $A_X = 1$ and all $B_{ij}^X = 0$, i.e. they are fully determined by the base models. We set

$$
\begin{aligned}
b_{\rm g}^{\rm base}(k,\chi) &= 1\,; & b_{\rm I}^{\rm base}(k,\chi) &= -C_1 \frac{\bar\rho(z)}{D(z)(1+z)}\,; \\
r_{\rm g}^{\rm base}(k,\chi) &= 1\,; & r_{\rm I}^{\rm base}(k,\chi) &= 1\,.
\end{aligned}
\tag{8.54}
$$

With the choice for $b_{\rm I}^{\rm base}$ and $r_{\rm I}^{\rm base}$ we reproduce the non-linear modification of the linear alignment model by Bridle & King (2007). Lacking solid physical motivation, it is yet in agreement with current observational evidence (Mandelbaum et al. 2006; see Bridle & King 2007 for a comparison) and the halo model studies by Schneider & Bridle (2010). It is based on the linear alignment model (Hirata & Seljak 2004) which is expected to provide a good description of intrinsic alignments on the largest scales. We assume the galaxy bias to be of order unity for our fiducial model, and set $r_{\rm g}^{\rm base}(k,\chi) = 1$. Note that most investigations of galaxy clustering consider much less flexibility in the galaxy bias.

In Fig. 8.3 we plot the fiducial angular power spectra of all considered signals for different combinations of photo-z bins. In the upper right panels the usual cosmic shear signal (GG) is

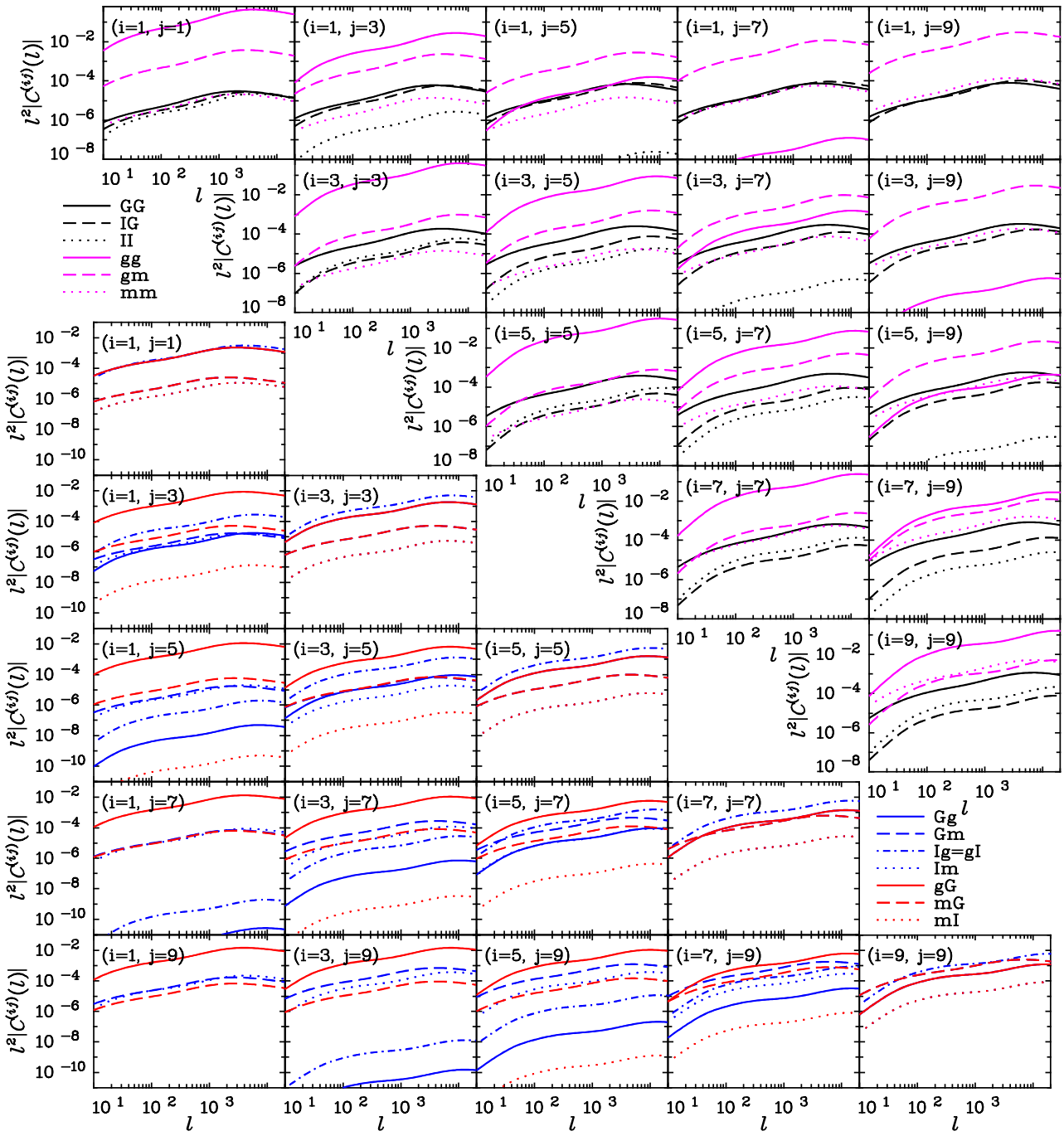

Figure 8.3: Fiducial power spectra for all considered correlations. The upper right panels depict the contributions to $\epsilon\epsilon$ (in black) and nn (in magenta) correlations. The lower left panels show the contributions to correlations between number density fluctuations and ellipticity. Since we only show correlations $C^{(ij)}_{\alpha\beta}(\ell)$ with $i \leq j$, we make in this plot a distinction between $n\epsilon$ (in red; number density contribution in the foreground, e.g. gG) and ϵn (in blue; number density contribution in the background, e.g. Gg) correlations. In each sub-panel a different tomographic redshift bin correlation is shown. For clarity only odd bins are displayed. See text for the explanation of the individual terms.

shown as a black solid lines; the intrinsic alignment GI term is shown by the black dashed lines; the intrinsic alignment II term is shown by the dotted black line; the usual galaxy clustering

signal (gg) is shown by the magenta solid line; the cross correlation between galaxy clustering and lensing magnification (gm) is shown by the magenta dashed line; the lensing magnification correlation functions (mm) are shown by the magenta dotted line. In the lower left panels the solid blue line shows the correlation between lensing shear and galaxy clustering (Gg); the blue dashed line shows the correlation between lensing shear and lensing magnification (gm); the blue dot-dashed line shows the correlation between intrinsic alignment and galaxy clustering (Ig or equivalently gI); the red solid line shows the correlation between galaxy clustering and lensing shear (gG), which is equivalent to the blue solid line with redshift bin indices i and j reversed; similarly the red dashed line shows the correlation between lensing magnification and lensing shear (mG), for cases where the magnification occurs at lower redshift than the shear ($i < j$); finally the dotted line shows the correlation between lensing magnification and intrinsic alignment (mI). Note that the ellipticity-number density cross-correlations are not symmetric under exchanging the photometric redshift bins. Hence, in this figure we treat nϵ and ϵn correlations, as well as all signals contributing to them, separately, keeping $i \leq j$ for all $C_{\alpha\beta}^{(ij)}(\ell)$.

The GG signal shows the usual behaviour of moderate increase with increasing redshift of the contributing photo-z-bins. The redshift scaling of the IG term is similar, but peaks when the source galaxies are at high redshift in the background (large j), while the galaxies that are intrinsically aligned are at low redshift (small i). For the model used here the IG contribution can even surpass the shear signal in this case. Due to the narrow kernel containing $p^{(i)}(\chi)\,p^{(j)}(\chi)$, see (8.37), the II signal is strong in the auto-correlations $i = j$, but drops off quickly as soon as the overlap of the redshift distributions decreases.

Due to the similar kernel, the scaling of the galaxy clustering contribution (gg) resembles the II term, but gg constitutes a much stronger signal. Lensing magnification (mm) adds the largest fraction of the galaxy number correlations at the highest redshifts, showing a slightly stronger redshift scaling than GG. However, the mm term always remains subdominant with respect to signals with a contribution from galaxy clustering; even for widely separated galaxy redshift distributions, say $i = 1$ and $j = 9$, and the gm cross-term is considerably stronger than mm. Such contributions might be a serious obstacle for probing cosmology with the lensing magnification signal as proposed by Broadhurst et al. (1995); Zhang & Pen (2005, 2006); van Waerbeke (2010). Yet in our approach, where the galaxy bias is taken into account and parametrised, the magnification signal yields a valuable contribution to the galaxy number correlations, which helps constraining the cosmological model.

The signals within the number density-ellipticity cross-correlations are not symmetric when swapping the photo-z bins. When the contribution by number density fluctuations stems from the foreground, the gG signal is strong, in particular if the photo-z bins are far apart in redshift, whereas the 'Gg' (in the notation of Fig. 8.3) drops off fast if $i < j$ because the shear signal of foreground galaxies is not correlated with the clustering of galaxies at much higher redshift. The mG, Gm, and GG signals differ only by the term including the slope of the luminosity function and thus have similar amplitudes. Correlations between intrinsic alignment and magnification (mI and Im) are subdominant throughout, obtaining their largest amplitudes if intrinsic alignments at low redshifts are combined with the magnification signal from galaxies far in the background, i.e. in the figure for Im at $i = 1$ and $j = 9$. Finally, the symmetric Ig term is the largest contribution for auto-correlations of number density-ellipticity observables, but decreases quickly in the cross terms, again due to the kernel $p^{(i)}(\chi)\,p^{(j)}(\chi)$ since we have assumed the photometric redshift errors are reasonably well behaved, without catastrophic outliers. Note that we have plotted the absolute values of the power spectra in Fig. 8.3 and that the correlations IG, gm, Gm, mG, and gI are negative.

8.2.4 Parameter constraints

We determine constraints on our parameters using a Fisher matrix analysis. To account for the errors and correlations of our observables, we compute covariances of the power spectra (8.4) to (8.6) in the Gaussian approximation, extending the results of Joachimi et al. (2008); see also Hu & Jain (2004). If we denote the difference between estimator and its ensemble average by $\Delta C_{\alpha\beta}^{(ij)}(\ell)$, one can write for the covariance

$$\begin{aligned}\left\langle \Delta C_{\alpha\beta}^{(ij)}(\ell)\, \Delta C_{\gamma\delta}^{(kl)}(\ell') \right\rangle &= \delta_{\ell\ell'} \frac{2\,\pi}{A \ell \Delta\ell} \left\{ \bar{C}_{\alpha\gamma}^{(ik)}(\ell)\, \bar{C}_{\beta\delta}^{(jl)}(\ell) + \bar{C}_{\alpha\delta}^{(il)}(\ell)\, \bar{C}_{\beta\gamma}^{(jk)}(\ell) \right\} \\ &\equiv \mathrm{Cov}_{\alpha\beta\gamma\delta}^{(ijkl)}(\ell)\,,\end{aligned} \tag{8.55}$$

where A is the survey size and $\Delta\ell$ the width of the corresponding angular frequency bin. As the Kronecker symbol $\delta_{\ell\ell'}$ indicates, the covariance is diagonal in ℓ in the Gaussian limit, which keeps the computation and inversion of (8.55) tractable. The subscripts $\{\alpha, \beta, \gamma, \delta\}$ can be either ϵ or n, where $C_{\epsilon n}^{(ij)}(\ell) \equiv C_{n\epsilon}^{(ji)}(\ell)$ holds. To account for the shot and shape noise contributions induced by the random terms in (8.1) and (8.2), we have defined

$$\bar{C}_{\alpha\beta}^{(ij)}(\ell) \equiv C_{\alpha\beta}^{(ij)}(\ell) + N_{\alpha\beta}^{(ij)}\,, \tag{8.56}$$

the second term given by

$$\begin{aligned} N_{\alpha\beta}^{(ij)} &= \delta_{ij}\, \frac{\sigma_\epsilon^2}{2\bar{n}^{(i)}} \quad \text{for } \alpha = \beta = \epsilon\,; \\ N_{\alpha\beta}^{(ij)} &= \delta_{ij}\, \frac{1}{\bar{n}^{(i)}} \quad \text{for } \alpha = \beta = n\,; \\ N_{\alpha\beta}^{(ij)} &= 0 \quad \text{for } \alpha \neq \beta\,. \end{aligned} \tag{8.57}$$

Here σ_ϵ^2 denotes the total intrinsic ellipticity dispersion, and $\bar{n}^{(i)}$ is the average galaxy number density per steradian in photo-z bin i.

Combining the observable power spectra, we compose the total data vector

$$\begin{aligned}\mathcal{D}(\ell) = \Big\{ & C_{\epsilon\epsilon}^{(11)}(\ell), \ldots, C_{\epsilon\epsilon}^{(N_\mathrm{zbin}N_\mathrm{zbin})}(\ell), C_{n\epsilon}^{(11)}(\ell), \ldots, \\ & C_{n\epsilon}^{(N_\mathrm{zbin}N_\mathrm{zbin})}(\ell), C_{nn}^{(11)}(\ell), \ldots, C_{nn}^{(N_\mathrm{zbin}N_\mathrm{zbin})}(\ell) \Big\}^\tau\end{aligned} \tag{8.58}$$

for every angular frequency considered. The corresponding covariance, again for every ℓ, reads

$$\mathrm{Cov}(\ell) = \left(\begin{array}{c|c|c} \mathrm{Cov}_{\epsilon\epsilon\epsilon\epsilon}^{(ijkl)}(\ell) & \mathrm{Cov}_{\epsilon\epsilon n\epsilon}^{(ijkl)}(\ell) & \mathrm{Cov}_{\epsilon\epsilon nn}^{(ijkl)}(\ell) \\ \hline \mathrm{Cov}_{n\epsilon\epsilon\epsilon}^{(ijkl)}(\ell) & \mathrm{Cov}_{n\epsilon n\epsilon}^{(ijkl)}(\ell) & \mathrm{Cov}_{n\epsilon nn}^{(ijkl)}(\ell) \\ \hline \mathrm{Cov}_{nn\epsilon\epsilon}^{(ijkl)}(\ell) & \mathrm{Cov}_{nnn\epsilon}^{(ijkl)}(\ell) & \mathrm{Cov}_{nnnn}^{(ijkl)}(\ell) \end{array} \right)\,, \tag{8.59}$$

with the block matrices given by (8.55). The number of galaxy ellipticity ($\epsilon\epsilon$) and number density (nn) observables entering $\mathcal{D}(\ell)$ is $N_\mathrm{zbin}\,(N_\mathrm{zbin}+1)\,/2$, respectively, while there are N_zbin^2 ellipticity-number density cross terms ($n\epsilon$), which are not symmetric. In the analysis that follows we will also consider $\epsilon\epsilon$ and nn correlations only. In these cases the covariance (8.59) is reduced accordingly to its upper left or lower right block.

For reasons of computational time the total number of parameters that we can consider is limited to a few hundred. As a consequence the k dependence of the galaxy bias can not be parametrised by more than about ten parameters per redshift grid node. This number might not provide enough freedom in b_g (and r_g) to represent a sufficiently general set of functional

z-bin	$z_{\rm med}$	$\ell^{\rm g}_{\rm max}$	$N_\ell^{\rm max}$
1	0.33	45	13
2	0.51	103	20
3	0.63	145	23
4	0.74	206	26
5	0.85	260	28
6	0.96	329	30
7	1.08	369	31
8	1.23	466	33
9	1.42	588	35
10	1.79	937	39

Table 8.4: Overview on the cuts in angular frequency for the default set of parameters with $N_{\rm zbin} = 10$ and $\sigma_{\rm ph} = 0.05$, using (8.60) and (8.61). For each photo-z bin the median redshift $z_{\rm med}$, the maximum angular frequency $\ell^{\rm g}_{\rm max}$, and the corresponding number of usable angular frequency bins $N_\ell^{\rm max}$ (out of the total of 50) is given.

forms, which inadvertently may cause strong constraints on cosmological parameters due to the strong signal of galaxy clustering. Hence, we follow existing studies of galaxy clustering by discarding the clustering contribution in the non-linear regime where the signal is largest and the form of the galaxy bias most uncertain.

Rassat et al. (2008) calculated wave vectors $k_{\rm lin}^{\rm max}$ as a function of redshift at which the three-dimensional power spectrum has to be cut off to avoid number density fluctuations above a certain threshold, used as an indicator for non-linearity. Since we do still have a fairly general parametrisation of the bias terms associated with galaxy bias, we can afford to include the mildly non-linear regime into our analysis. Consulting Fig. 2 of Rassat et al. (2008), we choose a simple linear parametrisation of the form

$$k_{\rm lin}^{\rm max}(z) \approx 0.132\, z\, h\,{\rm Mpc}^{-1}\,. \tag{8.60}$$

This relation roughly coincides with the fiducial curve in the figure, producing slightly more conservative cuts at low redshifts.

We do not cut the three-dimensional power spectrum in k-space, but instead exclude projected power spectra above a threshold angular frequency from the Fisher matrix analysis. This maximum angular frequency is computed via

$$\ell^{{\rm g}\,(i)}_{\rm max} = k_{\rm lin}^{\rm max}(z^{(i)}_{\rm med})\; f_{\rm k}\left(\chi(z^{(i)}_{\rm med})\right)\,, \tag{8.61}$$

where we choose as a characteristic redshift of bin i the median redshift $z^{(i)}_{\rm med}$. Hence, we obtain a cut-off ℓ for every photo-z bin. We choose that $\epsilon\epsilon$ correlations are not at all affected by this cut-off because they are not dominated by terms involving galaxy bias. We impose $\ell^{{\rm g}\,(i)}_{\rm max}$ on $n\epsilon$ correlations, where i is the photo-z bin from which the number density signal stems. For observables $C_{nn}^{(ij)}(\ell)$ we use the cut-off calculated for bin j. Note that, due to the fast drop-off of the galaxy clustering signal with increasingly different median redshifts of bins i and j, the more optimistic choice of bin j over i in the latter case should not influence our results decisively.

To compute the Fisher matrix, we use $N_\ell = 50$ angular frequency bins, spaced logarithmically between $\ell_{\rm min} = 10$ and $\ell_{\rm max} = 3000$, the latter value being a conservative maximum for future surveys. We assume that the covariance of the power spectra is independent of the cosmological parameters, so that it does not contribute to the constraints. Then the Fisher matrix reads (e.g. Tegmark et al. 1997, see also Appendix A)

$$F_{\mu\nu} = \sum_{m,n}^{N_d} \sum_{\ell}^{N_\ell^{\rm max}(m,n)} \frac{\partial \mathcal{D}_m(\ell)}{\partial p_\mu}\, {\rm Cov}^{-1}_{mn}(\ell)\, \frac{\partial \mathcal{D}_n(\ell)}{\partial p_\nu}\,, \tag{8.62}$$

where N_d is the dimension of $\mathcal{D}(\ell)$. The first summation in (8.62) runs over all $N_\ell^{\max}$ usable angular frequency bins. The number of usable bins depends on the type of correlation and is determined by the cut-off angular frequency as described above. For the default setup we have summarised $z_{\rm med}^{(i)}$, $\ell_{\max}^{{\rm g}\,(i)}$, and the number of usable bins for every photo-z bin in Table 8.4. The derivatives in (8.62) are taken with respect to the elements of the parameter vector

$$\boldsymbol{p} = \left\{ \Omega_{\rm m}, \sigma_8, h_{100}, n_{\rm s}, \Omega_{\rm b}, w_0, w_a; \sigma_{\rm ph}, \alpha^{(1)}, \,..\,, \alpha^{(N_{\rm zbin})}, B_{11}^{b_{\rm g}}, \;\; .. \;\; , B_{N_K\,N_Z}^{r_{\rm I}} \right\}^\tau . \tag{8.63}$$

The first seven entries of $\boldsymbol{p}$ correspond to the cosmological parameters that we are interested in, while the remaining nuisance parameters account for the uncertainty in the galaxy redshift distribution, the slope of the galaxy luminosity function, the intrinsic alignments, and the galaxy bias, see Table 8.3. In summary, we use a maximum of $N_\ell(2N_{\rm zbin}^2 + N_{\rm zbin})$ observables (actually significantly less due to the ℓ-cuts of the galaxy number density signals) to measure a total of $4N_ZN_K + N_{\rm zbin} + 8$ parameters. Note that since we have referred all signals contributing to the observables (8.4) to (8.6) to the matter power spectrum, they all constrain the set of cosmological parameters; none of them is fixed when calculating (8.62).

The minimum variance bound of the error on a parameter p_μ, if determined simultaneously with all other parameters, is given by $\sigma(p_\mu) = \sqrt{(F^{-1})_{\mu\mu}}$. This error provides us with a lower bound on the marginalised $1\,\sigma$-error on p_μ. To assess the statistical power of the survey by means of a single number, we use the figure of merit (FoM) suggested by the Dark Energy Task Force (DETF) Report (Albrecht et al. 2006),

$${\rm FoM}_{\rm DETF} = \frac{1}{\sqrt{\det\left(F^{-1}\right)_{w_0w_a}}} , \tag{8.64}$$

where the subscript 'w_0w_a' denotes the 2×2 sub-matrix of the inverse Fisher matrix that corresponds to the entries belonging to the two dark energy parameters. Note that different prefactors for (8.64) are used in the literature. To allow for direct comparison with Bridle & King (2007), divide our findings for the ${\rm FoM}_{\rm DETF}$ by four.

While (8.64) is restricted to the quality of constraints on dark energy, we also seek to consider the errors on all cosmological parameters of interest. We are interested in the total volume of the error ellipsoid in parameter space, which is measured by the determinant of the Fisher matrix. Hence, we define

$${\rm FoM}_{\rm TOT} \equiv \ln\left(\frac{1}{\det\left(F^{-1}\right)_{\rm cosm.}}\right) , \tag{8.65}$$

where only the sub-matrix of the inverse Fisher matrix that corresponds to the seven cosmological parameters under investigation is used in the determinant, as indicated by the subscript. The determinant of the inverse is computed in order to take the effect of marginalising over nuisance parameters into account.

8.3 Results

Based on the Fisher matrix formalism described in the foregoing section, we will now analyse the performance of a cosmological galaxy survey with combined number density and shear information. We are going to investigate the residual information content in the data after marginalising over models of the intrinsic alignments and the galaxy bias with varying degrees

of freedom. Furthermore, we will study the dependence of our FoM on the number of photo-z bins and the width of the bin-wise redshift distributions as well as on the priors imposed on the nuisance parameters. The information contained in the individual signals and their susceptibility to the nuisance parameters is also assessed. Throughout this section we use the default survey characteristics and parameter values unless specified otherwise.

8.3.1 Dependence on intrinsic alignments and galaxy bias

The four bias terms $\{b_\mathrm{g}, b_\mathrm{I}, r_\mathrm{g}, r_\mathrm{I}\}$ each comprise $N_K \times N_Z + 1$ nuisance parameters. The galaxy ellipticity ($\epsilon\epsilon$) power spectra only contain the two intrinsic alignment bias terms, whereas the number density correlations (nn) are only affected by the galaxy bias terms. The cross-correlations between ellipticity and number density link those signals which depend on both galaxy bias and intrinsic alignments and thus allow for their internal cross-calibration. An example is the study by Zhang (2008) which investigates the interrelations between the IG, gI, and gg terms.

In Fig. 8.4 both figures of merit are plotted as a function of N_K and N_Z, respectively. If we restrict our analysis to $\epsilon\epsilon$ correlations only, our setup is similar to the most realistic setup considered in Bridle & King (2007). We reproduce their result that the $\mathrm{FoM}_\mathrm{DETF}$ drops as a function of N_K, dropping most sharply at small N_K and then levelling off. It falls significantly below the reference value of the $\mathrm{FoM}_\mathrm{DETF}$ computed for a pure GG signal. However, while Bridle & King (2007) find a decrease by about a factor of 2 for $N_K = 10$ and $N_Z = 2$ compared to the lensing only case, our $\mathrm{FoM}_\mathrm{DETF}$ decreases by more than a factor of 4. This discrepancy can be traced back to the fact that Bridle & King (2007) limit the nuisance parameter gridding to the nonlinear regime in k-space.

We additionally plot the figures of merit as a function of N_Z, finding that the $\epsilon\epsilon$ results do in fact flatten as N_Z reaches high values around 10. We find a very similar behaviour in terms of the $\mathrm{FoM}_\mathrm{TOT}$. The dark energy parameters suffer more than other parameters from the uncertainty of the bias terms in the redshift direction, as the $\mathrm{FoM}_\mathrm{DETF}$ deteriorates faster than the $\mathrm{FoM}_\mathrm{TOT}$ as a function of N_Z.

With our default settings the pure nn correlations constrain cosmology much more weakly than ellipticity correlations. Recall that our galaxy clustering analysis uses a much more flexible bias parametrisation than most other work. Using a small number of nuisance parameters we get a $\mathrm{FoM}_\mathrm{DETF}$ which is marginally above unity. This result is of the same order of magnitude as the findings of Rassat et al. (2008) who determine $\mathrm{FoM}_\mathrm{DETF} = 4.2$ for a spectroscopic, space-based survey in the spherical harmonics approach. Contrary to us, Rassat et al. (2008) use a less flexible bias parametrisation and include BAO features, but neglect magnification effects in their study. The decrease in both figures of merit for a larger number of nuisance parameters is more pronounced than for $\epsilon\epsilon$ correlations, in particular as a function of N_Z.

We have also shown the results obtained without the additional angular frequency cuts in Fig. 8.4 (i.e. the maximum angular frequency is $\ell_\mathrm{max} = 3000$ for all angular power spectra). Because the full galaxy clustering signal is strong and a comparatively direct probe of the dark matter power spectrum if the galaxy bias is well known, the values of the figures of merit are much higher in this case and even surpass the lensing-only level if few nuisance parameters are used. This corresponds to the case where we have a reasonably good understanding of galaxy biasing over a large range of scales, into the deeply non-linear regime. For larger N_K and N_Z the decrease in FoM is considerable, but weaker than with ℓ-cuts.

In the limit of a large number of nuisance parameters we expect that the galaxy bias is parametrised in a sufficiently flexible way, such that the curves with and without ℓ-cuts should coincide or at least be of the same order of magnitude. Since this is not the case, and since there

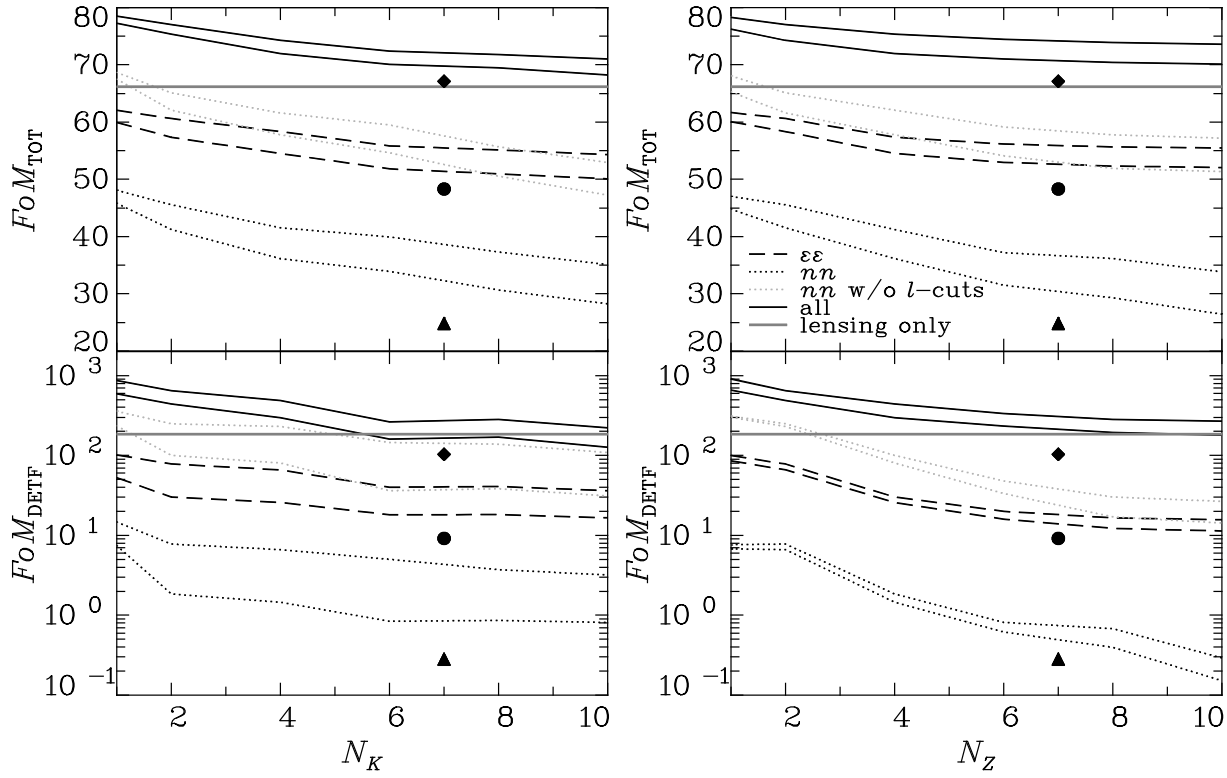

Figure 8.4: *Left panels*: Figures of merit as a function of the number of free parameters as a function of wave vector N_K in the bias terms. For each line type, the upper curve is obtained for a number of free bias parameters as a function of redshift $N_Z = 2$, the lower is for $N_Z = 4$. *Right panels*: Same as on the left, but as a function of N_Z, i.e. the number of redshift parameters in the bias terms. The upper curves for each set correspond now to $N_K = 2$ and the lower ones to $N_K = 4$, respectively. *Upper panels*: Figure of merit taking into account the full cosmological parameter space, $\mathrm{FoM}_{\mathrm{TOT}}$, see (8.65). *Lower panels*: Dark Energy figure of merit from the Dark Energy Task Force $\mathrm{FoM}_{\mathrm{DETF}}$, see (8.64). Dashed curves correspond to results using galaxy ellipticity correlations ($\epsilon\epsilon$) only, dotted black curves to galaxy number density correlations (nn) only, and solid black curves to results using all correlations ($\epsilon\epsilon$, nn and ϵn). The grey dotted lines show results for nn correlations without imposing cuts in angular frequency. The constant grey line marks the FoM computed for the pure lensing, i.e. GG, signal, assuming intrinsic alignments do not exist. In addition we show the resulting figures of merit when using our most flexible parametrisation with $N_K = N_Z = 7$ as filled symbols. Circles correspond to $\epsilon\epsilon$, triangles to nn, and diamonds to all correlations.

is no obvious sign of a lower boundary that the figures of merit are approaching, we hypothesise that this limit is only achieved for a very large, numerically and computationally prohibitive, number of nuisance parameters. Thus, the use of the additional angular frequency cuts in our default analysis is the most practical way to take into account our lack of understanding of galaxy biasing on small scales.

The simultaneous use of all available observables significantly boosts the parameter constraints, due to the addition of extra information from the survey, and due to breaking degeneracies between cosmological and nuisance parameters. The $\mathrm{FoM}_{\mathrm{DETF}}$ is up to a factor of about 50 higher than the lensing-only value. Both figures of merit decrease for larger N_K and N_Z, attaining mostly shallow slopes at $N_K, N_Z \approx 10$. Considering the most flexible model in each panel of Fig. 8.4, the $\mathrm{FoM}_{\mathrm{TOT}}$ remains above, but close to the value for a pure GG

Table 8.5: Marginalised parameter errors and the two Figures of Merit for a survey with ten photometric redshift bins used for tomography $N_{\rm zbin} = 10$ and a photometric redshift uncertainty parameter $\sigma_{\rm ph} = 0.05$. We have used the configuration with the maximum set of nuisance parameters, i.e. $N_K = N_Z = 7$ we consider. The cuts in angular frequency for number density correlations have been applied to restrict the analysis to the linear regime. Shown are the results using shear-shear correlations $\epsilon\epsilon$ only, observed galaxy clustering correlations nn only, all correlations, and the lensing-only signal (assuming no intrinsic alignments). The left-hand part of the table uses the standard Euclid-like survey parameters , i.e. $\sigma_\epsilon = 0.35$, $n = 35\,\mathrm{arcmin}^{-2}$, and the survey area $A = 20000\,\mathrm{deg}^2$. The right-hand part of the table uses parameters for a DES-like survey, i.e. $\sigma_\epsilon = 0.23$, $n = 10\,\mathrm{arcmin}^{-2}$, and the survey area $A = 5000\,\mathrm{deg}^2$.

par.	Euclid-like survey				DES-like survey			
	$\epsilon\epsilon$	nn	all	lensing	$\epsilon\epsilon$	nn	all	lensing
$\Omega_{\rm m}$	0.0228	0.1530	0.0079	0.0044	0.0636	0.3620	0.0233	0.0120
σ_8	0.0295	0.1800	0.0110	0.0065	0.0827	0.5941	0.0335	0.0180
h_{100}	0.2072	0.4273	0.0647	0.1099	0.5447	1.1092	0.1918	0.2837
$n_{\rm s}$	0.0721	0.2218	0.0312	0.0250	0.2117	1.0130	0.0973	0.0661
$\Omega_{\rm b}$	0.0224	0.0329	0.0063	0.0133	0.0557	0.0771	0.0166	0.0341
w_0	0.3242	1.6404	0.0939	0.0579	0.9064	4.3967	0.2895	0.1631
w_a	1.1995	5.6187	0.3051	0.2014	3.4754	18.2522	0.9865	0.5728
$\mathrm{FoM}_{\rm TOT}$	48.30	24.80	67.13	66.12	33.64	7.70	51.87	52.29
$\mathrm{FoM}_{\rm DETF}$	9.12	0.28	102.92	182.96	1.08	0.04	10.96	24.92

signal while the $\mathrm{FoM}_{\rm DETF}$ degrades slightly below the lensing-only value. In contrast to the setup with $\epsilon\epsilon$ or nn correlations only, the decrease is less pronounced with N_Z than N_K here, i.e. the cross-calibration between all correlations can partially compensate the loss in redshift information that affected the dark energy parameters in the former cases.

The most flexible configuration we consider has $N_K = N_Z = 7$ which corresponds to 200 nuisance parameters within the four bias terms. This limit is not inherent to our method, but is merely set for computational practicality. Both the intrinsic alignments and the galaxy bias have a physical origin and therefore are expected to produce smooth signals, which should not oscillate strongly or feature sharp peaks. Hence on the default angular scales used this model with 100 free parameters for each of intrinsic alignments and galaxy bias should yield a fairly general representation of the signals if one can rely on coarse prior information on the fiducial base model.

The figures of merit and the individual parameter errors for the most flexible model are given in Table 8.5, for the pure GG signal, $\epsilon\epsilon$, nn, and all correlations. Compared to lensing alone, the $\mathrm{FoM}_{\rm DETF}$ decreases by about a factor of 20 for $\epsilon\epsilon$ correlations, which means that cosmic shear is severely affected if one assumes very little prior knowledge about intrinsic alignments. There are hardly any dark energy constraints for nn correlations only, given this freedom in the galaxy bias. However, using all available correlation simultaneously, we can recover just over half of the pure cosmic shear DETF figure of merit. We find that the total error volume of the cosmological parameters, i.e. the $\mathrm{FoM}_{\rm TOT}$, is the same using all the correlation information as for the lensing-only case. Looking at the marginalised parameter errors, w_0 and w_a suffer particularly strongly in the $\epsilon\epsilon$ only and nn only case. Less information about the dark energy parameters is lost if all correlations are used, and the constraints on h_{100} and $\Omega_{\rm b}$ improve over the lensing-only case. In Fig. 8.5 we show in addition the marginalised $1\,\sigma$-error ellipses of all

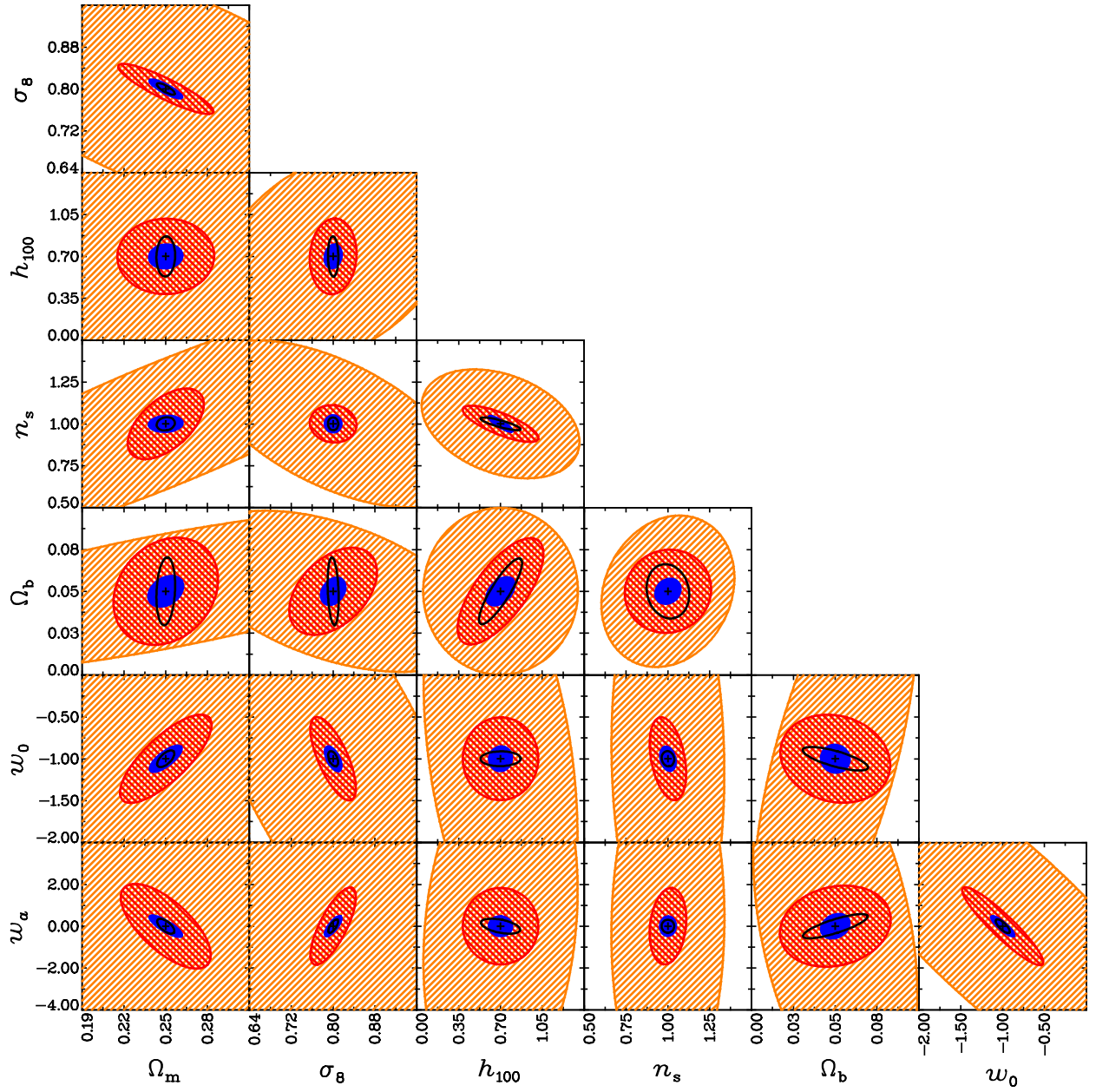

Figure 8.5: $1\,\sigma$-contours for all pairs of cosmological parameters considered, marginalised over all other parameters. We have used a photometric redshift uncertainty parameter value $\sigma_{\rm ph} = 0.05$, ten photometric redshift bins for tomography $N_{\rm zbin} = 10$, and the most flexible intrinsic alignment and bias model considered in this chapter, with over two hundred free parameters ($N_K = 7$, and $N_Z = 7$). Orange (light hatched) confidence regions result from using galaxy number density correlations (nn) (excluding the non-linear regime) only, red (dark hatched) regions use ellipticity correlations ($\epsilon\epsilon$) alone, and blue (filled) regions correspond to using all available information including density-ellipticity cross-correlations. For reference, the contours obtained from a pure lensing signal are shown as black lines. Flat priors on cosmological parameters have been applied.

possible pairs of cosmological parameters for the same setup. The degeneracy directions are fairly similar for the usual lensing only case and the results with all correlations presented in this chapter.

We repeat this analysis for a nearer term Stage-III-like survey such as the Dark Energy

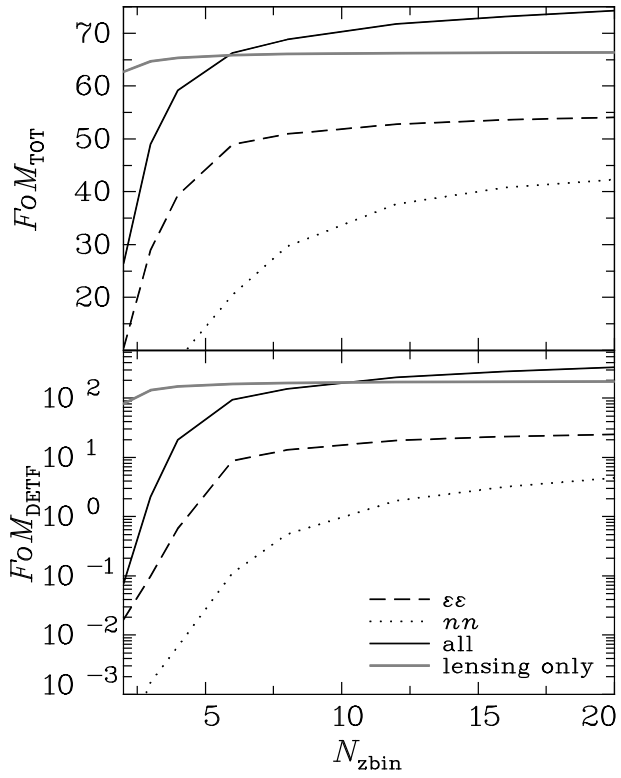

Figure 8.6: *Upper panel*: The Figure of Merit for all cosmological parameter space $\mathrm{FoM_{TOT}}$ as a function of the number of photo-z bins used for tomography N_{zbin}, shown for $\epsilon\epsilon$ (dashed line), nn (dotted line), and all (solid) correlations. The grey line corresponds to results for lensing only (GG). Throughout, $N_K = N_Z = 5$ nuisance parameters for the bias terms are used. These results are obtained for the standard set of parameters and $\sigma_{\mathrm{ph}} = 0.05$. *Lower panel*: Same as above, but in terms of the dark energy figure of merit $\mathrm{FoM_{DETF}}$.

Survey (DES). To this end, we use a survey size of $A = 5000\,\mathrm{deg}^2$, a median redshift of the overall redshift distribution of $z_{\mathrm{med}} = 0.8$, a total number density of galaxies of $n = 10\,\mathrm{arcmin}^{-2}$, and a total ellipticity dispersion of $\sigma_\epsilon = 0.23$, keeping all other parameters at their default values. We refer to this survey as DES-like for the rest of the chapter. Note that the DES and Euclid collaborations use different conventions for quoting the number density of galaxies and the corresponding ellipticity dispersion. The well-defined, physically meaningful quantity is the shape noise contribution given by $\sigma_\epsilon/\sqrt{n}$. Due to these different conventions, we use a smaller σ_ϵ for DES than Euclid, with a correspondingly low galaxy number density.

Our findings are also shown in Table 8.5. For the DES-like survey the $\mathrm{FoM_{TOT}}$ for all correlations is again about the same as in the lensing-only case, and the ratios of $\mathrm{FoM_{DETF}}$ values are slightly smaller than for the Stage-IV-like survey. The $\mathrm{FoM_{DETF}}$ values for $\epsilon\epsilon$, nn, and all possible correlations are about a factor of ten larger from the Stage-IV-like cosmic shear survey than the Stage-III-like survey, offering significant benefit beyond the minimal requirement of Albrecht et al. (2006).

8.3.2 Dependence on characteristics of the redshift distribution

It is well known that dividing the galaxy sample into several redshift photo-z bins greatly improves constraints from cosmic shear, but due to the broad lensing kernel (8.10) there is little benefit in having more distributions than three to five (e.g. Hu 1999; Simon et al. 2004; Ma et al. 2006). This result does not hold true anymore if one aims at controlling the intrinsic alignment contamination in the cosmic shear signal, mainly manifest via its characteristic redshift dependence. Using both marginalisation (Bridle & King 2007) and parameter-free approaches (Joachimi & Schneider 2008; see also Chap. 6), one finds that the figures of merit only start to stabilise when using ten redshift distributions or more.

In Fig. 8.6 our figures of merit are plotted as a function of the number of photo-z bins, using $N_K = N_Z = 5$ nuisance parameters per bias term. In agreement with the findings mentioned

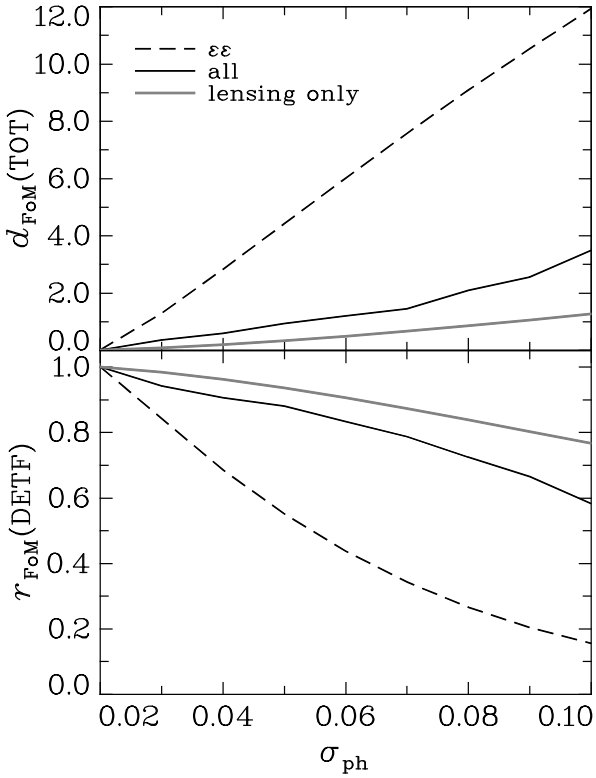

Figure 8.7: *Upper panel*: The difference $d_{\rm FoM}$, defined in (8.67), as a function of the photo-z dispersion $\sigma_{\rm ph}$, shown for $\epsilon\epsilon$ correlations (dashed line), all correlations (black solid line), and the lensing only signal (grey solid line). Throughout, nuisance parameters $N_K = N_Z = 5$ are used. These results are obtained for the standard set of parameters and $N_{\rm zbin} = 10$. *Lower panel*: Same as above, but in terms of the ratio $r_{\rm FoM}$, given in (8.66).

above both the $\mathrm{FoM}_{\rm TOT}$ and the $\mathrm{FoM}_{\rm DETF}$ in the case of a pure cosmic shear signal become approximately constant for $N_{\rm zbin} \gtrsim 5$, and increasing $N_{\rm zbin}$ beyond three has little effect. For $\epsilon\epsilon$ correlations the gain in FoM is considerable up to $N_{\rm zbin} \sim 7$; for larger $N_{\rm zbin}$ the curves rise only slowly.

Since nn correlations are more localised because of the compact kernel of the dominating galaxy clustering (gg) signal, increasing $N_{\rm zbin}$ proves beneficial for these observables up to the maximum number of photo-z bins we have considered, although the bins feature an increasing overlap of their corresponding redshift distributions as we keep $\sigma_{\rm ph} = 0.05$ fixed. As one would expect, we obtain an intermediate scaling with $N_{\rm zbin}$ for the complete set of available correlations. Our fiducial choice of $N_{\rm zbin} = 10$ is beyond the regime of strongly varying figures of merit at small $N_{\rm zbin}$, but the further increase in FoM is more pronounced than for a pure lensing signal or $\epsilon\epsilon$ correlations only with $\mathrm{FoM}_{\rm DETF}$ rising by an additional 80 % on increasing the number of photometric redshift bins from 10 to 20.

Figure 8.7 shows the figures of merit as a function of the photo-z dispersion, normalised to the value at $\sigma_{\rm ph} = 0.02$. Since the $\mathrm{FoM}_{\rm TOT}$ is a logarithmic quantity, we compute differences rather than ratios of the figure of merit, i.e.

$$r_{\rm FoM} = \mathrm{FoM}_{\rm DETF}(\sigma_{\rm ph})/\mathrm{FoM}_{\rm DETF}(\sigma_{\rm ph} = 0.02)\ ; \tag{8.66}$$

$$\begin{aligned} d_{\rm FoM} &= \mathrm{FoM}_{\rm TOT}(\sigma_{\rm ph} = 0.02) - \mathrm{FoM}_{\rm TOT}(\sigma_{\rm ph}) \\ &= \ln\left(\frac{[\det\left(F^{-1}\right)_{\rm cosm.}]\,(\sigma_{\rm ph})}{[\det\left(F^{-1}\right)_{\rm cosm.}]\,(\sigma_{\rm ph} = 0.02)}\right)\ . \end{aligned} \tag{8.67}$$

Hence the difference $d_{\rm FoM}$ is directly related to the change in volume of the error ellipsoid spanned by the set of cosmological parameters. We have returned to our default value of $N_{\rm zbin} = 10$.

The pure lensing signal needs merely coarse redshift information to attain its full statistical power, and hence its FoM hardly suffers from the increasing spread in the redshift distributions.

However, as redshift information is vital to account for intrinsic alignments, the figures of merit for the cosmic shear signal after marginalisation over intrinsic alignments decrease considerably by more than 80 % in terms of the $\mathrm{FoM}_{\mathrm{DETF}}$ on changing from $\sigma_{\mathrm{ph}} = 0.02$ to $\sigma_{\mathrm{ph}} = 0.1$, which is in line with Bridle & King (2007). For the same change in σ_{ph} the $\mathrm{FoM}_{\mathrm{TOT}}$ is reduced by about 12. It is interesting to note that the dependence of the $\mathrm{FoM}_{\mathrm{TOT}}$ on σ_{ph} is close to linear for both lensing and $\epsilon\epsilon$ signal.

Adding galaxy number density information largely alleviates the information loss. The degradation in FoM is only slightly stronger than for the pure lensing signals in the expected regime of high-quality photo-z information with $\sigma_{\mathrm{ph}} \lesssim 0.06$. For larger σ_{ph} the increasing overlap of the redshift distributions causes both figures of merit to decrease further. We have to add the caveat that in this investigation we consider only a single parameter that accounts for the uncertainty in the shape of the redshift distributions, σ_{ph}.

It remains to be seen how sensitive these conclusions are to greater levels of uncertainty in the photometric redshift distribution calibration. For example Zhang et al. (2010) consider the use of nn and ϵn terms for self-calibrating these uncertainties but do not include intrinsic alignments in their main calculations. If we assumed e.g. uncertain median redshifts of each individual distribution, which is beyond the scope of this work and under investigation elsewhere, we would have obtained significantly lower figures of merit; see Kitching et al. (2008) and also Bridle & King (2007) who consider this for the case of $\epsilon\epsilon$ correlations only. The curve for all correlations in Fig. 8.7 may hence approach the one for $\epsilon\epsilon$ correlations, especially for $\sigma_{\mathrm{ph}} \lesssim 0.06$. Consequently, redshift distributions with a small spread may turn out to be even more desirable when taking galaxy number density information into account.

8.3.3 Dependence on nuisance parameter priors

On all our nuisance parameters we can expect to have prior information to a certain extent, at least by the time large space-based cosmological surveys will be undertaken. Here we investigate the dependence of the resulting $\mathrm{FoM}_{\mathrm{TOT}}$ on tightening the priors on the different sets of nuisance parameters, employing our most general configuration with $N_K = N_Z = 7$. We show $d_{\mathrm{FoM}} = \mathrm{FoM}_{\mathrm{TOT}}(\sigma_{\mathrm{prior}}) - \mathrm{FoM}_{\mathrm{TOT}}(\sigma_{\mathrm{prior}}^{\mathrm{max}})$, i.e. the $\mathrm{FoM}_{\mathrm{TOT}}$, referred to its value for the widest priors we apply as default, as a function of the Gaussian prior width σ_{prior} in Fig. 8.8.

For reasons of numerical stability, we have imposed wide Gaussian priors on all nuisance parameters, i.e. 10 on both the $\alpha^{(i)}$ and σ_{ph}, and 50 on the parameters within the intrinsic alignment and galaxy bias terms. As the curves clearly indicate, these priors are non-informative since all of the curves have flattened off by this value. The strongest effect is achieved by tightening the priors on the bias terms (note the different scaling of the two panels). Prior knowledge on the galaxy bias tremendously improves constraints by nn correlations, raising the $\mathrm{FoM}_{\mathrm{TOT}}$ close to the values of the lensing-only case if the uncertainty of the bias term nuisance parameters is of the order 10^{-3}. Since in a situation with such excellent prior knowledge about galaxy bias, the cuts in angular frequency could be much less stringent, the increase in FoM would be even more pronounced.

The $\mathrm{FoM}_{\mathrm{TOT}}$ for $\epsilon\epsilon$ correlations changes from its value at the default configuration to the lensing-only value[2] (compare to Table 8.5) in the limited range between $\sigma_{\mathrm{prior}} \sim 1$ and $\sigma_{\mathrm{prior}} \sim 10^{-2}$. Thus coarse prior information about intrinsic alignments has little effect on the FoM, but, compared to the galaxy bias, a model with comparatively moderate precision can already bring the $\mathrm{FoM}_{\mathrm{TOT}}$ back close to its optimum. If all available correlations are used, the internal calibration works well to constrain the nuisance parameters, so that the priors only mildly

[2]In fact we expect the $\mathrm{FoM}_{\mathrm{TOT}}$ for $\sigma_{\mathrm{prior}} \to 0$ to be slightly above the lensing-only case since the intrinsic alignment signals also constrain cosmology if their form is perfectly known, see also Bridle & King (2007).

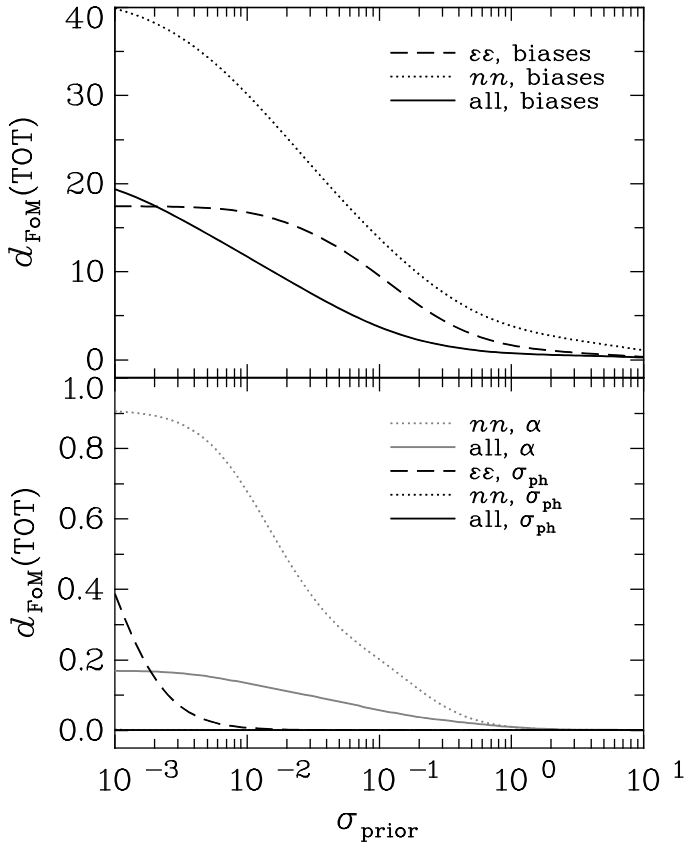

Figure 8.8: The difference d_{FOM} between the $\mathrm{FoM_{TOT}}$ for a given prior value σ_{prior} and the fiducial $\mathrm{FoM_{TOT}}$, obtained for the least stringent, default values of the different priors we apply. *Upper panel*: Effect of tightening the priors on the nuisance parameters in the bias terms for $\epsilon\epsilon$ (dashed line), nn (dotted line), and all (solid) correlations. *Lower panel*: Effect of tightening the priors on the slopes of the luminosity function $\alpha^{(i)}$, and for the prior on the uncertainty of σ_{ph}. Grey curves correspond to priors on $\alpha^{(i)}$, black curves to those on σ_{ph}. Except for the $\epsilon\epsilon$ case the latter remain very close to zero. As above, $\epsilon\epsilon$ correlations are shown as dashed lines, nn correlations as dotted lines, and all correlations as solid lines. Note that $\epsilon\epsilon$ correlations do not depend on the $\alpha^{(i)}$. For all curves, the remaining priors are each set to their default values of 50 for the bias term parameters, and 10 for priors on both $\alpha^{(i)}$ and σ_{ph}.

improve the $\mathrm{FoM_{TOT}}$. However, bear in mind that in spite of our flexible parametrisation, the choice of a fiducial base model for both intrinsic alignments and galaxy bias influences the results. Hence the base models should be as realistic as possible. It is questionable whether our knowledge about the bias terms will ever suffice to impose priors on the bias term nuisance parameters beyond the approximately correct form of the base models.

As already discussed in the foregoing section, the global parameter σ_{ph} is excellently constrained by the nn correlations. Therefore even tight priors do not have any effect on the $\mathrm{FoM_{TOT}}$ if nn correlations form part of the data vector. Priors below $\sigma_{\mathrm{prior}} = 10^{-2}$ increase the information content in $\epsilon\epsilon$ correlations marginally. As far as the uncertainty in the redshift distributions is concerned, our investigation is still to be regarded as idealistic. We defer the joint analysis of shape and number density correlations in presence of unknown parameters in each individual redshift distribution to future work.

The lack of knowledge in the slopes of the luminosity function $\alpha^{(i)}$ entering the lensing magnification signal is negligible in comparison with the effect of the galaxy bias nuisance parameters. If all correlations are considered, the $\alpha^{(i)}$ are well constrained since the improvement in FoM due to priors is below the 1 % level.

8.3.4 Information content in the individual signals

The question arises of which signals contributing to the observable power spectra contain most of the information about cosmology or suffer most strongly from the uncertainty in intrinsic alignments and galaxy bias. Bridle & King (2007) have studied the effect of the two intrinsic alignment terms on $\epsilon\epsilon$ correlations with a parametrisation very similar to ours. In the following

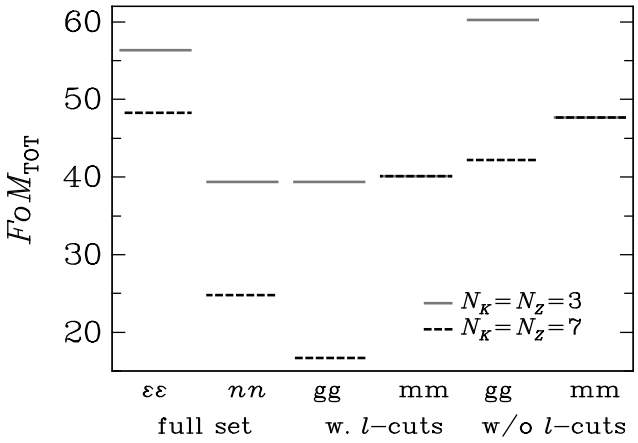

Figure 8.9: The $\mathrm{FoM}_{\mathrm{TOT}}$ for different subsets of correlations that form the nn signal. Throughout, we used $N_{\mathrm{zbin}} = 10$ and $\sigma_{\mathrm{ph}} = 0.05$. The marginalisation has been performed for $N_K = N_Z = 7$ nuisance parameters (black dashed bars) or $N_K = N_Z = 3$ nuisance parameters (grey solid bars). The two leftmost columns show the full set of $\epsilon\epsilon$ and nn correlations for reference. The two centre columns stand for gg and mm correlations only, employing the cuts in angular frequency. The rightmost columns show again gg and mm, but here the full information up to $\ell_{\mathrm{max}} = 3000$ is considered. Note that mm correlations depend neither on intrinsic alignments nor on galaxy bias and hence are independent of N_K and N_Z.

we consider nn correlations by repeating the Fisher matrix analysis twice: once assuming that there is no lensing magnification signal, i.e. only gg contributes to nn; and once assuming that there is no intrinsic galaxy clustering, i.e. only mm contributes to nn.

For this calculation we consider constraints from galaxy clustering information alone (nn), and assume that galaxy shape information ($\epsilon\epsilon$ and $n\epsilon$) is not used. We show the resulting $\mathrm{FoM}_{\mathrm{TOT}}$ for the most flexible model ($N_K = N_Z = 7$) and a model with somewhat less flexibility ($N_K = N_Z = 3$) in Fig. 8.9. On comparing the second, third and fourth columns from the left we see that the model with less freedom (solid grey lines) has approximately the same $\mathrm{FoM}_{\mathrm{TOT}}$ for the complete nn signal as when the nn signal is made up of either one of the pure gg and mm terms alone. We now examine how this conclusion is changed when increased flexibility is allowed in the galaxy bias model (dashed lines). Lensing magnification does not depend on any of our bias terms, so that its $\mathrm{FoM}_{\mathrm{TOT}}$ value is the same for the flexible model (the dashed and solid lines are on top of each other in the fourth column from the left). In contrast, constraints on cosmology from the intrinsic galaxy clustering information alone (gg) weaken significantly as greater flexibility is included in the galaxy bias model. Specifically, the constraint from the gg signal drops by more than 20 in the logarithmic $\mathrm{FoM}_{\mathrm{TOT}}$ when increasing the number of nuisance parameters per bias term by a factor of five (compare the solid and dashed lines in the third column from the left).

The nn correlations, containing both clustering and magnification, unsurprisingly have a $\mathrm{FoM}_{\mathrm{TOT}}$ in between (second column from the left). Hence, if the galaxy bias is well known, the galaxy clustering signal dominates the information from the nn correlations, but for very flexible bias models lensing magnification does allow more information on cosmology to be extracted, as compared to what might be expected if magnification did not take place (compare the dashed lines in the second and third columns).

The two right hand columns of Fig. 8.9 show the $\mathrm{FoM}_{\mathrm{TOT}}$ obtained when the full range of angular scales is used in the power spectra, thus including information from non-linear scales. As already seen in Fig. 8.4, the clustering constraints improve strongly when adding the signal from the non-linear regime. The magnification contribution remains trustworthy far into the non-linear regime, but is of course also affected by the ℓ-cuts. When using the full range of angular scales the $\mathrm{FoM}_{\mathrm{TOT}}$ of the mm signal is increased by about 7. The cosmological constraints from

intrinsic galaxy clustering (gg) alone are now much tighter than from the magnification effect alone (mm), when the smaller number of bias parameters are used (compare solid lines in the two right hand columns). However, the cosmological constraints from the maximally flexible model are still tighter from magnification alone than from galaxy clustering (dashed lines in the right hand two columns).

Note that the constraints from the isolated mm and gg signals are hypothetical – the full nn correlations including both terms are the only true observables. It is only possible to separate the contributions in an approximate fashion when making use of their characteristic scaling with redshift, see Fig. 8.3. But all of this available information is already included in our nn results when a large enough number of tomographic redshift bins are used.

We now assess the cosmological information available in the different subsets of observables when performing the Fisher matrix analysis for all correlations simultaneously. To this end, we split up the summation of the Fisher matrix (8.62) into three parts, corresponding to $\epsilon\epsilon$, nn, and $n\epsilon$ correlations. We also consider pairs of observables e.g. $\epsilon\epsilon$, and nn. The Fisher matrices of each part are then inverted separately to yield individual parameter errors and figures of merit. Thereby we split the total information into subsets of the data vector, which could in principle be observed independently.

However, the figures of merit we compute do not correspond to those which one would obtain for an independent analysis of $\epsilon\epsilon$, nn, or $n\epsilon$ correlations because we extract the relevant rows and columns of the inverse of the full covariance matrix (8.59) to insert into the Fisher matrix calculation (8.62). Due to the inversion, the covariance terms of the different subsets mix, thus accounting for the cross-correlations between the observables in the different subsets. This is desirable for our purposes because these terms add together in the full calculation. Consequently, it is possible that the FoM of a subset is larger than the one obtained for the complete data vector if there are anti-correlations with observables of other subsets which are not taken into account due to the splitting. Formally speaking, this means that due to anti-correlations of different observables, off-diagonal terms of the Fisher matrix can have negative entries, which produce negative terms in the sum in (8.62). We indeed observe this behaviour for one of the subsets.

The $\mathrm{FoM}_{\mathrm{TOT}}$ for the subsets of $\epsilon\epsilon$, nn, and $n\epsilon$ correlations, as well as all possible combinations thereof, are given in the upper panel of Fig. 8.10, again for the two parametrisations $N_K = N_Z = \{3; 7\}$. As part of the full set of observables, the $\epsilon\epsilon$ correlations, governed by the cosmic shear signal, yield the highest $\mathrm{FoM}_{\mathrm{TOT}}$ and contribute most to the cosmological information in the full set (second column). They are followed by cross-correlations between number density and ellipticity, which have a moderate $\mathrm{FoM}_{\mathrm{TOT}}$ (fourth column). This occurs in spite of the smaller range in angular frequency used for this observable. In addition, the least amount of information is lost when switching to the more flexible bias model. The subset of nn correlations has by far the lowest $\mathrm{FoM}_{\mathrm{TOT}}$, which becomes even more pronounced when the bias model has more nuisance parameters. This hierarchy in FoM is also mirrored in the results for the different combinations of two subsets.

To get a more explicit measure of the effect of the marginalisation over the galaxy bias and intrinsic alignments nuisance parameters, we compute the quantity

$$\begin{aligned} \Delta\mathrm{FoM} &\equiv \ln\left[\det F_{\mathrm{cosm.}}\right] - \mathrm{FoM}_{\mathrm{TOT}} \\ &= -\ln\left[\det\left(F_{\mathrm{cosm.}}\right)^{-1}\right] + \ln\left[\det\left(F^{-1}\right)_{\mathrm{cosm.}}\right] \end{aligned} \tag{8.68}$$

for each of the subsets. The first term in (8.68) is of a similar form as the $\mathrm{FoM}_{\mathrm{TOT}}$, but the cosmological elements are extracted before the inverse or determinant is taken i.e. it does not include the marginalisation over nuisance parameters. Hence, ΔFoM quantifies the depletion in FoM due to the marginalisation. As is evident from the lower panel in Fig. 8.10, the

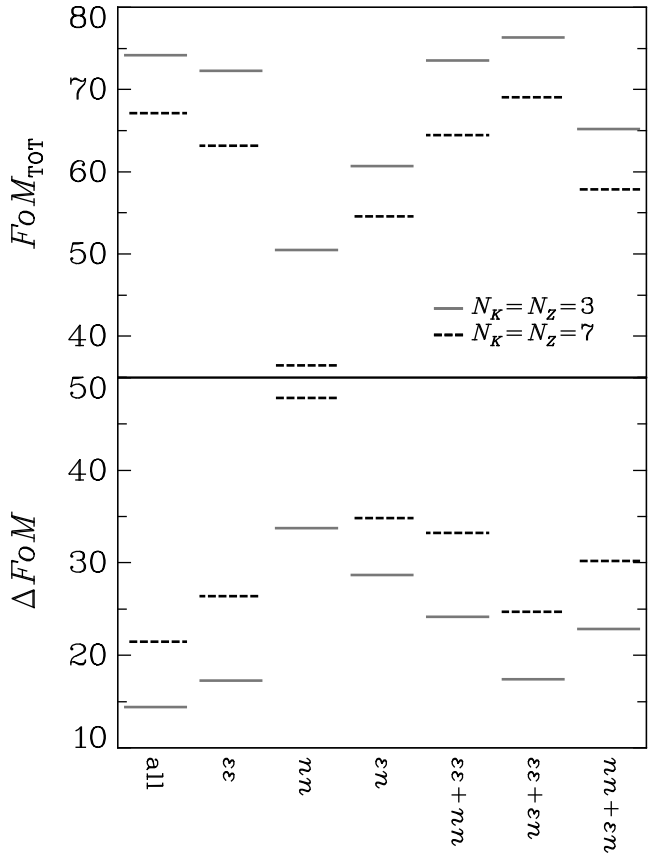

Figure 8.10: *Upper panel:* The $\mathrm{FoM}_{\mathrm{TOT}}$ for different subsets of correlations that are observable from a galaxy survey with galaxy shape and number density measurements. The Fisher matrix has been computed for the total data set containing all correlations, i.e. these results represent the information content of the subsets as a part of the total signal. Black dashed bars correspond to a marginalisation over $N_K = N_Z = 7$ nuisance parameters, grey solid bars to $N_K = N_Z = 3$ nuisance parameters. The labels on the abscissa indicate the different combinations of correlations used, where ϵn stands for the cross-correlations between number density and ellipticity. *Lower panel:* Difference Δ FoM, see (8.68), for the same subsets as above. This difference can be understood as a measure of the depletion of information in the subsets due to the marginalisation over nuisance parameters.

susceptibility of the subsets to the nuisance parameters is closely related to their contribution to the $\mathrm{FoM}_{\mathrm{TOT}}$ of the full set. Accordingly, ΔFoM is largest for the nn subset while the ellipticity-number density cross-correlations have substantially smaller ΔFoM although they contain all four bias terms. The effect of intrinsic alignments on the $\epsilon\epsilon$ subset is relatively small when compared to the effect of galaxy bias on the nn correlations.

Since the $\epsilon\epsilon$ correlations only depend on intrinsic alignments (b_{I} and r_{I}) whereas nn correlations only feature galaxy bias (b_{g} and b_{g}), combining them helps little in reducing ΔFoM, see the column labelled '$\epsilon\epsilon + nn$'. Both lines in this column remain higher than for the other combinations '$\epsilon\epsilon + \epsilon n$'and '$nn + \epsilon n$'. The ellipticity-number density cross-correlations instead have great potential in breaking degeneracies between cosmological and nuisance parameters. In particular, adding their subsets to the $\epsilon\epsilon$ correlations further decreases ΔFoM below the $\epsilon\epsilon$-only value for the most flexible bias term model. This synergy is presumably related to the internal calibration between the IG and gI signals, as investigated by Zhang (2008). Finally, the full set of shape and number density observables clearly calibrates the nuisance parameters best as it produces the smallest ΔFoM for both the most flexible and the more rigid bias term models.

8.4 Conclusions

In this work we studied the joint analysis of galaxy number density and shape correlations to constrain cosmological parameters in presence of contaminations by the intrinsic alignment of galaxies and the galaxy bias. We considered the signals due to gravitational shear, intrinsic shear, intrinsic galaxy clustering, and lensing magnification, explicitly computing all possible two-point correlations thereof. We introduced a two-dimensional grid parametrisation to ac-

count for the unknown scale and redshift dependence of both intrinsic alignments and galaxy bias. Further nuisance parameters were used to describe the uncertainty in the width of the photo-z bin-wise redshift distributions and in the slope of the galaxy luminosity functions within each bin.

Our Fisher matrix analysis demonstrates that the simultaneous use of ellipticity correlations, number-density correlations, and in particular ellipticity-number-density cross-correlations allows for a substantial amount of internal calibration of the bias terms. With flexible models that contain in total more than 200 nuisance parameters we can recover the volume of the error ellipsoid in parameter space when compared to assuming a pure gravitational lensing signal and using just the ellipticity correlation information. The dark energy parameters w_0 and w_a suffer more than other parameters on marginalisation over nuisance parameters, so that 56 % of the $\mathrm{FoM_{DETF}}$ are retained for a Euclid-like survey in this most flexible setup considered. The $\mathrm{FoM_{DETF}}$ for the combined set of shape and number density correlations is close to the pure lensing $\mathrm{FoM_{DETF}}$ if we choose a model which uses about 100 nuisance parameters to describe intrinsic alignments and galaxy bias. Our approach also proves beneficial for upcoming ground-based surveys with DES-like survey characteristics. The benefit is greatest for the more ambitious survey. In addition, we assumed the slopes of the galaxy luminosity functions in each photo-z bin to be unknown nuisance parameters and found that they are well calibrated internally from the data.

The information which we added on top of the standard cosmic shear analysis comes without any extra cost since galaxy number density measurements are directly available from imaging data. Given our encouraging findings, we hence suggest that the joint consideration of galaxy shape and number density information could become the standard technique whenever intrinsic alignments are suspected to make a significant contribution to the cosmic shear signal.

When interpreting our results, one has to keep in mind that our grid parametrisation of the bias terms has limited flexibility. On increasing the number of nuisance parameters in the grids, the curves for the figures of merit flatten off. However we are at present not able to say whether they approach a lower limit or continue to decrease for a large number of grid nodes. This issue, which is of considerable theoretical and practical interest, is currently under investigation, as well as a comparison with the performance of removal techniques such as nulling (Joachimi & Schneider 2008, 2009).

Due to the finite number of grid points the resulting angular power spectra will not span perfectly the range of possible physical models. Moreover, we found that of order 10 nuisance parameters in k per grid node in redshift do not suffice to represent all relevant functional forms of the galaxy bias. Therefore we removed all observables from the parameter estimation which have a significant contribution from the galaxy clustering signal at large k where the signal is strongest and the bias least known. However, since in the near future we expect to have at least coarse, but reliable knowledge about the functional forms of the galaxy bias on linear scales and the intrinsic alignment signals, the models used in our approach should still yield realistic results.

While the log-linear grid parametrisation is fairly general and intuitive, it may not be the most efficient way to represent freedom in intrinsic alignments and the galaxy bias. As all bias terms originate from physical processes, they are smooth and do not feature strong oscillations or isolated peaks. Thus, we presume that the bias terms can efficiently be parametrised in terms of complete sets of smooth functions such as the Fourier, Chebyshev, or Legendre series. Truncating the higher orders of these series will only limit the model to represent highly oscillatory or small-scale features. These parametrisations might therefore be more efficient in comprising the full set of realistic bias terms (see also Kitching et al. 2009) for a given number of nuisance parameters, this number in turn being dictated by the available computational

power. The latter will play a critical role when the approach suggested here is performed in a full likelihood analysis with several hundreds of nuisance parameters. We add that it might be necessary to furthermore consider the bias terms individually for different galaxy types and luminosities because it is known that both the intrinsic alignments and the galaxy bias vary considerably with galaxy type and luminosity (for recent examples see Mandelbaum et al. 2006; Hirata et al. 2007; McCracken et al. 2008; Swanson et al. 2008; Simon et al. 2009; Cresswell & Percival 2009; Wang et al. 2007).

Redshift information is crucial for discriminating the different signals that contribute to the observables. We investigated the dependence of the parameter constraints from the joint set of correlations on characteristics of the redshift distributions. We confirm the observation by foregoing works that the number of photo-z bins needed to retrieve the bulk of information about cosmology increases by at least a factor of two when using only ellipticity correlations and marginalising over the intrinsic alignment signals. Using the complete set of correlations, the figures of merit do not level off so quickly, but continue to increase as the number of tomographic bins is increased. This can be explained by the narrower kernel in the redshift integrations that link the projected and the three-dimensional power spectra involving galaxy number-density signals.

Moreover the figures of merit decrease substantially more slowly as a function of the photometric redshift dispersion $\sigma_{\rm ph}$ when adding galaxy number density information to the data. However, in our marginalisation we only used a single parameter accounting for the uncertainty in the spread of all bin-wise redshift distributions. This way the redshift cross-terms of the number-density correlations efficiently calibrate the shape of the redshift distributions. Therefore this result alone cannot be interpreted as a potential relaxation of the requirements for photometric redshift accuracy in cosmological surveys featuring cosmic shear. Conversely, the continuing increase in the figure of merit as a function of $N_{\rm zbin}$ makes an even larger number of well-separated and compact redshift distributions desirable in the case of the joint data set.

The recent work by Zhang et al. (2010) uses density-ellipticity correlations to self-calibrate photometric redshift parameters but a full approach may need to simultaneously deal with intrinsic alignments and photometric redshift properties if sufficient spectra cannot be obtained to calibrate the photometric redshifts independently. In forthcoming work we will investigate into a more realistic approach including uncertainty and outliers in the redshift distributions of each individual photo-z bin, as well as the benefits of spectroscopic redshift information for a subsample of the galaxy catalogue.

We emphasise that in the approach suggested here all considered correlations help in constraining cosmological parameters. Hence, none of the contributions is regarded as a systematic signal, and the different levels of uncertainty concerning the exact form of the signals are represented by nuisance parameters. By means of the joint analysis we increase the statistical power via the cross-calibration abilities of the signals, and reduce the risk of undetected systematic effects one faces when considering signals such as cosmic shear, galaxy clustering, or lensing magnification individually.

This integrative ansatz is not limited to two-point correlations, but can be generalised to the three-point level in a straightforward way. Future surveys will provide excellent data for studying three-point correlations whose exploitation can break parameter degeneracies and improve constraints considerably (e.g. Takada & Jain 2004). Our knowledge about intrinsic alignments and galaxy bias at the three-point level is currently even more limited than in the two-point case (however see Semboloni et al. 2008), so that a joint investigation of shape and number density observables, including a general parametrisation of the various bias terms, may be an appropriate way forward. However, limitations due to computational power will most likely play a dominant role in this case, but note that, if a subset of the parameters has a

probability distribution close to Gaussian, analytic marginalisation over the posterior could significantly relive the computational burden (Taylor & Kitching 2010).

One can also think of incorporating further sets of observables into the analysis. For instance, planned surveys like Euclid will also include a spectroscopic survey of a subset of the galaxies in order to determine the underlying redshift distributions of the photo-z bins. The spectroscopic data can be used to measure baryonic acoustic oscillations (note that the acoustic peaks are not included in our galaxy number-density correlations) and galaxy peculiar velocities. The latter allow for the measurement of redshift space distortions. Similar to the case considered here, the joint analysis of galaxy number density, shape, and velocity information (Guzik et al. 2010) will efficiently cross-calibrate nuisance terms such as the galaxy bias and tighten constraints on the cosmological model.

Chapter 9

Conclusions & Outlook

This thesis investigated various aspects of cosmic shear, the weak gravitational lensing of distant galaxies by the large-scale structure. We considered contributions to optimising the extraction of cosmological information from present and future cosmic shear surveys and elaborated on the properties of the intrinsic alignment of galaxies, as well as on methods to assess and control the contamination of cosmic shear data by this important systematic.

We conducted a stringent and detailed derivation of the covariance of the weak lensing convergence bispectrum which is vital for analysing three-point statistics of cosmic shear. Apparent discrepancies in the different flat-sky formalisms in the literature were resolved, and the treatment of parity clarified. Moreover we provided an illustrative geometrical interpretation of the covariance prefactors and presented simple and efficient approximation formulae. Our results were then applied to a prediction of the performance of combined two- and three-point cosmic shear statistics which formed part of the assessment study of the ESA Euclid mission, finding excellent constraints on e.g. dark matter abundance and dark energy equation of state, as well as great synergy with CMB experiments like Planck.

The forecasts of the errors on cosmological parameters employed the widespread Fisher matrix formalism which was also widely made use of in the remainder of this work. While it is an efficient means to demonstrate the feasibility of methods or determine general trends in the statistical errors of a survey, it lacks the accuracy for precise predictions due to the assumption of a Gaussian distribution both for the likelihood and the posterior probability in parameter space. The application of Gaussian likelihoods is ubiquitous in cosmology also for full likelihood analyses (and done throughout this work), simply due to the ignorance of the true probability distributions of the data. This also applies to cosmic shear surveys since, while the probability distribution of the matter density contrast is fairly well described by a log-normal law (Kayo et al. 2001), there is currently no compelling analogous prescription for projected quantities such as the convergence, let alone for two-point statistics like the power spectrum.

Hence, Gaussian likelihoods, which should at least yield a fair approximation to single-peak distributions close to the point of maximum likelihood, are likely to continue to prevail in cosmic shear analyses in the near future. In parameter space however, progress beyond Gaussianity may be possible, without resorting to high-dimensional parameter grid sampling or Marcov Chain Monte Carlo methods, by transforming the set of cosmological parameters such that the distribution in parameter space is well approximated by a multivariate Gaussian (e.g. Box & Cox 1964). This transformed set could then be used in a standard Fisher matrix computation whose in this case precise results would subsequently be transformed back to the original set of parameters. We note that the parameter forecast for Euclid assumed in addition Gaussianity for the covariances, even for three-point statistics which have vanishing expectation values for purely Gaussian random fields. This further over-simplification results

from demands of numerical tractability and the absence of precise model predictions for four-, five-, and six-point statistics of the matter distribution.

Moreover we presented a novel method named functional form filling (Kitching et al. 2009) which robustly quantifies the effect on the total error budget of cosmological parameters by a systematic whose form is unknown except for upper and lower limits defined by a boundary function. The formalism determines the worst possible parameter bias among all the systematic signals within these bounds for a given resolution. Functional form filling yields the same mean square error as the standard approach of marginalisation over nuisance parameters if in the latter case the systematic can be represented by the chosen parametrisation. In case this parametrisation is too rigid to capture the true form of the systematic, marginalisation will yield biased, usually too optimistic results in contrast to functional form filling which is independent of the parametrisation that samples the region allowed for the systematic signal. Recently, this ansatz has been generalised by Kitching & Taylor (2010) to the marginalisation over sets of nuisance functions instead of parameters by employing path integrals.

Several modelling details in the first fully tomographic cosmic shear analysis of the HST COSMOS survey (Schrabback et al. 2010) were also discussed. The cosmological results are consistent with other established probes and have a low level of systematics, providing a strong case for weak lensing studies from space. However, while this investigation constitutes one of the most detailed and careful cosmic shear studies to date, it is also likely to be one of the last for which first-generation shape measurement techniques as well as simple approximations in the signal and covariance modelling are still sufficiently accurate.

One of the main challenges for future cosmic shear surveys with substantially higher constraining power than COSMOS is the improvement of galaxy shape measurements beyond KSB-like approaches which generally yield biased estimates and rely on empirical corrections (Kaiser et al. 1995; Bernstein & Jarvis 2002). Currently, none of the recent developments including Bayesian modelling, wavelet decomposition, or Fourier-space analyses (see Bridle et al. 2010 for an overview) fulfil the accuracy requirements of surveys like Euclid, even for the still idealised image simulations.

Furthermore future measurements will have to tackle complications such as a wavelength dependence of the PSF in addition to spatial variations (Cypriano et al. 2010), which is particularly relevant for diffraction-limited observations from space. Thus, the shape determination process has to take into account the variation of colour between different galaxies. Even more intricately, accuracy goals could also be threatened by the spatial variability in the colour within a single galaxy image (Euclid consortium, private communication), or a radial change of the ellipticity of galaxy isophotes (Bernstein 2010). Shape measurement remains a critical issue for cosmic shear, and data challenges addressing this problem like STEP (Heymans et al. 2006a; Massey et al. 2007a) and GREAT (Bridle et al. 2010) will be continued over the coming years.

The second point for which the COSMOS analysis probably reached the current accuracy limit is the modelling of cosmic shear signals and their covariances. The fits to the non-linear contributions to the matter power spectrum by Peacock & Dodds (1996) and Smith et al. (2003) are still prevailing in weak lensing analyses as in all of cosmology, although mismatches with ΛCDM N-body simulations by at least 10 % have been found (Hilbert et al. 2009). To incorporate parameters of dynamical dark energy or parameters indicative of a departure from general relativity, one either has to rely on crude approximations as outlined in Sect. 4.3.2 or sets of simulations covering usually only a small region of parameter space (e.g. McDonald et al. 2006).

The situation is even more difficult for higher-order shear statistics, e.g. the matter bispectrum is mostly determined from perturbation theory in combination with a fit formula that was matched to simulations and accounts for non-linear evolution (Fry 1984; Scoccimarro &

Couchman 2001). The halo model (Cooray & Sheth 2002) is a potential alternative but also decreases strongly in accuracy for higher-order statistics. As mentioned above, the ignorance of precise bispectra, trispectra, etc. also hinders the calculation of covariances which are often – like in this work – evaluated under a Gaussian approximation which is known to fail below angular scales of about 10 arcmin (Semboloni et al. 2007; Pielorz et al. 2010).

However, large-volume N-body simulations are in principle capable of solving all these issues, except perhaps for the smallest scales where baryonic physics become important. Since the computational power grows alongside with the size of cosmic shear surveys and their demands on precision, it should be possible within the next couple of years to produce and store Millennium-like simulations on a dense grid in a multi-dimensional cosmological parameter space, possibly aided by analytical treatments as for instance suggested by Angulo & White (2010).

Besides theoretical and measurement issues, the preparation of cosmic shear for high-precision cosmology also needs to include an assessment of astrophysical contaminations to the signal. The most important one is the intrinsic alignment of galaxies which mimics the correlations between galaxy shapes induced by gravitational lensing. We reviewed the research about intrinsic alignments and argued that the current models are still crude due to the limited understanding of the processes of galaxy alignment, thus hampering a straightforward correction of this effect. Analytical progress in modelling intrinsic alignments is not to be expected beyond e.g. simple halo model calculations (Schneider & Bridle 2010), so that the best chances to improve the physical insight into alignment processes are via the combination of large-scale N-body simulations at high mass resolution with accurate semi-analytic galaxy models (e.g. Guo et al. 2010) and small-scale hydrodynamical galaxy simulations in the spirit of Hahn et al. (2010).

We measured correlations between the matter distribution and intrinsic shear in a set of early-type galaxy samples from SDSS, finding that all samples are consistent with a simple three-parameter intrinsic alignment model. Strong evidence was obtained for an increase of the intrinsic alignment amplitude with galaxy luminosity. It was also demonstrated that the redshift evolution of the most widespread intrinsic alignment model based on Hirata & Seljak (2004) is not compatible with observations, but that the corrections we proposed for the redshift evolution of the linear alignment paradigm agree with our constraints at the $2\,\sigma$ level. We used for the first time a galaxy sample which is restricted to photometric redshift information and developed a formalism that includes photometric redshift uncertainty, opening up the possibility to apply our measurement technique to other large galaxy samples with photometric redshifts. Under the idealistic assumption that the mean intrinsic alignment contribution can be modelled and subtracted from the cosmic shear signal, we showed that the constraints on the intrinsic alignment model by the combination of the samples analysed can reduce the scatter of the biases on cosmological parameters below the statistical $1\,\sigma$ error for a present-day cosmic shear survey.

While these constraints on intrinsic alignments are unprecedented in accuracy, this type of measurement does not suffice to calibrate intrinsic alignments in future cosmic shear surveys, e.g. due to the limited statistical power, hindering the fitting of more flexible models, and the necessary exclusion of small, non-linear scales. In absence of a compelling model for intrinsic alignments, one requires model-independent techniques that guarantee the removal of this systematic from cosmic shear data. This lead us to developing the nulling technique, exploiting only the well-known characteristic redshift dependence of gravitational shear-intrinsic ellipticity correlations to eliminate them from tomographic cosmic shear surveys. We derived the transformation central to nulling, deriving several ways to optimally construct the weightings involved. It was proven that nulling can be understood as a rotation of the cosmic shear data vector with a subsequent truncation, thereby creating a simple formalism that can readily be applied to

real data. We demonstrated that nulling robustly reduces gravitational shear-intrinsic ellipticity correlations by an order of magnitude in presence of realistic survey parameters, especially a wide range of photometric redshift scatters and outlier rates.

The price to pay for model independence is a considerable loss of cosmological information, for instance a decrease in the DETF figure of merit by an order of magnitude for a Euclid-like survey. This loss is inevitable due to the similar redshift dependencies of shear-intrinsic correlations and the lensing signal. Consequently, the nulling technique constitutes a valuable consistency check, but will not serve as the intrinsic alignment removal method of choice for future cosmic surveys. In an extension of the nulling technique currently under investigation we aim at mitigating the reduction of constraints on cosmological parameters by incorporating prior information on the intrinsic alignment signal, either obtained from external data in the spirit of our SDSS analysis or from the cosmic shear survey itself via a further geometrical method introduced in this work, the boosting technique.

Boosting follows an inverse approach to nulling in that the cosmic shear signal is suppressed while amplifying the intrinsic alignment contribution in relation to it. We exemplified that it is indeed possible under realistic conditions to extract the intrinsic alignment signal out of cosmic shear data, albeit with comparatively large errors which again can be ascribed to the similar redshift dependence of intrinsic alignment and lensing correlations. Allowing for a measurement of intrinsic alignments in the same sample used for the cosmic shear analysis, the boosting technique can verify extrapolations of intrinsic alignment models to the typically faint and high-redshift galaxies in cosmic shear data and thus serves as a further helpful consistency check for future weak lensing campaigns.

In search for a standard tool of intrinsic alignment control in cosmic shear surveys we furthermore investigated the simultaneous analysis of galaxy ellipticity correlations, galaxy number density correlations, and number density-ellipticity cross-correlations, all of which are readily available from cosmic shear data. This self-calibration ansatz unites a standard cosmic shear analysis with the principle of intrinsic alignment measurements via number density-shape cross-correlations applied in Chap. 5, which in turn requires the galaxy bias obtained from galaxy clustering (e.g. Zhang 2008; Bernstein 2009). To remain essentially model-independent, we employed a general and flexible parametrisation for both intrinsic alignments and galaxy bias, also extending into the non-linear regime, resulting in a maximum of over 200 nuisance parameters. For this maximal case we found that 56 % of the DETF figure of merit are preserved in the joint analysis of a Euclid-like survey, performing even better on cosmological parameters other than those entering the dark energy equation of state.

To obtain these promising results, we modelled a realistic scatter in photometric redshifts and included a global parameter accounting for the uncertainty in the corresponding redshift distributions. Yet, to be fully representative of real cosmic shear data, one has to allow for further free parameters such as an uncertainty in the mean of the bin-wise redshift distributions or a fraction of catastrophic failures in the photometric redshift determination. Zhang et al. (2010) showed that the same type of analysis can self-calibrate photometric redshifts excellently, so that now the performance of the simultaneous calibration of intrinsic alignments, galaxy bias, and photometric redshifts remains to be investigated.

Moreover it should be straightforward to include more information into the self-calibration formalism, such as external data serving as prior information on intrinsic alignments or the galaxy bias. Future cosmic shear surveys will be accompanied by spectroscopic surveys of a subset of the galaxies which, when jointly analysed with the imaging data yielding the aforementioned correlations, can help calibrating photometric redshifts and possibly add peculiar velocity information, the latter also probing the local tidal gravitational field at least on large scales and hence also constraining intrinsic alignments.

So far most work on the control of intrinsic alignments has focused on cosmic shear two-point statistics, with the exception of the generalisation of the nulling technique to three-point statistics by Shi et al. (2010). As cosmic shear at the three-point level features substantial and complementary cosmological information (e.g. Bergé et al. 2010), and as the work by Semboloni et al. (2008) suggests an even more severe contamination by intrinsic alignments than at the two-point level, more efforts concerning modelling, observational constraints, and removal techniques are required. We note that interesting cosmological information could also be extracted from higher-oder lensing distortions such as flexion (e.g. Bacon et al. 2009) which may profit from a smaller intrinsic shape dispersion as well as less intrinsic alignment.

Ultimately, for both cosmic shear measurements and the capabilities of intrinsic alignment control, a plethora of opportunities will open up by the transition from optical observations to the radio regime (or combining the two). At present cosmic shear is observed at optical wavelengths mainly because galaxy number densities are highest, but radio surveys will eventually become competitive with instruments like the Square Kilometer Array (e.g. Schneider 1999). Instead of mitigating the shortcomings of optical PSFs with their complex, non-circular shapes and spatial or spectral variations, one will be able to define desired properties of the PSF at radio wavelengths to a certain extent in the process of aperture synthesis. A second major issue for optical cosmic shear surveys, the determination of redshifts for billions of galaxies, would also largely be resolved by the frequency tunability of radio receivers and the resulting easy measurement of spectra.

Observations at radio wavelengths can also provide new information about intrinsic galaxy ellipticities as e.g. Patel et al. (2010) recently found that the intrinsic ellipticities in optical and radio images are uncorrelated and hence provide an independent shape sample which should also have different intrinsic alignment properties. Furthermore, intrinsic and gravitational shear could be decoupled, at least partially, if spatially resolved radial velocity (Blain 2002; Morales 2006) or polarisation (Brown & Battye 2010) data are incorporated. Finally, the intricacies of galaxy shape measurements and potential intrinsic alignments are completely circumvented by using hundreds of tomographic slices of 21 cm radiation maps of neutral hydrogen before the epoch of reionisation instead of distant galaxies as the sources for weak lensing studies of the large-scale structure (Metcalf & White 2007). The joint analysis of the CMB in combination with the complementary 21 cm and galaxy weak lensing surveys would have outstanding constraining power and self-calibration capabilities (Metcalf & White 2009).

In summary, weak gravitational lensing on cosmological scales is indeed one of the most promising probes of the Universe for high-precision cosmology in the coming years. To achieve its full potential, cosmic shear still has to overcome a number of important issues such as the intrinsic alignment effect covered in depth in this work. However, it should be kept in mind that these caveats also applied in a similar fashion to other, nowadays established techniques such as for instance CMB and Supernova Type Ia measurements, only that these methods have by now been investigated by a large number of scientists over the course of several decades. Cosmic shear is a young field and has rapidly matured from first detection to aspiring competitor for cosmological space missions within a decade. Based on a continuing effort including the contributions presented in this thesis, the achievements of the next decade will consolidate cosmic shear as an indispensable tool to shed light on the nature of the Universe.

Acknowledgements

First of all, I would like to thank my supervisor Peter Schneider whom I owe as to every aspect of my PhD, be it guidance and advice on my work whenever needed, encouragement and opportunities galore to get involved into various activities, or editing and proof-reading services on thesis and papers. Most importantly, I have profited and will continue to profit from the many conversations in which I learnt how a scientist thinks, how a scientist works, and how one gets along in science.

I am also deeply indebted to Sarah Bridle who kindly accepted me as a visiting PhD student at UCL, reserved a lot of time for productive discussions and work, and had great share in making my stay a very pleasant and fruitful part of my PhD.

Moreover I would like to thank Prof. Eckart for being my BCGS mentor during my PhD, and for being the second examiner of my thesis. I also thank Dr. Metsch and Prof. Simmer for agreeing to join my PhD exam panel.

I am grateful to Filipe Abdalla, Adam Amara, Tim Eifler, Jan Hartlap, Martin Kilbinger, Tom Kitching, Rachel Mandelbaum, Alexandre Réfrégier, Tim Schrabback, Elisabetta Semboloni, Xun Shi, and Patrick Simon whom I have had the pleasure to collaborate with during my PhD. In particular, I would like to thank Rachel Mandelbaum and Filipe Abdalla for kindly providing me with the correlation functions and redshifts needed to perform the intrinsic alignment analysis presented in Chap. 5. Furthermore I appreciated helpful and stimulating discussions with many colleagues, especially Joel Bergé, Gary Bernstein, Alan Heavens, Martin Hendry, Catherine Heymans, Bhuvnesh Jain, Ofer Lahav, Masahiro Takada, Andy Taylor, and the members of the Euclid Weak Lensing Working Group.

Work would have been dreary in the past three years without my colleagues at the Argelander-Institut and in the astrophysics group at UCL. I am grateful for insightful discussions, pleasant chats, a lot of help, and good company. I am indebted to the computer departments at UCL and especially at AIfA for providing and – most of the time – fixing problems with the computational infrastructure that was necessary to complete this thesis.

During all of my studies my wife shared the good and the bad times with me, and I would be very happy if she kept on reminding me for the rest of my life that there is more to life than work. I would also like to thank my parents for giving me the opportunity, the encouragement, and the long-standing support to venture into such an 'unremunerative' field as astrophysics.

I acknowledge financial support by the Deutsche Telekom Stiftung and the Bonn-Cologne Graduate School of Physics and Astronomy during the three years of my PhD. Projects contributing to this thesis were supported by the RTN-Network 'DUEL' of the European Commission, and the Deutsche Forschungsgemeinschaft under the Transregional Collaborative Research Center TR33 'The Dark Universe', the project SCHN 342/6–1, and the Priority Program 1177 'Galaxy Evolution'.

Bibliography

Abazajian, K. N., Adelman-McCarthy, J. K., Agüeros, M. A., Allam, S. S., et al. 2009, ApJS, 182, 543

Abdalla, F. B., Amara, A., Capak, P., et al. 2007, MNRAS, 387, 969

Abdalla, F. B., Banerji, M., Lahav, O., & Rashkov, V. 2008, astro-ph/0812.3831, submitted to MNRAS

Adelman-McCarthy, J. K., Agüeros, M. A., Allam, S. S., Allende Prieto, C., et al. 2008, ApJS, 175, 297

Adelman-McCarthy, J. K., Agüeros, M. A., Allam, S. S., Anderson, K. S. J., et al. 2006, ApJS, 162, 38

Albrecht, A., Bernstein, G., Cahn, R., et al. 2006, astro-ph/0609591

Alcock, C., Allsman, R. A., Alves, D. R., et al. 2000, ApJ, 542, 281

Amara, A. & Réfrégier, A. 2007, MNRAS, 381, 1018

Amara, A. & Réfrégier, A. 2008, MNRAS, 391, 228

Amsler, C. et al. 2008, Physics Letters, B667, 1, update for the 2010 edition by M. Drees, G. Gerbier

Angulo, R. E. & White, S. D. M. 2010, MNRAS, 405, 143

Armendariz-Picon, C., Mukhanov, V., & Steinhardt, P. J. 2000, Phys. Rev. Lett., 85, 4438

Bacon, D. J., Amara, A., & Read, J. I. 2009, astro-ph/0909.5133, submitted to MNRAS

Bacon, D. J., Réfrégier, A. R., & Ellis, R. S. 2000, MNRAS, 318, 625

Bardeen, J. M., Bond, J. R., Kaiser, N., & Szalay, A. S. 1986, ApJ, 304, 15

Barger, V., Guarnaccia, E., & Marfatia, D. 2006, Phys. Lett. B, 635, 61

Bartelmann, M. & Schneider, P. 1999, A&A, 345, 17

Bartelmann, M. & Schneider, P. 2001, Phys. Reports, 340, 291

Bartolo, N., Komatsu, E., Matarrese, S., & Riotto, A. 2004, Phys. Reports, 402, 103

Basilakos, S. & Plionis, M. 2009, A&A, 507, 47

Bean, R. 2009, astro-ph/0909.3853

Bean, R. & Tangmatitham, M. 2010, Phys. Rev. D, 81, 083534

Bekenstein, J. D. 2010, in Particle Dark Matter: Observations, Models and Searches, Cambridge Univ. Press, ed. G. Bertone

Benjamin, J., Heymans, C., Semboloni, E., et al. 2007, MNRAS, 381, 702

Bergé, J., Amara, A., & Réfrégier, A. 2010, ApJ, 712, 992

Bernardeau, F., Colombi, S., Gaztañaga, E., & Scoccimarro, R. 2002a, Phys. Reports, 367, 1

Bernardeau, F., Mellier, Y., & van Waerbeke, L. 2002b, A&A, 389, L28

Bernstein, G. M. 2009, ApJ, 695, 652

Bernstein, G. M. 2010, MNRAS, accepted

Bernstein, G. M. & Huterer, D. 2010, MNRAS, 401, 1399

Bernstein, G. M. & Jarvis, M. 2002, AJ, 123, 583

Bett, P., Eke, V., Frenk, C. S., Jenkins, A., & Okamoto, T. 2010, MNRAS, 404, 1137

Beynon, E., Bacon, D. J., & Koyama, K. 2010, MNRAS, 403, 353

Blain, A. W. 2002, ApJ, 570, L51

Blake, C. & Bridle, S. 2005, MNRAS, 363, 1329

Blake, C., Collister, A., Bridle, S., & Lahav, O. 2007, MNRAS, 374, 1527

Blandford, R. D., Saust, A. B., Brainerd, T. G., & Villumsen, J. V. 1991, MNRAS, 251, 600

Blanton, M. R., Brinkmann, J., Csabai, I., Doi, M., et al. 2003, AJ, 125, 2348

Bordoloi, R., Lilly, S. J., & Amara, A. 2010, MNRAS, accepted

Borodin, K. S., Kroshilin, A. E., & Tolmachev, V. V. 1978, TMF, 34, 110

Bower, R. G., Benson, A. J., Malbon, R., et al. 2006, MNRAS, 343, 679

Box, G. E. P. & Cox, D. R. 1964, J. Roy. Statist. Soc. Ser. B, 26, 211

Bradač, M., Allen, S. W., Treu, T., Ebeling, H., et al. 2008, ApJ, 687, 959

Brainerd, T., Agustsson, I., Madsen, C. A., & Edmonds, J. A. 2009, astro-ph/0904.3095, submitted to ApJ

Brandenberger, R. H. 2000, in COSMO-99, International Workshop on Particle Physics and the Early Universe, ed. B. Sadoulet

Bridle, S. & Abdalla, F. B. 2007, ApJ, 655, L1

Bridle, S. & King, L. 2007, NJPh, 9, 444

Bridle, S., Sreekumar, S. T., Bethge, M., et al. 2010, MNRAS,accepted

Broadhurst, T. J., Taylor, A. N., & Peacock, J. A. 1995, ApJ, 438, 49

Brown, M. L. & Battye, R. A. 2010, astro-ph/1005.1926, submitted to MNRAS

Brown, M. L., Taylor, A. N., Hambly, N. C., & Dye, S. 2002, MNRAS, 333, 501

Cacciato, M., van den Bosch, F. C., More, S., Li, R., et al. 2009, MNRAS, 394, 929

Camera, S., Kitching, T. D., Heavens, A. F., Bertacca, D., & Diaferio, A. 2010, astro-ph/1002.4740, submitted to MNRAS

Cannon, R., Drinkwater, M., Edge, A., Eisenstein, D., et al. 2006, MNRAS, 372, 425

Carroll, S. M., Press, W. H., & Turner, E. L. 1992, Annu. Rev. Astron. Astrophys., 30, 499

Catelan, P., Kamionkowski, M., & Blandford, R. D. 2001, MNRAS, 320, 7

Chevallier, M. & Polarski, D. 2001, Int. J. Mod. Phys., D10

Clowe, D., Bradac, M., Gonzalez, A. H., et al. 2006, ApJ, 648, 109

Collister, A. & Lahav, O. 2004, Public. Astron. Soc. Pacific, 116, 345

Collister, A., Lahav, O., Blake, C., et al. 2007, MNRAS, 375, 68

Cooray, A., Sarkar, D., & Serra, P. 2008, Phys. Rev. D, 77, 123006

Cooray, A. & Sheth, R. 2002, Phys. Reports, 372, 1

Cresswell, J. G. & Percival, W. J. 2009, MNRAS, 392, 682

Crittenden, R. G., Natarajan, P., Pen, U., & Theuns, T. 2001, ApJ, 559, 552

Crittenden, R. G., Natarajan, P., Pen, U., & Theuns, T. 2002, ApJ, 568, 20

Croft, R. A. C. & Metzler, C. A. 2000, ApJ, 545, 561

Cypriano, E. S., Amara, A., Voigt, L. M., et al. 2010, MNRAS, 405, 494

Dalal, N., Doré, O., Huterer, D., & Shirokov, A. 2008, Phys. Rev. D, 77, 123514

Daniel, S. F., Linder, E. V., Smith, T. L., Caldwell, R. R., et al. 2010, Phys. Rev. D, 81, 123508

Das, S. & Spergel, D. N. 2009, Phys. Rev. D, 79, 043509

Davis, M. & Peebles, P. J. E. 1977, ApJS, 34, 425

de Bernardis, F., Kitching, T. D., Heavens, A., & Melchiorri, A. 2009, PhysRevD, 80, 123509

Debono, I., Rassat, A., Réfrégier, A., Amara, A., & Kitching, T. D. 2010, MNRAS, 404, 110

Dodelson, S. 2004, Modern cosmology (Academic Press)

Dolney, D., Jain, B., & Takada, M. 2006, MNRAS, 366, 884

Durrer, R. & Maartens, R. 2008, astro-ph/0811.4132

Dvali, G., Gabadadze, G., & Porrati, M. 2000, Phys. Lett. B, 485, 208

Eddington, A. S. 1920, Space, time and gravitation (Cambridge University Press)

Efstathiou, G., Bond, J. R., & White, S. D. M. 1992, MNRAS, 258, 1

Eifler, T., Schneider, P., & Hartlap, J. 2009, A&A, 502, 721

Einstein, A. 1916, AnP, 354, 769

Einstein, A. 1936, Science, 84, 506

Eisenstein, D. J., Annis, J., Gunn, J. E., Szalay, A. S., et al. 2001, AJ, 122, 2267

Eisenstein, D. J., Hogg, D. W., Fukugita, M., Nakamura, O., et al. 2003, ApJ, 585, 694

Eisenstein, D. J. & Hu, W. 1998, ApJ, 496, 605

Erben, T., van Waerbeke, L., Bertin, E., Mellier, Y., & Schneider, P. 2001, A&A, 366, 717

Etherington, I. M. H. 1933, Phil. Mag. ser. 7, 15, 761

Feng, J. L. 2010, astro-ph/1003.0904, to appear in Annu. Rev. Astron. Astrophys.

Fergusson, J. R. & Shellard, E. P. S. 2007, Phys. Rev. D, 76, 083523

Freedman, W. L., Madore, B. F., Gibson, B. K., Ferrarese, L., et al. 2001, ApJ, 553, 47

Friedmann, A. 1922, Z. Phys., 10, 377

Friedmann, A. 1924, Z. Phys., 21, 326

Fry, J. N. 1984, ApJ, 279, 449

Fu, L., Semboloni, E., Hoekstra, H., et al. 2008, A&A, 479, 9

Giannantonio, T., Crittenden, R. G., Nichol, R. C., et al. 2006, Phys. Rev. D, 74, 063520

Giannantonio, T. & Porciani, C. 2010, Phys. Rev. D, 81, 063530

Gradshteyn, I. S., Ryzhik, I. M., Jeffrey, A., & Zwillinger, D. 2000, Tables of Integrals, Series, and Products (Academic Press)

Gunn, J. E. 1967, ApJ, 147, 61

Guo, Q., White, S. D. M., Boylan-Kolchin, M., de Lucia, G., et al. 2010, astro-ph/1006.0106, submitted to MNRAS

Guth, A. H. 1981, Phys. Rev. D, 23, 347

Gutiérrez, C. M. & Lopéz-Corredoira, M. 2010, ApJ, 713, 46

Guzik, J., Jain, B., & Takada, M. 2010, Phys. Rev. D, 81, 023503

Guzik, J. & Seljak, U. 2001, MNRAS, 321, 439

Guzik, J. & Seljak, U. 2002, MNRAS, 335, 311

Hahn, O., Carollo, C. M., Porciani, C., & Dekel, A. 2007, MNRAS, 381, 41

Hahn, O., Teyssier, R., & Carollo, C. M. 2010, MNRAS, 405, 274

Hartlap, J., Simon, P., & Schneider, P. 2007, A&A, 464

Heavens, A. 2003, MNRAS, 343

Heavens, A. 2009, Nuclear Physics B Proceedings Supplements, 194, 76

Heavens, A., Réfrégier, A., & Heymans, C. 2000, MNRAS, 319

Hetterscheidt, M., Simon, P., Schirmer, M., et al. 2007, A&A, 468, 859

Heymans, C., Brown, M., Heavens, A., et al. 2004, MNRAS, 347, 895

Heymans, C. & Heavens, A. 2003, MNRAS, 339, 711

Heymans, C., van Waerbeke, L., Bacon, D., Bergé, J., et al. 2006a, MNRAS, 368, 1323

Heymans, C., White, M., Heavens, A., Vale, C., & van Waerbeke, L. 2006b, MNRAS, 371, 750

Hilbert, S., Hartlap, J., White, S. D. M., & Schneider, P. 2009, A&A, 499, 31

Hirata, C. M., Mandelbaum, R., Ishak, M., et al. 2007, MNRAS, 381, 1197

Hirata, C. M., Mandelbaum, R., Seljak, U., et al. 2004, MNRAS, 353, 529

Hirata, C. M. & Seljak, U. 2004, Phys. Rev. D, 70, 063526

Hivon, E., Górski, K. M., Netterfield, C. B., et al. 2002, ApJ, 567, 2

Hoekstra, H., Franx, M., Kuijken, K., & Squires, G. 1998, ApJ, 504, 636

Hoekstra, H., Mellier, Y., van Waerbeke, L., et al. 2006, ApJ, 647, 116

Hoekstra, H., Yee, H. K. C., & Gladders, M. D. 2002, ApJ, 577, 595

Hu, W. 1999, ApJ, 522, 21

Hu, W. 2000, Phys. Rev. D, D62, 043007

Hu, W. 2002a, Phys. Rev. D, 65, 023003

Hu, W. 2002b, Phys. Rev. D, 66, 083515

Hu, W. & Jain, B. 2004, Phys. Rev. D, 70, 043009

Hubble, E. 1929, Proc. N. A. S., 15, 168

Huterer, D. 2002, Phys. Rev. D, 65, 063001

Huterer, D. & Takada, M. 2005, APh, 23, 369

Huterer, D., Takada, M., Bernstein, G., & Jain, B. 2006, MNRAS, 366, 101

Huterer, D. & White, M. 2005, Phys. Rev. D, 72, 043002

Ilbert, O., Capak, P., Salvato, M., et al. 2009, ApJ, 690, 1236

Israel, H., Erben, T., Reiprich, T. H., Vikhlinin, A., et al. 2010, A&A, accepted

Jarvis, M., Bernstein, G., & Jain, B. 2004, MNRAS, 352, 338

Jarvis, M., Jain, B., Bernstein, G., & Dolney, D. 2006, ApJ, 644, 71

Jing, Y. P. 2002, MNRAS, 335, 89

Joachimi, B. 2007, Analysis of second-order statistics of cosmic shear (diploma thesis)

Joachimi, B. & Bridle, S. L. 2009, astro-ph/0911.2454, submitted to A&A

Joachimi, B. & Schneider, P. 2008, A&A, 488, 829

Joachimi, B. & Schneider, P. 2009, A&A, 507, 105

Joachimi, B. & Schneider, P. 2010, A&A, accepted

Joachimi, B., Schneider, P., & Eifler, T. 2008, A&A, 477, 43

Joachimi, B., Shi, X., & Schneider, P. 2009, A&A, 508, 1193

Johnston, D. E., Sheldon, E. S., Tasitsiomi, A., Frieman, J. A., et al. 2007, ApJ, 656, 27

Kaiser, N. 1992, ApJ, 388, 272

Kaiser, N. 1998, ApJ, 498, 26

Kaiser, N. & Squires, G. 1993, ApJ, 404, 441

Kaiser, N., Squires, G., & Broadhurst, T. 1995, ApJ, 449, 460

Kaiser, N., Wilson, G., & Luppino, G. 2000, astro-ph/0003338

Kasai, M., Asada, H., & Futamase, T. 2006, Prog. Theor. Phys., 115, 827

Kayo, I., Taruya, A., & Suto, Y. 2001, ApJ, 561, 22

Kilbinger, M. & Schneider, P. 2004, A&A, 413, 465

Kim, A. G., Linder, E. V., Miquel, R., & Mostek, N. 2004, MNRAS, 347, 909

King, L. J. 2005, A&A, 441, 47

King, L. J. & Schneider, P. 2002, A&A, 396, 411

King, L. J. & Schneider, P. 2003, A&A, 398, 23

Kirk, D., Bridle, S., & Schneider, M. 2010, astro-ph/1001.3787, submitted to MNRAS

Kitching, T. D., Amara, A., Abdalla, F. B., Joachimi, B., & Réfrégier, A. 2009, MNRAS, 399, 2107

Kitching, T. D. & Taylor, A. N. 2010, astro-ph/1005.2063, submitted to MNRAS

Kitching, T. D., Taylor, A. N., & Heavens, A. F. 2008, MNRAS, 389, 173

Kochanek, C. S. 2006, in Saas-Fee Advanced Course 33: Gravitational Lensing: Strong, Weak and Micro, ed. G. Meylan, P. Jetzer, P. North, P. Schneider, C. S. Kochanek, & J. Wambsganss, 91

Kolb, E. W. & Lamb, C. R. 2009, astro-ph/0911.3852

Kolb, E. W. & Turner, M. S. 1990, The Early Universe (Addison-Wesley)

Komatsu, E., Smith, K. M., Dunkley, J., et al. 2010, astro-ph/1001.4538, submitted to ApJS

Kowalski, M., Rubin, D., Aldering, G., et al. 2008, ApJ, 686, 749

Krause, E. & Hirata, C. 2009, astro-ph/0910.3786, submitted to A&A

Kuijken, K. 1999, A&A, 352, 355

Kunz, M. & Sapone, D. 2007, Phys. Rev. Lett., 98, 121301

Lahav, O. & Suto, Y. 2004, Liv. Rev. Relativ., 7, 8

Landy, S. D. & Szalay, A. S. 1993, ApJ, 412, 64

Laureijs, R. et al. 2009, Euclid Assessment Study Report for the ESA Cosmic Visions, ESA/SRE(2009)2, astro-ph/0912.0914

Lee, J. & Pen, U.-L. 2000, ApJ, 532, L5

Lemaître, G. 1927, Ann. Soc. Sci. Bruxelles, A47, 49

Lemaître, G. 1933, Ann. Soc. Sci. Bruxelles, A53, 51

Limber, D. N. 1953, ApJ, 117, 134

Linde, A. D. 1982, Phys. Lett., 108B, 389

Linder, E. V. 2003, Phys. Rev. Lett., 90, 091301

Liu, C. T., Capak, P., Mobasher, B., et al. 2008, ApJ, 672, 198

LSST Science Collaborations. 2009, astro-ph/0912.0201

Ma, Z., Hu, W., & Huterer, D. 2006, ApJ, 636, 21

Mackey, J., White, M., & Kamionkowski, M. 2002, MNRAS, 332, 788

Mandelbaum, R., Blake, C., Bridle, S., Abdalla, F. B., et al. 2009, astro-ph/0911.5347, submitted to MNRAS

Mandelbaum, R., Hirata, C. M., Ishak, M., Seljak, U., & Brinkmann, J. 2006, MNRAS, 367, 611

Mandelbaum, R., Hirata, C. M., Seljak, U., et al. 2005, MNRAS, 361, 1287

Marinucci, D. & Peccati, G. 2010, JMP, 51, 043301

Massey, R., Heymans, C., Bergé, J., et al. 2007a, MNRAS, 376, 13

Massey, R., Kitching, T., & Richard, J. 2010, Rep. Prog. Phys., accepted

Massey, R., Rhodes, J., Ellis, R., Scoville, N., et al. 2007b, Nature, 445, 286

Massey, R., Rhodes, J., Leauthaud, A., et al. 2007c, ApJS, 172, 239

Matarrese, S., Verde, L., & Heavens, A. F. 1997, MNRAS, 290, 651

McCracken, H. J., Ilbert, O., Mellier, Y., Bertin, E., et al. 2008, A&A, 479, 321

McDonald, P., Trac, H., & Contaldi, C. 2006, MNRAS, 366, 547

Metcalf, R. B. & White, S. D. M. 2007, MNRAS, 381, 447

Metcalf, R. B. & White, S. D. M. 2009, MNRAS, 394, 704

Milgrom, M. 1983a, ApJ, 270, 365

Milgrom, M. 1983b, ApJ, 270, 371

Milgrom, M. 1983c, ApJ, 270, 384

Miralda-Escudé, J. 1991, ApJ, 380, 1

Moffat, J. W. 2009, astro-ph/0910.2723

Morales, M. F. 2006, ApJ, 650, L21

Narayan, R. 1989, ApJ, 339, L53

Newman, J. A. 2008, ApJ, 684, 88

Okumura, T. & Jing, Y. P. 2009, ApJ, 694, L83

Okumura, T., Jing, Y. P., & Li, C. 2009, ApJ, 694, 214

Padmanabhan, N., Schlegel, D. J., Seljak, U., Makarov, A., et al. 2007, MNRAS, 378, 852

Patel, P., Bacon, D. J., Beswick, R. J., Muxlow, T. W. B., & Hoyle, B. 2010, MNRAS, 401, 2572

Peacock, J. A. 1999, Cosmological physics (Cambridge University Press)

Peacock, J. A. & Dodds, S. J. 1996, MNRAS, 280, L19

Peacock, J. A., Schneider, P., Efstathiou, G., et al. 2006, in ESA-ESO Working Group on "Fundamental Cosmology", ed. E. J. A. Peacock et al.

Pen, U.-L., Lee, J., & Seljak, U. 2000, ApJ, 543, L107

Percival, W. J., Reid, B. A., Eisenstein, D. J., et al. 2010, MNRAS, 401, 2148

Pielorz, J., Rödiger, J., Tereno, I., & Schneider, P. 2010, A&A, 514, 79

Press, W. H., Teukolsky, S. A., Vetterling, W. T., & Flannery, B. P. 1992, Numerical recipes in C. The art of scientific computing (Cambridge University Press)

Rassat, A., Amara, A., Amendola, L., et al. 2008, astro-ph/0810.0003, submitted to MNRAS

Réfrégier, A. 2003, MNRAS, 338, 35

Réfrégier, A., Amara, A., Kitching, T., & Rassat, A. 2008, astro-ph/0810.1285, submitted to A&A

Réfrégier, A., Amara, A., Kitching, T., et al. 2010, astro-ph/1001.0061

Réfrégier, A., Boulade, O., Mellier, Y., et al. 2006, SPIE, 6265, 62651Y

Réfrégier, A., Massey, R., Rhodes, J., et al. 2004, AJ, 127, 3102

Refsdal, S. & Surdej, J. 1994, Rep. Prog. Phys., 56, 117

Reyes, R., Mandelbaum, R., Seljak, U., et al. 2010, Nature, 464, 256

Robertson, H. P. 1935, ApJ, 82, 284

Robertson, H. P. 1936, ApJ, 83, 187

Sandick, P. 2010, in Proceedings of the Frank N. Bash Symposium 2009, ed. L. Stanford, L. Hao, Y. Mao, & J. Green

Schäfer, B. M. 2009, IJMPD, 18, 173

Schmidt, F., Rozo, E., Dodelson, S., Hui, L., & Sheldon, E. 2009, Phys. Rev. Lett., 103, 051301

Schneider, M., Knox, L., Zhan, H., & Connolly, A. 2006, ApJ, 651, 14

Schneider, M. D. & Bridle, S. 2010, MNRAS, 402, 2127

Schneider, P. 1996, MNRAS, 283, 837

Schneider, P. 1999, in Perspectives on Radio Astronomy, Scientific Imperatives at cm and m wavelengths

Schneider, P. 2003, A&A, 408, 829

Schneider, P. 2006, in Saas-Fee Advanced Course 33: Gravitational Lensing: Strong, Weak and Micro, ed. G. Meylan, P. Jetzer, P. North, P. Schneider, C. S. Kochanek, & J. Wambsganss, 269

Schneider, P., Eifler, T., & Krause, E. 2010, astro-ph/1002.2136, submitted to A&A

Schneider, P. & Kilbinger, M. 2007, A&A, 462, 841

Schneider, P. & Lombardi, M. 2003, A&A, 397, 809

Schneider, P. & Rix, H.-W. 1997, ApJ, 474, 25

Schneider, P., van Waerbeke, L., Jain, B., & Kruse, G. 1998, MNRAS, 296, 873

Schneider, P., van Waerbeke, L., Kilbinger, M., & Mellier, Y. 2002a, A&A, 396, 1

Schneider, P., van Waerbeke, L., & Mellier, Y. 2002b, A&A, 389, 729

Schrabback, T., Erben, T., Simon, P., et al. 2007, A&A, 468, 823

Schrabback, T., Hartlap, J., Joachimi, B., et al. 2010, A&A, accepted

Scoccimarro, R. 2000, ApJ, 544, 597

Scoccimarro, R. & Couchman, H. M. P. 2001, MNRAS, 325, 1312

Scoccimarro, R., Feldman, H. A., Fry, J. N., & Frieman, J. A. 2001, ApJ, 546, 652

Scoville, N., Abraham, R. G., Aussel, H., et al. 2007, ApJS, 172, 38

Sefusatti, E., Crocce, M., Pueblas, S., & Scoccimarro, R. 2006, Phys. Rev. D, 74, 023522

Seitz, C. & Schneider, P. 1997, A&A, 318, 687

Seljak, U. 2002, MNRAS, 337, 769

Seljak, U., Makarov, A., Mandelbaum, R., Hirata, C. M., et al. 2005, Phys. Rev. D, 71, 043511

Semboloni, E., Heymans, C., van Waerbeke, L., & Schneider, P. 2008, MNRAS, 388, 991

Semboloni, E., Mellier, Y., van Waerbeke, L., et al. 2006, A&A, 452, 51

Semboloni, E., van Waerbeke, L., Heymans, C., et al. 2007, MNRAS, 375, 6

Serra, P., Cooray, A., Holz, D. E., Melchiorri, A., et al. 2009, Phys. Rev. D, 80, 121302

Shi, X., Joachimi, B., & Schneider, P. 2010, astro-ph/1002.0693, submitted to A&A

Simon, P. 2007, A&A, 473, 711

Simon, P., Hetterscheidt, M., Wolf, C., et al. 2009, MNRAS, 398, 807

Simon, P., King, L. J., & Schneider, P. 2004, A&A, 417, 873

Smail, I., Ellis, R. S., & Fitchett, M. 1994, MNRAS, 270, 245

Smith, R. E., Peacock, J. A., Jenkins, A., et al. 2003, MNRAS, 341, 1311

Spergel, D. N., Bean, R., Doré, O., et al. 2007, ApJS, 170, 377

Springel, V., White, S. D. M., Jenkins, A., et al. 2005, Nature, 435, 629

Stoughton, C., Lupton, R. H., Bernardi, M., Blanton, M. R., et al. 2002, AJ, 123, 485

Sugiyama, N. 1995, ApJS, 100, 281

Swanson, M. E. C., Tegmark, M., Blanton, M., & Zehavi, I. 2008, MNRAS, 385, 1635

Taburet, N., Aghanim, N., Douspis, M., & Langer, M. 2009, MNRAS, 392, 1153

Takada, M. & Jain, B. 2004, MNRAS, 348, 897

Takada, M. & White, M. 2004, ApJ, 601, 1

Tasitsiomi, A., Kravtsov, A. V., Wechsler, R. H., & Primack, J. R. 2004, ApJ, 614, 533

Taylor, A. N. & Kitching, T. D. 2010, astro-ph/1003.1136, submitted to MNRAS

Taylor, A. N., Kitching, T. D., Bacon, D. J., & Heavens, A. F. 2007, MNRAS, 374, 1377

Tegmark, M., Taylor, A. N., & Heavens, A. F. 1997, ApJ, 480, 22

Tereno, I., Doré, O., van Waerbeke, L., & Mellier, Y. 2005, A&A, 429, 383

Thomas, S. A., Abdalla, F. B., & Lahav, O. 2010, Phys. Rev. Lett., accepted

Thomas, S. A., Abdalla, F. B., & Weller, J. 2009, MNRAS, 395, 197

Uzan, J. P. 2009, in Special Issue on Gravitational Lensing, ed. P. Jetzer, Y. Mellier, & V. Perlick

van den Bosch, F. C., Abel, T., Croft, R. A. C., Hernquist, L., & White, S. D. M. 2002, ApJ, 576, 21

van Waerbeke, L. 2010, MNRAS, 401, 2093

van Waerbeke, L. & Mellier, Y. 2003, astro-ph/0305089

van Waerbeke, L., Mellier, Y., Erben, T., et al. 2000, A&A, 358, 30

van Waerbeke, L., Mellier, Y., & Hoekstra, H. 2005, A&A, 429, 75

Voigt, L. M. & Bridle, S. L. 2010, MNRAS, 404, 458

Wake, D. A., Nichol, R. C., Eisenstein, D. J., Loveday, J., et al. 2006, MNRAS, 372, 537

Walker, A. G. 1936, Proc. Lon. Math. Soc., 42, 90

Walsh, D., Carswell, R. F., & Weymann, R. J. 1979, Nature, 279, 381

Wang, Y., Yang, X.-H., Mo, H. J., & van den Bosch, F. C. 2007, ApJ, 664, 608

Wiltshire, D. L. 2008, in Dark Matter in Astroparticle and Particle Physics, ed. H. V. Klapdor-Kleingrothaus & G. F. Lewis

Wittman, D. M., Tyson, J. A., Kirkman, D., Antonio, I. D., & Bernstein, G. 2000, Nature, 405, 143

Wolf, C., Meisenheimer, K., Rix, H.-W., et al. 2003, A&A, 401, 73

Yoo, J., Tinker, J. L., Weinberg, D. H., et al. 2006, ApJ, 652, 26

Zhan, H. 2006, JCAP, 0608, 008

Zhang, P. 2008, astro-ph/0811.0613, submitted to ApJ

Zhang, P. & Pen, U.-L. 2005, Phys. Rev. Lett., 95, 241302

Zhang, P. & Pen, U.-L. 2006, MNRAS, 367, 169

Zhang, P., Pen, U.-L., & Bernstein, G. 2010, MNRAS, 405, 359

Zhao, G.-B., Giannantonio, T., Pogosian, L., Silvestri, A., et al. 2010, Phys. Rev. D, 81, 103510

Zwicky, F. 1937a, Phys. Rev., 51, 290

Zwicky, F. 1937b, Phys. Rev., 51, 679

Appendix

A Parameter estimation

This work focuses on methods that help optimising and debiasing constraints on cosmological models, and consequently the estimation of the parameters of these models plays a vital role. In this appendix we briefly summarise the statistical framework of parameter estimation used in the different studies presented above.

Throughout it is assumed that the random variables at consideration, i.e. in the context of this work usually a set of second-order cosmic shear measures, follow a multivariate Gaussian distribution. This is motivated by the fact that the density perturbations in the early Universe were close to Gaussian, as the anisotropies of the cosmic microwave background suggest. The density fluctuations continue to follow a Gaussian distribution as long as their evolution is linear, which applies to large cosmic scales (see Kayo et al. 2001 for distributions of the full matter density contrast including non-linear evolution). According to the central limit theorem, Gaussianity is also expected for the distribution of the weighted sum, so for instance the average, of independently and identically distributed random variables. Therefore, despite mildly non-linear evolution, a Gaussian distribution also holds to good approximation for the weak lensing convergence κ down to intermediate scales at which a considerable number of matter density fluctuations are integrated over along the line of sight.

Second-order cosmic shear measures are square in the convergence, so that they are generally not exactly Gaussian distributed even if κ is, but still the assumption of Gaussianity should hold to fair accuracy. In the strongly non-linear regime on small angular scales below about 10 arcmin however, the assumption of Gaussian errors for correlation functions or power spectra breaks down (Semboloni et al. 2007). As a consequence we underestimate the errors on these scales, due to neglecting an increase in the variance and cross-correlation between different angular scales induced by non-Gaussianity.

The fundamental statistical quantity for parameter estimation is the likelihood $L(\boldsymbol{x}|\boldsymbol{p}, M)$, which returns the probability of obtaining a data vector $\boldsymbol{x}$, given the set of parameters $\boldsymbol{p}$ of the underlying model M. Since model selection, i.e. the comparison of different models, is not considered in this work, M acts as a background variable and is not explicitly given in the main body of the text. Assuming Gaussianity and a data vector of dimension n, the likelihood reads

$$L(\boldsymbol{x}|\boldsymbol{p}, M) = \frac{1}{(2\pi)^{\frac{n}{2}}\sqrt{\det C(\boldsymbol{p}, M)}} \exp\left\{-\frac{1}{2}\left[\boldsymbol{x} - \bar{\boldsymbol{x}}(\boldsymbol{p}, M)\right]^{\tau} C(\boldsymbol{p}, M)^{-1}\left[\boldsymbol{x} - \bar{\boldsymbol{x}}(\boldsymbol{p}, M)\right]\right\} , \quad \text{(A.1)}$$

where $\bar{\boldsymbol{x}}$ is the prediction of the model, and C is the covariance matrix of $\boldsymbol{x}$, both depending on the parameters in general. The best fit to the data is then given by the set of parameters that maximises the likelihood.

Throughout this work we assume in addition that the covariance does not depend on the cosmological parameters. Otherwise the covariance would contain further cosmological information, so that constraints would tighten (Eifler et al. 2009), hence this assumption is conservative.

degrees of freedom	$1\,\sigma$	$2\,\sigma$	$3\,\sigma$
1	1.00	4.00	9.00
2	2.30	6.18	11.80
3	3.53	8.02	14.20

Table A.1: Values of $\Delta\chi^2$ for different degrees of freedom, indicating the probability of obtaining values smaller than $\Delta\chi^2$ to be 68.3 % ($1\,\sigma$), 95.4 % ($2\,\sigma$), and 99.7 % ($3\,\sigma$).

Then maximising (A.1) is equivalent to determining the minimum of the quantity

$$\chi^2_\nu(\boldsymbol{p}, M) = \sum_{\alpha,\beta=1}^{n} \left[\boldsymbol{x} - \bar{\boldsymbol{x}}(\boldsymbol{p}, M)\right]_\alpha \left(C^{-1}\right)_{\alpha\beta} \left[\boldsymbol{x} - \bar{\boldsymbol{x}}(\boldsymbol{p}, M)\right]_\beta \ , \tag{A.2}$$

where ν indicates the dimension of the parameter vector $\boldsymbol{p}$. This step corresponds to a weighted least-squares fit to the data.

Errors to the best-fit parameter values can be assigned via a procedure of frequentist statistics. If $\boldsymbol{x}$ follows a Gaussian distribution, then the sum over squares of $\boldsymbol{x}$ should be distributed according to a χ^2-distribution. In this situation the number of the degrees of freedom of the χ^2-distribution is just the number of parameters to be fitted ν (e.g. Press et al. 1992). If $\Delta\chi^2(\boldsymbol{p}')$ denotes the difference between the minimum χ^2 and $\chi^2(\boldsymbol{p}')$ for a given set of parameters $\boldsymbol{p}'$, then the cumulative χ^2 probability $\mathcal{P}\left(\Delta\chi^2(\boldsymbol{p}')\right)$ returns the probability to get $\Delta\chi^2$-values smaller than this $\Delta\chi^2(\boldsymbol{p}')$.

Hence, drawing the contour for a fixed $\Delta\chi^2$ in the model parameter plane, the probability is $\mathcal{P}(\Delta\chi^2)$ that the fitted parameters lie within this contour. Evaluating the cumulative χ^2 probability, we determine the values of $\Delta\chi^2$ for the standard error contours of $1\,\sigma$ (contains parameters with a probability of 68.3 %), $2\,\sigma$ (95.4 %), and $3\,\sigma$ (99.7 %), as listed in Table A.1.

Switching to a Bayesian treatment which is more versatile for our purposes, one interprets the likelihood (A.1) as the probability of obtaining a data vector $\boldsymbol{x}$ for a given model M with parameters $\boldsymbol{p}$. For the inference on parameters one is interested in the posterior probability of $\boldsymbol{p}$ given an observation $\boldsymbol{x}$, which is linked to the likelihood via Bayes theorem,

$$P(\boldsymbol{p}|\boldsymbol{x}, M) = \frac{P(\boldsymbol{p}|M)\ L(\boldsymbol{x}|\boldsymbol{p}, M)}{P(\boldsymbol{x}|M)} \ , \tag{A.3}$$

where $P(\boldsymbol{p}|M)$ is the prior on the set of parameters in a given model M. The evidence

$$P(\boldsymbol{x}|M) = \int \mathrm{d}\boldsymbol{p}\ P(\boldsymbol{p}|M)\ L(\boldsymbol{x}|\boldsymbol{p}, M) \tag{A.4}$$

describes the probability of obtaining the observed data vector for a given model, irrespective of the parameter values of this model. It is the key quantity to compare the performance of different models, but serves in this context only as the normalisation of the posterior. If the prior is flat or a top hat which is truncated far outside the region where the likelihood deviates significantly from zero, the analysis of the posterior yields exactly the same best-fit parameters and errors as the χ^2-fit discussed above.

The Bayesian treatment allows us to additionally calculate marginal errors or confidence contours[1], taking the uncertainty in the remaining parameters in the model into account. The marginalised posterior is given by

$$P(p_1, \ldots, p_d|\boldsymbol{x}, M) = \int \mathrm{d}p_{d+1} \ldots \int \mathrm{d}p_\nu\ P(\boldsymbol{p}|\boldsymbol{x}, M) \ , \tag{A.5}$$

[1]Strictly speaking, this expression is a frequentist term. The Bayesian equivalent is 'credible region'. We use these terms interchangeably as there is not practical difference between the two in the context of this work.

where the parameters p_{d+1} to p_ν were marginalised over. We use $d = 1$ to quote marginalised errors on every cosmological parameter individually, and $d = 2$ to compute marginalised confidence contours.

The majority of this work is not based on actual data, but predicts the performance of cosmological probes and analysis methods on future data. One option to proceed in absence of a real data vector is to choose a model data vector with a specific fiducial parameter set $\boldsymbol{p}_\mathrm{f}$ as the mock data to be employed subsequently in the likelihood analysis. Computationally more favourable is the use of the Fisher information matrix, defined by

$$F_{\mu\nu} \equiv \left\langle \frac{\partial^2 \mathcal{L}}{\partial p_\mu \, \partial p_\nu} \right\rangle \Bigg|_\mathrm{f} \; , \tag{A.6}$$

where $\mathcal{L}(\boldsymbol{x}|\boldsymbol{p}, M) \equiv -\ln L(\boldsymbol{x}|\boldsymbol{p}, M)$ is the log-likelihood, and where $|_\mathrm{f}$ indicates derivatives evaluated at the fiducial set of parameters $\boldsymbol{p}_\mathrm{f}$. The Fisher matrix is the expectation value of the Hessian matrix of the log-likelihood, evaluated at its minimum given by the fiducial model. At this minimum the first derivatives of $\mathcal{L}$ with respect to the parameters vanish. Since around its peak the likelihood can always be approximated locally by a Gaussian, third and higher-order derivatives of $\mathcal{L}(\boldsymbol{x}, \boldsymbol{p})$ are expected to be small, so that the width and the shape of the peak at the maximum of $L(\boldsymbol{x}, \boldsymbol{p})$ are well described by the Hessian matrix. Note that if the likelihood is Gaussian, the Fisher matrix fully describes its local features.

Intuitively, the larger the entries of the Fisher matrix, the narrower is the peak of the likelihood, and the smaller are consequently the errors on the parameters. As Tegmark et al. (1997) have shown, the inverse Fisher matrix serves as an estimate for the parameter covariance,

$$\mathrm{Cov}\,(p_\mu, p_\nu) = \left(F^{-1}\right)_{\mu\nu} \; . \tag{A.7}$$

Accordingly, $1\,\sigma$-errors are bound by the Cramér-Rao inequality

$$\sigma(p_\mu) \geq \left(\sqrt{F_{\mu\mu}}\right)^{-1} \quad \text{(fixed)} \; ; \quad \sigma(p_\mu) \geq \sqrt{\left(F^{-1}\right)_{\mu\mu}} \quad \text{(marg.)} \; , \tag{A.8}$$

where the first equation holds if all other parameters are known, whereas the second equation is valid if the other parameters are marginalised over, i.e. if the cross-correlation with these other parameters is taken into account. One usually quotes the minimum variance bound, i.e. the error resulting from using the equality in (A.8), which in most cases is valid if one employs a maximum likelihood estimator on a large data set (Tegmark et al. 1997).

In order to calculate the Fisher matrix explicitly, assume once more that the random variables are Gaussian distributed. Then, inserting (A.1), the corresponding log-likelihood reads

$$\mathcal{L}(\boldsymbol{x}, \boldsymbol{p}) = \frac{1}{2} \ln\left[\det C(\boldsymbol{p})\right] + \frac{1}{2} \left[\boldsymbol{x} - \bar{\boldsymbol{x}}(\boldsymbol{p})\right]^\tau C(\boldsymbol{p})^{-1} \left[\boldsymbol{x} - \bar{\boldsymbol{x}}(\boldsymbol{p})\right] + \mathrm{const} \; . \tag{A.9}$$

The calculation of the Fisher matrix, plugging (A.9) into (A.6), yields (Tegmark et al. 1997, see also the following section)

$$F_{\mu\nu} = \frac{1}{2} \, \mathrm{tr} \left\{ C^{-1} \frac{\partial C}{\partial p_\mu} \, C^{-1} \frac{\partial C}{\partial p_\nu} + C^{-1} \left(\frac{\partial \bar{\boldsymbol{x}}}{\partial p_\mu} \frac{\partial \bar{\boldsymbol{x}}^\tau}{\partial p_\nu} + \frac{\partial \bar{\boldsymbol{x}}}{\partial p_\nu} \frac{\partial \bar{\boldsymbol{x}}^\tau}{\partial p_\mu} \right) \right\} \; . \tag{A.10}$$

Since throughout this study the covariance is assumed to be independent of the set of parameters, one subsequently obtains the form of the Fisher matrix used in the foregoing chapters,

$$F_{\mu\nu} = \sum_{\alpha,\beta} \frac{\partial \bar{x}_\alpha}{\partial p_\mu} \left(C^{-1}\right)_{\alpha\beta} \frac{\partial \bar{x}_\beta}{\partial p_\nu} \; . \tag{A.11}$$

It is possible to incorporate Gaussian priors into the Fisher matrix formalism. If p_μ has a prior of width $\sigma_{\rm pr}$, one simply adds $\sigma_{\rm pr}^{-2}$ to $F_{\mu\mu}$. While the errors (A.8) are $1\,\sigma$ constraints, one can derive others by multiplying with the square root of the corresponding $\Delta\chi^2$ with one degree of freedom, see Table A.1. Confidence contours are obtained by extracting the 2×2 sub-matrix from F^{-1} for the parameter combination to be plotted. Diagonalising this matrix yields the semi-major axes and the orientation of the error ellipse. Note that the length of the semi-major axes needs to be adapted accordingly by factors of $\sqrt{\Delta\chi^2}$, using 2 degrees of freedom.

B Fisher matrix for a parameter-dependent data vector

The Fisher matrix is a measure for the information content in a data set. An invertible, parameter-independent transformation of the data vector should not alter the amount of information in it and thus results in the same Fisher matrix. In the following we are going to explicitly calculate the Fisher matrix for a data vector $\boldsymbol{y}$, transformed according to (6.70), i.e. via $\boldsymbol{y} = \boldsymbol{T}\,\boldsymbol{x}$, where the transformation $\boldsymbol{T}$ depends on the parameters to be determined. Such transformations occur in the nulling technique, and we need to assess the potential change in the information content originating from applying $\boldsymbol{T}$.

We closely follow the derivation of the Fisher matrix presented in Tegmark et al. (1997). A comma notation is used to indicate derivatives with respect to parameters, and the dependence of the likelihood on an underlying model is suppressed throughout. For $\boldsymbol{y}$ the Gaussian log-likelihood reads

$$-\ln L_y(\boldsymbol{y}|\boldsymbol{p}) = \frac{N_{\rm d}}{2}\ln 2\pi + \frac{1}{2}\ln\det C_y + \frac{1}{2}\left[\boldsymbol{y}-\bar{\boldsymbol{y}}\right]^\tau C_y^{-1}\left[\boldsymbol{y}-\bar{\boldsymbol{y}}\right] \ , \tag{B.1}$$

where we dropped the arguments of $\boldsymbol{y}$ and C_y for notational convenience. The expectation value of a data vector is indicated by a bar over the corresponding variable name. Making use of the matrix identity $\ln\det C = \mathrm{tr}\ln C$, and defining the matrix $D_y \equiv (\boldsymbol{y}-\bar{\boldsymbol{y}})\,(\boldsymbol{y}-\bar{\boldsymbol{y}})^\tau$, one arrives at

$$-\ln L_y(\boldsymbol{y}|\boldsymbol{p}) = \frac{N_{\rm d}}{2}\ln 2\pi + \frac{1}{2}\,\mathrm{tr}\left\{\ln C_y + C_y^{-1}D_y\right\} \ . \tag{B.2}$$

According to the derivation in Tegmark et al. (1997), the second derivative of (B.2) reads[2]

$$\begin{aligned} -\left\{\ln L_y(\boldsymbol{y}|\boldsymbol{p})\right\}_{,\mu\nu} \ &= \ \frac{1}{2}\,\mathrm{tr}\Big\{C_y^{-1}C_{y,\mu\nu} - C_y^{-1}C_{y,\mu\nu}C_y^{-1}D_y \\ &\quad + C_y^{-1}C_{y,\nu}C_y^{-1}C_{y,\mu}C_y^{-1}D_y - C_y^{-1}C_{y,\mu}C_y^{-1}D_{y,\nu} - C_y^{-1}C_{y,\nu}C_y^{-1}D_{y,\mu} + C_y^{-1}D_{y,\mu\nu}\Big\} \ , \end{aligned} \tag{B.3}$$

where the rules $(\ln C)_{,\mu} = C^{-1}C_{,\mu}$ and $(C^{-1})_{,\mu} = -C^{-1}C_{,\mu}C^{-1}$ were applied. The expectation value of (B.3) yields the Fisher matrix, see the definition in (A.6). We compute the matrix D_y and its derivatives in terms of the original data set,

$$\begin{aligned} D_y \ &= \ \boldsymbol{T}D_x\boldsymbol{T}^\tau \ ; \\ D_{y,\mu} \ &= \ \boldsymbol{T}_{,\mu}D_x\boldsymbol{T}^\tau + \boldsymbol{T}D_x\boldsymbol{T}_{,\mu}^\tau - \boldsymbol{T}\bar{\boldsymbol{x}}_{,\mu}\,(\boldsymbol{x}-\bar{\boldsymbol{x}})^\tau\boldsymbol{T}^\tau - \boldsymbol{T}\,(\boldsymbol{x}-\bar{\boldsymbol{x}})\,\bar{\boldsymbol{x}}_{,\mu}^\tau\boldsymbol{T}^\tau \ ; \\ D_{y,\mu\nu} \ &= \ \boldsymbol{T}_{,\mu\nu}D_x\boldsymbol{T}^\tau - \left(\boldsymbol{T}_{,\mu}\bar{\boldsymbol{x}}_{,\nu} + \boldsymbol{T}_{,\nu}\bar{\boldsymbol{x}}_{,\mu} + \boldsymbol{T}\bar{\boldsymbol{x}}_{,\mu\nu}\right)(\boldsymbol{x}-\bar{\boldsymbol{x}})^\tau\boldsymbol{T}^\tau + \boldsymbol{T}D_x\boldsymbol{T}_{,\mu\nu}^\tau \\ &\quad - \boldsymbol{T}\,(\boldsymbol{x}-\bar{\boldsymbol{x}})\left(\boldsymbol{T}_{,\mu}\bar{\boldsymbol{x}}_{,\nu} + \boldsymbol{T}_{,\nu}\bar{\boldsymbol{x}}_{,\mu} + \boldsymbol{T}\bar{\boldsymbol{x}}_{,\mu\nu}\right)^\tau + \boldsymbol{T}_{,\mu}D_x\boldsymbol{T}_{,\nu}^\tau \\ &\quad - \boldsymbol{T}\bar{\boldsymbol{x}}_{,\mu}\,(\boldsymbol{x}-\bar{\boldsymbol{x}})^\tau\boldsymbol{T}_{,\nu}^\tau - \boldsymbol{T}_{,\mu}\,(\boldsymbol{x}-\bar{\boldsymbol{x}})\,\bar{\boldsymbol{x}}_{,\nu}^\tau\boldsymbol{T}^\tau + \boldsymbol{T}\bar{\boldsymbol{x}}_{,\mu}\bar{\boldsymbol{x}}_{,\nu}^\tau\boldsymbol{T}^\tau + \boldsymbol{T}_{,\nu}D_x\boldsymbol{T}_{,\mu}^\tau \\ &\quad - \boldsymbol{T}\bar{\boldsymbol{x}}_{,\nu}\,(\boldsymbol{x}-\bar{\boldsymbol{x}})^\tau\boldsymbol{T}_{,\mu}^\tau - \boldsymbol{T}_{,\nu}\,(\boldsymbol{x}-\bar{\boldsymbol{x}})\,\bar{\boldsymbol{x}}_{,\mu}^\tau\boldsymbol{T}^\tau + \boldsymbol{T}\bar{\boldsymbol{x}}_{,\nu}\bar{\boldsymbol{x}}_{,\mu}^\tau\boldsymbol{T}^\tau \ , \end{aligned} \tag{B.4}$$

[2]Note that there is a typo in Eq. (14) of Tegmark et al. (1997): A factor C^{-1} should be eliminated from the last term.

where D_x is defined in analogy to D_y. Using $\langle \boldsymbol{x} \rangle = \bar{\boldsymbol{x}}$ and $\langle \boldsymbol{x}\boldsymbol{x}^\tau \rangle = C_x + \bar{\boldsymbol{x}}\bar{\boldsymbol{x}}^\tau$, we obtain the expectation values of the former quantities,

$$\begin{aligned} \langle D_y \rangle &= \boldsymbol{T} C_x \boldsymbol{T}^\tau = C_y \; ; \\ \left\langle D_{y,\mu} \right\rangle &= \boldsymbol{T}_{,\mu} C_x \boldsymbol{T}^\tau + \boldsymbol{T} C_x \boldsymbol{T}^\tau_{,\mu} \; ; \\ \left\langle D_{y,\mu\nu} \right\rangle &= \boldsymbol{T}_{,\mu\nu} C_x \boldsymbol{T}^\tau + \boldsymbol{T} C_x \boldsymbol{T}^\tau_{,\mu\nu} + \boldsymbol{T}_{,\mu} C_x \boldsymbol{T}^\tau_{,\nu} + \boldsymbol{T}_{,\nu} C_x \boldsymbol{T}^\tau_{,\mu} + \boldsymbol{T} \left(\bar{\boldsymbol{x}}_{,\mu} \bar{\boldsymbol{x}}^\tau_{,\nu} + \bar{\boldsymbol{x}}_{,\nu} \bar{\boldsymbol{x}}^\tau_{,\mu} \right) \boldsymbol{T}^\tau \; . \end{aligned} \tag{B.5}$$

With these expressions at hand we calculate the expectation value of (B.3),

$$\begin{aligned} F^y_{\mu\nu} &= \left\langle - \left\{ \ln L_y(\boldsymbol{y}|\boldsymbol{p}) \right\}_{,\mu\nu} \right\rangle \\ &= \frac{1}{2} \operatorname{tr} \Big\{ C_y^{-1} \left(\boldsymbol{T}_{,\nu} C_x \boldsymbol{T}^\tau + \boldsymbol{T} C_{x,\nu} \boldsymbol{T}^\tau + \boldsymbol{T} C_x \boldsymbol{T}^\tau_{,\nu} \right) C_y^{-1} \left(\boldsymbol{T}_{,\mu} C_x \boldsymbol{T}^\tau + \boldsymbol{T} C_{x,\mu} \boldsymbol{T}^\tau + \boldsymbol{T} C_x \boldsymbol{T}^\tau_{,\mu} \right) \\ &\quad - C_y^{-1} \left(\boldsymbol{T}_{,\nu} C_x \boldsymbol{T}^\tau + \boldsymbol{T} C_{x,\nu} \boldsymbol{T}^\tau + \boldsymbol{T} C_x \boldsymbol{T}^\tau_{,\nu} \right) C_y^{-1} \left(\boldsymbol{T}_{,\mu} C_x \boldsymbol{T}^\tau + \boldsymbol{T} C_x \boldsymbol{T}^\tau_{,\mu} \right) \\ &\quad - C_y^{-1} \left(\boldsymbol{T}_{,\mu} C_x \boldsymbol{T}^\tau + \boldsymbol{T} C_{x,\mu} \boldsymbol{T}^\tau + \boldsymbol{T} C_x \boldsymbol{T}^\tau_{,\mu} \right) C_y^{-1} \left(\boldsymbol{T}_{,\nu} C_x \boldsymbol{T}^\tau + \boldsymbol{T} C_x \boldsymbol{T}^\tau_{,\nu} \right) \\ &\quad + C_y^{-1} \big(\boldsymbol{T}_{,\mu\nu} C_x \boldsymbol{T}^\tau + \boldsymbol{T} C_x \boldsymbol{T}^\tau_{,\mu\nu} + \boldsymbol{T}_{,\mu} C_x \boldsymbol{T}^\tau_{,\nu} + \boldsymbol{T}_{,\nu} C_x \boldsymbol{T}^\tau_{,\mu} + \boldsymbol{T} \left(\bar{\boldsymbol{x}}_{,\mu} \bar{\boldsymbol{x}}^\tau_{,\nu} + \bar{\boldsymbol{x}}_{,\nu} \bar{\boldsymbol{x}}^\tau_{,\mu} \right) \boldsymbol{T}^\tau \big) \Big\} \; . \end{aligned} \tag{B.6}$$

Note that the first two terms in (B.3) cancel due to $\langle D_y \rangle = C_y$. We now make extensive use of the fact that the trace is invariant under cyclic permutations of matrices. Then one readily finds that many terms in (B.6) cancel. Expanding $C_y^{-1} = \boldsymbol{T}^{\tau\,-1} C_x^{-1} \boldsymbol{T}^{-1}$, more terms cancel, either directly or after cyclic permutation. This way (B.6) reduces to

$$\begin{aligned} F^y_{\mu\nu} &= \frac{1}{2} \operatorname{tr} \Big\{ C_x^{-1} C_{x,\nu} C_x^{-1} C_{x,\mu} + C_x^{-1} \left(\bar{\boldsymbol{x}}_{,\mu} \bar{\boldsymbol{x}}^\tau_{,\nu} + \bar{\boldsymbol{x}}_{,\nu} \bar{\boldsymbol{x}}^\tau_{,\mu} \right) \\ &\qquad + \boldsymbol{T}^{-1} \boldsymbol{T}_{,\mu\nu} + \boldsymbol{T}^\tau_{,\mu\nu} \boldsymbol{T}^{\tau\,-1} - \boldsymbol{T}^{-1} \boldsymbol{T}_{,\nu} \boldsymbol{T}^{-1} \boldsymbol{T}_{,\mu} - \boldsymbol{T}^{\tau\,-1} \boldsymbol{T}^\tau_{,\nu} \boldsymbol{T}^{\tau\,-1} \boldsymbol{T}^\tau_{,\mu} \Big\} \; . \end{aligned} \tag{B.7}$$

The first two terms of this expression correspond to the Fisher matrix $F^x_{\mu\nu}$ of the data vector $\boldsymbol{x}$, see (A.10). Finally, by employing in addition that $\operatorname{tr} C^\tau = \operatorname{tr} C$ and $(C^\tau)^{-1} = (C^{-1})^\tau$, one arrives at

$$F^y_{\mu\nu} = F^x_{\mu\nu} + \operatorname{tr} \left\{ \ln \boldsymbol{T} \right\}_{,\mu\nu} \; . \tag{B.8}$$

If we apply the condition $\det \boldsymbol{T} = 1$, as required in Sect. 6.4, we find $\operatorname{tr} \ln \boldsymbol{T} = \ln \det \boldsymbol{T} = 0$, and hence, the Fisher matrices of the original data vector $\boldsymbol{x}$ and the transformed one $\boldsymbol{y}$ are equivalent. Note that if the transformation matrix is independent of the parameters, we recover the initial statement that the Fisher matrix is invariant under invertible transformations. This result is in agreement with (6.71), which, when transformed to log-likelihood, reads

$$\begin{aligned} - \ln L_y(\boldsymbol{y}|\boldsymbol{p}) &= \ln \det \boldsymbol{T}(\boldsymbol{p}) \; - \ln L_x(\boldsymbol{x}|\boldsymbol{p}) \\ &= \operatorname{tr} \left\{ \ln \boldsymbol{T}(\boldsymbol{p}) \right\} \; - \ln L_x(\boldsymbol{x}|\boldsymbol{p}) \end{aligned} \tag{B.9}$$

and reproduces (B.8) after taking derivatives and expectation value. Employing the further simplification that the original covariance C_x does not depend on the parameters, the Fisher matrix can be written as

$$\begin{aligned} F_{\mu\nu} &= \frac{1}{2} \operatorname{tr} \left\{ C_x^{-1} \left(\bar{\boldsymbol{x}}_{,\mu} \bar{\boldsymbol{x}}^\tau_{,\nu} + \bar{\boldsymbol{x}}_{,\nu} \bar{\boldsymbol{x}}^\tau_{,\mu} \right) \right\} \\ &= \frac{1}{2} \operatorname{tr} \left\{ C_y^{-1} \boldsymbol{T} \left(\bar{\boldsymbol{x}}_{,\mu} \bar{\boldsymbol{x}}^\tau_{,\nu} + \bar{\boldsymbol{x}}_{,\nu} \bar{\boldsymbol{x}}^\tau_{,\mu} \right) \boldsymbol{T}^\tau \right\} \; , \end{aligned} \tag{B.10}$$

which, after converting the trace to a sum, yields (6.72).

C Validity of the bias formalism

As is evident from Sect. 6.5.3, a GI systematic that fits within the error bounds of current observations can attain values of similar order of magnitude as the lensing power spectrum. Besides, due to the similar dependence on geometry, see (3.34) and (5.16), the effect of adding a GI systematic acts similarly to a change of cosmological parameters, in particular those determining the amplitude of the lensing power spectrum. Consequently, we expect the systematic to produce a strong bias, possibly much larger than the statistical error bounds. While this does not hamper the performance of the nulling technique, it may render the bias formalism as given by (6.73) invalid. In the following we provide a general derivation of the parameter bias in the Fisher matrix formalism from the log-likelihood, taking special care of approximations and the resulting limitations.

Since we keep the assumption that the signal covariance C_P does not depend on the parameters to be determined, the calculations can be directly done in terms of the χ^2, which is then twice the log-likelihood. For a similar approach see e.g. Taburet et al. (2009). We define a fiducial data vector $\boldsymbol{P}^{\mathbf{f}}$, i.e. the signal in absence of systematic effects, and assume this signal to be contaminated by a systematic $\boldsymbol{P}^{\mathbf{sys}}$. A set of models $\boldsymbol{P}(\boldsymbol{p})$, depending on a set of parameters $\boldsymbol{p}$, is fitted to the signal, where $\boldsymbol{p}^{\mathbf{f}}$ denotes the fiducial set of parameters such that $\boldsymbol{P}(\boldsymbol{p}^{\mathbf{f}}) = \boldsymbol{P}^{\mathbf{f}}$. Then the χ^2 reads

$$\chi^2(\boldsymbol{p}) = \sum_{\alpha,\beta} \left(P_\alpha(\boldsymbol{p}) - P_\alpha^{\mathrm{tot}}\right) \left(C_P^{-1}\right)_{\alpha\beta} \left(P_\beta(\boldsymbol{p}) - P_\beta^{\mathrm{tot}}\right) \ , \tag{C.1}$$

where $P_\alpha^{\mathrm{tot}} \equiv P_\alpha^{\mathrm{f}} + P_\alpha^{\mathrm{sys}}$. Writing the unbiased χ^2 as

$$\chi_0^2(\boldsymbol{p}) = \sum_{\alpha,\beta} \left(P_\alpha(\boldsymbol{p}) - P_\alpha^{\mathrm{f}}\right) \left(C_P^{-1}\right)_{\alpha\beta} \left(P_\beta(\boldsymbol{p}) - P_\beta^{\mathrm{f}}\right) \ , \tag{C.2}$$

one can expand (C.1) to yield

$$\chi^2(\boldsymbol{p}) = \chi^2(\boldsymbol{p}^{\mathbf{f}}) + \chi_0^2(\boldsymbol{p}) - 2 \sum_{\alpha,\beta} P_\alpha^{\mathrm{sys}} \left(C_P^{-1}\right)_{\alpha\beta} \left(P_\beta(\boldsymbol{p}) - P_\beta^{\mathrm{f}}\right) \ , \tag{C.3}$$

where $\boldsymbol{p}^{\mathbf{f}}$ produces the maximum likelihood (or minimum χ^2) in absence of a systematic. Since $\boldsymbol{P}(\boldsymbol{p}^{\mathbf{f}}) = \boldsymbol{P}^{\mathbf{f}}$, $\chi^2(\boldsymbol{p}^{\mathbf{f}})$ contains only the systematic power spectrum and causes an irrelevant overall rescaling of the χ^2 in parameter space. Hence, the modification of the χ^2 due to the systematic is contained in the last term of (C.3). It can shift the point of maximum likelihood and deform the likelihood in its vicinity, depending on both the parameters and the form of the systematic.

Considering (C.1) again, $\chi^2(\boldsymbol{p})$ can be written as a Taylor expansion around the fiducial set of parameters,

$$\chi^2(\boldsymbol{p}) = \chi^2(\boldsymbol{p}^{\mathbf{f}}) + \sum_\mu \left.\frac{\partial\chi^2}{\partial p_\mu}\right|_{\mathrm{f}} \left(p_\mu - p_\mu^{\mathrm{f}}\right) + \frac{1}{2} \sum_{\mu,\nu} \left(p_\mu - p_\mu^{\mathrm{f}}\right) \left.\frac{\partial^2\chi}{\partial p_\mu\, \partial p_\nu}\right|_{\mathrm{f}} \left(p_\nu - p_\nu^{\mathrm{f}}\right) + \mathcal{O}\left(p^3\right) \ , \tag{C.4}$$

where the subscript f indicates that the derivatives are evaluated at $\boldsymbol{p}^{\mathbf{f}}$. Making again use of $\boldsymbol{P}(\boldsymbol{p}^{\mathbf{f}}) = \boldsymbol{P}^{\mathbf{f}}$, one obtains for the derivatives from (C.3)

$$\left.\frac{\partial\chi^2}{\partial p_\mu}\right|_{\mathrm{f}} = -2 \sum_{\alpha,\beta} P_\alpha^{\mathrm{sys}} \left(C_P^{-1}\right)_{\alpha\beta} \left.\frac{\partial P_\beta}{\partial p_\mu}\right|_{\mathrm{f}} \ ; \tag{C.5}$$

$$\left.\frac{\partial^2\chi^2}{\partial p_\mu\, \partial p_\nu}\right|_{\mathrm{f}} = 2 \sum_{\alpha,\beta} \left\{ \left.\frac{\partial P_\alpha}{\partial p_\mu}\right|_{\mathrm{f}} \left(C_P^{-1}\right)_{\alpha\beta} \left.\frac{\partial P_\beta}{\partial p_\nu}\right|_{\mathrm{f}} - P_\alpha^{\mathrm{sys}} \left(C_P^{-1}\right)_{\alpha\beta} \left.\frac{\partial^2 P_\beta}{\partial p_\mu\, \partial p_\nu}\right|_{\mathrm{f}} \right\} . \tag{C.6}$$

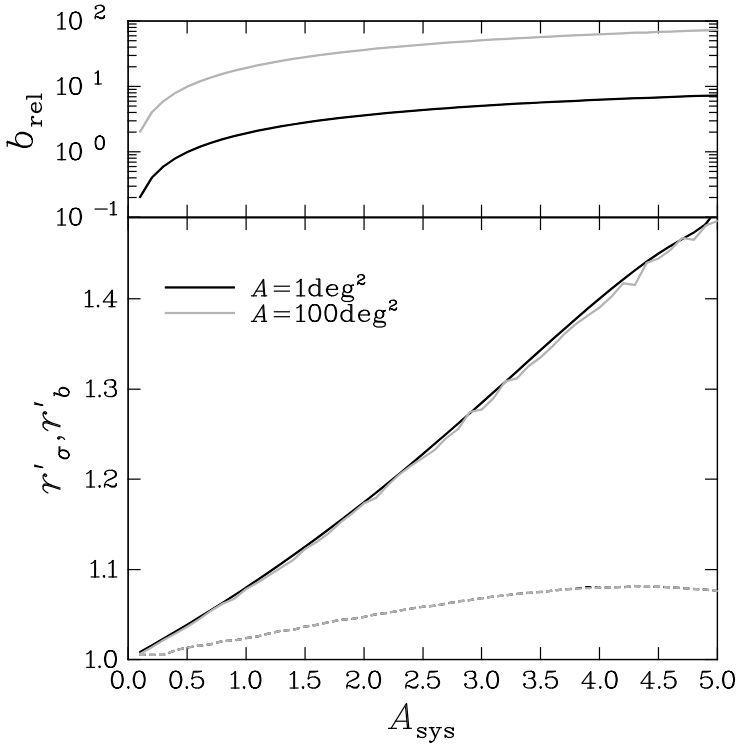

Figure C.1: Comparison of statistical errors and biases obtained by Fisher matrix and χ^2 calculations. *Top panel*: Ratio of bias over statistical error $b_{\rm rel}$ as a function of the scaling of the systematic $A_{\rm sys}$. Results for a $1\,{\rm deg}^2$ survey are shown as black curves, and for a $100\,{\rm deg}^2$ survey as grey curves. *Bottom panel*: Ratios of the statistical errors r'_σ and biases r'_b as a function of the scaling of the systematic $A_{\rm sys}$. Solid lines correspond to r'_σ, dashed lines to r'_b. As above, results for a $1\,{\rm deg}^2$ and a $100\,{\rm deg}^2$ survey are shown as black and grey curves, respectively. Note that the curves showing r'_b for the two survey sizes are almost indistinguishable.

Dividing (C.6) by 2 yields the Fisher matrix, so that in the case of a biased χ^2 one can define an equivalent to the Fisher matrix as

$$F'_{\mu\nu} \equiv F_{\mu\nu} - \sum_{\alpha,\beta} P_\alpha^{\rm sys} \left(C_P^{-1}\right)_{\alpha\beta} \left.\frac{\partial^2 P_\beta}{\partial p_\mu\, \partial p_\nu}\right|_{\rm f} \,. \tag{C.7}$$

We want to determine the bias $\boldsymbol{b} \equiv \boldsymbol{p}^{\rm b} - \boldsymbol{p}^{\rm f}$, where $\boldsymbol{p}^{\rm b}$ is the point in parameter space where the biased χ^2 attains its minimum. The biased parameter set $\boldsymbol{p}^{\rm b}$ is computed from (C.4), using the expansion up to second order, which results in

$$\left.\frac{\partial \chi^2}{\partial p_\mu}\right|_{\rm b} = -2 \sum_{\alpha,\beta} P_\alpha^{\rm sys} \left(C_P^{-1}\right)_{\alpha\beta} \left.\frac{\partial P_\beta}{\partial p_\mu}\right|_{\rm f} + 2 \sum_\nu F'_{\mu\nu} b_\nu = 0 \,, \tag{C.8}$$

where the derivative of the χ^2 has been evaluated at $\boldsymbol{p}^{\rm b}$. Provided that the biased Fisher matrix (C.7) has an inverse, too, one can solve for the bias and obtain

$$b_\mu = \sum_\nu \left(F'^{-1}\right)_{\mu\nu} \sum_{\alpha,\beta} P_\alpha^{\rm sys} \left(C_P^{-1}\right)_{\alpha\beta} \left.\frac{\partial P_\beta}{\partial p_\nu}\right|_{\rm f} \,. \tag{C.9}$$

If one assumes that the systematic is small such that the second term in (C.7) becomes subdominant, (C.9) reproduces the known bias formula (6.73).

In summary, the differences in employing the exact likelihood/ χ^2 formalism (C.1) or the Fisher matrix approach (6.72, 6.73) can be reduced to cutting the Taylor expansion in (C.4) after the second order in $\boldsymbol{p}$, and dropping the second term in (C.7). Both approximations are fair if the amplitude of the systematic and the bias it produces are sufficiently small.

To quantify the validity of these approximations in the context of this work we create a cosmic shear tomography survey with $N_z = 10$ redshift bins without photometric redshift errors. The GI signal is calculated via the linear intrinsic alignment model, with a free overall

scaling of $A_{\rm sys}$ to control the amplitude of the systematic. The original GI model corresponds to $A_{\rm sys} = 1$. We use $\Omega_{\rm m}$ as the only parameter to be constrained, setting a fiducial value of 0.4 for this exemplary analysis. Thereby, as the GI signal biases $\Omega_{\rm m}$ low, we allow for large biases in a range of still reasonable parameter values. To achieve a suitable magnitude of statistical errors, the survey size is set to $1\,\mathrm{deg}^2$ and $100\,\mathrm{deg}^2$, respectively, the remaining parameters kept at the values given in Sect. 6.5. The exact errors are calculated via (C.1) on a grid in parameter space with steps of 10^{-4} between $\Omega_{\rm m} = 0.1$ and $\Omega_{\rm m} = 0.5$. While the minimum χ^2 is simply read off the grid values, the 1σ-errors are computed by linear interpolation on the grid, with $\Delta\chi^2 \approx 1$ from the minimum for one degree of freedom.

We define the ratios

$$r'_\sigma \equiv \frac{\sigma_{\chi^2}}{\sigma_{\rm F}} \,; \qquad r'_b \equiv \frac{b_{\chi^2}}{b_{\rm F}} \,, \tag{C.10}$$

where σ_{χ^2} denotes the statistical error on $\Omega_{\rm m}$ obtained by the likelihood calculation, and where $\sigma_{\rm F}$ is the statistical error resulting from the computation of the Fisher matrix. Likewise definitions hold for the bias b_{χ^2} and $b_{\rm F}$. In Fig. C.1 the ratios r'_σ and r'_b are plotted as a function of $A_{\rm sys}$. Apart from uncertainties due to the finite grid resolution the results for both survey sizes agree very well, but since the bias does not depend on the survey size A, and $\sigma \propto 1/\sqrt{A}$, the ratios of bias over statistical error $b_{\rm rel} = b/\sigma$ differ by a factor of 10. Thus, the limits within which the bias formalism yields accurate results do not depend on $b_{\rm rel}$. Instead, the deviations from the exact χ^2 results are a function of the amplitude of the systematic with respect to the original signal.

For $A_{\rm sys} = 1$, i.e. the default GI signal, we find a deviation of the bias obtained from the full likelihood from the one computed via the Fisher matrix formalism of only 2.4 %, despite the strong systematic. The true bias does not deviate more than 10 % from the Fisher matrix prediction throughout, even for a very large systematic that dominates the signal by far. In the analysis considered here, both the second derivatives of the weak lensing convergence power spectrum and the power spectrum of the systematic are negative, so that the second term in (C.7) should in general be negative as well. Consequently, $F'_{\mu\nu} < F_{\mu\nu}$, causing (C.9) to produce larger biases than (6.73). Hence, the correction of the Fisher matrix via (C.7) renders the parameter biases closer to the actual values found for the likelihood analysis, see Fig. C.1.

If the amplitude of the systematic increases, the second term in (C.7) becomes more important, so that, due to the dependence of F' on $A_{\rm sys}$, the departure from the proportionality between the bias and $A_{\rm sys}$ is more significant. Then, as is evident from (C.9), the increase of the bias as a function of $A_{\rm sys}$ becomes smaller than in the standard formalism (6.73). Hence, assuming that the more accurate approximation (C.9) traces the results for the full likelihood well, the ratio of biases can level off and start to decrease for large $A_{\rm sys}$ because the bias, as computed from (6.73), continues to scale with $A_{\rm sys}$, an effect which is also seen in the figure. A similar behaviour may be expected from the inclusion of the third-order in (C.4) as it leads to a term with bias squared in (C.8), thereby placing the term scaling with $P^{\rm sys}$ under a square root when solving for $\boldsymbol{b}$.

In the presence of a systematic a more accurate way to obtain statistical errors would be to use F' instead of the original Fisher matrix. As opposed to the default Fisher matrix formalism, the statistical errors become dependent on the systematic. Inspecting (C.7), errors scale linearly with $A_{\rm sys}$ and should increase because of $F'_{\mu\nu} < F_{\mu\nu}$. Again Fig. C.1 demonstrates that this holds true to good approximation, yielding already a 8 % effect at $A_{\rm sys} = 1$. Downscaling the systematic to $A_{\rm sys} = 0.2$, the bias formalism should produce results that are very close to the full likelihood calculation, even for the full set of cosmological parameters.